FINAL REPORT

Investigation of Erosion Rates of Field Samples Using FDOT's Enhanced Sediment Erosion Rate Flume (SERF)

BDK75 977-53

Submitted by:

Raphael Crowley, Ph.D., P.E.
Department of Construction Management
University of North Florida
Jacksonville, FL 32224

David Bloomquist, Ph.D., P.E.
D. Max Sheppard, Ph.D.
Department of Civil and Coastal Engineering
University of Florida
Gainesville, Florida 32611

Developed for the

Rick Renna, P.E., Project Manager
September 2013

DISCLAIMER

The opinions, findings, and conclusions expressed in this publication are those of the author and not necessarily those of the State of Florida Department of Transportation.

SI (MODERN METRIC) CONVERSION FACTORS (FROM FHWA)

APPROXIMATE CONVERSIONS TO SI UNITS

SYMBOL	WHEN YOU KNOW	MULTIPLY BY	TO FIND	SYMBOL
LENGTH				
in	inches	25.4	millimeters	mm
ft	feet	0.305	meters	m
yd	yards	0.914	meters	m
mi	miles	1.61	kilometers	km
SYMBOL	**WHEN YOU KNOW**	**MULTIPLY BY**	**TO FIND**	**SYMBOL**
AREA				
in^2	square inches	645.2	square millimeters	mm^2
ft^2	square feet	0.093	square meters	m^2
yd^2	square yard	0.836	square meters	m^2
ac	acres	0.405	hectares	ha
mi^2	square miles	2.59	square kilometers	km^2
SYMBOL	**WHEN YOU KNOW**	**MULTIPLY BY**	**TO FIND**	**SYMBOL**
VOLUME				
fl oz	fluid ounces	29.57	milliliters	mL
gal	gallons	3.785	liters	L
ft^3	cubic feet	0.028	cubic meters	m^3
yd^3	cubic yards	0.765	cubic meters	m^3
NOTE: volumes greater than 1000 L shall be shown in m^3				
SYMBOL	**WHEN YOU KNOW**	**MULTIPLY BY**	**TO FIND**	**SYMBOL**
MASS				
oz	ounces	28.35	grams	g
lb	pounds	0.454	kilograms	kg
T	short tons (2000 lb)	0.907	megagrams (or "metric ton")	Mg (or "t")
SYMBOL	**WHEN YOU KNOW**	**MULTIPLY BY**	**TO FIND**	**SYMBOL**
TEMPERATURE (exact degrees)				
^oF	Fahrenheit	5 (F-32)/9 or (F-32)/1.8	Celsius	^oC
SYMBOL	**WHEN YOU KNOW**	**MULTIPLY BY**	**TO FIND**	**SYMBOL**
ILLUMINATION				
fc	foot-candles	10.76	lux	lx
fl	foot-Lamberts	3.426	candela/m^2	cd/m^2
SYMBOL	**WHEN YOU KNOW**	**MULTIPLY BY**	**TO FIND**	**SYMBOL**
FORCE and PRESSURE or STRESS				
lbf	pound force	4.45	newtons	N
lbf/in^2	pound force per square inch	6.89	kilopascals	kPa

APPROXIMATE CONVERSIONS TO ENGLISH UNITS

SYMBOL	WHEN YOU KNOW	MULTIPLY BY	TO FIND	SYMBOL
LENGTH				
mm	millimeters	0.039	inches	in
m	meters	3.28	feet	ft
m	meters	1.09	yards	yd
km	kilometers	0.621	miles	mi
SYMBOL	**WHEN YOU KNOW**	**MULTIPLY BY**	**TO FIND**	**SYMBOL**
AREA				
mm^2	square millimeters	0.0016	square inches	in^2
m^2	square meters	10.764	square feet	ft^2
m^2	square meters	1.195	square yards	yd^2
ha	hectares	2.47	acres	ac
km^2	square kilometers	0.386	square miles	mi^2
SYMBOL	**WHEN YOU KNOW**	**MULTIPLY BY**	**TO FIND**	**SYMBOL**
VOLUME				
mL	milliliters	0.034	fluid ounces	fl oz
L	liters	0.264	gallons	gal
m^3	cubic meters	35.314	cubic feet	ft^3
m^3	cubic meters	1.307	cubic yards	yd^3
SYMBOL	**WHEN YOU KNOW**	**MULTIPLY BY**	**TO FIND**	**SYMBOL**
MASS				
g	grams	0.035	ounces	oz
kg	kilograms	2.202	pounds	lb
Mg (or "t")	megagrams (or "metric ton")	1.103	short tons (2000 lb)	T
SYMBOL	**WHEN YOU KNOW**	**MULTIPLY BY**	**TO FIND**	**SYMBOL**
TEMPERATURE (exact degrees)				
^oC	Celsius	1.8C+32	Fahrenheit	^oF
SYMBOL	**WHEN YOU KNOW**	**MULTIPLY BY**	**TO FIND**	**SYMBOL**
ILLUMINATION				
lx	lux	0.0929	foot-candles	fc
cd/m^2	$candela/m^2$	0.2919	foot-Lamberts	fl
SYMBOL	**WHEN YOU KNOW**	**MULTIPLY BY**	**TO FIND**	**SYMBOL**
FORCE and PRESSURE or STRESS				
N	newtons	0.225	pound force	lbf
kPa	kilopascals	0.145	pound force per square inch	lbf/in^2

*SI is the symbol for the International System of Units. Appropriate rounding should be made to comply with Section 4 of ASTM E380.(Revised March 2003)

TECHNICAL REPORT DOCUMENTATION PAGE

<table>
<tr><td>1. Report No.</td><td>2. Government Accession No.</td><td colspan="2">3. Recipient's Catalog No.</td></tr>
<tr><td colspan="2" rowspan="2">4. Title and Subtitle
Investigation of Erosion Rates of Field Samples using FDOT's Enhanced Sediment Erosion Rate Flume (SERF)

BDK75 977-53</td><td colspan="2">5. Report Date
September 2013</td></tr>
<tr><td colspan="2">6. Performing Organization
University of Florida</td></tr>
<tr><td colspan="2">7. Author(s)
Raphael Crowley, David Bloomquist, D. Max Sheppard</td><td colspan="2">8. Performing Organization Report No.
0094522 & 0094523</td></tr>
<tr><td colspan="2" rowspan="2">9. Performing Organization Name and Address
Department of Civil and Coastal Engineering
365 Weil Hall
University of Florida
Gainesville, Florida 32611</td><td colspan="2">10. Work Unit No.</td></tr>
<tr><td colspan="2">11. Contract or Grant No.
BDK TWO 977-53</td></tr>
<tr><td colspan="2" rowspan="2">12. Sponsoring Agency Name and Address
Florida Department of Transportation
605 Suwannee Street, MS 30
Tallahassee, FL 32399</td><td colspan="2">13. Type of Report and Period Covered
Draft Report
05/12/2011 – 09/12/2013</td></tr>
<tr><td colspan="2">14. Sponsoring Agency Code</td></tr>
<tr><td colspan="4">15. Supplementary Notes</td></tr>
<tr><td colspan="4">16. Abstract
The first part of this project was to enhance and improve the Florida Department of Transportation's Sediment Erosion Rate Flume (SERF) device. Notable improvements include a pump repair, laser system enhancement, installation of a digital video camera, an updated graphical user interface, a rebuilt pump drive, and a large-capacity filter. Additionally, attempts were made to install a sand injection system in the SERF, although these efforts proved unsuccessful. A computational model of the SERF was prepared using CD-adapco's Star-CCM+. Results appeared to indicate that a conservative, smooth-wall approximation must be used to estimate shear stress when testing sediment samples in the SERF. Using these new shear stress approximation guidelines, a series of erosion tests was conducted on several sediment specimens. Results appeared to show that field specimens exhibit layering during testing. Three distinct layering events were observed and described. Results also appear to show that in addition to depth-layering, erosion functions may be governed by spatial variability. Future sampling guidelines were developed based upon these results. Finally, a dataset from the Rotating Erosion Testing Apparatus (RETA) was re-analyzed. Results appear to show a preliminary correlation between erosion rate and rock cohesion. Lastly, a new operating manual was written for the SERF device.</td></tr>
<tr><td colspan="2">17. Key Word
Scour, Erosion, Rock Scour, Water Erosion, Cohesive Scour, Local Scour, Bridge Scour</td><td colspan="2">18. Distribution Statement
No restrictions.</td></tr>
<tr><td>19. Security Classif. (of this report):
Unclassified</td><td>20. Security Classif. (of this page):
Unclassified</td><td>21. No. of Pages
384</td><td>22. Price</td></tr>
</table>

EXECUTIVE SUMMARY

The first part of this project was to enhance and improve the Florida Department of Transportation's Sediment Erosion Rate Flume (SERF) device. Notable improvements include a pump repair, laser system enhancement, installation of a digital video camera, an updated graphical user interface, a rebuilt pump drive, and a large-capacity filter. Additionally, attempts were made to install a sand injection system in the SERF, although these efforts proved unsuccessful.

A computational model of the SERF was prepared using CD-adapco's Star-CCM+. Results appeared to indicate that a conservative, smooth-wall approximation must be used to estimate shear stress when testing sediment samples in the SERF. Using these new shear stress approximation guidelines, a series of erosion tests was conducted on several sediment specimens. Results appeared to show that field specimens exhibit layering during testing. Three distinct layering events were observed and described. Results also appear to show that in addition to depth-layering, erosion functions may be governed by spatial variability. Future sampling guidelines were developed based upon these results.

Finally, a dataset from the Rotating Erosion Testing Apparatus (RETA) was re-analyzed. Results appear to show a preliminary correlation between erosion rate and rock cohesion. Lastly, a new operating manual was written for the SERF device.

TABLE OF CONTENTS

page

LIST OF TABLES

LIST OF FIGURES

CHAPTER 1
INTRODUCTION

1.1 Background Statement

Scour is the most common cause of bridge failure in the United States (Briaud, 2004). Although predicting scour depths and erosion rates for cohesionless sediment (sand) has been studied and is now fairly well understood, much less is known about scour and erosion associated with rock, rock-like material, clay, and sand-clay mixtures. According to the current edition of *Hydraulic Engineering Circular No. 18, Evaluating Scour at Bridges* (HEC-18; Arneson et al., 2012), when a foundation is to be built on cohesive bed materials such as these, a site-specific design procedure is to be used. First, a conservative hydrograph is to be developed to describe flow conditions during the structure's lifetime. Then, this hydrograph is to be used to compute maximum local shear stresses associated with each flow rate according to Equation 1-1:

$$\tau_{\max} = \frac{\gamma}{y_1^{1/3}}\left(\frac{nKV_1}{K_u}\right)^2 \tag{1-1}$$

where τ_{max} is the maximum shear stress associated with velocity, V_1; K is the velocity coefficient (2.0 for circular piers; 2.5 for square piers); n is Manning's roughness coefficient; y_1 is the water depth; and K_u is a unit-specific calibration factor (1.0 for SI units and 1.486 for English units).

HEC-18 then says that given infinite time, cohesive materials will erode to the same depth as non-cohesive materials. This statement is controversial, and it has been questioned by other researchers (Bloomquist and Crowley, 2010; Sheppard et al., 2005). If one abides by this assumption, an equation is provided by which scour may be computed for each shear stress developed during application of Equation 1-1:

$$y_s = \frac{t}{\frac{1}{\dot{z}} + \frac{t}{y_s}} \quad (1\text{-}2)$$

where t is time; $\dot{z}$ is the erosion rate at a given shear stress; and y_s is the maximum scour depth that would be obtained by applying the sand scour equations.

There are two issues with this method. First, as discussed, its initial assumption that clays and rocks will eventually erode to the same depth as sand may be incorrect. Secondly, it relies on performing an accurate, site-specific erosion test so that a relationship may be developed between erosion rate and shear stress. In an effort to address these issues, FDOT sponsored construction of the Sediment Erosion Rate Flume (SERF), a device that measures erosion rate and associated shear stress for intact rock core and Shelby tube samples, at the University of Florida (UF). While devices similar to the SERF had been built in the past (McNeil et al. 1996, Roberts et al. 1998, Briaud et al. 2001 for example), the SERF was unique because it provided automation during testing which is believed to reduce user-error.

From 2008-2010, a study was conducted to enhance the SERF and run a series of tests with the instrument. Because of these enhancements and these tests, researchers came to a number of important conclusions (Bloomquist and Crowley 2010):

- Inferring shear stress on eroding material in flume-style erosion rate testing devices (the SERF and other similar devices) may not be accurately determined by measuring the pressure difference from ports upstream and downstream from the sample. Previously, researchers had thought that pressure-drop shear stress estimates were sufficient. However, there is still a need to estimate shear stresses if sediment erosion functions (erosion rate versus shear stress relationships) are to be developed.
- The newly installed laser-leveling system appears to allow the SERF to function properly when cohesive sediment (sand-clay mixtures and clay) are tested in the

instrument. Previously, an ultrasonic sensor was used to keep samples level with the flume bottom. When cohesive sediment was used in conjunction with the ultrasonic array, researchers noticed that ultrasonic pulses tended to penetrate into the sample, thereby creating a "false-bottom reading." As a result, as originally constructed, it was difficult to use the SERF with cohesive material. The laser array seems to have corrected this issue.

- Sheppard et al. (2005) developed a rudimentary correlation between erosion rate and cohesion using data from FDOT's Rotating Erosion Testing Apparatus (RETA). The advantage to such a relationship is that if it can be proven, it may eliminate the need for labor and time-intensive erosion rate testing. Bloomquist and Crowley (2010) developed a new relationship between cohesion and erosion; however as of the 2010 study, investigators concluded that more analysis was required.

- Because of the new laser array, researchers were able to measure real-time erosion rates for a variety of synthetic sand-clay mixtures (Figure 1-1). Synthetic sand-clay mixtures tended to exhibit "step-like" erosion behavior – i.e., portions of rapid erosion followed by portions of slow erosion. Researchers believe that this "step-like" erosion pattern was due to the mixing procedure of the synthetic samples. During sample preparation, sand-clay was placed into molds and compacted in a number of discrete lifts. Slow erosion appears to correspond to the location of the compacted surfaces. Researchers speculated that a similar mechanism may occur with natural samples because many natural sediments are created through a series of deposition events and settlement/consolidation. Since the SERF is the only instrument known to exist that can measure real-time erosion data, previous tests in similar instruments were incapable of picking up these differential erosion signals. Field-tests are required to determine if erosion rate is nearly constant for natural samples or if similar step-like patterns remain.

  Determining erosion patterns of field samples is important for a number of reasons. First, the SERF was designed to test intact Shelby tube or rock core samples. When this project began, no field samples had been tested in the device. Secondly, the SERF is designed to generate a material's erosion rats vs. shear stress relationship for use in scour prediction equations. Currently, the assumption behind an erosion test in the SERF is that a sample's surface will erode nearly uniformly. Step-like erosion on synthetic samples as demonstrated in Figure 1-1 seems to contradict this assumption because during "flat" erosion regimes, "chunking" or "blocking" was often dominant when compared with steady, particle-like erosion. If cohesive field samples erode uniformly, the SERF should be an effective device for determining a material's erosion rate vs. shear stress relationship. In other words, while the synthetic data is interesting, from a practical standpoint its importance can be minimized when compared with field data. If field samples do not erode uniformly (i.e., if periods of quick erosion and periods of sediment "chunking" or "blocking" persist as was seen in the synthetic samples), a testing procedure would need to be developed to ensure a conservative physical test when the SERF is used for design.

As mentioned previously, the SERF is the only known device that can generate real-time erosion data for an intact sample. Determining exactly "how" a natural sample erodes would allow researchers to assess the feasibility of predicting scour by measuring erosion rate vs. shear stress relationships in a laboratory.

- During synthetic sand-clay testing, investigators noticed that the filtration system was incapable of keeping up with erosion testing because recirculating SERF water became extremely cloudy. While turbidity was not measured directly, researchers qualitatively approximated that there was less than four inches of visibility through SERF water after an erosion test. Recirculating sediment may affect erosion rate and associated shear stress, but because of recirculating sediment, it was impossible to isolate sediment concentration from other variables that govern the erosion problem.

- Recirculating sediment also caused three more issues. First, it precluded investigators from installing and calibrating the sand injector – a device that was believed to be designed to carefully regulate the amount of suspended material upstream from the eroding sample. Secondly, recirculating sediment caused one of the pumps that pushes water through the SERF to begin leaking. Researchers believe that this leaking is caused by a damaged seal. Third, the pump for the device's water chiller similarly failed due to the same mechanism.

- While the new laser system allowed researchers to obtain excellent erosion date, over time the lasers and corresponding photoelectric sensors became damaged because of harsh conditions in the SERF. This damage was unanticipated. Investigators concluded that the lasers needed to be repaired and that next time around, protection should be installed to prevent future damage.

- There is a need to determine the magnitude and dynamic properties of several hydrodynamic parameters under prototype scale conditions for clays. Of particular interest is cohesive equilibrium scour depth and associated stress information. For design, these data would be used in conjunction with SERF results to provide design scour information.

1.2 Objectives

The objectives of this project were aimed to address some of the concerns emanating from the previous study and to continue to advance research in cohesive bridge scour. Objectives are listed as follows:

- Repair damaged SERF components so that the device can be used regularly.

- Add lasers to the instrument to improve sample leveling during cohesive sediment tests, rebuild the laser system, and add a protective shield to prevent future damage.

- Run a series of tests on field samples to determine if their erosion rates mimic erosion rates of synthetic samples and to validate that the SERF is capable of being used with intact samples.

- Run a series of tests on field samples under suspended sediment conditions to determine how suspended sediment affects erosion rate.

- Develop a series of tests under prototype conditions to determine if stress and erosion data is properly captured in the SERF.

- Determine a better method of estimating shear stress in the SERF.

- Re-investigate the link between erosion rate and cohesion.

- Install the sand injector, and run a series of tests to preliminarily quantify water column sand's effect on sediment erosion rate.

1.3 Methodology

To meet these objectives, the following tasks were completed:

- A number of improvements, enhancements, and repairs were made to the SERF.

- Data analysis was conducted on RETA data to develop a better link between erosion rate and cohesion.

- A series of computer models was programmed to simulate stress conditions in the SERF.

- A number of tests were conducted on natural sand-clay mixtures.

- A study was conducted to determine the best method to conduct prototype-scale tests.

- Attempts were made to install the sand injector. Because of issues with the device, it was not possible to successfully complete this task.

1.4 Organization

Organization of this report is as follows:

- Chapter 2 provides a brief description of the devices used in this study – the SERF and the RETA. For comprehensive details about these instruments and scour, please refer to Bloomquist and Crowley 2010.

- Chapter 3 describes all improvements, enhancements, and repairs that were made to the SERF.

- Chapter 4 discusses an updated erosion model based upon cohesion.
- Chapter 5 describes SERF computer modeling aimed at better-understanding shear stresses in the instrument.
- Chapter 6 describes field tests on SERF specimens.
- Chapter 7 discusses the next step needed in scour research including the implementation of a prototype-scale scour test.
- Chapter 8 discusses the sand injector and associated issues with the device.
- Appendix A contains an updated SERF users' manual.
- Appendix B contains raw erosion versus time data from all SERF tests on field specimens.

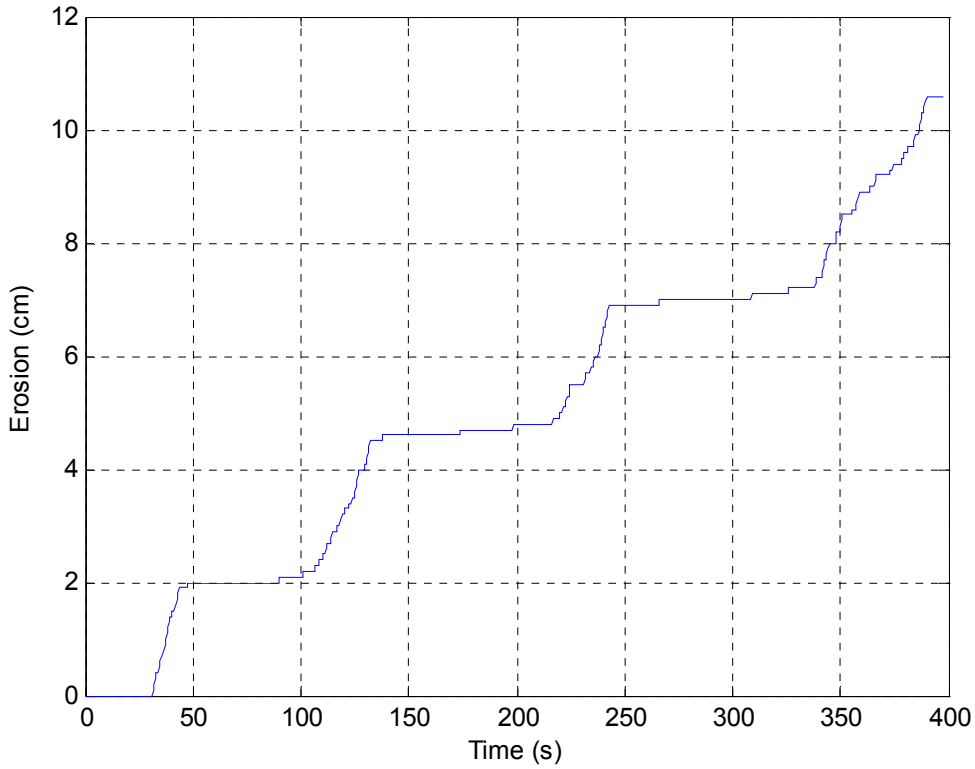

Figure 1-1. Typical erosion vs. time for SERF for sand-clay mixtures; figure shows 75:25 sand-clay ratio at 11 Pa (1.6×10^{-3} psi)

CHAPTER 2
DESCRIPTION OF EROSION RATE TESTING DEVICES

As mentioned in Chapter 1, two erosion rate testing devices were used throughout this study. While the focus of this work was the Sediment Erosion Rate Flume (SERF) device, Rotational Erosion Testing Apparatus (RETA) data were also used to develop the relationship between erosion rate and cohesion discussed in Chapter 4. This chapter briefly describes the two instruments. For a thorough explanation of the SERF and an updated discussion of its components, please refer to Appendix A.

2.1 The Sediment Erosion Rate Flume (SERF)

The SERF is typical "piston-style" or "flume-style" erosion rate testing instrument as described by HEC-18 (Arneson et al., 2012). However, it has a number of enhancements that appear to make it more accurate than previous instruments.

2.1.1 Previous Piston-Style Erosion Rate Testing Devices

As mentioned in Chapter 1, "piston-style" devices have been built in the past. These devices include the Adjustable Shear Stress Erosion and Transport Flume (ASSET, McNeil et al., 1996), the Sediment Erosion at Depth Flume (SEDFlume, Roberts et al., 1998), and the Erosion Function Apparatus (EFA, Briaud et al., 2001).

The principles of all these previous flume-style erosion rate testing-devices are similar (Figure 2-1). First, an in situ sample is collected using a Shelby tube or rock core. A piston is inserted into the Shelby Tube's end and the assemblage attached to a lead screw. This lead-screw assembly is fed into a rectangular duct with a circular cutout such that advancement of the piston forces the sample to protrude into the flume. Visual observation is used to keep the sample flush with the flume floor. Water is run

over the sample and as it erodes, a manual crank, attached to the lead screw, is used to keep the sample level with the bottom of the flume.

When a test is run, a timestamp is taken at the beginning and end of the test. The erosion rate, $\Delta y/\Delta t$ (where Δy is the change in piston position and Δt, the elapsed time), is measured directly. Shear stress is estimated using one of two mechanisms. Earlier erosion-rate testing devices assumed that shear stress on an eroding sample could be approximated using a smooth wall using the following expressions:

$$\frac{1}{\sqrt{f}} = 2.0\log\left[\frac{UD\sqrt{f}}{\upsilon}\right] - 0.8 \tag{2-1}$$

$$D = \frac{2hw}{h+w} \tag{2-2}$$

$$f = \frac{8\tau}{\rho U^2} \tag{2-3}$$

where U is average flow velocity, f is wall friction factor, τ is wall shear stress, D is hydraulic radius defined by flume height h and flume width w, ρ is the density of water, and ν is the kinematic viscosity of water. In the EFA, it is assumed that the Moody Diagram (described by the Colebrook-White Equation – Equation 2-4) can accurately describe the friction factor:

$$\frac{1}{\sqrt{f}} = -2.0\log\left[\frac{k_s/D}{3.7} + \frac{2.51}{\mathrm{Re}\sqrt{f}}\right] \tag{2-4}$$

In this expression, k_s is the roughness height, and Re, the Reynolds Number with respect to hydraulic diameter. Reynolds Number is given in Eq. (2-5):

$$\mathrm{Re} = \frac{UD}{\nu} \tag{2-5}$$

The advantage of flume-style instruments is that they are capable of measuring bulk erosion rates of in situ soil samples upon their surfaces as would be seen in nature. Despite this attribute, there are several drawbacks to these designs. First, because previous devices were manually advanced, they were operator-dependent. Thus, it was possible to over or under advance a sample. During an erosion event or an erosion test, even small stress deviations caused by slightly imprecise advancement may lead to large erosion rate differences.

Secondly, none of these previous devices were capable of providing real-time erosion rate data. Because erosion is defined as $\Delta y/\Delta t$ as opposed to dy/dt, or small change in sample position divided by a small time step, the assumption was that erosion rate was nearly constant from top-to-bottom throughout a sample. A better method for estimating erosion rate is to continually monitor piston position at smaller time intervals. If piston position is plotted as a function of time, then the slope of the best-fit line through these sample position versus time data points should correspond to erosion rate. If erosion rate is constant, the slope of this curve should be linear. If on the other hand the soil is non-uniform from top-to-bottom, a non-linear relationship will be a more appropriate data fit. Hence, a differential erosion rate based on layering depth can be determined. For cohesive soil and rock, layering may affect rates.

Finally, these devices did not measure shear stress directly on an eroding sample nor do they provide a check between one shear stress estimation technique versus another. Hence, shear stresses may be incorrect. This may alter the shear stress-erosion rate relationship, which in turn will alter computed local scour depth. In an effort to address these deficiencies, a the SERF was developed

2.1.2 SERF Description

The SERF (Crowley et al. 2012b, Bloomquist and Crowley 2010, Slagle 2006, Sheppard et al. 2005, Trammel 2004; Figure 2-2) is based on similar principles to the aforementioned devices. As of 2010, the major components of the device included:

- Two 1,000 GPM Vertiflo pumps (Figure 2-3), one equipped with a GE Electronic variable frequency drive/Labview computer control and the other equipped with a simple on/off relay.

- Aluminum flume, 2.0 in. x 8.0 in. (5.08 cm x 20.32 cm) cross-sectional area, 0.5 in. (15.24 cm) wall thickness, and 9.0 ft. (2.74 m) in length.

- Five rectangular flume sections. The first and second are one foot long, and the first contains a rectangular flow straightener. The third section, which is two feet in length, contains a series of two pressure ports and a direct shear stress sensor with a topside access hatch.

- Following the two-foot section is the one-foot test section. The test cylinder is inserted into the bottom of this section, and an ultrasonic ranging system is mounted over top of the sample portion. Flush with the flume bottom on one side of the sample are three fiber optic lasers; on the other side are three corresponding fiber optic photoelectric sensors. Two pressure taps are positioned on either side of the sample. The test section and the section with the shear stress sensor are both equipped with viewing windows for observation/recording. Following the test section is a four-foot section which contains the temperature probe.

- One, one-foot long aluminum transition section located between the circular CPVC pipes and the rectangular flume (at the flume entrance and exit).

- A shear stress sensor and signal amplifier (0 Pa – 100 Pa with 4 data ranges) (Fig. 2-4).

- A RT5-603 six-ton Rite-Temp water chiller, a Triton-II commercial grade sand filter to protect the chiller, and a 1.5-hp pool pump to supplement the water chiller pump.

- Connective plumbing (six-inch CPVC pipe from tank to pumps, four-inch pipe from pumps to flume, four-inch discharge hose from flume to tank, two-inch connective pipe from tank to filter, one-inch connective pipe from filter to chiller and from chiller to tank).

- 1,100 gallon stainless steel reservoir, equipped with baffles and drain.

- SEATEK 12 element 5MHz ultrasonic ranging system (Fig. 2-5). This ultrasonic array consists of eight individual crystals that sit "inside" the sample such that they monitor distance from the top of the flume to the top of the sample. Four other crystals are positioned "outside" of the sampling area such that they measure distance from the top of the flume to its bottom.

- Keyence FU-59 fiber optic lasers (Fig. 2-6) and corresponding photoelectric sensors, and control boxes. In its original configuration, three lasers were installed; as will be discussed in Chapter 3, fives lasers were added during this project for a total of 8 lasers.

- A Haydon-Kerk linear actuator powered by Servo Systems power drive, and controlled by National Instruments (NI) UMI-7764 motion controller/PCI-7330 stepper motor interface.

- Two Omega FX2300-.5BDI differential pressure transducers; 0.5 psi, bi-directional range, 0.2% F.S. accuracy.

- Omega type T thermocouple probe.

- NI data acquisition system consisting of a PCI 6014 DAQ card and a SC-2345 signal conditioning terminal block capable of recording pressure, laser, shear stress, and temperature data.

- Two Watec auto-focus, color cameras for real-time viewing and recording of the erosion and shear stress tests.

- A 4CM CPCam MPEG-4 DVR with networking capabilities for recording and remote viewing of SERF tests.

- An Omega FPB151 paddlewheel flowmeter.

As with the other flume-style devices, the SERF was designed as a rectangular cross-sectional flume since the shape allows the flow to become fully developed over a relatively short length (Trammel, 2004). The device was built in sections because a partitioned flume permits testing of different sections varying in length, design, roughness, etc. which can be inserted into the flume relatively quickly. Additionally, the numerous test sections can be modified such that each accepts a different size sample diameter.

The flume is mounted on two five-and-one-half foot stands. Stiff rubber bushings were inserted between the stands and the flume to reduce vibration. The 1,100 gallon reservoir is equipped with a series of baffles to reduce turbulence in the tank and to aid in the settling of the suspended sediment. The tank is equipped with a two foot port on its top and a drain valve on its bottom to allow cleaning between tests. The piping between the tank and the two pumps is six inch schedule 80, CPVC, and the discharge from the pumps to the flume is carried through four inch schedule 80, CPVC.

The two pump motors are mounted on inertial bases, and the discharge end of each pump is equipped with expansion joints to reduce potential damage to the pipe due to pump movement or vibration. There is a series of shut off valves at both the discharges of the tank and at the discharges of the motors to prevent backflow of water into the pumps. Water discharged through the pumps is carried through the four inch pipe, past the paddlewheel flowmeter, and enters the flume through a one foot circular to rectangular transition section.

As water enters the flume, it first passes through a one foot flow straightener. This aids in the transition to a hydraulically smooth, fully turbulent flow. The flow passes through a second one foot rectangular section followed by a two foot rectangular section. The shear stress sensor and the access hatch are located approximately eighteen inches from the upstream edge of the two foot section. The shear sensor has a removable disc that is level with the flume bottom. This disc can be replaced with discs of different roughness. The access hatch allows replacement without removing the sensor. On either side of the sensor are two pressure taps which lead to one of the two differential pressure transducers. This provides a comparison between computed

shear stress from a pressure drop and actual shear stress readings from the sensor. A 1.4 inch diameter viewing window is located on the side of the flume parallel with the shear stress sensor so that real-time viewing and recording can be conducted either via closed-circuit television (CCTV) or remotely via the Internet.

Once through the two foot section, the flow passes through the sediment sample test section. The test cylinder consists of an acrylic cylinder, a PVC cylinder, or a Shelby tube secured by two compression plates. The top plate is mounted to the bottom of the test section of the flume, while the bottom plate is attached to the top plate through four threaded rods (Figure 2-7). This supports and secures the cylinder in compression, permitting sample removal without disassembling the entire test section. The top of the test section is equipped with a port where the ultrasonic ranging system is mounted.

Along the flume bottom, 0.06 in. (1.5 mm) grooves house the fiber-optic lasers and photoelectric sensors. Located on the side of the test section is another 1.4 inch diameter viewing port with camera. On either side of the sample, two additional pressure taps are connected to a second differential pressure transducer.

The lead screw stepper motor is bolted to a variable elevation stand (mounted to the floor underneath the test section) and is positioned directly under the test cylinder. As the sample erodes, a piston attached to the lead screw advances the sample inside the test cylinder. Once through the test section, water proceeds through a four-foot-long duct section, and exits the flume. The temperature probe is located approximately three and one-half feet from the upstream edge of this section. At the flume exit is a

one-foot rectangular-to circular transition, which is bolted to a four inch rubber hose back to the reservoir.

2.1.3 Shear Stress Sensor

The first unique feature that distinguishes the SERF from other flume-style erosion rate testing devices is the shear stress sensor. With it, the SERF is capable of directly measuring shear stress of a sample with a given roughness (Figure 2-4). Fifty millimeter diameter (1.97 in.) discs of varying roughness can be attached to the top of the apparatus. The discs' surfaces are leveled with the flume's bottom by tightening the springs. The disc-spring assembly sits on top of a movable platform that is suspended from two bronze leaf springs. Below the platform sits a Servo magnet and Hall sensor. As water flows over the test disc, the disc-platform-leaf spring deflects. Deflection is measured using the Hall sensor. Two brass rods are connected to the underside of the platform on which two electro magnets are attached. When the platform deflects, the brass rods and magnets deflect along with it. Two PVC-encased solenoids are wrapped around the magnet. Based on the deflection read by the Hall sensor, the upstream solenoid energizes the magnets to return the disc back to its original position. A signal is sent from this solenoid proportional to the shear stress imposed on it. The upstream solenoid is used to calibrate the device by sending a control-voltage to it.

In an analysis of the EFA, Annandale (2006) speculated that the Moody Diagram may not accurately estimate shear stress. A force balance between average shear stress and the average pressure differential upstream and downstream from the sample was hypothesized to be a better method. If pressure differential could be used to estimate shear stress, the following expression should govern this parameter:

$$\tau_b = \frac{\Delta phw}{(2h + 2w)L} \quad (2\text{-}6)$$

where Δp is the pressure differential, h, the flume's width, w, the flume's height, τ_b, the average bed shear stress, and L, the spacing between pressure ports (Trammel, 2004).

Comparisons between the shear stress sensor and pressure differential expression allowed investigators to evaluate the applicability of Equation 2-6. Investigators concluded that using a pressure drop to estimate shear stress was not accurate (Crowley et al., 2012a, Bloomquist et al., 2010).

2.1.4 Erosion Depth-Monitoring System

Because of the sensitivity of erosion rate to stress, it is essential to keep the sample level with the flume-bottom during testing. If the sample is recessed below the flume bottom, shear stress may be lower than it would be for a flush sample. Conversely, if the sample protrudes into the flow, it will be subjected to a normal or bearing stress, which may produce irregularly high erosion rates. To keep the sample flush with the flume bottom, the ultrasonic depth array, temperature probe, laser system, and stepper motor are used in concert via several feedback loops. The algorithm for these loops is as follows:

1. Water temperate is taken and the data is fed to the ultrasonic sensor array so that the sensor array uses the correct sonic speed to calculate distance.
2. A 5 MHz ultrasonic burst is sent from the array, which sits atop the flume, toward the flume-bottom and the sample. Each of the array's twelve crystals sends and receives 20 pulses from this burst. An average is taken for each crystal.
3. Data processing is performed to ensure that depth readings are accurate.
4. Twelve individual crystals are positioned such that eight strike the sample while the other four reflect off the flume bottom. Both datasets (eight-crystal and four-crystal) are isolated from one another.

5. The maximum and minimum values from each datasets are eliminated.

6. A search is conducted where error readings are removed from each dataset (an error reading returns an average depth "value" of 0.00).

7. An average is computed for both the eight-crystal and four-crystal truncated datasets.

8. The two averages are compared with one another. If average depth from the four-crystal, "outside" dataset deviates from average depth from the eight-crystal "inside" dataset by more than 0.5 mm (0.02 in.), a sample advancement signal is generated.

9. The laser system is initiated. Lasers and photoelectric sensors are located along grooves across the sample from one another. If a laser's sensor can "see" its corresponding laser beam, a portion of the sample must have eroded. If two of the three photoelectric sensors (middle and either on the outer edge), are exposed, another advancement signal is generated.

10. Before a test, an operator can choose to use "and logic" or "or logic" for the ultrasonic array and laser system. When cohesive soil is tested, investigators have found that ultrasonic pulses tend to penetrate slightly into the sample, producing false bottom readings. Hence, under these conditions, it is advantageous to use the lasers alone. On the other hand, when sand or rock is tested, penetration is not an issue, and using the two systems as a redundant check of one another may be more appropriate. Using the signal(s) from Step 5 and/or Step 6, the stepper motor is initiated.

    a. When the ultrasonic system is used, bottom deviation can be computed directly. Thus, if an advancement signal is generated in Step 5, the motor advances the sample according to the computed offset.

    b. The lasers, whose diameter is 0.06 in., do not provide a direct computation for bottom offset. Because of this, when they are used as a stand-alone system a different advancement algorithm must be used. If an advancement signal was generated in Step 7, then discrete 0.03 in. steps are used to advance the sample until the lasers and photoelectric sensors no longer produce an advancement signal.

2.1.5 Other SERF Systems

Before each test, the temperature control system is activated, since during long duration tests a temperature rise of approximately 2^{o} C per hour develops. This could affect erosion rates and may damage equipment. The cooling system is designed to maintain a constant temperature during testing.

The two centrifugal pumps are controlled separately. If the sample is a soft clay or loose sand, only the computer controllable, pump is used. Its range is 0 to 60 Hz, with 0.01 Hz increments. For less erodible samples such as rock or stiff clay, both pumps are used. First the variable speed pump is slowly brought up to full speed. It is then shut off and the on/off pump started. The variable speed motor is then adjusted until the desired velocity and shear stress is achieved.

2.1.6 SERF Testing Procedure

Because shear stress and erosion rates are measured separately, there are different procedures for shear stress and erosion rate tests.

2.1.6.1 Shear Stress Test

1. A test-disc is attached to the shear stress sensor, and data range, sampling rate (typical rates are ~1 kHz), and sampling time are set (default is 1 min.).
2. The temperature control system is initiated and temperature is adjusted using the chiller's thermostat.
3. The flume is filled and air remove is removed from the pressure transducers.
4. The shear stress sensor is calibrated using pre-defined voltage parameters. For example, an input of 10V should correspond to a shear stress of 100 Pa when operating in the 100 Pa range.
5. A flow velocity is chosen. Once flow has stabilized, shear stress, temperature, and pressure readings are recorded.
6. Step 5 is repeated for a number of velocities (shear stresses).

Please note that a more detailed testing procedure is presented in Appendix A.

2.1.6.2 Erosion Rate Test

1. The sample is inserted into the flume's test-section.
2. The temperature control system is initiated and temperature is adjusted using the chiller's thermostat.
3. The flume is filled using the pumps.

4. Flow speed is slowly increased until critical velocity is observed. This flow speed/shear stress is recorded.

5. A new flow speed is chosen. Water is allowed to flow at this rate for a user-specified time interval (for example, 24 hours). The ultrasonic array and laser system should keep the sample level with the flume bottom.

6. Step 5 is repeated for a number of flow velocities/shear stresses.

2.2 The Rotating Erosion Testing Apparatus (RETA)

2.2.1 Description

The RETA (Figure 2-8) takes a different approach to measure erosion rate and shear stress than in flume-style devices. It utilizes a water-filled rotating outer-cylinder (Figure 2-9) surrounding a sample to generate the shear stress. Rotating cylinder devices have been built in the past to measure erosion and shear stress (Moore and Masch 1962, Rektorik and Smerdon 1964, Arulanandan et al. 1973, Sargunam et al. 1973, Alizadeh 1974, and Chapius and Gatien (1986). The concept behind all of these devices, including the RETA, is similar. A sample is inserted into a larger diameter cylinder thus forming an annular space which is filled with a fluid (usually water). The cylinder is rotated, which induces a flow in the annulus. This flow imparts a shear stress on the outer surface of the sample. The cylinder is rotated for a specified period of time, stopped and the mass of eroded material measured. Knowing the mass density of the sample and the duration of the test, the average eroded surface thickness and erosion rate can be computed. Since the diameter of the sample, length of the sample, and the measured torque during the test are known, the average shear stress acting on the outer surface of the sample can be computed.

The control/monitoring system for the RETA allows the desired torque (shear stress) to be specified. During a test, torque is monitored, and the rotational speed of

the cylinder is adjusted to maintain the specified shear stress throughout the test. The unique features of the RETA are its torque-cell/clutch arrangement and its control/monitoring system. The components of the RETA include:

- A vibration-damped housing that contains an electric motor and drive mechanism,
- A Plexiglas cylinder with inserts (liners) for different size samples,
- A support frame with slide-rails for retrieving the eroded material,
- A sample support shaft that connects to the clutch and torque-cell (Figure 2-10), and
- A digital touch-screen control/monitoring unit (Figure 2-11).

2.2.2 Torque Cell and Clutch Assembly

An adjustable slip clutch is used to limit the torque applied to the torque-cell. Should a piece of the sample break free and become lodged in the annulus, the clutch will slip and the controller will stop the motor, thus preventing damage to the torque-cell and assembly.

The torque cell comprises a strain gauged-equipped cantilever arm which is attached to the sample shaft at one end and the housing at the other end. Two mechanical stops are used (1) to insure no gap exists between the arm and its support and (2) to provide a stop so as to not exceed the limit of the gauges. The torque-cell is calibrated using a thin wire, a pulley system, and a series of weights. The torque is produced by the shear stress acting over the cylindrical surface area of the sample, i.e.,:

$$T = \tau AR = \tau(2\pi RL)R \tag{2-7}$$

where R is the sample radius, L is the sample length, T is torque, and τ is the average shear stress acting on the sample surface. The shear stress in terms of the torque and sample dimensions is therefore:

$$\tau = \frac{T}{2\pi R^2 L} \tag{2-8}$$

The mass of material eroded is obtained by evaporating the water from the annulus container at the end of a test in an oven and weighing the resulting content. Knowing the eroded mass and the average mass density of the sample, the average eroded thickness can be computed:

$$\Delta R \equiv \text{Average Eroded Thickness} = \sqrt{\frac{\Delta m}{2\pi\rho L}} \tag{2-9}$$

where Δm is the chance in sample mass, ρ is sample density, and other terms have previously been defined. The average rate of erosion can then be computed using the change in radius and test duration:

$$E \equiv \text{Erosion Rate} \equiv \frac{\Delta R}{\Delta t} = \frac{\Delta m}{2\pi\rho RLD} \tag{2-10}$$

2.2.3 Control/Monitoring System

The control/monitoring system, which has a touch-screen operator interface, allows the desired torque (shear stress) to be input directly. The rotational speed of the outer cylinder is increased in a prescribed manner until it reaches the required speed to achieve this torque. Since variations in water temperature or sample roughness during the test can affect the shear stress, the rotational speed is adjusted during testing to maintain the input torque value.

2.2.4 RETA Testing Procedure

2.2.4.1 Sample preparation

A 4.0 in. (10.16 cm) long cylindrical sample is cut from a standard rock core or stiff clay sample. If, for some reason, the sample is “out-of-round” it is placed in a lathe, and a fine cut is made to insure a uniform diameter along its length. The out-of-roundness must be less than 1/32 in. (0.079 cm). A 5/16 in. (0.79 cm) diameter hole is drilled

through the center of the sample. A support rod is inserted into the hole, and end platens are connected to both ends (Figure 2-12). The sample is then soaked in water for a minimum of 24 hours to ensure saturation. The sample and rod are attached to the clutch-torque-cell assembly shaft and lowered into the cylinder (Figure 2-13). The annulus between the sample and the insert is filled with water and the cover attached to the cylinder. The sample is ready for the preconditioning run.

2.2.4.2 Sample preconditioning

The surface of the sample can be disturbed by 1) the sampling procedure; 2) transport from the field to lab; and 3) test preparation. For these reasons, a preconditioning run is used to remove any surface artifacts. The duration of the precondition run and the magnitude of the preconditioning torque depend on the estimated impact erosion would have on the proposed structure. If the duration and/or torque are insufficient, this will be obvious during the test runs, i.e., the rate of erosion will decrease with increasing shear stress for the first runs. Guidelines based on soil-type were developed (Table 1 and Table 2) for determining the torque and duration of the conditioning run but engineering judgment should also be used. The RETA is run at the specified torque for the required duration, the sample rinsed, lowered back into the cylinder, and the annulus' water replaced. The sample is then ready for testing.

2.2.4.3 Testing

A series of appropriate shear stresses are selected with a minimum of three and preferably five tests performed. The lowest shear stress is input to the controller and the RETA started and allowed to run for the specified duration: short duration for stiff clays and longer for erosion resistant rock. Recommended durations are included in

Table 2-1 and Table 2-2. At the end of the prescribed time the sample is carefully raised and rinsed off into the annulus container holding the eroded material. The container, which was weighed prior to the test, is placed in an oven, and the water evaporated. It and the eroded material are weighed and the eroded mass determined. A new container is installed, the sample lowered, filled with water, and a new shear stress is applied for the next test. This procedure is repeated until the testing sequence is completed.

Table 2-1. Preconditioning and test guidelines for 2.4 in. diameter rock core

Material	Preconditioning Torque; Duration (N-mm; hr)	3 Test Torques (N-mm)	5 Test Torques (N-mm)	Test Duration (hr)
Stiff Clay	7; 1	10, 15, 20	8, 11, 14, 17, 20	3-6
Soft Rock	20; 12	10, 20, 30	10, 15, 20, 25, 35	24
Hard Rock	25; 15	20, 30, 40	15, 20, 25, 35, 45	72

Table 2-2. Preconditioning and test guidelines for 4.0 in. diameter rock core

Material	Preconditioning Torque; Duration (N-mm; hr)	3 Test Torques (N-mm)	5 Test Torques (N-mm)	Test Duration (hr)
Stiff Clay	10; 1	16, 24, 32	14, 18, 22, 28, 32	3-6
Soft Rock	32; 12	16, 32, 48	16, 24, 32, 40, 56	24
Hard Rock	40; 15	32, 52, 72	24, 32, 40, 56, 72	72

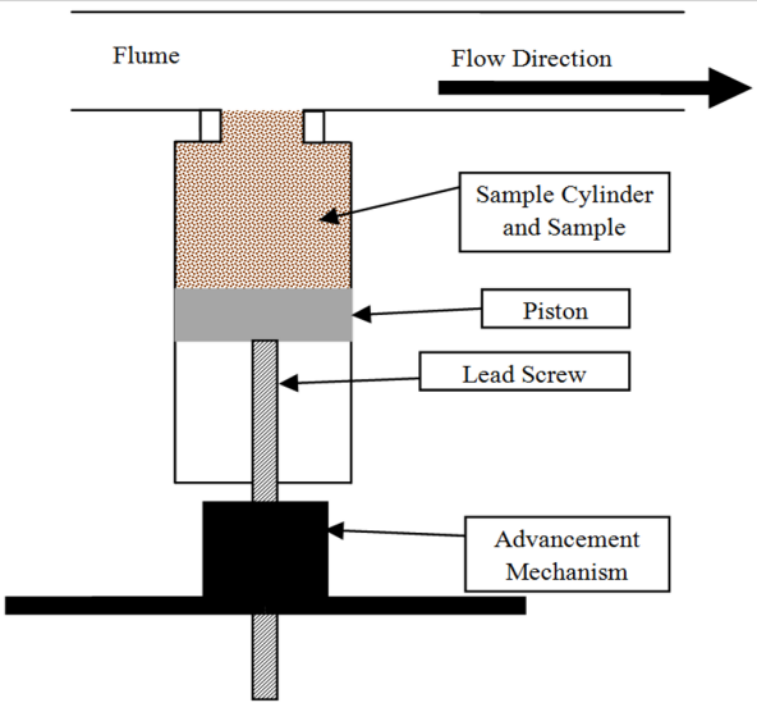

Figure 2-1. Piston-style erosion rate testing device schematic

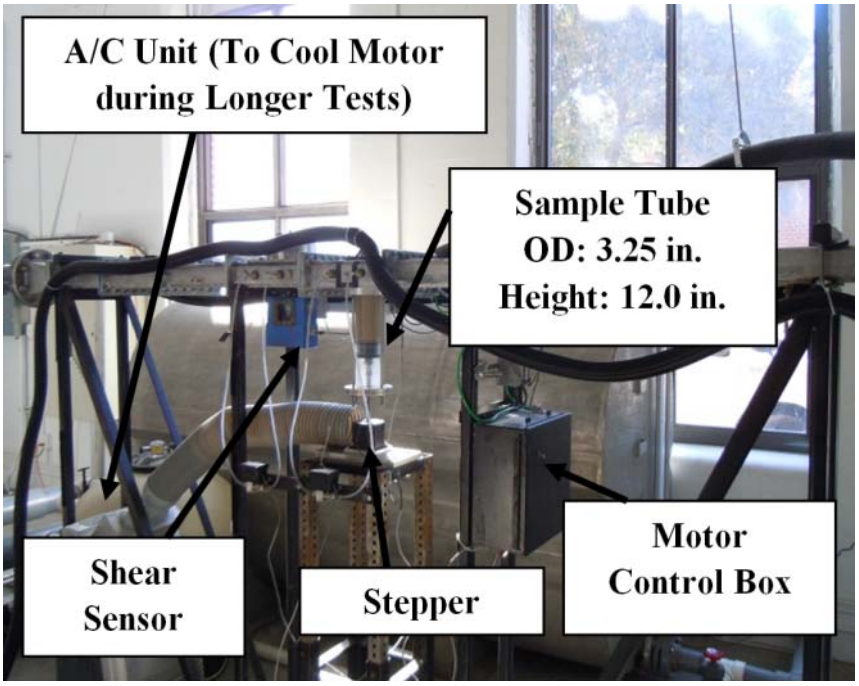

Figure 2-2. Photograph of the SERF

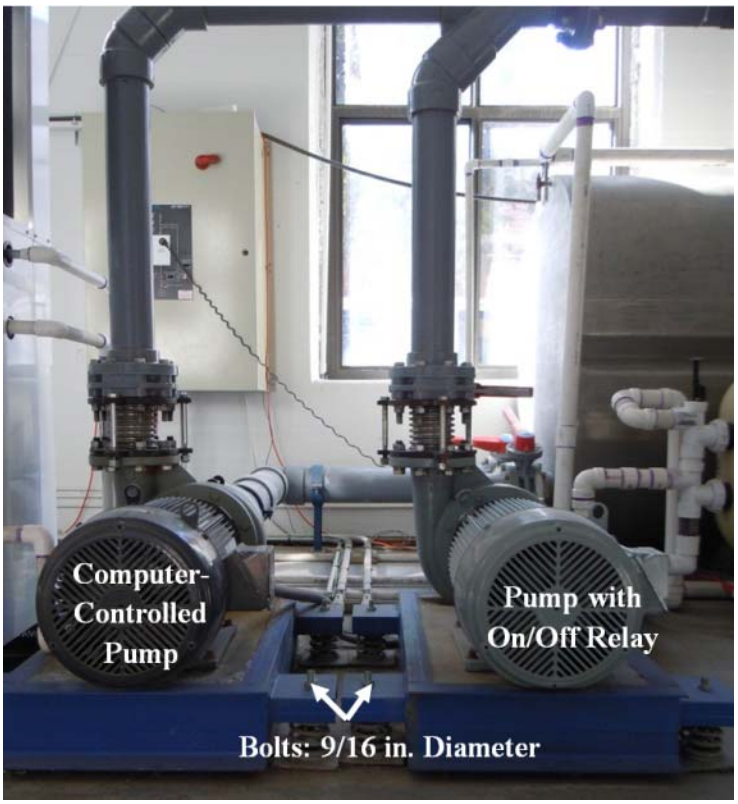

Figure 2-3. Photograph of SERF pumps

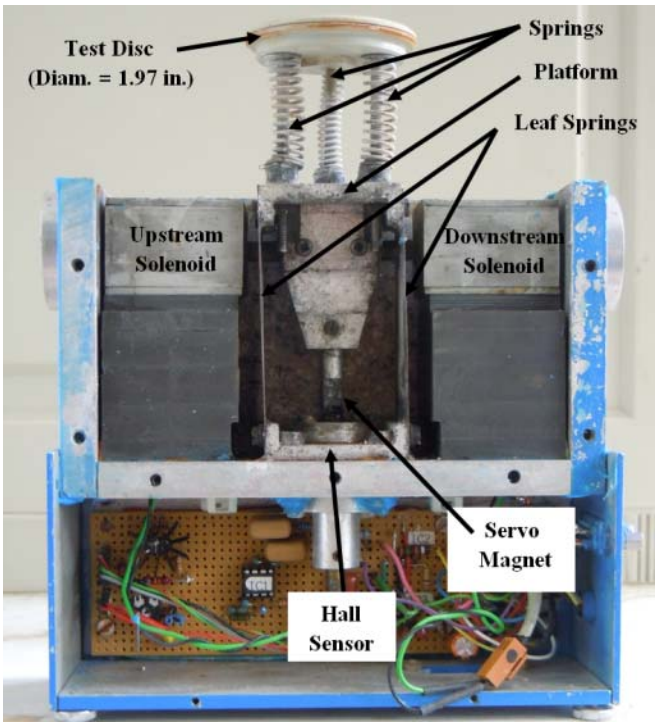

Figure 2-4. Photograph of shear stress sensor

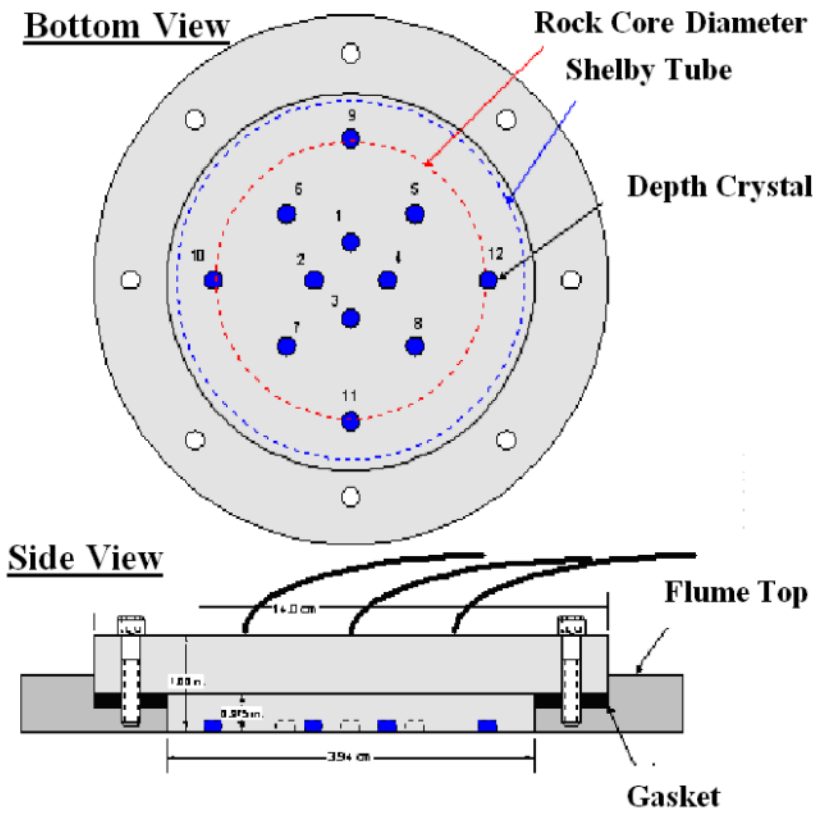

Figure 2-5. SEATEK ultrasonic sensor schematic

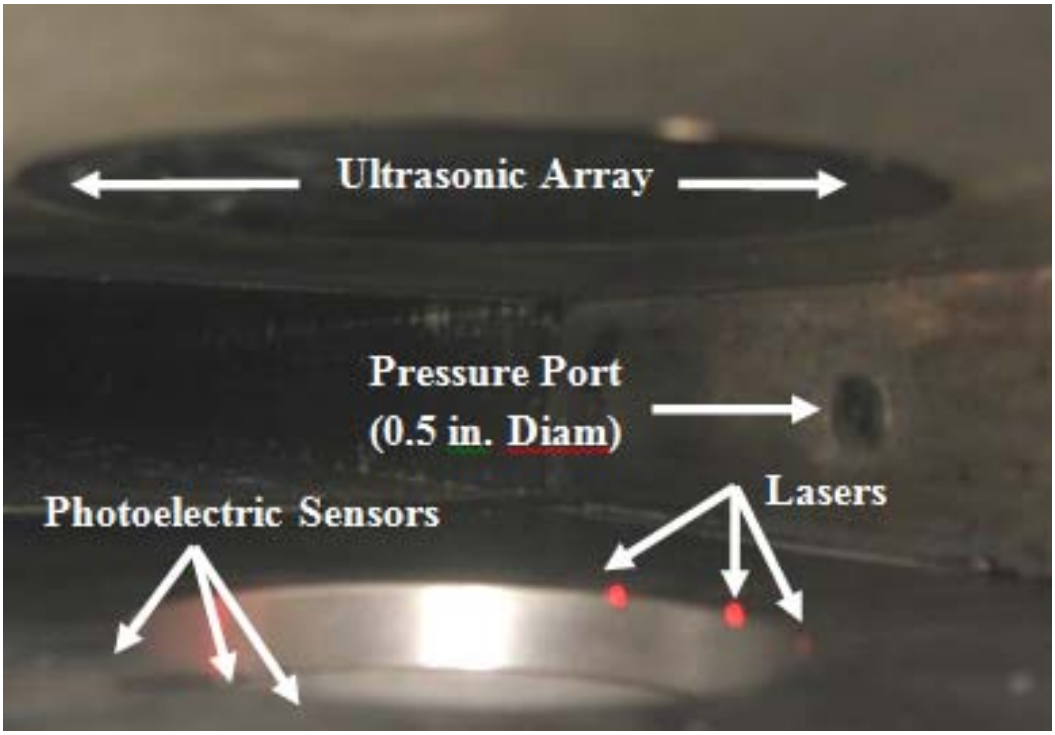

Figure 2-6. Photograph inside SERF (2010 configuration shown)

Figure 2-7. SERF close-up


Figure 2-8. The rotating erosion testing apparatus

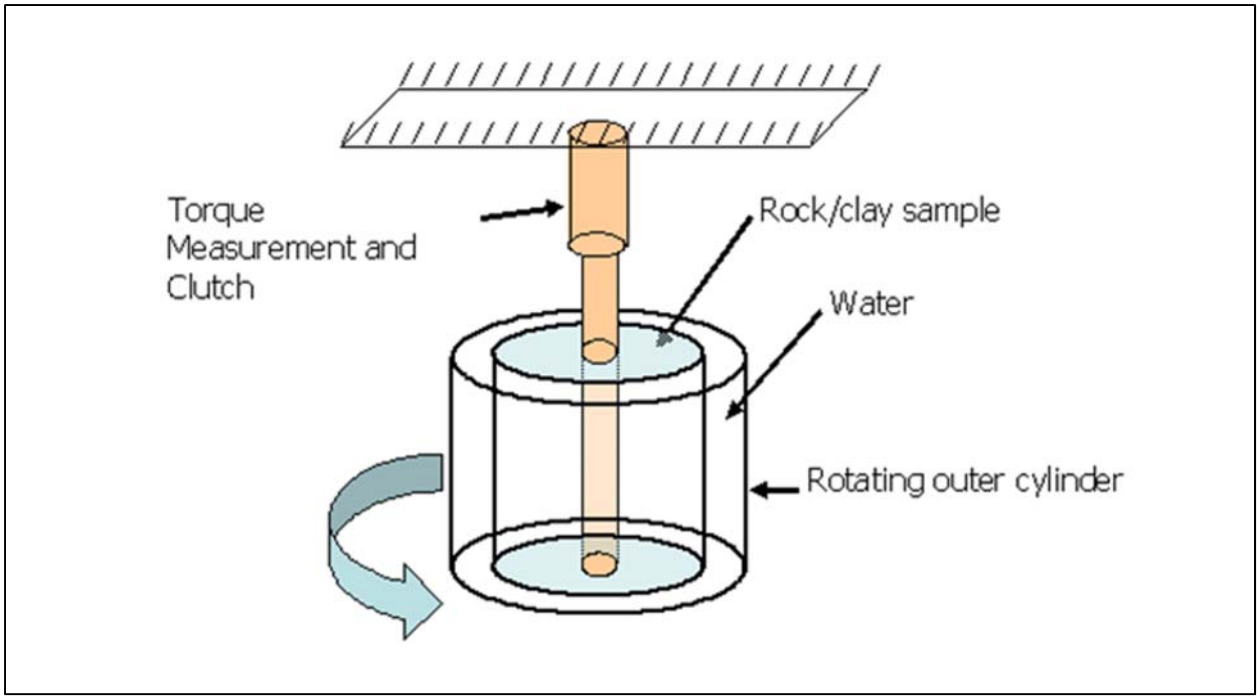

Figure 2-9. RETA schematic

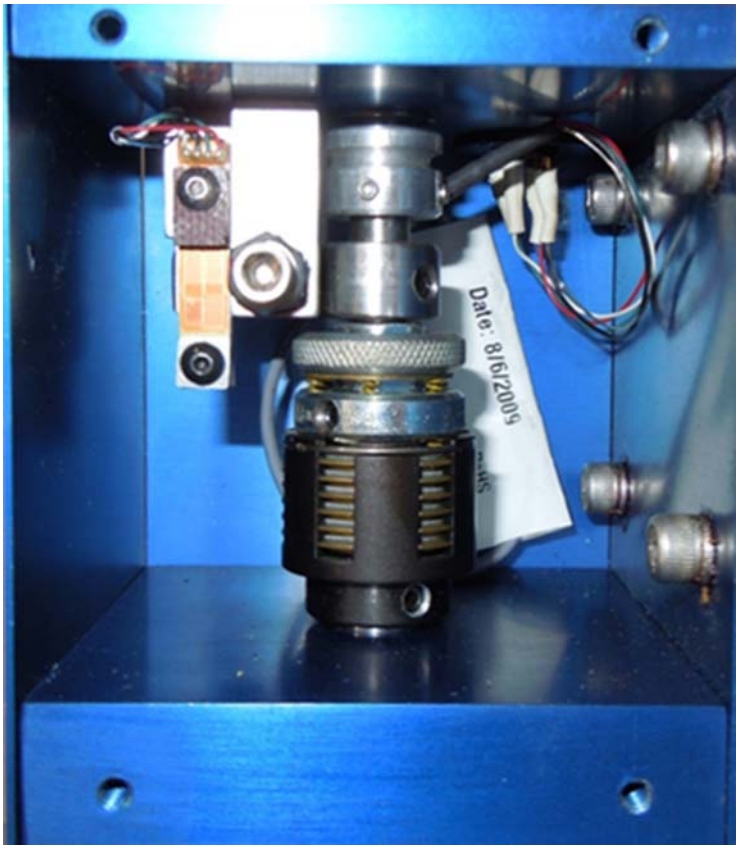

Figure 2-10. RETA torque cell and clutch

Figure 2-11. RETA control screen

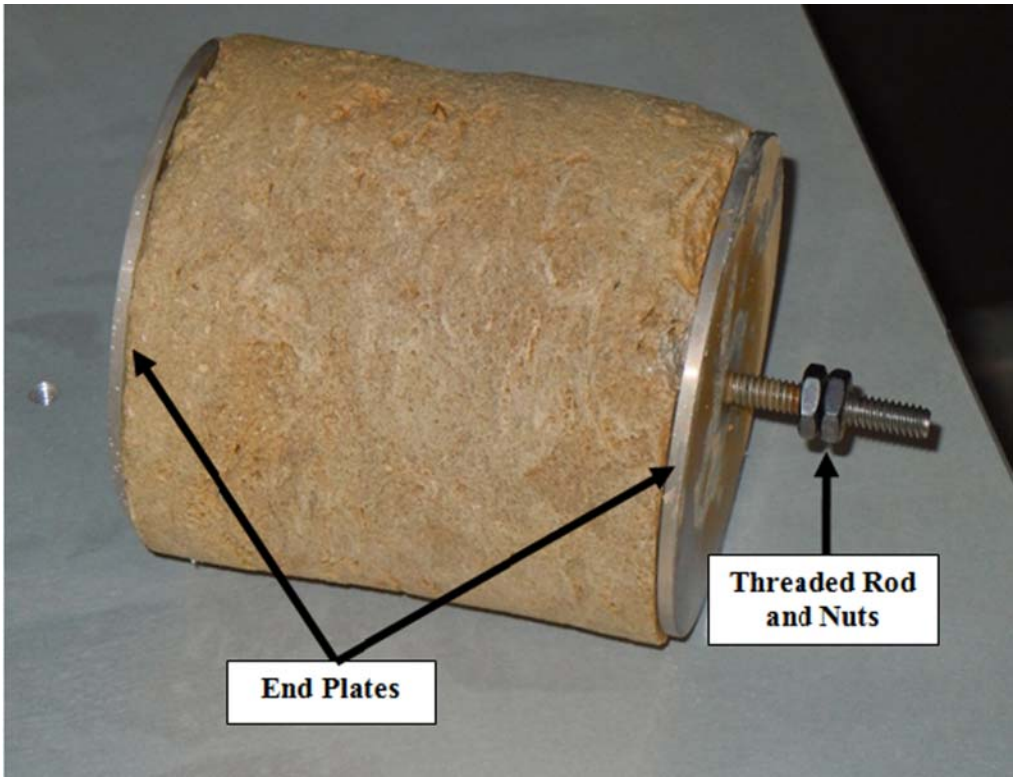

Figure 2-12. RETA sample ready for an erosion test

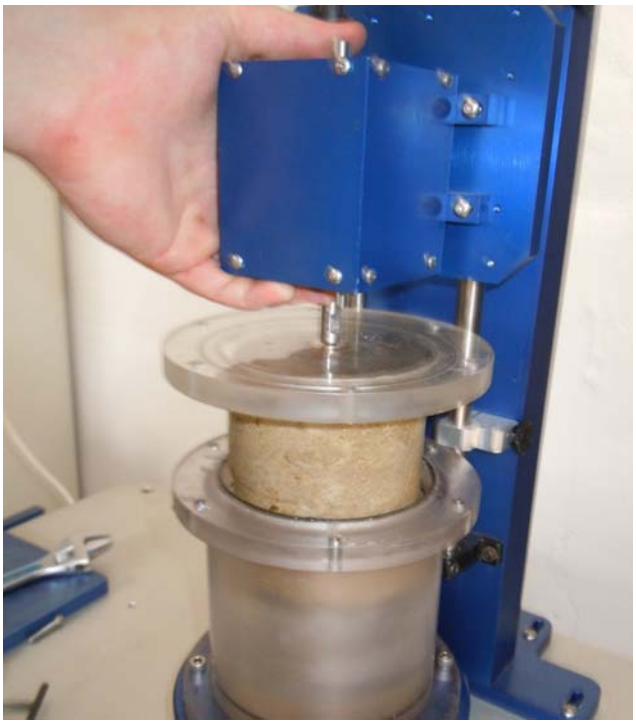

Figure 2-13. Lowering the RETA sample into position

CHAPTER 3
IMPROVEMENTS, ENHANCEMENTS, AND REPAIRS TO SERF

3.1 Pump Repair

As discussed in Section 1.1, due to recirculating sand, the SERF's primary pump's mechanical seal had become damaged during the previous round of SERF tests. Westside Electric of Jacksonville, FL was contracted to repair the damage. The pump's mechanical seal was replaced, the pump was reassembled, and it was reinstalled. Similarly, the water chiller's pump had also become damaged. For the water chiller, it was more cost-effective to replace the pump. This new pump was also installed as part of this project.

3.2 Laser Repair and Enhancement

As discussed in Section 1.1, and in this project's Scope, the laser system had become damaged due to harsh testing conditions. Additionally, the resolution of the previous laser system was not small enough. Because of this, often, large portions of eroding sediment would protrude into the flume – thereby defeating the purpose of the laser system. Additionally, investigators needed to increase the SERF test-section's sampling diameter to match a standard Shelby tube so that field tests could be conducted. This would further reduce the laser system's resolution if only three lasers were used.

To address these issues, the SERF's laser system was replaced and enhanced. Rafferty's Machine and Tool of Gainesville, FL was contracted to remove the SERF test-section's bottom, cut small channels into a new bottom section, epoxy the laser/photoelectric sensor fiber optics into these channels, and weld the device back together (Figure 3-1). To improve the laser system's resolution, the number of

laser/photoelectric sensor fiber optic lines was increased from three to eight. To guard against future damage, a series of sacrificial Plexiglas inserts (Figure 2-2) were fabricated so that they would become scratched instead of the lasers/photoelectric sensors themselves.

Once the lasers had been installed, the SERF was rewired to accommodate them (Figure 3-3 and Figure 3-4). A photograph of the final version of the laser system is provided in Figure 3-5.

To accommodate Shelby tubes, several new testing tubes and pistons were machined (Figure 3-6). A steel plate was attached to the bottom of each tube so that its hole pattern matched the hole pattern of FDOT's Shelby tube extractor at the State Material Office (SMO, Figure 3-7). The SERF's threaded rods/compression plate were modified to accommodate the new tubes' bolt patterns. A photograph of the new testing apparatus is presented in Figure 3-8.

3.3 Large-Capacity Filter

As discussed in Section 1.1 and in this project's Scope, the most pressing issue with the SERF was recirculating sediment. To prevent recirculating sediment from continuing to damage the device, a large-capacity filter was installed.

Three bids were obtained for the filter, and ultimately, ISC Liquid Filtration of Plano, TX was chosen to fabricate the device. ISC's filter had another of advantages compared with the other two filters investigated. Specifically, ISC's filter was less expensive (by about $3,000), could achieve a greater filtration level (0.5 microns as opposed to 1.0 micron), and could be built more quickly (6 weeks as opposed to 3 months) than either of the other two filters.

During fabrication, ISC indicated that there had been an issue on their production line. The filter that had been specified had been built, but it did not meet their internal quality-control specifications. To make the situation right, ISC substituted a filter that could accommodate 3,500 gpm flow rates (as opposed to the original 2,000 gpm design) that was soon coming off their production line. In other words, FDOT obtained a significant upgrade at no cost.

The filter (Figure 3-9) consists of a carbon steel housing that uses 24 filter bags. Half of these filter housings are filled with 1.0 micron-mesh filter bags while the other half are filled with 0.5 micron-mesh filter bags. Two 12.0 in. diameter flanges provide inflow and outlet to the filter bags. Two aluminum plates were machined to transition from the filter's twelve-inch inlet/outlet flanges to the SERF's nominal four inch Sch. 80 PVC sections. The device was painted to prevent corrosion to its carbon steel.

During installation, a series of valves were installed to improve SERF functionality. Ball valves were added between the filter intake and the flume; and the filter outlet and the reservoir tank. Additionally, a drainpipe and a corresponding valve was added to the SERF itself (shown in Appendix A). This valve system allows operators to drain the SERF without draining the filter, and they allow operators to change samples and start a new SERF test without refilling the instrument (which takes several hours).

3.4 Camera

Previously, SERF erosion video had been obtained using antiquated techniques. Sheppard et al. (2005) recorded video using cassette tapes and a Hi-8 recorder. Bloomquist and Crowley (2010) recorded video using an external digital video recorder (DVR). While this represented an improvement, the best-case scenario would be to

capture video to the SERF's computer directly. An iCube NS4133CU capable of 25 fps video capture at 1.3 MP (up to 1280x720 video resolution) and a M118FM08 8 lens were installed to bring video capture to the 21st century (Figure 3-10).

3.5 Computer

As discussed in this project's scope and in Section 1.1, the previous SERF computer was obsolete. Because of the computer's lack of processing power, the SERF typically struggled to complete its computer-controlled feedback loops such that sample advancement only occurred once every two to three seconds (this is due to the computer taking time to complete its control program). This sampling resolution was not fast enough to capture quick erosion changes.

A new machine was installed to address this issue. A Dell Optiplex with a 2 TB slave drive, a 320 GB operating system drive, 12 GB of RAM, and an Intel i7 processor (3.40 GHz, quad-core) was designed and installed. The system is capable of storing up to twenty hours of uncompressed video footage at 640x480 resolution, and it appears to be an improvement in terms of "keeping up" with an erosion test. Several codecs are available to compress captured video; these are detailed in Appendix A. To accommodate a larger GUI and computer-captured video, the SERF's dual-monitor system that had previously operated on a hard VGA-BNC switch was replaced with a 24 in. widescreen unit.

Because the new computer only had one open PCI slot, the SERF's analog DAQ card needed to be replaced with an external unit. A National Instruments USB-6251 was installed to read data from the SERF's existing NI SC-2345 analog control box to its computer. As implied in its name, the USB-6251 connects to the computer via a

universal serial bus connection. A photograph of the control room with these updated components is presented in Figure 3-11.

3.6 Graphical User Interface

To accommodate the SERF's improvements and enhancements, the device's Graphical User Interface (GUI) needed to be updated. Several control programs were written to control the SERF. A thorough description of these programs including screenshots of their LabVIEW block diagrams is provided in Appendix A.

3.7 Pump Drive

During this project, the SERF's computerized pump drive control component became damaged. Westside Electric of Jacksonville, FL was once again contracted to conduct repairs. Westside believed that the damage to the unit was due to its age (almost 10 years). According to Westside, the most likely cause of the damage was that a capacitor had discharged improperly. This appeared to cause damage to the unit's control board. The pump drive was shipped to General Electric (its manufacturer), but GE indicated that the correct control board was no longer produced. As a result, a board was individually manufactured in one of GE's Japan facilities. The board was reinstalled, and the pump drive was reconnected to the SERF. The unit now functions correctly.

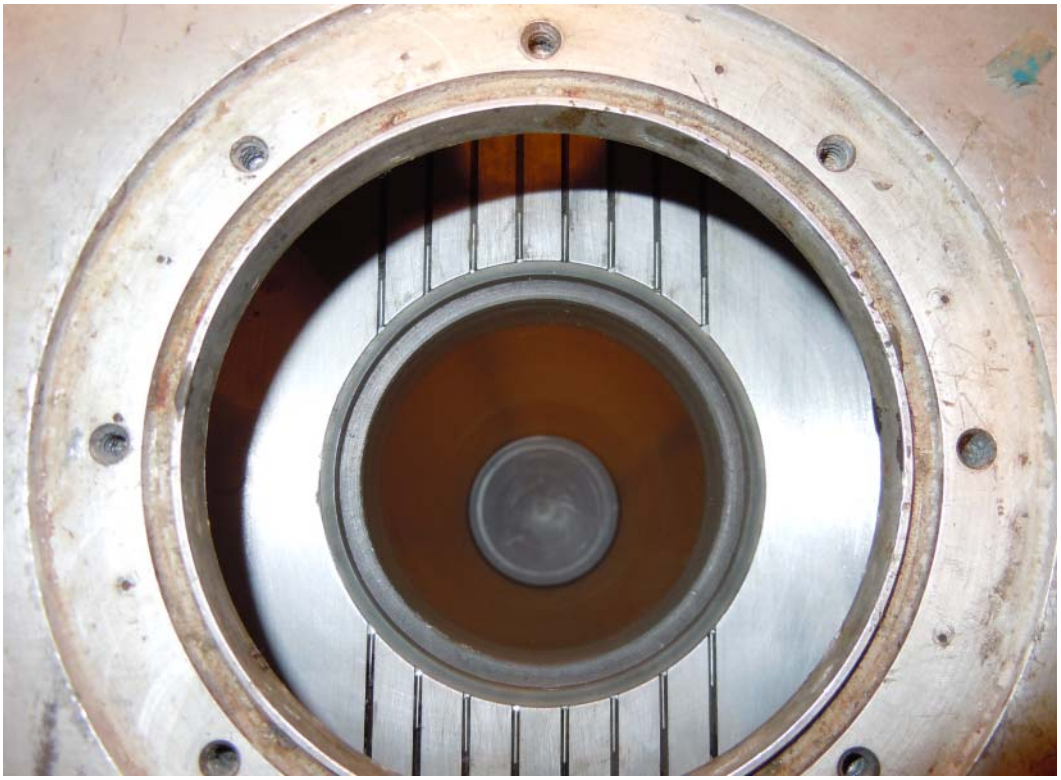

Figure 3-1. New laser bank (top looking down into sample tube). Please note that lasers/photoelectric sensors have been set up to alternate

Figure 3-2. Plexiglas insert for use in the laser system

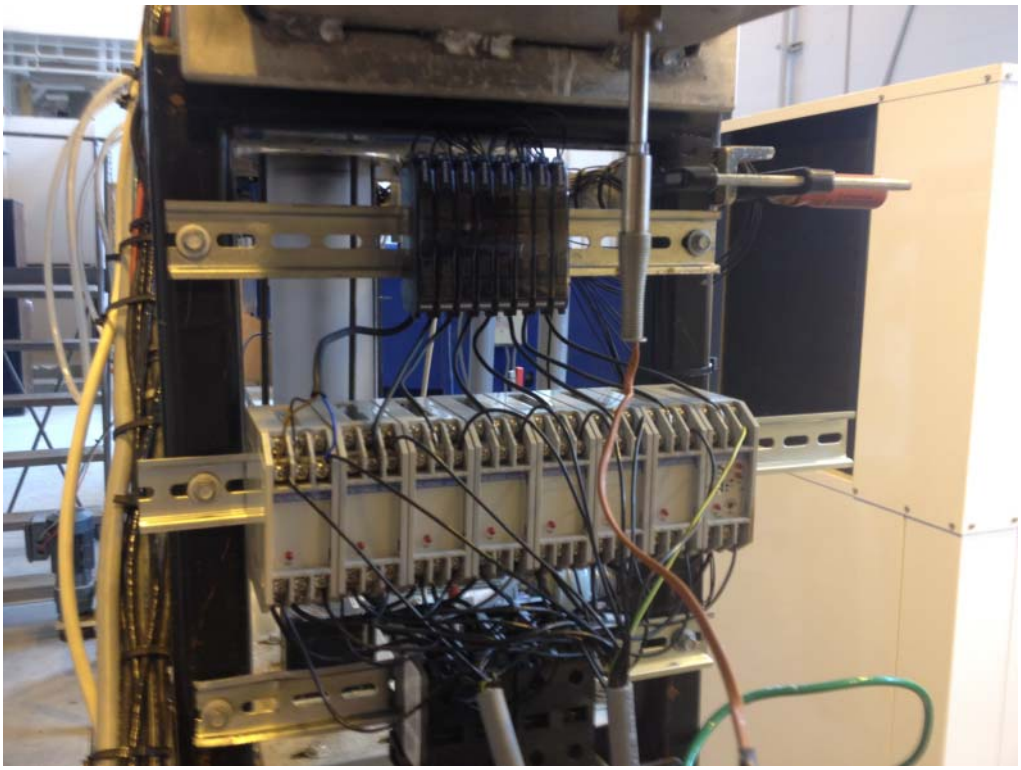

Figure 3-3. Laser amplifiers, control boxes, and AC power splitters

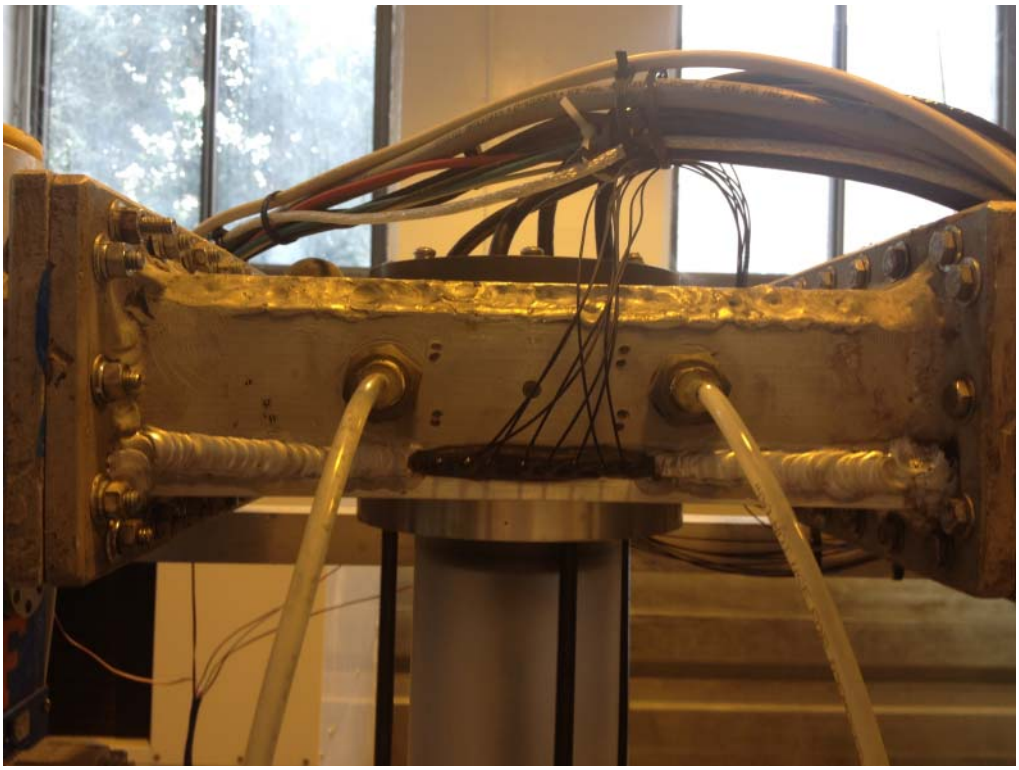

Figure 3-4. Outside of SERF showing laser fiber optic lines headed into the device

Figure 3-5. SERF laser system looking into flume

Figure 3-6. Example of new SERF testing tube

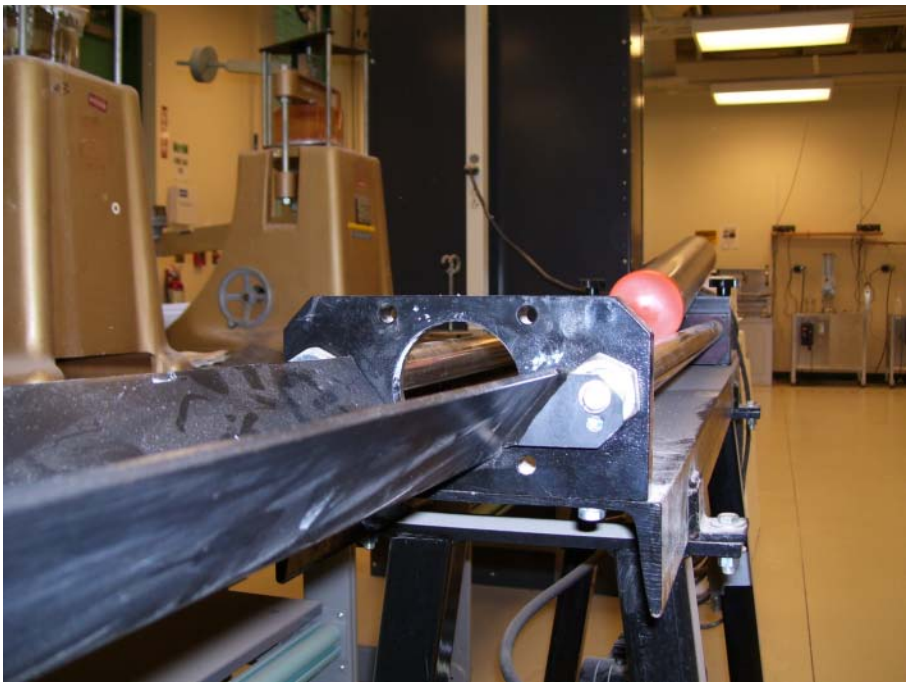

Figure 3-7. Photograph of FDOT's SMO Shelby tube extractor

Figure 3-8. SERF with new testing tube

Figure 3-9. SERF large-capacity filter

Figure 3-10. New SERF camera

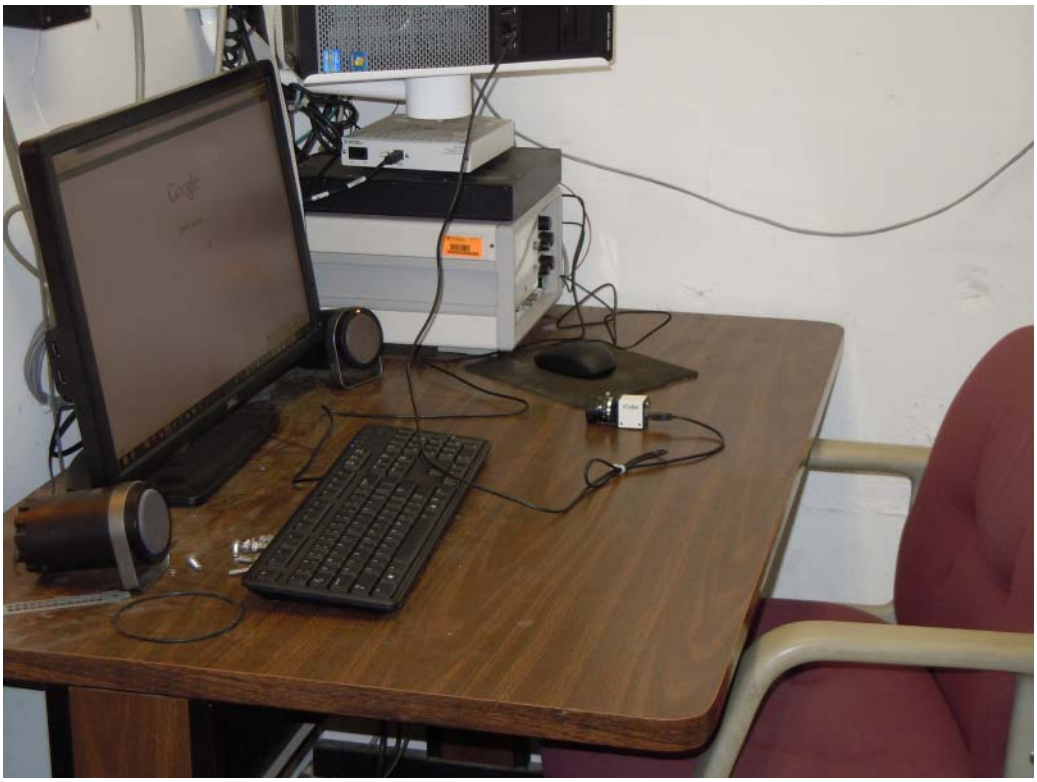

Figure 3-11. Updated SERF control room

CHAPTER 4
NEW EROSION MODEL BASED UPON COHESION

4.1 Introduction

As mentioned in Chapter 1, it may be beneficial to develop a relationship between erosion rate and another geotechnical parameter. Development of such a relationship may reduce the need for time-intensive and labor-intensive erosion tests in devices similar to the SERF and the RETA. In 1991, Gordon issued an interim memorandum to guide engineers when designing on erodible rock. He indicates that "only a generalized correlation exists between unconfined compressive strength and scourability," but he does acknowledge that as intuitively expected, stronger rock erodes more slowly than weaker rock.

As implied throughout this report, previous research has shown that there appears to be a relationship between erosion rate and bed shear stress. Several studies (Einstein and El-Samni, 1949, Partheniades, 1965, Kandiah, 1974) have confirmed that erosion appears to be related to shear stress via:

$$E = M(\tau_b - \tau_c) \tag{4-1}$$

In 2006, Slagle argued that a rock's cohesion may have some potential as a variable that could parameterize erosion rate. Slagle's argument for cohesion was based upon a McVay et al. (1992) derivation and tested samples involving drilled shafts in soft rock. Cohesion, *C*, is simply a bed material's shear strength defined by:

$$C = \frac{\sqrt{q_u}\sqrt{q_t}}{2} \tag{4-2}$$

where q_u is the rock's compressive strength and q_t is its tensile strength.

Slagle collected a number of erodible rock samples from Jewfish Creek in Key Largo FL. Erodibility was tested using the RETA while compressive and tensile strength were tested on adjoining sections. For each sample, Slagle developed an erosion rate versus shear stress relationship. Using these relationships, erosion was computed at shear stress intervals and plotted as a function of cohesion (Figure 4-1). Slagle chose to fit power-law best-fit regression curves to his shear stress/cohesion data of the form:

$$E = kC^{-n} \tag{4-3}$$

where constants *k* and *n* were fit from data at each shear stress. There are two issues with this approach. First, his relationships would be simpler to use if he found a way to collapse his data onto one curve. Secondly, and much more importantly, model results in Equation 4-2 imply that as cohesion approaches zero, erosion becomes infinite.

Tests were conducted in the SERF on sand specimens with diameters of 0.1 mm, 0.2 mm, 0.4 mm, 0.8 mm, and 2.0 mm. Results (Figure 4-2) indicate that Equation 4-1 appears to remain valid for sands and that the material-constant in Equation 4-1 appears to be a function of grain size; as grain size increases, material constant decreases. This implies that the material constant in Equation 4-1 represents a bed material's resistance to erosion from a critical shear stress deficit. Investigators hypothesize that *M* may also be a function of particle shape and particle density for cohesionless soil. For a cohesive soil, it would appear that material strength should become dominant. But, unlike Slagle's relationship, a cohesionless situation should not yield an infinite erosion rate.

4.2 Data Analysis

Slagle's RETA data from Jewfish Creek was supplemented with RETA/cohesion test data from erodible rock samples acquired at the Aucilla River approximately 20 miles south of Lamont, FL, in Tallahassee, FL, and Mill Creek, approximately 25 miles south of Portland, OR. Erosion was plotted as a function of shear stress, and best-fit regression lines of the form:

$$E = N\tau_b - Z \tag{4-4}$$

were fit to each dataset where *N* and *Z* are regression coefficients. *N* and *Z* were plotted as a function of cohesion (Figure 4-3 and Figure 4-4). Results appeared to indicate correlations between cohesion and each parameter. Best-fit exponential regression curves of the form:

$$N, Z = a + b\exp\left(\frac{-C}{c}\right) \tag{4-5}$$

were fit to the data where *a*, *b*, and *c* are regression constants.

Using the coefficients shown in Figure 4-3 and Figure 4-4, erosion rate was back-calculated and plotted against erosion data (Figure 4-5). A y=x line was fit to the data and residuals were calculated. Results appear to indicate good agreement between erosion model results and data (R^2 = 0.722; slope of best-fit line = 0.86).

4.3 Discussion

A comparison between this new rock erosion model and Slagle's model indicates that this model appears to be an improvement. Slagle's average R^2 value for his power-law curves was 0.52 while relationships obtained for *N* and *Z* yielded R^2 values of 0.91 and 0.62 respectively.

If one examines the mathematics behind modelled results, they do appear to correspond to the known relationship for cohesive and noncohesive scour in Equation 4-1. Erosion was modelled as:

$$E = N\tau_b - Z \tag{4-6}$$

$$N = a_1 + b_1 \exp\left(\frac{C}{c_1}\right) \tag{4-7}$$

$$Z = a_2 + b_2 \exp\left(\frac{C}{c_2}\right) \tag{4-8}$$

Dividing Equation 4-6 by *N* yields:

$$E = N\left(\tau_b - \frac{Z}{N}\right) \tag{4-9}$$

which is of the same form as Equation 4-1. *Z/N* should be precisely equal to the classically-defined critical shear stress parameter because it was based upon erosion versus shear stress curves' x-intercepts. The material-specific coefficient, *N,* remains as a multiplier of shear stress deficit. Interestingly however, when classically-defined critical shear stress is plotted as a function of cohesion, no strong correlation was found (Figure 4-6).

This is not unexpected. Both the slope coefficient and the intercept coefficient were modeled as functions of cohesion. Curves of the same form were fit to both parameters. Dividing both parameters by one another to give critical shear stress would appear to "cancel" cohesion's contribution to critical shear stress. A more appropriate relationship is shown in Figure 4-7 – modeled critical shear stress (Equation 4-8 divided by Equation 4-7) as a function of measured critical shear stress (*Z/N* from Equation 4-9). As shown, while erosion data appears to become reproduced relatively accurately

(Figure 4-7), critical shear stress data does not (R^2 = 0.45). This is probably due to the fact that solving for modeled critical shear stress compounds the errors resulting from curve-fitting slope coefficients, intercept-coefficients, and erosion rate versus shear stress relationships.

Beyond this, it should be noted that this model does have other limitations. First, model-dependency between *N* and grain size appears to be lost. While for rock it appears likely that erosion-resistive forces would be dominated by material-strength, it would be beneficial to reconcile Equation 4-7 with Equation 4-1 and results in Figure 4-2 through the introduction of a grain-size parameter. It should also be noted that this model does not take joints or fractures in rock into account. Erosion rate may ultimately be more dependent on these variables than cohesion.

Finally, this model implies that as cohesion approaches zero, critical shear stress becomes constant. This is known to be incorrect. Critical shear stress should be a function of roughness, Reynolds number, grain size, and sample density. With the present limited dataset however, one cannot reconcile this discrepancy.

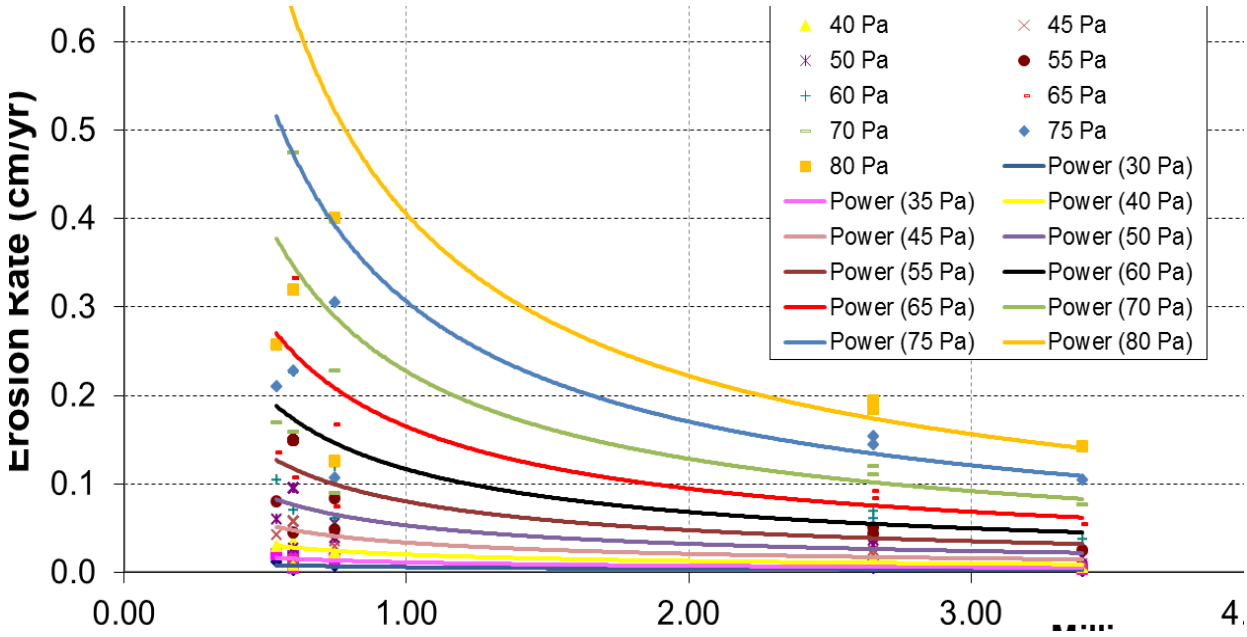

Figure 4-1. Erosion rate as a function of cohesion and shear stress (From Slagle's 2006 data)

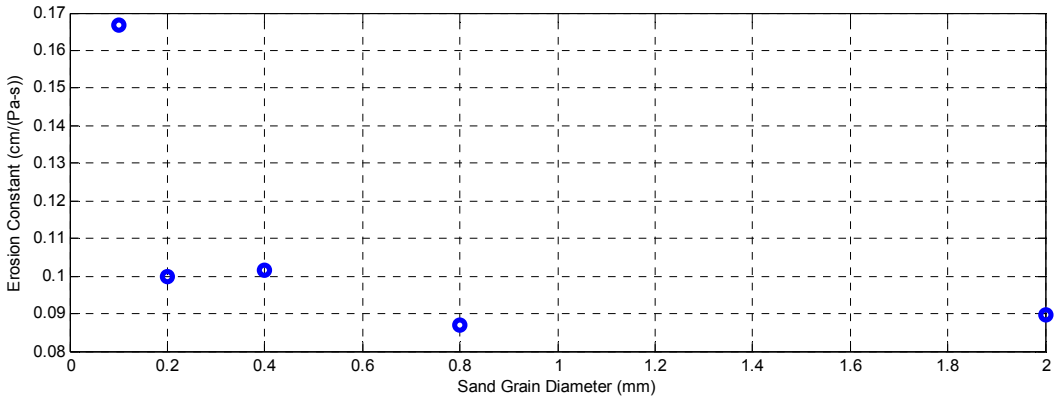

Figure 4-2. Erosion material constant as a function of grain size

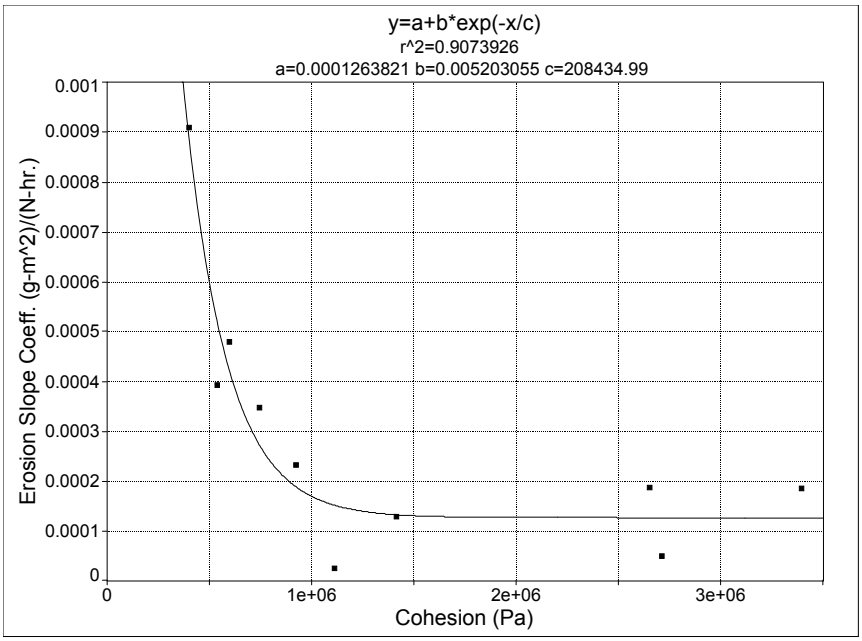

Figure 4-3. Erosion slope coefficient as a function of cohesion

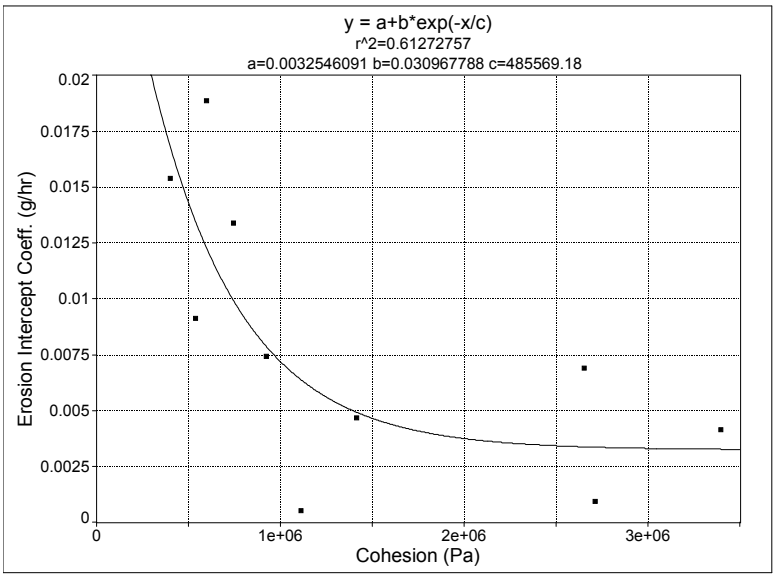

Figure 4-4. Erosion intercept coefficient as a function of cohesion

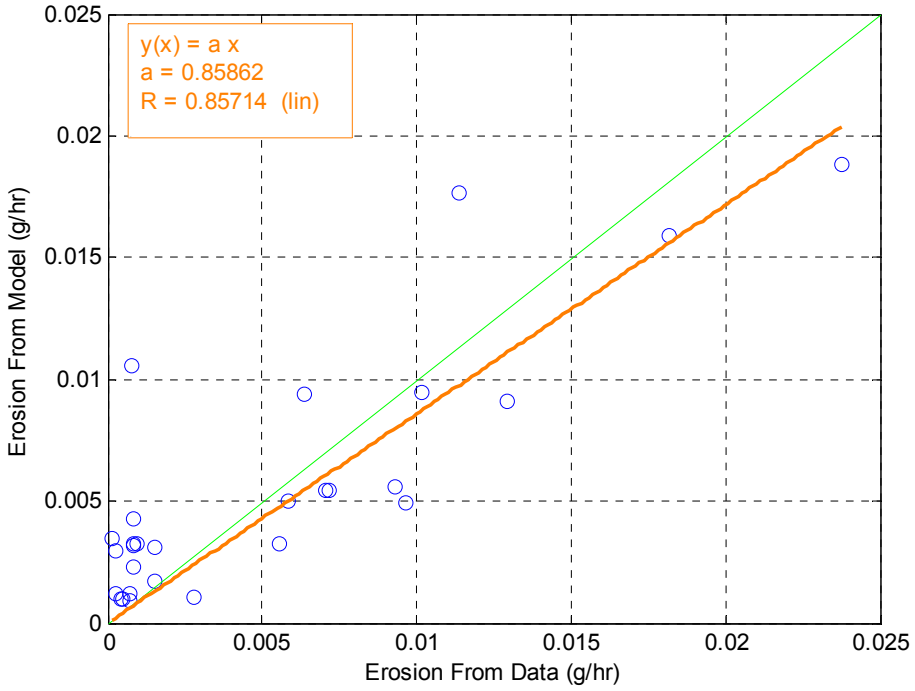

Figure 4-5. Modelled erosion results vs. erosion data

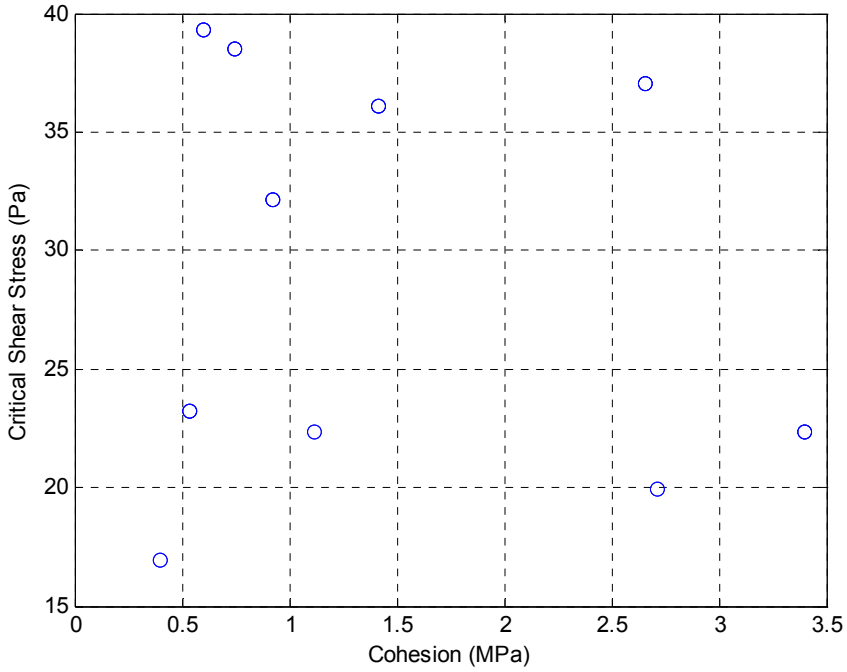

Figure 4-6. Cohesion versus critical shear stress

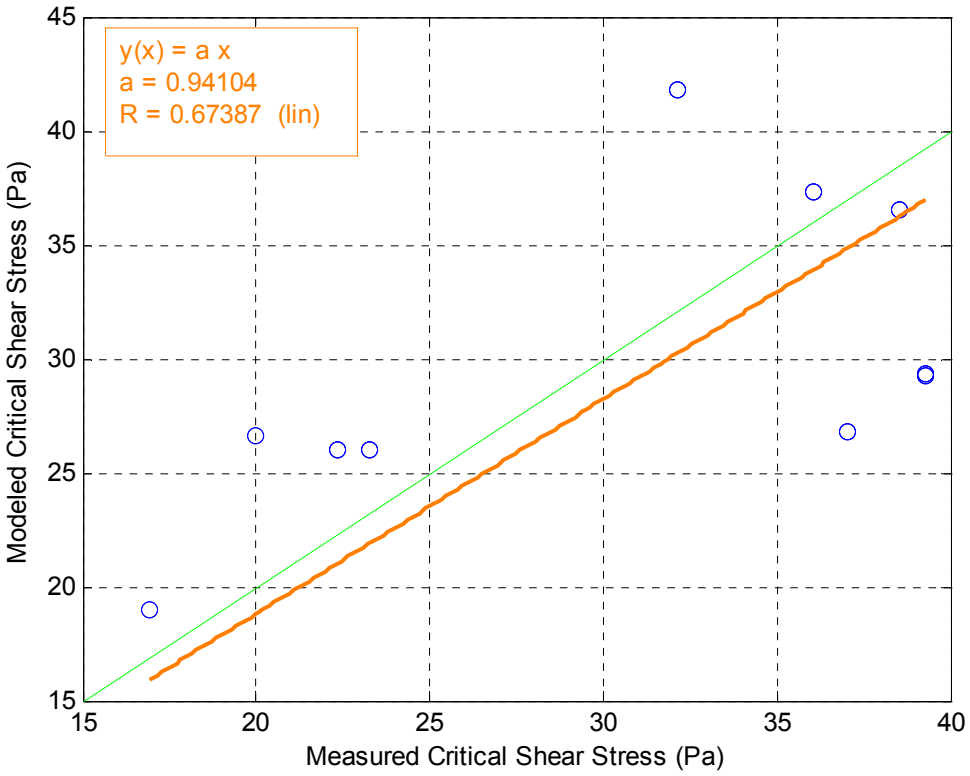

Figure 4-7. Modeled critical shear stress versus measured data

CHAPTER 5
SERF COMPUTER MODELING

5.1 Introduction

As discussed in Section 2.1.3, during the previous study, investigators concluded that using a pressure drop to estimate shear stress during an erosion test (Equation 2-6) did not provide accurate results. However, if the SERF was still to be used to develop sediments' erosion functions, a shear stress estimate needed to be made.

During previous erosion tests in the SERF, investigators noted that samples often displayed "blocking" or "chunking" whereby erosion of smaller particles is interspersed by events where large chunks of material erode (Crowley et al. 2012b, Bloomquist and Crowley 2010). Under these conditions, it would appear to be incorrect to assume a uniform surface roughness to estimate shear stress because localized shear stress should govern erosion rate.

In concept, the distribution of shear stress over a flat, rough sample should show some similarity to development of the boundary layer over a flat plate. At the leading edge of the flat plate, both boundary layer thickness and shear stress begin at zero and grow with distance downstream. In the case of a rough sample in a piston-style device like the SERF, the initial shear stress at the sample's upstream edge should be equal to the shear on a smooth duct boundary. And presumably, the shear over the remaining portion of the sample should increase as the flow moves downstream (at a faster rate than shear stress growth for a smooth sample). This increase in shear development may be responsible for "blocking" or "chunking" often observed during testing.

However, Crowley et al. (2012b) appear to show that from a design perspective, assuming nearly-uniform surface conditions in the testing device may be conservative

because estimating a lower shear stress for a given erosion rate forces the design erosion function to translate toward the y-axis and to become steeper. Therefore, the most conservative design approximation would be to use smooth-wall approximations. This presumption assumes that “blocking” or “chunking” do not significantly reduce the localized shear stress.

Investigators sought to determine: (1) if computational results verify experimental pressure drop results; and (2) if using protruding, recessed, or “chunked” samples has a significant effect on shear stresses. Question (2) bears some further discussion beyond non-uniform erosion. Briaud et al.’s (2001) EFA testing procedure stipulates that during testing, samples should protrude 1.0 mm into their duct. Presumably, this is done to ensure conservative results. Causing the sample to protrude into the flume will induce a normal stress upon its leading edge, which in turn should increase erosion rate for a given estimated shear stress. On the other hand, Crowley et al. (2012b), Roberts et al. (1998) and McNeil et al. (1996) recommend keeping the sample approximately level with the flume bottom so that field shear stress alone is approximated.

5.2 Methodology

To evaluate these questions, a computational model of the SERF (Crowley et al. 2012b) was generated using CD-adapco’s Star-CCM+. Details of the model are discussed below:

5.2.1 Mesh Geometry

A detailed, three-dimensional drawing of the SERF was prepared using AutoCAD by Autodesk, Inc. All volume meshing was performed within Star-CCM+. First investigators attempted to adapt a polyhedral volume meshing scheme to the geometry.

However, due to convergence issues with the model, researchers eventually were forced to abandon the polyhedral mesh and revert to a tetrahedral scheme. Between 1.5 and 2 million cells were used depending on the simulation. Cell resolution was approximately 0.5 mm per cell near the shear stress sensor and sample sections. Resolution was expanded to approximately 10.0 mm further away from these areas of interest in improve computational efficiency (Figure 5-1).

5.2.2 Turbulence Model Formulation

A realizable, two-layer, *k*-ε model with two-layer all-y+ wall treatment was chosen for this study. This realizable model was developed by Shih et al. (1994), and it contains a different transport equation for the turbulent dissipation rate, ε, than the traditional *k*-ε approach. It also parameterizes the model coefficient, C_μ as a function of mean flow and turbulence. In the standard *k*-ε approach, this term is assumed to be constant. This parameterization appears to be consistent with experimental observations in boundary layers (CD-adapco, 2012).

Specifically, in the realizable *k*-ε model, the standard transport equations are:

$$\frac{d}{dt}\int_V \rho k dV + \int_A \rho k\left(v - v_g\right)\cdot da =$$

$$\int_A \left(\mu + \frac{\mu_t}{\sigma_k}\right)\nabla k \cdot da + \int_V \left[G_k + G_b - \rho\left((\varepsilon - \varepsilon_0) + \Gamma_M\right) + S_k\right]dV \qquad (5\text{-}1)$$

$$\frac{d}{dt}\int_V \rho \varepsilon dV + \int_A \rho \varepsilon\left(v - v_g\right)\cdot da =$$

$$\int_A \left(\mu + \frac{\mu_t}{\sigma_k}\right)\nabla \varepsilon \cdot da + \int_V [C_{\varepsilon 1} S\varepsilon + \frac{\varepsilon}{k}(C_{\varepsilon 1} C_{\varepsilon 3} G_b) - \frac{\varepsilon}{k+\sqrt{\nu\varepsilon}} C_{\varepsilon 2}\rho(\varepsilon - \varepsilon_0) + S_\varepsilon]dV \qquad (5\text{-}2)$$

in which ρ is the density of the fluid; *k* is the turbulent kinetic energy; *V* is the cell volume; *v* is the velocity; v_g is the grid velocity; *a* is the face-area vector; μ is the dynamic viscosity of the fluid; μ_t is the turbulent viscosity; σ_k and σ_ε are the turbulent

Schmidt numbers; ε is the turbulent dissipation rate; ε_0 is the ambient turbulence value in the source terms that counteracts turbulence decay; Γ_M is the dilation dissipation coefficient; ν is the kinematic viscosity of the fluid; and S_k and S_ε are user-specified source terms (CD-adapco, 2012).

The turbulent terms, G_k and G_b for production and production due to buoyancy are given by Equation 5-3 and Equation 5-4 respectively:

$$G_k = \mu_t S^2 - \frac{2}{3}\rho k \nabla \cdot v - \frac{2}{3}\mu_t (\nabla \cdot v)^2 \tag{5-3}$$

$$G_b = \beta \frac{\mu_t}{\sigma_t} (\nabla T \cdot g) \tag{5-4}$$

In these equations, T is the temperature (although flow was assumed to be isothermal); β is the coefficient of thermal expansion; g is the acceleration due to gravity; and S is the modulus of the mean rate of strain tensor, $\boldsymbol{S}$, given by:

$$S = |\boldsymbol{S}| = \sqrt{2S:S^T} = \sqrt{2S:S} \tag{5-5}$$

$$\boldsymbol{S} = \frac{1}{2}(\nabla v + \nabla v^T) \tag{5-6}$$

The dilation coefficient, Γ_M is expected to be small since the SERF was modeled as a single-phase volume of water. However, for completeness, its formulation is presented below:

$$\Gamma_M = \frac{C_M k \varepsilon}{c^2} \tag{5-7}$$

where c is the speed of sound and C_M = 2 (CD-adapco, 2012).

The turbulent viscosity is defined as:

$$\mu_t = \rho C_\mu \left(\frac{k^2}{\varepsilon}\right) \tag{5-8}$$

where, as mentioned, unlike the standard k-ε approach, C_μ is variable and is given by:

$$C_\mu = \frac{1}{A_0 + A_s U^{(*)}\left(\frac{k}{\varepsilon}\right)} \tag{5-9}$$

$$U^{(*)} = \sqrt{\boldsymbol{S}:\boldsymbol{S} - \boldsymbol{W}:\boldsymbol{W}} \tag{5-10}$$

$$A_s = \sqrt{6}\cos\phi \tag{5-11}$$

$$\phi = \frac{1}{3}\cos^{-1}(\sqrt{6}W) \tag{5-12}$$

$$W = \frac{S_{ij}S_{jk}S_{ki}}{\sqrt{S_{ij}Sij}^3} \tag{5-13}$$

$$A_0 = 4.0 \tag{5-14}$$

$\boldsymbol{W}$ is the rotation tensor:

$$\boldsymbol{W} = \frac{1}{2}(\nabla v - \nabla v^T) \tag{5-15}$$

The model coefficient, $C_{\varepsilon 1}$ is defined as:

$$C_{\varepsilon 1} = max\left(0.43, \frac{\eta}{5+\eta}\right) \tag{5-16}$$

where η is defined as:

$$\eta = \frac{Sk}{\varepsilon} \tag{5-17}$$

And the balance of the model coefficients are given as $C_{\varepsilon 2}$ = 1.9, σ_κ = 1.0, and σ_ε = 1.2 (CD-adapco, 2012).

This realizable model was combined with a two-layer approach (Rodi, 1991) which allows the *k*-ε model to be applied in the viscous sublayer. In this approach (as implied), the computation is divided into two layers. In the layer near the walls, ε and μ_t are specified as functions of wall distance. Values for ε are blended smoothly with values computed by solving Equation 7 far from the wall using blending functions described in detail by Jongen (1998). Meanwhile, Equation 6 is solved throughout the entire flow regime (CD-adapco, 2012). Specifically, the near-wall model is

parameterized as a length-scale function and a turbulent viscosity ratio function (Wolftshtein, 1969):

$$l_\varepsilon = f(y, Re_y) = c_l y \left[1 - \exp\left(-\frac{Re_y}{A_\varepsilon}\right)\right] \tag{5-18}$$

$$A_\varepsilon = 2c_l \tag{5-19}$$

$$c_l = \kappa C_\mu^{-\frac{3}{4}} \tag{5-20}$$

$$\frac{\mu_t}{\mu} = f(Re_y) = Re_y C_\mu^{0.25} \kappa \left[1 - \exp\left(-\frac{Re_y}{A_\mu}\right)\right] \tag{5-21}$$

$$Re_y = \frac{\sqrt{\kappa} y}{\nu} \tag{5-22}$$

where C_μ = 0.09, κ = 0.42, A_m = 70. The dissipation rate is simply:

$$\varepsilon = \frac{k^{3/2}}{l_\varepsilon} \tag{5-23}$$

The use of this two-layer approach allows for the flexibility of a two-layer all-y+ wall treatment.

5.2.3 Wall Treatment Formulation

A two-layer all-y+ wall treatment implies that no assumptions are made about how well the viscous sublayer is resolved. Instead, a blended wall law was used to estimate shear stress. Blending is achieved between high y+ wall treatment and low y+ wall treatment. High-y+ wall treatment is similar to a wall-function type approach in that near-wall cells are assumed to lie within the logarithmic region of the boundary layer. Low-y+ wall treatment is similar to the traditional low-Reynolds number approach where no modeling beyond the assumption of laminar flow is needed in the wall cells. In other words, it assumes that the viscous sublayer is properly resolved (CD-adapco, 2012). All-y+ wall treatment attempts to mimic high-y+ wall treatment when a mesh is coarse

and low-y+ wall treatment when a mesh is fine. Specifically, a blending function, $\boldsymbol{g}$ is defined as a function of Re_y:

$$\boldsymbol{g} = \exp\left(-\frac{Re_y}{11}\right) \tag{5-24}$$

Next, a reference (friction) velocity is defined:

$$u^* = \sqrt{\frac{g\nu u}{y} + (1-\boldsymbol{g})C_\mu^{0.5}k} \tag{5-25}$$

in which y is the normal distance from the wall. Wall-cell turbulence production is defined as:

$$G_k = \boldsymbol{g}\mu_t S^2 + (1-\boldsymbol{g})\left(\frac{1}{\mu}\right)\left(\rho u^*\left(\frac{u}{u^+}\right)\right)^2\left(\frac{\partial u^+}{\partial y^+}\right) \tag{5-26}$$

where u^+ is the wall-parallel velocity nondimensionalized with u^* and y^+ is the nondimensional wall coordinate given by:

$$y^+ = \frac{yu^*}{\nu} \tag{5-27}$$

Wall-cell dissipation is given the same formulation as Equation 27 to provide two-layer approach consistency. At the walls, a Neumann boundary condition is used for k such that $\partial k/\partial t = 0$.

In the viscous sublayer, velocity distribution is modeled as:

$$u_{lam}^+ = y^+ \tag{5-28}$$

In the logarithmic layer, velocity distribution is modeled as:

$$u_{turb}^+ = \frac{1}{\kappa}\ln\left(\frac{Ey^+}{f}\right) \tag{5-29}$$

where E is a constant (9.0) and f is the roughness function (friction factor). Obviously, a discontinuity exists between the viscous sublayer and the logarithmic layer – i.e., the

buffer region. A blended wall law (Reichardt, 1951) is used to model the velocity distribution in this region:

$$u^+ = \frac{1}{\kappa}\ln(1+\kappa y^+) + C[1-\exp\left(\frac{y^+}{D}\right) - \frac{y^+}{D}\exp(-by^+) \quad (5\text{-}30)$$

where *D* is the intersection point between the logarithmic layer and the viscous sublayer, and:

$$C = \frac{1}{\kappa}\ln\left(\frac{E'}{\kappa}\right) \quad (5\text{-}31)$$

$$b = \frac{1}{2}\left(\frac{Dk}{C} + \frac{1}{D}\right) \quad (5\text{-}32)$$

Wall friction factor is defined through introduction of a wall roughness number:

$$\mathrm{Re}^+ = \frac{u^* r}{\upsilon} \quad (5\text{-}33)$$

where *r* is a roughness parameter (analogous to k_s); and ν is the kinematic viscosity of water. Friction factor, *f*, is related to Re+ via:

$$f = \begin{cases} \left[B\left(\dfrac{\mathrm{Re}^+ - \mathrm{Re}^+_{smooth}}{\mathrm{Re}^+_{rough} - \mathrm{Re}^+_{smooth}}\right) + C\,\mathrm{Re}^+ \right]^a & \text{for } \mathrm{Re}^+ \le \mathrm{Re}^+_{smooth} \\ B + C\,\mathrm{Re}^+ & \text{for } \mathrm{Re}^+_{smooth} < \mathrm{Re}^+ < \mathrm{Re}^+_{rough} \\ & \mathrm{Re}^+ > \mathrm{Re}^+_{rough} \end{cases} \quad (5\text{-}34)$$

where the exponent, *a* is given by:

$$a = \sin\left[\frac{\pi}{2}\frac{\log\left(\mathrm{Re}^+ / \mathrm{Re}^+_{smooth}\right)}{\log\left(\mathrm{Re}^+_{rough} / \mathrm{Re}^+_{smooth}\right)}\right] \quad (5\text{-}35)$$

where *C* and *B* are calibration coefficients and Re^+_{smooth} and Re^+_{rough} are constant roughness Reynolds Numbers representing “fully rough” and “hydraulically smooth” conditions. By default, *B* = 0; *C* = 0.253; Re^+_{smooth} = 2.25; and Re^+_{rough} = 90 (CD-adapco, 2012).

5.2.4 Inlet Formulation

The inlet into the SERF was modeled as a "velocity inlet," and its velocity vectors were specified explicitly in the normal direction. The boundary face pressure was extrapolated from cells adjacent to the inlet boundary using a hybrid Gauss-least square method (LSQ) reconstruction gradient. The unlimited (superscript *u*) reconstruction (subscript *r*) of data value ϕ is given by:

$$(\nabla\phi)_r^u = \sum_f (\phi_n - \phi_0) w_0^f \tag{5-36}$$

$$w_f^0 = \beta w_f^{lsq} + (1-\beta) w_f^G \tag{5-37}$$

$$w_f^{lsq} = \left[\sum_f \frac{\boldsymbol{ds}\times\boldsymbol{ds}}{\boldsymbol{ds^2}}\right]^{-1} \left(\frac{\boldsymbol{ds}}{\boldsymbol{ds^2}}\right) \tag{5-38}$$

$$\boldsymbol{ds} = \boldsymbol{x_n} - \boldsymbol{x_0} \tag{5-39}$$

$$w_f^G = \frac{A_f}{V_0 + V_n} \tag{5-40}$$

where $\boldsymbol{x_0}$ and $\boldsymbol{x_n}$ are the centroids of cell-0 and its neighboring cell *n* through face *f*; ϕ_0 and ϕ_n are data values in cell-0 and its neighbor; A_f is the face-area vector; V_0 and V_f are cell volumes; and β is the geometric Gauss-LSQ gradient blending factor field function. The blending factor is user-specified, and it determines the weight given to the Gauss/LSQ computed gradients (CD-adapco, 2012). Initial turbulent kinetic energy, *k*, was specified through introduction of a turbulence intensity parameter, *I* such that:

$$k = \frac{3}{2} I v^2 \tag{5-41}$$

where *v* is local velocity magnitude and *I* was manually set at 5%. Inlet turbulent dissipation rate was derived using an initial turbulent viscosity ratio, μ_t/μ, of 30 such that:

$$\varepsilon = \frac{\rho C_\mu k^2}{\left(\frac{\mu_t}{\mu}\right)\mu} \tag{5-42}$$

5.2.5 Outlet Formulation

An outlet flow boundary condition (internally, called a “flow-split outlet” in Star-CCM+) was used to specify the flume’s downstream edge. Star-CCM+ defines the velocity at a flow-split outlet as:

$$v_f = v_0^r + \frac{x_i}{\rho}\left(\frac{a}{|a|}\right) \tag{5-43}$$

Where $v_o^r$is the velocity that is extrapolated from the adjacent cell value using reconstruction gradients; *a/|a* is the outward-normal vector; and x_i is a scale factor that is computed for outlet boundary *i* as per Eq. 48 through Eq. 50 (CD-adapco, 2012):

$$x_i = -\frac{f_i}{\sum_{j=1}^{n\ outlets} f_i}\frac{\dot{m_{in}} - \dot{m_i^*}}{\sum_{outlet\ i\ faces}|a|} \tag{5-44}$$

where f_i is the specified fraction of the flow leaving outlet *i* (in the case of the SERF, 100%); and $\dot{m}_{in}$ is the total inlet flow defined as:

$$\dot{m_{in}} = \sum_{non-outlet\ faces} \rho(v_f * a - g) \tag{5-45}$$

And $\dot{m_i^*}$ is the unscaled outlet mass flow rate through outlet *i*:

$$\dot{m_i^*} = \sum_{outlet\ i\ faces} \rho(v_0 * a - g, 0) \tag{5-46}$$

where $\rho_{fmax}$is the maximum density of the fluid.

5.2.6 Model Computation Scheme

Initial conditions of the model were established such that the SERF was filled with stagnant water, and a “step” increase of velocity, v_0 was specified at the velocity inlet. Over time, flow became fully developed as the velocity “step” migrated downstream. Average wall shear stress across the model’s sample section and sensor section was used as an approximate indicator of a fully developed flow condition. Once

these average shear stresses approached a constant value, or leveled off, the flow was assumed to be fully developed. Then, a modeled "reading" was taken. Fully developed conditions were typically achieved in approximately 4-5 seconds of modeled time. This time approximately corresponded to observations during physical tests in previous studies. Modeled readings were compared with data from Crowley et al. 2012a. Typically, average *y*+ values near the sample-section and sensor section were between 75 and 80, which would tend to shift all-y+ wall treatment toward the high-y+, wall-function style of wall boundary. This technique was deemed acceptable because modeled "readings" tended to match physical data (please see below).

5.2.7 Justification

The models that were used in this study were chosen for a number of reasons. Researchers' previous experience in Star-CCM+ appeared to indicate that the combination of models described here would provide accurate results. Investigators conducted several discussions with researchers at Argonne National Laboratories' (ANL) Transportation Research and Computing Center (TRACC) and the J. Sterling Jones Hydraulics Laboratory at the Turner-Fairbank Highway Research Center (TFHRC) concerning modeling choices (Lottes, 2012). Based upon these researchers' experiences, they agreed that the aforementioned modeling choices appeared to be appropriate. Review of the Star-CCM+ user's manual indicated that for a flow situation similar to the one described here, the models used in this paper were appropriate for this particular commercially-available software (CD-adapco 2012).

Finally, models discussed here have been compared with other modeling options in literature. For example, Davis et al. (2012) compared Star-CCM+'s realizable *k*-ε

model with its k-ω model and its *V2F* k-ε variant for flows over a wall-mounted cylinder. The traditional k-ε approach was not studied because of its known deficiencies in resolving flows in the viscous sublayer. This study concluded that the realizable k-ε model consistently performed better than the other two models in almost every measurable aspect.

5.3 Results

Several simulations were conducted using this setup at varying flow rates. First, a "smooth-wall" approximation was used. Because wall functions were used during the computation, researchers wanted to be sure that these wall functions accurately replicated real data for the selected mesh geometry and associated y^+ values. Once smooth data had been verified, the roughness parameter, r from Eq. 37, was varied to match data for grain sizes of 0.125 mm, 0.25 mm, and 0.5 mm at each velocity (as reported in Crowley et al. 2012a). Averaged modeled shear stress across the sensor section was plotted as a function of measured shear stress from Crowley at el. (2012a) to demonstrate quality of fit (Figure 5-2). Note that the same roughness parameter was used at each velocity for a given grain size to preserve physical significance. For rougher sediments, increases in r led to increases in y^+. This, in turn led to increases in the near-wall-cell centroids near the areas of interest in the flume (recall that resolution near the sample/sensor was approximately 0.5 mm). To account for this, a "maximum" r value was defined as approximately 0.3 mm – the approximate distance from the wall to the adjacent cells' centroids. Then, B from Equation 5-34 was adjusted to fit the measured data (C in Equation 5-34 was left untouched so that modeling conditions were changed as minimally as possible). As an unintended consequence of this

procedure, very rough data (grain sizes 1.0 mm and 2.0 mm) at lower velocities (less than 4.0 m/s) failed to match data; however, at higher velocities, matching was achieved. Data that failed to match was omitted from further analysis.

The grain diameters reported in Crowley et al. 2012a appear to be on the order of magnitude of sand grains, and the SERF (and other piston-style devices) is designed to measure the erosion rates of cohesive material. However, previous research with the device showed that during an erosion tests, “blocking” or “chunking” often occurred during a cohesive erosion test (Crowley et al. 2012b). Use of a uniform sample (or shear stress) section with a high roughness could approximate an infinitely-chunked specimen. In other words, it is not difficult to imagine a scenario where many clay flocs erode from a smooth clay specimen’s surface and the remaining sample surface approximates a sample with the roughness of a sand specimen surface. Likewise, previous research has shown that the introduction of a small amount of cohesive material to a sand specimen may cause the specimen to erode like a cohesive material (Mitchener and Torfs 1996 for example). These specimens may have surface roughnesses on the order of magnitude of a typical, uniform-sand specimen, but they may erode slowly like a cohesive soil and exhibit higher, cohesive-style critical shear stresses.

Next, mean values of r were found by integrating across the model’s sensor-section. These data appear to correspond to previous research in that r appears to be approximately an order-one multiplier of d (Einstein and El Samni, 1949, Einstein and Krone, 1962, Kamphuis 1974, Bayazit 1976, Dancey et al. 2000, Rahman and Webster 2005, Camenen et al. 2006, etc.). In fact, when data from this study was plotted

alongside data in a similar range (Kamphuis 1974, Rahman and Webster, 2005) results followed a very similar trend (Figure 5-3). Additionally, modeled pressure differentials were used to compute shear stresses via Equation 5 (Figure 5-4). Pressure differentials were computed just upstream and just downstream from the sensor-section to mimic Crowley et al.'s (2012a) previous experiments. Total distance between pressure ports was approximately 4.0 in. (10.16 cm).

To verify these results, a convergence study was conducted using a representative flow rate (5.0 m/s), a smooth sample-section, and a smooth sensor-section. The refined portions of the mesh (across the sample-section and across the sensor section), were replaced with several finer and coarser meshes. Average shear stress was computed across the sensor-section and the sample section, and results were plotted as a function of cell size. A best-fit, linear regression curve was established, and shear stresses for a cell-size of zero were computed (i.e., a Richardson extrapolation). Results (Figure 5-5) appear to indicate that using average cell-sizes of 1.0 mm produces cell-size computational errors less than 5.0%, which is why the ~0.5 mm grid size was deemed to be acceptable.

Next, the SERF's sample section (circled portion of Figure 5-1) was replaced with four configurations (Figure 5-6) to approximate differential erosion rates observed by Crowley et al. (2012b), Annandale et al. (2006), and recommendations from Briaud et al.'s (1999, 2001, 2004a, 2004b) testing procedure to determine their effect on localized shear stresses. Configurations were dubbed conical protrusion configuration, 1 mm protrusion configuration, differential erosion configuration, and wavy configuration. These configurations and the rationale for their selection are described below:

- Conical protrusion configuration (Figure 5-6a). As discussed in Crowley et al. (2012a), piston advancement in the SERF is controlled through a feedback loop between an ultrasonic depth sensor array and a Servo stepper motor. The ultrasonic array consists of twelve crystals that measure distance from the top of the flume to the top of the sample. When the average of these differences is within the tolerance of the stepper motor, an advancement signal is triggered. Sometimes, a sample may over-advance because of an errant ultrasonic signal. When sand is tested and an error occurs, a small conical shaped slope as illustrated in Figure 5a is often generated because sand grains tend to roll from the center of the eroding sample toward its edges. For this configuration, the conical sample protrudes 1.50 in. (3.81 cm) into the flume.

- 1 mm protrusion configuration (Figure 5-6b). As discussed, Briaud et al. (2001) recommend a 1.0 mm protrusion into their EFA device when cohesive samples are tested. While this will probably increase erosion rate due to a normal force along their samples' front-face, it was unclear how this affected shear stress along the sample's surface. As implied, Figure 5b shows this 1.0 mm protrusion.

- Differential erosion configuration (Figure 5-6c). During previous SERF testing with cohesive sediment and rock, investigators often found that the upstream portions of the samples eroded much more slowly than their downstream portions. A photograph in Annandale (2006, p. 287) appears to show similar behavior during an EFA test. Figure 5c is meant to approximate this phenomenon. In this configuration, the front half of the sample is held flush with the flume bottom, while its back edge is recessed 0.50 in. (1.27 cm) below the flume floor and a linear plane is used to connect the two points.

- Wavy configuration (Figure 5-6d). The "wavy" configuration represents a worst-case "blocking" or "chunking" scenario often observed during cohesive and rock tests with flume-style devices. A random pattern of recesses was prepared to illustrate forcing on a very rough sample during an erosion test. This configuration was tested in two different ways. First, its top edge was held level with the flume bottom. Then, average elevation was held flush with the flume bottom.

Smooth bed assumptions were made for each configuration, and results were compared with smooth, flush results. Amplification factors were computed by dividing non-uniform configuration shear stresses by flush configuration shear stresses. Because the grid points did not align exactly with one another, an interpolation algorithm was used. Results are presented from Figure 5-7 through Figure 5-11. A table of average amplification factors was also prepared (Table 5-1).

Finally, the sample-portion of the SERF was roughened using the same roughness coefficients developed in Figure 5-2. Simulated flow was applied at 5.0 m/s to illustrate a representative worst-case flow condition. Contour maps were generated of bed shear stress as a function of downstream flume distance to quantify shear stress development along the sample-length as a function of roughness (Figure 5-11). Similarly, the centerlines of each contour plot were compared with one another (Figure 5-12). The hope from this analysis was to provide a possible explanation for "blocking" or "chunking" during erosion testing.

5.4 Discussion

Figure 5-2 and Figure 5-3 appear to show strong agreement with Crowley et al. (2012a). The trend in Figure 5-2 looks nearly identical in shape to a similar relationship that was developed by previous researchers. In the previous study, the relationship was developed by back-solving Equation 2-4 for k_s using measured shear stress data. Of course, previously reported values for k_s do not match r found during this study because k_s was based upon an instrument-specific hydraulic diameter. But, it is encouraging that the shape of the relationships between roughnesses and grain sizes is similar.

Figure 5-4 appears to confirm previous results in that as roughness increases, pressure differential does not significantly increase. This is believed to be caused by small rough sample area relative to the flume's hydraulic diameter. And, this appears to solidify previous arguments that using Δp to estimate shear stress in piston-style erosion equipment is ineffective.

Results for variable-testing configurations appeared to show that small changes in sample geometry may have large effects on localized shear stresses. For the case of protruding samples (conical protrusion configuration and 1 mm protrusion configuration), average surface shear stress was similar to shear stresses for a flush specimen. However, as demonstrated in Figure 5-7, localized amplification factors for a protruding specimen may become quite large – as much as 6.0 times that for a flush specimen. This may affect localized erosion rates, and brings into question the validity of assuming a constant shear stress for the entire sample surface.

The recessed specimens exhibit more significant problems. As samples become more recessed, average shear stress appears to become significantly affected. For the differential erosion configuration, average shear stress was on average only approximately 0.72 times the shear stress for a flush sample on average. However, as demonstrated in Figure 5-9, localized shear stresses near the sample's downstream-edge may reach values as high as 2.5 times the stress for a flush sample. Likewise, shear stress amplification factor appears to reach a similar maximum at the point where the sample begins to slope downward. This would appear to indicate that if differential erosion was to occur over time (and as discussed, it has been repeatedly observed during testing), the issue will exacerbate itself. In other words, because differential erosion occurred, a higher downstream-edge shear stress was produced in some locations. Ultimately, this may lead to higher downstream-edge erosion rates, which in turn would produce higher downstream stresses at certain localized positions. Meanwhile, the presence of these high-stress concentration regions appears to be somewhat balanced by other localized areas where shear stress is reduced. Thus, in

certain regions, “blocking” or “chunking” would appear to be encouraged based upon sample geometry and turbulent flow fluctuations.

The “wavy” configuration provided the most interesting results. As shown in Figure 5-10, random recesses may produce large amplification factors, although on average, shear stress appears to decrease. Conversely, in Figure 5-11 – where the sample was on-average level with the flume bottom – the average shear stress on the sample surface appears to be much closer to smooth wall results. The presence of localized large amplification factors in both cases appeared to correspond to “hills” or “valleys” along the sample. This would appear to indicate a similar phenomenon to the differential erosion configuration in terms of “blocking” or “chunking” encouragement. In other words, once “blocking” begins, the phenomenon exacerbates itself because of localized stress amplification. Meanwhile, areas that failed to erode will continue to fail to erode because the stresses upon these regions of the sample are too low.

Results in Figure 5-12 and Figure 5-13 appear to provide some explanation for the “blocking” or “chunking” phenomenon often observed during testing. As illustrated, when roughness is added to the flume (as would be the case when a sample is eroded), shear stress increases as a function of distance downstream. And, as roughness increases, the average shear stress upon the sample becomes and increasingly poor estimator of actual stress conditions. All samples appeared to exhibit approximately equal localized shear stresses for 2.0 mm. Very rough samples (samples with equivalent grain sizes of 1.0 mm and 2.0 mm) appeared to exhibit a local shear stress maximum just beyond this upstream 2.0 mm edge; while intermediate roughness specimens (specimens with roughnesses of 0.125 mm, 0.25 mm, and 0.5 mm) showed

maximum shear stresses closer to the samples' downstream edges. As shown in Figure 12, for very rough samples, once the localized maximum is reached, shear stress appears to level off and slightly decrease. This would appear to indicate that the sudden introduction of high roughness acts as a sort of "turbulent shock" to the flow system. Thus, adding high roughness generates enormous localized shear stresses that require some distance to resemble a more developed flow condition. This result appears to show, from a stress perspective, why "blocking" and "chunking" begin and persist throughout an erosion event. And it calls into question the accuracy of using an averaged shear stress to develop a sediment's erosion function during a piston-style erosion test.

For conservative testing results, estimated average shear stress must be lower than actual sample shear stress, or estimated erosion rate must be higher than actual sample erosion rate for a given shear stress. If erosion rate and shear stress are correlated to one another, then these results provide interesting clues as to how to properly implement flume-style erosion testing. First, it appears to be incorrect to keep the sample recessed relative to the flume bottom when differential erosion, blocking, or chunking occur because doing so reduces shear stress in regions of the sample. This in turn may reduce localized erosion rates, which would lead to a non-conservative erosion function. A better solution is to keep an eroding sample in a piston-style device level with the flume bottom on average. Briaud et al.'s (2001) recommendation for a 1.0 mm protrusion appears to be close to correct, although even this recommendation may not go far enough. The Briaud et al. (2001) recommendation does not take into account a situation where a localized portion of the sample erodes more than 1.0 mm. From the

results in this chapter, for a situation such as Briaud et al.'s EFA where it may be difficult to quantify average sample elevation, the most conservative method for an erosion test would be to keep the sample's lowest elevation point flush with the flume bottom, regardless of any protrusion into the device.

Table 5-1. Average amplification factors for each SERF configuration

Configuration	Average Amplification Factor
Conical protrusion	1.01
1 mm protrusion	0.98
Differential erosion	0.72
Wavy – top portion level with flume bottom	0.37
Wavy – average elevation level with flume bottom	1.16

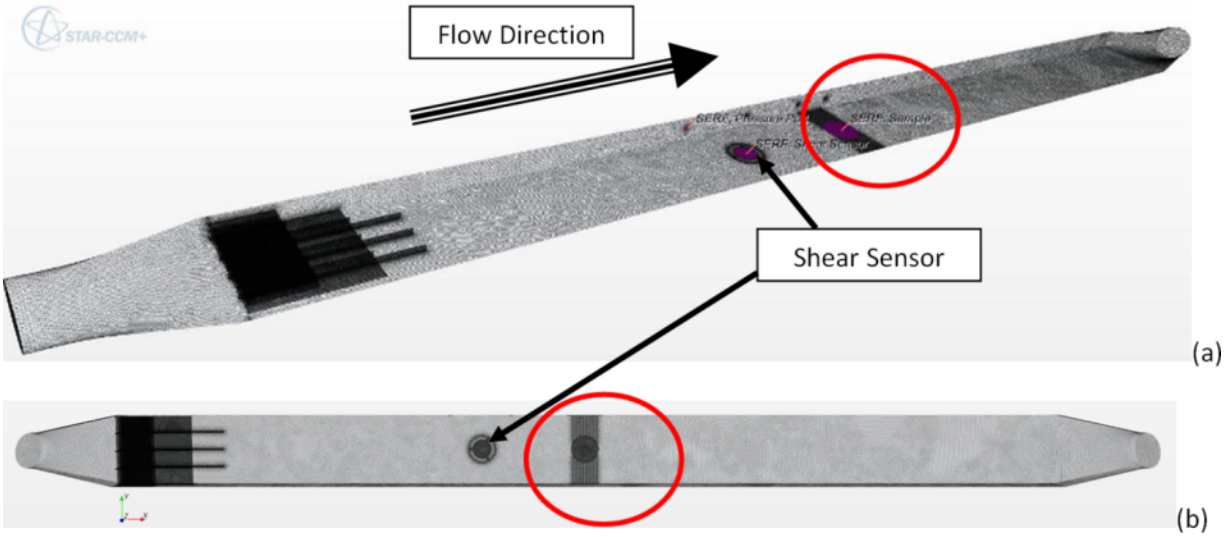

Figure 5-1. SERF grid showing (a) three-dimensional view and (b) top-view. The circled portion of the grid is an approximate representation of the location of the sample.

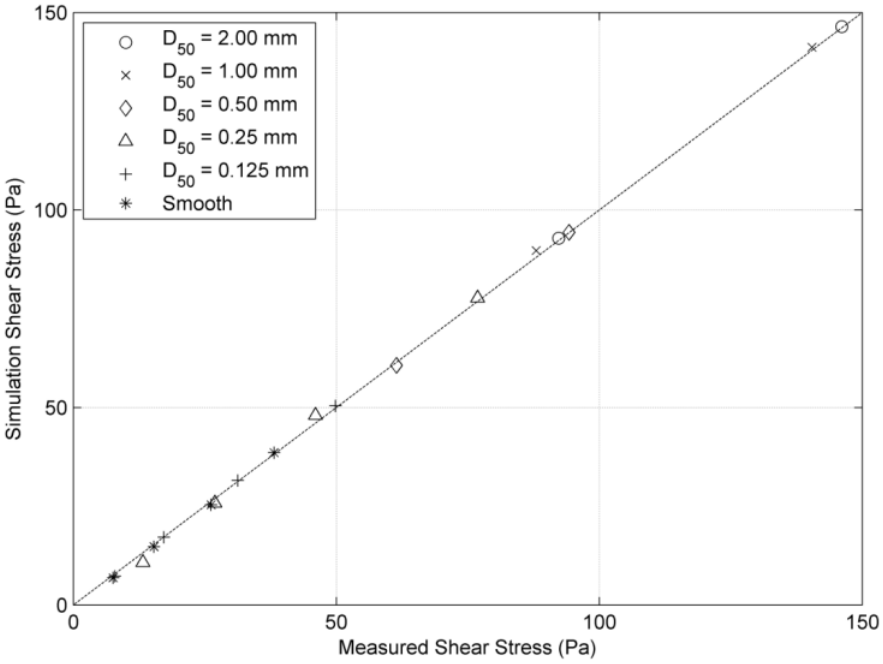

Figure 5-2. Modeled shear stress versus measured shear stress

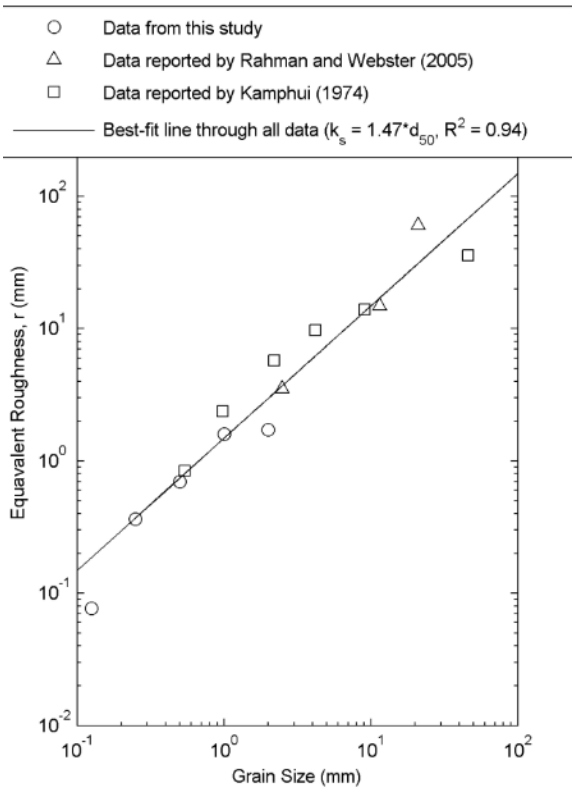

Figure 5-3. Relationship between grain size and equivalent roughness

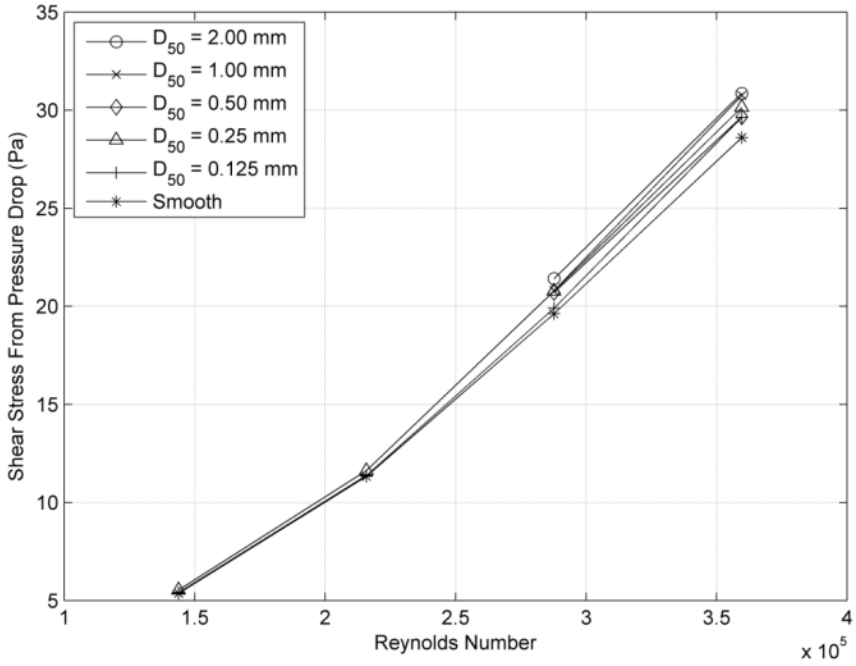

Figure 5-4. Computed shear stress using pressure drop from CFD model for varying roughnesses

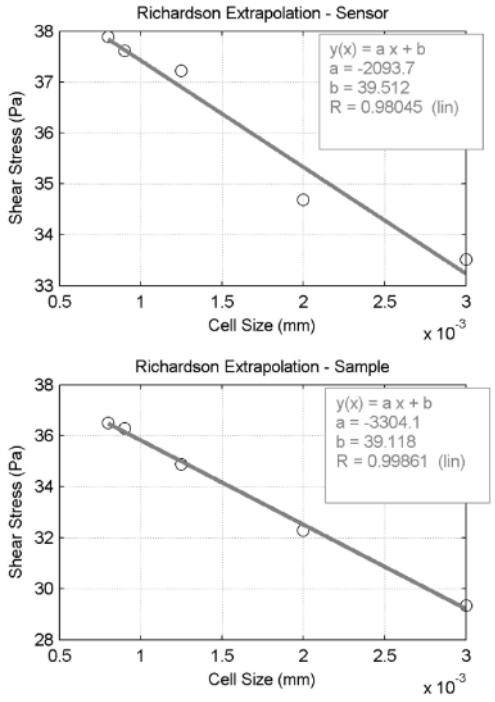

Figure 5-5. Grid sensitivity study results

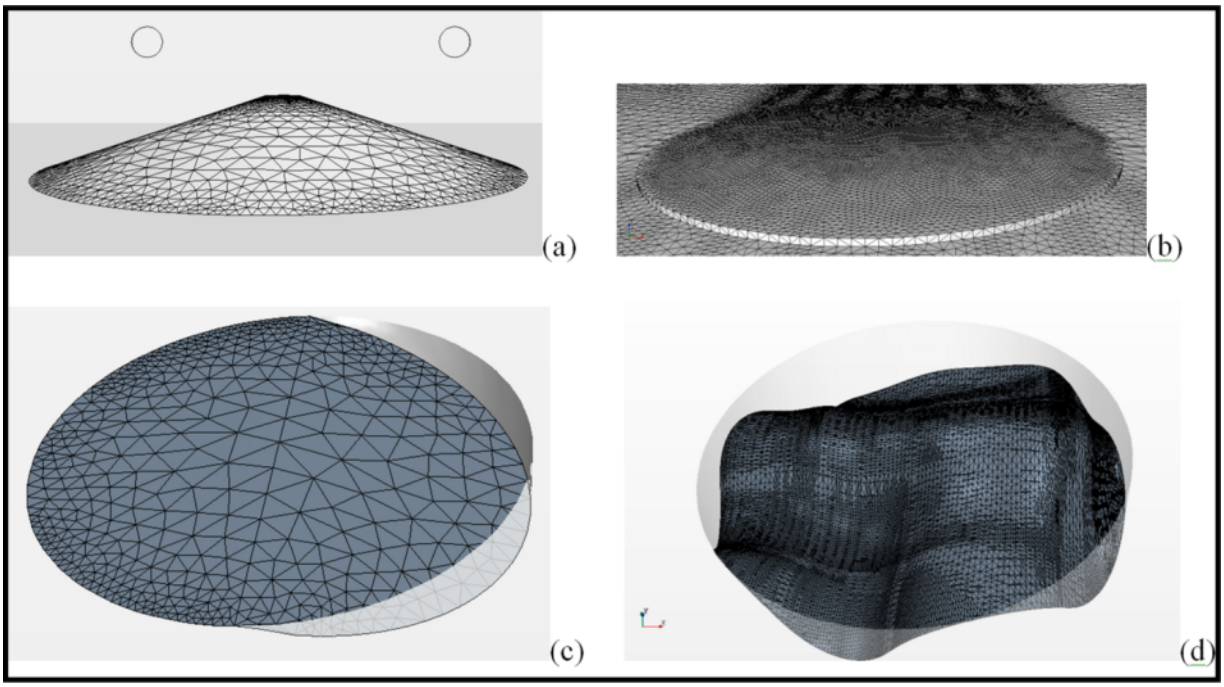

Figure 5-6. SERF sample-section configurations showing (a) conical protrusion configuration; (b) 1 mm protrusion configuration; (c) differential erosion configuration; and (d) wavy configuration. Flow is from left-to-right for all configurations.

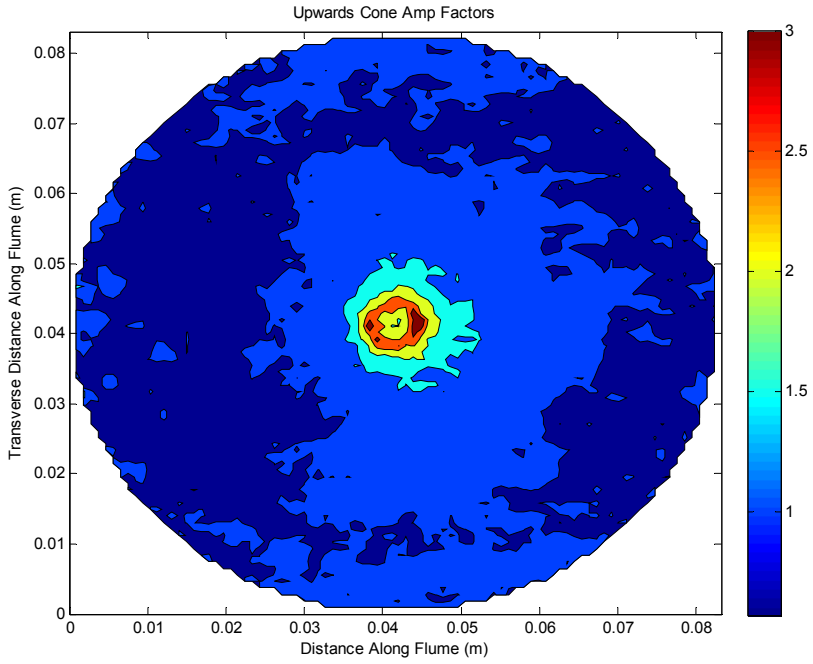

Figure 5-7. Amplification factors for conical protrusion configuration. Flow direction is along the x-axis.

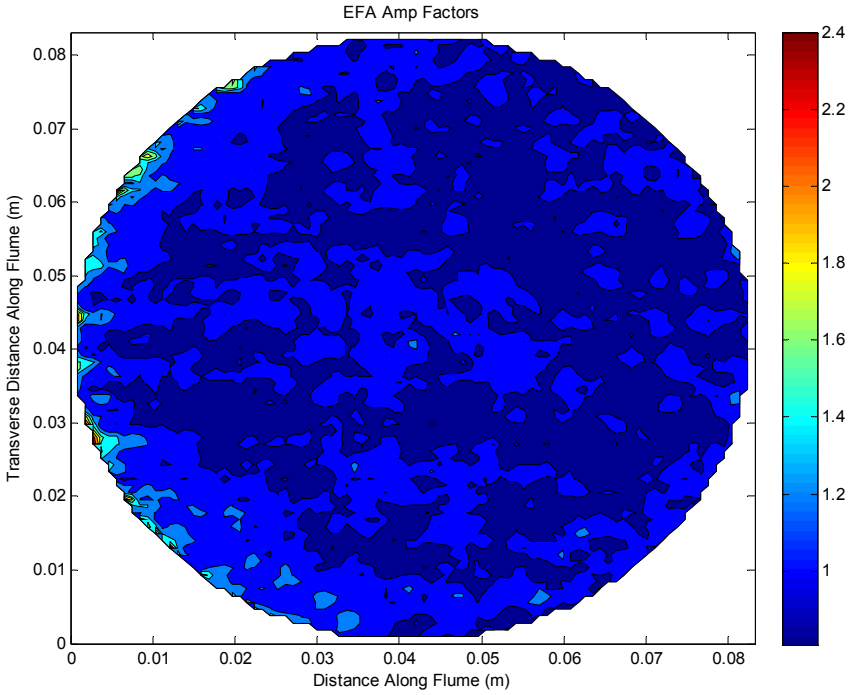

Figure 5-8. Amplification factors for 1 mm protrusion configuration. Flow direction is along the x-axis.

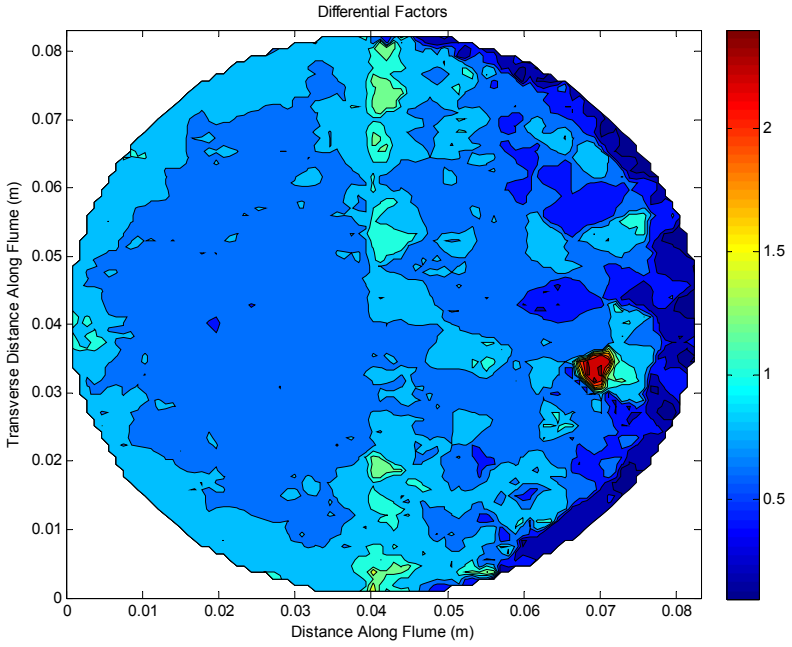

Figure 5-9. Amplification factors for differential erosion configuration. Flow direction is along the x-axis.

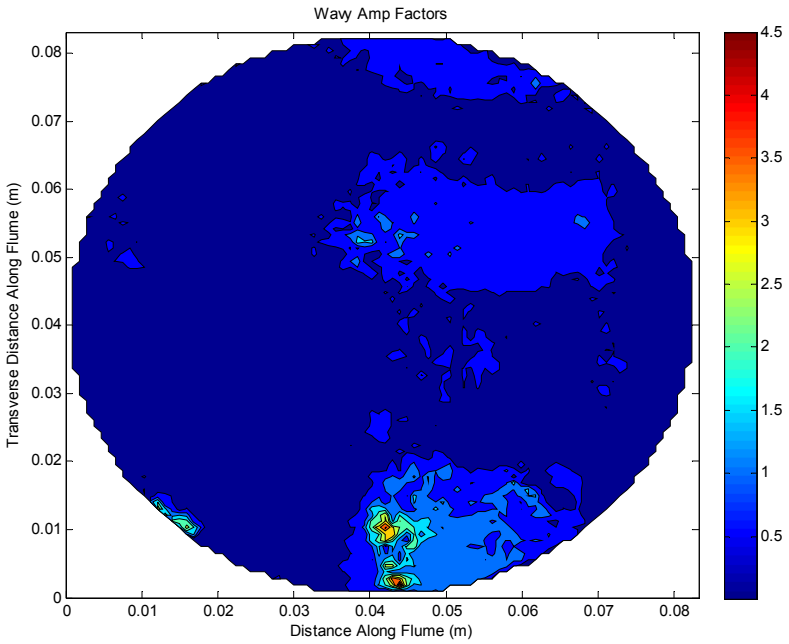

Figure 5-10. Amplification factors for wavy configuration when top edge is held flush with flume bottom. Flow direction is along the x-axis.

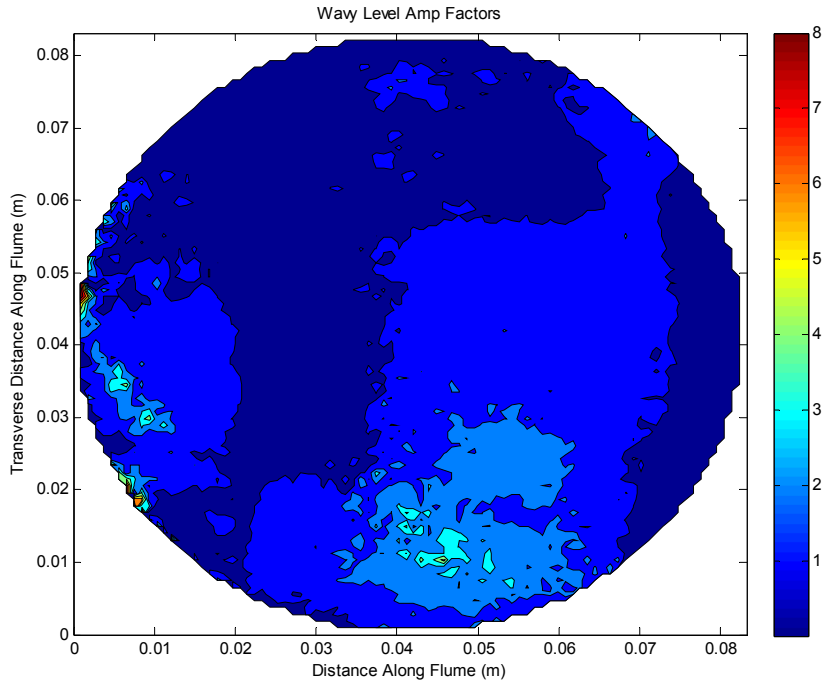

Figure 5-11. Amplification factors for wavy configuration when average elevation is held flush with flume bottom. Flow direction is along the x-axis.

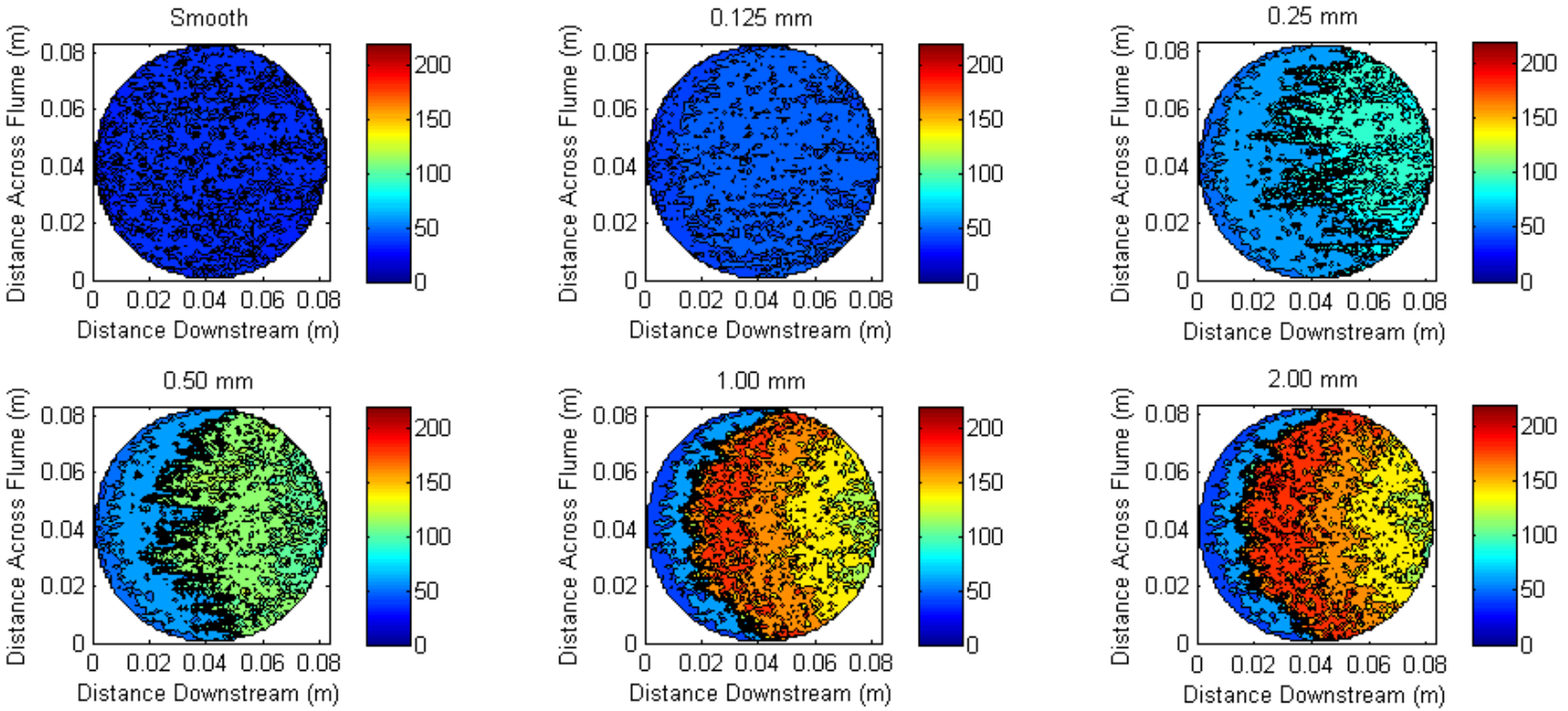

Figure 5-12. Local shear stress variations for uniformly rough samples (contour units are in Pa)

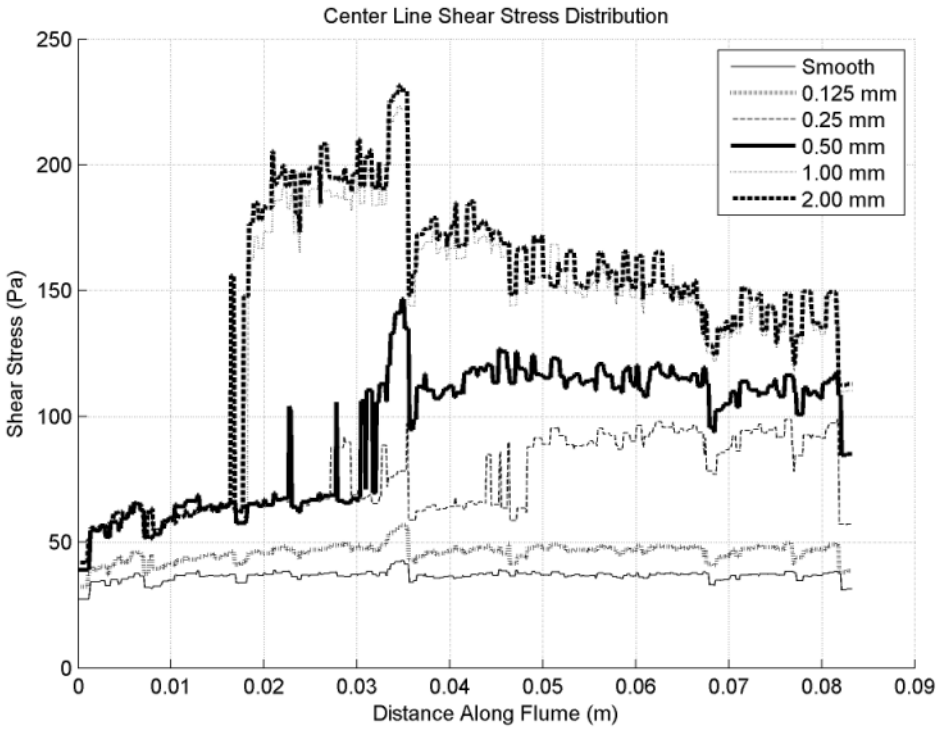

Figure 5-13. Centerline shear stress variations for uniformly rough samples

CHAPTER 6
FIELD TESTING SAMPLES IN THE SERF

6.1 Introduction

Recall, that one of the original goal of this project was to determine if field samples displayed differential erosion characteristics throughout their sample lengths. During the previous SERF project, several synthetic samples showed periods of rapid erosion interspersed with periods of very slow erosion (Bloomquist and Crowley, 2010). Slow erosion appeared to correspond to lift-interfaces. As of the conclusion of the previous project, it remained unclear whether or not natural samples would behave similarly. Since the SERF is the only known device that can measure real-time erosion (as a function of length through a sample), this project was proposed. As a secondary goal, it would be beneficial to estimate erosion functions for several materials using the SERF to demonstrate that the instrument is capable of functioning in this capacity. Based upon the shear stress analysis discussed throughout this project, conservative shear stress approximations can be made to develop these erosion functions.

6.2 Methodology

Prior to testing, samples were saturated for a minimum of 24 hours to mimic field conditions. For erosion function development tests, a flow rate was randomly chosen. This flow rate was held constant until certain criteria were met. Early-on during testing, a minimum of 5.0 cm of erosion or 15.0 minutes of sample testing time were used as a baseline. However, eventually stiffer sediments were observed, and these criteria were changed such that 4.0 hours of testing time became the minimum. Eventually, as investigators became comfortable working with stiff specimens, “final” criteria were

established whereby a minimum of 4.0 cm of erosion or 1.0 hour of testing represented minimum testing conditions.

Once the time/erosion criterion had been satisfied for a given flow rate (shear stress), a new flow rate was chosen, and the procedure was repeated. Flow rate was converted to shear stress by assuming smooth-wall approximations using empirical data from the previous SERF project (Figure 6-1). As discussed in Chapter 5, due to localized stress variability, the smooth-wall approximation is the only known method whereby investigators can be assured of generating a conservative erosion function. As implied by the previous statement, all sediments were kept at least on-average level with the flume bottom.

Then, for each shear stress (flow rate), erosion was plotted as a function of time, and a best-fit linear regression line was fit to the data (of the form $y = ax + b$ or $y = ax$ depending on the dataset). The slopes from these erosion lines were then plotted as a function of estimated shear stress (from Figure 6-1), and erosion functions were developed.

For sample-variability tests, a constant flow rate was chosen where moderate erosion was qualitatively observed. This erosion rate persisted throughout the test. Again, specimens were kept at least on-average level with the flume bottom so that minimum shear stress criteria were met during the test.

Tests were conducted on specimens from various FDOT job sites around Florida to determine the erosion behavior of local sediments. In total, sediments from four sites were examined – Anderson Street (AS), River Road at Gum Creek (RR), District 5 (D5), and Jewfish Creek (JCB).

Additionally, some out-of-state specimens from an undisclosed location were made available for testing. These out-of-state specimens were particularly valuable for a number of reasons. First, they were from an existing river near an existing bridge. Because of this, investigators could determine how river geometry and the existing structure affected local scour for virgin soil near the existing structure. As implied, these specimens were obtained from depths that would be typical for scour – between the mudline and 25 feet below the mudline. This allowed investigators to analyze the role of depth on erosion function development. Finally, these specimens were all very close to one another spatially (within 2.75 miles of each other). This allowed investigators to approximate the role of shoreline proximity on erodibility.

All specimens (both from Florida and out-of-state) were similar in that they were a combination of sand and silty/clayey material.

6.3 Results

Raw testing (and approximate grain size distributions when available) are presented in Appendix B (for Florida specimens) and Appendix C (for non-Florida specimens). Erosion functions that were developed from these tests are presented in Appendix D (for Florida-specimens) and Appendix E (for non-Florida specimens). Additionally, results are reproduced in tabular form (Table 6-1 through Table 6-5). Note that apparent decreases in erosion versus time raw data graphs are a result of the SERF's ultrasonic sensor-stepper motor feedback system. The ultrasonic sensor is continually monitoring specimen position. Thus, if the computer "thinks" that a sample has over-advanced, it will attempt to correct the situation and retract the specimen.

Because of the proximity of out-of-state specimens to one another, a more in-depth analysis was conducted to analyze the roles of depth and spatial variability on erosion function development (please see below). Please note, some highlights from the appendices have been reproduced at the end of this Chapter to add to the discussion presented below.

6.4 Discussion

6.4.1 Florida Specimens

Successful erosion functions were developed for two AS specimens, one RR specimen, one D5 specimen, and one JCB specimen. Investigators were unable to produce erosion rate versus shear stress relationships for one JCB specimen, one RR specimen, and one AS specimen due to the low erodibility of these materials.

When successful erosion rate versus shear stress relationships were obtained, testing usually followed a similar pattern. Specimens were usually uniform, and during testing, little to no layering was observed. At times during testing, a sediment layer became obvious. This allowed investigators to eliminate some data points (grayed rows in Table 6-1 and Table 6-2) and develop physically-meaningful curves from the data. To illustrate the presence of sediment layers, tests AS-UF2 and AS-UF3 were conducted (Figure 6-2 and Figure 6-3). As shown, through the tests, the sediment appeared to become stiffer and more erosion-resistant. This leads to perhaps the most important finding from this study – <u>erosion of specimen that appears to be qualitatively the same from top-to-bottom may nonetheless be hypersensitive to erosion</u>.

Understanding the implications of this result is essential if in the future, the SERF is to be used for design. First, if SERF results are to be used to predict scour depths,

sediment specimens must be taken at varying locations and varying depths. Secondly, it is essential that an experienced operator with the instrument has the expertise to identify soil layers. If a layer is suspected, the operator should retest a previous shear stress to confirm the existence of a layer. Third, during scour computations, it is incorrect to simply assign a “bulk erosion rate” to a certain bed material. In fact, it is more useful to assign several erosion rates based upon depth.

Successful erosion function development usually occurred when stiffness was a function of depth. When stiffness was no longer a function of depth, it was not possible to distinguish between “hard” layers and “soft” layers. As a result, “chunking” during these tests increased; and it became impossible to develop a meaningful erosion rate versus shear stress relationship. This phenomenon occurred during test AS-UF4 for example. Sometimes, the reasons for layering were obvious. For example, during test RR B3 9’-11’, a large piece of organic matter was obviously obstructing erosion for much of the test (Figure 6-4, Figure 6-5, and Figure 6-6).

The failure of development of an erosion function for all Jewfish creek specimens is interesting. As shown in Figure 6-7, investigators were able to develop an erosion function for one specimen from 12 ft. to 14 ft. However, the 10 ft. to 12 ft. specimen was highly erosion-resistant. As shown in Table 6-1, one specimen was tested at varying shear stresses up to 200 Pa for 2.5 hours and then tested for an additional 2.5 hours at 200 Pa. No significant erosion was observed (Figure 6-8 and Figure 6-9).

The sample was dried for two days to get a qualitative gauge on water content’s effect on erosion. This specimen did erode, and an erosion function was developed (Figure 6-10). Another “dry” JCB specimen was tested immediately thereafter, but this

specimen also did not erode. These discrepancies are not necessarily indicative of testing inconsistencies. As shown in the previous SERF study, results were repeatable for synthetic specimens. It is more likely that these seemingly conflicting results demonstrate erosion's hypersensitivity to soil spatial variability.

6.4.2 Out-of-State Specimens

Results from out-of-state tests appeared to confirm results from Florida-tests. Additionally, because these specimens were spaced so closely together both spatially and in terms of depth, results from out-of-state tests was able to significantly enhance investigators' understanding of the process of erosion function development using the SERF.

In general, most out-of-state tests obeyed the "higher erosion rate at higher shear stress" principle. Sometimes, organic matter would affect erosion function development (Figure 6-10, Figure 6-11, and Figure 6-12 for example). Similar results in Florida would probably be expected for situations where specimens are taken near the coast in a shallow-water environment. This is important to note if the SERF is to be used for design. The presence of large shells appears to cause inaccurate SERF testing results because the large shells tend to block erosion. Capturing these shells may be unpredictable during boring; therefore, it is recommended that several erosion testing specimen be obtained if the device is to be used for design.

In addition to the organic anomalies, layering during testing was also a large issue, as it was during Florida-specimen testing. Examination of the out-of-state dataset allowed investigators to categorize three distinct layering events. The first layering event is similar to the layering that was discussed in Section 6.4.1 and will be named

“depth layering” because as implied, like the Florida samples, specimens appeared to stiffen as a function of localized depth.

While quantitative data were not obtained to illustrate this trend for the out-of-state specimens, there were several instances where lower erosion rates were presumably shown at higher shear stresses. Qualitatively, this was easily observed. For example, suppose the following shear stress sequence was conducted: 10.0 Pa, 5.0 Pa, 20.0 Pa, 15.0 Pa, 25.0 Pa (assumed shear stresses using a smooth wall). Under such a scenario, rapid erosion would be seen at 15.0 Pa but not 25.0 Pa. Usually, under these conditions, the erosion versus time curve for the penultimate test for a given specimen would “level off” (as illustrated in Figure 6-14). Thus, investigators would “know” that the sample was stiffening. This observation of “localized layering” introduces an interesting testing paradox that would probably be best resolved in the future by obtaining “sample clusters” from the same depths and approximately same locations. Each sample from a “cluster” could be tested at a single stress to a meaningful “stiffening cutoff point.”

The second “layering event” will be called “localized layering.” During this phenomenon, a stiff layer would be observed partway through a specimen. As soon as the water eroded the stiff layer, rapid erosion would resume in the looser sediment below the stiff obstruction. Sometimes, the reverse of this phenomenon occurred where a loose layer would be surrounded by stiff sediment. These layers are undoubtedly due to a non-uniform deposition event. A similar phenomenon should be expected in Florida in the vicinity of rivers (particularly the Suwannee and St. John’s River) and coastal

inlets because of differing rates of deposition/erosion at these locations due to different flow events.

The third layering event will be called “blocking” or “chunking” and it appears to resemble rock-like erosion. This phenomenon has been repeatedly observed in Florida specimens as well, and it has been discussed in previous Geotechnical Research in Progress meetings and the 2010 SERF Final Report (Bloomquist and Crowley, 2010). In the past, this layering event was referred to as “blocking” or “chunking.” Analysis of the out-of-state specimens allowed investigators to distinguish this layering event from “depth layering” and “localized layering.” An illustration of data associated with “blocking” or “chunking” is presented in Figure 6-15. Essentially, during a “flat-line” portion of an erosion versus time curve, small flocs of clay eroded from the specimen. These flocs were too small to trigger sample advancement, but they were visually observed. After some time of small floc removal, a large “chunk” of material would erode. The sample would advance, and the “floc-weakening” cycle would repeat.

Investigators developed a hypothesis for the cause of this “floc-weakening” cycle associated with “blocking” or “chunking.” A portion of a “failed” test was allowed to dry; it was broken in half; and several distinct layers were observed (Figure 6-16). “Floc-weakening” is believed to occur until enough of an exposed sand layer is uncovered to cause an entire clay-sand layer to erode. Then, the cycle repeats until the next clay-sand layer is removed. This is very similar to “localized layering” except that the stiff/loose cycle appears to repeat.

As implied in Table 6-3 through Table 6-5, some data points were eliminated due to layering so that physically-meaningful erosion functions could be developed (as

illustrated in dark-grey; exactly as was the case for the Florida specimens). Sometimes, specimens were too layered for meaningful erosion functions to be developed (OS-51, OS-44, and OS-26); or meaningful erosion was not observed (OS-5 and OS-6). These scenarios are illustrated in light-grey and strikethrough font in Table 6-3, Table 6-4, and Table 6-5.

Meaningful erosion data were compiled an approximated as a function of estimated shear stress (Figure 6-17). This is uniquely acceptable for this dataset because of its proximity – which was the advantage of including data from out-of-state in this report.

According to previous research (Partheniades 1965 for example), erosion of cohesive soils may be approximated a critical shear stress deficit times a material-specific erosion constant:

$$E = M(\tau_b - \tau_c) \tag{6-1}$$

where τ_b is the bed shear stress; τ_c is the critical shear stress, or stress required for incipient motion; and *M* is the material-specific constant. For each erosion function dataset, zero-erosion points were eliminated at lower stresses so that a critical shear stress could be developed by fitting a best-fit y=mx+b equation to erosion function data and determining the x-intercept. Then, erosion data were used to solve for *M* for each specimen, and an average *M* value was obtained (Table 6-6). Note that average shear stresses were approximately 10.6 Pa and average values for *M* were 44.5 cm/Pa-hr. However, standard deviations of these variables were 11.7 Pa and 71.0 Pa/cm-hr respectively. This would appear to indicate large variability among the data. Erosion was nondimensionalized by *M* and τ_c while τ_b was nondimensionalized by τ_c so that

nondimensionalized erosion plot could be developed (Figure 6-18). A best-fit line was fit to the data of the form y=ax-1 to determine error associated with the computation of *M*. The slope of this line was 0.99, while its R^2 value was 0.9025.

As shown in Figure 6-17, it is very difficult to generalize an erosion curve for these data. This was unexpected – especially because specimens were relatively close to one another both in terms of depth and spatial proximity. However, investigators knew that the specimens that failed to erode were obtained near the river's shoreline. Knowing this, investigators hypothesized that spatial variability may affect erosion at this particular site. Several "groupings" were generated in the hopes of producing more useful data. Data were divided into three categories – near the shoreline, near the main channel, and near the river's existing bridge. Results (Figure 6-19) appeared to show three distinct erosion patterns. Finally, depth was analyzed for data near the main channel by splitting main channel data between specimens taken at depths greater than 15 feet and specimens taken from depths less than 15 feet. Results (Figure 6-20) appeared to indicate that no significant difference was observed. As indicated, depth layering was repeatedly observed throughout testing; but recall that when it occurred, investigators removed these data points.

Conclusions

As indicated throughout this discussion, a number of important conclusions about the behavior of field specimens were generated from this study:

- Using the stress approximations discussed in Chapter 5, development of an erosion functions appears to be effective using the SERF device.
- Erosion for a similar soil-type may be highly affected by depth and layering. This appears to confirm previous results using synthetic specimens; and it calls into

further question the pre-SERF method of assigning a bulk erosion rate based upon $\Delta y/\Delta t$ to a specimen.

- To properly determine a sediment's erosion function, an experienced SERF operator is needed who fully understands testing with the instrument and data analysis. It should be expected that due to layering, testing patterns will need to be adjusted, stresses (flow rates) may need to be repeated, and some data points may need to be eliminated to account for layering.

- Virgin sediment near an existing structure may exhibit high erosion rates when compared with virgin soil further away from the existing structure. This should be expected due to previous scour from the previous structure. It appears to be important to take this variable into account for design.

- The most important conclusion from this study pertains to use of the SERF for future design. The SERF test is somewhat unique in that a test in the instrument necessarily destroys a soil specimen. Therefore, as the test persists, a paradox exists if "layering" is observed whereby the only way to "prove" layering (and quantitatively account for it) would be to erode an entire specimen at one shear stress. However, eroding the specimen at one shear stress would destroy it and render development of an erosion function impossible. The solution is to rethink sample collection when specimens are to be used for SERF tests. At locations of interest (i.e., near proposed bridge piers), multiple samples should be obtained from the same depth. Each specimen should be tested at a single shear stress, and erosion should be quantified as a function of both stress and depth.

  Physically, depth-dependence for cohesive sediment should be expected because stiffness/density should increase as a function of depth due to consolidation. Still, the depth dependence shown during these tests is interesting because it was displayed over relatively short (a few centimeters) sampling lengths. And the difference between one set of results and another was often quite dramatic. Again, the "sampling-cluster method" is highly recommended if/when the SERF is to be used for design so that depth-dependence can be quantified.

Table 6-1. SERF results from Florida specimens part 1

Sample Designation	Pump Frequency (Hz)	Shear Stress (Pa)	Erosion Rate (cm/s)	Sample Starting Point (cm)	Sample End Point (cm)
	10	2.35	0.00E+00	0.00	0.00
	15	4.05	1.37E-04	0.00	0.14
	20	6.72	0.00E+00	0.14	0.23
	25	10.37	0.00E+00	0.23	0.22
	30	14.98	5.24E-05	0.22	0.33
	35	20.56	2.09E-02	0.33	5.66
	31	16.02	2.50E-03	5.66	7.90
	33	18.21	1.18E-04	7.90	8.17
	34	19.37	1.02E-03	8.17	8.75
AS-UF1	20	6.72	0.00E+00	8.75	8.75
	25	10.37	0.00E+00	8.75	8.75
	30	14.98	0.00E+00	8.75	8.75
	35	20.56	1.12E-02	8.75	13.75
	34	19.37	6.63E-03	13.75	16.60
	36	21.80	2.40E-03	16.60	18.24
	37	23.07	1.91E-04	18.24	18.33
	38	24.38	0.00E+00	18.33	18.37
	40	27.12	0.00E+00	18.37	18.37
	35	20.56	0.00E+00	18.37	18.37
AS-UF2	30	14.98	Varied	0.00	12.48
AS-UF3	35	20.56	Varied	0.00	12.18
	20	6.72	5.92E-02	0.00	1.93
	25	10.37	4.47E-03	1.93	4.14
	30	14.98	3.89E-03	4.14	5.39
AS-UF4	35	20.56	5.78E-04	5.39	5.43
	31	16.02	1.88E-02	5.43	11.14
	29	13.98	1.10E-02	11.14	13.61
	25	10.37	1.16E-02	13.61	15.50
	20	6.72	0.00E+00	0.00	-0.11
	25	10.37	0.00E+00	-0.11	-0.11
AS-100 #5	30	14.98	0.00E+00	-0.11	-0.11
	35	20.56	2.68E-03	-0.11	8.95
	34	19.37	1.44E-02	8.95	14.57
	33	18.21	4.36E-03	14.57	16.88
	25	10.37	4.42E-04	0.00	0.36
	30	14.98	3.02E-03	0.36	5.99
RR B-1E	28	13.02	1.89E-03	5.99	7.73
	29	13.98	0.00E+00	7.73	8.80
	20	6.72	1.26E-04	0.00	0.06
	25	10.37	1.51E-03	0.06	0.56
	30	14.98	1.36E-02	0.56	7.25
	28	13.02	2.59E-03	7.25	10.57
	28	13.02	9.15E-04	10.57	10.99
RR B3 9'-11'	29	13.98	0.00E+00	10.99	10.90
	30	14.98	2.88E-04	10.90	11.15
	35	20.56	9.91E-04	11.15	11.36
	40	27.12	9.30E-04	11.36	11.51
	45	34.64	8.07E-04	11.51	12.60
	50	43.13	1.83E-03	12.60	13.18

Table 6-2. SERF results from Florida specimens part 2

Sample Designation	Pump Frequency (Hz)	Shear Stress (Pa)	Erosion Rate (cm/s)	Sample Starting Point (cm)	Sample End Point (cm)
D-5 S-2	20	6.72	3.89E-05	0.00	0.53
	30	14.98	0.00E+00	0.53	0.55
	35	20.56	6.39E-05	0.55	0.55
	40	27.12	3.94E-04	0.55	0.82
	45	34.64	8.13E-04	0.82	1.07
	50	43.13	6.91E-03	1.07	6.50
	48	39.62	5.76E-02	6.50	10.72
JCB 12'-14'	20	6.72	3.30E-04	0.00	0.13
	25	10.37	5.47E-02	0.13	7.31
	21	7.37	4.90E-03	7.31	9.68
	22	8.06	2.24E-03	9.68	10.69
	23	8.79	2.09E-03	10.69	12.18
	24	9.56	0.00E+00	12.18	12.11
	25	10.37	0.00E+00	12.11	11.92
	30	14.98	0.00E+00	11.92	11.92
JCB 10'-12' (wet) (lasers only)	20	6.72	0.00E+00	Note: Sample did not erode. Indicated Shear stresses were held for a minimum of 10 minutes (approx. 2.5 hrs. of total testing time). Then, 200 Pa was held for an additional 2.5 hours. Still no erosion.	N/A
	25	10.37	0.00E+00		N/A
	30	14.98	0.00E+00		N/A
	35	20.56	0.00E+00		N/A
	40	27.12	0.00E+00		N/A
	45	34.64	0.00E+00		N/A
	50	43.13	0.00E+00		N/A
	55	52.60	0.00E+00		N/A
	60	63.03	0.00E+00		N/A
	65	74.43	0.00E+00		N/A
	70	86.80	0.00E+00		N/A
	75	100.15	0.00E+00		N/A
	80	114.46	0.00E+00		N/A
	85	129.74	0.00E+00		N/A
	90	145.99	0.00E+00		N/A
	95	163.21	0.00E+00		N/A
	100	181.40	0.00E+00		N/A
	105	200.57	0.00E+00		N/A
JCB 10'-12' (dry, test 1) (lasers only)	20	6.72	0.00E+00	0.00	0.00
	25	10.37	0.00E+00	0.00	0.00
	30	14.98	0.00E+00	0.00	0.00
	35	20.56	0.00E+00	0.00	0.00
	40	27.12	0.00E+00	0.00	0.00
	45	34.64	0.00E+00	0.00	0.00
	50	43.13	0.00E+00	0.00	0.00
	55	52.60	3.82E-03	0.00	1.70
	60	63.03	1.31E-02	1.70	10.29
	59	60.86	5.47E-04	10.29	10.59
	58	58.74	6.18E-03	10.59	16.69
JCB 10'-12' (dry, test 2) (lasers only)	20	6.72	0.00E+00	Note: Sample did not erode. Indicated Shear stresses were held for a minimum of 10 minutes (approx. 2.5 hrs. of total testing time).	N/A
	25	10.37	0.00E+00		N/A
	30	14.98	0.00E+00		N/A
	35	20.56	0.00E+00		N/A
	40	27.12	0.00E+00		N/A
	45	34.64	0.00E+00		N/A
	50	43.13	0.00E+00		N/A
	55	52.60	0.00E+00		N/A
	60	63.03	0.00E+00		N/A

Table 6-3. SERF results from out-of-state specimens part 1

SAMPLE NAME	PUMP FREQUENCY (HZ)	APPROX. SHEAR STRESS (ASSUMING SMOOTH WALL, PA)	ESTIMATED EROSION RATE (CM/HR)
OS-35 60-62, TOP	15.00	4.05	0.138
	20.00	6.72	0.041
	22.00	8.06	0.931
OS-35 60-62, BOTTOM	14.90	4.01	0.000
	18.80	5.99	0.000
	25.54	10.82	0.009
	28.00	13.02	49.570
	32.40	17.54	55.570
	38.47	25.01	215.540
OS-34 52-54, TOP	17.70	5.37	220.200
	24.56	10.01	260.680
	30.02	15.00	1344.000
OS-34 52-54, BOTTOM	17.00	5.00	80.016
	25.56	10.84	442.590
	30.02	15.00	84.511
~~OS-51, TOP~~	~~17.00~~	~~5.00~~	~~11.710~~
	~~24.56~~	~~10.01~~	~~5.890~~
	~~30.02~~	~~15.00~~	~~30.410~~
~~OS-51, BOTTOM~~	~~17.00~~	~~5.00~~	~~7.708~~
	~~24.56~~	~~10.01~~	~~49.570~~
OS-23 U-1 30-32, TOP	17.00	5.00	10.162
	24.56	10.01	780.020
	30.02	15.00	176.110
OS-23 U-1 30-32, BOTTOM	14.89	4.00	0.000
	21.91	8.00	61.607
	26.90	12.01	46.166
	32.82	18.01	212.450
	36.17	22.01	2000.000
OS-34 63-66 TOP	17.00	5.00	0.070
	24.56	10.01	0.586
	30.02	15.00	189.490
	21.91	8.00	54.280
	26.90	12.01	7.576
OS-34 63-66 BOTTOM	30.02	15.00	209.800
	26.90	12.01	12.893
	21.90	7.99	10.312
OS-33 TOP	17.00	5.00	478.170
	21.19	7.50	307.520
	24.56	10.01	111.940
	27.45	12.51	154.250
	30.02	15.00	176.250
	32.37	17.51	754.800
	34.54	20.01	333.360
	36.56	22.50	576.660
	38.47	25.01	455.750
	40.28	27.51	506.650
	42.00	30.01	494.170
OS-33 BOTTOM	17.00	5.00	436.620
	30.02	15.00	80.502
	34.54	20.01	81.228
	38.57	25.14	134.430
	42.00	30.01	184.930

Table 6-4. SERF results from out-of-state specimens part 2

SAMPLE NAME	PUMP FREQUENCY (HZ)	APPROX. SHEAR STRESS (ASSUMING SMOOTH WALL, PA)	ESTIMATED EROSION RATE (CM/HR)
OS-35 46-48 TOP	17.00	5.00	280.460
	34.54	20.01	432.340
	42.00	30.01	1035.700
~~OS-44 BOTTOM~~	~~17.00~~	~~5.00~~	~~69.469~~
	~~24.56~~	~~10.01~~	~~316.930~~
	~~30.02~~	~~15.00~~	~~137.610~~
	~~21.19~~	~~7.50~~	~~7.433~~
	~~27.45~~	~~12.51~~	~~9.955~~
	~~32.37~~	~~17.51~~	~~20.204~~
~~OS-44 VERY BOTTOM~~	~~32.37~~	~~17.51~~	~~274.430~~
	~~34.54~~	~~20.01~~	~~211.890~~
	~~38.47~~	~~25.01~~	~~215.240~~
OS-28 TOP	17.00	5.00	66.297
	24.56	10.01	108.420
	30.02	15.00	157.240
	34.54	20.01	225.390
	38.47	25.01	67.485
OS-28 BOTTOM	21.19	7.50	59.580
	27.45	12.51	210.700
	32.37	17.51	163.210
	36.56	22.50	334.950
OS-104 BOTTOM	17.00	5.00	9.571
	24.56	10.01	0.000
	30.02	15.00	1.919
	34.54	20.01	0.000
	38.47	25.01	113.860
	42.00	30.01	707.850
	40.28	27.51	126.640
OS-104 TOP	21.19	7.50	3.615
	32.37	17.51	142.480
	36.56	22.50	331.670
	34.54	20.01	92.294
	38.47	25.01	521.980
~~OS-26 TOP~~	~~17.00~~	~~5.00~~	~~0.00~~
	~~24.56~~	~~10.01~~	~~9.72~~
	~~30.02~~	~~15.00~~	~~42.90~~
~~OS-26 BOTTOM~~	~~21.19~~	~~7.50~~	~~0.00~~
	~~27.45~~	~~12.51~~	~~0.00~~
OS-102 TOP	17.00	5.00	0.000
	24.56	10.01	0.000
	30.02	15.00	0.000
	34.54	20.01	698.740
	34.54	20.01	0.000
	38.47	25.01	0.000
	42.00	30.01	780.780
OS-102 BOTTOM	17.00	5.00	0.000
	45.23	35.01	0.702
	45.23	35.01	0.067
	45.23	35.01	0.000
	45.23	35.01	1411.400
	40.32	27.57	2.295
	42.00	30.01	237.440

Table 6-5. SERF results from out-of-state specimens part 3

SAMPLE NAME	PUMP FREQUENCY (HZ)	APPROX. SHEAR STRESS (ASSUMING SMOOTH WALL, PA)	ESTIMATED EROSION RATE (CM/HR)
~~OS-5 TOP~~	~~17.00~~	~~5.00~~	~~0.000~~
	~~30.02~~	~~15.00~~	~~0.000~~
	~~38.47~~	~~25.01~~	~~52.028~~
	~~48.23~~	~~40.02~~	~~0.000~~
	~~51.03~~	~~45.00~~	~~1.780~~
	~~53.68~~	~~50.00~~	~~0.000~~
	~~60.00~~	~~63.03~~	~~0.000~~
~~OS-6 TOP~~	~~17.00~~	~~5.00~~	~~0.000~~
	~~24.56~~	~~10.01~~	~~0.000~~
	~~30.02~~	~~15.00~~	~~0.000~~
	~~34.54~~	~~20.01~~	~~0.000~~
	~~38.47~~	~~25.01~~	~~0.000~~
	~~51.03~~	~~45.00~~	~~454.080~~
OS-42 TOP	17.00	5.00	0.000
	24.56	10.01	0.000
	30.02	15.00	0.000
	34.54	20.01	2.206
	38.47	25.01	0.000
	42.00	30.01	0.174
	45.23	35.01	0.219
	48.23	40.02	1.422
	51.03	45.00	10.803
	53.68	50.00	36.121
	60.00	63.03	445.570
OS-42 BOTTOM	17.00	5.00	6.711
	24.56	10.01	98.754
	30.02	15.00	3.728
	34.54	20.01	0.228
	56.20	55.01	97.038
OS-66 TOP	24.56	10.01	0.093
	34.54	20.01	3.579
	42.00	30.01	9.068
	48.23	40.02	19.146
	38.47	25.01	7.196
	40.28	27.51	0.570
OS-66 BOTTOM	45.23	35.01	0.501

Table 6-6. Further analysis of out-of-state specimens

Specimen Name	Estimated Critical Shear Stress (Pa)	Average M (cm/[hr-Pa])	Approximate Depth (ft)	Avg. Depth (ft)
OS-44	N/A	N/A	19-21	20
OS-5	N/A	N/A	11-13	12
OS-26	N/A	N/A	10-12	11
OS-6	N/A	N/A	7-9	8
OS-51	N/A	N/A	5-7	6
OS-42	44.1936	13.0725	19-21	20
OS-102	17.559	112.1509	10-12	11
OS-104	12.9769	22.9431	17-19	18
OS-35	10.7582	15.0817	20-22	21
OS-34 #2	7.3065	21.3732	23-25	24
OS-33 BOT	6.0911	7.4301	26-27	26.5
OS-33 TOP	4.9799	22.5652	25-26	25.5
TCZ-34 #1	4.85585	250.4746	13-15	14
OS-23	4.6314	17.0025	13.5-15.5	14.5
OS-28	1.412	13.702	14-16	15
OS-66	12.5381	0.3384	25-27	26
OS-35 #2	0.0709	37.7324	4-6	5

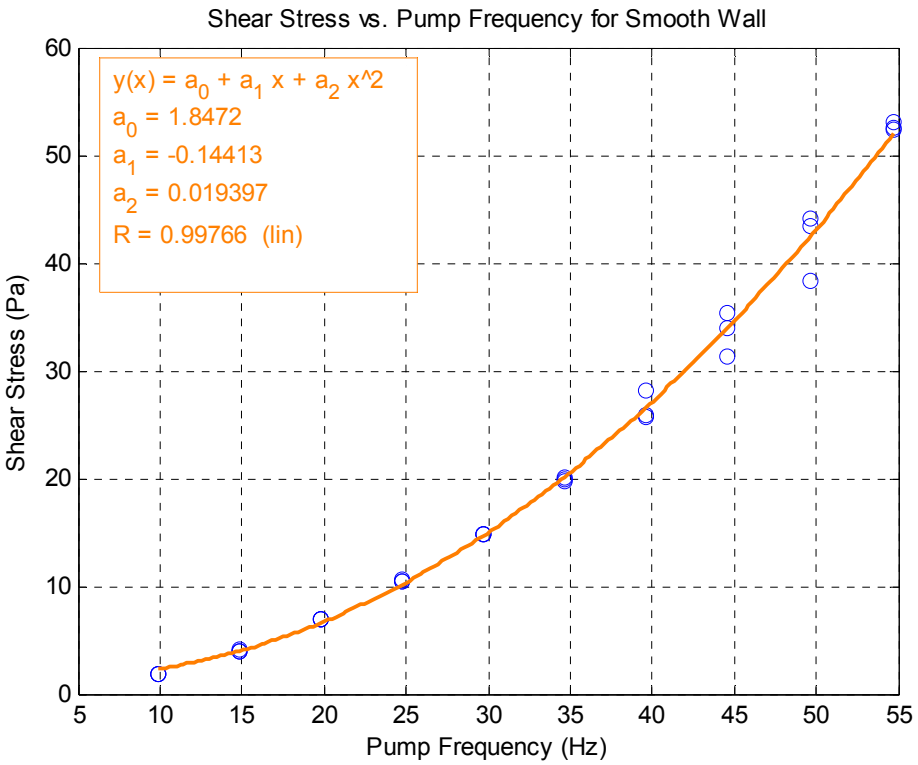

Figure 6-1. Pump frequency versus smooth wall shear stress in SERF

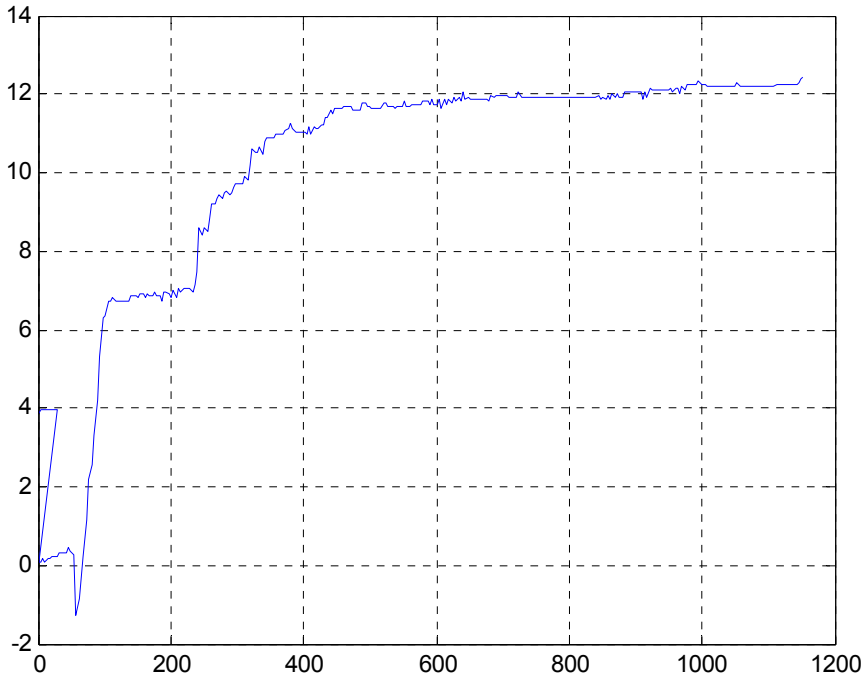

Figure 6-2. Evidence of varied erosion rates (specimen AS-UF2 at 14.98 Pa; reproduced from Appendix B)

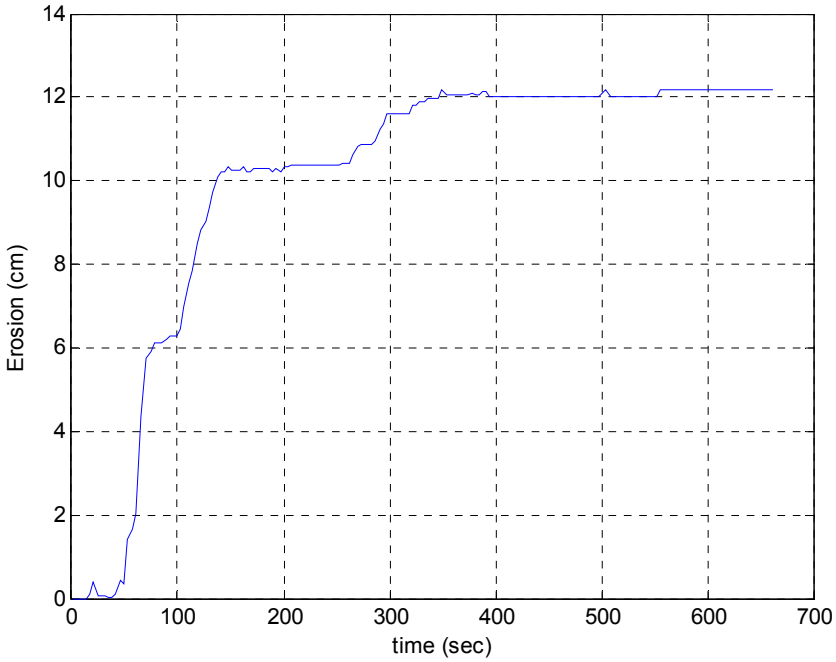

Figure 6-3. More evidence of varied erosion rates (specimen AS-UF3 at 20.56 Pa; reproduced from Appendix B)

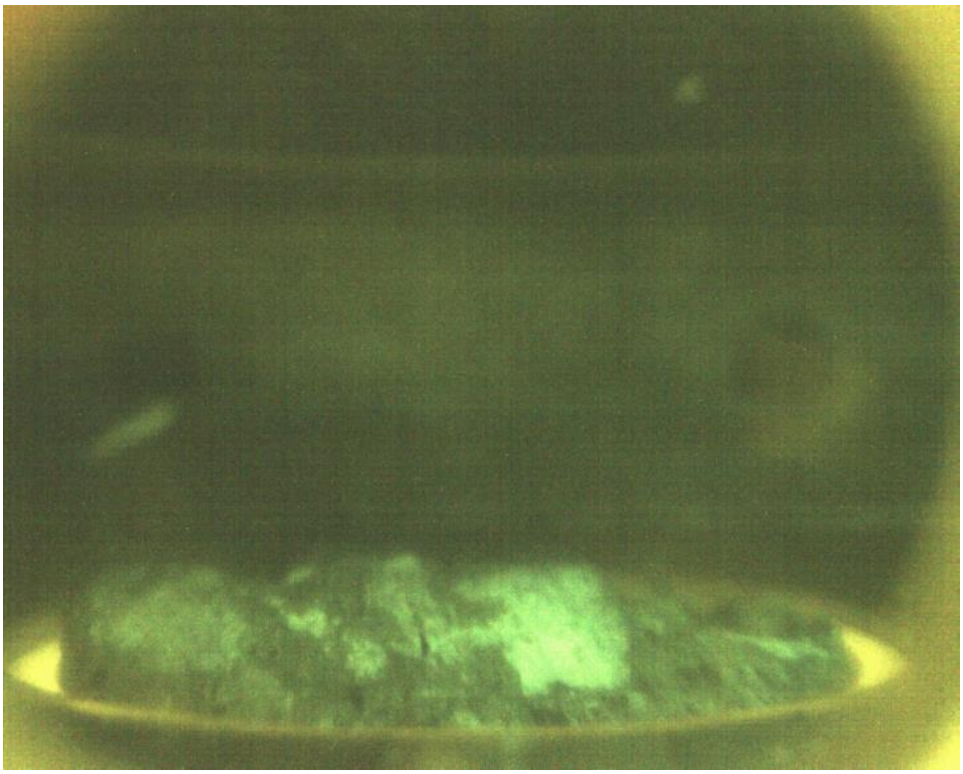

Figure 6-4. Photograph of large piece of organic matter obstructing erosion (during erosion test RR-B1E)

Figure 6-5. Evidence of organic matter obstructing erosion

Figure 6-6. More evidence of organic matter responsible for erosion disturbances

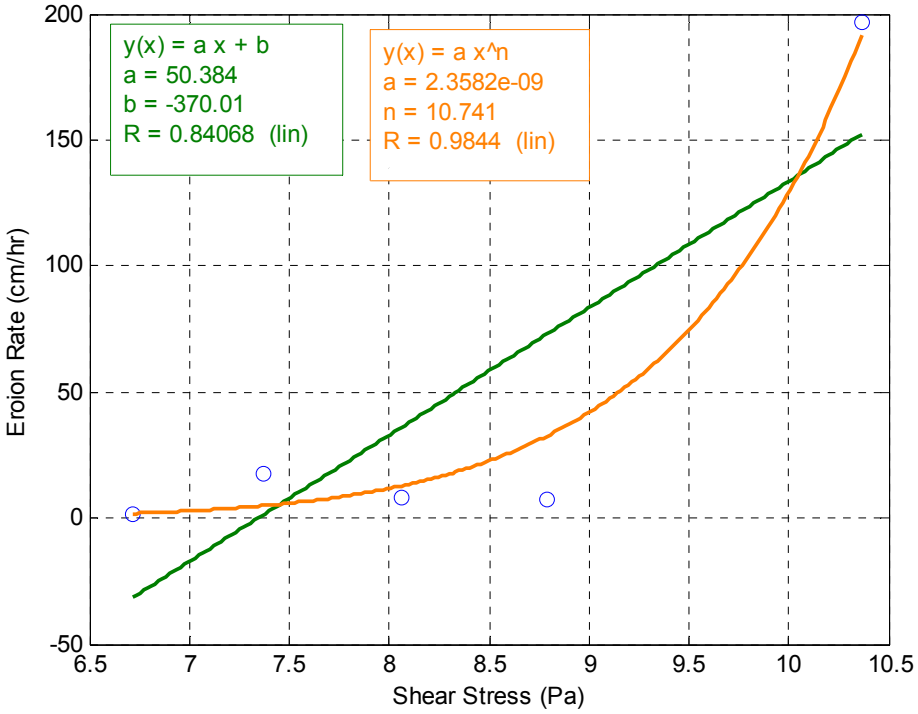

Figure 6-7. Erosion rate versus shear stress for specimen JBC 12'-14' (reproduced from Appendix C)

Figure 6-8. Photograph of JCB 10'-12', dry, test 1 after application of approximately 5 hours of very high shear stresses

Figure 6-9. Close-up of specimen from Figure 6-8

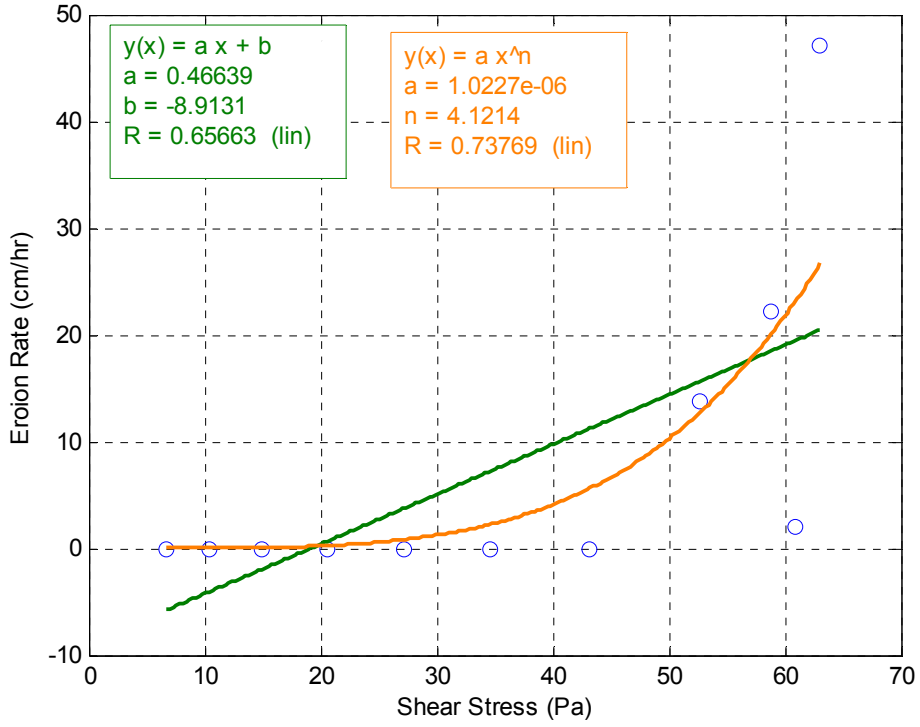

Figure 6-10. Erosion rate versus shear stress for specimen JBC 10'-12' (dry; reproduced from Appendix C)

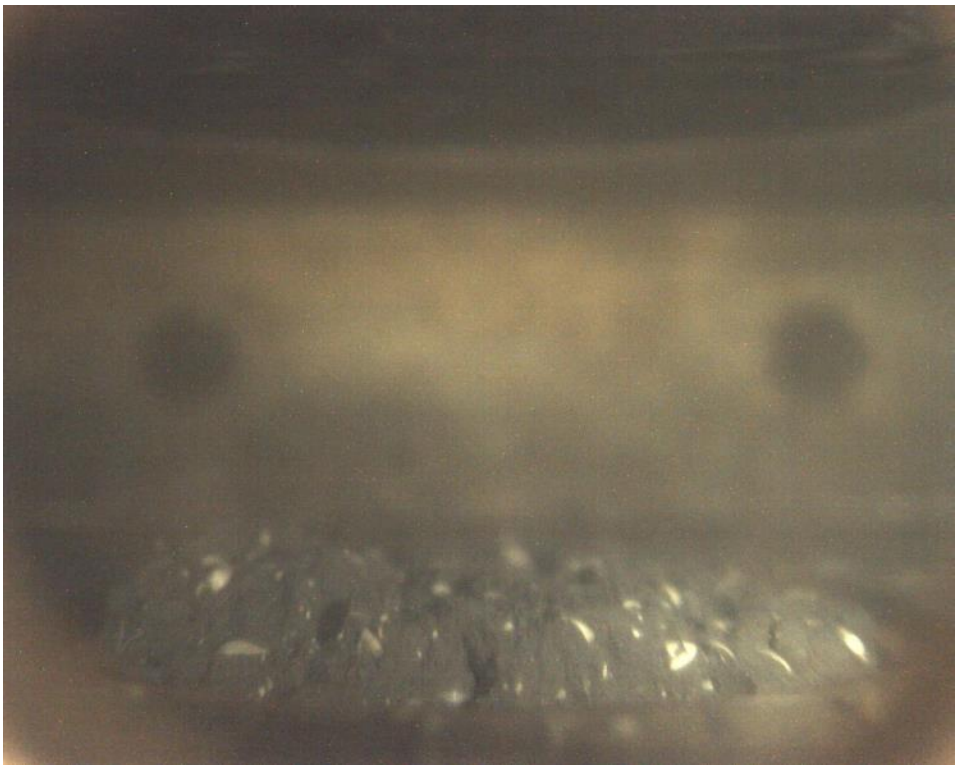

Figure 6-11. Example of organic matter during test OS-44

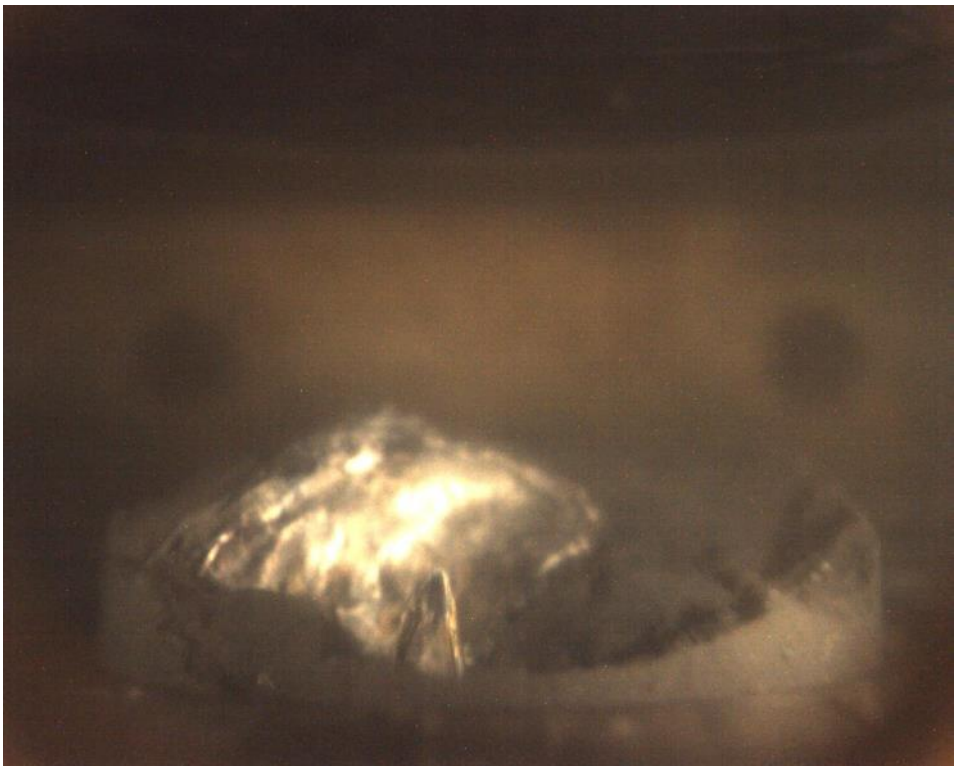

Figure 6-12. Example of organic matter during test OS-26

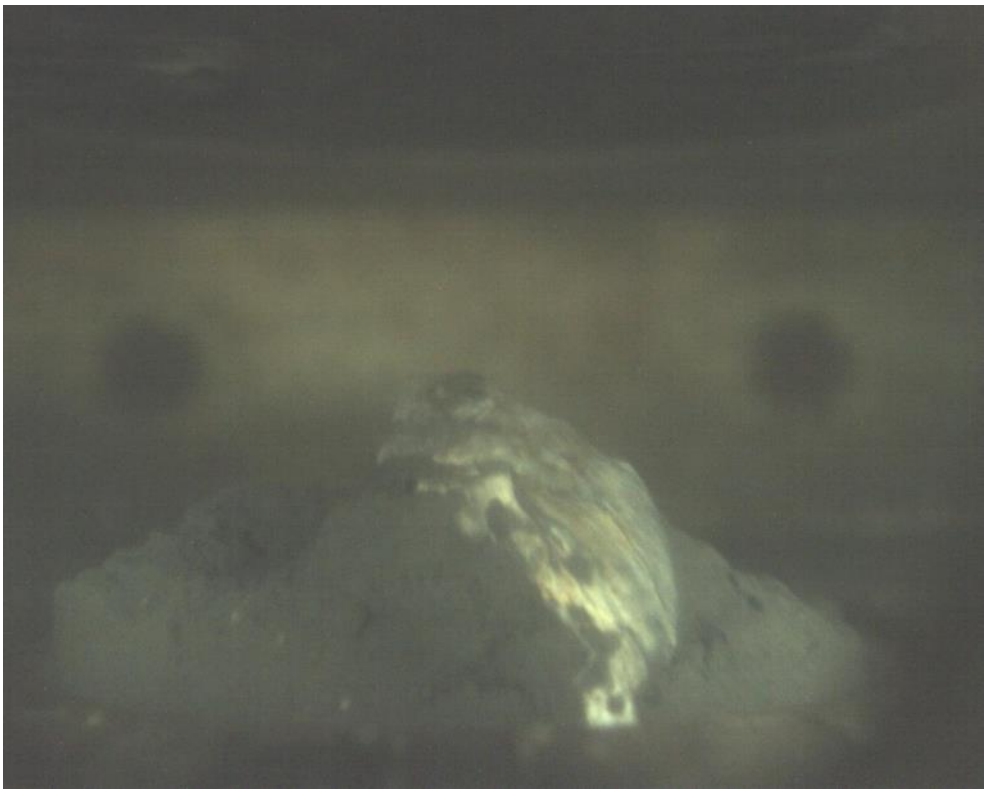

Figure 6-13. Photograph of organic matter during test OS-51

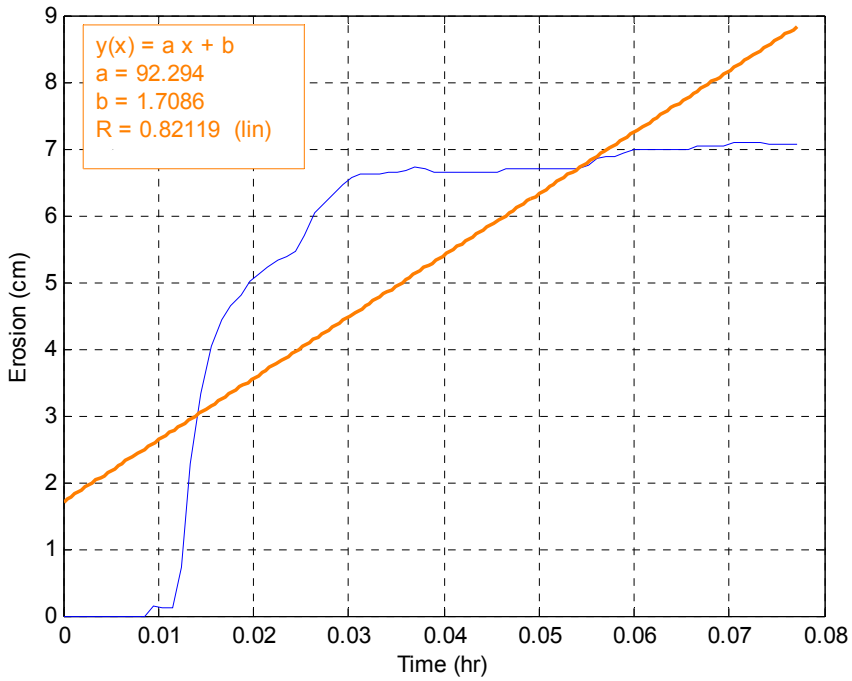

Figure 6-14. Erosion versus time for OS-104 (reproduced from Appendix D)

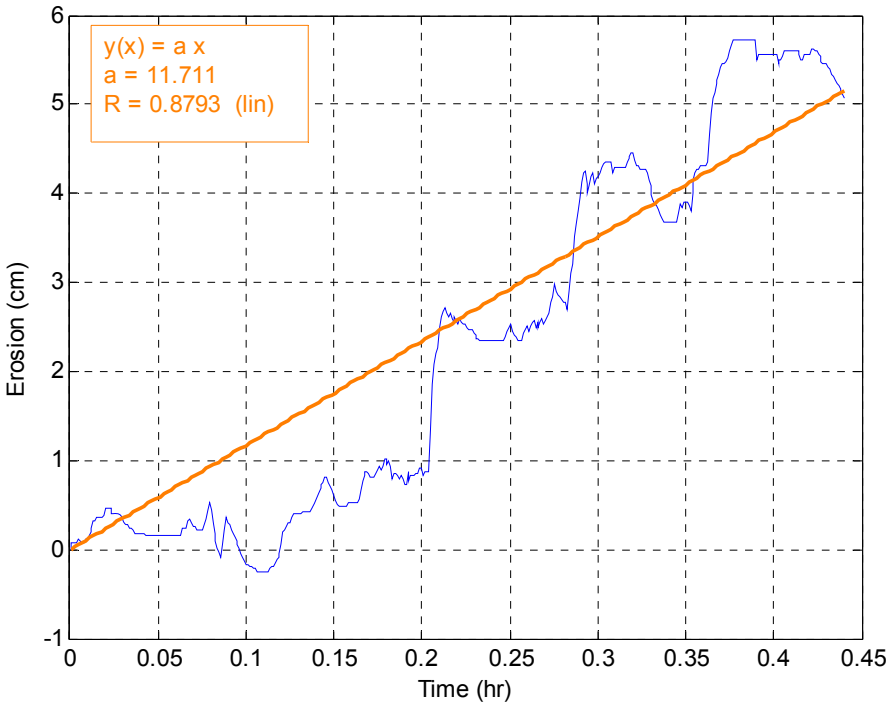

Figure 6-15. Illustration of “blocking” or “chunking” data (from OS-51; reproduced from Appendix D

Figure 6-16. Possible explanation for “blocking” or “chunking”

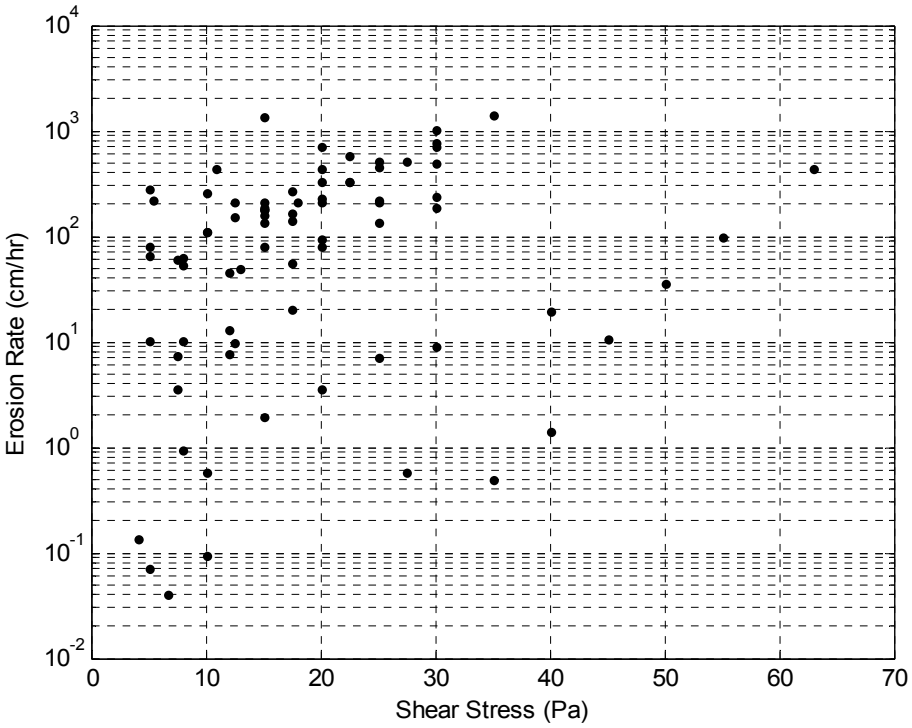

Figure 6-17. Erosion rate versus shear stress for all out-of-state data points

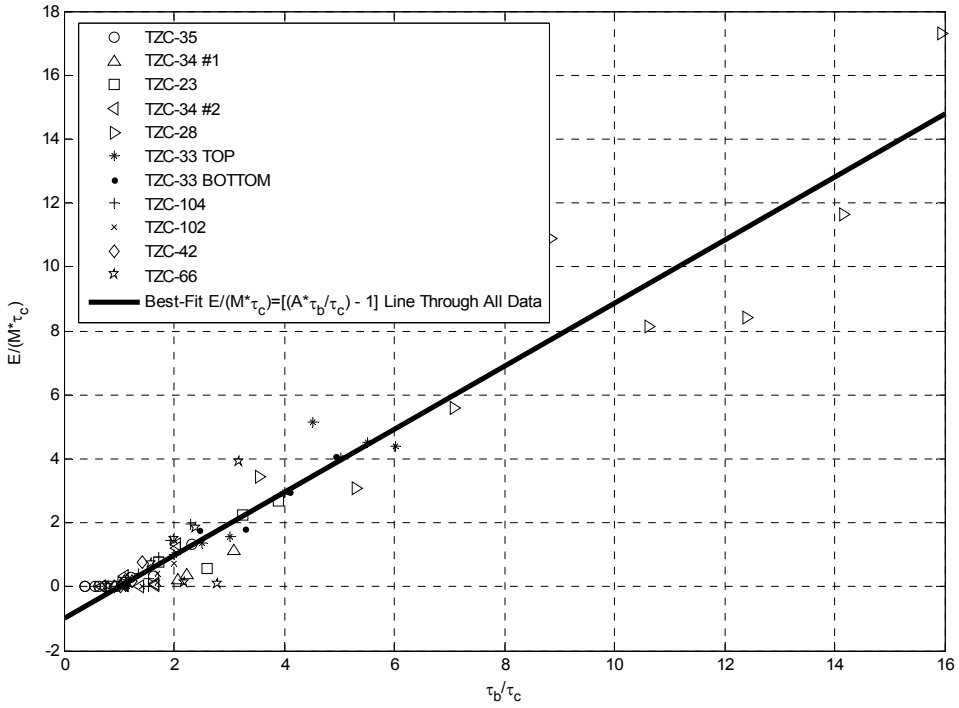

Figure 6-18. Nondimensionalized erosion plot for all out-of-state data

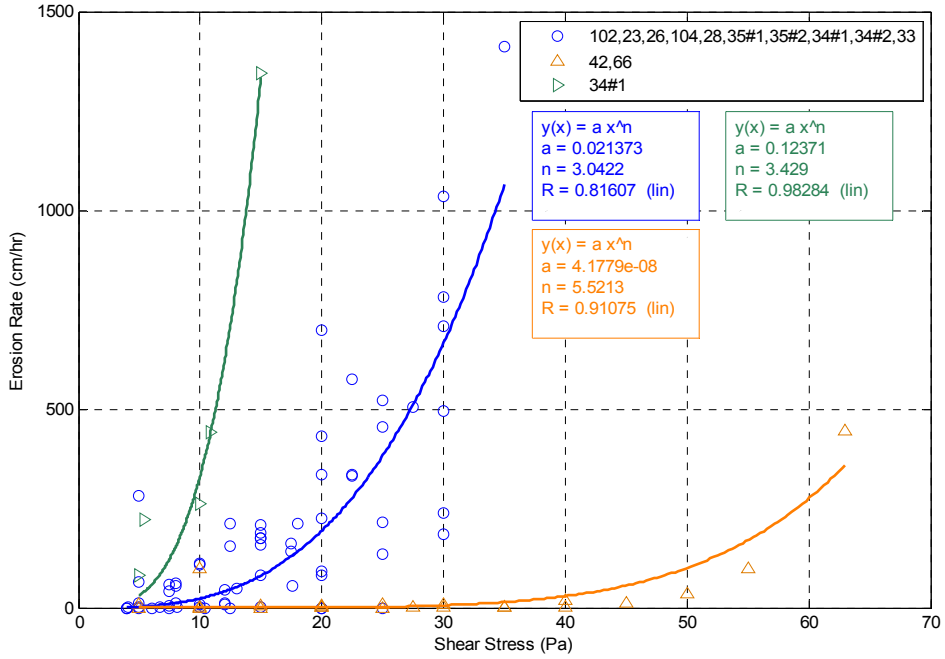

Figure 6-19. Grouped data plot showing erosion function near the existing bridge (green line); near the main channel (blue line); and near the shore (orange line)

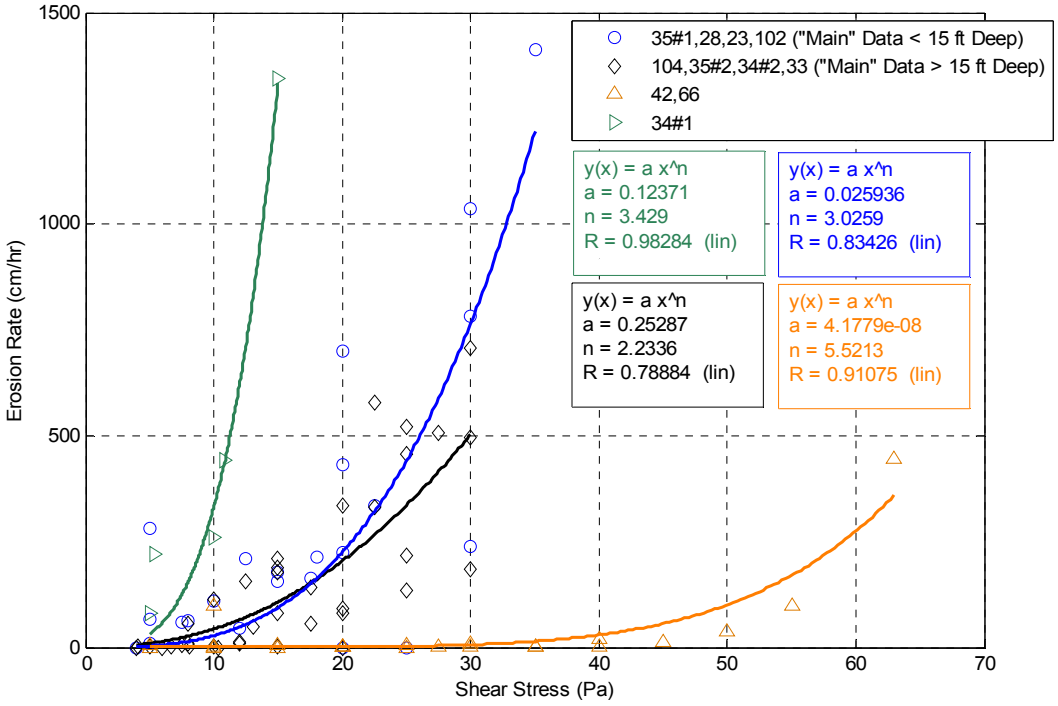

Figure 6-20. Apparent role of depth for data near the main channel (black line are data greater than 15 ft; blue line are data less than 15 ft.)

CHAPTER 7
PROTOTYPE-SCALE SCOUR TESTING PROPOSED FUTURE RESEARCH

7.1 Background Statement

Development of the SERF and other erosion rate testing devices, including FDOT's RETA (Bloomquist et al., 2012), Briaud et al.'s EFA (Briaud et al., 1999), McNeil's et al.'s ASSET (McNeil et al., 1996) and Roberts et al.'s SedFlume (Roberts et al., 1998), has presumed that the scour problem may be reduced to a situation whereby a bed material's shear stress and erosion rate (erosion function) need to be measured. If maximum shear stress in the field is known, erosion rate and subsequently scour depth may be computed using the measured erosion function.

The assumptions behind this method are: (1) erosion is truly governed primarily by shear stress; (2) shear stress in the field can be adequately quantified; and (3) maximum shear stress is truly indicative of field shear stress conditions throughout development of a scour hole. Research from Einstein and El Samni(1949), Einstein and Krone (1962), Partheniades (1965), Kandiah (1974), and Van Prooijen and Winterwerp (2008) appears to indicate that the former assumption may be true under "baseline conditions" – i.e., conditions where no obstruction is present, and erosion obeys a classical critical shear stress pattern.

A number of researchers (Melville and Sutherland, 1989, Melville, 1997, Melville and Chiew, 1999, Sheppard, 2003, Sheppard, 2004, Sheppard and Miller, 2006) have found that equilibrium local scour depths depend on the ratio of structure width to sediment diameter. One possible explanation for this dependence was given by Sheppard (2004) who showed that pressure gradients in the flow field near the structure created by the presence of the structure can produce large forces on sediment grains

that diminish with increasing structure to grain size ratios. Work from Bloomquist and Crowley (2010) appears to indicate that when cohesive sediment and rock erode, a normal forcing component may play an additional role in governing erosion. Kerenyi came to a similar conclusion during testing at the Turner-Fairbank Highway Research Center (TFHRC; Kerenyi, 2012). Bollaert and Schleiss (2003a, 2003b) developed a model whereby a fluctuating normal velocity component was quantified for dam spillways. Bollaert (2010) developed a similar model for rock scour around a bridge pier.

Several computational fluid dynamic (CFD) studies have been conducted to validate the semi-empirical method's second assumption. Horseshoe vortex (HV) evolution under both fixed bed and movable bed conditions has been simulated using Reynolds-Averaged Navier Stokes (RANS) models that relied upon the input of calibration coefficients. Kirkil et al. (2005) indicate that the RANS movable bed models (Wei et al., 1997, Olsen and Kjellesvig, 1998, Roulund et al., 2002, Chen, 2002) appear to capture some HV/scour evolution, and they predict scour depth reasonably well. Briaud et al.'s semi-empirical EFA-SRICOS method relies upon shear stress estimates from Wei et al.'s RANS model. In 2005 and 2008, Kirkil et al. developed large-eddy simulation (LES) models to improve upon previous RANS models for HV development. Because of the nature of their LES simulation, no adjustable constants were necessary.

Several physical tests have also been performed to mirror data from numerical simulations. The first test series from Schwind (1962) and Hjorth (1975) appear to indicate that fluid shear stresses upon the bottom beneath HV are significantly amplified (as much as twelve-fold) when compared to shear stresses associated with the

undisturbed freestream. Dargahi (1987, 1990) visualized “coherent structures” (i.e., streamlines) during scour hole development using tracer dye. In recent years, a number of tests have been performed using combinations of particle image velocimetry (PIV), large-scale particle image velocimetry (LSPIV), digital particle image velocimetry (DPIV) and acoustic Doppler velocity probes (ADVP). Examples include Gosselin and Sheppard (1997), Vlachos (2000), Wei et al. (2001), Graf and Istiarto (2002), Roulund et al. (2005), Unger and Hager (2007), and Kirkil et al. (2008).

With the exception of Roulund et al. none of these studies measured bed shear stress directly. Rather, velocity was measured or inferred, and these values were used to estimate shear stress. Roulund et al. used a conical-film probe to measure shear stress directly. Roulund et al.’s study was also the only series of tests conducted using a near-prototype-scale. Their pile was 1.75 ft. (53.6 cm) wide while their flumes were a maximum of 13.1 ft. (4.0 m) wide. Work from Sheppard (2004) appears to indicate that scaling effects may influence scour rate.

In addition to tests aimed specifically toward developing a semi-empirical, generalized method for predicting scour, a number of “traditional scour tests” have been conducted using cohesionless sediment. In these tests, a noncohesive sediment bottom with an obstruction (bridge pier) was eroded until equilibrium scour depth was obtained. Sometimes, time-rate of scour was recorded. Usually, this style test was concerned with scour depth and not flow-field dynamics. With the exception of Sheppard 2004, most of this style test was also conducted in smaller-scale flumes. For an excellent summary of relevant work, please refer to Melville and Coleman 2007.

Perhaps more relevant to the current goal – quantifying scour for cohesive material and rock – very little data exist that compare cohesionless scour with cohesive scour. Briaud et al. (2004a) claim that for a given flow rate, cohesive scour will eventually approach noncohesive scour if sufficient time has elapsed. They cite Ting et al. (2001) and Gudavalli (1997) where 43 scour tests were conducted on different clays and sands. The Briaud research group's original formula for ultimate scour depth (for both noncohesive and cohesive sediment) is given in Equation 7-1:

$$y_s(mm) = 0.18\left(\frac{aV_1}{\upsilon}\right)^{0.635} \tag{7-1}$$

where *a* is pier width, V_1 is upstream velocity, and *n* is kinematic viscosity of water. This expression appears to lack the dependency terms between sediment diameter and pier width which were reported by Sheppard (2004) and Sheppard et al. (2004) and have become standards according to the FDOT *Bridge Scour Manual* (2005).

In 2004, Briaud et al. published a series of formulae for estimating scour depth for complex pier configurations. Similar to Equation 7-1, their original equation lacked dependency terms between sediment diameter and pier width. However, in 2009 and 2011, Oh and Oh et al. reanalyzed the Briaud dataset. Equation 7-2 shows the new formulation for scour depth below a complex bridge pier:

$$\frac{y_s}{a} = 2.2K_w K_1 K_L K_{sp}\left(2.6Fr_{(pier)} - Fr_{c(pier)}\right)^{0.7} \tag{7-2}$$

with K_w a correction for pier width; K_1 a correction for pier shape, K_{sp} a correction for pile group spacing; $Fr_{(pier)}$ the pier Froude Number (Eq. 4-3); and $Fr_{c(pier)}$ the Froude number based upon critical velocity (Equation 7-5).

$$Fr_{(pier)} = \frac{V_1}{\sqrt{ga'}} \tag{7-3}$$

$$Fr_{c(pier)} = \frac{V_c}{\sqrt{ga'}} \tag{7-4}$$

where *a'* is the projected pier width and V_c is the critical velocity.

Upon first glance, these new expressions appear to take scaling effects into account in the sense that Equation 7-4 is a function of critical velocity, which in turn should be a function of sediment size and sediment density. In Oh's dissertation, he recommends using the HEC-18 formulation for finding critical shear stress (Arneson et al. 2012):

$$V_o = \sqrt{\frac{\tau_0 y^{1/3}}{\rho g n^2 V_1^2}} \tag{7-5}$$

where *n* is Manning's roughness and τ_o is bed shear stress. Critical values are substituted for stresses and velocities.

This method may be questionable because Oh appears to indicate that Gudavalli obtained his shear stress data from EFA tests. As discussed in Crowley et al. (2012a) and in Chapter 5 the EFA uses a Moody Diagram (described by the Colebrook-White equation) to estimate shear stress. Crowley et al. (2012a) show that a different Colebrook-White roughness height could be developed for any flume-style erosion rate testing device based solely upon flume geometry (excluding roughness). Furthermore, work presented in this report (Chapter 5) would appear to indicate that any assumptions about stresses in the EFA would be questionable. Since the Briaud research group assumes that roughness height is simply half the sediment diameter (Crowley et al. 2012a, Crowley et al. 2013, and Chapter 5 provide relatively strong evidence to show

that this is probably not the case), Li and Oh's critical shear stress assumption may be dubious.

Even if one overlooks this, there are other issues with the Briaud research group's assumptions. Using Equation 7-5 for computing critical velocity and comparing the Briaud ultimate scour depth with computed scour depths from the FDOT Bridge Scour Manual (Sheppard et al. 2004) for sands, a plot comparing the results as a function of the grain size to pier width ratio may be prepared (Figure 7-1). It should be noted that this plot was obtained by using the Briaud et al. "upper envelope limit" – i.e., 1.5 times Equation 7-2.

However, according to the FDOT *Bridge Scour Manual* (2005), there is an alternative method for computing critical shear stress which does not rely upon the introduction of a Manning's roughness coefficient. Essentially, if one knows the relationship between roughness height and grain size (recall that previous research was supplemented in Chapter 5 to provide such a relationship), then it should be possible to use this information to solve for the friction velocity. Using the friction velocity, critical shear stress can be found directly.

The decay in the Briaud et al. scour depth results as a function of grain size to pier width ratio presented in Figure 7-1 appears to be due mostly to the method by which critical shear stress was computed. Note that Equation 7-5 is strongly dependent on empirical Manning's roughness values due to the n^2 in its denominator. If one uses the FDOT method for computing critical shear stresses (thereby bypassing the need for Manning's roughness) and combines these stresses with Equation 7-2, then a new plot is generated (Figure 7-2). In Figure 7-2, maximum scour appears to decay quickly as a

function of the ratio between grain size and pier width when the FDOT method is used. By comparison, the Briaud et al. method appears to predict significantly more scour; and it appears to only show a slight decay in maximum scour depth with respect to grain size/pier width ratio.

The Briaud et al. analysis may not be in error with respect to their dataset. For example, according to Roulund et al. (2005), both Froude number of the ratio between grain size and pier width should be factors that control equilibrium scour depth. However, as discussed in Sheppard (2003), even though there have been almost 40 years of research in bridge scour, it appears that researchers cannot agree upon which variables are most important for nondimensionalization of scour; and which nondimensional variables should be used for equilibrium computations. Roulund et al. (2005) and Melville and Coleman (2007) state that beyond a D/D_{50} ratio of approximately 50, scour appears to stabilize for a given set of flow conditions. In terms of this recommendation, the Briaud et al. conclusions follow suit. But, data used to draw these conclusions were mostly collected at smaller-scales.

The apparent lack of maximum scour depth decay as a function of grain size/pier width ratio has yet to be satisfactorily reconciled. This becomes especially troubling when juxtaposed with Briaud's proposition that all sediment will scour to the same depth given sufficient time. If this were truly the case, then decay rates from the Briaud correlation should be similar to the Sheppard et al. decay rates since Briaud's group developed their equations using both cohesive and noncohesive sediment. One possible explanation for the discrepancy has already been briefly mentioned. Specifically, the Briaud/Oh/Li/Ting datasets were obtained using relatively small-scale

flumes. Tests were conducted with 1.0 in. (25 mm) and 3.0 in. (75 mm) bridge piers in an 18 in. (0.46 m) wide flume; and 3.0 in., 6.0 in. (150 mm), and 8.3 in. (210 mm) diameter bridge piers in a 5.0 ft. (1.52 m) wide flume. More concerning, the Texas A&M data appears to contradict results from Hosny (1995) who reported that cohesive sediment will reduce equilibrium scour depth. Ting et al. acknowledges this. No known explanation has been found to reconcile this discrepancy.

Qualitatively, Ting et al. describe cohesive scour around bridge piers. Notably, they point out that the shape of a cohesive scour hole is different than a noncohesive hole. Specifically, cohesive scour holes form primarily toward the rear of the pier. Conversely, maximum scour depth for a sandy scour hole is located near the pier's front. Flow dynamics around a circular pile should form a scour hole due to a flow-balance problem (essentially). If holes are differently-shaped when cohesive sediments erode, it stands to reason that cohesive holes should erode to a different equilibrium depth than their non-cohesive counterparts.

7.2 Objectives

While much small-scale scour and flow field data is available, there is the notable absence of studies conducted under prototype-scale conditions. Based upon the Roulund et al. results, which appeared to indicate that the Hjorth (1975) dataset is a reasonable predictor of maximum stress in the vicinity of a bridge pier, it is not unreasonable to conclude that a suitable "target" for maximum stress has already been established before the scour hole begins to form. However, there is still a need to find an "upper-limit" for scour when cohesive sediments erode – particularly because of the known dependencies concerning inclusion of a bridge pier width to sediment grain size

nondimensional computational group. Therefore, the primary objective of the work proposed herein is to conduct prototype-scale scour tests to determine the maximum scour depth for cohesive sediments under prototype-scale conditions.

Sand scour occurs relatively quickly, and the FDOT design equations for sand scour are reflective of this in that they may be represented as functions of the following nondimensional variables:

$$\frac{y_s}{D} = f\left(\frac{D}{D_{50}}, \frac{V}{V_c}, \frac{y_0}{D}\right) \quad (7\text{-}6)$$

where D is the pier width; D_{50} is the grain size; V is the upstream velocity; V_c is the critical velocity; and y_0 is the upstream water depth. Note, that while stresses are known to change throughout the hole's development, they are not used to compute sand scour according to HEC-18. These equations are presented here as the "standard" because of the documented successes of the FDOT Bridge Scour Method when compared to other prediction equations.

Cohesive scour on the other hand occurs much more slowly than sand scour. Ultimately, the SERF is to be used to develop an erosion function. The erosion function is to be related to actual field stress conditions so that local scour can be computed. If maximum scour is assumed throughout development of the scour hole, it is likely that this assumption will lead to overly-conservative predicted scour. Therefore, as a corollary to this project's primary objective, its secondary objective is to determine stress magnitudes throughout development of a cohesive scour hole under prototype-scale conditions.

7.3 Testing Location

Prototype-scale or full-scale testing implies two alternatives: (1) testing may be conducted in the field; or (2) testing may be conducted in a large-scale laboratory. Based upon investigators' previous experience with large-scale scour tests (Sheppard et al., 2004), the latter alternative is strongly recommended.

Laboratory testing offers several advantages compared with field-testing. First, laboratory testing allows researchers to control environmental variables – flow rate, sediment size, sediment distribution, and water depth, for example. Doing this allows one to isolate the more significant variables from one another more easily.

Investigators recommend conducting large-scale tests at the United States Geological Survey's (USGS) Conte Laboratory in Turners-Falls, MA. This laboratory houses three large-scale flumes. All flumes measure 126 ft. (38.40 m) in length by 21 ft. (6.40 m) in depth. The larger flume is 20 ft. (6.10 m) wide while the two smaller flumes are both 10 ft. (3.05 m) wide. Because of the smaller flumes' cross-sectional areas, they are capable of producing higher flow rates. The larger flume would allow researchers to install larger-scale bridge piers during testing.

Water moves through the Conte Laboratory flumes via gravity-driven flow from the Connecticut River. A valve is opened on the flumes' upstream end to divert water through the devices. A downstream weir that may be used to control water-levels is present in each flume. Head difference between the upstream valve and the downstream valve is approximately 30 ft. The advantage to this design is that pumps are not used to drive flow; the disadvantage to this setup is that flow rates are

necessarily governed by flow depth. In the past, scour tests were run using a 9.0 ft. depth (Sheppard et al., 2004).

Another apparent disadvantage to this setup is that since the USGS facility is a "flow through" flume only clear water tests can be performed; suspended sediment concentration during testing cannot be controlled. Sheppard did observe an apparent dependence between equilibrium local scour depths on the presence of suspended fine sediment which he attributed to changes in bed shear stress (for approximately the same flume discharge) caused by the suspended sediment. However, for flow rates and flow conditions in typical Florida scour situations in cohesive soil, the effect of suspended sediment is expected to be minor relative to the effects of flow rates and cohesion.

The flume's flow-through design does present one notable advantage. In recirculating flumes, it is difficult to test cohesive erosion. Recirculating cohesive particles often cannot be filtered; and these particles may damage recirculating pumps. Conducting cohesive tests in a flow-through facility eliminates this possibility of breakage.

7.4 Supporting Tasks

To complete this project's objectives, the following tasks will be completed:

Task 1. Develop instrumentation for a full-scale scour test.

Task 1 is to develop all necessary equipment for the full-scale cohesive scour tests. Because computer modeling is to be used for a significant portion of this project (please see below), the only sensor that will be required will be a movable, trolley-style ultrasonic depth sensor. This system will be similar to the TFHRC large-scale flume sensor system in that three motors will be installed to allow a depth sensor to move laterally up-and-down the flume; horizontally across the flume; and downward into the flume water column so that measurements may be taken. The system

will be fully-automated using LabVIEW. Depth readings will be taken as a function of time at pre-defined sets of coordinates so that accurate bathymetry contour maps may be developed. Because the system will be automated, it will be possible to take readings around the clock.

Task 2. Move the SERF from the University of Florida to the University of North Florida.

As the PM is aware, Dr. D. M. Sheppard and Dr. D. Bloomquist have both retired from the University of Florida. Additionally, Dr. R. Crowley recently accepted an appointment at the University of North Florida. As a result, there are no active faculty at UF who understand how to use the SERF. Because Dr. Crowley's goal is to remain at UNF for the long-term, it makes a certain amount of sense to move the SERF to UNF because of Dr. Crowley's expertise with the instrument. Task 2 involves dismantling the SERF (as minimally as possible), loading it onto a truck, and installing it at UNF.

Task 3. A series of tests on simple bridge piers will be tested at the USGS Conte Laboratory in Turner-Falls, MA.

One simple bridge pier (1.0 ft. diameter circular pile) will be installed in the small (10 ft.) USGS flume. Similar to Sheppard et al.'s series of tests, 5.0 ft. of cohesive sediment will be used to coat the flume's bottom. However, because clay is to be used for these experiments, coating the bottom of the flume will require a specialized technique. To prepare the bed, a series of clay "boxes" will be prepared, brought to an appropriate water contents, and lifted into the flume.

Once the clay is installed, water will be made to run through the flume so that a scour hole begins to form around the simple bridge pier. Scour hole bathymetry (both temporal and spatial) will be monitored throughout the test. Results will be compared with existing cohesionless data to determine if scour reaches the same depth when cohesive sediment is used and to determine if cohesive and noncohesive scour holes are similarly shaped. Additionally, the pier width to grain size relationship will be analyzed for these cohesive sediments. Investigators hypothesize that this nondimensional variable may become less important because cohesion may become the controlling factor for equilibrium scour depth.

The smaller USGS flume is specified for two reasons. First, it will be much more feasible to install 10 ft. wide clay sections along the flume bed than it would be to install 20 ft. sections. Secondly, the smaller flume is believed to be more readily available than the larger flume.

Task 4. A series of erosion tests will be conducted in the SERF using the same sediment used in the USGS Conte experiments.

Task 4 involves testing the sediment that is to be used during the USGS Conte Laboratory experiments in the SERF. Using expertise reported in Bloomquist and Crowley (2010), a method will be developed to create nearly-uniform clay specimens. Then, these specimens will be tested in the SERF at a minimum of five shear stresses. Tests will be repeated at least once to ensure consistency. Using these erosion data, erosion rate versus shear stress relationships will be obtained for these specimens using the shear stress assumptions discussed in Chapter 5.

Because of issues with the sand injector (please refer to Chapter 8), the injector will be removed from the SERF and replaced with a schedule 80 PVC-pipe as part of this task.

Task 5. Develop a computational model to describe stress reduction associated with scour hole development.

Task 4 is to be conducted as a prelude to Task 5. Recall that the secondary goal of this project was to study the effect of shear stress reduction during scour hole development on equilibrium scour depth.

There are two practical ways to study this problem. The first involves measuring a limited number of flow variables during Task 3. For example, bed shear stress could be measured somewhere in the flume using a shear stress sensor similar to FDOT's SERF sensor or a sensor from TFHRC. Similarly, a portable PIV device could be adapted to measure velocity profiles somewhere in the flume. Then, a RANS computational model could be developed of the scour experiment. LES should not be used because of its significant computational expense (several months of computational time would be required to obtain one dataset). RANS modeling coefficients would be modified so that computational data matched experimental "flow measurement" results.

Next, similar to Chapter 5, a series of modified bed configurations would be modeled based upon bathymetry changes measured during Task 3. A discrete number of bed time steps would be specified. For each bed configuration time step, the RANS computational bed would be modified to match measured bathymetry. Shear stress contours and maximum shear stresses would be taken from each modified computational dataset. Then, maximum shear stress would be plotted as a function of time/scour depth. The issue with this approach is that measuring these variables precisely during a large-scale scour test may be unfeasibly difficult. Without precise "matched" data, this approach will not produce accurate results.

The alternative is to match the data that is more likely to be measured precisely – i.e., depth. Recently, colleagues at the ANL TRACC Center have developed a computational erosion model whereby the bed "morphs" when certain stress criteria are met. Their issue thus-far in employing this

model is that they do not yet know the “stress targets” that should govern morphing and modifying their bed. In other words, while the code is written to couple Star-CCM+ with an erosion rate versus shear stress curve, programmers at ANL are unsure what the erosion function should look like. Similarly, even if they were to assume an erosion function, there would be no way to verify their results.

During Task 5, the erosion rate versus shear stress curve from the Conte Laboratory sediment that was obtained during Task 2 will be applied to a morphing computational model of the flume experiment. Eventually, an equilibrium scour depth will be computed. This scour depth will be compared with measured data. Computational modeling coefficients will be varied to achieve approximate matching between modeled and experimental results.

Once data are matched, stress information may be obtained from the computational model to develop maximum shear stress versus time/scour depth information that may be used for design. This procedure will be repeated for several experimental configurations (i.e., flow rates) studied as part of Task 1.

An additional advantage to the depth matching approach is that if it is successful, it may represent a new state-of-the-art in scour modeling in that measured erosion data will be coupled to computational results. Please note that while ANL has used the erosion function coupled approach to approximate sand scour, they have yet to use the approach for cohesive sediment. However, it is believed that cohesive modeling will perform even better than sand modeling because there will be no “sand slide” effects during a cohesive scour event.

Also note that while investigators recommend the depth-matching approach for quantifying stress reduction please note that the flow-matching approach is also better than the third alternative – directly measuring stress in the hole during a large-scale test. Due to the complexity of such a test, obtaining accurate direct measurements does not appear to be feasible. Additionally, there would be significant cost associated with developing and installing the necessary instrumentation for such a series of experiments. To achieve the goals discussed in this chapter, it will be more efficient and more cost effective to combine computational modeling with measured data than it would be to strictly rely on prototype-scale measurements.

Task 6. <u>Preparation of Progress Reports, the Draft Final Report, and the Final Report.</u>

FDOT-required submittals including quarterly progress reports, a Draft Final Report, and a Final Report will be completed in accordance with standard specifications (please see below).

7.5 Use of Graduate Student(s) and other Research Assistants

Due to the complexity of the work proposed here, two research assistants will be requested to complete this study. The first student would be a M.S. student at the University of North Florida. This student would be charged with conducting all SERF experiments described in Task 2 and developing all computational models associated with Task 3. His or her graduation would be dependent upon successful completion of this project. As implied then, this student would either have to (1) regularly travel from Jacksonville to Gainesville; or (2) the SERF should be moved from Gainesville to Jacksonville. Because of the retirement of Dr. Sheppard and Dr. Bloomquist and Dr. Crowley's recent appointment at UNF, we believe that it may be more effective to move the SERF because of Dr. Crowley's expertise with the instrument. Because of the complexity of the instrumentation associated with Task 1, a full-time research assistant would be requested to conduct these experiments. This research assistant would be under the direct supervision of Dr. Crowley at UNF, and his or her full-time responsibilities would include conducting the full-scale scour tests.

7.6 Equipment

Limited equipment will be required to complete the experiments associated with Task 1. This equipment is as follows:

- *Trolley-Style Depth Sensor*. As mentioned above, completion of this project is dependent upon installation of a trolley-style ultrasonic depth sensor similar to the TFHRC large-scale flume system. Components for this system will include three computer-controlled motors; belt/gear systems to move the sensor along its three movable axes; and the ultrasonic sensor itself.

- *Digital Video Camera*. A video camera will be installed to record scour testing associated with Task 1. Video data will be used to qualitatively verify depth sensor data throughout Task 1.

- *Computer with Data Acquisition Capabilities*. A computer will be installed at the USGS Conte Laboratory that will be used to record depth information and send signals to the trolley-style depth sensor apparatus. Data acquisition (DAQ) cards and LabVIEW must be installed on this computer. The computer will be returned to FDOT upon completion of this project.

7.7 Travel

The MA-based research assistant will be permanently based at the USGS Conte facility. This will eliminate the need for him or her to travel back-and-forth from Florida to Massachusetts. However, a travel allowance will still be required for the PI to occasionally visit Massachusetts to troubleshoot and assist in setting up the large-scale experiment. Therefore, funds are requested for six trips to/from the USGS facility. All travel shall be in accordance with Section 112.061, Florida Statutes. FDOT employees may not travel on research contracts.

7.8 Project Kickoff Meeting

A kick-off meeting shall be scheduled to occur within the first 30 days of execution by the University of Florida. The preferred method for the kick-off meeting is via teleconference or video conference. As a minimum, the project manager and the principal investigator will attend. The Research Center staff must be advised of the meeting and given the option to attend. Other parties may be invited, as appropriate. The subject of the meeting will be to review and discuss the project's tasks, schedule, milestones, deliverables, reporting requirements, and deployment plan. A summary of the kick-off meeting shall be included in the first progress report.

7.9 Deliverables

The following is a list of deliverables that will be produced under this project:

- Quarterly progress reports
- A Draft final report
- A final report
- An updated user's manual for the SERF

7.9.1 Progress Reports

The University of Florida will submit quarterly progress reports to the Research Center. The first report will cover the activity that occurred in the 90 days following the issuance of the task work order.

Reports will be submitted within 30 days of the end of the reporting period. Reports will be given even if little or no progress has occurred (in which case, the report will explain delays and/or lack of progress). Progress reports will be sent in MS Word to Sandra Bell, sandra.bell@dot.state.fl.us.

Progress reports will include the following information:

1. Contract number, task work order number, and title
2. Work performed during the period being reported
3. Work to be performed in the following period
4. Anticipated modifications (i.e., to funding, schedule, or scope). If an amendment is requested, the project manager will be provided with the appropriate information (i.e., what is being requested with justification) in the required format.
5. A progress schedule updated to reflect activities for the period being reported.

We understand that failure to submit progress reports in a timely manner may result in termination of the work order.

7.9.2 Draft Final Report

The Draft Final Report will be submitted 90 days prior to the end date of the task work order. The Draft Final Report will be submitted to Sandra Bell,

sandra.bell@dot.state.fl.us. It will be edited for technical accuracy, grammar, clarity, organization, and format prior to submission to the Department for technical approval. The document will be a well-written, high-quality reports that address the objectives defined by the scope of service. The Draft Final Report will be prepared in accordance with the "Guidelines for Preparing Draft Final and Final Reports" posted at: http://www.dot.state.fl.us/research%2Dcenter/Program_Information/Guidelines%20for%20Preparing%20a%20Final%20Report%2012-07.pdf.

7.9.3 Final Reports

Once the draft final report has been approved, the University of North Florida shall prepare the final report. The university will deliver a minimum eight (8) copies on CD or DVD – seven (7) CDs should contain the final report in PDF format, one (1) CD should contain the final report in PDF format, MS Word format and a Summary of the Final Report.

The CD/DVDs will be labeled in a professional manner and include at a minimum the contract number, task work order number, project title and date.

The Final Report will be delivered to the following address:

The Florida Department of Transportation
Research Center, MS 30
605 Suwannee Street
Tallahassee, FL 32399-0450

7.10 Project Closeout Meeting

A closeout meeting shall be conducted to review project performance, the deployment plan, and next steps. Attendees shall include, as a minimum, the project manager, the principal investigator, and the Research Center performance coordinator. This meeting will occur prior to the expiration of the contract and subsequent to the

approval of the draft final report (i.e., it will be scheduled sometime during the final 30 days of the project).

7.11 Project Schedule & Budget Sheet

The project schedule and an approximate budget sheet are provided in Figure 7-3 and Figure 7-4.

7.12.1 Contact Information

7.12.1 Principal Investigators

Dr. Raphael W. Crowley, P.E.
Department of Construction Management
University of North Florida
Building 50, Room 2400
Jacksonville, FL 32224
Phone: 904-620-1847
rcrowley@ufl.edu

Dr. D. Max Sheppard
Department of Civil & Coastal Engineering
University of Florida
365 Weil Hall / PO Box 116580
Gainesville, FL 32611
Phone: 352-392-9537 ext 1428
sheppard@ufl.edu

7.12.2 Project Manager

Rick Renna, P.E.
Florida Department of Transportation
605 Suwannee Street
Tallahassee, FL 32399
Phone: 850-414-4351
rick.renna@dot.state.fl.us

7.13 Other Considerations/Menu of Options

As presented in this chapter, the cost of completion of the proposed research is approximately $350,000. Please note however that the work proposed here is almost

two distinct projects – one involving full-scale scour testing and the other involving computational modeling and SERF testing.

As discussed in Section 7.2, the most important objective is to obtain equilibrium scour depth for cohesive sediments – i.e. to run the full-scale scour tests. A modified project schedule and budget worksheet were prepared to reflect the cost of achieving this objective alone (Figure 7-4 and Figure 7-5).

Additionally, a modified schedule and budget worksheet were prepared to show the time and costs of computational modeling and SERF testing on their own (Figure 7-6 and Figure 7-7). While it would not be possible to compare computational results with measured data until full-scale tests are conducted, there is some value in verifying that the computational code will function as anticipated. Alternatively, this schedule/budget are presented if FDOT chooses to split the work proposed here into two “phases.”

Please note that costs presented here for equipment, shipping the SERF, and space-rental from the USGS Conte Laboratory need to be finalized. These numbers will be confirmed for the Final Report. However, investigators do not believe these values will change drastically. As of the Draft Final Report, these budgets are intended to give an approximate order-of-magnitude approximation for future work.

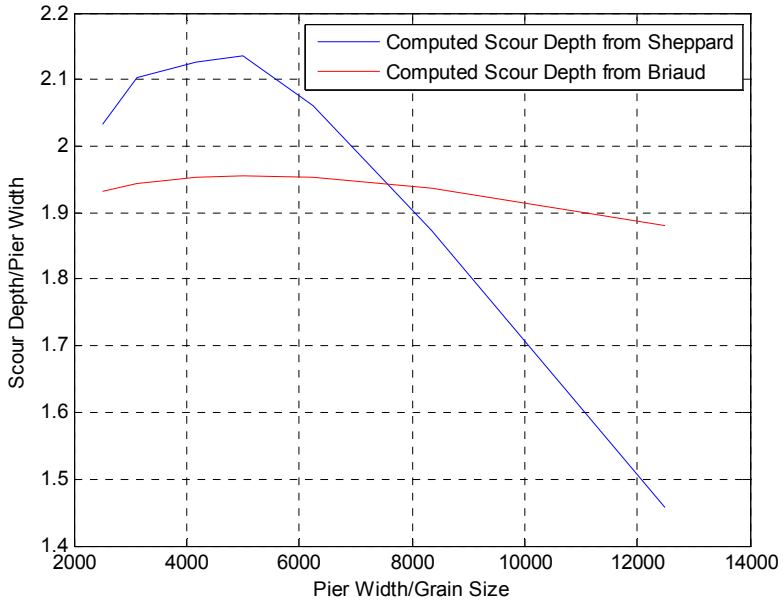

Figure 7-1. Comparison of FDOT Bridge Scour Manual and EFA-SRICOS maximum scour depths for sands

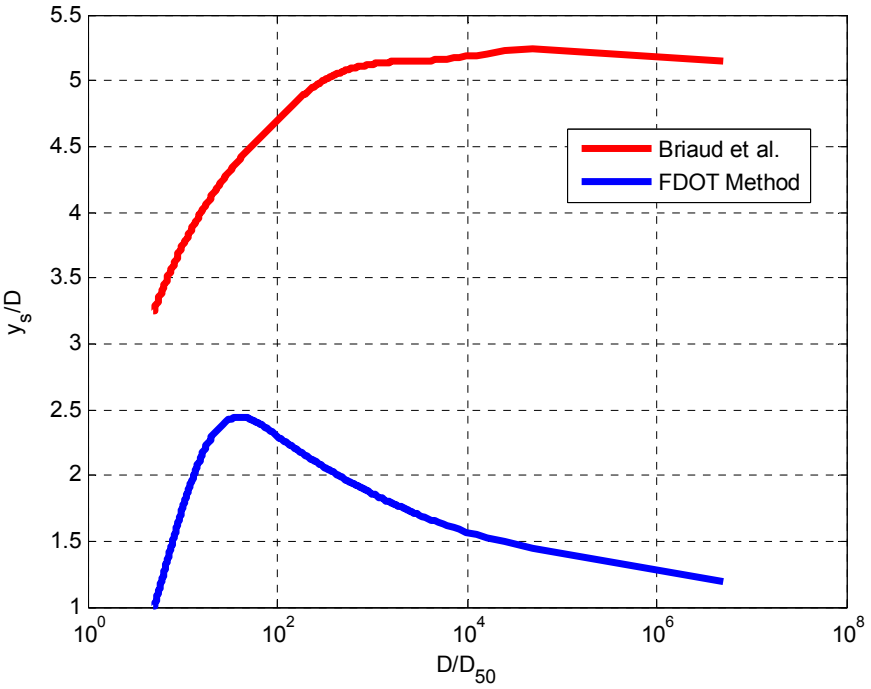

Figure 7-2. Comparison of FDOT Bridge Scour Manual and EFA-SRICOS maximum scour depths for several sediment sizes using the FDOT method for computing critical shear stress

FLORIDA DEPARTMENT OF TRANSPORTATION

RESEARCH CENTER

PROJECT SCHEDULE

Project Title	Prototype-scale scour testing of cohesive soil																								FY	2013	Month	September			
FDOT Project No.																															
Research Agency	University of North Florida-University of Florida																														
Principal Investigator	Dr. Raphael Crowley, P.E. (UNF)-Dr. D. Max Sheppard (UF)																														
RESEARCH	1	2	3	4	5	6	7	8	9	10	11	12	13	14	15	16	17	18	19	20	21	22	23	24	25	26	27	28	29	30	ESTIMATED %
TASK																															COMPLETION
Task 1: Preparation of full-scale																															
scour instrumentation																															
Task 2: Moving the SERF																															
Task 3: Full-scale scour tests																															
Task 4: SERF tests																															
Task 5: Computational Modeling																															
Task 6: Draft Final Report																															
Task 7: Final Report																															
Overall % Complete																															
Projected	2%	4%	6%	9%	11%	13%	15%	17%	21%	26%	28%	30%	32%	34%	38%	43%	47%	51%	55%	62%	68%	74%	79%	83%	87%	91%	94%	96%	98%	100%	
Overall % Complete																															
Actual																															

FIG. A -- OVERALL PROJECT SCHEDULE

Figure 7-3. Proposed overall project schedule

		Raphael W. Crowley/Prototype-Scale Scour Testing of Cohesive Soil				
		Project Dates				
CAS needed?	Object Code	Budget Items	Year 1 1/1/2014 - 1/1/2015	Year 2 1/1/2015 - 1/1/2016	Year 3 1/1/2016 - 1/1/2017	Total
		Salaries (UNF Faculty and A&P)				
No	611001	Faculty 9-month during AY	$ 27,500	$ 28,325	$ 14,587	
No	611002	Faculty 9-month during summer				
No	611000	Faculty 12-month				
Maybe	612000	A&P				
		Sub-total	$ 27,500	$ 28,325	$ 14,587	$ 70,412
		Wages (UNF Students, OPS, USPS) - show name (if known) hourly wage, number of hours or				
No	712006	Faculty Supplemental Compensation (OPS)				
No	712003	Part Time Faculty Contracts (OPS)				
Yes	613000	USPS				
No	711004	Graduate Research Assistant:	$ 5,000	$ 20,000	$ 20,000	
Maybe	711001	Undergraduate Student				
Maybe	713001	OPS/Part-Time Employment	$ 40,000	$ 40,000		
		Sub-total	$ 45,000	$ 60,000	$ 20,000	$ 125,000
		Employee Benefits - use one line per category				
No	629996	Faculty @ 28.8%	$ 7,920	$ 8,158	$ 4,201	
No	629996	Faculty Summer term @ 7.65%	$ -			
No	629996	Faculty Supplemental compensation and Part Time @ 7.65%	$ -			
No	629996	A&P @ 32.7%	$ -			
No	629996	USPS @ 44.2%	$ -			
No	719996	OPS / Students @ 7.65%	$ 3,443	$ 4,590	$ 1,530	
No	719996	OPS FICA Alternative @ 1.45% (NOT Phased/Returning/Active Retiree, Grad/Undergrad Student, USPS/A&P)	$ 73			
		Sub-total	$ 11,435	$ 12,748	$ 5,731	$ 29,914
		Contractual - Any non-UNF individuals or entities				
No	721080	Subawards ≤ $25,000				
No	721081	Subawards > $25,000	$ 5,000	$ 5,000	$ 2,500	
No	721082	Other Contractual Services				
		Sub-total	$ 5,000	$ 5,000	$ 2,500	$ 12,500
		Equipment - ≥ $5,000 with at least a 1 year life PER item				
No	792080	Desktop Computer				
No	792082	Laptop Computer				
No	792083	Server				
No	793080	Audio-Visual Technology-Overhead Projector				
No	793080	Audio-Visual Technology-Video Projector				
No	793080	Audio-Visual Technology-Projection Screen				
No	793080	Audio-Visual Technology-TV Monitor				
No	793080	Audio-Visual Technology-DVD/CD Player/Recorder				
No	793080	Audio-Visual Technology-Camera and Accessories				
No	791082	Lab Equipment	$ 30,000			
Yes	791083	Office Equipment				
Yes	791081	Office Furniture				
Maybe	794180	Communication Device				
		Sub-total	$ 30,000			$ 30,000
		Travel -				
No	772180	In State Travel				
No	772280	Out of State Travel	$ 2,500	$ 2,500	$ -	
No	772380	Foreign Travel				
		Sub-total	$ 2,500	$ 2,500	$ -	$ 5,000
		Materials and Supplies				
No	740881	Laboratory/Technical Supplies				
Yes	740880	Office Materials and Supplies				
Maybe	740882	Educational Materials				
No	740883	Medical Supplies				
No	740884	Computer Equipment < $5,000				
No	740885	Audio-Visual Technology < $5,000				
No	741881	Lab Equipment < $5,000	$ 500			
	741881	Lab Equipment:				
Maybe	741887	Communication Devices < $5,000 (PDAs / GIS / Wireless Card)				
No	741883	Desktop Computer	$ 1,500			
No	741884	Laptop Computer				
No	741885	Server				
No	741886	Audio-Visual Technology-Overhead Projector				
No	741886	Audio-Visual Technology-Video Projector				
No	741886	Audio-Visual Technology-Projection Screen				
No	741886	Audio-Visual Technology-TV Monitor				
No	741886	Audio-Visual Technology-DVD/CD Player/Recorder				
No	741886	Audio-Visual Technology-Camera and Accessories				
Yes	741882	Office Equipment				
Yes	741880	Office Furniture				
Maybe	776000	Software - Licenses				
Maybe	776002	Software - Packages				
		Sub-total	$ 2,000			$ 2,000
		Other				
Maybe	715080	Cell Phone Allowance				
Maybe	721013	Advertising Promotional				
Maybe	731005	Utilities-Other				
Yes	732001	Local Phone Service - Monthly service charge				
Yes	732001	Local Phone Service - Monthly service charge (Wireless Card Service)				
Yes	732001	Telephone Service Charges for set-up or repair (new/add'l Line, change of number, etc.)				
No	732005	Long-Distance Phone Charges (Suncom)				
Maybe	751080	Repairs / Maintenance-Commodities				
Maybe	752080	Repairs / Maintenance-Services				
No	761000	UNF Student Tuition / Scholarships / Educational Assistance	$ 12,000	$ 12,600	$ 13,230	
No	771006	Freight / Courier Postage	$ 3,000			
Yes	771010	Local Postage				
No	771025	Stipends/Non-UNF Scholarship Payments				
No	771880	Publications - Reprints, Journal Page Charges				
No	771881	Participant Incentives				
Yes	771882	Memberships				
Yes	771883	Subscription				
No	771885	Food (non-entertainment meals or non-travel meals for events associated with SOW only)				
No	771886	UNF Fee-For-Service/Recharge Centers-PORL				
No	771887	UNF Fee-For-Service/Recharge Centers-FIE				
Maybe	771980	Rental of Space	$ 5,000	$ 5,000	$ -	
No	771981	Rental of Equipment				
No	775080	Printing/Design Services				
		Sub-total	$ 20,000	$ 17,600	$ 13,230	$ 50,830
		Construction (not usually allowed)				
	N/A	Renovation				
	N/A	New Construction				
		Sub-total	$ -			$ -
		Participant Support Costs - Conference/Event Attendees				
No	771025	Stipend				
No		Travel - use applicable account code above based on type of travel				
No	771885	Food				
No		Other				
		Sub-total	$ -			$ -
		Total Direct Costs	$ 325,656			$ 325,656
	771080	**F&A at 10% of Total Direct Costs** Indirect Costs	$ 27,366			$ 27,366
		TOTAL COSTS	$ 353,022			$ 353,022
		Prepared by: R. Crowley				
		Indirect Cost Basexxx (modify with appropriate subcontract calculation):	$ 273,656			

Figure 7-4. Overall project budget sheet

FLORIDA DEPARTMENT OF TRANSPORTATION

RESEARCH CENTER

PROJECT SCHEDULE

Project Title	Prototype-scale scour testing of cohesive soil - phase I, large-scale test	FY	2013
FDOT Project No.		Month	September
Research Agency	University of North Florida-University of Florida		
Principal Investigator	Dr. Raphael Crowley, P.E. (UNF)-Dr. D. Max Sheppard (UF)		

RESEARCH TASK	1	2	3	4	5	6	7	8	9	10	11	12	13	14	15	16	17	18	19	20	21	22	23	24	25	26	ESTIMATED % COMPLETION
Task 1: Preparation of full-scale scour instrumentation																											
Task 2: Full-scale scour tests																											
Task 3: Draft Final Report																											
Task 4: Final Report																											
Overall % Complete Projected	3%	6%	9%	12%	15%	18%	21%	24%	27%	30%	33%	36%	39%	42%	45%	52%	58%	64%	70%	76%	82%	88%	91%	94%	97%	100%	
Overall % Complete Actual																											

FIG. A -- OVERALL PROJECT SCHEDULE

Figure 7-5. Proposed schedule excluding SERF testing and computational modeling

		Raphael W. Crowley/Prototype-Scale Scour Testing of Cohesive Soil				
		Project Dates				
CAS needed?	Object Code	Budget Items	Year 1 1/1/2014 - 1/1/2015	Year 2 1/1/2015 - 1/1/2016	Year 3 1/1/2016 - 1/1/2017	Total
		Salaries (UNF Faculty and A&P)				
No	611001	Faculty 9-month during AY	$ 27,500	$ 28,325	$ 2,431	
No	611002	Faculty 9-month during summer				
No	611000	Faculty 12-month				
Maybe	612000	A&P				
		Sub-total	$ 27,500	$ 28,325	$ 2,431	$ 58,256
		Wages (UNF Students, OPS, USPS) - show name (if known) hourly wage, number of hours or				
No	712006	Faculty Supplemental Compensation (OPS)				
No	712003	Part Time Faculty Contracts (OPS)				
Yes	613000	USPS				
No	711004	Graduate Research Assistant:				
Maybe	711001	Undergraduate Student				
Maybe	713001	OPS/Part-Time Employment	$ 40,000	$ 40,000		
		Sub-total	$ 40,000	$ 40,000	$ -	$ 80,000
		Employee Benefits - use one line per category				
No	629996	Faculty @ 28.8%	$ 7,920	$ 8,158	$ 700	
No	629996	Faculty Summer term @ 7.65%	$ -			
No	629996	Faculty Supplemental compensation and Part Time @ 7.65%	$ -			
No	629996	A&P @ 32.7%	$ -			
No	629996	USPS @ 44.2%	$ -			
No	719996	OPS / Students @ 7.65%	$ 3,060	$ 3,060	$ -	
No	719996	OPS FICA Alternative @ 1.45% (NOT Phased/Returning/Active Retiree, Grad/Undergrad Student, USPS/A&P)	$ -			
		Sub-total	$ 10,980	$ 11,218	$ 700	$ 22,898
		Contractual - Any non-UNF individuals or entities				
No	721080	Subawards ≤ $25,000				
No	721081	Subawards > $25,000	$ 5,000	$ 5,000	$ 833	
No	721082	Other Contractual Services				
		Sub-total	$ 5,000	$ 5,000	$ 833	$ 10,833
		Equipment - ≥ $5,000 with at least a 1 year life PER item				
No	792080	Desktop Computer				
No	792082	Laptop Computer				
No	792083	Server				
No	793080	Audio-Visual Technology-Overhead Projector				
No	793080	Audio-Visual Technology-Video Projector				
No	793080	Audio-Visual Technology-Projection Screen				
No	793080	Audio-Visual Technology-TV Monitor				
No	793080	Audio-Visual Technology-DVD/CD Player/Recorder				
No	793080	Audio-Visual Technology-Camera and Accessories				
No	791082	Lab Equipment	$ 30,000			
Yes	791083	Office Equipment				
Yes	791081	Office Furniture				
Maybe	794180	Communication Device				
		Sub-total	$ 30,000			$ 30,000
		Travel -				
No	772180	In State Travel				
No	772280	Out of State Travel	$ 2,500	$ 2,500	$ -	
No	772380	Foreign Travel				
		Sub-total	$ 2,500	$ 2,500	$ -	$ 5,000
		Materials and Supplies				
No	740881	Laboratory/Technical Supplies				
Yes	740880	Office Materials and Supplies				
Maybe	740882	Educational Materials				
No	740883	Medical Supplies				
No	740884	Computer Equipment < $5,000				
No	740885	Audio-Visual Technology < $5,000				
No	741881	Lab Equipment < $5,000	$ 500			
	741881	Lab Equipment:				
Maybe	741887	Communication Devices < $5,000 (PDAs / GIS / Wireless Card)				
No	741883	Desktop Computer	$ 1,500			
No	741884	Laptop Computer				
No	741885	Server				
No	741886	Audio-Visual Technology-Overhead Projector				
No	741886	Audio-Visual Technology-Video Projector				
No	741886	Audio-Visual Technology-Projection Screen				
No	741886	Audio-Visual Technology-TV Monitor				
No	741886	Audio-Visual Technology-DVD/CD Player/Recorder				
No	741886	Audio-Visual Technology-Camera and Accessories				
Yes	741882	Office Equipment				
Yes	741880	Office Furniture				
Maybe	776000	Software - Licenses				
Maybe	776002	Software - Packages				
		Sub-total	$ 2,000			$ 2,000
		Other				
Maybe	715080	Cell Phone Allowance				
Maybe	721013	Advertising Promotional				
Maybe	731005	Utilities-Other				
Yes	732001	Local Phone Service - Monthly service charge				
Yes	732001	Local Phone Service - Monthly service charge (Wireless Card Service)				
Yes	732001	Telephone Service Charges for set-up or repair (new/add'l Line, change of number, etc.)				
No	732005	Long-Distance Phone Charges (Suncom)				
Maybe	751080	Repairs / Maintenance-Commodities				
Maybe	752080	Repairs / Maintenance-Services				
No	761000	UNF Student Tuition / Scholarships / Educational Assistance				
No	771006	Freight / Courier Postage	$ 3,000			
Yes	771010	Local Postage				
No	771025	Stipends/Non-UNF Scholarship Payments				
No	771880	Publications - Reprints, Journal Page Charges				
No	771881	Participant Incentives				
Yes	771882	Memberships				
Yes	771883	Subscription				
No	771885	Food (non-entertainment meals or non-travel meals for events associated with SOW only)				
No	771886	UNF Fee-For-Service/Recharge Centers-PORL				
No	771887	UNF Fee-For-Service/Recharge Centers-FIE				
Maybe	771980	Rental of Space	$ 5,000	$ 5,000	$ -	
No	771981	Rental of Equipment				
No	775080	Printing/Design Services				
		Sub-total	$ 8,000	$ 5,000	$ -	$ 13,000
		Construction (not usually allowed)				
	N/A	Renovation				
	N/A	New Construction				
		Sub-total	$ -			$ -
		Participant Support Costs - Conference/Event Attendees				
No	771025	Stipend				
No		Travel - use applicable account code above based on type of travel				
No	771885	Food				
No		Other				
		Sub-total	$ -			$ -
		Total Direct Costs	$ 221,987			$ 221,987
	771080	**F&A at 10% of Total Direct Costs** Indirect Costs	$ 18,199			$ 18,199
		TOTAL COSTS	$ 240,186			$ 240,186
		Prepared by: R. Crowley				
		Indirect Cost Basexxx (modify with appropriate subcontract calculation):	$ 181,987			

Figure 7-6. Budget sheet for prototype-scale tests only

FLORIDA DEPARTMENT OF TRANSPORTATION

RESEARCH CENTER

PROJECT SCHEDULE

Project Title	Prototype-scale scour testing of cohesive soil - phase II: computational and SERF modeling	FY	2013
FDOT Project No.		Month	September
Research Agency	University of North Florida-University of Florida		
Principal Investigator	Dr. Raphael Crowley, P.E. (UNF)-Dr. D. Max Sheppard (UF)		

RESEARCH TASK	1	2	3	4	5	6	7	8	9	10	11	12	13	14	15	16	17	18	19	20	21	22	23	24	ESTIMATED % COMPLETION
Task 1: Moving the SERF																									
Task 2: SERF tests																									
Task 3: Computational Modeling																									
Task 4: Draft Final Report																									
Task 5: Final Report																									
Overall % Complete Projected	0%	0%	4%	8%	8%	8%	8%	8%	13%	17%	21%	25%	29%	33%	42%	50%	58%	67%	75%	83%	88%	92%	96%	100%	
Overall % Complete Actual																									

FIG. A -- OVERALL PROJECT SCHEDULE

Figure 7-7. Proposed schedule excluding large-scale test

Raphael W. Crowley/Prototype-Scale Scour Testing of Cohesive Soil

Project Dates

CAS needed?	Object Code	Budget Items	Year 1 1/1/2014 - 1/1/2015	Year 2 1/1/2015 - 1/1/2016	Total
		Salaries (UNF Faculty and A&P)			
No	611001	Faculty 9-month during AY	$ 27,500	$ 28,325	
No	611002	Faculty 9-month during summer			
No	611000	Faculty 12-month			
Maybe	612000	A&P			
		Sub-total	$ 27,500	$ 28,325	$ 55,825
		Wages (UNF Students, OPS, USPS) - show name (if known) hourly wage, number of hours or			
No	712006	Faculty Supplemental Compensation (OPS)			
No	712003	Part Time Faculty Contracts (OPS)			
Yes	613000	USPS			
No	711004	Graduate Research Assistant:	$ 20,000	$ 20,000	
Maybe	711001	Undergraduate Student			
Maybe	713001	OPS/Part-Time Employment			
		Sub-total	$ 20,000	$ 20,000	$ 40,000
		Employee Benefits - use one line per category			
No	629996	Faculty @ 28.8%	$ 7,920	$ 8,158	
No	629996	Faculty Summer term @ 7.65%	$ -		
No	629996	Faculty Supplemental compensation and Part Time @ 7.65%	$ -		
No	629996	A&P @ 32.7%	$ -		
No	629996	USPS @ 44.2%	$ -		
No	719996	OPS / Students @ 7.65%	$ 1,530	$ 1,530	
No	719996	OPS FICA Alternative @ 1.45% (NOT Phased/Returning/Active Retiree, Grad/Undergrad Student, USPS/A&P)	$ 290		
		Sub-total	$ 9,740	$ 9,688	$ 19,428
		Contractual - Any non-UNF individuals or entities			
No	721080	Subawards ≤ $25,000			
No	721081	Subawards > $25,000	$ 5,000	$ 5,000	
No	721082	Other Contractual Services			
		Sub-total	$ 5,000	$ 5,000	$ 10,000
		Equipment - ≥ $5,000 with at least a 1 year life PER item			
No	792080	Desktop Computer			
No	792082	Laptop Computer			
No	792083	Server			
No	793080	Audio-Visual Technology-Overhead Projector			
No	793080	Audio-Visual Technology-Video Projector			
No	793080	Audio-Visual Technology-Projection Screen			
No	793080	Audio-Visual Technology-TV Monitor			
No	793080	Audio-Visual Technology-DVD/CD Player/Recorder			
No	793080	Audio-Visual Technology-Camera and Accessories			
No	791082	Lab Equipment			
Yes	791083	Office Equipment			
Yes	791081	Office Furniture			
Maybe	794180	Communication Device			
		Sub-total	$ -		$ -
		Travel -			
No	772180	In State Travel			
No	772280	Out of State Travel			
No	772380	Foreign Travel			
		Sub-total	$ -	$ -	$ -
		Materials and Supplies			
No	740881	Laboratory/Technical Supplies			
Yes	740880	Office Materials and Supplies			
Maybe	740882	Educational Materials			
No	740883	Medical Supplies			
No	740884	Computer Equipment < $5,000			
No	740885	Audio-Visual Technology < $5,000			
No	741881	Lab Equipment < $5,000			
	741881	Lab Equipment:			
Maybe	741887	Communication Devices < $5,000 (PDAs / GIS / Wireless Card)			
No	741883	Desktop Computer			
No	741884	Laptop Computer			
No	741885	Server			
No	741886	Audio-Visual Technology-Overhead Projector			
No	741886	Audio-Visual Technology-Video Projector			
No	741886	Audio-Visual Technology-Projection Screen			
No	741886	Audio-Visual Technology-TV Monitor			
No	741886	Audio-Visual Technology-DVD/CD Player/Recorder			
No	741886	Audio-Visual Technology-Camera and Accessories			
Yes	741882	Office Equipment			
Yes	741880	Office Furniture			
Maybe	776000	Software - Licenses			
Maybe	776002	Software - Packages			
		Sub-total	$ -		$ -
		Other			
Maybe	715080	Cell Phone Allowance			
Maybe	721013	Advertising Promotional			
Maybe	731005	Utilities-Other			
Yes	732001	Local Phone Service - Monthly service charge			
Yes	732001	Local Phone Service - Monthly service charge (Wireless Card Service)			
Yes	732001	Telephone Service Charges for set-up or repair (new/add'l Line, change of number, etc.)			
No	732005	Long-Distance Phone Charges (Suncom)			
Maybe	751080	Repairs / Maintenance-Commodities			
Maybe	752080	Repairs / Maintenance-Services			
No	761000	UNF Student Tuition / Scholarships / Educational Assistance	$ 12,000	$ 12,600	
No	771006	Freight / Courier Postage			
Yes	771010	Local Postage			
No	771025	Stipends/Non-UNF Scholarship Payments			
No	771880	Publications - Reprints, Journal Page Charges			
No	771881	Participant Incentives			
Yes	771882	Memberships			
Yes	771883	Subscription			
No	771885	Food (non-entertainment meals or non-travel meals for events associated with SOW only)			
No	771886	UNF Fee-For-Service/Recharge Centers-PORL			
No	771887	UNF Fee-For-Service/Recharge Centers-FIE			
Maybe	771980	Rental of Space			
No	771981	Rental of Equipment			
No	775080	Printing/Design Services			
		Sub-total	$ 12,000	$ 12,600	$ 24,600
		Construction (not usually allowed)			
	N/A	Renovation			
	N/A	New Construction			
		Sub-total	$ -		$ -
		Participant Support Costs - Conference/Event Attendees			
No	771025	Stipend			
No		Travel - use applicable account code above based on type of travel			
No	771885	Food			
No		Other			
		Sub-total	$ -		$ -
		Total Direct Costs	$ 149,853		$ 149,853
	771080	**F&A at 10% of Total Direct Costs** Indirect Costs	$ 13,285		$ 13,285
		TOTAL COSTS	$ 163,138		$ 163,138
		Prepared by: R. Crowley			
		Indirect Cost Base xxx (modify with appropriate subcontract calculation)	$ 132,853		

Figure 7-8. Budget sheet for computational modeling and SERF testing only

CHAPTER 8
THE SAND INJECTOR

8.1 Introduction

During Sheppard's work that led to the current specifications for designing for bridge scour in Florida (Florida Department of Transportation, 2005), Sheppard noticed that when the amount of sand trapped in the water column during an erosion event increased, scour depth appeared to decrease. Sheppard (2012) believes that the increase in sand particle concentration may decrease turbulent eddy generation. This in turn may reduce the shear stress upon the bed, which in turn would lead to reduced erosion during a scour event.

In an effort to test this hypothesis, a sand injection device was built to be used during a series of SERF tests (Bloomquist and Crowley, 2010, Figure 8-1). Unfortunately, as discussed in Chapter 1, the SERF lacked an adequate filtration system; therefore, the sand injector was never connected or used during the previous SERF-related, FDOT-sponsored research project (Bloomquist and Crowley, 2010).

During this project, investigators attempted to get the sand injection system connected so that test could be conducted in the SERF with suspended sediment in the water column. Unfortunately, as mentioned in Chapter 1, investigators were unable to get the sand injector to function as designed. This chapter describes the attempts that were made to install a sand injection system and a discussion about the suspected relative effects of suspended sediment in the water column on erosion functions.

8.2 First Attempt to Connect Sand Injector

First, investigators tried to connect the sand injector that had been built during FDOT project no. BDK75 977-09. Because investigators were unsure about the

effectiveness of the device, a series of bypass valves were installed so that the device could be closed-off during non-sand injection tests (Figure 8-2). This allowed investigators to focus on this project's biggest priority – investigating erosion rates of field samples using the SERF – without being preoccupied with the sand injector's performance.

Once all field sample tests were completed, the sand injector was wired and turned on. Investigators noticed that the feed screw rotated backwards. Therefore, the wiring was reversed, and the screw turned as designed. The sand reservoir was filled with Ottawa 50/70 testing sand and water, and immediately, issues with the design became apparent. Because the sand was wet (as would always be the case during a SERF test), apparent cohesion appeared to take effect such that the sand appeared to stiffen. As a result, the feed screw "seized" and failed to move. This issue was temporarily remedied by "helping" the screw achieve initial movement by pulling on the sand injector's belt.

However, once the screw began turning, it became obvious that the device would not push sand upward into the flume. There were two reasons for this. First, as mentioned, the sand was moist and apparent cohesion had begun to play a role in the soil dynamics associated with it. As a result, the sand failed to "fall" into the feed screw's threads. Instead, the screw was effectively boring a hole into the sand – which was not how the device was designed to function. The sand was dried, and another attempt was made to push sand upward into the flume using the feed screw. This test also failed because the dry sand tended to slip from the PVC threads.

8.3 Sand Injector Redesign

As a result of these failures, the device was redesigned (Figure 8-3). After experimenting with the feed screw mechanism, investigators realized that it would push sand if it was turned horizontally. Therefore, a trough-type system was designed and implemented (Figure 8-4). The barrel-style reservoir system was replaced with a Plexiglas hopper. As the feed screw turned, sand was pushed horizontally until it fell into the flume at a ninety-degree angle. Meanwhile, sand was free to fall through the hopper, onto the trough so that it could be pushed. A valve was provided to allow investigators to "close-off" the system when a non-sand-injection test was to be conducted. The hopper was filled halfway with Ottawa 50/70 testing sand, and the device was tested.

Once again, issues with the design became apparent. When sand height in the hopper was relatively low, the screw was capable of moving sand into the flume. However, as sand height increased, the screw began to seize and fail to turn. When water was added to the hopper, the screw would turn and push sand to some extent, but its rate appeared to be a function of hopper sand height and inconsistent.

Next, investigators attempted a sand injection test. Two methods were used for this. First, the valve was opened, and the SERF's primary pump was started. At low flow speeds (less than 20 Hz pump frequency), the hopper failed to fill with water. As a result, the SERF system failed to pressurize – thereby creating a pseudo-open-channel-flow situation. When the reverse methodology was employed so that the SERF duct was pressurized and then the sand injector valve was opened, sand was injected to some extent, although injection rate appeared to be inconsistent. Additionally, when the

valve was opened after flow was started in the SERF, the sand injector's hopper failed to fill/become pressurized. This is believed to be the cause of the apparently inconsistent injection rates (combined with variable hopper sand heights). More importantly, because the system failed to pressurize, it would not have been possible to determine if changes in erosion rate for a given pump speed were the result of sand in the water column or the flow "splitting" between the injector and the remainder of the SERF.

It must be noted that to overcome motor seizure issues, the low flow-rate tests were conducted at relatively high screw rotational speeds. As a result, sand was injected into the flume so quickly that the filter ceased to be effective. To avoid further breakage to the pumps, investigators chose to shut down testing at lower flow speeds.

At higher SERF flow speeds, the sand-water mixture that was created in the hopper was observed to be much "looser." Therefore, the feed screw would turn at lower rotational speeds. However, the sand became so loose that investigators realized that feed screw rotation had almost no effect on injection rate. Instead, at higher rotational speeds, a pressure gradient was created between the water in the hopper and the water moving through the flume. Because of the pressure gradient, the sand-water mixture from the hopper was "sucked" down the feed screw even when the screw was stagnant. This "sucking" mechanism was so fast that all sand was removed from the hopper in less than one minute. This was not long enough to obtain erosion data; and as previously implied, the filter ceased to be effective under these conditions.

In summary, the only combination of steps that appeared to be somewhat effective was the following:

1. Start an erosion test without the sand injector (i.e. close the sand injector valve).
2. Open the sand injector valve.
3. Start the feed screw and hope that conditions in the hopper were such where the screw would not “seize” at a given rotational speed.

Of course, this set of steps was not repeatable from test-to-test; and therefore, it was not possible to obtain a repeatable set of data to show whether or not sand had an effect on erosion rate at a given shear stress.

8.4 Discussion

Ultimately, it may be possible to calibrate a feed screw type injection system, but investigators ultimately concluded that this would constitute a significant research project in-and-of itself. The idea from a feed screw was meant to mimic a similar injection-style system that was seen by on of this project’s principle investigators (D. M. Sheppard). In the previous example, an injector was used in an open-channel flume. Therefore, in the previous configuration, sand could be kept dry until it was injected into the flume – at which point, it entered the water column. Of course, the SERF is a pressurized, closed-flume-style instrument. This is the source of the errors associated with the feed screw system.

It is also worth noting that while on the surface it appears that investigators found a method for the injection system that was pseudo-effective some of the time, (steps 1 – 3 in Section 8.2), it is doubtful that this procedure is actually useful. The SERF is designed to measure erosion functions for cohesive sediment so that these values may be used for cohesive design scour depths. FDOT already has a relatively in-depth understanding of scour depths for sand; therefore, there is not a large need for conducting SERF sand injection tests at the low flow rates associated with sand

erosion. For clays, a higher shear stress would be required – which in turn would cause the pressure gradient issue. Even with a redesign, it is likely that this pressure gradient issue would still be apparent.

A possible solution to the pressure gradient issue during a cohesive erosion test is to install a large piston. The piston would be similar to the SERF sample testing piston, although it would have a much larger diameter and a much larger stroke length. A longer stroke length could be achieved by boring into the floor in Reed lab and installing a motor in the borehole that would turn at a constant rate. The motor would be connected to a lead screw using a worm gear. As long as injection rate remained relatively low, it should be sufficient for a cohesive erosion test. Of course, the motor in such a setup would need to provide relatively high torque to overcome the friction of a larger piston. Or, alternatively, high torque could be achieved by using a small worm-gear combined with a large-diameter lead screw gear.

Finally, it may be wise to rethink the effect of suspended sediment during a cohesive erosion test. While Sheppard's 2004 tests showed an apparent effect for sand, it is likely that clay erosion rates become dominated by cohesion. As such, investigators hypothesize that the effect of sand injection may be minor relative to other effects. The preparer of this report understands that the motivation for much of this scour research is to develop more accurate scour equations so that scour depths are not over-predicted. While the effect of sand injection may have some marginal effect on cohesive scour depth, it is far more likely that taking shear stress reduction during scour hole development into account will play a much larger role in improving scour equations'

predictive accuracy. Therefore, moving forward, it is recommended that FDOT put future efforts toward the stress-reduction modeling discussed in Chapter 7.

LIST OF REFERENCES

Alizadeh, A. (1974). Amount and type of clay and pore fluid influences on the critical shear stress and swelling of cohesive soils. Ph.D. dissertation, University of California, Davis.

Annandale, G.W. (2006). *Scour Technology*. McGraw-Hill, New York.

Arneson, L. A., Zevenbergen, L. W., Lagasse, P. F., and Clopper, P. E. (2012) *Evaluating Scour at Bridges, Fifth Edition*. U. S. Department of Transportation, Federal Highway Administration, Washington, D. C.

Arulanandan, K., Sargunam, A., Loganathan, P., and Krone, R.B. (1973). Application of chemical and electrical parameters to prediction of erodibility. Soil Erosion: Causes and Mechanisms; Prevention and Control, Conference Workshop on Soil Erosion, Highway Research Board Special Report 135, Washington, DC.

Attaway, S. (2013). *MATLAB: a PRACTICAL Introduction to Programming and Problem Solving Third Edition*, Elsevier Inc., Waltham, MA.

Bayazit, M. (1976). Free surface flow in a channel of large relative roughness. *J. of Hydraulic Res.*, 14, 115-126.

Bloomquist, D., and Crowley, R. W. (2010). Enhancement of FDOT's SERF device and a study of erosion rates of rock, sand, and clay mixtures using FDOT's RETA and SERF equipment. Final Report No. BDK75 977-09. Florida Department of Transportation, Tallahassee, FL.

Bloomquist, D., Sheppard, D. M., Schofield, S., and Crowley R. W. (2012). The rotating erosion testing apparatus (RETA): a laboratory device for measuring erosion rates versus shear stresses of rock and cohesive materials. *ASTM Geotechnical Testing Journal*, 35 (4), 990-994.

Bollaert, E. and Schleiss, A. (2003a). Scour of rock due to the impact of plunging high velocity jets part I: a state-of-the-art review. *Journal of Hydraulics Research*, 41(5), 451-464.

Bollaert, E. and Schleiss, A. (2003b). Scour of rock due to the impact of plunging high velocity jets part II: experimental results of dynamic pressures at pool bottoms in one- and two-dimensional closed end rock joints. *Journal of Hydraulics Research*, 41 (5), 465-480.

Bollaert, E. F. R. (2010). Numerical modeling of scour at bridge foundations on rock. *Proc. ASCE Fifth International Conference on Scour and Erosion*, San Francisco, CA.

Briaud, J.L. (2004). Scour #1 killer of bridges. *Geostrata*. The Geotechnical Institute of the American Society of Civil Engineers, Fall.

Briaud, J.L., Chen, H. C., Li, Y., Nurtjahyo, P., and Wang, J. (2004a). Pier and contraction scour in cohesive soils. *NCHRP Report 516*, Transportation Research Board, Washington, D.C.

Briaud, J. L., Chen, H. C., Li, Y., Nurtjahyo, P., and Wang, J. (2004b). SRICOS-EFA method for complex piers in fine-grained soils. *J. of Geotechnical and Geoenvironmental Engineering*, 130(11), 1180-1191.

Briaud, J. L., Ting, F.C.K., Chen, H. C., Gudavalli, R., Perugu, S., and Wei, G. (1999). SRICOS: Prediction of scour rate in cohesive soils at bridge piers. *J. of Geotechnical and Geoenvironmental Engineering*, 125(4), 237 – 246.

Briaud, J.L., Ting, F., Chen, H.C. Cao, Y., Han, S.-W., Kwak, K (2001). Erosion function apparatus for scour rate predictions. *J. of Geotechnical and Geoenvironmental Engineering,* 127 (2), 105-113.

Camenen, B., Bayram, A., and Larson, M. (2006). Equivalent roughness height for plane bed under steady flow. *J. Hydraulic Engineering*, 132(11), 1146-1158.

CD-adapco (2012). *User Guide Star-CCM+ Version 7.06.* CD-adapco, Melville, NY.

Chapius, R., and Gatien, T. (1986). An improved rotating cylinder technique for quantitative measurements of the scour resistance of clays. *Canadian Journal of Geotechnical Engineering,* 23, 83-87.

Chen, H. C. (2002). Numerical simulation of scour around complex piers in cohesive soil. *Proc. First Int. Conf. on Scour and Erosion*, Texas A&M University, College Station, TX.

Crowley, R., Bloomquist, D., Hayne, J., and Holst, C. (2012a). Estimations and measurements of shear stresses on bed materials in erosion rate testing devices. *Journal of Hydraulic Engineering*, 138 (11), 990-994.

Crowley, R., Bloomquist, D., Shah, F., and Holst, C. (2012b). The sediment erosion rate flume (SERF): a new testing device for measuring erosion rates and shear stresses. *Geotechnical Testing Journal*, 35 (4), 649-659.

Crowley, R., Robeck, C., and Thieke, R.J. (2013). Computer modeling of bed material shear stresses in piston-type erosion ate testing devices. *Journal of Hydraulic Engineering*, posted online ahead of print, http://ascelibrary.org/doi/abs/10.1061/%28ASCE%29HY.1943-7900.0000797.

Dancey, C. L., Balakrishnan, M., Diplas, P., and Papanicolaou, A. N. (2000). The spatial inhomogeneity of turbulence above a fully rough, packed bed in open channel flow. Exp. Fluids, 29, 402-410.

Dargahi, B. (1987). Flow-field and local scouring around a cylinder. *Bulletin No. TRITA-VBI-137*, Royal Inst. Of Tech., Hydraulics Laboratory, Stockholm, Sweden.

Dargahi, B. (1990). Controlling mechanism of local scouring. *J. of Hydraulic Engr.*, 116 (10), 1196-1214.

Davis, P. L., Rinehimer, T., and Uddin, M. (2012). A comparison of RANS-based turbulence modeling for flow over a wall-mounted square cylinder. Proc. 20th Annual Conference of the CFD Society of Canada, Canmore, AB, May 9-12.

Einstein, H. A. and Krone, R. B. (1962). Experiments to determine modes of cohesive sediment transport in salt water. *J. Geophysical Research*, 67(4), 1451-1461.

Einstein, H. A and El Samni, E. A. (1949). Hydrodynamic forces on a rough wall. *Rev. Modern Physics*, 21, 520-524.

Florida Department of Transportation, Tallahassee, FL (2005). *Bridge Scour Manual.*

Gordon, S. (1992). Scourability of rock formations. Federal Highway Administration Memorandum, July 19, Washington, D.C.

Gosselin, M. S. and Sheppard, D. M. (1997). Physical and numerical experiments on the time-rate of scour. Report No. UFL/COEL/MP-96-02, University of Florida, Gainesville, FL.

Graf, W.H. and Istiarto, I. (2002). Flow pattern in the scour hole around a cylinder. *J. Hydraulic Research,* 40 (1), 13-19.

Gudavalli, S. R. (1997). Prediction model for scour rate around bridge piers in cohesive soils on the basis of flume tests. Ph.D. Dissertation, Texas A&M University, College Station, TX.

Gust, G. (1988). Skin friction probes for field applications. *Journal of Geophysical Research*, vol. 93 (C11), 14121-14132.

Hjorth, P. (1975). Studies on the nature of local scour. Dept. of Water Resource Engineering, Lund Inst. Of Tech., Bulletin Series A., No. 14.

Hosny, M. M. (1995). Experimental study of local scour around circular piers in cohesive soils. Ph.D. dissertation, Colorado State University, Fort Collins, CO.

Jongen, T. (1998). Simulation and modeling of turbulent incompressible flows. Ph.D. thesis, Lausanne EPFL.

Kamphuis, J. W. (1974). Determination of sand roughness for fixed beds. *J. Hydraulic Res.,* 12, 193-203.

Kandiah, A. (1974). Fundamental aspects of surface erosion of cohesive soils. Ph.D. dissertation, University of California, Davis, CA.

Kerenyi, K. (2012). Personal conversations. *FHWA Turner-Fairbank Highway Research Center*, McLean VA.

Kirkil, G., Constantinescu, G., and Ettema, R. (2005). The horseshoe vortex system around a circular bridge pier on equilibrium scour bed. *World Water and Environmental Resources Congress*, Canada.

Kirkil, G., Constantinescu, G., and Ettema, R. (2008). Coherent structures in the flow field around a circular cylinder with scour hole. *J. of Hydraulic Engr*, 134(5) 572-587.

Li, Y. (2002). Bridge pier scour and contraction scour in cohesive soils on the basis of flume tests. Ph.D. Dissertation, Texas A&M University, College Station, TX.

Lottes, S. (2012). Principle Mechanical Engineer, Energy Systems Division, Argonne National Laboratories Transportation Research and Computing Center. Personal conversations.

McNeil, J., Taylor, C., and Lick, W. (1996). Measurements of erosion of undisturbed bottom sediments with depth. *J. of Hydraulic Engineering*, 122(6), 316 – 324.

McVay, M.C., Townsend, F. C., and Williams, R. C. (1992). Design of socketed drilled shafts in limestone. *J. of Geotechnical Engr.*, 118 (10) 1626-1637.

Melville, B.W., and Sutherland, A.J. (1989). Design method for local scour at bridge piers. *J. of Hydraulic Engineering*, 114 (10), 1210-1266.

Melville, B.W. (1997). Pier and abutment scour: integrated approach. *J. of Hydraulic Engr.*, 123 (2), 125-136.

Melville, B.W. and Chiew, Y.M. (1999). Time scale for local scour at bridge piers. *J. Hydraulic Engineering*, 125 (1) 59-65.

Melville, B.W. and Coleman, S.E. (2007). *Bridge Scour*, Water Resources Publication, LLC, Highlands Ranch, Colorado.

Mitchener, H., and Torfs, H. (1996). Erosion of mud/sand mixtures. *Coastal Engineering* 29, 1-25.

Moore, W.L. and Masch. F.D. (1962). Experiments on the scour resistance of cohesive sediments. *Journal of Geophysical Research*, 67(4), 1436-1446.

Oh, S. J. (2009). Experimental study of bridge scour in cohesive soil. Ph.D. Dissertation, Texas A&M University, College Station, TX.

Oh, S. J., Briaud, J. L., Chang, K. A., and Chen, H. C. (2011). Maximum pier scour depth in fine grained soil. *Journal of Geotechnical and Geoenvironmental Engineering*, cited in Briaud et al. 2011.

Olsen, R. R. B., and Kjellesvig, H. M. (1998). Three dimensional numerical flow modeling for estimation of maximum local scour depth. *J. of Hydraulic Research*, IAHR, 36 (4), 579-590.

Partheniades, E. (1965). Erosion and deposition of cohesive soils. *Journal of Hydraulics Division of ASCE*, 91(1), 105-138.

Rahman, S. and Webster, D. R. (2005). The effect of bed roughness on scalar fluctuations in turbulent boundary layers. *Experiments in Fluids*, 28, 372-384.

Reichardt, H. (1951). Vollstaendige darstellung der turbulenten geschwindigkeitsverteilung in glatten leitungen. *Z. Andrew. Math. Mech*, 31(7), 208-219.

Rektorik, R.J., and Smerdon, E.T. (1964). Critical shear stress in cohesive soils from a rotating shear stress apparatus. *Paper No. 64-216, American Society of Agricultural Engineers*, June.

Roberts, J., Gotthard, D., and Lick, W. (1998). Effects of particle size and bulk density on erosion of quartz particles. *Journal of Hydraulic Engineering*, 124, 1261-1267.

Rodi, W. (1991). Experience with two-layer models combining the k-e model with a one-equation model near the wall. *29th Aerospace Sciences Meeting*, January 6-10, Reno, NV, AIAA 91-0216.

Roulund, A., Sumer, B. M., Fredsoe, J., and Michelsen, J. (2002). 3-D numerical modeling of flow and scour around a pile. *Proc. First Int. Conf. on Scour and Erosion,* Texas A&M University, College Station, TX, 795-809.

Roulund, A., Sumer, B. M., Fredsoe, J., and Michelsen, J. (2005). Numerical and experimental investigation of flow and scour around a circular pile. *J. Fluid Mech.* 534, 351-401.

Sargunam, A., Riley, P., Arulanandan, K., and Krone, R.B., (1973). Effect of physicochemical factors on the erosion of cohesive soils. *Journal of the Hydraulic Divisions, Proceedings of the American Society of Civil Engineers*, 99 (HY3), March, 555-558.

Schwind, R. (1962). The three-dimensional boundary layer near a strut. Gas Turbine Lab. Rep., MIT.

Sheppard, D.M. (2003). Scour at complex piers. Final Report, Florida Department of Transportation, Tallahassee, FL.

Sheppard, D. M. (2004). An overlooked local scour mechanism. *Transportation Research Record: Journal of the Transportation Research Board*, no. 1890, TRB, National Research Council, Washington, DC, 106-111.

Sheppard, D.M. (2012). Personal conversations. Professor Emeritus, University of Florida; former-president Ocean Engineering Associates, Inc.

Sheppard, D. M., Bloomquist, D., Marin, J., and Slagle, P. (2005). Water erosion of Florida rock materials. Final Report No. BC354 RPWO #12, Florida Department of Transportation, Tallahassee, FL.

Sheppard, D.M., Odeh, M., and Glass, T. (2004) Large scale clear water local pier scour experiments. *J. Hydraulic Engineering*, 130 (10), 957-963.

Sheppard, D.M., and Miller, W. (2006). Live-bed local pier scour experiments. *Journal of Hydraulic Engineering*, 132 (7), 635-642.

Shih, T.-H., Liou, W. W., Shabbir, A., Yang, Z., and Zhu, J. (1994). A new k-ε eddy viscosity model for high Reynolds number turbulent flows – model development and validation. NASA TM 106721.

Slagle, P (2006). Correlations of erosion rate-shear stress relationships with geotechnical properties of rock and cohesive sediments. M.S. thesis, Univ. of Florida, Gainesville, FL.

Ting, C. K., Briaud, J. L., Chen, H. C., Gudavalli, R., Perugu, S., and Gengsheng, W. (2001). Flume tests for scour in clay at circular piers. *Journal of Hydraulic Engineering,* vol. 127 (11), 969-978.

Trammel, M. A. (2004). Laboratory apparatus and methodology for evaluating water erosion rates of erodible rock and cohesive sediments. M.S. thesis, Univ. of Florida, Gainesville, FL.

Unger, J., and Hager W. H. (2007). Down-flow and horseshoe vortex characteristics of sediment embedded bridge piers. *Exp. Fluids* 42, 1-19.

Van Prooijen, B. C. and Winterwerp, J. C. (2008). A stochastic formulation for erosion of cohesive sediments. *Journal of Geophysical Research*, Draft Copy, December 9, 2008.

Vlachos, P. P. (2000). An experimental spatio-temporal analysis of separated flows over bluff bodies using quantitative flow visualization. Ph.D. Thesis, Virginia Polytechnic University, Blacksburg, VA.

Wei, G., Chen, H.C., Ting, F., Briaud, J.L., Gudavalli, R, and Perugu, S. (1997). Numerical simulation to study scour rate in cohesive soils. *Report for the Texas Department of Transportation, Department of Civil Engineering*, Texas A&M University, College Station, TX.

Wei, Q.-D., Chen, G., and Du, X.-D. (2001). An experimental study on the structure of juncture flows. *Journal of visualization,* 3(4) 341-348.

White, F. (1986). *Fluid mechanics,* McGraw-Hill, New York, 302-304.

Wolfshtein, M (1969). The velocity and temperature distribution in one-dimensional flow with turbulence augmentation and pressure gradient. *International Journal of Heat and Mass Transfer*, 12, 301-318.

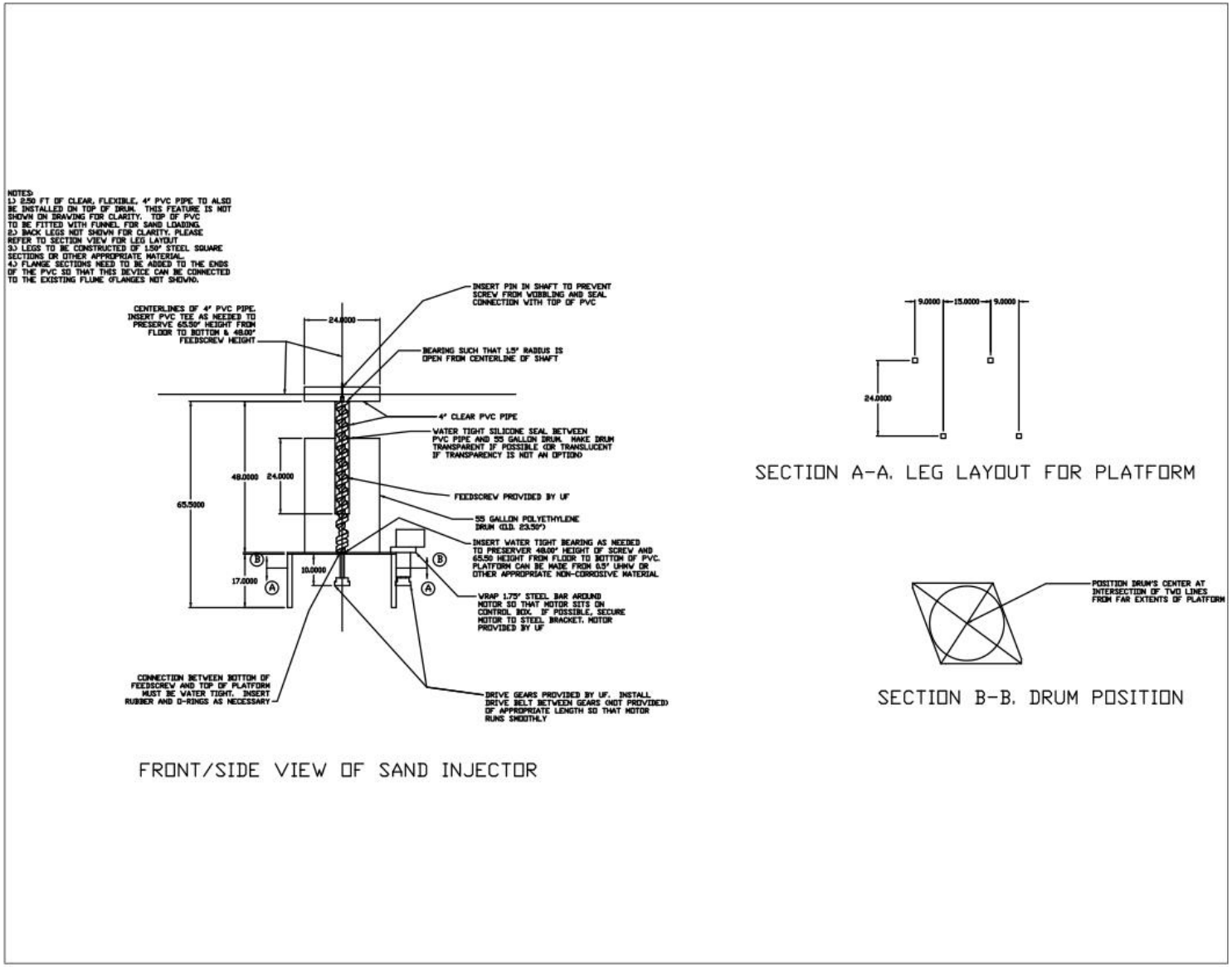

Figure 8-1. Schematic of old sand injector

Figure 8-2. Photograph of original sand injector installed in SERF with valve system

Figure 8-3. Photograph of redesigned sand injector

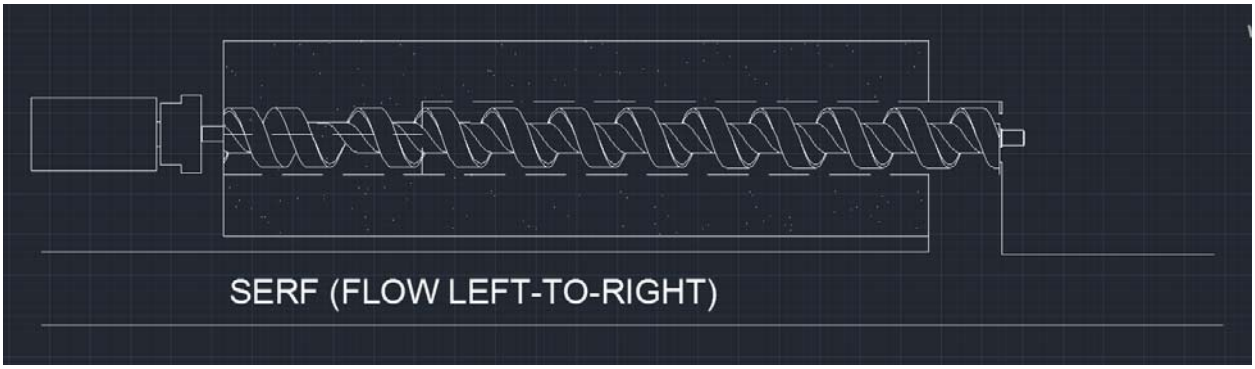

Figure 8-4. Schematic of new sand injector

APPENDIX A
SERF OPERATING MANUAL

The Sediment Erosion Rate Flume (SERF) is the second of two apparatuses developed at the University of Florida for the purpose of measuring the rate at which sediments erode when subjected to a water flow-induced shear stress (the other apparatus, the Rotating Erosion Testing Apparatus or RETA is detailed in Sheppard et al., 2005). Development of the SERF began in the early 2000's and has continued through 2013. In December of 2005, the original manual for SERF testing was developed and in October 2010, the second manual was developed to reflect a number of enhancements and improvements that had been made to the device. Since then, the SERF has been enhanced and improved even more. This manual describes the updated version of the flume, the sediment sample preparation, and the test procedure. This manual is meant to replace the previous versions of the SERF manual.

A.1 Previous Piston-Style Erosion Rate Testing Devices

As mentioned in Chapter 1, "piston-style" devices have been built in the past. These devices include the Adjustable Shear Stress Erosion and Transport Flume (ASSET, McNeil et al., 1996), the Sediment Erosion at Depth Flume (SEDFlume, Roberts et al., 1998), and the Erosion Function Apparatus (EFA, Briaud et al., 2001).

The principles of all these previous flume-style erosion rate testing-devices are similar (Figure A-1). First, an in situ sample is collected using a Shelby tube or rock core. A piston is inserted into the Shelby Tube's end and the assemblage attached to a lead screw. This lead-screw assembly is fed into a rectangular duct with a circular cutout such that advancement of the piston forces the sample to protrude into the flume. Visual observation is used to keep the sample flush with the flume floor. Water is run

over the sample and as it erodes a manual crank (attached to the lead screw) is used to keep the sample level with the bottom of the flume.

When a test is run, a timestamp is taken at the beginning and end of the test. The erosion rate, $\Delta y/\Delta t$ (where Δy is the change in piston position and Δt the elapsed time), is measured directly. Shear stress is estimated using one of two mechanisms. Earlier erosion-rate testing devices assumed that shear stress on an eroding sample could be approximated using a smooth wall using the following expressions:

$$\frac{1}{\sqrt{f}} = 2.0\log\left[\frac{UD\sqrt{f}}{\upsilon}\right] - 0.8 \tag{A-1}$$

$$D = \frac{2hw}{h+w} \tag{A-2}$$

$$f = \frac{8\tau}{\rho U^2} \tag{A-3}$$

where U is average flow velocity, f is wall friction factor, τ is wall shear stress, D is hydraulic radius defined by flume height h and flume width w, ρ is the density of water, and ν is the kinematic viscosity of water. In the EFA, it is assumed that the Moody Diagram (described by the Colebrook-White Equation – Equation A-4) can accurately describe the friction factor:

$$\frac{1}{\sqrt{f}} = -2.0\log\left[\frac{k_s/D}{3.7} + \frac{2.51}{\mathrm{Re}\sqrt{f}}\right] \tag{A-4}$$

In this expression, k_s is the roughness height and *Re* represents the Reynolds Number with respect to hydraulic diameter. Reynolds Number is given in Equation (A-5):

$$\mathrm{Re} = \frac{UD}{\nu} \tag{A-5}$$

The advantage of flume-style instruments is that they are capable of measuring bulk erosion rates of in situ soil samples upon their surfaces as would be seen in nature. Despite this attribute, there are several drawbacks to these designs. First, because previous devices were manually advanced, they were operator-dependent. Thus, it was possible to over or under advance a sample. During an erosion event or an erosion test, even small stress deviations caused by slightly imprecise advancement may lead to large erosion rate differences.

Secondly, none of these previous devices were capable of providing real-time erosion rate data. Because erosion is defined as $\Delta y/\Delta t$ as opposed to dy/dt, or a small change in sample position divided by a small time step, the assumption was that erosion rate was nearly constant from top-to-bottom throughout a sample. A better method for estimating erosion rate is to continually monitor piston position at smaller time intervals. If piston position is plotted as a function of time, then the slope of the best-fit line through these sample position versus time data points should correspond to erosion rate. If erosion rate is constant, the slope of this curve should be linear. If on the other hand the soil is non-uniform from top-to-bottom, a non-linear relationship will be a more appropriate data fit. Hence, a differential erosion rate based on layering depth can be determined. For cohesive soil and rock, layering may affect rates.

Finally, these devices did not measure shear stress directly on an eroding sample nor did they provide a check one shear stress estimation technique against another. Hence, shear stresses may be incorrect. This may alter the shear stress-erosion rate relationship, which in turn will alter computed local scour depth. In an effort to address these deficiencies, the SERF was developed

A.2 SERF Description

The SERF (Crowley et al. 2012b, Bloomquist and Crowley 2010, Slagle 2006, Sheppard et al. 2005, Trammel 2004; Figure A-2) is based on similar principles to the aforementioned devices. The major components of the device include:

- Two 1,000 GPM Vertiflo pumps (Figure A-3). One equipped with a GE Electronic variable frequency drive/LabVIEW computer control and the other equipped with a simple on/off relay.
- Aluminum flume, 2.0 in. x 8.0 in. (5.08 cm x 20.32 cm) cross sectional area, 0.5 in. (15.24 cm) wall thickness, and 9.0 ft. (2.74 m) in length.
- Five 2.87 in. (7.3 cm) diameter tubes with permanently attached base plates (Figure A-4). These tubes are specifically designed to fit FDOT's Shelby tube extractor (Figure A-5).
- Five rectangular flume sections. The first and second are one foot long, and the first contains a rectangular flow straightener. The third section, which is two feet in length, contains a series of two pressure ports and a direct shear stress sensor with a topside access hatch.
- Following the two foot section is the one foot test section. The test cylinder is inserted into the bottom of this section and an ultrasonic ranging system is mounted over top of the sample portion. Flush with the flume bottom on one side of the sample are three fiber optic lasers; on the other side are three corresponding fiber optic photoelectric sensors. Two pressure taps are positioned on either side of the sample. The test section and the section with the shear stress sensor are both equipped with viewing windows for observation/recording. Following the test section is a four foot section which contains the temperature probe.
- One, one foot long aluminum transition section located between the circular CPVC pipes and the rectangular flume (at the flume entrance and exit).
- A shear stress sensor and signal amplifier (0 Pa – 100 Pa with 4 data ranges) (Figure A-6).
- A RT5-603 six ton Rite-Temp water chiller.
- Connective plumbing. (six-inch CPVC pipe from tank to pumps, four-inch pipe from pumps to flume, four-inch discharge hose from flume to tank, two inch connective pipe from tank to filter, one inch connective pipe from filter to chiller and from chiller to tank).

- 1,100 gallon stainless steel reservoir, equipped with baffles and drain.

- SEATEK 12 element 5MHz ultrasonic ranging system (Figure A-7). This ultrasonic array consists of eight individual crystals that sit “inside” the sample such that they monitor distance from the top of the flume to the top of the sample. Four other crystals are positioned “outside” of the sampling area such that they measure distance from the top of the flume to its bottom.

- Eight Keyence FU-59 fiber optic lasers (Figure A-8) and corresponding photoelectric sensors, and control boxes (Figure A-9).

- Several sacrificial acrylic protective casings for the lasers (Figure A-10).

- A Haydon-Kerk linear actuator powered by Servo Systems power drive, and controlled by National Instruments (NI) UMI-7764 motion controller/PCI-7330 stepper motor interface.

- Two Omega FX2300-.5BDI differential pressure transducers; 0.5 psi, bi-directional range, 0.2% F.S. accuracy.

- Omega type T thermocouple probe.

- A control room housing a National Instruments data acquisition system consisting of a USB-6251 external data acquisition card, a SC-2345 signal conditioning terminal block capable of recording pressure, laser, shear stress, and temperature data and an Intel i7, 2 TB, 12 gB random access memory computer (Figure A-11).

- An iCube NS4133CU capable of 25 fps video capture at 1.3 MP (up to 1280x720 video resolution) and a M118FM08 8 lens (Figure A-12).

- An Omega FPB151 paddlewheel flowmeter.

- A large-scale filter with filter bags that is capable of removing sediment with diameters as low as 0.5 μm (Figure A-13).

- A sand injection system. While as of the date of this report, the sand injection system does not function properly, a photograph of it is included for completeness (Figure A-14).

- A series of valves to drain the flume and bypass the sand injector during tests where sand injection is not to be measured.

As with the other flume-style devices, the SERF was designed as a rectangular cross-sectional flume since the shape allows the flow to become fully developed over a

relatively short length (Trammel, 2004). The device was built in sections because a partitioned flume permits testing of different sections varying in length, design, roughness, etc. which can be inserted into the flume relatively quickly. Additionally, the numerous test sections can be modified such that each accepts a different size sample diameter.

The flume is mounted on two five-and-one-half foot stands. Stiff rubber bushings were inserted between the stands and the flume to reduce vibration. The 1,100 gallon reservoir is equipped with a series of baffles to reduce turbulence in the tank. The tank is equipped with a two foot port on its top and a drain valve on its bottom to allow cleaning between tests. The piping between the tank and the two pumps is six inch schedule 80, CPVC, and the discharge from the pumps to the flume is carried through four inch schedule 80, CPVC.

The two pump motors are mounted on inertial bases, and the discharge end of each pump is equipped with expansion joints to reduce potential damage to the pipe due to pump movement or vibration. There is a series of shut off valves at both the discharges of the tank and at the discharges of the motors to prevent backflow of water into the pumps. Water discharged through the pumps is carried through the four inch pipe until it reaches the sand-injector valve (Figure A-15). If the valve is closed, the sand injection system is bypassed.

As water enters the flume, it first passes through a one-foot flow straightener. This aids in the transition to a hydraulically smooth, fully turbulent flow. The flow passes through a second one foot rectangular section followed by a two foot rectangular section. The shear stress sensor and the access hatch are located approximately

eighteen inches from the upstream edge of the two foot section. The shear sensor has a removable disc that is level with the flume bottom. This disc can be replaced with discs of different roughness. The access hatch allows replacement without removing the sensor. On either side of the sensor are two pressure taps which lead to one of the two differential pressure transducers. This provides a comparison between computed shear stress from a pressure drop and actual shear stress readings from the sensor. A 1.4 inch diameter viewing window is located on the side of the flume parallel with the shear stress sensor so that real-time viewing and recording can be conducted either via closed-circuit television (CCTV) or remotely via the Internet.

Once through the two foot section, the flow passes through the sediment sample test section. The test cylinder consists of an acrylic cylinder secured by two compression plates. The top plate is mounted to the bottom of the test section of the flume, while the bottom plate is attached to the top plate through four threaded rods (Figure A-16). This supports and secures the cylinder in compression, permitting sample removal without disassembling the entire test section. The top of the test section is equipped with a port where the ultrasonic ranging system is mounted.

Along the flume bottom, eight 0.06 in. (1.5 mm) grooves house the fiber-optic lasers and photoelectric sensors (Figure A-17). Located on the side of the test section is another 1.4 inch diameter viewing port with camera. On either side of the sample, two additional pressure taps are connected to a second differential pressure transducer.

The lead screw stepper motor is bolted to a variable elevation stand (mounted to the floor underneath the test section) and is positioned directly under the test cylinder. As the sample erodes, a piston attached to the lead screw advances the sample inside

the test cylinder. Once through the test section, water proceeds through a four-foot-long duct section. The temperature probe is located approximately three and one-half feet from the upstream edge of this section.

At the flume exit is a one foot rectangular-to circular transition. Water passes through this transition and past two more ball valves. The valve that points downward, which is closed during testing, is used to drain the flume after a test. The downstream valve isolates the filter from the flume when it is being drained (Figure A-18). Water flows through the filter, through its filter bags, past another valve (which isolates the filter from the reservoir tank during draining; Figure A-19) and back into the reservoir tank.

A.3 Shear Stress Sensor

The first unique feature that distinguishes the SERF from other flume-style erosion rate testing devices is the shear stress sensor. With it, the SERF is capable of directly measuring shear stress of a sample with a given roughness. Fifty millimeter diameter (1.97 in.) discs of varying roughness can be attached to the top of the apparatus. The discs' surfaces are leveled with the flume's bottom by tightening the springs. The disc-spring assembly sits on top of a movable platform that is suspended from two bronze leaf springs. Below the platform sits a Servo magnet and Hall sensor. As water flows over the test disc, the disc-platform-leaf spring deflects. Deflection is measured using the Hall sensor. Two brass rods are connected to the underside of the platform on which two electromagnets are attached. When the platform deflects, the brass rods and magnets deflect along with it. Two PVC-encased solenoids are wrapped around the magnet. Based on the deflection read by the Hall sensor, the upstream solenoid

energizes the magnets to return the disc back to its original position. A signal is sent from this solenoid proportional to the shear stress imposed on it. The upstream solenoid is used to calibrate the device by sending a control-voltage to it.

In an analysis of the EFA, Annandale (2006) speculated that the Moody Diagram may not accurately estimate shear stress. A force balance between average shear stress and the average pressure differential upstream and downstream from the sample was hypothesized to be a better method. If pressure differential could be used to estimate shear stress, the following expression should govern this parameter:

$$\tau_b = \frac{\Delta phw}{(2h + 2w)L} \tag{A-6}$$

where Δp is the pressure differential, w is the flume's width, h, the flume's height, τ_b, the average bed shear stress, and L, the spacing between pressure ports (Trammel, 2004).

Comparisons between the shear stress sensor and pressure differential expression allowed investigators to evaluate the applicability of Equation A-6. Investigators concluded that using a pressure drop to estimate shear stress was not accurate (Crowley et al. 2012a, Bloomquist and Crowley 2010, Chapter 5 of this report).

A.4 Erosion Depth-Monitoring System

Because of the sensitivity of erosion rate to stress, it is essential to maintain the proper sample elevation during testing. To conduct an erosion test, the following algorithm is followed:

1. Water temperate is taken and the data is fed to the ultrasonic sensor array so that the sensor array uses the correct sonic speed to calculate distance.
2. A 5 MHz ultrasonic burst is sent from the array, which sits atop the flume, toward the flume-bottom and the sample. Each of the array's twelve crystals sends and receives 3000 pulses from this burst. An average is taken for each crystal.

3. Data processing is performed to ensure that depth readings are accurate.

4. Twelve individual crystals are positioned such that eight strike the sample while the other four reflect off the flume bottom. Both datasets (eight-crystal and four-crystal) are isolated from one another.

5. The maximum and minimum values from each datasets are eliminated.

6. A search is conducted where error readings are removed from each dataset (an error reading returns an average depth "value" of 0.00).

7. An average is computed for both the eight-crystal and four-crystal truncated datasets.

8. The two averages are compared with one another. If average depth from the four-crystal, "outside" dataset deviates from average depth from the eight-crystal "inside" dataset by more than 0.5 mm (0.02 in.), a sample advancement signal is generated.

9. If the lasers are to be used during an erosion test, its algorithm is run in parallel with the ultrasonic sensor algorithm. As mentioned, lasers and photoelectric sensors are located along grooves across the sample from one another. If a laser's sensor can "see" its corresponding laser beam, a portion of the sample must have eroded. If four of the eight photoelectric sensors are exposed, another advancement signal is generated.

10. Before a test, an operator can choose to use "AND" logic or "OR" logic for the ultrasonic array and laser system (by manipulating the LabVIEW GUI. When cohesive soil is tested, investigators have found that ultrasonic pulses tend to penetrate slightly into the sample, producing false bottom readings. Hence, under these conditions, it is advantageous to use the lasers alone. On the other hand, if erosion is expected to be such where large specimen advancement would occur, it is sometimes more advantageous to use the ultrasonic array alone. Finally, there may be instances where one would want to use the laser/ultrasonic system as a redundant check (for example, a highly-layered specimen).

11. Using the signal(s) from Step 8 and/or Step 10, the stepper motor is initiated.

    a. When the ultrasonic system is used, bottom deviation can be computed directly. Thus, if an advancement signal is generated in Step 5, the motor advances the sample according to the computed offset.

    b. The lasers, whose diameter is 0.06 in., do not provide a direct computation for bottom offset. Because of this, when they are used as a stand-alone system a different advancement algorithm must be used. If an advancement signal was generated in Step 10, then discrete 0.03 in.

steps are used to advance the sample until the lasers and photoelectric sensors no longer produce an advancement signal.

A.5 Other SERF Systems

Before each test, the temperature control system is activated, since during long duration tests a temperature rise of approximately 2^{o} C per hour develops. This could affect erosion rates and may damage equipment. The cooling system is designed to maintain a constant temperature during testing.

The two centrifugal pumps are controlled separately. If the sample is a soft clay or loose sand, only the computer controllable pump is used. Its range is 0 to 60 Hz, with 0.01 Hz increments. For less erodible samples such as rock or stiff clay, both pumps are used. First the variable speed pump is slowly brought up to full speed. It is then shut off and the on/off pump started. The variable speed motor is then adjusted until the desired velocity and shear stress is achieved.

The large flow-capacity filter is designed to filter sediment up to 0.5 μm. Every now and then (approximately 6 months of regular SERF use), its filter bags need to be changed because they become full of sediment due to repeated tests.

A.6 SERF Testing Procedure and Flume Operation

Because shear stress and erosion rates are measured separately, there are different procedures for shear stress and erosion rate tests that are described in this section.

A.6.1 Shear Stress Test

A.6.1.1 Disc preparation

Before a shear stress test may begin, a test-disc needs to be prepared. The following are instructions for preparing a disc:

1. Obtain a removable test-disc (Figure A-20).

2. A uniformly, evenly mixed batch of aggregate should be set aside.

3. The acrylic disk should be coated with epoxy. Experience has shown that JB Weld two-part epoxy (Figure A-21) works the most effectively. Be sure to spread the epoxy evenly and level.

4. Press the epoxy coated disk onto a random portion of the aggregate so that the disk coats with sediment particles.

5. Multiple disks should be prepared to ensure that a true random sampling form the aggregate is achieved (Figure A-22)

A.6.1.2 Shear sensor preparation

The following are instructions for affixing the test disc to the shear stress sensor:

1. Remove the shear stress sensor top-hatch by loosening the PVC plug's top screw (Figure A-23).

2. Below the PVC plug are a spring and an aluminum plug. Remove these as well.

3. To lower/raise the shear stress sensor platform, its springs must be tightened/loosened. Pick a platform elevation, and test with the appropriate test disc to make sure the disc is level with the flume bottom. Tighten/loosen the springs as necessary.

4. When the platform has been placed at the proper elevation, affix the appropriate test disc to the platform using the screw in its center (Figure A-24).

A.6.1.3 Flume preparation

The following are instructions for filling the flume with water:

1. Open the appropriate upstream butterfly valves (Figure A-25). If only using one pump, open the valves for the pipe closer to the wall. If using both pumps, open both sets of valves.

2. Open the downstream flow valve and close the downstream drain valve (Figure A-26).

3. Open the downstream butterfly drain valve (Figure A-27).

4. Close the sand injector valve.

5. The flume is now ready to be filled with water. Turn on the pump frequency drive, and be sure to set its control to “local” and “drive.” Additionally, open the air valve on the top of the filter to prime it.

6. Using the buttons on the pump controller (Figure A-29), adjust the pump speed to approximately 20 Hz, and press “FWD” on the pump controller. The pump should start filling the flume. Once the flume is full (as evidenced by water coming from the filter’s air valve), the shear stress sensor is ready to be calibrated. Close the filter’s air valve.

7. Stop the pumps by bringing the flow velocity down to zero.

A.6.1.4 Shear stress sensor and pressure transducer calibration

To calibrate the shear stress sensor, please refer to Figure A-30 and the following instructions:

1. Zero the sensor using the knobs (1) and (2) as shown in Figure A-30. The coarse adjustment knob is knob (2) and the find adjustment knob is knob (1). When the sensor is properly zeroed, the ammeter on the front of the amplifier should read 0.

2. Press and hold the CAL button on the shear stress sensor (4). This sends a voltage to the calibration solenoid based on the position of knob (5), which causes the deflection solenoid to react. Turn knob (3) such that the ammeter on the amplifier deflects to the corresponding correct stress reading. For example, if knob (5) is turned to 50, the corresponding stress read on the ammeter should be 50 Pa. Release the CAL button (4).

3. Repeat for several values of (5) to make sure the sensor is working. Note that the shear sensor runs at 4 different ranges: 10 Pa, 20 Pa, 50 Pa, and 100 Pa. To set the range of the sensor, turn knob (6). Keep in mind that if the range is set to anything less than 100 Pa, a calibration voltage of 100 Pa will rail the instrument. Likewise, if the range is 20 Pa a calibration voltage of 50 Pa will do the same thing. When the range goes below 100 Pa, the scale on the ammeter adjusts accordingly. Therefore, a calibration voltage of 50 Pa when the range is on 50 Pa will still deflect the ammeter to full deflection (this is correct and it is how the instrument was designed).

4. Restart the pump (approximately 20 Hz again), and remove the bubbles from the pressure transducer tubes by unplugging the tube from the flume to the transducer (so some water drains from the flume). Make sure to unplug the downstream tube first. The transducers are designed to tolerate over pressurization on the positive side only. Let the water continue to flow from the transducer’s tube until bubbles are eliminated. Then, plug the tube back into the transducer. Repeat for all pressure transducer tubes.

A.6.1.5 Running a shear stress test

1. Open the shear stress control program (Figure A-31). Note that this program has a non-working input for pump control. This feature stopped functioning as a result of variable frequency drive replacement, and it was not repaired during this project due to time constraints. The reason it was included originally was to accommodate remote operation. However, experience has shown that remote operation is not advisable; therefore, repairing this feature did not appear to be a high priority. Still, the code for it has remained in the program if future researchers want to allow for remote operation in the future.

2. Initiate the temperature control system (i.e., turn on the water chiller), and adjust the temperature using the device's thermostat. Be sure that the water chiller's overflow valve is opened (Figure A-32).

3. Start the control program and specify a location for its output file. Using the pump control box, bring the pump to the desired flow speed, and wait approximately 30 seconds for conditions in the flume to stabilize. Real-time graphs should be generated as soon as the shear stress control program begins to run. Stabilization is achieved when these graphs show a nearly-constant shear stress.

4. When conditions have stabilized, press the "RUN" button on the LabVIEW GUI screen. This will stop the generation of the graphs for a length of time that is dependent on the Sampling Rate Parameter (default is 1 kHz) and the Number of Samples Parameter (default is 10,000). Both these values can be changed as the LabVIEW program runs to allow for different sampling frequencies and different sampling lengths.

5. When the graphs start moving again, data collection has been completed. Bring the pump to the next desired flow rate, wait for it to stabilize, press the run button to collect data, repeat.

6. Repeat for flow rates that are to be investigated.

7. When testing is done, gradually bring the pump speed down to zero. For example, if a pump frequency of 30 Hz was used for the test, bring the pump down to 25 Hz, let it run for 5 seconds, then bring it to 20 Hz, let it run for 5 seconds, etc. all the way down to 0 Hz pump frequency. This gradual velocity reduction allows the shear sensor to "catch up" with changing flow conditions and can help prevent breakage to the instrument.

8. The test may now be repeated, or a new sample disk may be installed. It is recommended to repeat each test at least three times and to recalibrate the shear sensor after every test.

A.6.1.6 Draining the flume

1. When all tests are completed, close the valves on the pressure transducer tubes to prevent damage to the instruments.
2. Close the flume valves in the following order:
    a. Downstream butterfly valve
    b. Downstream flow ball valve
    c. Upstream pump valves
3. Open the downstream flume drain valve. Wait approximately 30 seconds. The flume should drain, and a new disc may be installed by opening the access hatch.

A.6.2 Erosion Rate Test

A.6.2.1 Shelby tube extraction and sample preparation

Before an erosion test can be conducted, the specimen needs to be extracted from its Shelby tube and placed in a SERF test-tube. While the original design of the instrument was to allow for direct insertion of Shelby tubes, colleagues at FDOT indicated that often, Shelby tubes may become asymmetric when they are pushed into the ground. Asymmetry would cause leakage during SERF testing if round pistons did not properly fit into the Shelby tubes. To prevent leakage during testing, the SERF test tubes were designed. The following is the procedure for Shelby tube extraction using the FDOT Shelby tube extractor at the SMO:

1. Cut a Shelby tube to the appropriate length using the SMO's band saw. Experience has shown that specimens between 8 and 9 inches appear to function the best.
2. Remove all burs from the Shelby tube using a file (Figure A-33).
3. Affix one of the SERF test tubes to the SMO Shelby tube extractor using four screws (Figure A-34). Be sure the opening in the test tube aligns with the opening of the Shelby tube extractor.
4. Place the Shelby tube in the extractor (Figure A-35).

5. Place a piece of wax paper upon the Shelby tube extractor's piston.

6. Start the Shelby tube extractor, and begin pushing its piston toward the Shelby tube.

7. Once the piston makes contact with the specimen tube, extract the specimen using one continuous push from the piston.

8. If the piston arm is not long enough to extract the entire specimen, retract the piston, and place a spacer between the piston and the specimen (Figure A-36). Begin extraction again.

9. Once the specimen has been extracted, place a plug in the top and the SERF plastic piston in the bottom of the SERF tube to prevent moisture loss. Cover the tube with plastic to further minimize the chances for moisture loss (Figure A-37).

10. When transporting the specimens, be sure to keep them upright to avoid disturbances.

11. Soak the samples for a minimum of 24 hours so that saturated field conditions are mimicked.

A.6.2.2 Inserting a specimen into the SERF

The following is the procedure for inserting samples into the SERF:

1. Add an O-ring to the top of the sample tube (Figure A-38).

2. Line up the specimen with the SERF false bottom and the threaded compression rods (Figure A-42). Carefully raise the specimen into position.

3. Attach and tighten the wing nuts onto the compression rods below the sample tube's compression plate (Figure A-40). Tighten the nuts as if tightening lug nuts on a car tire – i.e. tighten one a bit, then another, then another, etc. This ensures a proper seal between the top of the specimen and the flume while preventing damage to the SERF test tube.

A.6.2.3 Flume preparation

The following are instructions for filling the flume with water and initiating an erosion test (note, this procedure is very similar to preparing the flume for a shear stress test):

1. Open the appropriate upstream butterfly valves (Figure A-25). If only using one pump, open the valves for the pipe closer to the wall. If using both pumps, open both sets of valves.

2. Open the downstream flow valve and close the downstream drain valve (Figure A-26).

3. Open the downstream butterfly drain valve (Figure A-27).

4. Close the sand injector valve.

5. Open the iCube control program (iControl). Press the green triangle button on the upper-left of the program (Figure A-41) to start the camera. Note, while there is a version of the SERF program that utilizes NI LabVIEW IMAQ controls, this program does not function well with digital inputs. It is better to use the iCube program because it appears to run in parallel with NI.

6. Turn on the LED lights located inside the flume on either side of the camera viewport. The switch for these lights is located in the control room.

7. Manually adjust the color settings within the iControl program until the view of the material and flume is as desired. This process can also be assisted by placing a light blocking object above and around the camera and viewport, resulting in less glare from ambient lighting and a better view into the flume itself.

8. The flume is now ready to be filled with water. Turn on the pump, and be sure to set its control to "local." Open the air valve on top of the filter to prime the filter.

9. Fill the flume with water using the pump control box and a flow rate of approximately 20 Hz.

10. Once the flume is full and pressurized (as evidenced by the lack of bubbles in the camera's image and water shooting out of the filter's air valve), reduce the flow rate to approximately 8.0 Hz and close the filter's air valve. The SEATEK is now ready to be calibrated.

A.6.2.4 SEATEK Calibration

The following are instructions for calibrating the SEATEK ultrasonic depth sensor array:

1. Manually turn on the SEATEK Ranging System in the Control Room.

2. Open TeraTerm.

3. Within TeraTerm, Go to Setup → Serial Port.

4. Within the Serial Port Setup menu, make sure the following values are entered (Figure A-28):

    a. Baud rate: 9600

b. Data: 8 bit

c. Parity: none

Leave all other entries with their default settings.

5. Type a "?" and press "Enter" while in the TeraTerm interface. This function returns a list of all the valid operations and inputs TeraTerm accepts/recognizes.

6. Type "te 20" to change the approximate water temperature to 20 degrees Celsius. While this number is probably not exact, it is close enough for calibration of the SEATEK.

7. Type "v 0250" and press "Enter" while in the TeraTerm interface. This function will set the Threshold Voltage to 250 mV. Depending on the organic content, looseness, and other characteristics of the sample, this setting may have to be altered to another value within the allowable quantities.

8. Type "b 0025" and press "Enter" while in the TeraTerm interface. This function will set the Blanking Distance to 25 mm. Depending on the organic content, looseness, and other characteristics of the sample, this setting may have to be altered to another value within the allowable quantities.

9. Type "p" and press "Enter" while in the TeraTerm interface. This function will use ultrasonic pings to determine the distance between the SEATEK array and the top of the material sample.

10. If the returned data seems unreasonable or impossible, repeat Steps 6 through 8 using various numerical values for each setting until reasonable depth values are returned.

11. Disconnect from the serial port interface in TeraTerm. This is <u>important</u> because the serial port cannot communicate with TeraTerm and LabVIEW simultaneously. Failure to disconnect from the serial port in TeraTerm will result in an error when attempting to run an erosion test.

A.6.2.4 Running an Erosion Test

1. Turn on the water chiller, and adjust the temperature settings using the thermostat. Be sure that the chiller's overflow valve is opened.

2. Turn on the motor control box (black box on the SERF frame).

3. Turn on the lasers using the power strip in the control room.

4. Open the erosion control program (Figure A-42) and the motor mover program (Figure A-43). Note that like that shear stress program, code remains in the

"main" program for a pump control. In the future, it should not be too terribly difficult to get this working again, but as stated previously, as of the date of this report, remote SERF operation was not deemed a priority.

5. On the main control program, click the "soft" motor on/off, lasers on/off, and SEATEK on/off buttons to the off position.

6. If directions have been followed properly up until this point, the flume should still be running at approximately 8.0 Hz. Next, the sample needs to be raised into position. Within the motor mover program, incrementally move the specimen upward by specifying a number of steps, pressing the run button, specifying a new number of steps, pressing the run button, etc. Usually, 5,000 steps is a good approximation for coarse adjustments while 1,000 steps are sufficient for fine adjustments. Do not use more than 10,000 steps because doing so may cause the motor to seize.

7. Once the specimen is approximately level, press start on the main control program.

8. The control program will ask where to save its output file. Specify a location. Some analog data should begin to be generated on the GUI screen (timestamps, temperatures, etc.).

9. If lasers are to be used, turn on the "soft" laser button now. Analog data should begin to appear in the GUI screen from the lasers.

10. If the SEATEK is to be used, turn on the "soft" SEATEK button now. Depth data should begin appearing on the GUI screen.

11. Verify that the SEATEK is functioning properly by checking the depth numbers on the GUI screen. If depth numbers are not correct, (average should be approximately 4.92 cm if the specimen is approximately level), stop the program and recalibrate using TeraTerm. Alternatively, if it is obvious that one or two crystals are causing the incorrect readings, their "soft" on/off buttons may be turned off. Once satisfied with SEATEK numbers, move on to Step 12.

12. Once the majority of SEATEK numbers are coming back acceptably (or the lasers appear to be functioning properly), turn on the "soft" motor button. Within a couple of seconds, the specimen should become almost completely-level with the flume bottom.

13. Specify a flow rate of interest and input this flow rate using the pump control. If the flowmeter is not attached, note the flow rate in a .txt file. If the flow meter is attached, flow rate should be recorded automatically.

14. Once the flow rate has been established, press the "RESET" button on the GUI. The "garbage" data points that were collected during setup can be taken out during data analysis.

15. Once 4.0 cm of a specimen has eroded or one hour of time has elapsed, press the reset button, and specify a new flow rate.

16. Repeat step 15 for all flow rates of interest.

17. Throughout the test, make a careful note of any anomalies, qualitative observations of layering, etc. as these notes will become important during data analysis.

A.7 Data Analysis

The methods used to reduce data output from the data acquisition programs are briefly presented here. However, future operators are encouraged to read this report and Bloomquist and Crowley (2010) for more-detailed descriptions about some of the purposes of these control programs. Additionally, all data analysis programs are written in MATLAB. Users are encouraged to work in MATLAB (and not MS Excel) because of its versatility in manipulating large data strings. Several references are available for users to familiarize themselves with MATLAB (Attaway 2013 for example).

A.7.1 Analog Signal Analysis

Analog signal analysis is usually most important for data obtained during a shear stress test. Of particular interest are data from the shear stress sensor and the pressure transducers. Before averages are to be computed, a spectral analysis is important to ensure that unusual vibrations or functions are not aliased within the instruments' signals. The following MATLAB script is useful for spectral analysis:

```
function [freq,SPT]=basicSpt(allTS,dt,fbounds,Nft)
      hfNft=round(Nft/2); Nft=2*hfNft;
      freq=(0:hfNft-1)/dt/Nft;
      kmask=find(freq>=fbounds(1) & freq<=fbounds(2)); freq=freq(kmask);
      SPT=[];
      for kpt=1:length(allTS(1,:))
            TS=detrend(allTS(:,kpt)); [Nts,Npt]=size(TS);
            DOF=floor(Nts/hfNft-1);
            kseq=zeros(2*hfNft,DOF);
            for k=1:DOF, kseq(:,k)=((k-1)*hfNft+1:(k+1)*hfNft)'; end
            Han=hanning(2*hfNft); nHan=Han./sqrt(sum(Han.^2)/length(Han));
            TF=fft(detrend(TS(kseq).*(nHan*ones(1,DOF))));
```

```
        spt=2*mean((TF.*conj(TF)),2)/Nft*dt;
        spt=spt(1:hfNft);spt=spt(kmask);
    SPT=[SPT,spt(:)];
End
```

This script was used extensively for spectral analysis in Bloomquist and Crowley (2010). This script performs a fast Fourier transform and computes the spectral density for a signal defined by *allTS*, where *dt* is the sampling rate, *fbounds* is the upper and lower computed frequency limit, and *Nft* is the number of records in a sequence. For details on running MATLAB and incorporating this script with a dataset, operators are encouraged to consult any number of MATLAB tutorials available online regarding using functions in MATLAB.

If unusual spectral data is present in a signal, it is possible to filter the dataset using MATLAB. MATLAB offers a number of filtering options. For example, to use a 4th order Butterworth filter, the following syntax should be used:

```
f = 1000;
cutoff = [4/(f/2) 23/(f/2)];
order = 4;
[B,A] = butter(order,cutoff,'bandpass');
pse_filt = filter(B,A,pse_dm);
pse_filt_avg = mean(pse_filt);
```

In this code sequence, the signal that is filtered is called *pse_filt*, and the filter mechanism is a bandpass filter with upper and lower limits defined by *f* and *cutoff*.

To use either the filtering script or the spectral analysis script, return data from the LabVIEW program must be rearranged. LabVIEW returns a series of numbers in a .dat file that corresponds to the sampling frequency and sampling rate. For example, if 10 analog bursts are taken at a sampling rate of 1000 Hz, LabVIEW will generate a 1x10,000 (10*1000) number array in its .dat file. To rearrange this array to a more usable format such as a 10x1000 array, MATLAB's *reshape* command should be used.

Once spectral analysis and filtering has been completed, MATLAB's averaging command, *mean(X)*, and MATLAB's plot command, *plot(X,Y,'properties')* should be used to present data. Because of the length of LabVIEW output files, SERF operators should not use MS Excel because Excel often has difficulty dealing with arrays with several thousand entries. Rearrangement from LabVIEW to a matrix-style Excel-style array would also be difficult and require the use of several Visual Basic (VB) Excel scripts. Since the MATLAB code for analysis has already been developed, operators are encouraged to use this instead.

A.7.2 Erosion Rate Test

The following is a description of analyzing data after an erosion rate test using the SERF:

A.7.2.1 Erosion versus time analysis

Before 2010, erosion rate in the SERF was measured by simply subtracting piston start position from piston end position and dividing by the total length of the test. While this method will provide an average erosion rate, it will not produce instantaneous erosion rates. When certain samples are tested (for example, sand-clay mixtures), they often respond such that localized portions of a sample erode much more slowly than other portions of the sample. These localized differential erosion rates need to be captured because they may be significant.

The best method then for estimating erosion rate from SERF data is to plot a sample position vs. time graph using MATLAB; and to plot a best-fit erosion versus time line to determine erosion rate. However, if the RESET button was used during testing, the data files will need to be slightly manipulated to ensure that only usable data are

analyzed. The following script was developed to “split” a dataset based upon application of the reset button:

```
clc; clear all; close all;
A = load(uigetfile('*.*','All files (*.*)'));
E = A(:,4);
t = A(:,5);
f = find(t == 0);
for i = 1:length(f)-1
    if length(f) == 1
        LL = f(i);
        UL = f(i + 1);
        t_plot = t(LL:UL);
        E_plot = E(LL:UL);

    else
        LL = f(i);
        UL = f(i + 1);
        t_plot = t(LL:UL-1);
        E_plot = E(LL:UL-1);
    end

    figure(i)
    plot(t_plot,E_plot)
    grid on
    xlabel('time (sec)')
    ylabel('Erosion (cm)')
end
```

The script looks for zeros in the time-column (column 5). Each time a new zero has been found, a new graph is generated. Assuming the user knows how many times he/she pressed “RESET,” it should be easy to determine which graphs require further analysis.

Next, best-fit regression lines need to be fit to the data. The best method found so far is to install the EzyFit MATLAB toolbox, and it to use it to fit regression data. Directions on installation of this toolbox and utilizing EzyFit can be found here: http://www.fast.u-psud.fr/ezyfit/.

Using EzyFit, best-fit regression lines (of the form y=ax + b or y = ax) should be fit to each graph. While it is possible to program a script whereby these lines are automatically fit, this procedure is not recommended so that users will be “forced” to

think about the statistics of each line that is being fit to their graph. Slopes from these best-fit regression lines and slopes associated with each graph should be recorded in a table or in another MATLAB script.

If a “negative-slope” is found, it probably means that there was no erosion at that stress. Under these conditions, manually entering a zero is usually reasonable. Note, that fitting these regression curves is not an exact science. Due to differential erosion rates, often one curve may not make physical sense. Operators are encouraged to use their engineering judgment when assigning erosion rates to the data.

A.7.2.2 Erosion function development

Development of an erosion function is relatively less complicated than analyzing erosion versus time data. Assuming flow rates (or pump frequencies) were recorded, these values need to be converted to shear stress. Figure A-44 shows the known relationship between pump frequency and smooth-wall shear stress while Figure A-45 shows the known relationship between pump frequency and flow rate. Using these relationships, shear stress can be computed. As per the discussion in Chapter 5, the smooth-wall shear stress shall be assumed to ensure conservative results.

Once shear stress is computed, it should be plotted against erosion rate. At this point during analysis, it may become obvious that some data points need to be eliminated. If during testing, the operator properly noted all qualitative anomalies, it should be pretty easy to justify eliminating certain data points. Again, this is not an exact science. Sometimes for example, a “loose” or a “stiff” layer will become obvious based upon erosion data. Elimination of one or two points is left to the engineer’s discretion.

Once a graph has been massaged so that it will generate a positive relationship between erosion rate and shear stress, a best-fit power-law curve should be fit to the data using EzyFit. The reason a power-law curve should be used is that presumably there would be zero-points for erosion at lower shear stresses.

A.7.2.3 Critical shear stresses and development of Partheniades-style curves

To develop a critical shear stress for a sediment, all zero-points for erosion at lower shear stresses should be removed. Then, a best-fit y=ax + b line should be fit to the remaining, positive data points. If "b" from the best-fit line is divided by "a" (i.e., the x-intercept is set equal to zero), the result is a bed material's classically-defined critical shear stress.

If one wishes to fit an Einstein-Partheniades-style equation to the data of the form $E = M(\tau_b - \tau_c)$, critical shear stress should be subtracted from each shear stress to generate a series of critical shear stress deficits. Then, each erosion rate should be divided by each critical shear stress deficit to yield a value for M (for each data point). An average value of M should be computed for each bed-material. If one wishes to nondimensionalize data, τ_b/τ_c can be divided by $E/(M\tau_c)$.

A.8 SERF Control Programs

As discussed above, the pump control program that was presented as part of the 2010 report malfunctioned when the pump frequency drive's motherboard was replaced. As a result, there are only three programs that need to be discussed for SERF operation:

1. Motor Mover
2. Shear Stress Sensor Data Program

3. Full Erosion Rate Program

Of these, only the full erosion rate program is significantly different from the 2010 versions of control programs.

A.8.1 Motor Mover

The motor mover program has been one of the constants of the SERF over the years. Its front-panel was already displayed in Figure A-42. Its source code is presented in Figure A-46.

A.8.1.1 Block diagram discussion

The algorithm for the motor mover is as follows:

1. Specify the movement axis. For the stepper motor, only one axis, Axis 1, moves.
2. Specify the Board ID. Board ID corresponds to the slot in which the motion controller (a National Instruments PCI 7330 Card) is plugged in the control computer. With the current SERF setup, the PCI 7330 is plugged into Slot #1.
3. Specify the velocity, acceleration, deceleration, and jerk quantities. If the motor starts to stall, reduce the velocity and/or the acceleration. When temperature approach 100 degrees Fahrenheit, slower velocities are often required.
4. Read the current motor position. The default is for the motor to start at 0 when the Motor Mover program is first run. If the user wants to reset its overall position, press the reset switch on the front panel and press start.
5. Read relative vs. absolute position. The current setting as shown is relative position. This should not be changed.
6. Set the target position.
7. Initiate movement.
8. Continually move the motor and monitor movement for errors.
9. Stop movement when target position is reached.

A.8.1.2 Front panel discussion

First, input the target position in steps. One centimeter equals 787.4 steps. Then, press start. The motor should move. Press the reset switch and press start to move

the computer position back to zero. The End Position Indicator should return the motor's position every time the program is run. The program will stop automatically when the final position is reached.

A.8.2 Shear Stress Control Program

A description of the control program for conducting shear stress tests is presented below. Additionally, a screenshot of its source code is presented in Figure A-47. Note, that this program has not changed since the 2010 report.

A.8.2.1 Block diagram discussion

The block diagram for the shear stress sensor program is designed as a "flat-sequence structure" in that certain commands execute sequentially (note, this is not always the case in LabVIEW). A description of what occurs during a programming "step" is provided below.

SC-2345 Channels

First, SC-2345 channels are specified (Figure A-48). To explain the shear stress sensor's wiring, the sub-vi in Figure A-48 needs to be explained. A screenshot of this sub-vi is shown in Figure A-49.

On the front panel for the SERF Control No Motor Program, one of the inputs is for the shear stress sensor's range. Recall from above, that range can be adjusted on the shear stress sensor's amplifier so that more accurate readings can be obtained at lower shear stresses. The range on the instrument must equal the range on the control program for data to be read properly.

Four wires come from the shear stress sensor; each wire corresponds to a different output range. The sub-vi shown in Figure A-49 takes the user input range and

compares it with the possibilities from the from the shear stress sensor – 10 Pa, 20 Pa, 50 Pa, and 100 Pa. Then, an array is built with three zero values. The last value in this array corresponds to an actual channel in the SC-2345 based on the results from the four case structures shown in the figure. The array max/min command returns the maximum value from this array so that the computer knows which channel is the correct channel from which to read during shear stress tests.

In addition to specifying which SC modules are to be read, the VI also asks where the user wants to save data. In general programs were written so that .dat files were generated. This makes MATLAB analysis the easiest. The .dat extension can be changed to .xls for an Excel file or .txt for a text file.

Pump Input

The next step in this program is to send a signal to the pump (Figure A-50). Again, due to wiring issues with the new frequency drive motherboard, this feature is not currently operational. But, the coding has been left in the control program so that it would be easy to bring a computerized pump back to the system at a later date.

Analog Output

The last step in the shear stress sensor data collection program is to read the data and split it according to its position in the analog signal stream (Figure A-51 and Figure A-52). Note that in the configuration shown, the signal is split five times.

Miscellaneous Details

The case structure surrounding the analog-read portion of the base vi is to allow for manual data acquisition. During a shear stress test, a SERF operator specifies a flow rate, waits for flow to stabilize, and collects data. Then, he or she presses “Run” in

the base vi and data is collected. The “true” case for the case structure corresponds to when the “Run” button is pressed while the “false” case corresponds to when no button is pressed.

As the base vi runs, real-time graphs are generated because of this true-false sequence. During “false” execution, analog signals are sampled one time through the loop, and the results are plotted immediately. During “true” execution, raw data is sampled at the specified sampling rate according to the Samples Per Channel input parameter. Then, this data sequence is written to the appropriate .dat file. This portion of the program is much different than previous versions. Previous programs both captured an analog block of data every time through the LabVIEW loop, averaged it, and wrote the average to the output file. The acquisition of raw data allows for more advanced data analysis.

A.8.2.2 Front panel operation

To operate the shear stress control program:

1. Specify the shear stress range using the drop down menu.
2. Specify the number of samples per analog channel.
3. Specify the sampling rate in Hz.
4. Press the LabVIEW “Run” button
5. Initialize the Pump by pressing “FWD”
6. Bring the pump to the desired flow speed using the computerized pump dial. Record the flow rate.
7. When flow speed and shear stress have leveled out, press “Run” to record a burst of raw data. Data time can be computed by $t = N/f$ where N is the number of samples per channel and f is the sampling frequency.

8. When data are taken, the real-time graphs on the front panel will freeze. When data are done being taken, the graphs will resume moving. If this happens, it means the program is working as designed.

9. Pick a new flow rate and repeat steps 6 through 8 for all flow rates that are to be studied.

A.8.3 Erosion Control Program

The SERF erosion control program has been updated significantly. Its front panel is shown in Figure A-53 while its source code is shown in Figure A-54 and Figure A-55.

A.8.3.1 Block diagram discussion

Like the previous erosion control program, the updated version of the program is designed as a flat sequence structure. The following is a discussion of this sequence:

SC-2345 Channels

As with the shear stress sensor control program, first the SC-2345 channels are specified (Figure A-56). These channels are hard-wired for the laser system, flow meter, and thermocouple.

Pump Input and Timer

Similar to the Shear Stress Sensor program, a pump input subroutine has been setup so that computerized pump control could be reestablished at a later date (Figure A-57). Because this subroutine has already been described, a detailed description will not be repeated here.

Additionally, a timer-structure is added alongside the pump input sequence as shown in Figure A-57. This timer structure starts a new timestamp at the beginning of each “loop” through the program so that time can be tracked during testing.

Laser Sequence

Next, the control program moves onward to the laser sequence. Figure A-58 shows the associated sub-VI with output voltages from each laser. These output voltages are added together, and a laser-sum is computed. Later in the sequence, if this sum is greater than or less than a certain pre-defined number, certain advancement signals are sent to the stepper motor. The laser-read sub-VI is presented in Figure A-59 (block diagram) and Figure A-60 (front panel). This is simply an analog collection algorithm that has already been described in detail and will not be repeated here.

SEATEK Pre-Input Sequence

The SEATEK pre-input sequence (Figure A-61) runs in parallel with the laser sequence. The sub-vi in Figure A-61 was taken verbatim from the NI examples folder and should not be changed. The sub-vi sends a “N 1; Enter” command to the SEATEK, waits for 200 ms, and then reveals an optional output that shows that the number of samples to be taken per SEATEK burst is indeed one. Previous SERF testing procedures (prior to 2010) called for a user to open a HyperTerminal session, specify the number of samples to be taken during a test, and start a data run. When a SEATEK data run is started, the SEATEK pings each of its crystals at 5 MHz, takes an average over 1 s, and then outputs its result. The SEATEK “N” command corresponds to the number of times this pinging-averaging is to repeat itself. Once a SEATEK data run is started, output data will continue to be generated until the number of bursts from the SEATEK equals N. When a data run is started, new input parameters cannot be added to the SEATEK until N is met. For the temperature patch to function properly, the SEATEK’s input temperature needs to be updated continuously. Put another way, after each 5 MHz SEATEK burst-average, the SEATEK needs to know that it should stop

taking data and wait for a new temperature command. Inputting the “N 1” command as the SEATEK is initialized guarantees that this will occur properly.

SEATEK Data Collection

Once the pre-input sequence has been conducted, the SEATEK must collect its data. The SEATEK data collection component of the control program is shown in Figure A-62. As with the updated 2010 version of this program, this module contains individual buttons whereby the user can turn “off” a malfunctioning SEATEK crystal by pressing an electronic button. Additionally, because the physical testing hole in the SERF was changed to accommodate Shelby tubes, the SEATEK portion of the control program has been updated so that the four outside crystals may be turned “off.”

As with the 2010 version of the SERF program, this program contains a temperature patch (sub-VI in Figure A-63; Figure A-64; Figure A-65). The patch reads writes temperature data to the SEATEK just before every SEATEK depth reading. The algorithm for this temperature patch is as follows:

1. Figure A-64 – first part of stacked sequence structure
    a. The serial port is specified
    b. The input temperature is converted to a string
    c. The letters “TE” and the input temperature are written to the SEATEK
    d. The program waits for 200 ms.
2. Figure A-65 – second part of the stacked sequence structure
    a. The letter “D” is written to the SEATEK to indicate that data collection is to be conducted.
    b. The program waits 3000 ms. This is approximately the amount of time it takes the SEATEK to read its data.

Once the data are collected from the SEATEK, they are split between crystals 1-8 and crystals 9-12. Then the correct string characters are isolated from one another and converted from a string to numbers (Figure A-66). Once the data are recognized as numbers, they filter through their appropriate “on/off” checks. Thus, if a crystal is malfunctioning, data is replaced with a zero here (Figure A-67).

Next, data are transmitted to a zero-checker (Figure A-68). As implied, this sequence checks data for zeros. And, if a zero is found, it is eliminated. Then, the high value and the low value from the SEATEK data string are eliminated (Figure A-69). Finally, the data are averaged, and a bottom offset is computed based upon the height of the SERF duct (4.92 cm by default; Figure A-70).

Please note that the entire SEATEK portion of the sequence structure is wrapped in a case structure. Therefore, if the SEATEK is not to be used for a test, the entire SEATEK algorithm may be skipped by pressing the soft-button on the program’s front panel.

Motor Movement

Once depth and laser data are collected, movement signals are sent to the motor (Figure A-71). Note that this part of the sequence structure is also wrapped in a case structure. This allows a user to test that the SEATEK and the lasers are functioning properly without having to worry about specimen movement.

As shown in Figure A-71, step and position data are output from a sub-VI and written to an array in .dat format. Additionally, timestamp information, temperature data, and flow meter voltages are written to this data file. Finally, output from the pump has also been setup so that this feature may be available in future versions of the program.

The sub-VI for step and position data is shown in Figure A-72. This sub-VI's inputs are true/false commands for "laser-only test," "SEATEK-only-test," and "laser-and-SEATEK test." Additionally, data from the SEATEK and laser systems are input as well. As shown, a sub-VI labeled "6" is shown multiple times here. This program is simply the motor mover that was previously discussed.

The left-hand-block in Figure A-72 represents conditions for a laser-only test. A case-structure is programmed such that if the sum of the laser voltages is less than 60 V, an advancement signal of one millimeter (79 steps) is generated. The 60 V number comes from testing the SERF power supplies that power the lasers, and it implies that 3 lasers become uncovered (a very conservative approximation). This number can easily be changed to be made more or less conservative depending on the material being tested in the device.

The middle block in Figure A-73 represents a SEATEK-only test. This portion of the code reads data from the SEATEK, and compares it with pre-defined precision values. If the bottom-offset is greater than 0.025 cm, an advancement signal is generated equal to the offset converted to the appropriate number of steps (i.e., multiplied by 787.4). Likewise, if the offset is less than 0.025 cm, a retraction signal is generated.

The third block in Figure A-73 represents the both-laser-and-SEATEK test. As shown here, "and" logic is used such that if both the laser system and the SEATEK generate advancement signals, the motor is told to advance. As implied, because the SEATEK and the laser system are being used together, advancement may be related to offset position, and not a predefined step increment as specified with the laser-only test.

Similarly, the addition of the SEATEK allows for retraction if the specimen has over-advanced in the flume.

Repetition and Reset

As implied, this feedback loop was programmed to repeat continuously until the "STOP" button is pressed by wrapping the program in a "WHILE LOOP." A wait timer of 10 ms is included in the program to help with computer memory issues.

The "RESET" button bears some further discussion as well. This button is wired so that if pressed, the sample position will reset to zero in the output data file. Similarly, the timestamp will reset to zero. This allows a user to change a flow rate and isolate one test from another without starting a new data file.

A.9 Troubleshooting

This section presents solutions to problems that may occur while operating the SERF. The problems listed have at some point been encountered, and knowledge of how to handle these situations is very valuable. If there are other problems encountered in the SERF, solutions to these problems should be added to this section.

A.9.1 Water Leaking at the Test Cylinder

Unfortunately, leaks are frustrating problems that usually require unexpected additional time and effort to solve. Leaks can either occur from the outside of the test cylinder or at the piston. Leaks outside of the cylinder are much easier to stop than leaks at the plunger.

To stop a leak at the outside of the cylinder, the solution is usually to tighten the wing nuts on the bottom compression plate with a wrench. Eventually, the leak should stop. If, however, leaks still occur, the O-ring in the top compression plate will need to

be replaced. This requires that the operator drain the flume, lower the piston to the edge of the cylinder, remove the lead screw-piston pin, and remove the test cylinder. Remove and the O-ring in the upper compression plate and install a new, greased O-ring. Reload the cylinder, and no further leaks should occur.

Leaks at the piston are due to damaged O-rings due to over use. To stop a leak at the piston, the flume must be drained, the cylinder removed as described in the previous paragraph, and the piston should be removed from the cylinder. Replace the worn O-rings on the plunger with two cleaned and greased O-rings. Reload the piston and the cylinder into the SERF, and no further leaks should occur.

A.9.2 Stepper Motor

If the LabVIEW controls indicate that the stepper motor is in a reset state, it means that due to a computer update/restart, the PCI-7330 needs to be reinitialized. To reinitialize the motor, close all Labview programs and open Measurement and Automation Explorer (MAX). Click initialize (same button indicated in previous paragraph) and close MAX. The stepper motor should now function properly.

The stepper motor also tends to “stick” if the piston is not greased properly. Under these conditions, the motor will “try” to move, fail, and keep trying. From an operations perspective, this would mean that the control program would indicate that the piston has moved further than it actually has moved. To correct this issue, re-grease the piston.

Finally, the motor tends to stall if it is moved too quickly when the temperature approaches 100 degrees Fahrenheit (as of the date of this report, the SERF is not housed in an air conditioned facility). To correct this issue, change the velocity and acceleration values in the motor mover program.

A.9.3 Erosion Rate Program not Receiving Valid SEATEK Data

When running an erosion rate program and either no data or invalid data appears in the SEATEK window, the program is not receiving readable data from the SEATEK. This is usually due to not closing TeraTerminal before opening any LabVIEW program. To correct this problem, make sure that the SEATEK unit is turned on, then close all LabVIEW applications. Close TeraTerminal. Re-open LabVIEW. The SEATEK should now function properly.

A.9.4 Invalid Pressure Sensor Data

Although the need for extensive pressure transducer tests has been reduced because of work presented in this report, troubleshooting information for these sensors is included here for completeness.

If the user suspects that data sent from the pressure transducer is incorrect, this may be due to either a clog in the tube connecting the flume to the pressure transducer, the presence of a trapped air bubble at the transducer or in the line, or due to damage to the pressure transducer.

Sediment clogs may be removed by disconnecting the tube from the valve and using a wire or unwound paper clip to dislodge the blockage. Also, shaking or flicking the tube will be required to remove all sediment. Once water flows easily again, re-establish the connection to the valve and shake the tube to remove any introduced air bubbles.

Most often, trapped air bubbles are the reason for invalid pressure readings. Air bubbles will probably be trapped at the tubes with side tap connections. As the tubes make a horizontal connection into the flume wall, air bubbles will often lodge here. To

remove the bubbles, slowly lift the tubing above the flume so the air bubbles trapped inside are pulled out from the wall, rapidly pull down the tubing, and repeat. This will force the air bubbles to shoot back into the wall of the flume, where they may be picked up by the flow inside the flume and carried away. Air bubbles trapped in the transducer require removing the pressure transducer from its seat and turning the transducer around to encourage air to escape up the pressure line and into the flume.

To determine if a pressure transducer is damaged, MAX can be opened to display direct pressure sensor signals. If moving the pressure tube lines does not affect the output, the sensor is damaged.

A.9.5 Air Bubbles in the Flume

Air in the flume will lead to invalid SEATEK data readings. Air is easily observable from the camera, and it must be eliminated for the SEATEK to function properly. To eliminate air from the flume, increase the flow rate until the flume fills. Once the flume is full/pressurized, decrease the flow rate. The SEATEK should now function properly.

A.9.6 Shear Stress Sensor Problems

The shear stress sensor is very temperamental and the source of most problems in the SERF. Because of the high sensitivity of the device, this is to be expected, although problems with the shear stress sensor can be frustrating. Generally, operators will become aware of a shear stress sensor problem if the device fails to calibrate properly. If this occurs, there must be something wrong with the mechanical setup of the device. These mechanical issues are common, and they must be addressed before a shear stress test can commence. If the shear stress sensor will not calibrate properly:

1. The most common mechanical issue with the shear sensor is pollution (see step 5). First, recheck to make sure the gap between the Servo magnet and the Hall Sensor is present. If not, re-clean and recalibrate.

2. If the gap between magnet and sensor is present, the next most common mechanical issue is the connection between the deflection magnet and the platform. Open the round upstream access hatch on the left side of the sensor as the sensor is observed from the middle of Reed Lab (Figure A-73).

3. When looking into the round hole in the sensor, there should be a small gap between the magnet battery and the solenoid. When the connection slips, an illustration as shown in Figure A-74 is what will be seen instead.

4. If it looks as though the magnet battery is rubbing against the deflection solenoid as shown in this figure, loosen the screw shown in Figure A-75 and reposition the brass rod so that there is an air gap present between the deflection solenoid and the magnet battery.

   Try to recalibrate the sensor. If it still does not work, remove the brass rod and magnet battery completely and check to make sure the connection between the magnet and the brass rod is not broken (it often breaks). Reattach using a two-part plastic super glue. DO NOT USE METAL EPOXY SUCH AS JB WELD. IT WILL CAUSE AN ERROR IN THE SOLENOID BECAUSE JB WELD IS MAGNETIC.

5. If the sensor will still not calibrate, repeat steps 1 – 5 with the calibration solenoid (although this malfunctions much less often).

6. This should fix the sensor. The only other possible explanation could be that the leaf springs have become permanently deformed and they need to be replaced (contact Raf Crowley for procedure on how to do that; r.crowley@unf.edu) or water has leaked into the dry portion of the sensor.

7. If leakage is suspected at any time when using the shear sensor, open the panel exposing the electronics (Figure A-76), UNPLUG THE SENSOR, and assess the damage. The sensor may need to be resealed and/or IC's may need to be replaced. Usually though, if the sensor is given time to dry out, it will begin working again.

A.9.7 Sacrificial Protection Replacement for Lasers

As mentioned in Chapter 3, sacrificial Plexiglas cylinders were prepared for the laser system. If the Plexiglas screen becomes too scratched, it must be replaced. To replace the protective cylinder, remove the top of the compression cylinder from the underside of the SERF. The protective cylinder should slide out. Slide in a new

protective cylinder (ten were prepared as part of this project), and reattach the compression cylinder. The laser system should now be ready for testing.

A.9.8 Filter Bag Replacement

If water in the SERF becomes "cloudy," it means that the filter bags need to be replaced. To replace the filter bags, the following procedure is used:

1. Drain the filter by opening its drain valve. Be sure that all other valves "out" are closed (i.e., reservoir drain valve, flume drain valve, water chiller overflow valve).
2. Once the filter is drained, loosen the filter's eye bolts using a crow bar. Once loose, rotate the bolts downward.
3. Use the hydraulic jack to carefully lift the filter's lid. To use the jack, close its hydraulic valve and begin pumping the jack. The lid should lift up.
4. Once the lid has been lifted, lower the lid onto the steel safety latch to remove the stress from the jack.
5. Rotate the lid approximately 45 degrees in one direction. Do not place any body parts under the lid!
6. Remove the filter bags and discard them. Remove the screens housing the filter bags and wash them with a hose.
7. Use a hose to rinse the inside of the filter.
8. Replace the bags in the filter. Use 1.0 μm bags on the filter's perimeter and 0.5 μm bags on its inside. Extra bags are located in Reed Laboratory, room 103.
9. Once half the bags have been replaced, rotate the filter's lid 45 degrees in the other direction. Replace the other bags using the same guidelines discussed in Step 8.
10. Once all bags have been replaced, be sure to clean the filter's large rubber gasket and the area on which the gasket sits. Be sure to straighten the gasket.
11. Align the lid back onto the filter. Be sure that the filter's outer alignment tabs are such where the lid will not rest upon them when lowered.
12. Lower the filter lid by releasing the hydraulic valve. It should sit directly onto the gasket. If it does not, the lid may need to be manually tilted by re-raising it with the hydraulic jack. Readjust and re-lower the lid.

13. Once in-place, verify that the lid correctly aligned with the eye-bolts. If it does not align, raise the lid slightly with the jack, rotate it, and lower it again.

14. Once aligned, verify that that the gasket was not “caught” during the procedure and that the bolts are aligned.

15. If (14) is true, tighten the eye bolts. The eye bolts should be tightened like one would change a car tire – i.e., slightly tighten one; slightly tighten one on the opposite side; etc. Once all bolts are hand tight, tighten them further using a crow bar.

Note – filter bag replacement can be dangerous, and it should not be undertaken by only one operator. Replacing the filter bags is a two-man operation, and it is very labor intensive. Experience with the SERF has shown that with regular use, replacement should only be necessary approximately once a year.

A.9.9 Other SERF Problems

Other problems in the SERF are much less common, and they will not be discussed further. If a problem comes up that a novice operator cannot solve, Raf Crowley should be contacted (r.crowley@unf.edu) so that he can help to troubleshoot. If future operators suspect a problem with the shear stress sensor, Hans Prechtel should be contacted (elekt@aon.at).

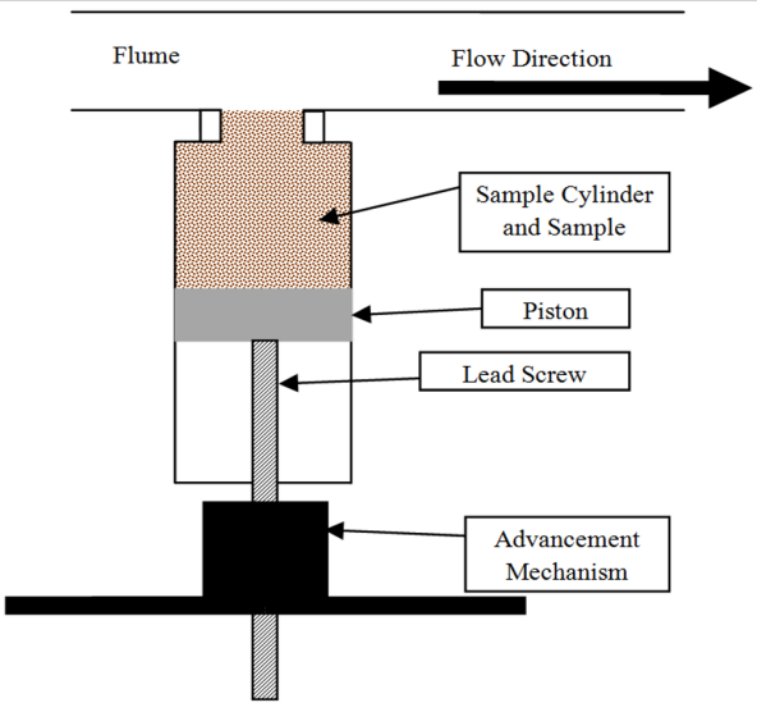

Figure A-1. Piston-style erosion rate testing device schematic

Figure A-2. Birds-eye view of the SERF

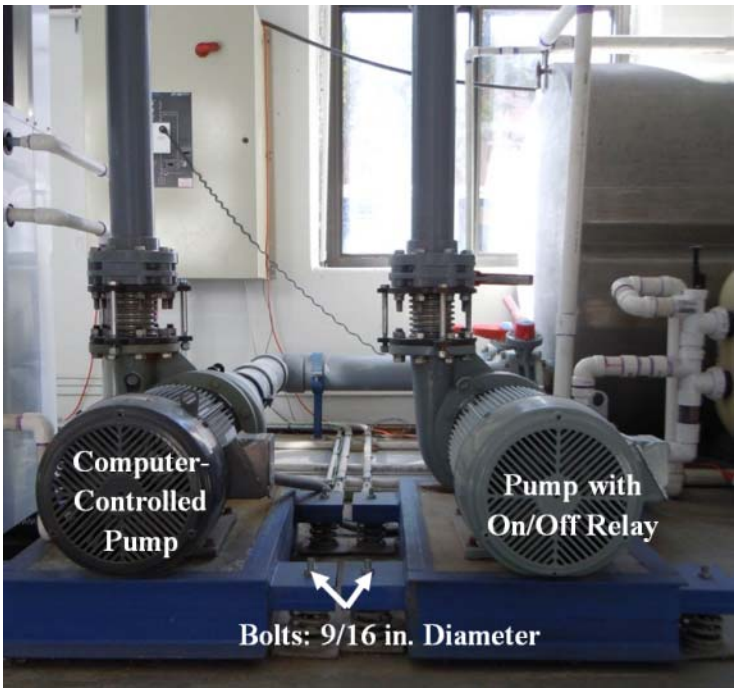

Figure A-3. Photograph of SERF pumps


Figure A-4. One of the SERF testing tubes with permanent base plate

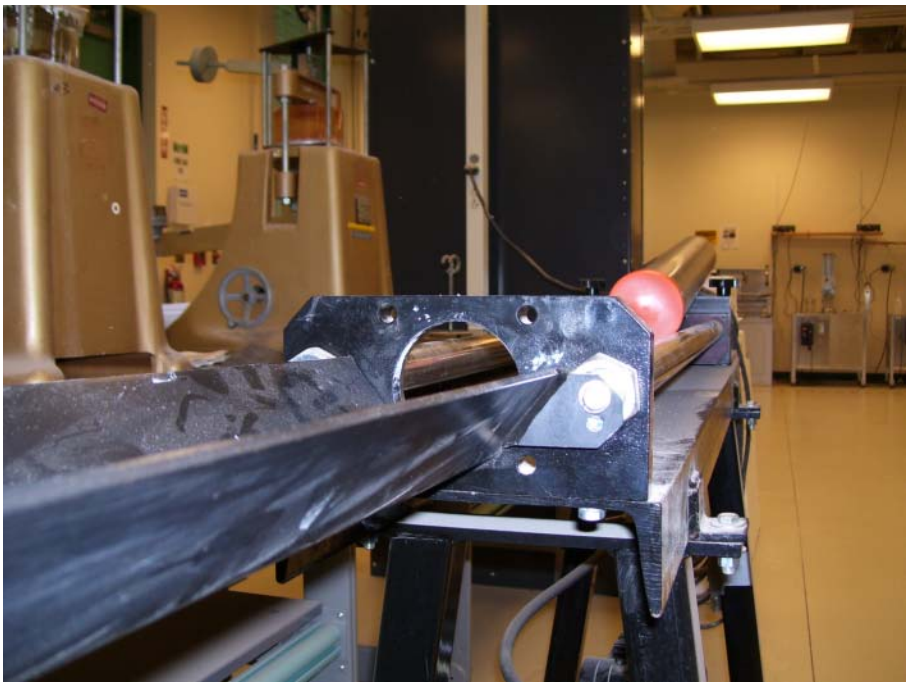

Figure A-5. FDOT Shelby tube extractor to be used with SERF test tubes

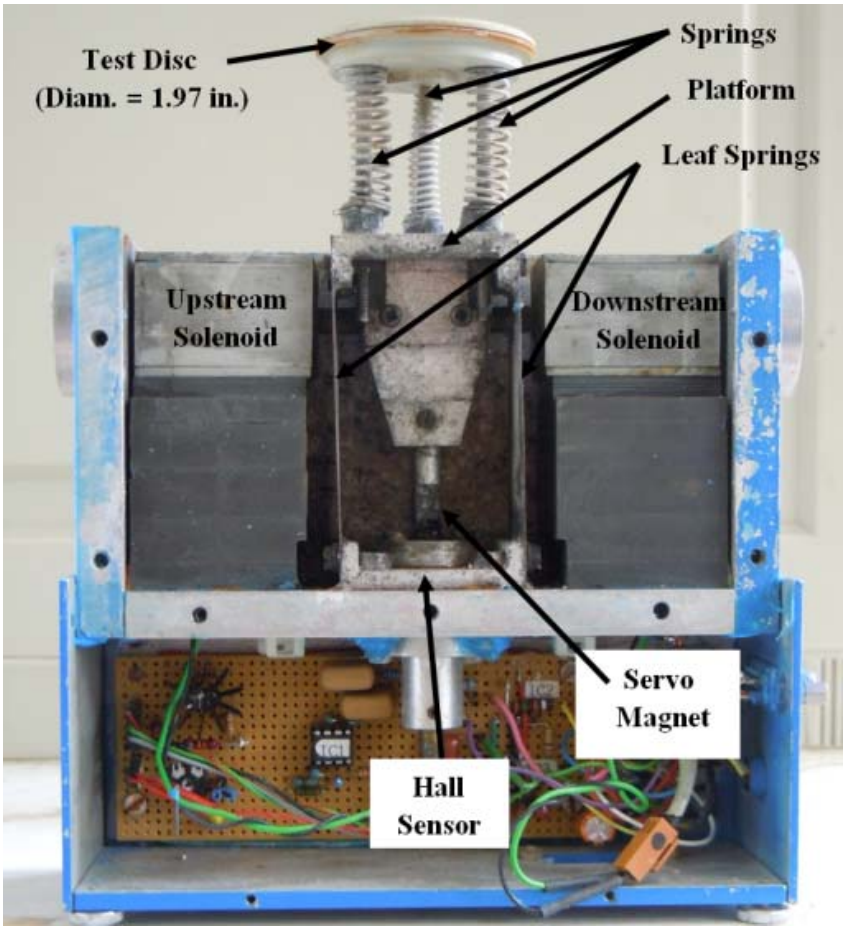

Figure A-6. Photograph of shear stress sensor

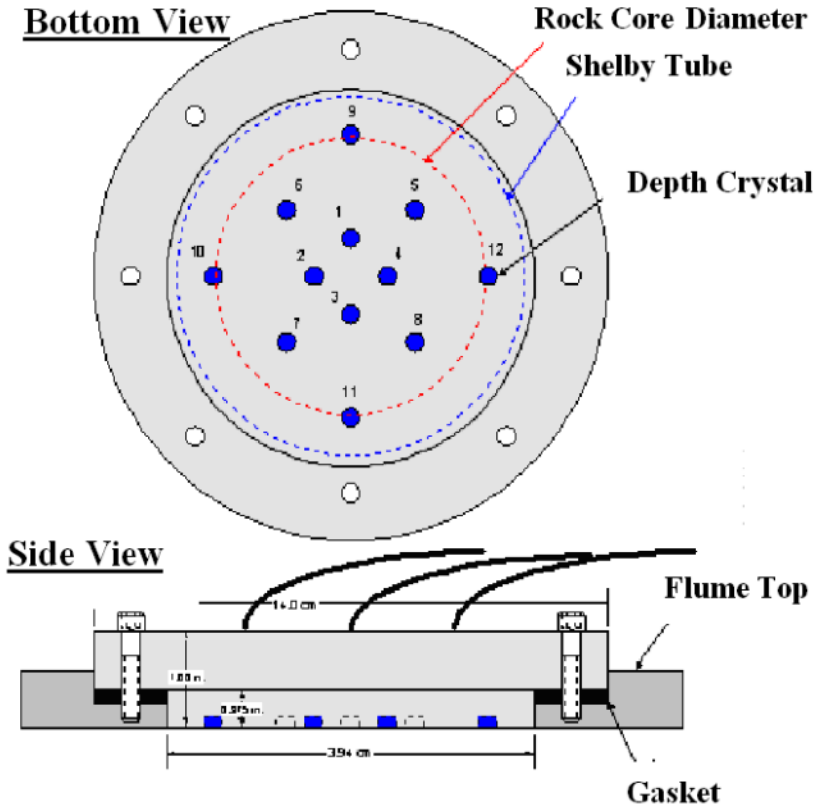

Figure A-7. SEATEK ultrasonic sensor schematic

Figure A-8. Photograph inside SERF showing lasers (note 4 laser point one direction and 4 lasers point another direction to minimize interference)

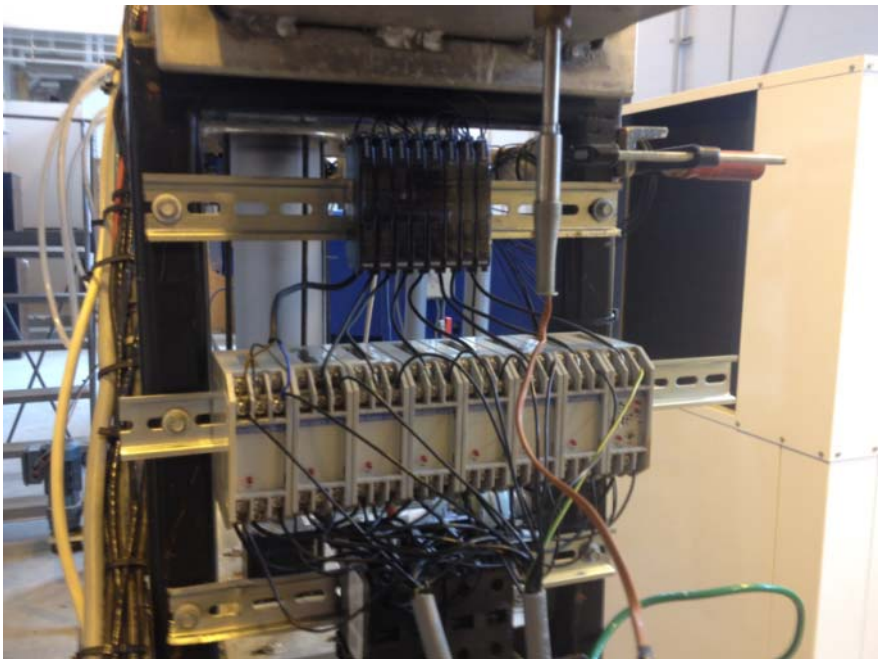

Figure A-9. Photograph of the SERF laser control boxes

Figure A-10. Example of sacrificial acrylic laser protector

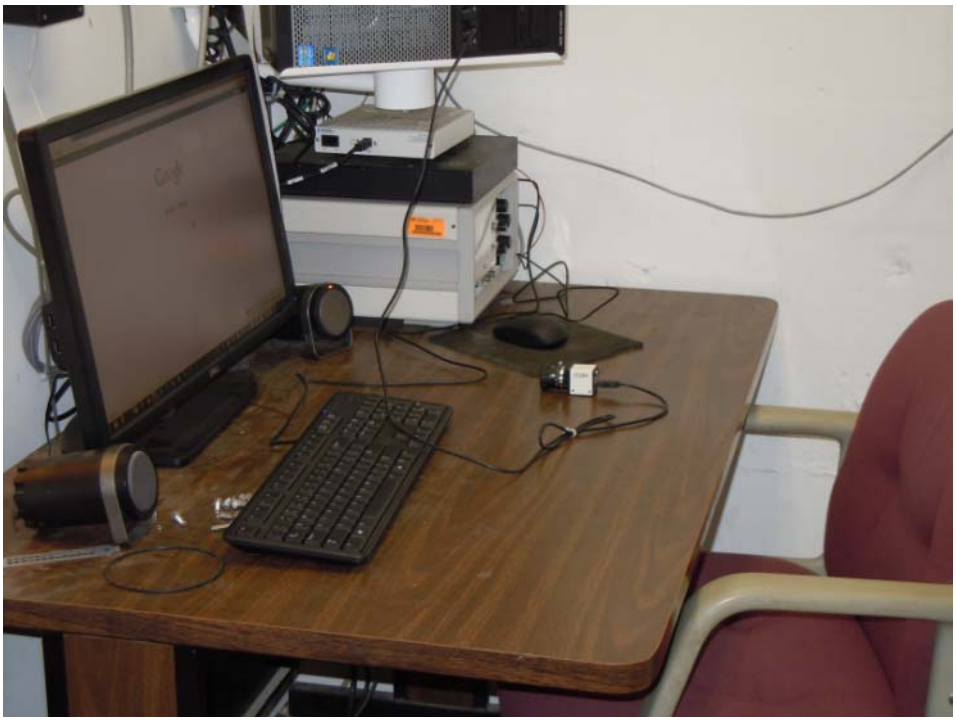

Figure A-11. SERF control room

Figure A-12. iCube SERF camera

Figure A-13. Large-capacity filter

Figure A-14. SERF sand injector

Figure A-15. Sand injector shut-off valve

Figure A-16. SERF close-up showing the compression plate

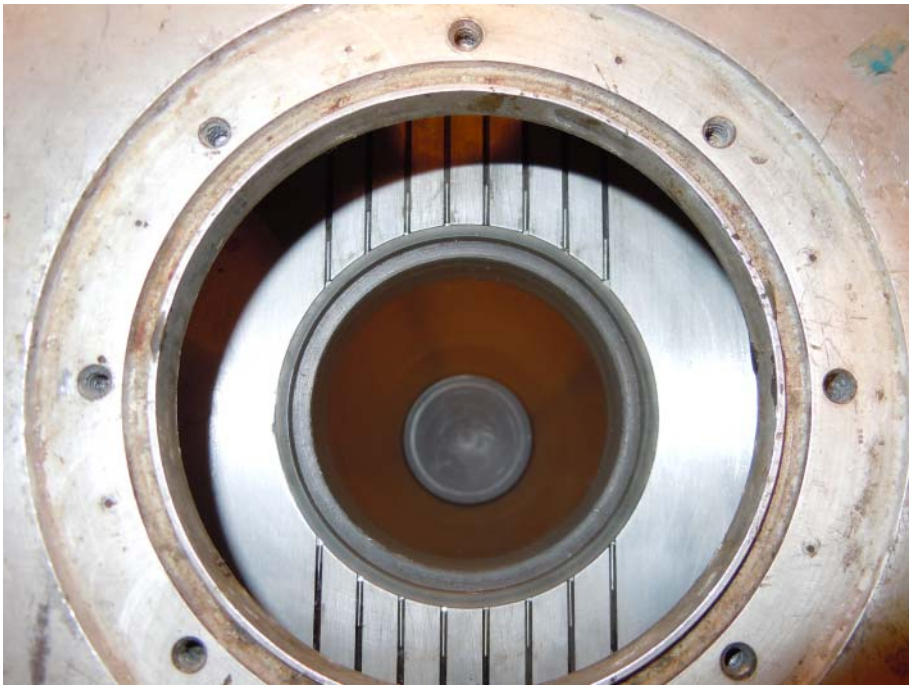

Figure A-17. Top-view into SERF (SEATEK removed) showing laser and photoelectric sensor grooves

Figure A-18. SERF downstream valve system

Figure A-19. Downstream pump butterfly valve

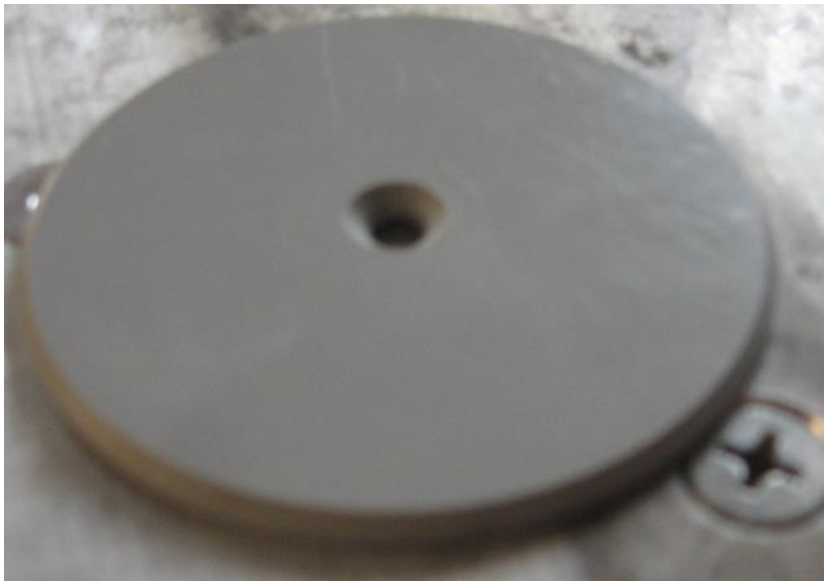

Figure A-20. Example of shear stress sensor removable test-disc

Figure A-21. J-B Weld epoxy


Figure A-22. Several shear stress sensor test-discs

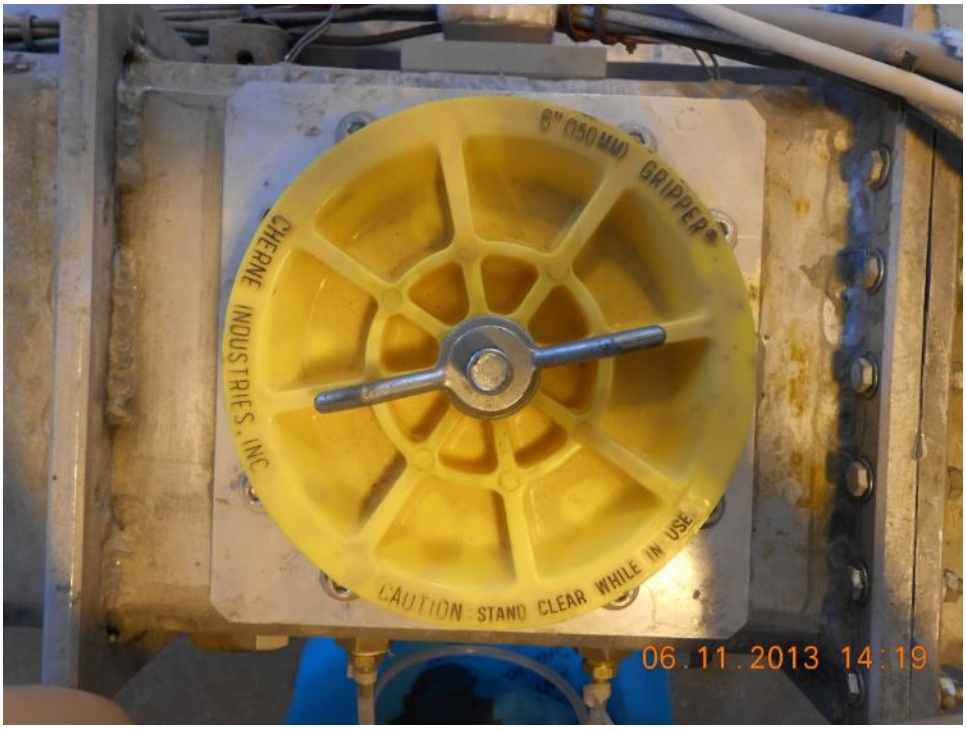

Figure A-23. Shear stress sensor top hatch PVC plug


Figure A-24. Illustration of affixing a test-disc to the shear stress sensor

Figure A-25. Upstream butterfly valves in the “open” position showing configuration when one pump is used


Figure A-26. Downstream flow valve and drain valve in open and closed positions, respectively

Figure A-27. Downstream butterfly valve in open position

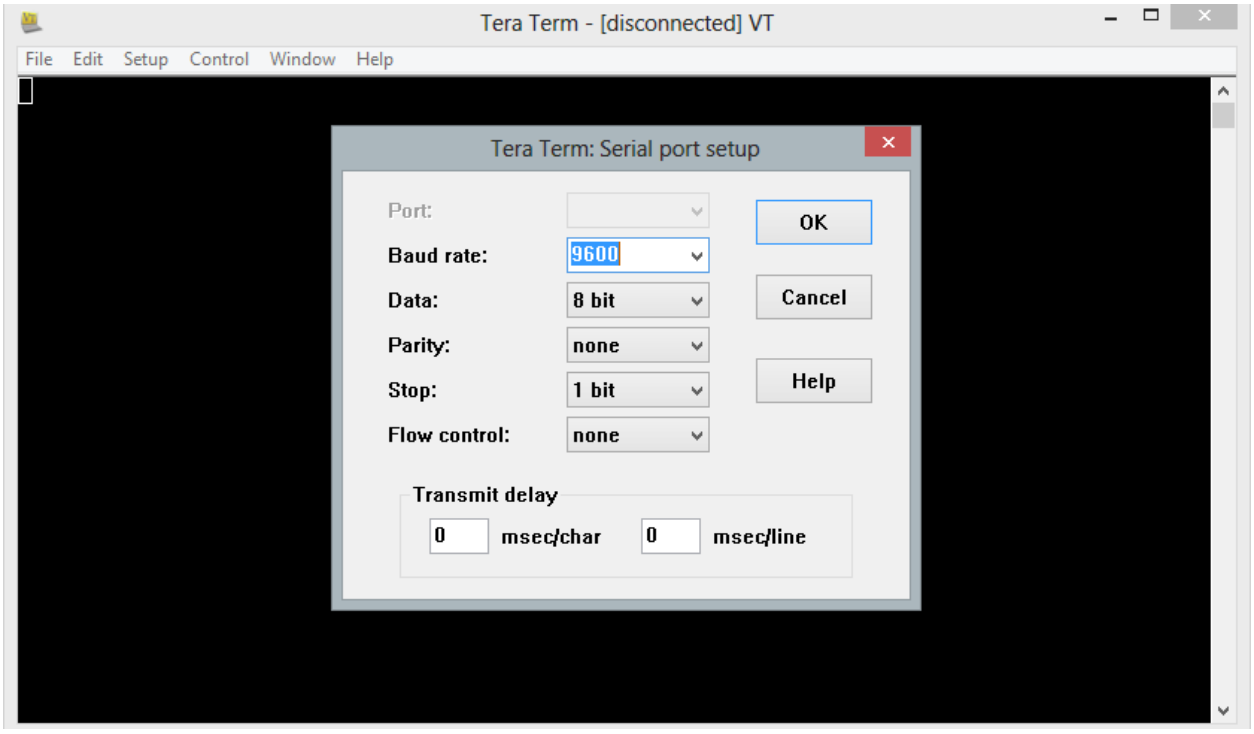

Figure A-28. TeraTerm with the proper settings

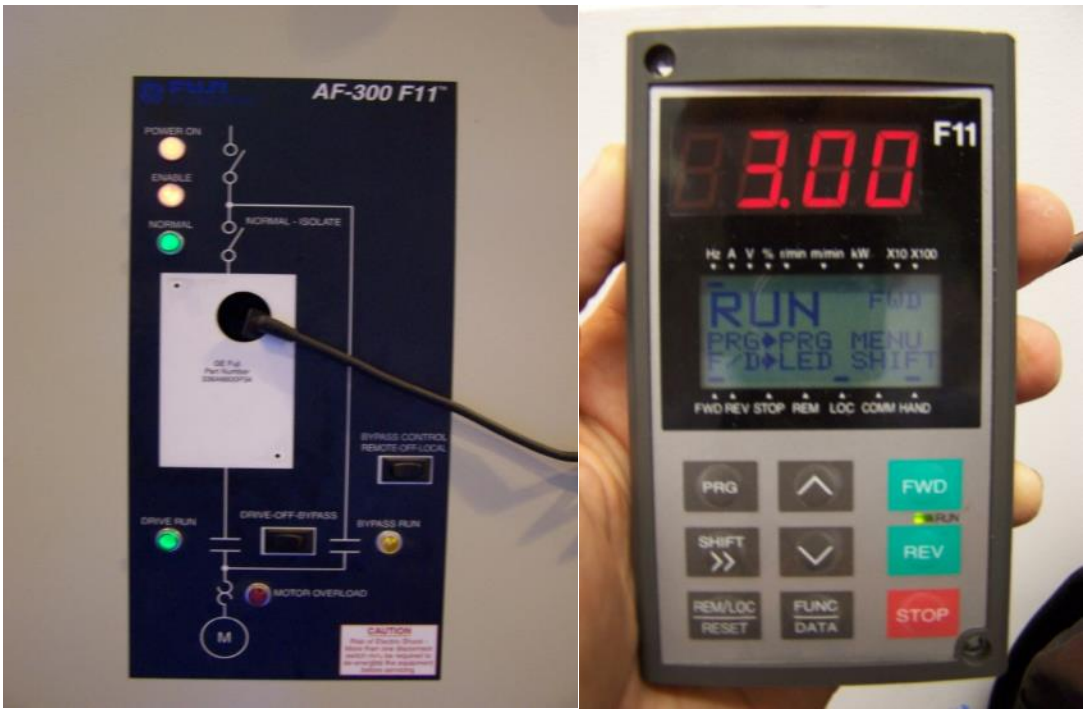

Figure A-29. Photograph of pump controller; frequency drive on left and control box on right

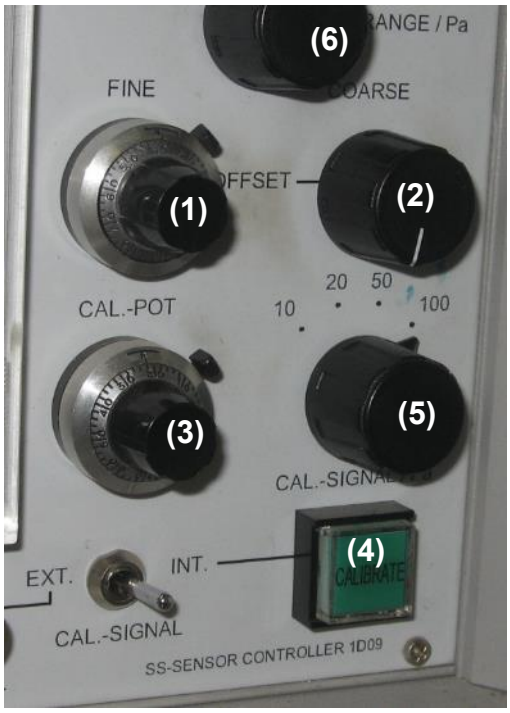

Figure A-30. Knobs on shear stress sensor amplifier

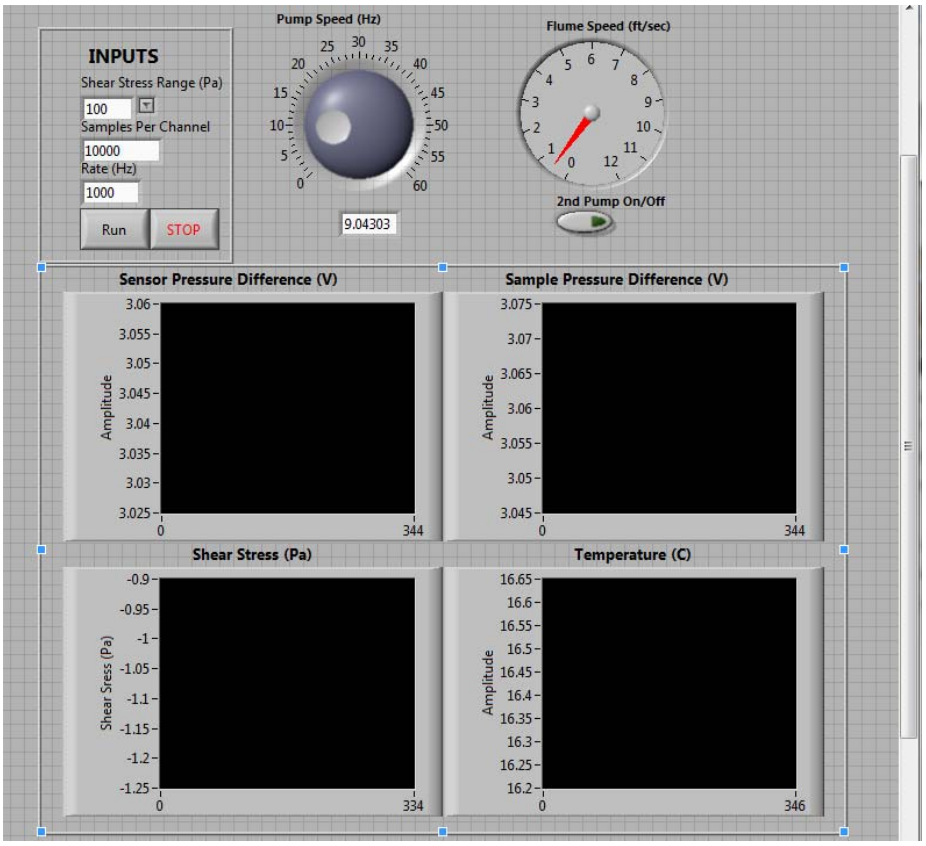

Figure A-31. SERF shear stress test program

Figure A-32. Water chiller overflow valve in the “open” position

Figure A-33. Removing Shelby tube burs using a file

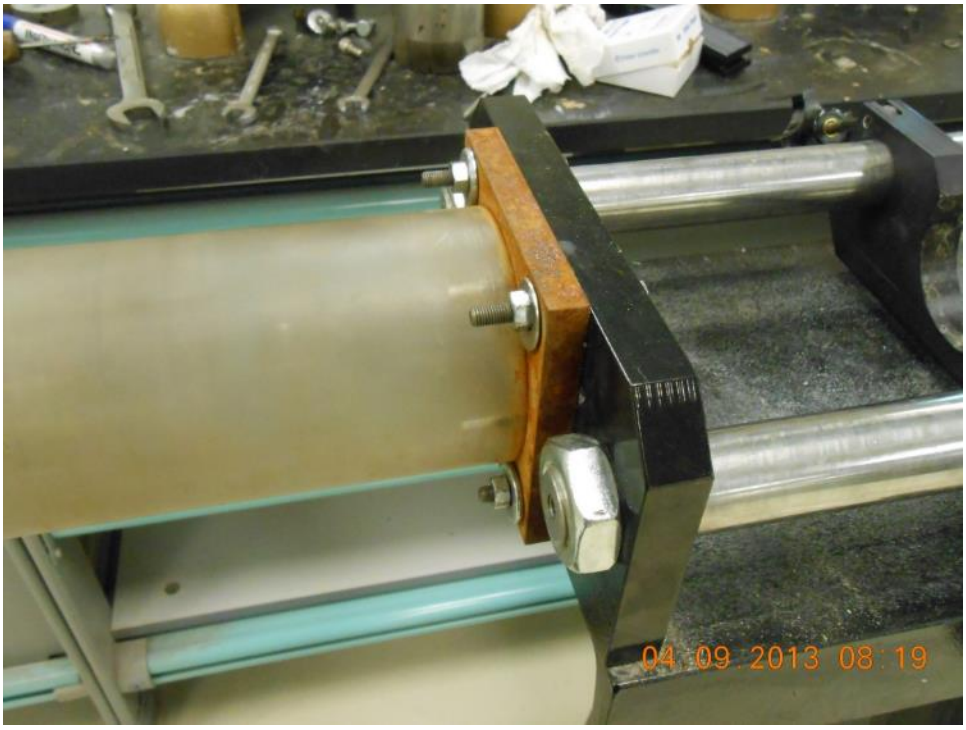

Figure A-34. SERF tube attached to Shelby tube extractor

Figure A-35. Shelby tube in extractor

Figure A-36. Spacer in Shelby tube extractor

Figure A-37. Extracted specimen with plug

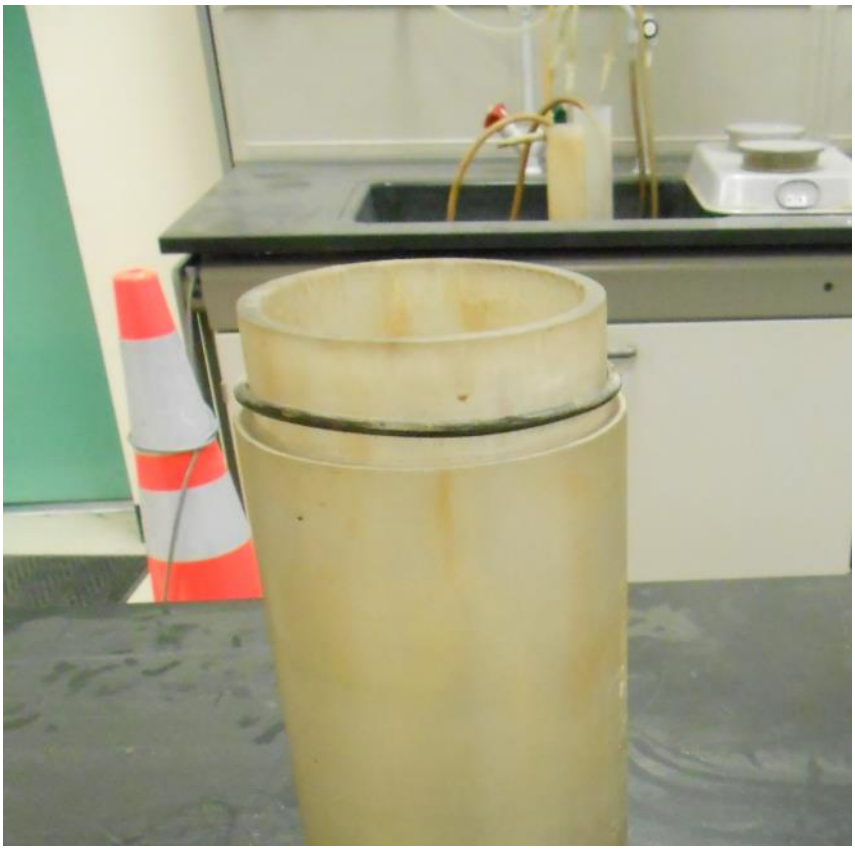
Figure A-38. O-ring on top of SERF sample tube

Figure A-39. SERF specimen aligned with flume bottom

Figure A-40. Attaching wing nuts to SERF compression plate

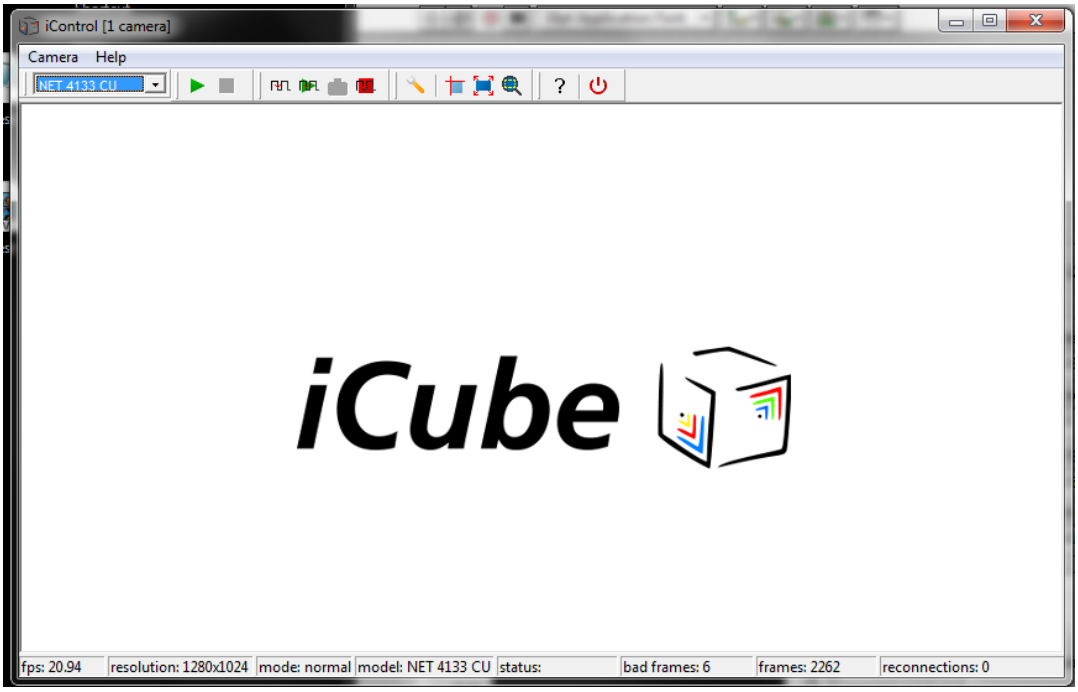

Figure A-41. iCube control program

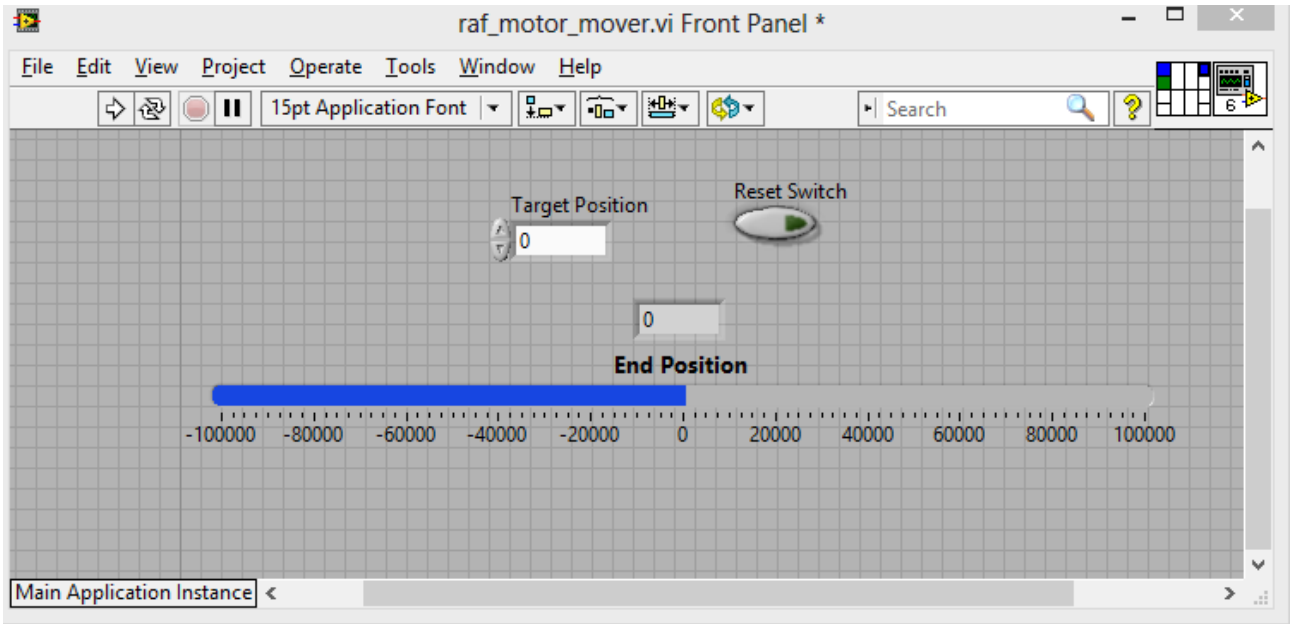

Figure A-42. Motor mover front panel

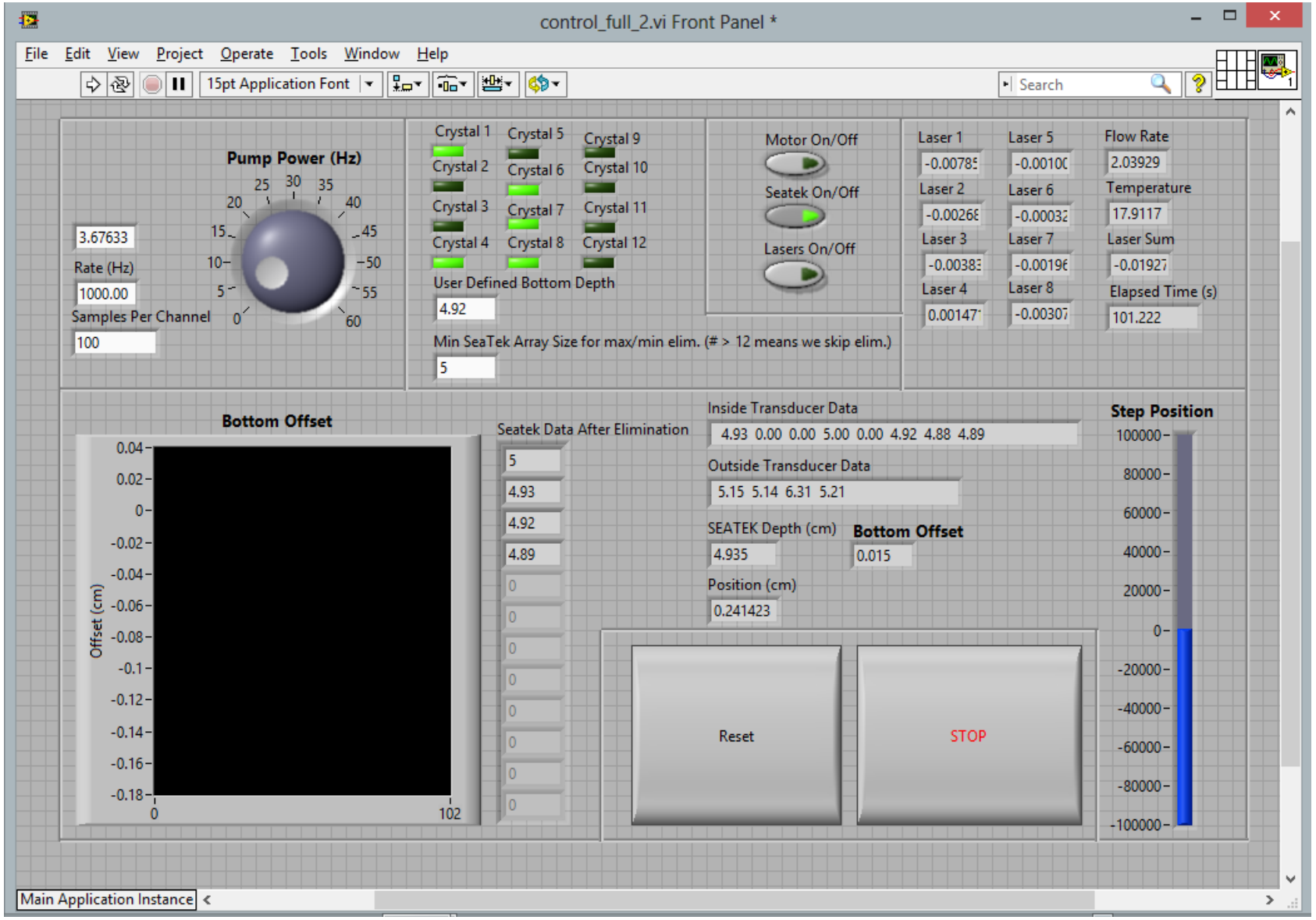

Figure A-43. SERF erosion control program front panel

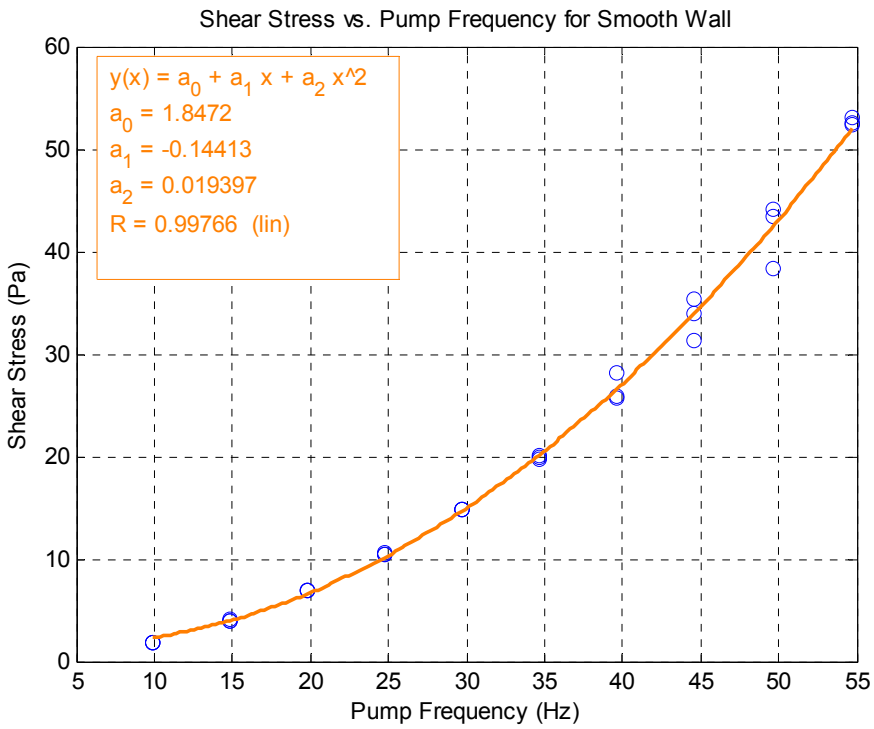

Figure A-44. Pump frequency versus shear stress in the SERF (based upon 2010 data)

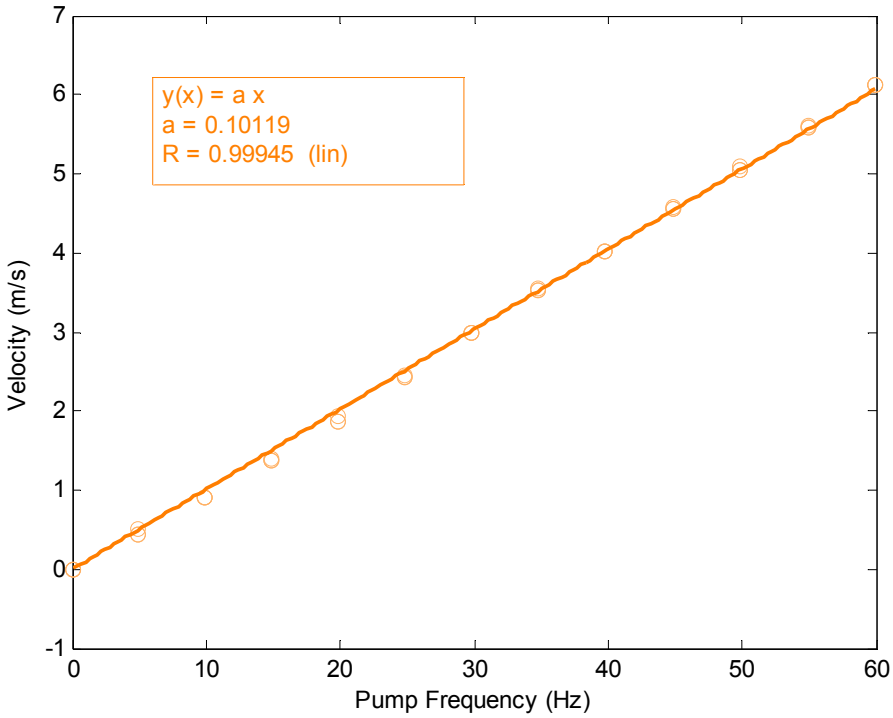

Figure A-45. Pump frequency versus velocity in the SERF (based upon 2010 data)

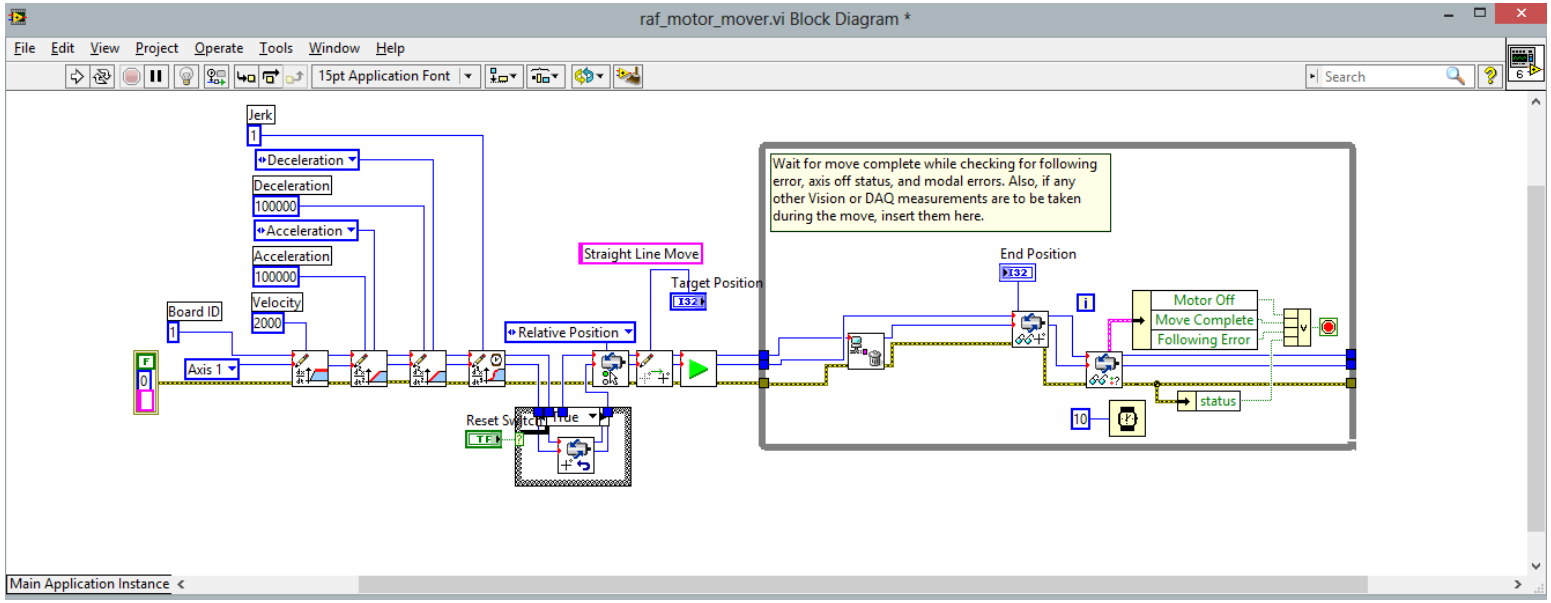

Figure A-46. Source code for motor mover program

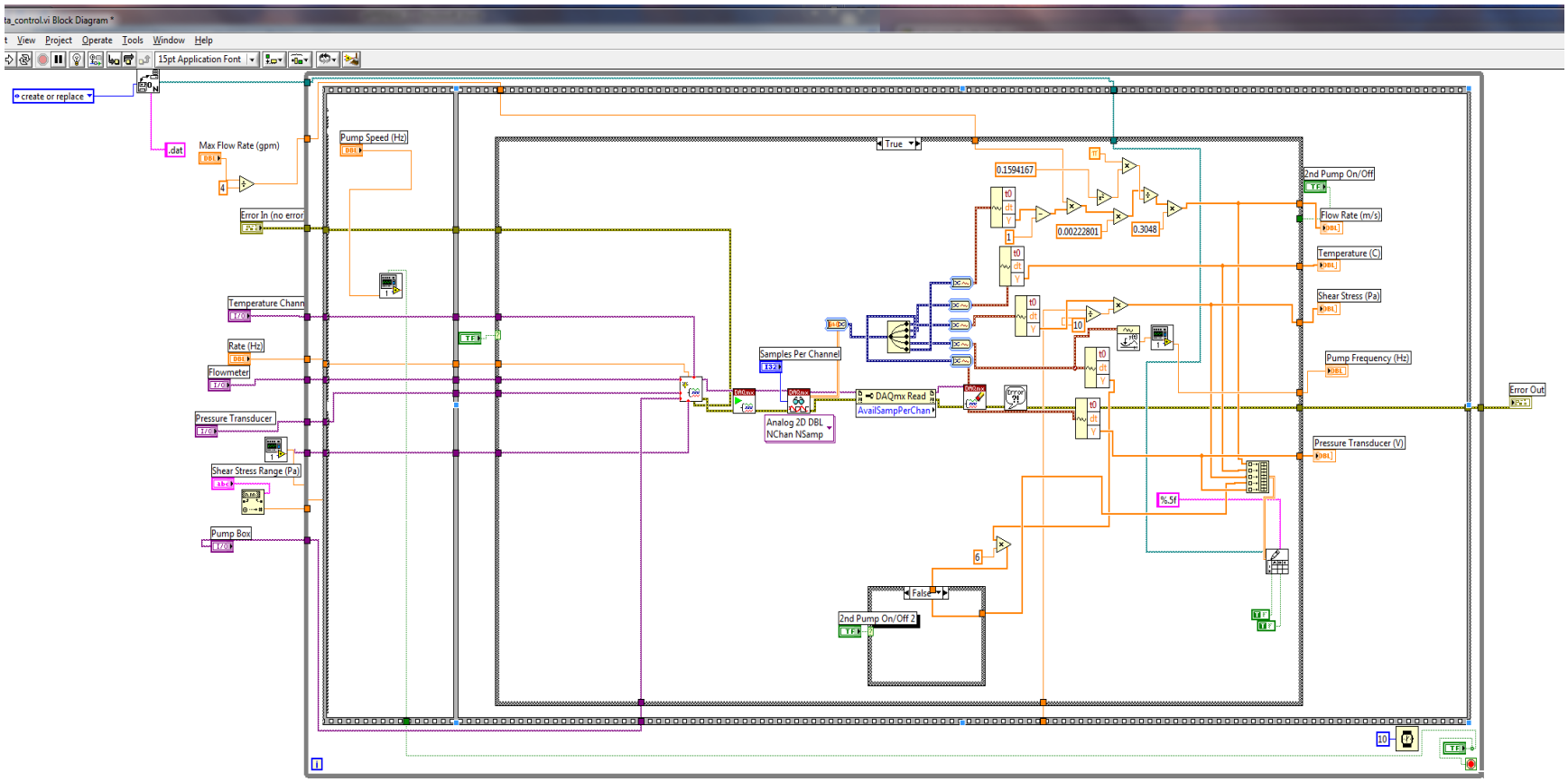

Figure A-47. Screenshot of the shear stress sensor control program

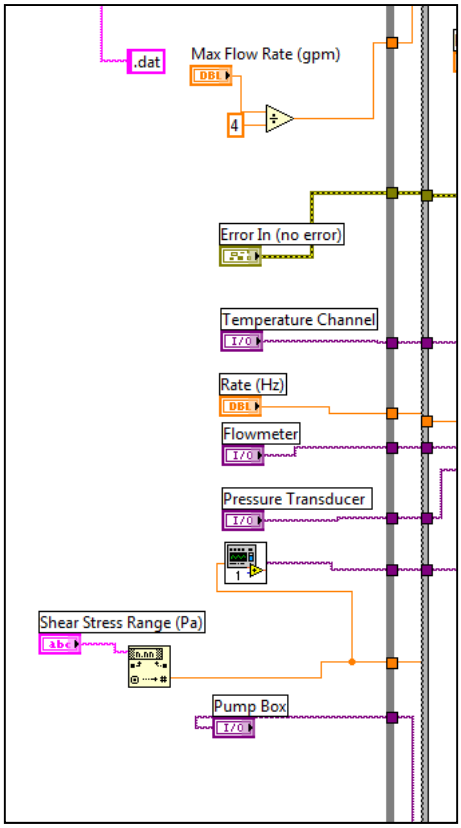

Figure A-48. Zoom-in on SC-2345 channels

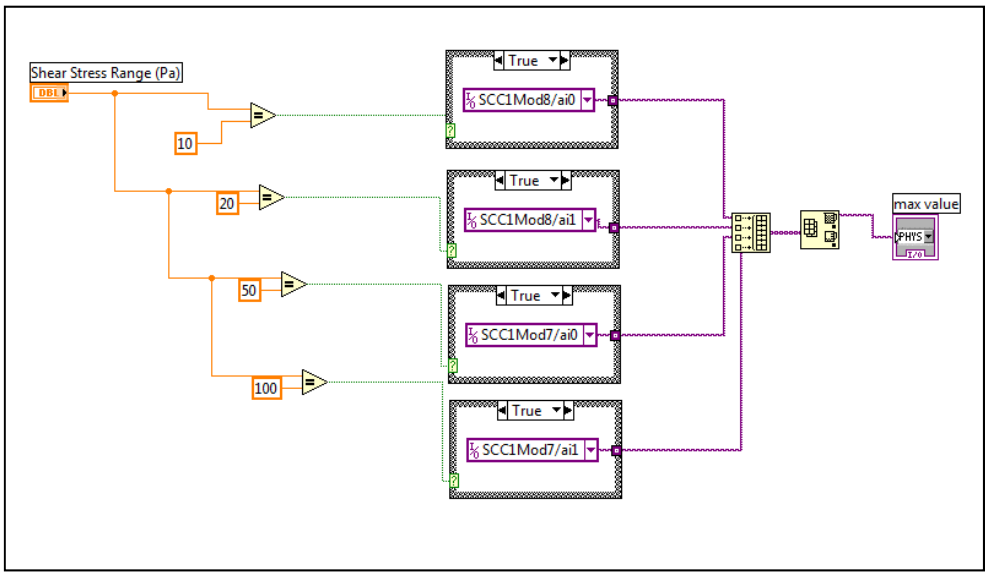

Figure A-49. Shear Stress Calibration Sub-vi (raf_shear_module.vi)

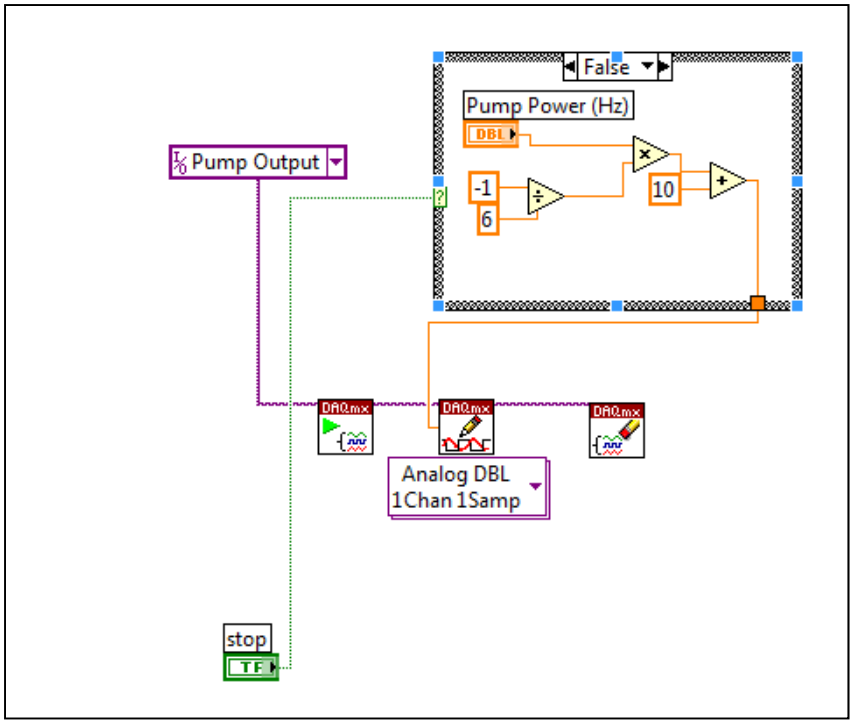

Figure A-50. Sub-vi Showing First Portion of Pump Control Program (raf_pump_on.vi)

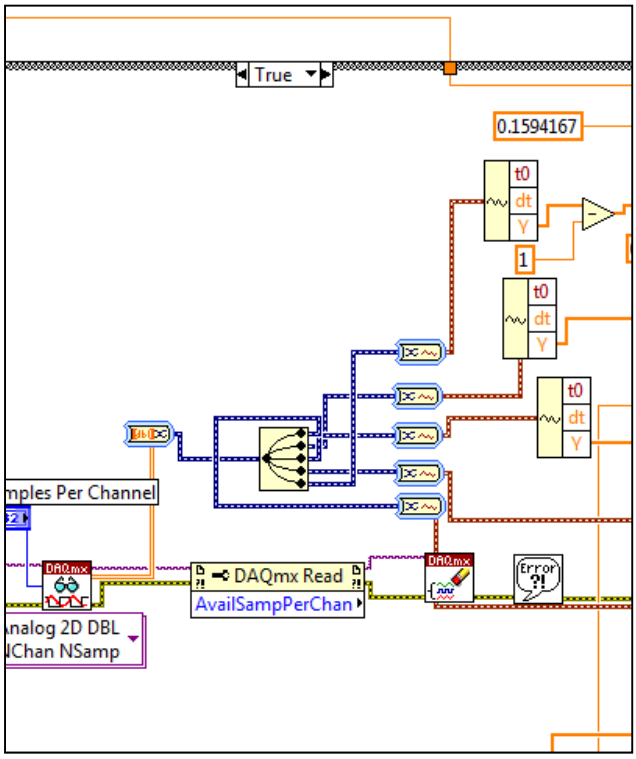

Figure A-51. Five Signal Split in Pump Control No Motor

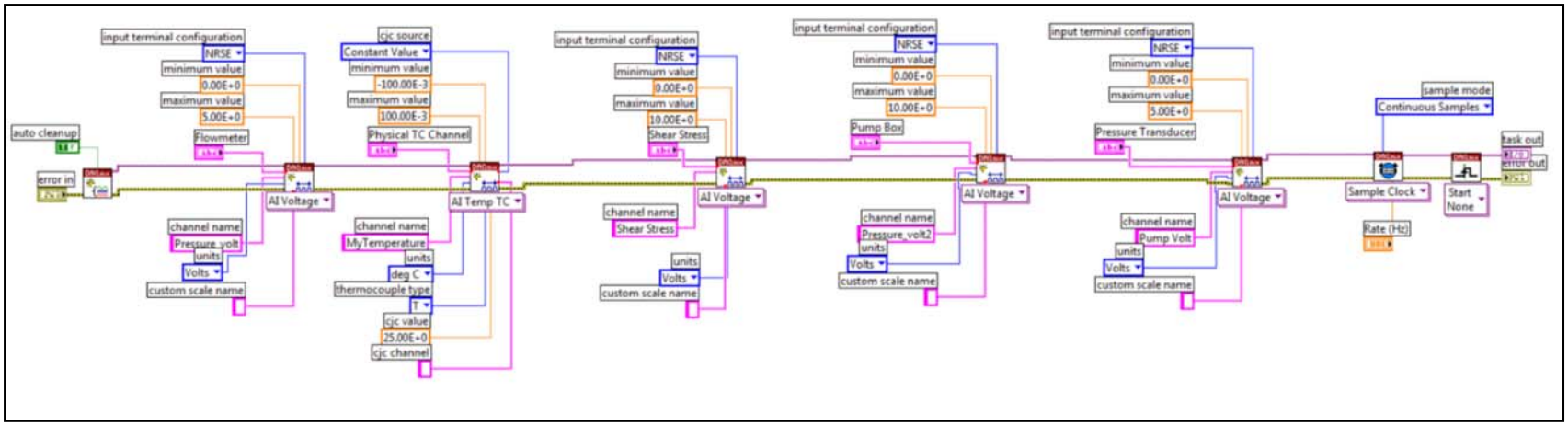

Figure A-52. Analog Reader for shear stress sensor program

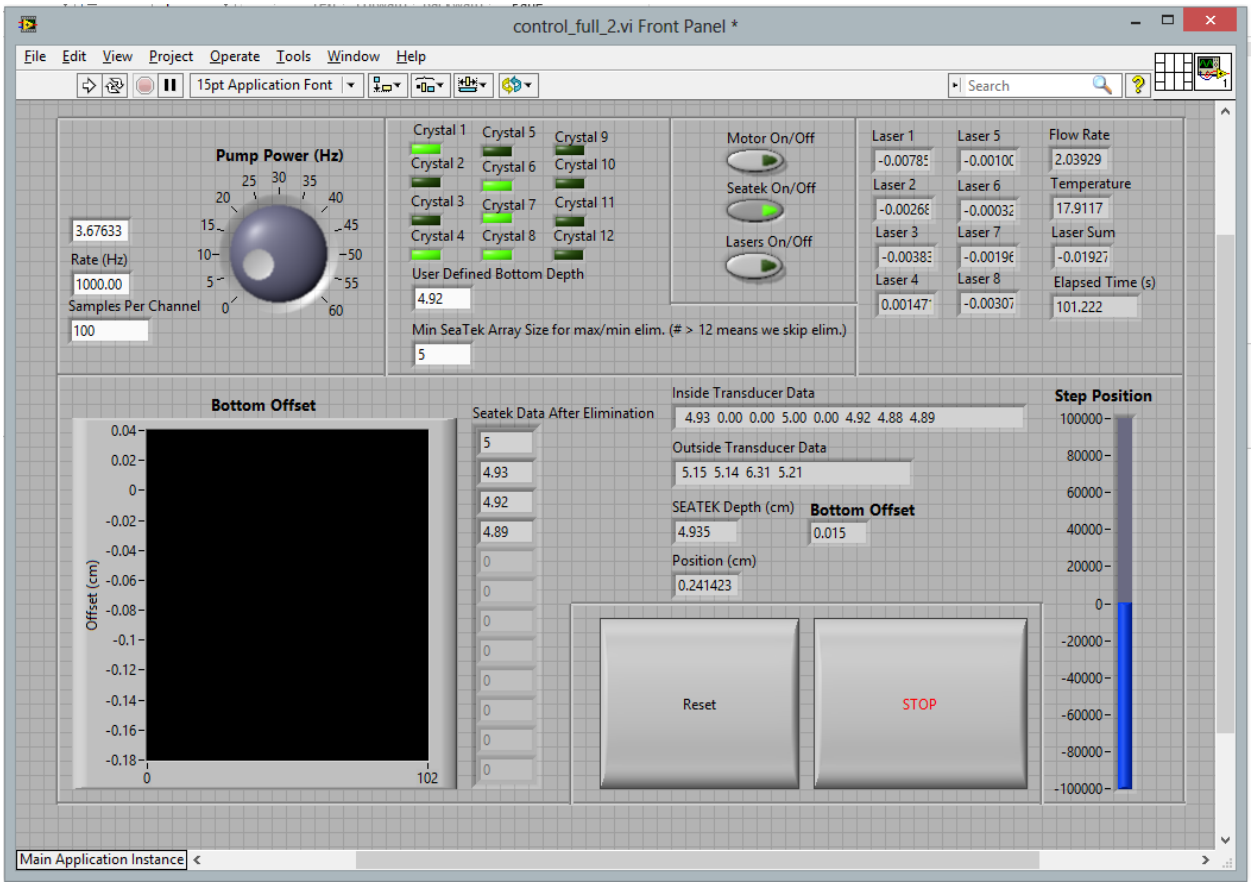

Figure A-53. SERF full control front panel

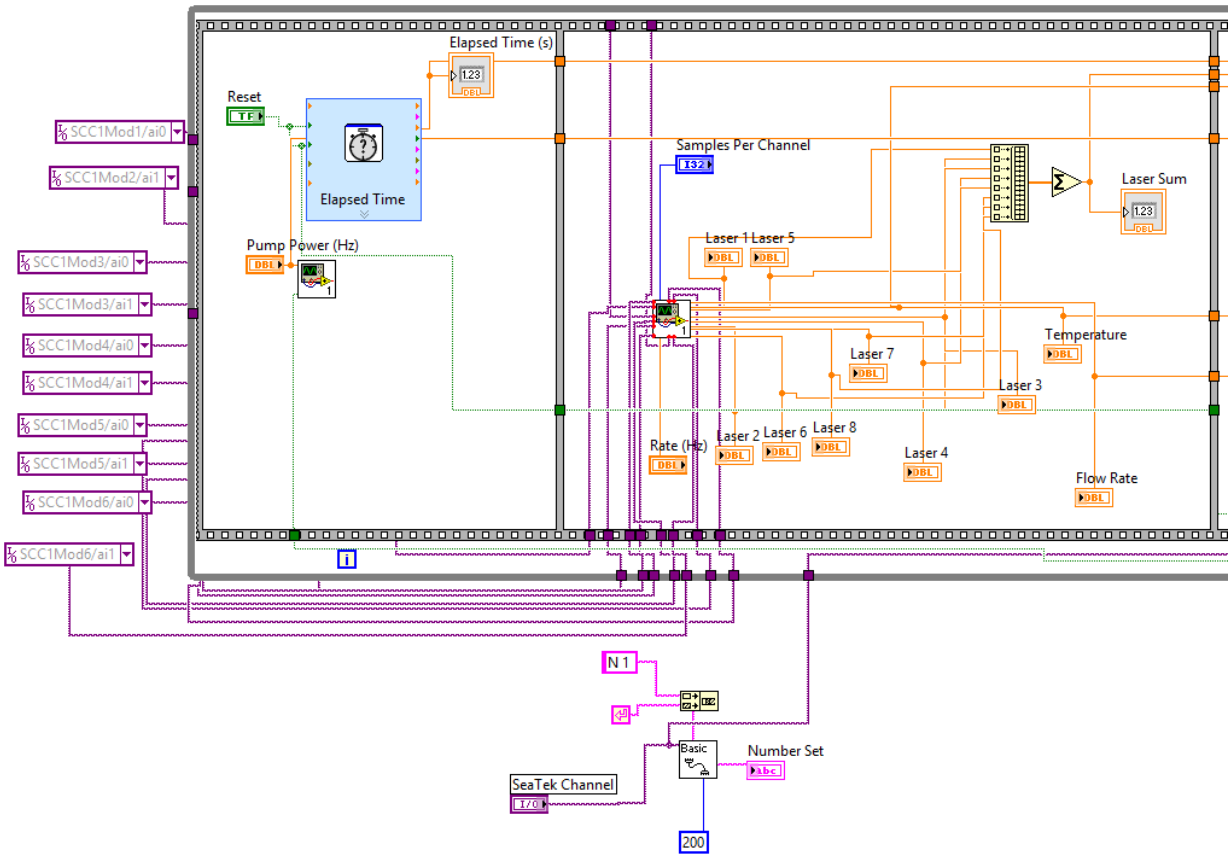

Figure A-54. First half (left side) of SERF full control source code

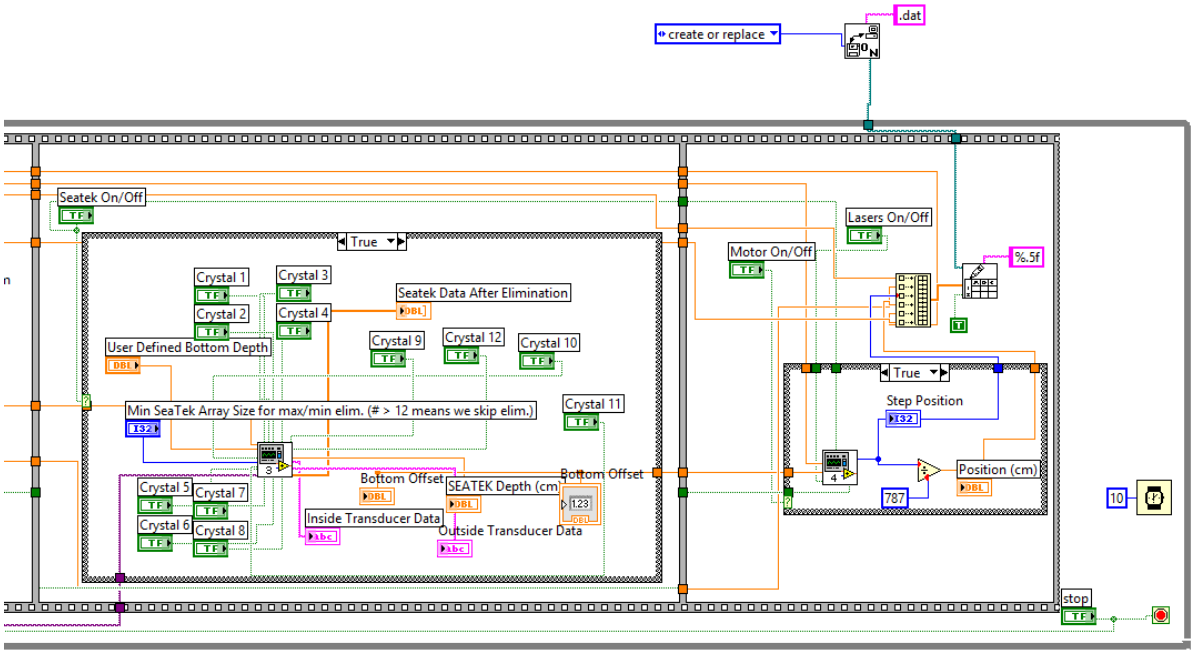

Figure A-55. Second half (right side) of SERF full control source code

Figure A-56. SC-2345 channels for full SERF control program

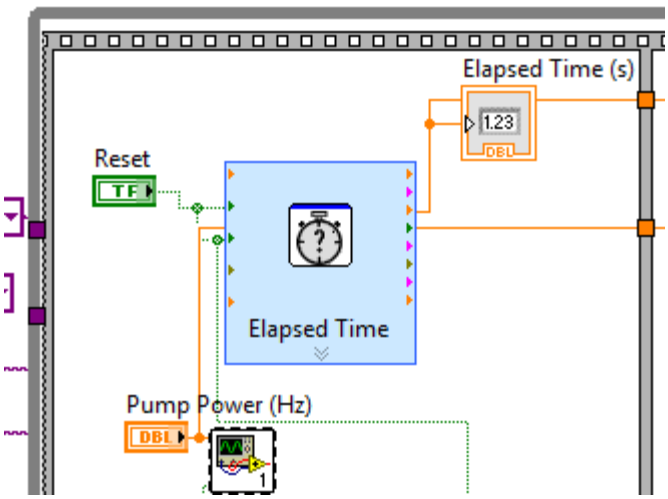

Figure A-57. Pump subroutine and timer structure in main SERF program

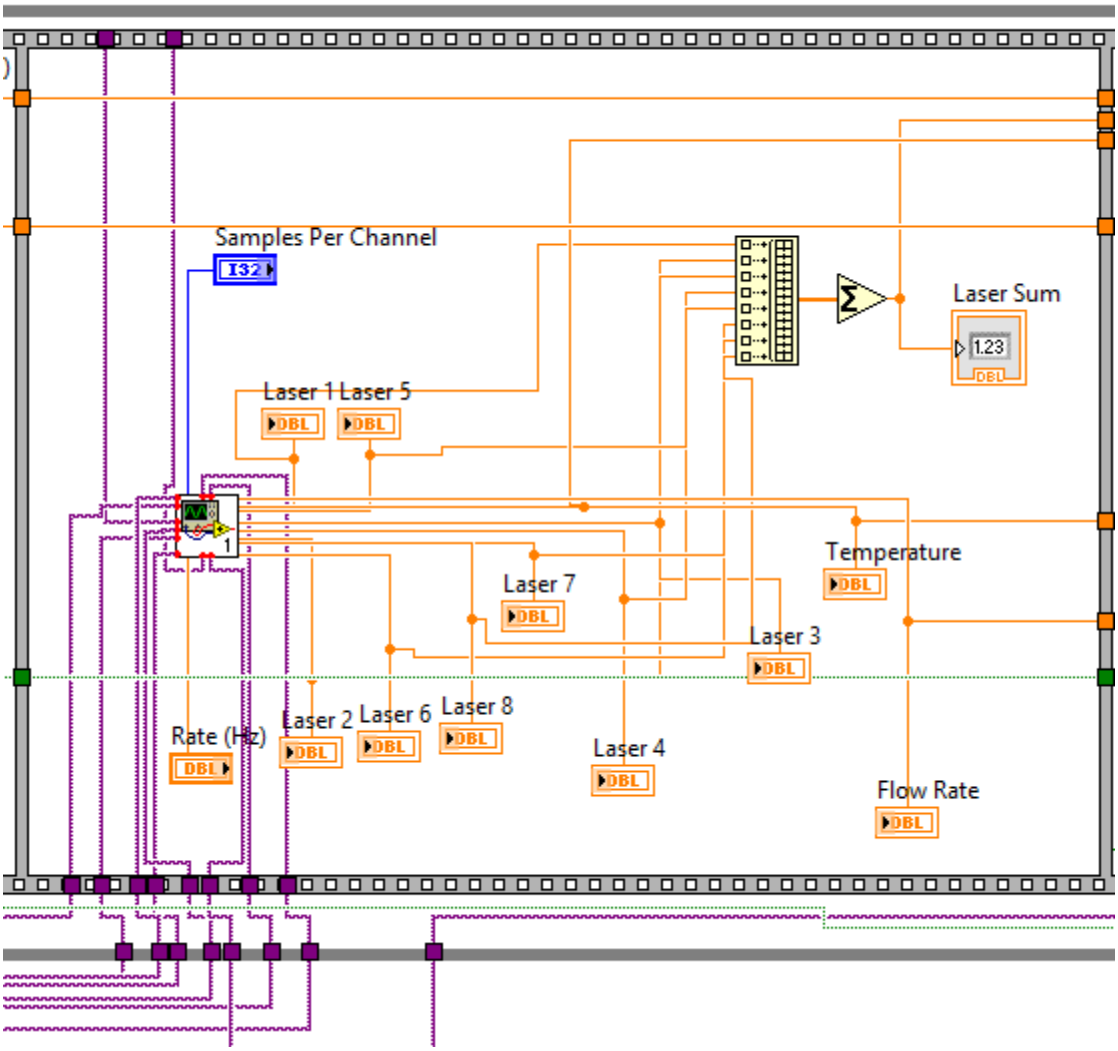

Figure A-58. Laser sequence

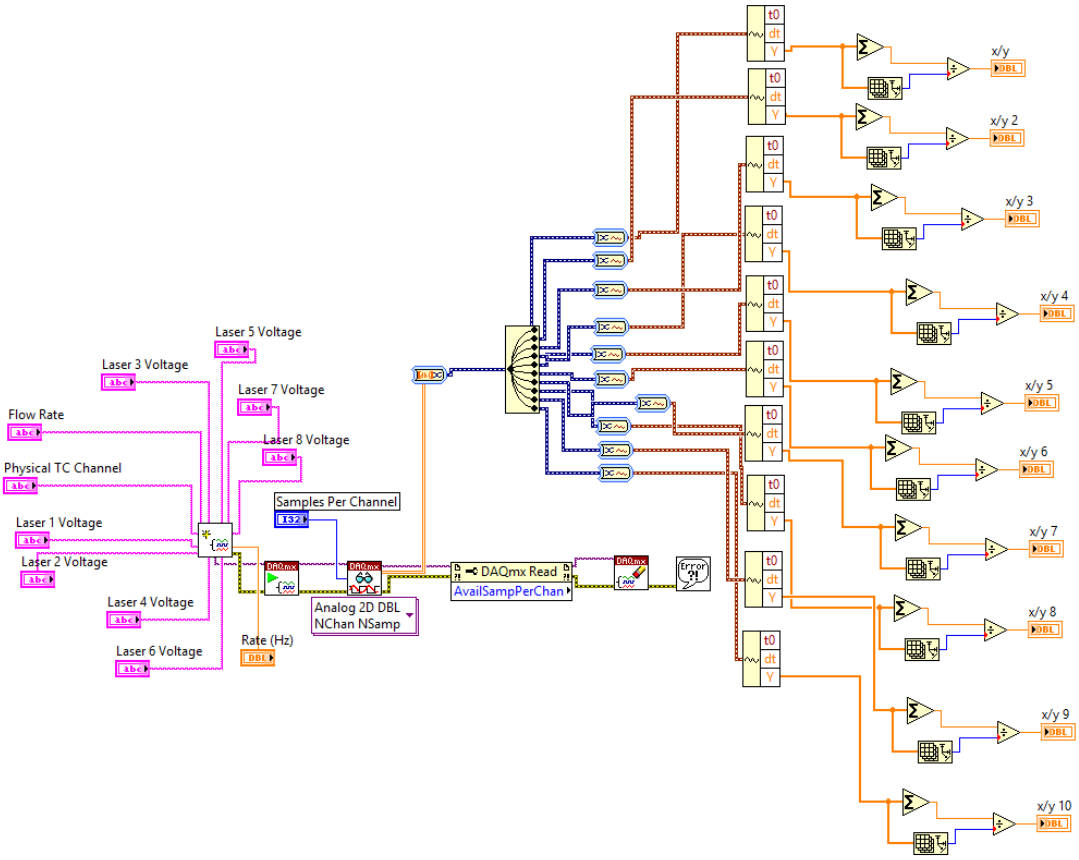

Figure A-59. Laser program sub-VI block diagram

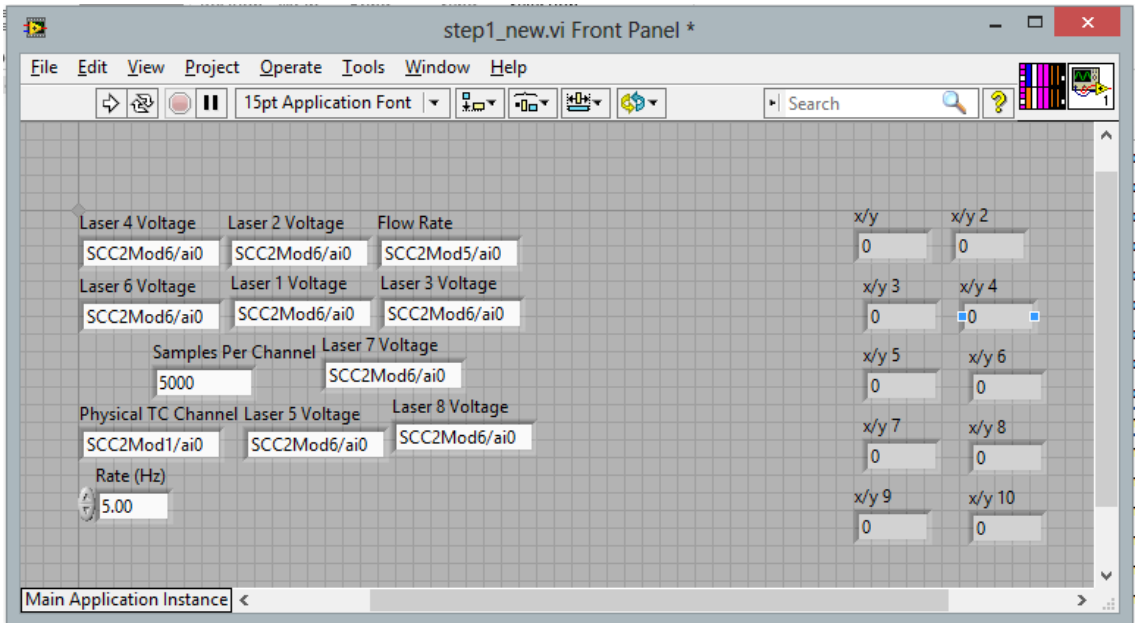

Figure A-60. Laser sub-VI front panel

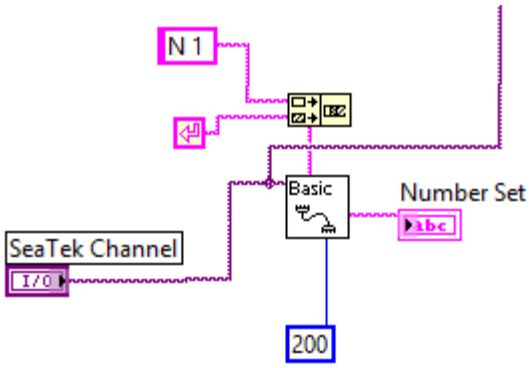

Figure A-61. SEATEK pre-input sequence

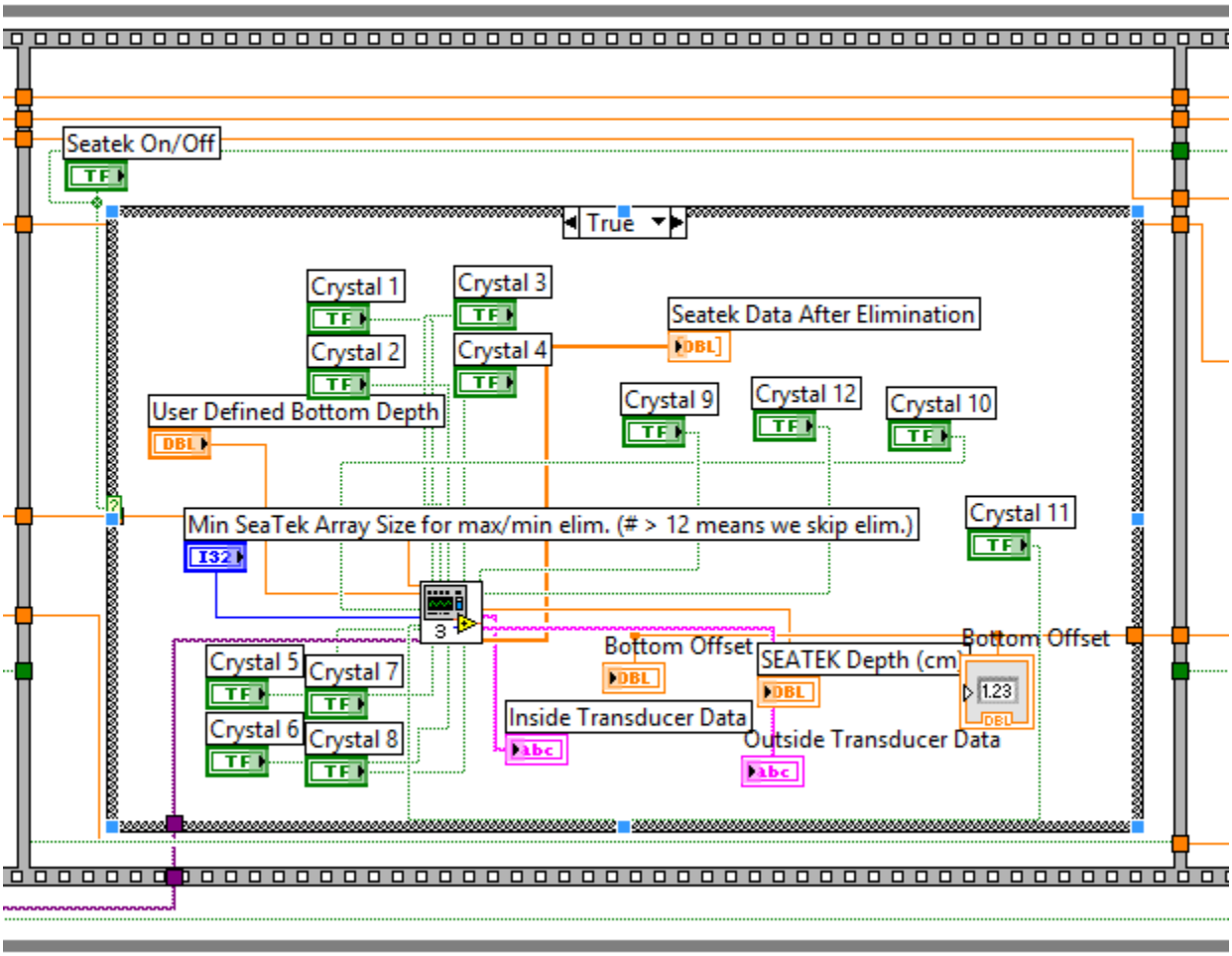

Figure A-62. SEATEK data collection algorithm of main SERF program

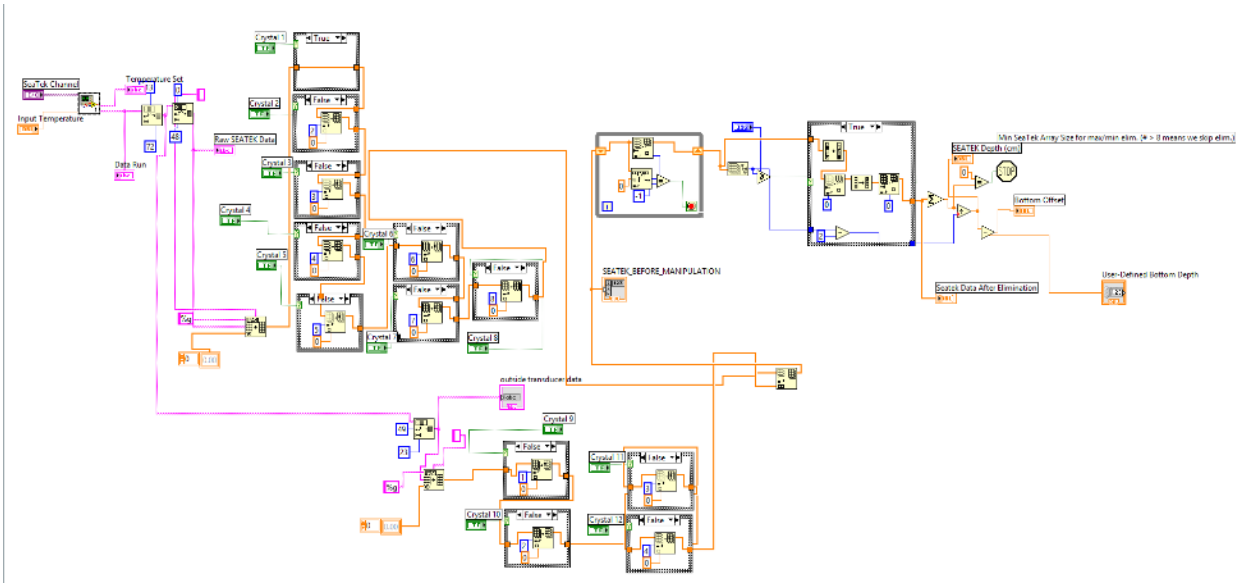

Figure A-63. SEATEK data collection sub-VI

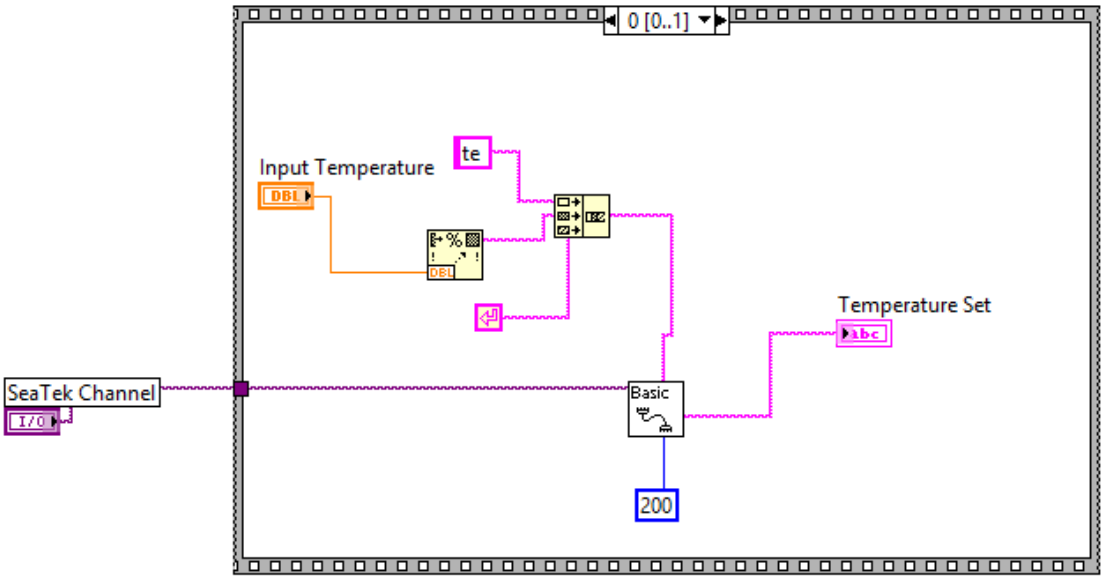

Figure A-64. First sequence in temperature patch

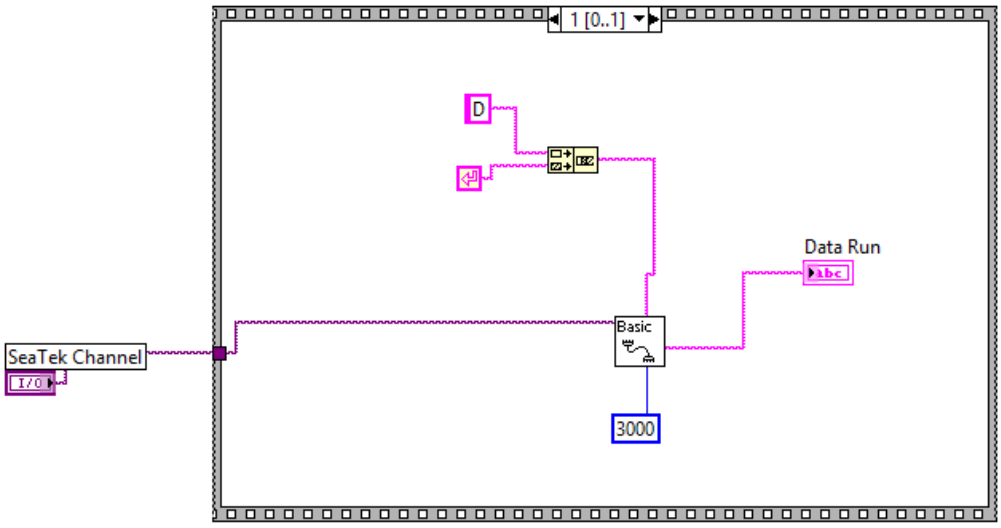

Figure A-65. Second sequence in temperature patch

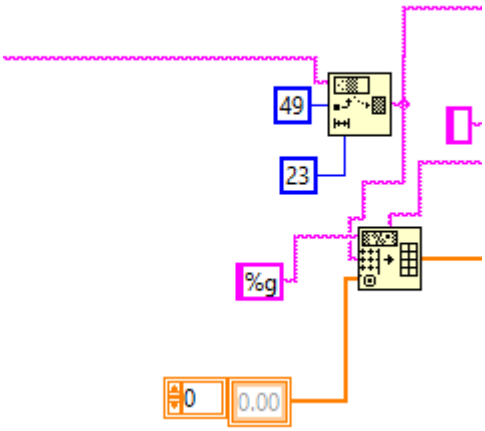

Figure A-66. Correct character isolation and array conversion in SEATEK control program (crystals 9-12)

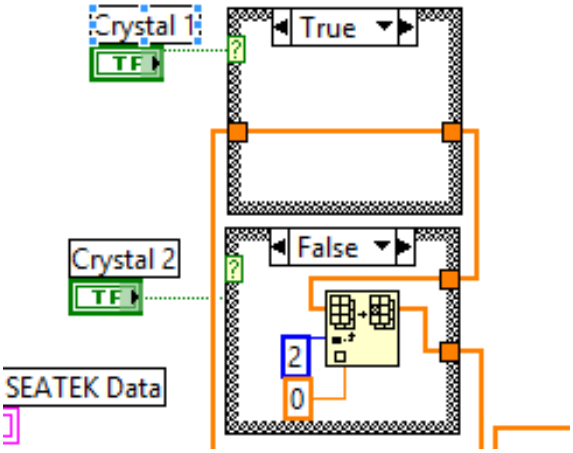

Figure A-67. Crystal on/off soft-wire for crystals 1 and 2 showing the “on” case (top) and the “off” case (bottom)

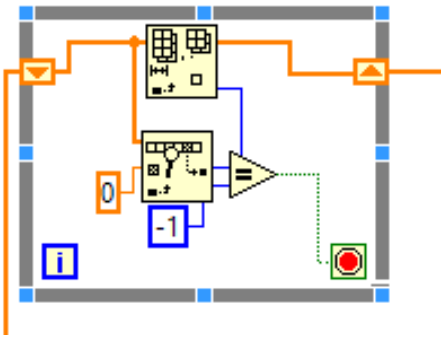

Figure A-68. SEATEK zero-checker

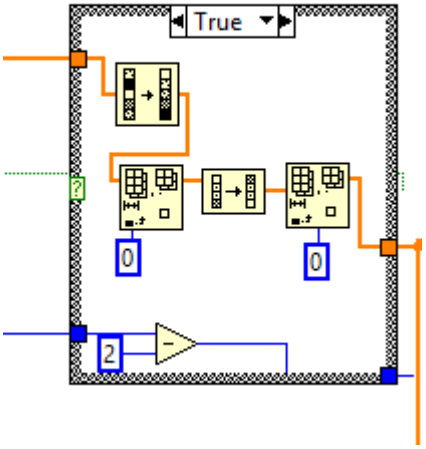

Figure A-69. SEATEK high/low elimination sequence

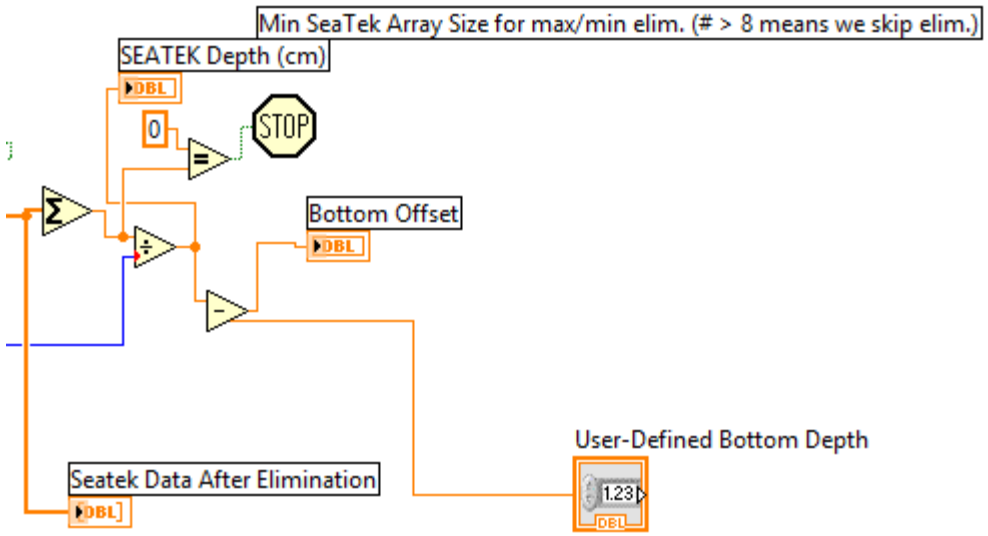

Figure A-70. SEATEK bottom offset computation

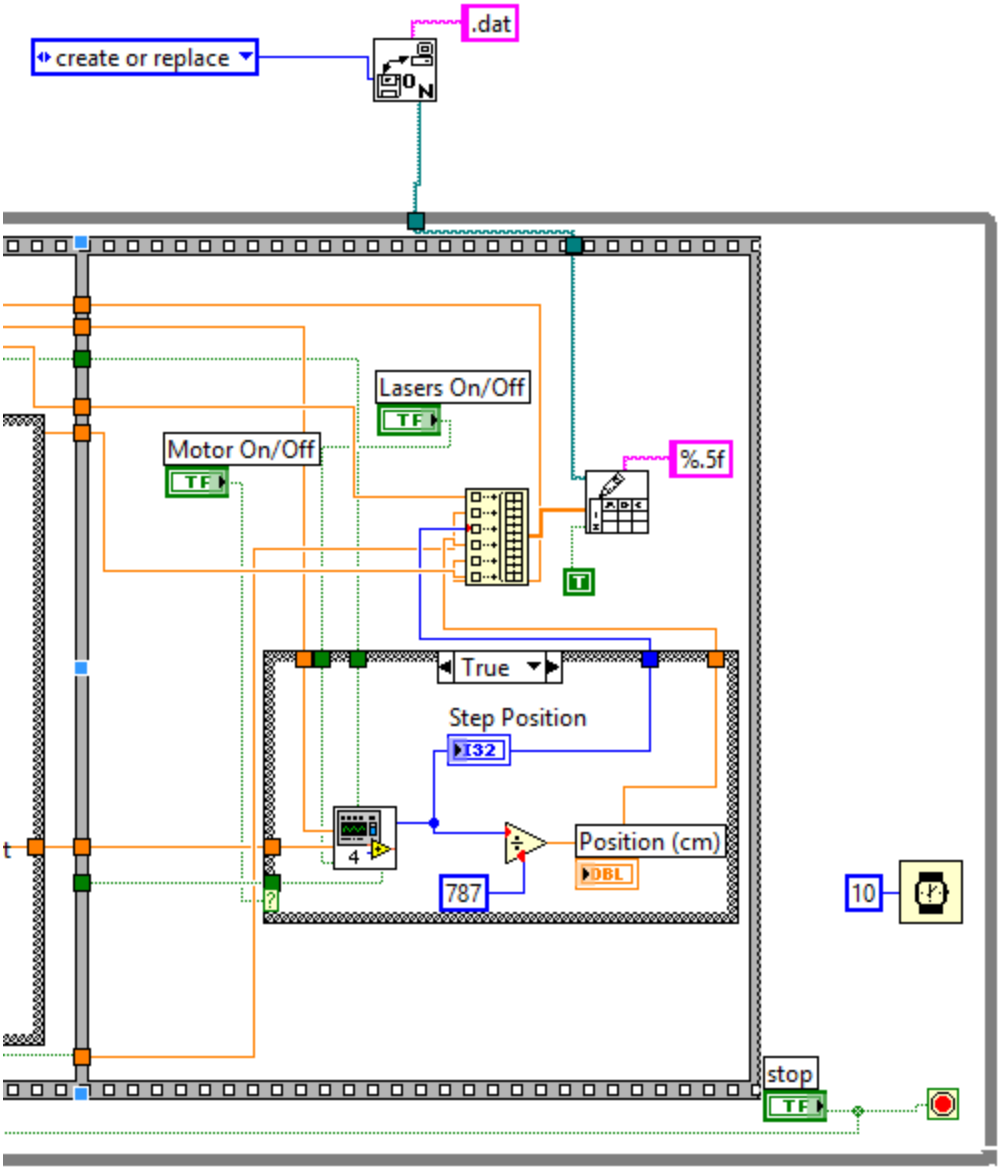

Figure A-71. Motor movement sequence in SERF control program

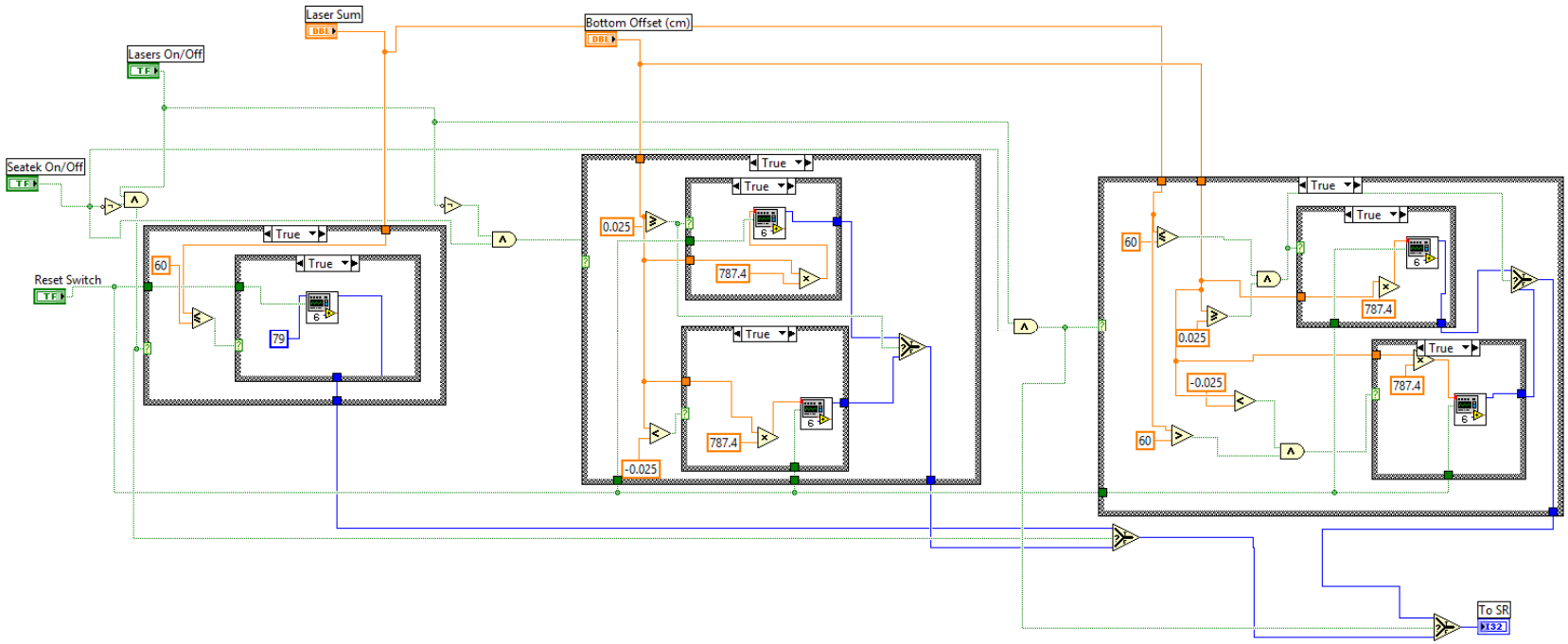

Figure A-72. Motor sub-VI in SERF full control program

Figure A-73. Round Access Hatch on Shear Sensor

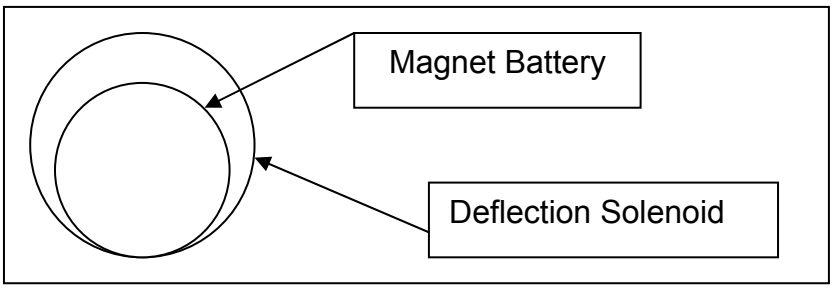

Figure A-74. Schematic of a Slipped Brass Rod Connection

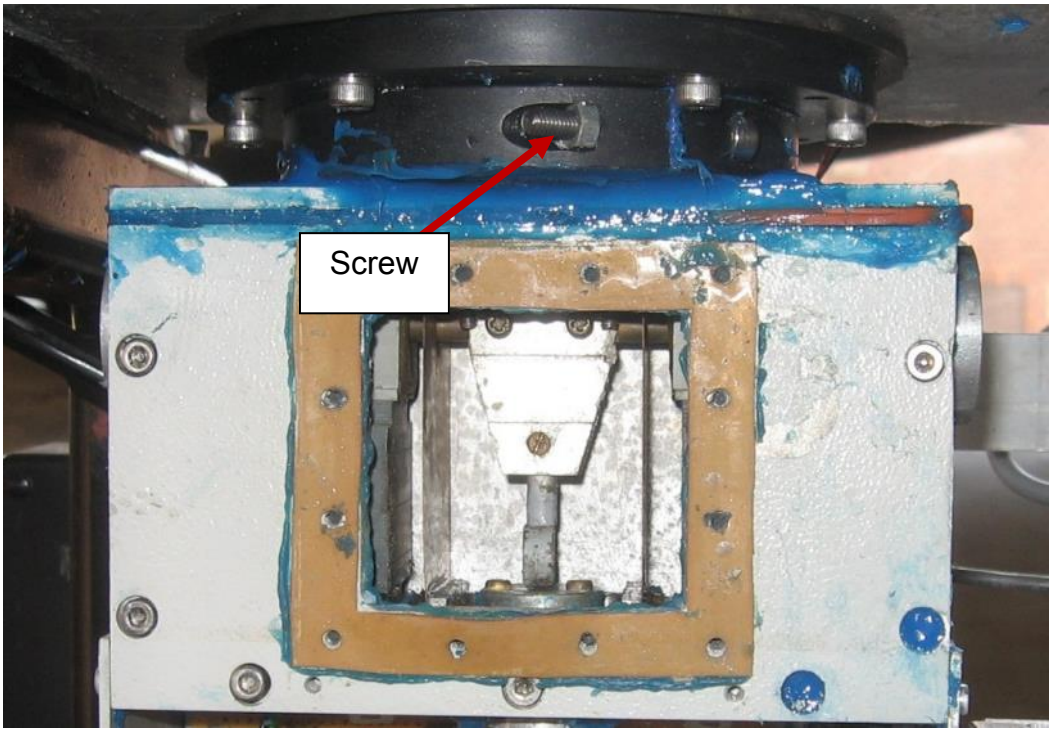

Figure A-75. Screw holding brass rod to platform.

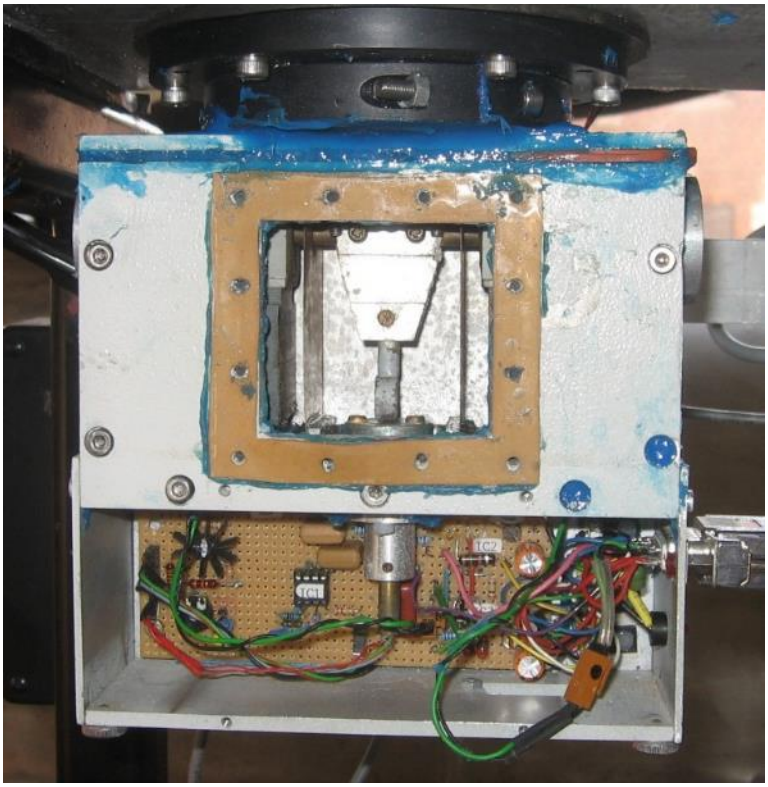

Figure A-76. Exposed Electronics in “Dry” Portion of Sensor

APPENDIX B
RAW EROSION DATA FOR FLORIDA SPECIMENS

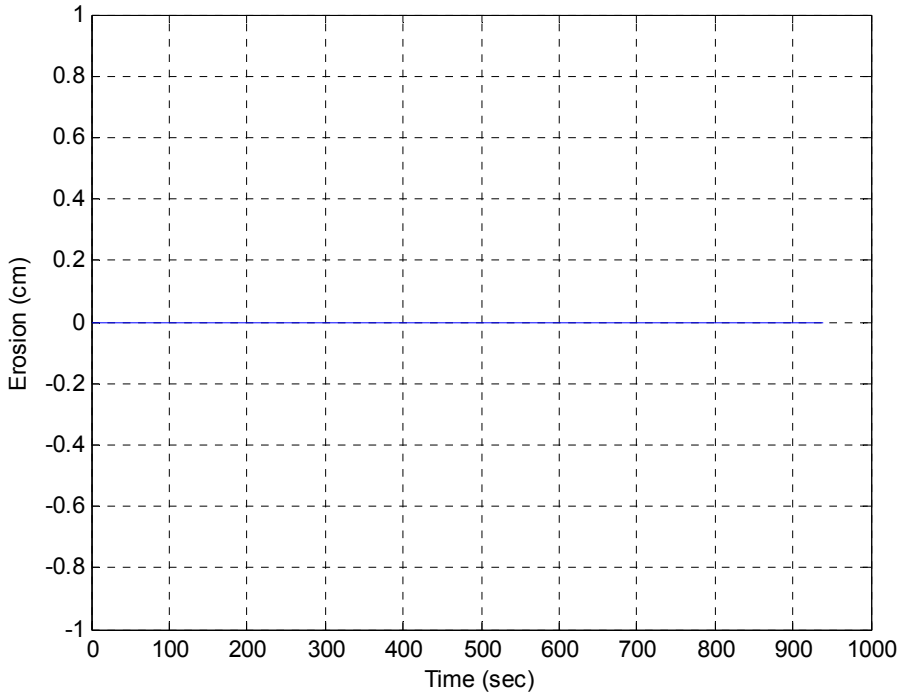

Figure B-1. Erosion versus time for specimen AS-UF1 at 2.35 Pa.

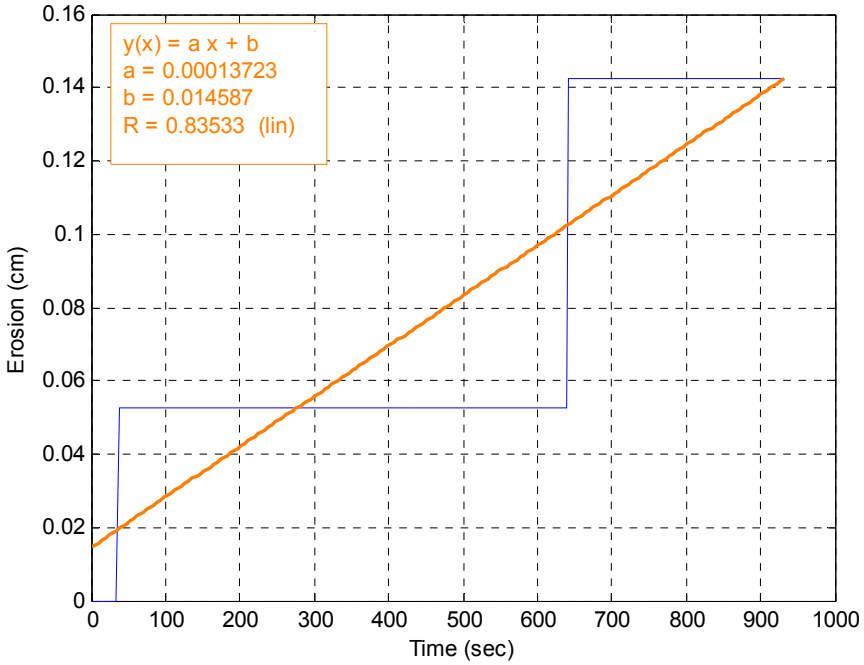

Figure B-2. Erosion versus time for specimen AS-UF1 at 4.05 Pa

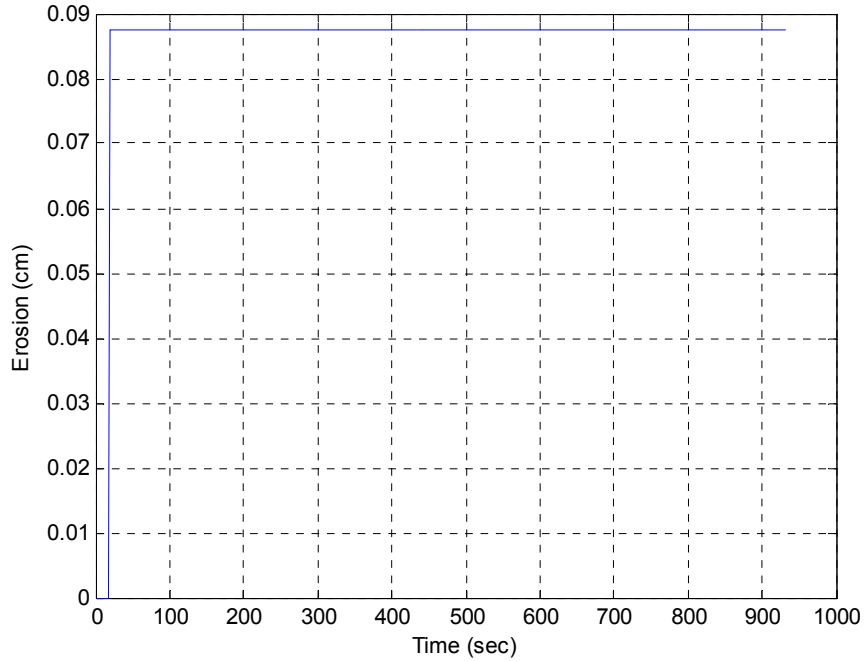

Figure B-3. Erosion versus time for specimen AS-UF1 at 6.72 Pa

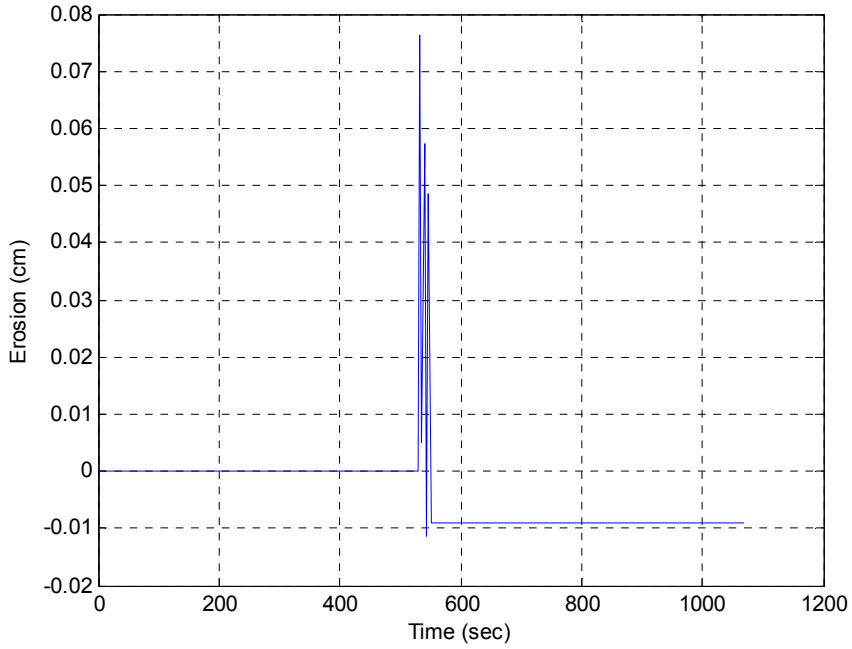

Figure B-4. Erosion versus time for specimen AS-UF1 at 10.37 Pa

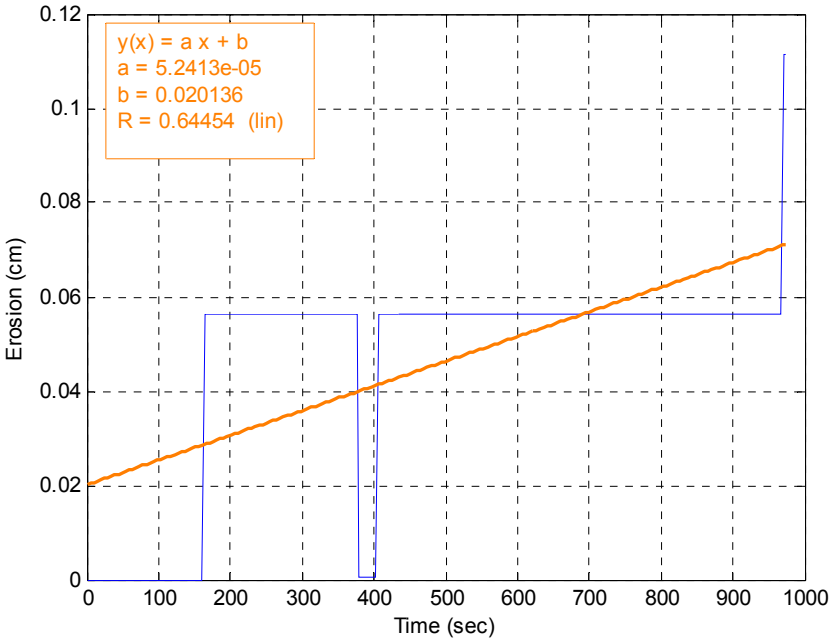

Figure B-5. Erosion versus time for specimen AS-UF1 at 14.98 Pa

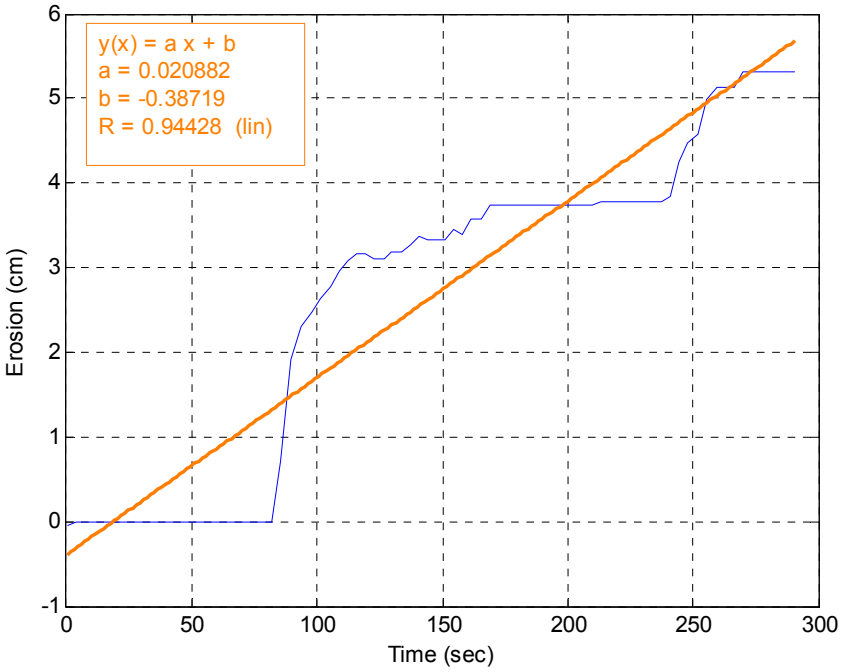

Figure B-6. Erosion versus time for specimen AS-UF1 at 20.56 Pa

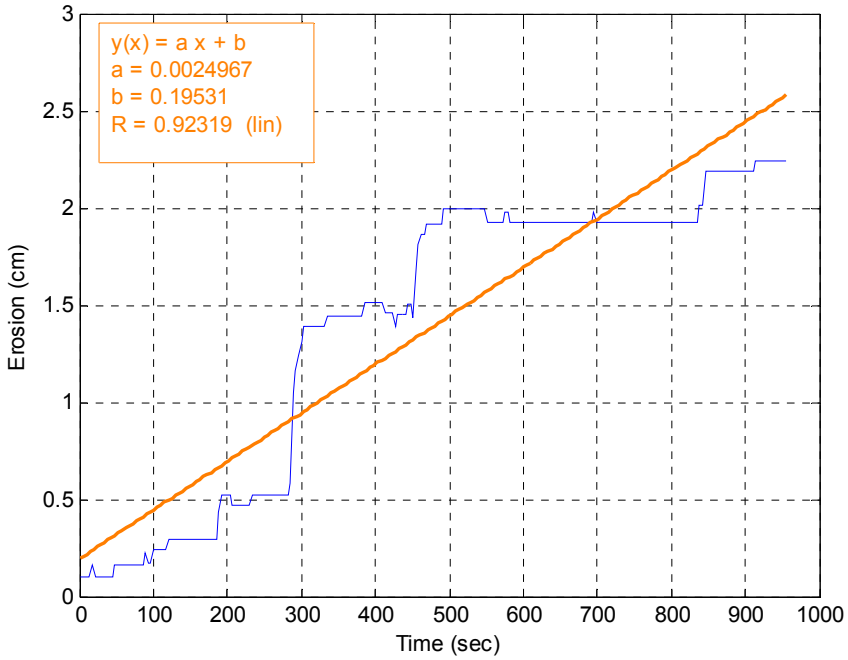

Figure B-7. Erosion versus time for specimen AS-UF1 at 16.02 Pa

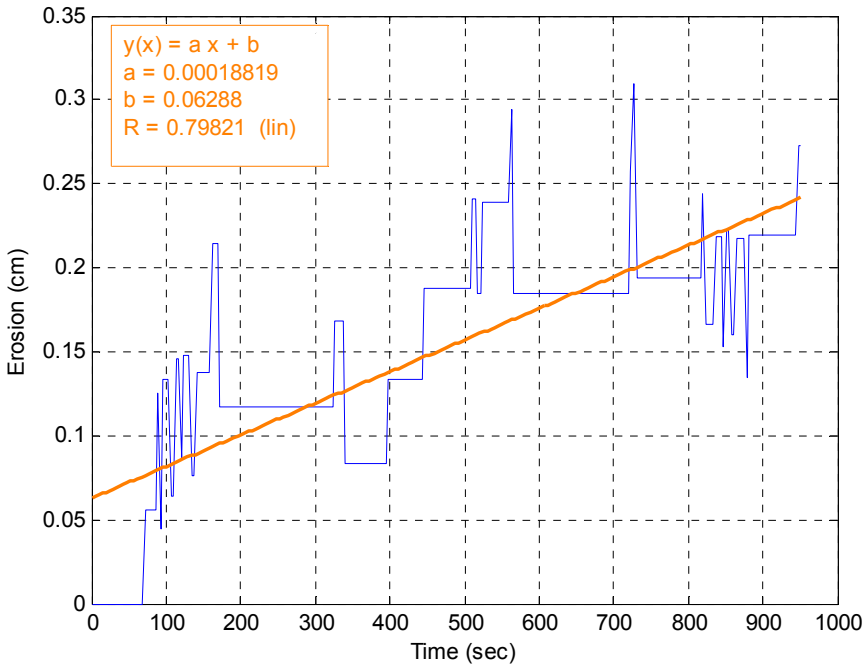

Figure B-8. Erosion versus time for specimen AS-UF1 at 18.21 Pa

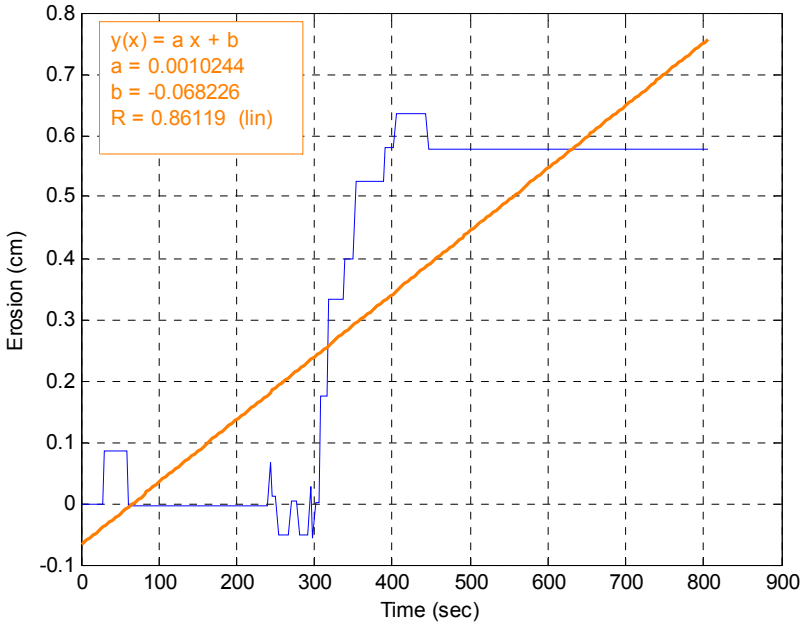

Figure B-9. Erosion versus time for specimen AS-UF1 at 19.37 Pa

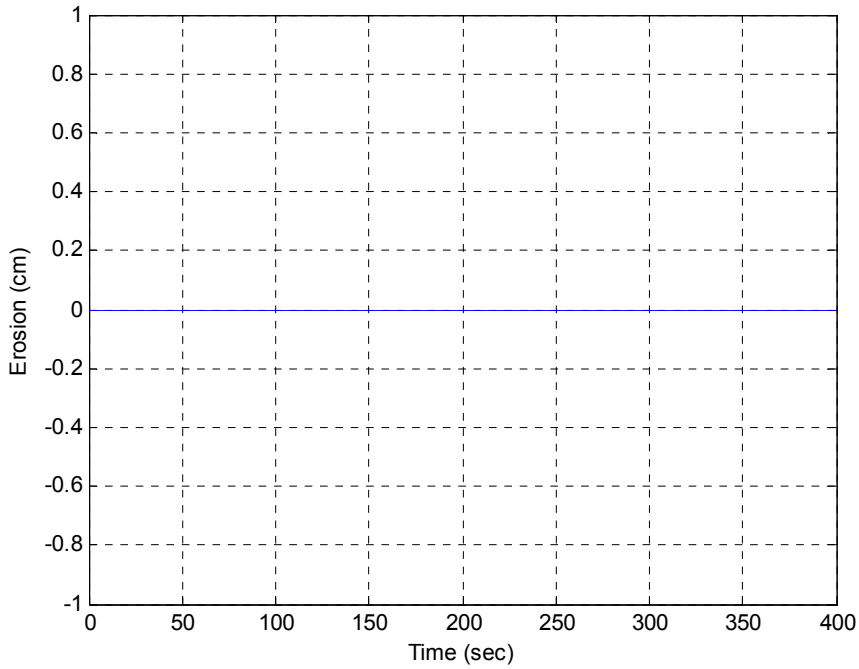

Figure B-10. Erosion versus time for specimen AS-UF1 at 6.72 Pa

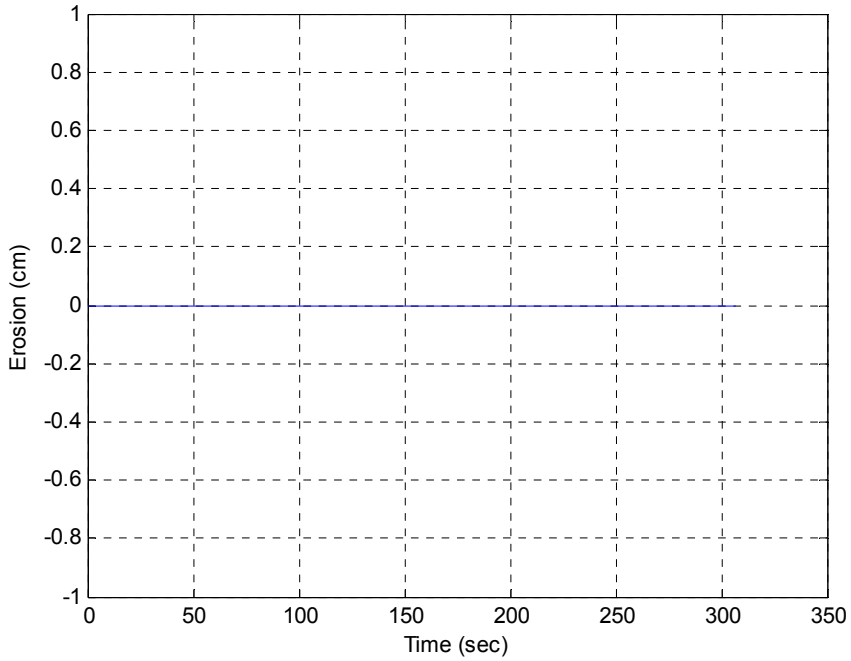

Figure B-11. Erosion versus time for specimen AS-UF1 at 10.37 Pa

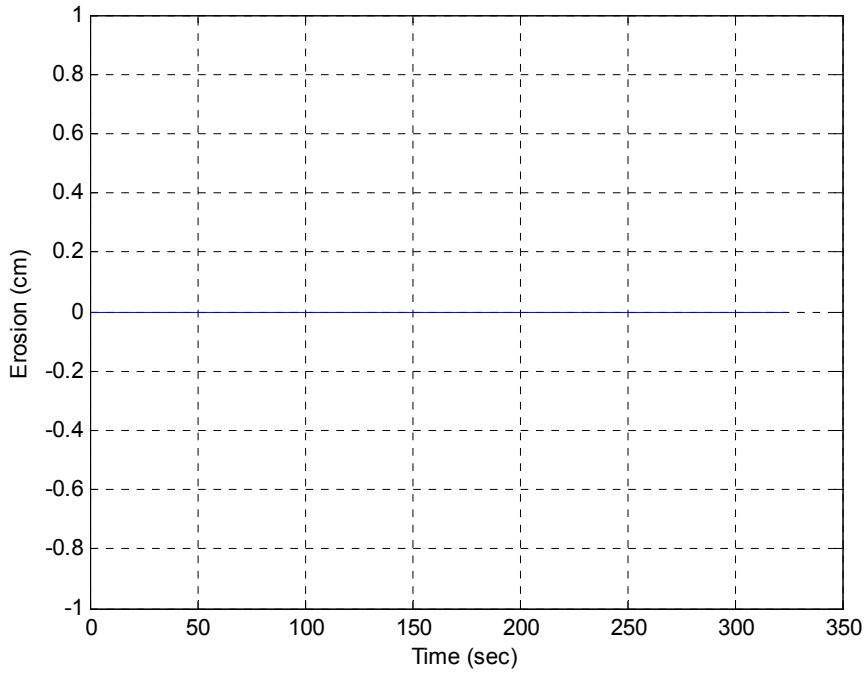

Figure B-12. Erosion versus time for specimen AS-UF1 at 14.98 Pa

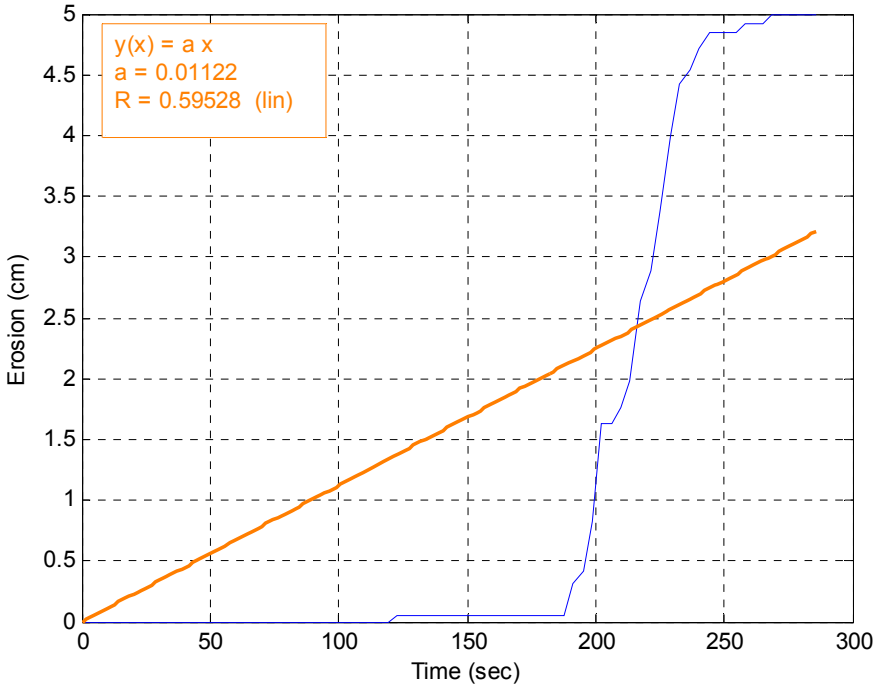

Figure B-13. Erosion versus time for specimen AS-UF1 at 20.56 Pa

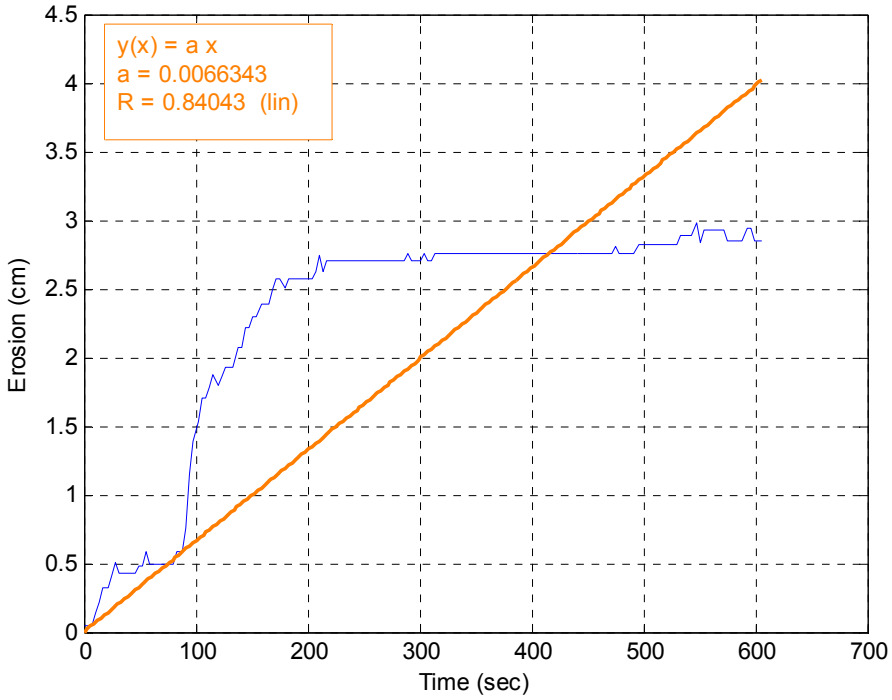

Figure B-14. Erosion versus time for specimen AS-UF1 at 19.37 Pa (data eliminated from erosion function due to suspected layering)

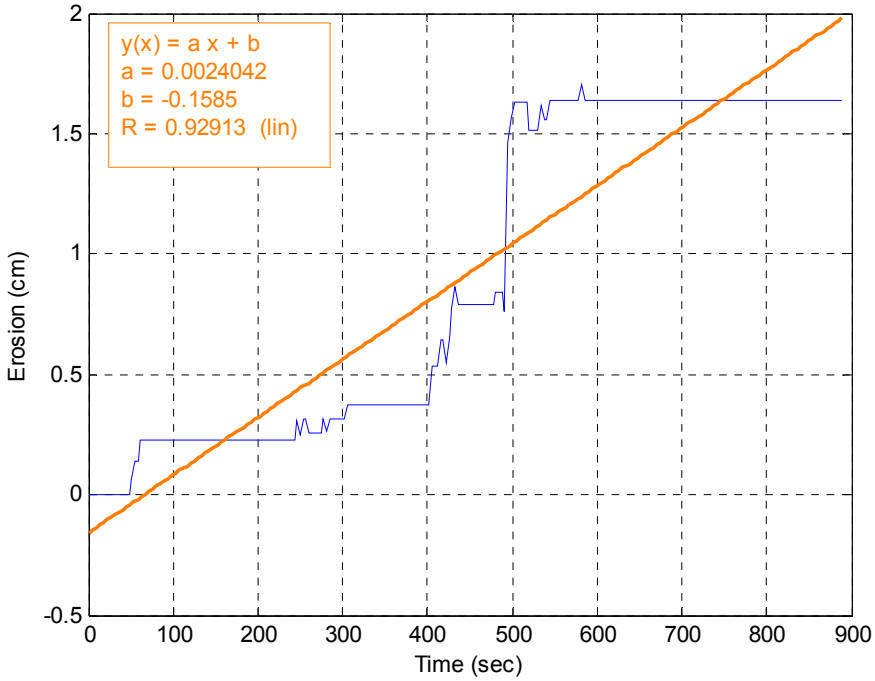

Figure B-15. Erosion versus time for specimen AS-UF1 at 21.80 Pa (data eliminated from erosion function due to suspected layering)

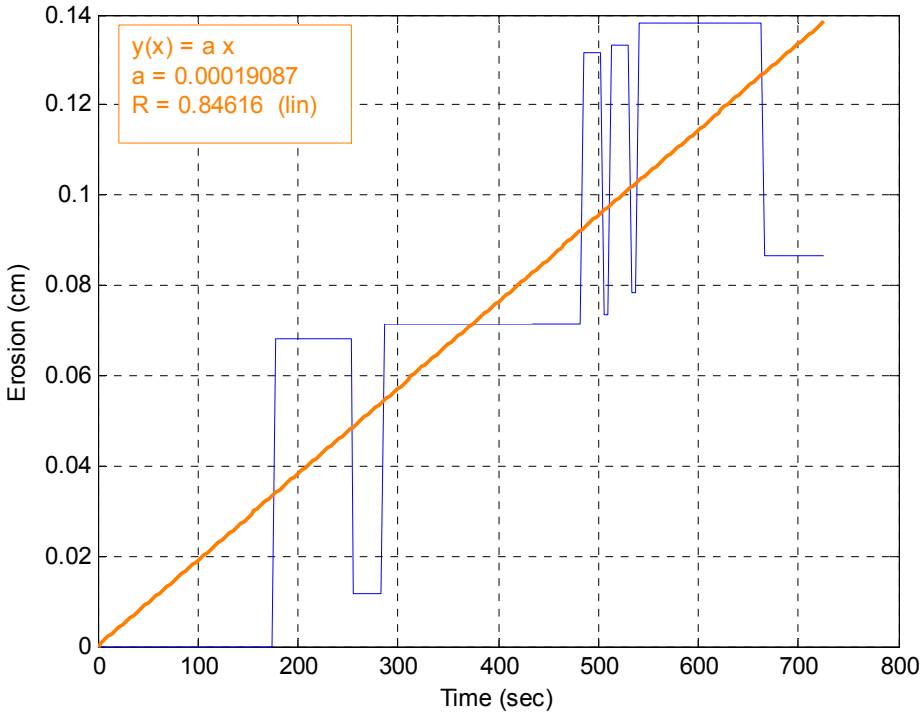

Figure B-16. Erosion versus time for specimen AS-UF1 at 23.07 Pa (data eliminated from erosion function due to suspected layering)

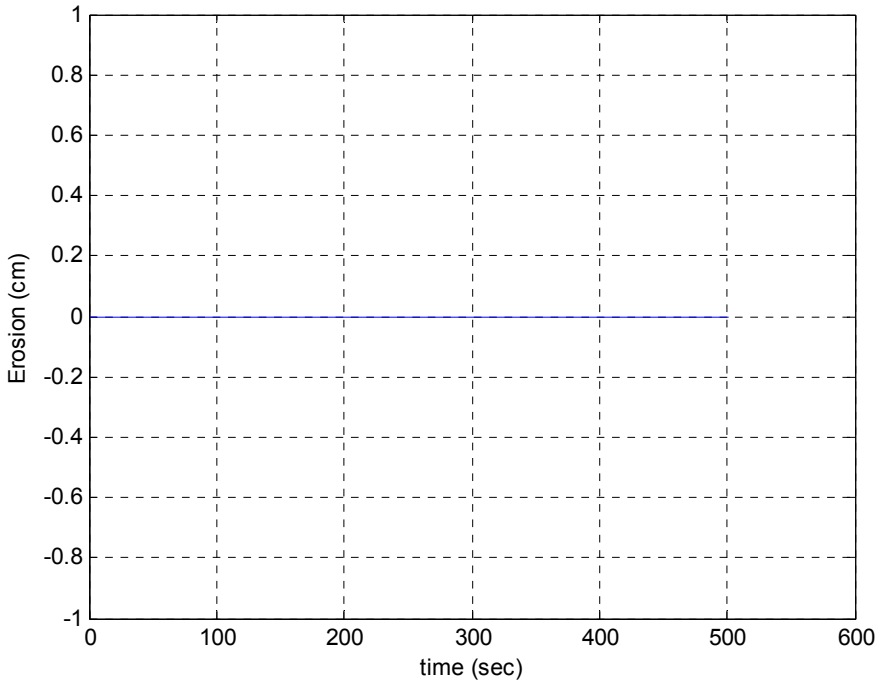

Figure B-17. Erosion versus time for specimen AS-UF1 at 20.56 Pa (data eliminated from erosion function due to suspected layering)

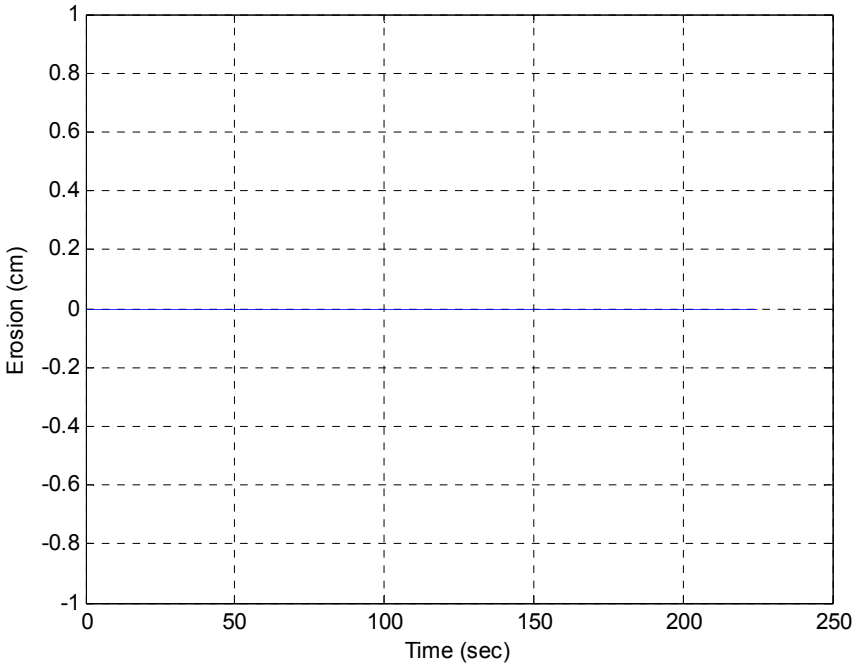

Figure B-18. Erosion versus time for specimen AS-UF1 at 27.12 Pa (data eliminated from erosion function due to suspected layering)

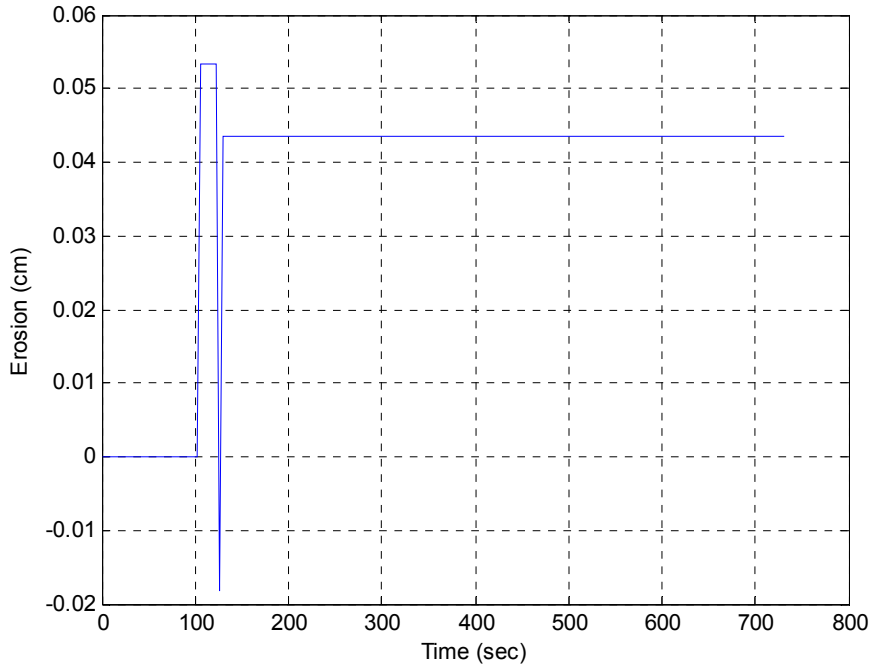

Figure B-19. Erosion versus time for specimen AS-UF1 at 24.38 Pa (data eliminated from erosion function due to suspected layering)

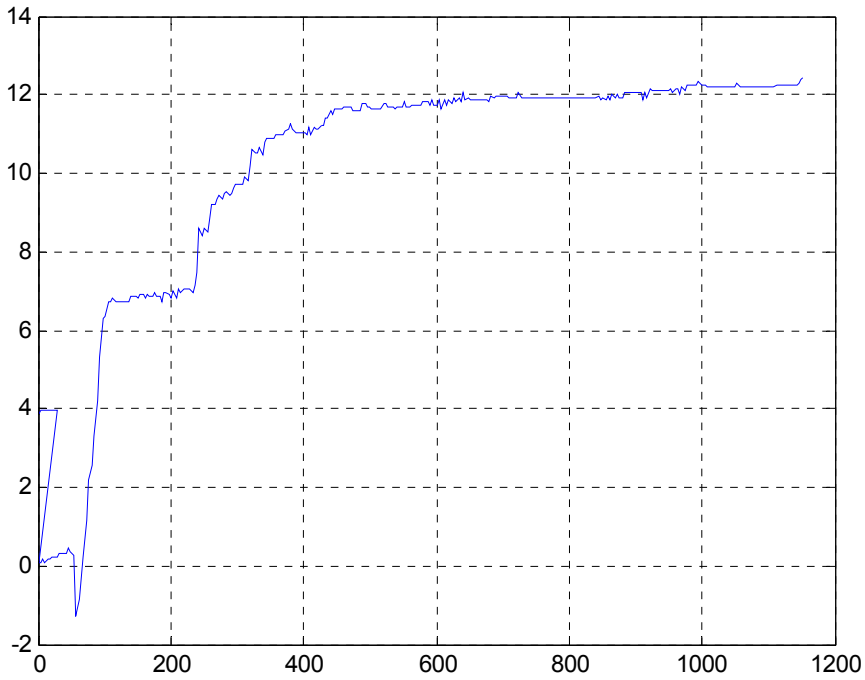

Figure B-20. Evidence of varied erosion rates (specimen AS-UF2 at 14.98 Pa)

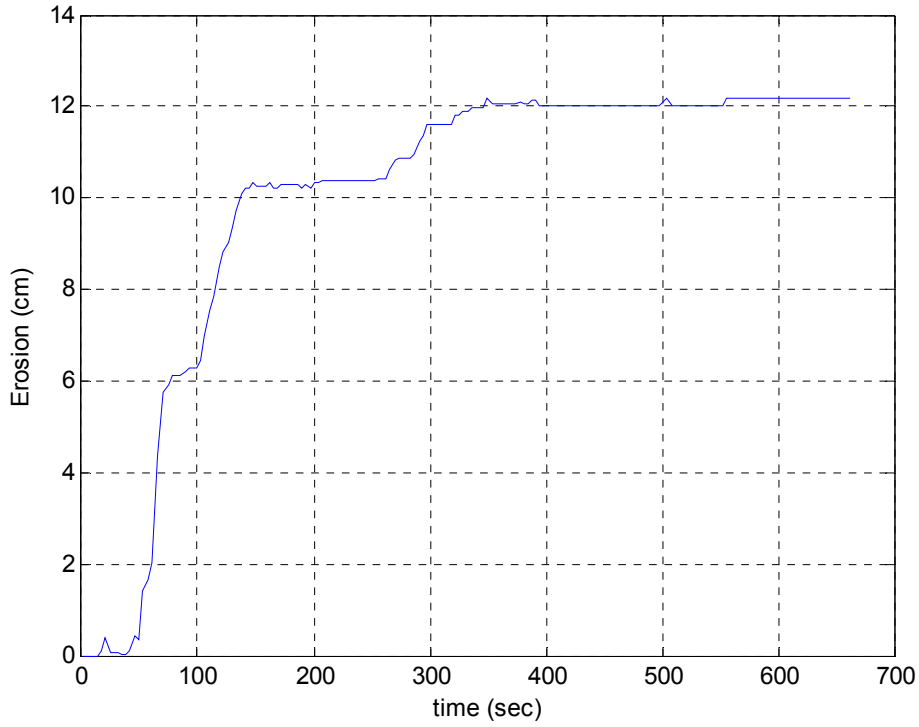

Figure B-21. More evidence of varied erosion rates (specimen AS-UF3 at 20.56 Pa)

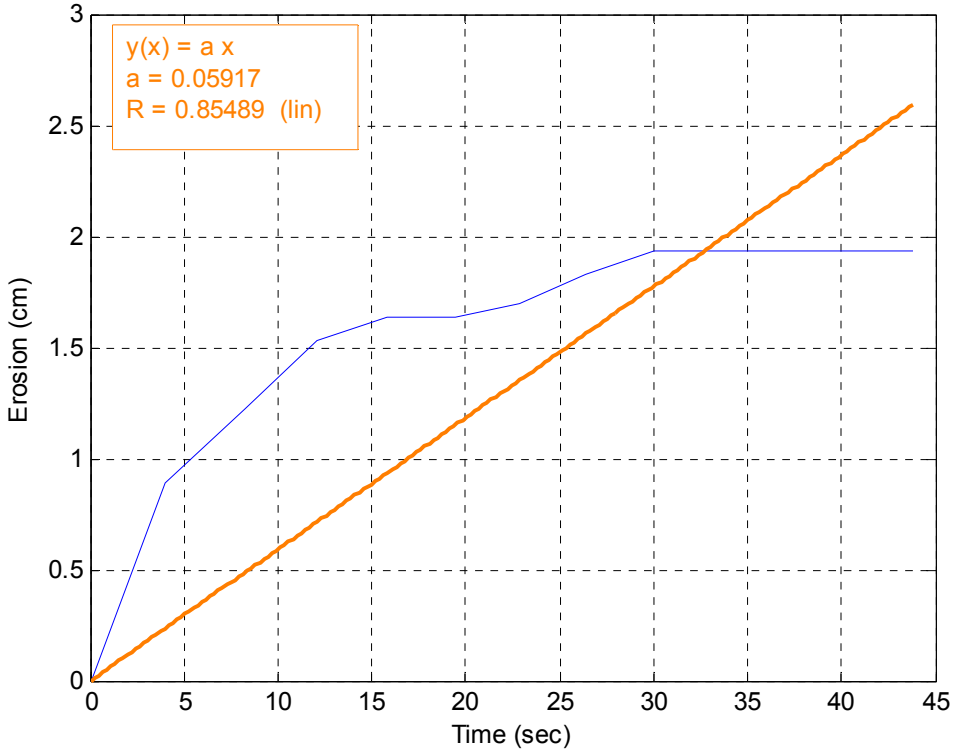

Figure B-22. Erosion versus time for specimen AS-UF4 at 6.72 Pa

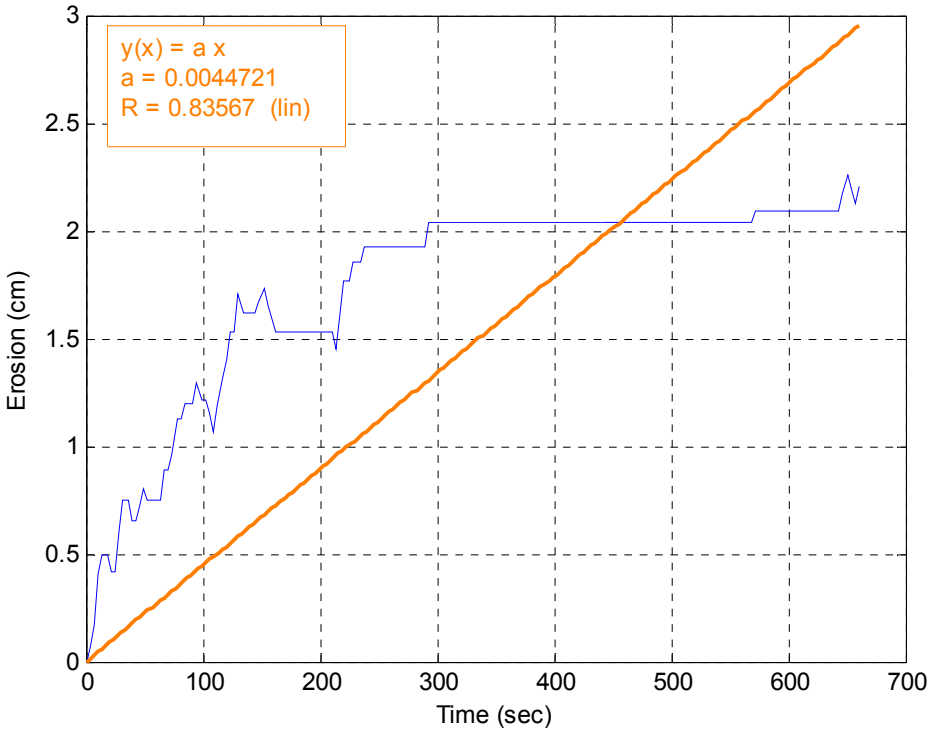

Figure B-23. Erosion versus time for specimen AS-UF4 at 10.37 Pa

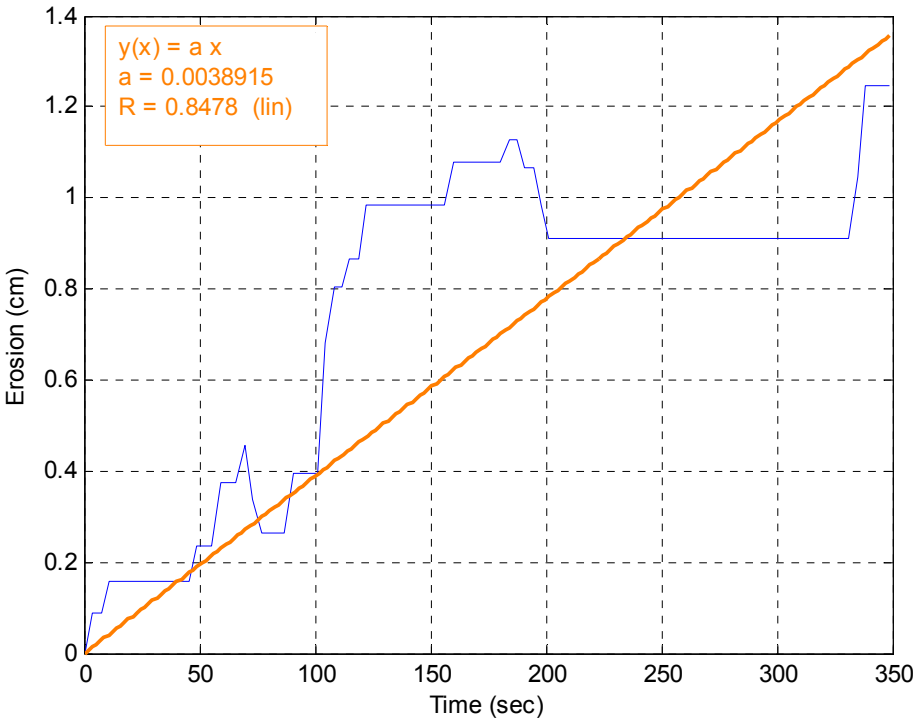

Figure B-24. Erosion versus time for specimen AS-UF4 at 14.98 Pa

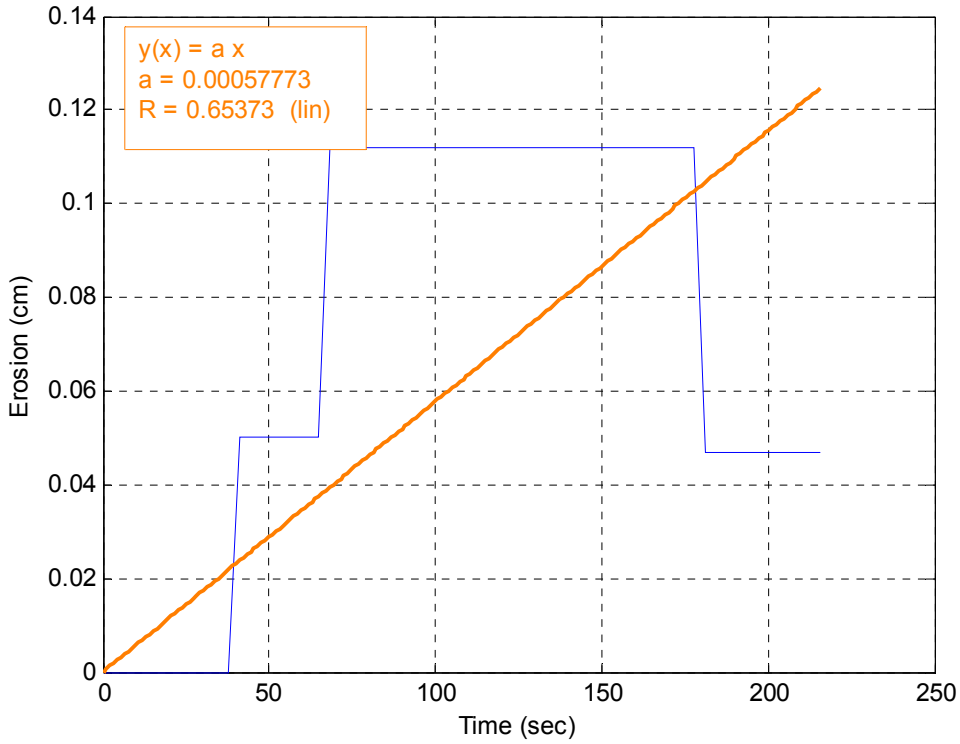

Figure B-25. Erosion versus time for specimen AS-UF4 at 20.56 Pa

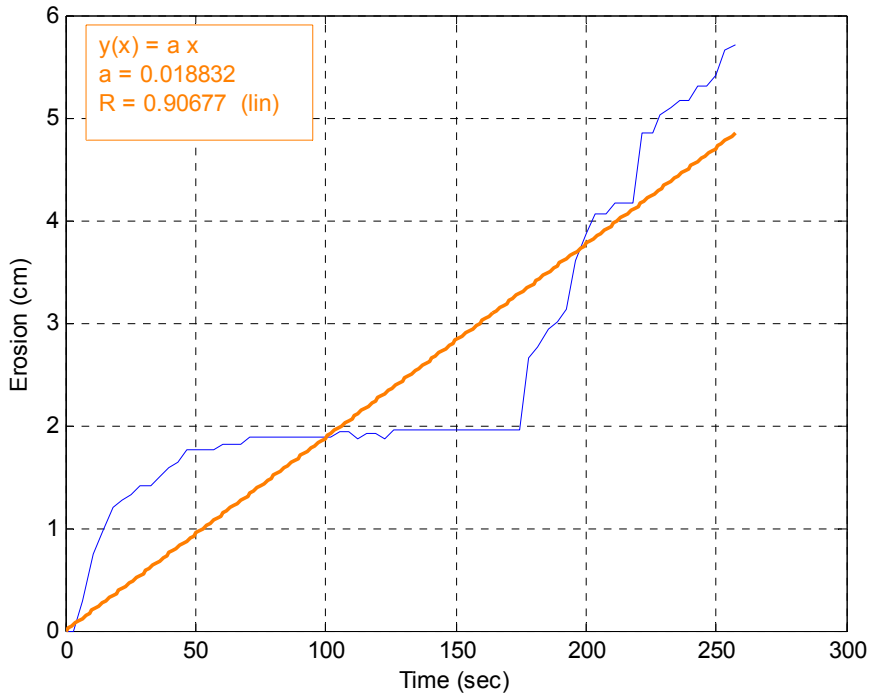

Figure B-26. Erosion versus time for specimen AS-UF4 at 16.02 Pa

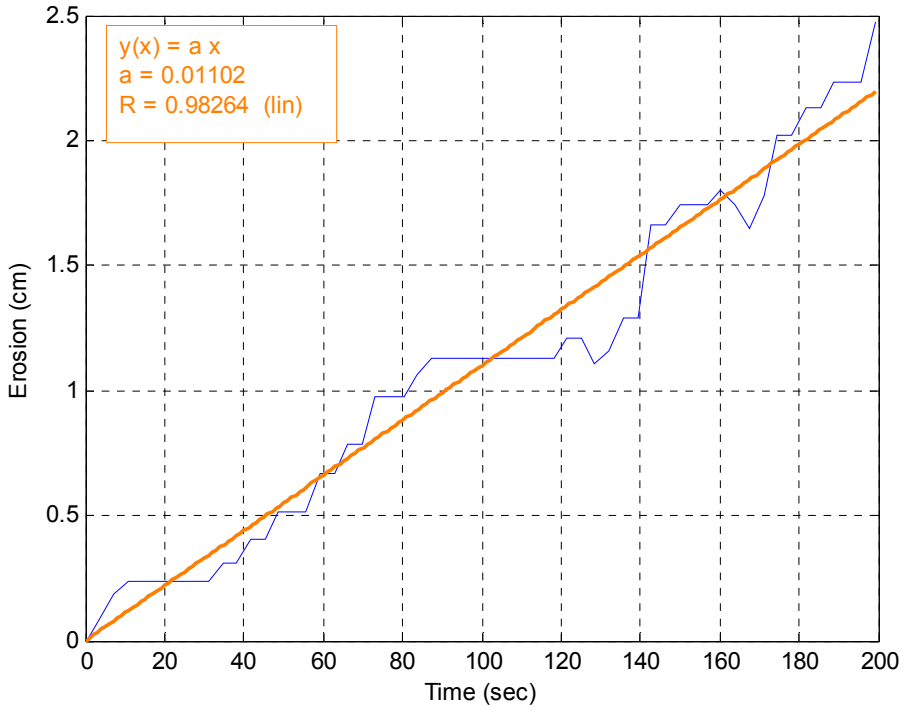

Figure B-27. Erosion versus time for specimen AS-UF4 at 13.98 Pa

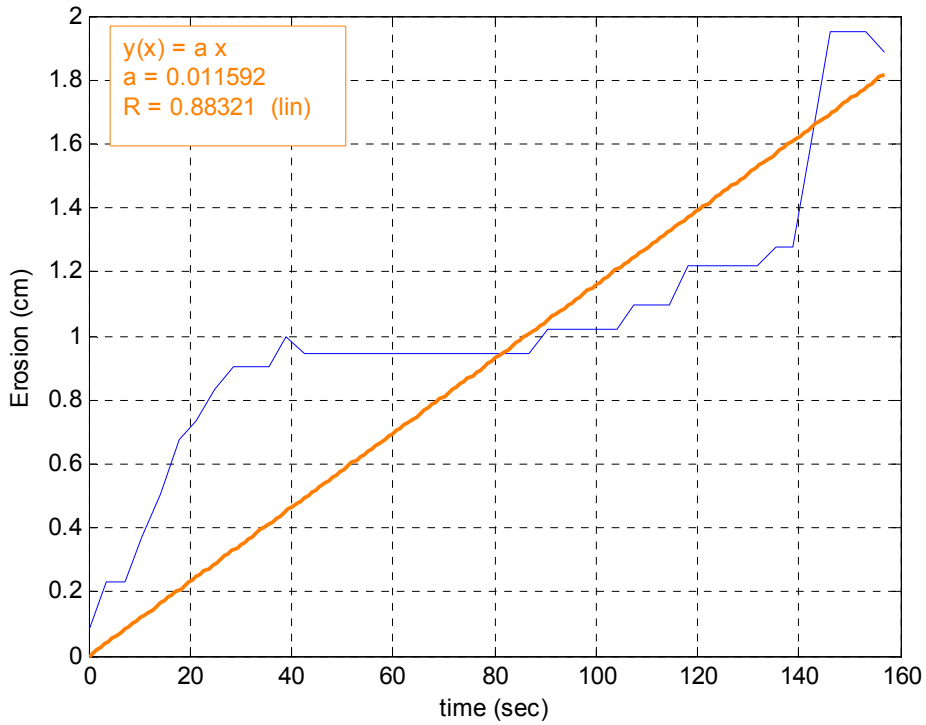

Figure B-28. Erosion versus time for specimen AS-UF4 at 10.37 Pa

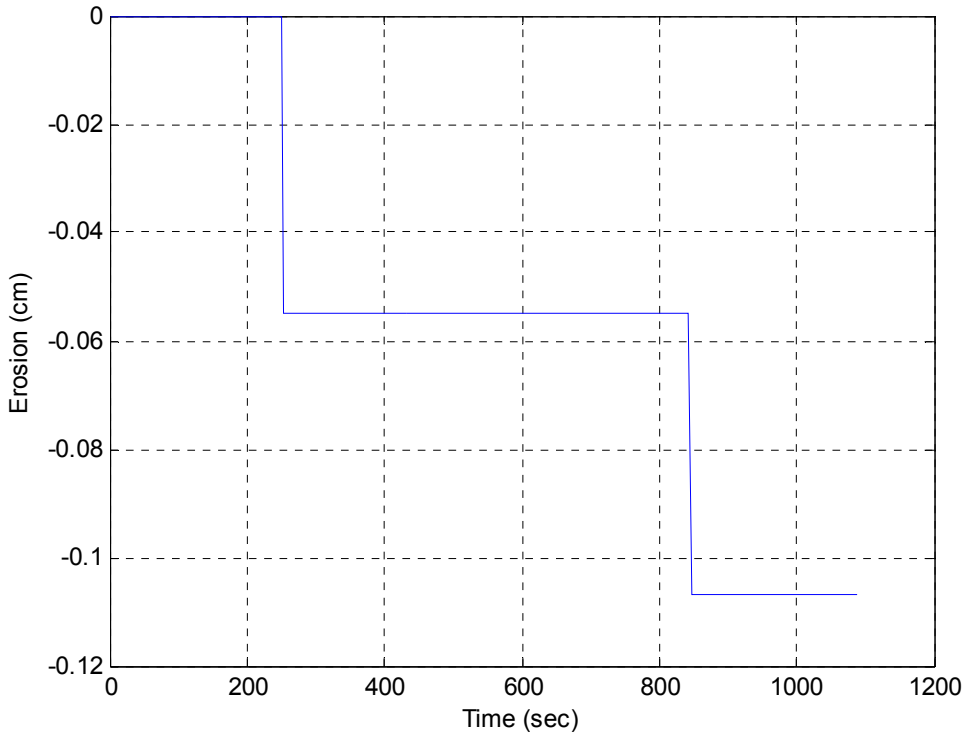

Figure B-29. Erosion versus time for specimen AS-100 #5 at 6.72 Pa

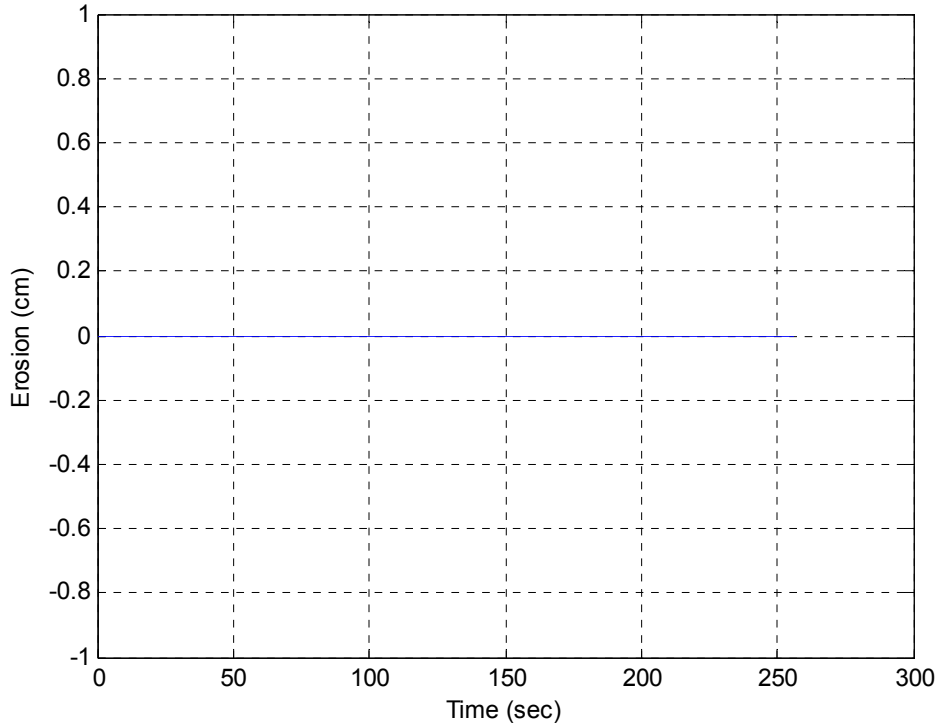

Figure B-30. Erosion versus time for specimen AS-100 #5 at 10.37 Pa

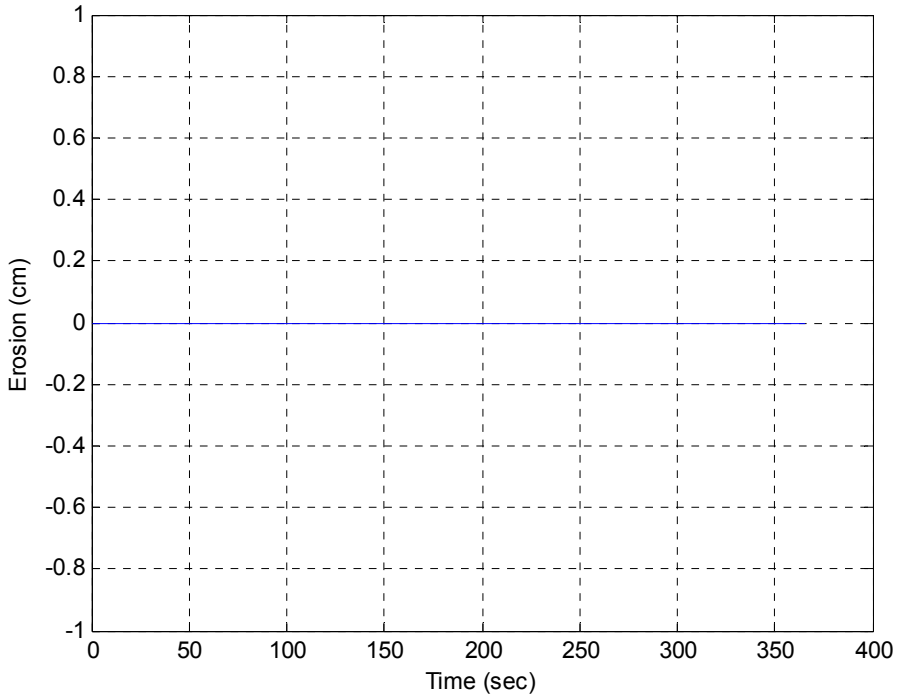

Figure B-31. Erosion versus time for specimen AS-100 #5 at 14.98 Pa

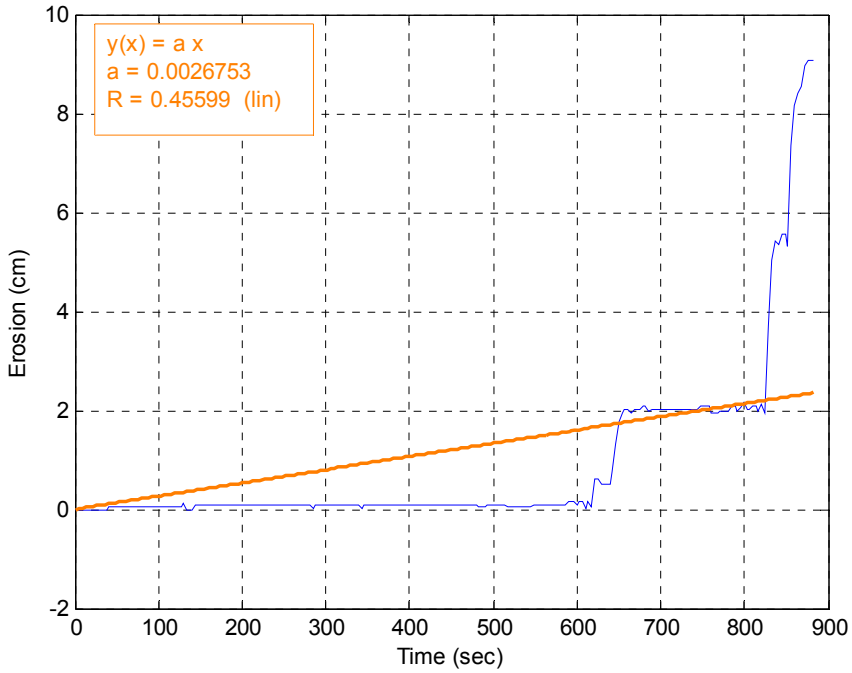

Figure B-32. Erosion versus time for specimen AS-100 #5 at 20.56 Pa

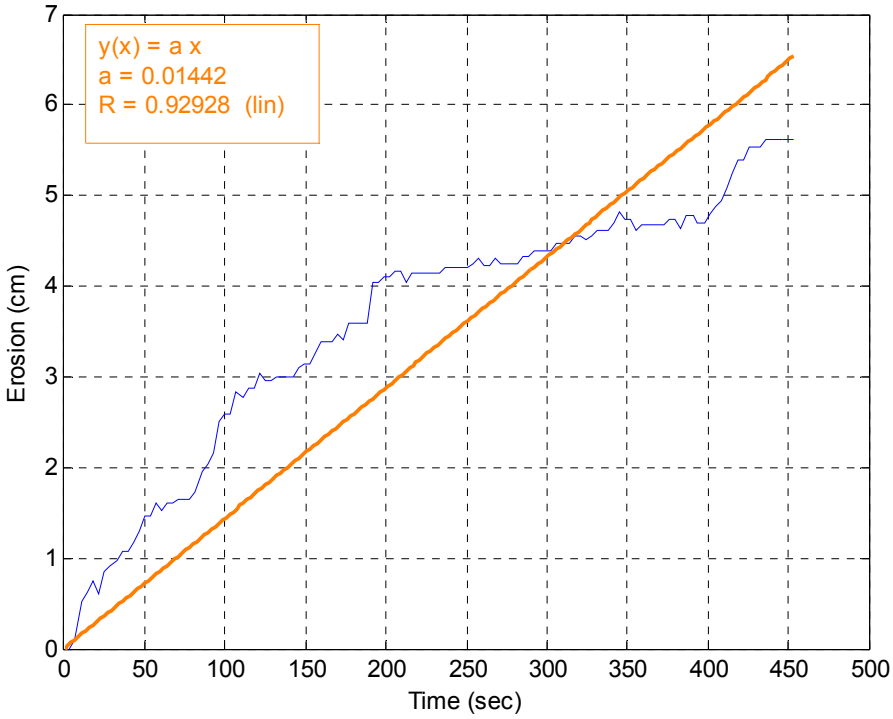

Figure B-33. Erosion versus time for specimen AS-100 #5 at 19.37 Pa

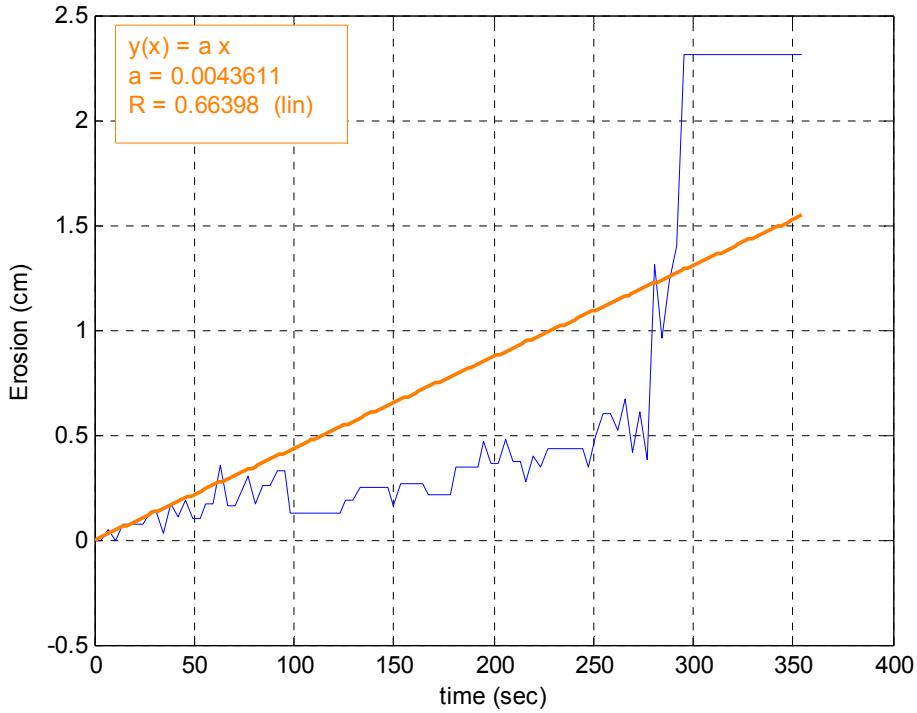

Figure B-34. Erosion versus time for specimen AS-100 #5 at 18.21 Pa

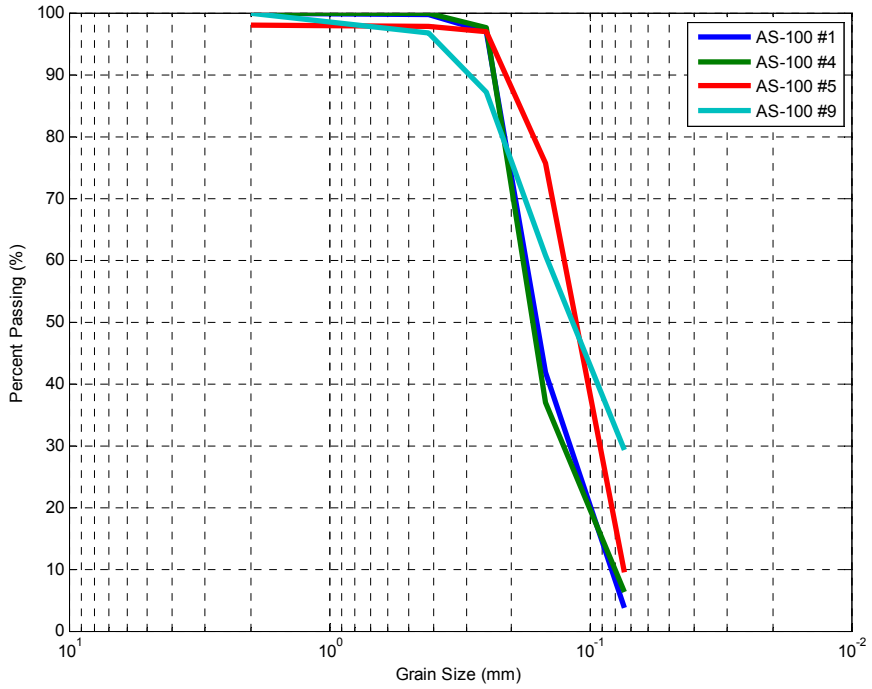

Figure B-35. Grain size distributions for Anderson Street specimens

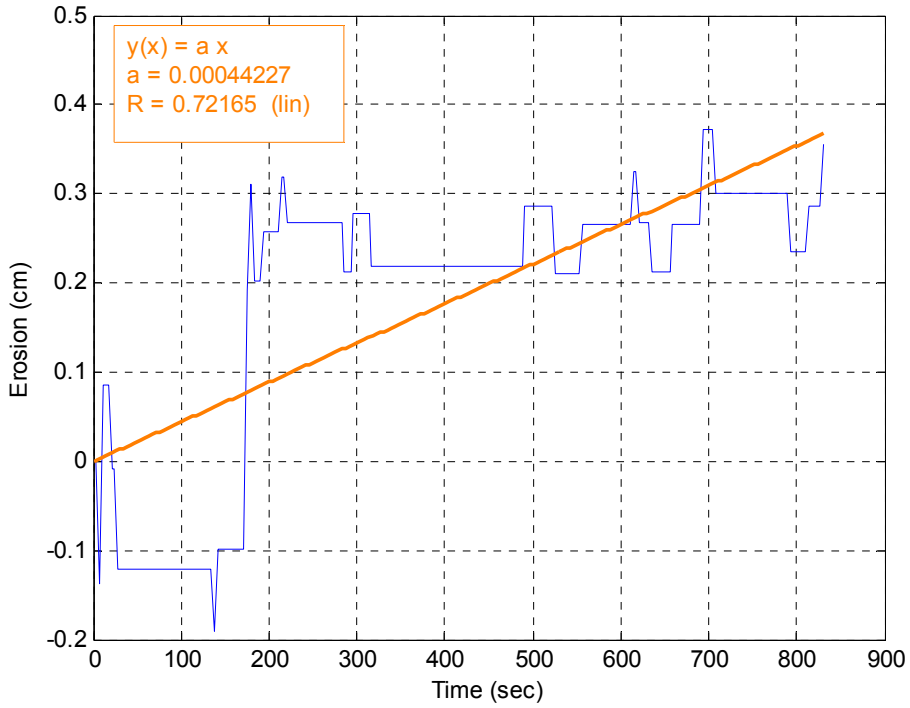

Figure B-36. Erosion versus time for specimen RR B-1E at 10.37 Pa

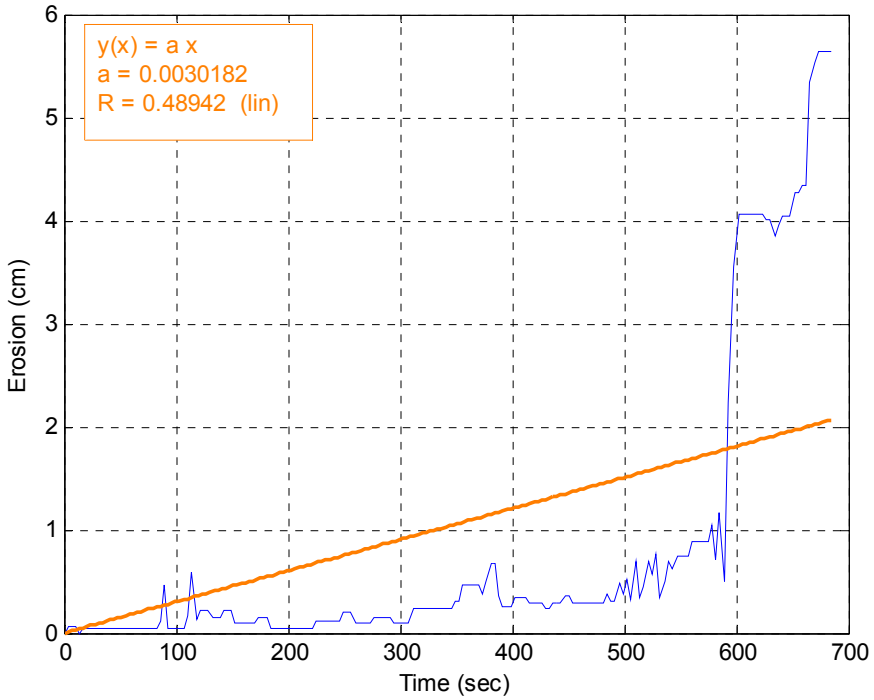

Figure B-37. Erosion versus time for specimen RR B-1E at 14.98 Pa

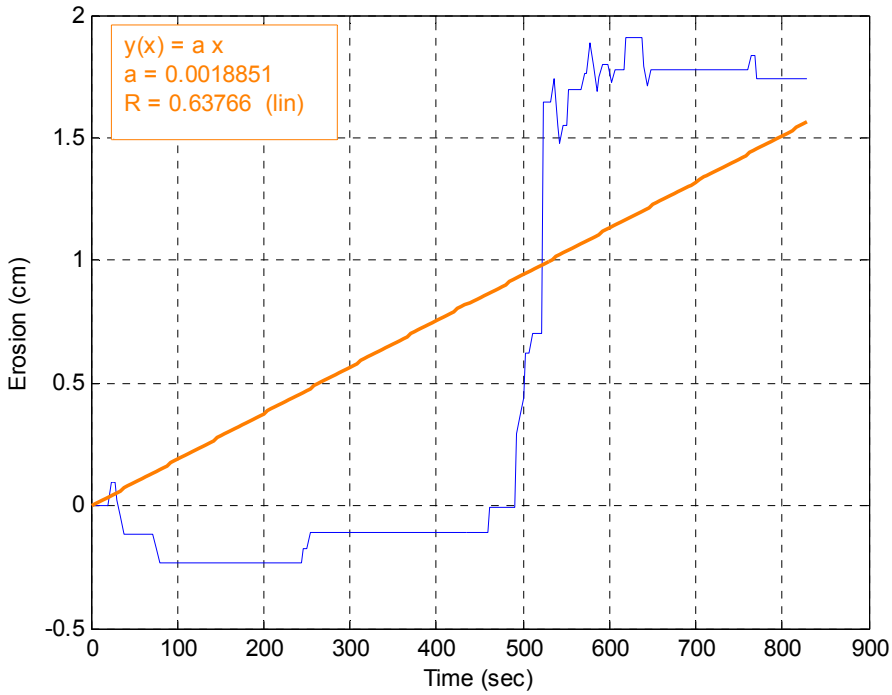

Figure B-38. Erosion versus time for specimen RR B-1E at 13.02 Pa

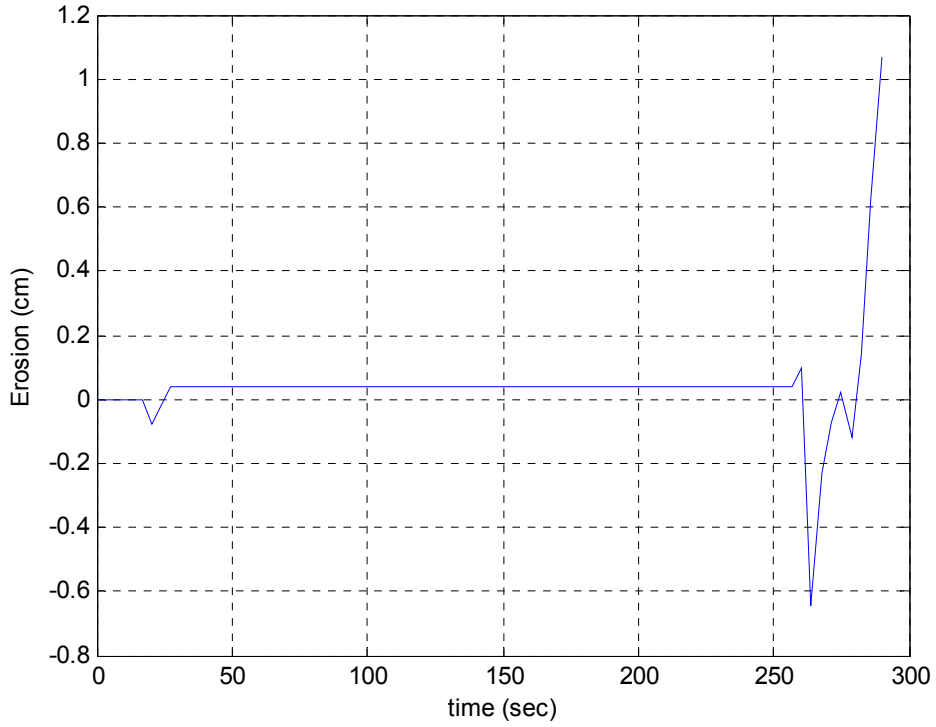

Figure B-39. Erosion versus time for specimen RR B-1E at 13.98 Pa

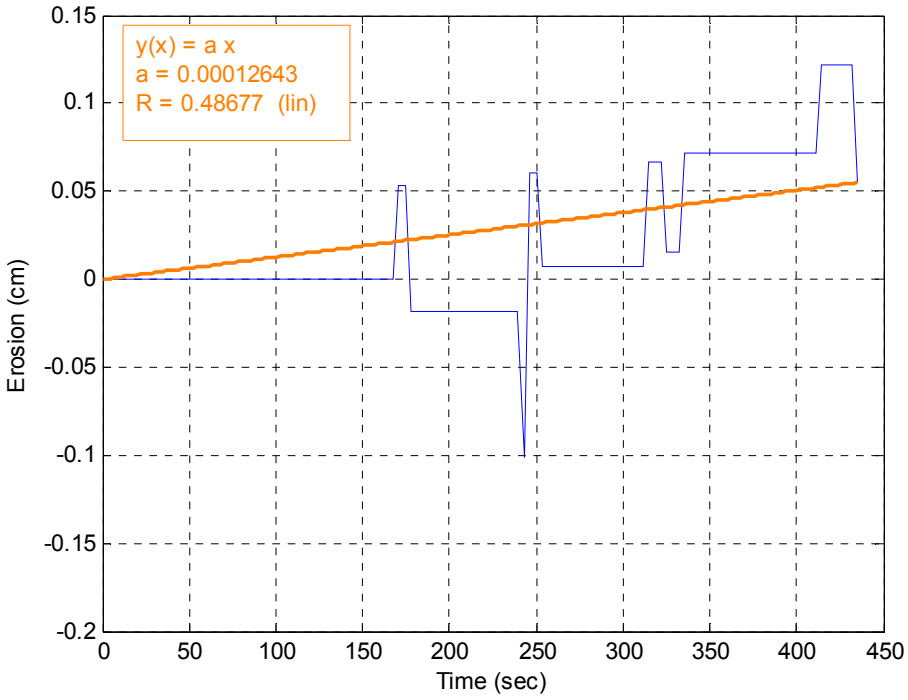

Figure B-40. Erosion versus time for specimen RR B3 at 6.72 Pa

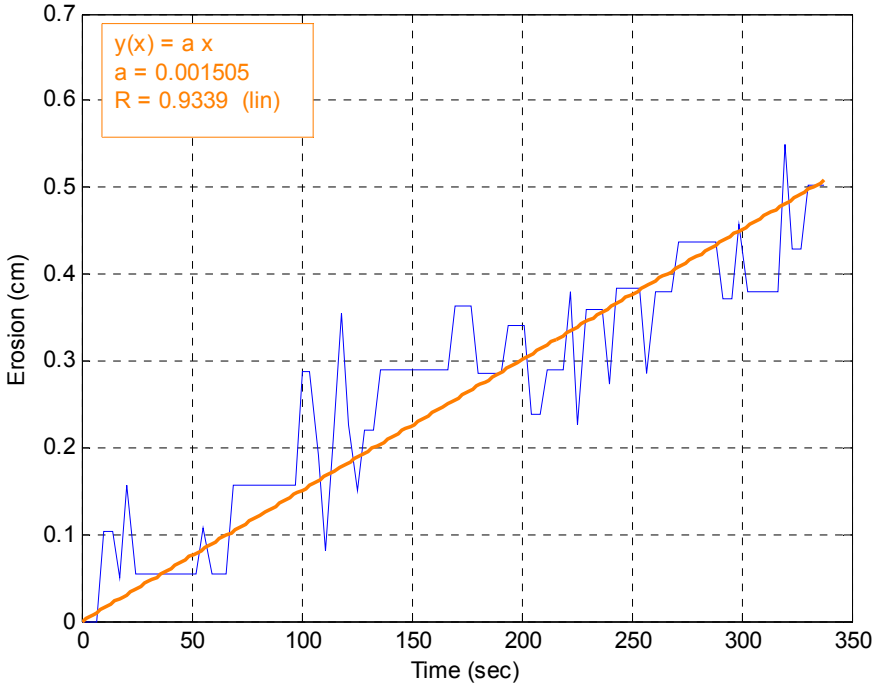

Figure B-41. Erosion versus time for specimen RR B3 at 10.37 Pa

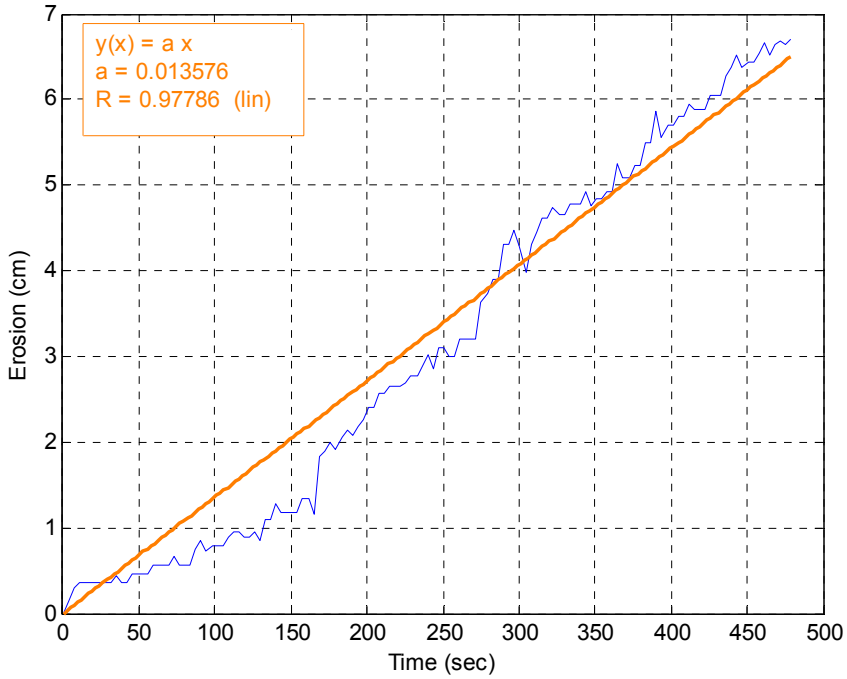

Figure B-42. Erosion versus time for specimen RR B3 at 14.98 Pa

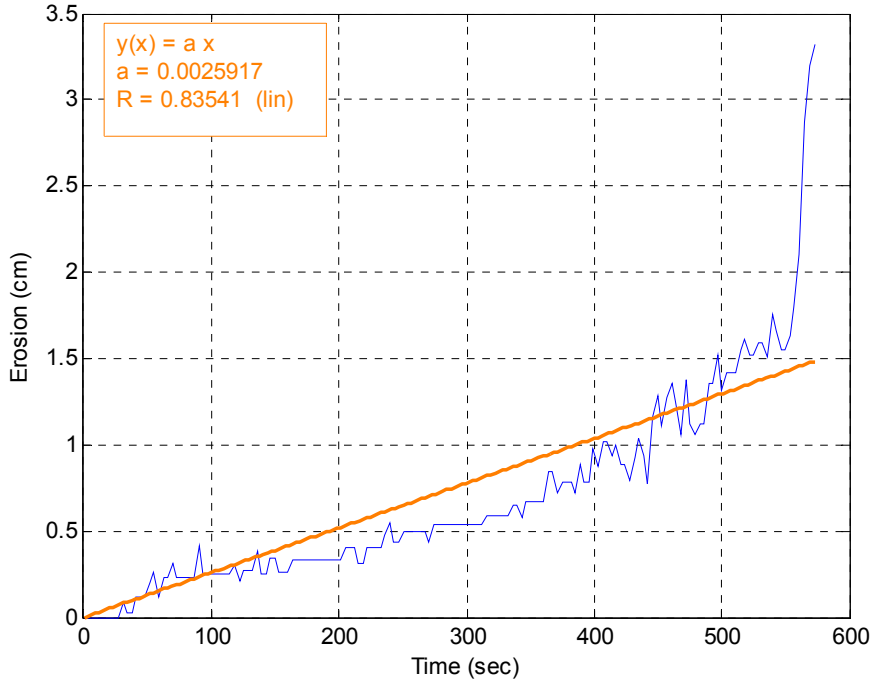

Figure B-43. Erosion versus time for specimen RR B3 at 13.02 Pa

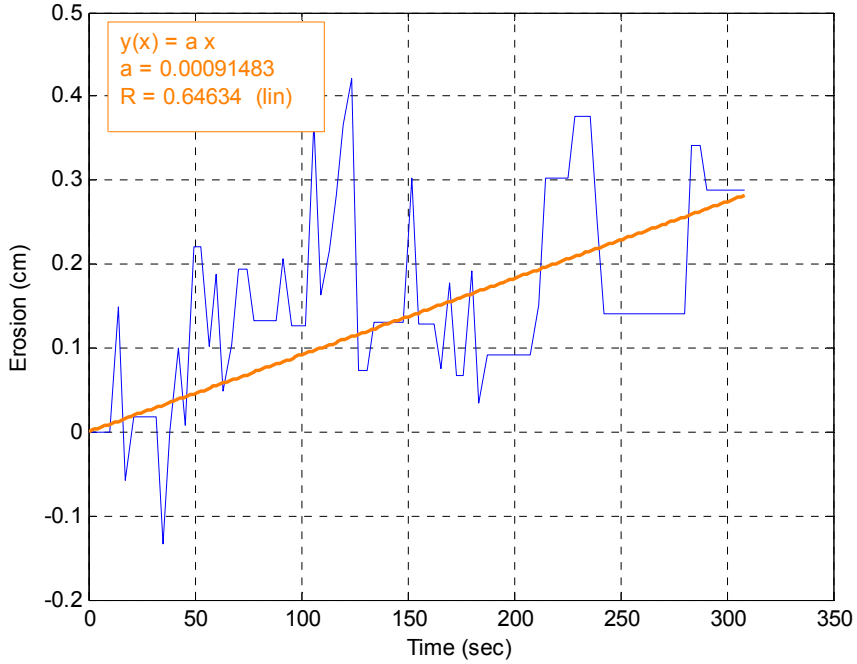

Figure B-44. Erosion versus time for specimen RR B3 at 13.02 Pa

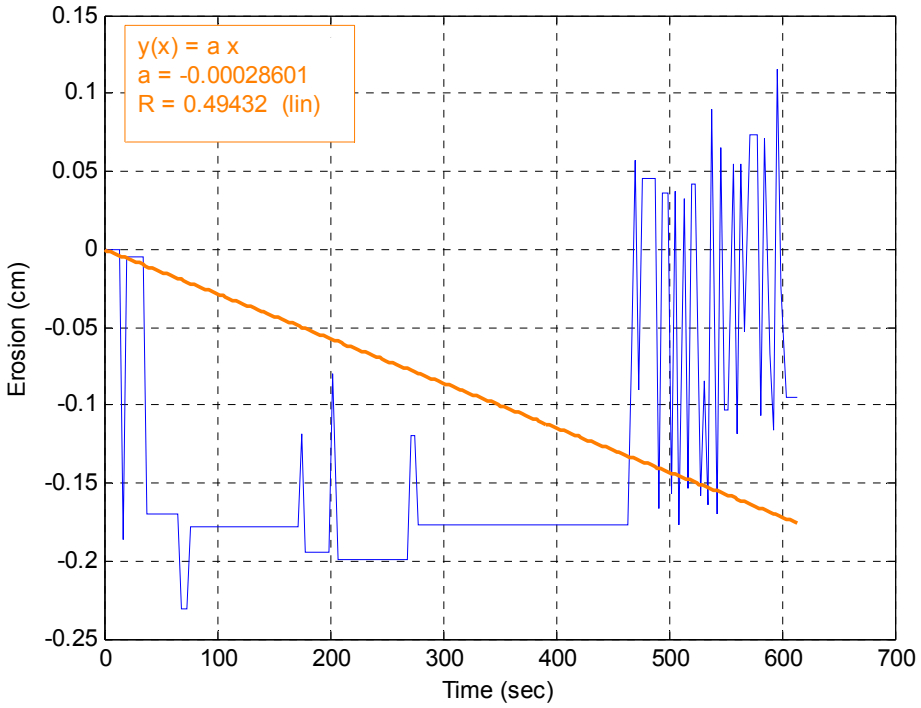

Figure B-45. Erosion versus time for specimen RR B3 at 13.98 Pa

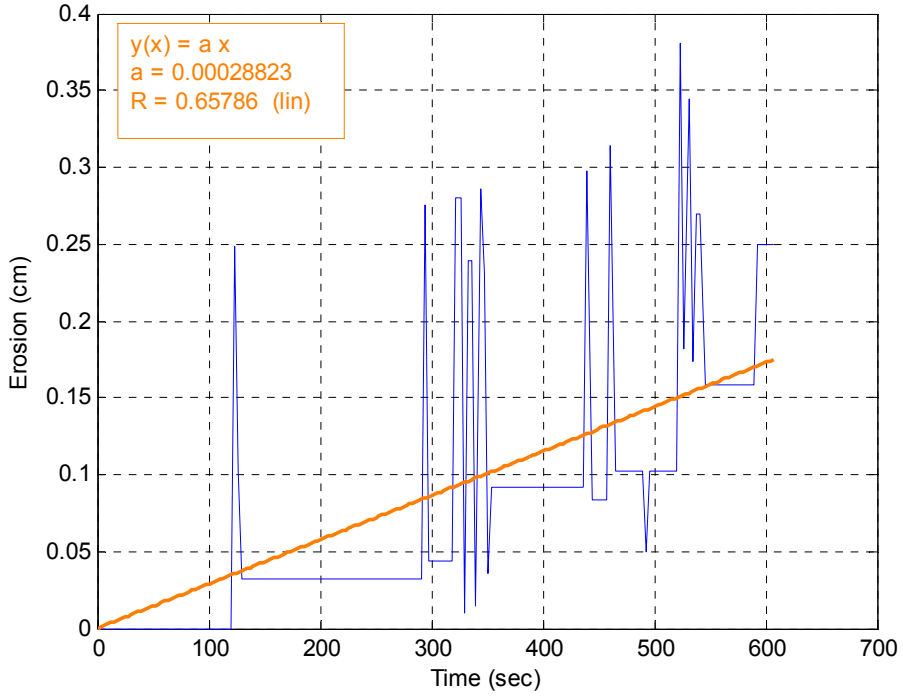

Figure B-46. Erosion versus time for specimen RR B3 at 14.98 Pa

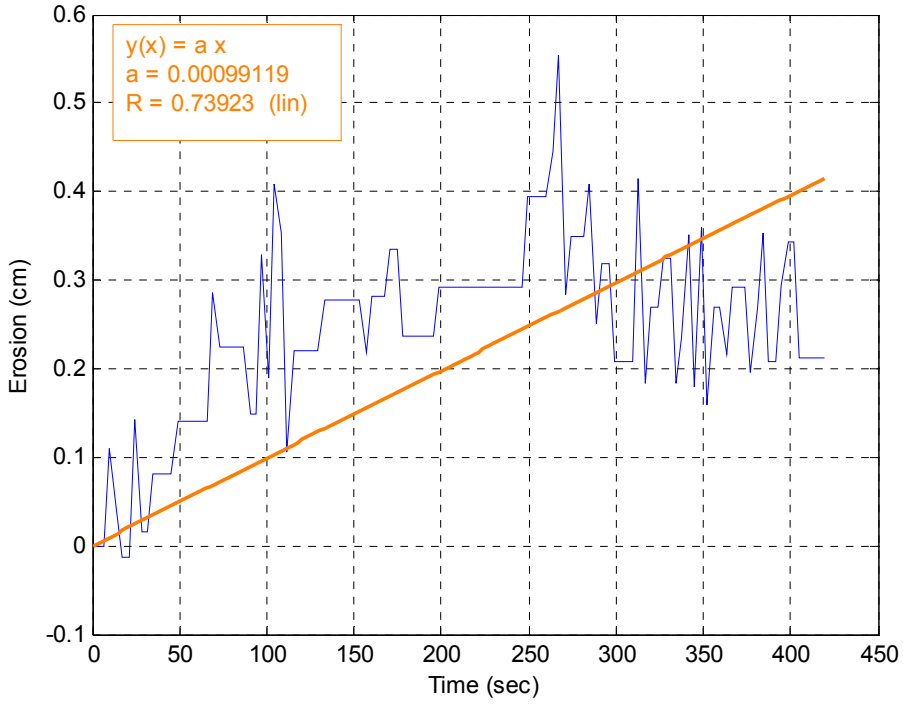

Figure B-47. Erosion versus time for specimen RR B3 at 20.56 Pa

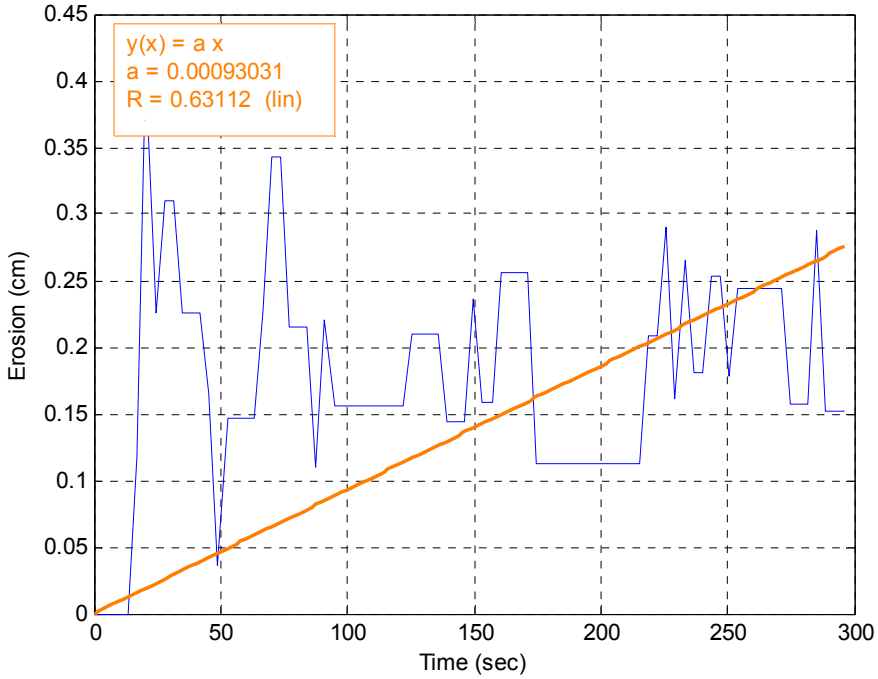

Figure B-48. Erosion versus time for specimen RR B3 at 27.12 Pa

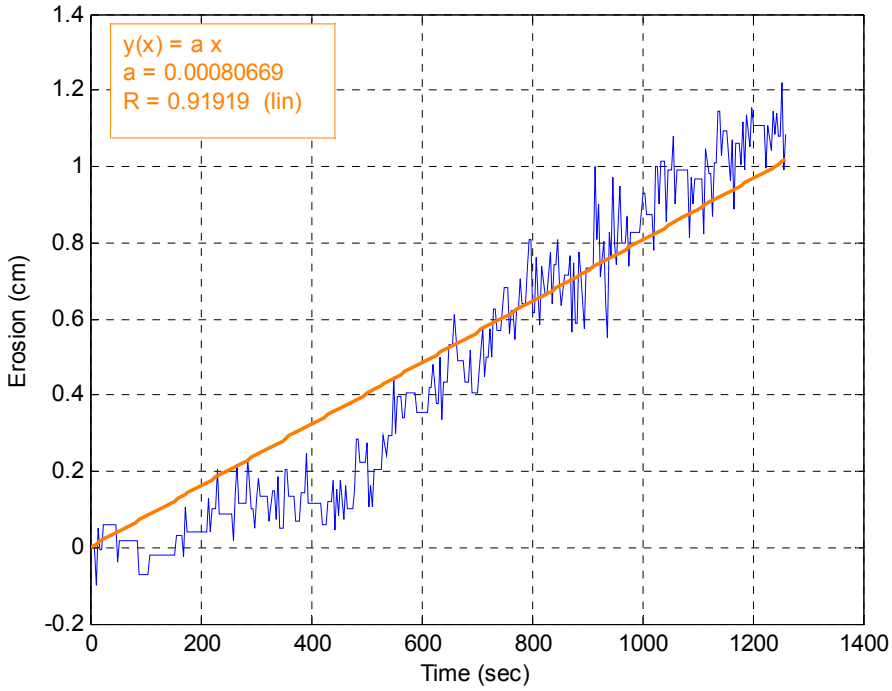

Figure B-49. Erosion versus time for specimen RR B3 at 34.64 Pa

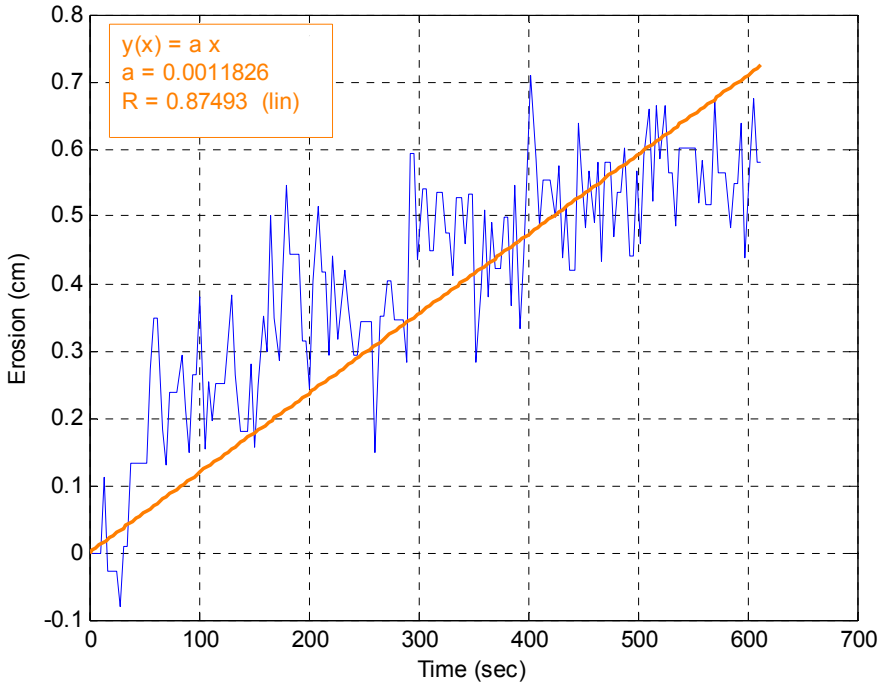

Figure B-50. Erosion versus time for specimen RR B3 at 43.13 Pa

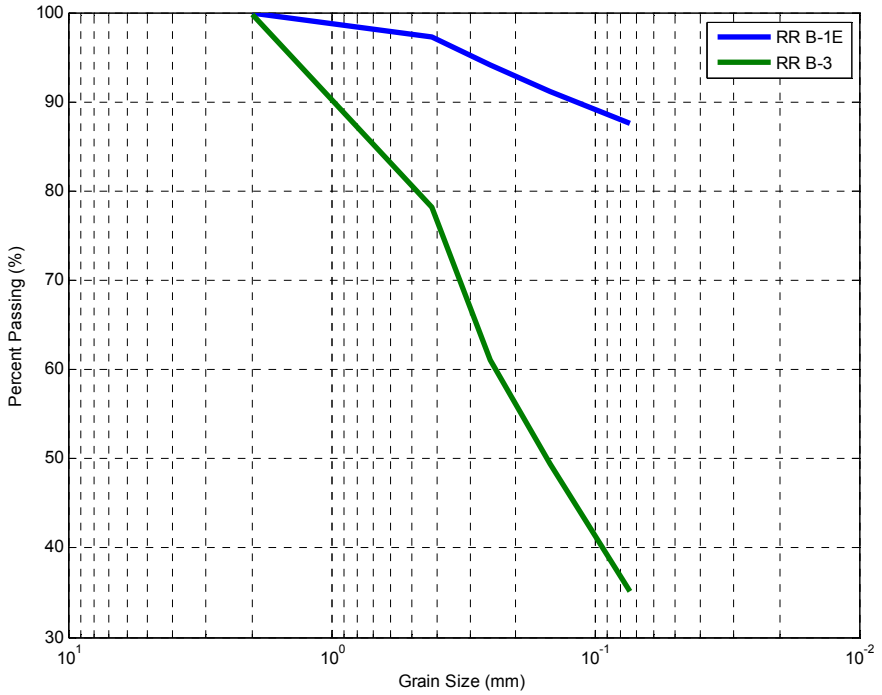

Figure B-51. Grain size distributions for River Road over Gum Creek specimens

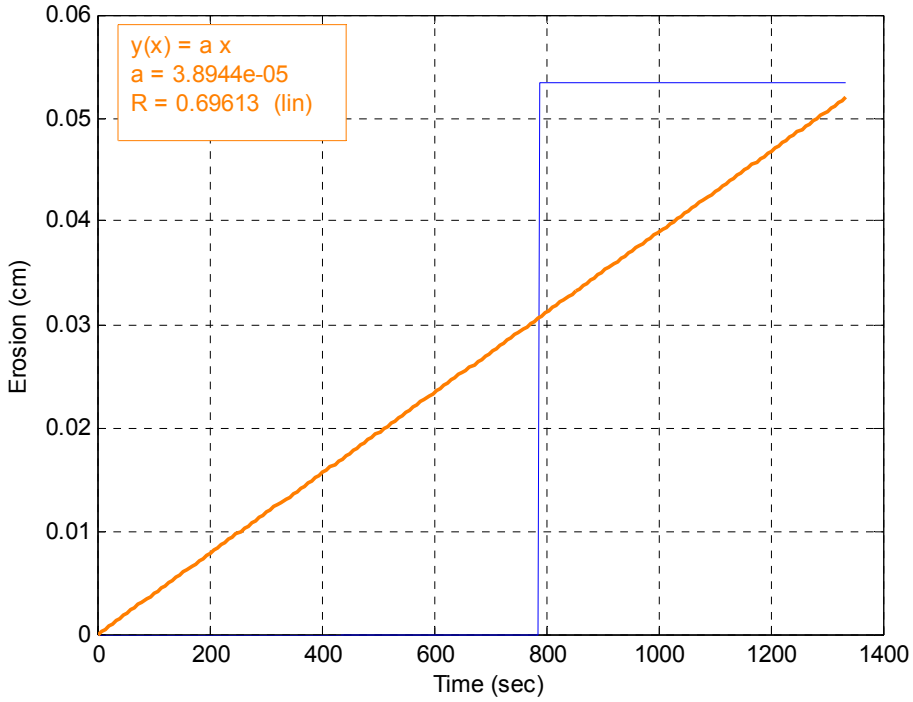

Figure B-52. Erosion versus time for specimen D-5 S-2 at 6.72 Pa

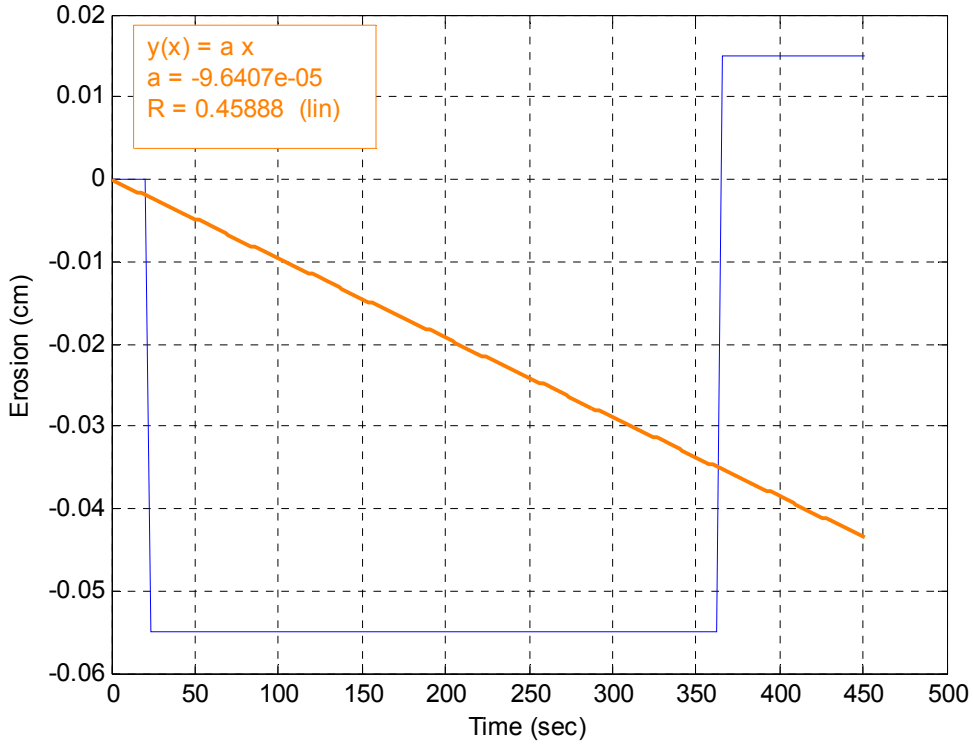

Figure B-53. Erosion versus time for specimen D-5 S-2 at 14.98 Pa

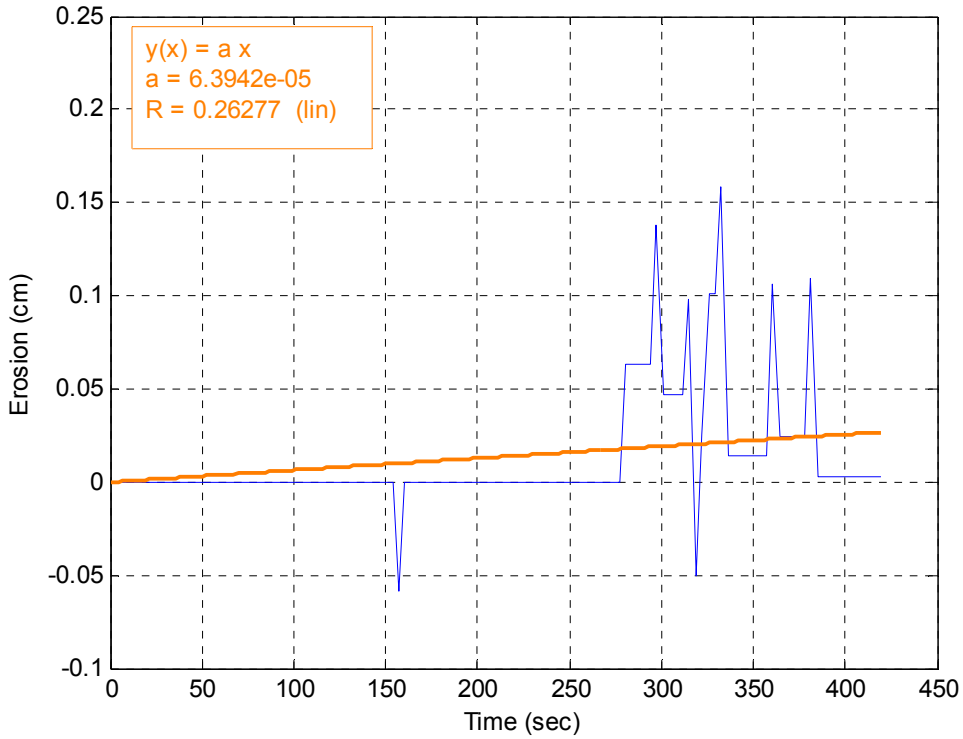

Figure B-54. Erosion versus time for specimen D-5 S-2 at 20.56 Pa

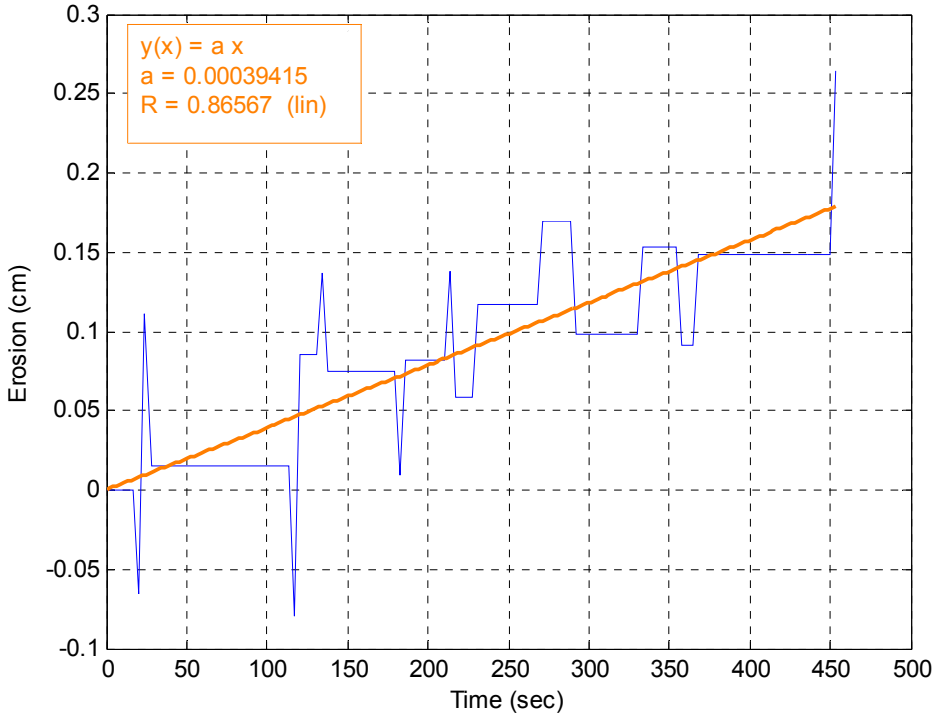

Figure B-55. Erosion versus time for specimen D-5 S-2 at 27.12 Pa

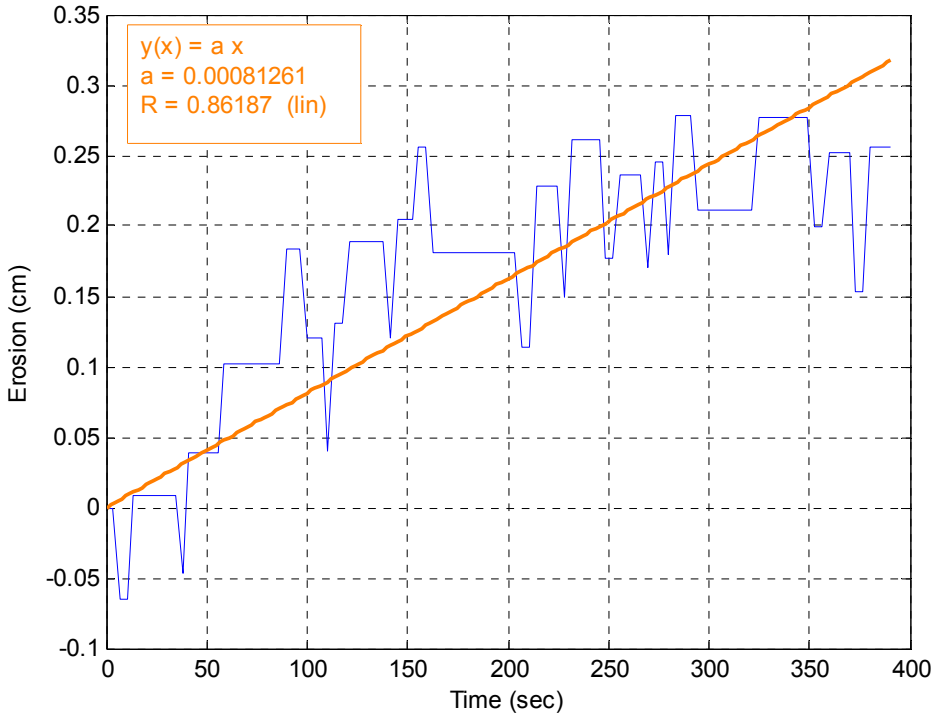

Figure B-56. Erosion versus time for specimen D-5 S-2 at 34.64 Pa

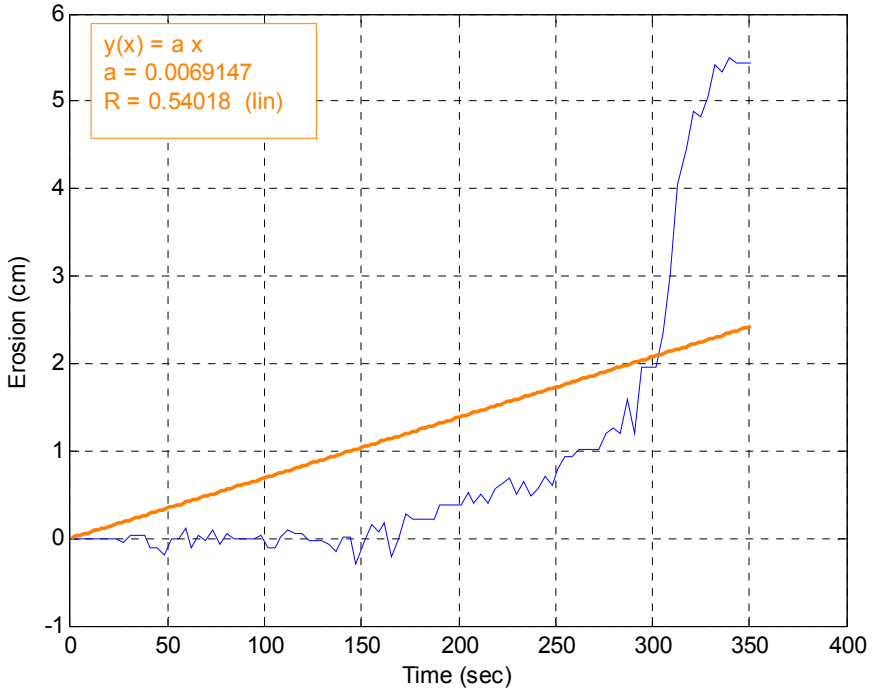

Figure B-57. Erosion versus time for specimen D-5 S-2 at 43.13 Pa

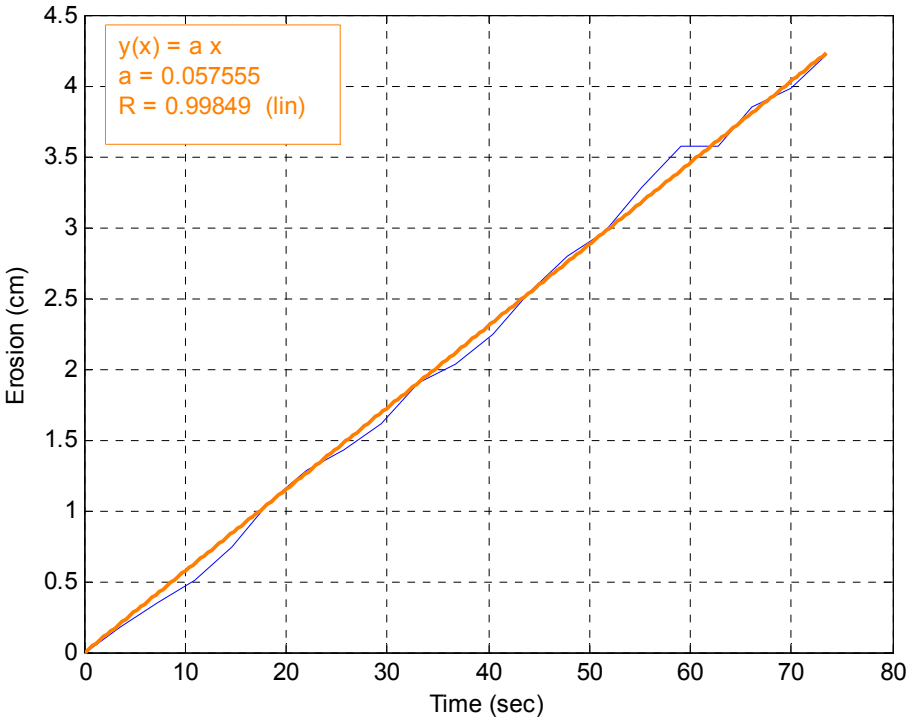

Figure B-58. Erosion versus time for specimen D-5 S-2 at 39.62 Pa

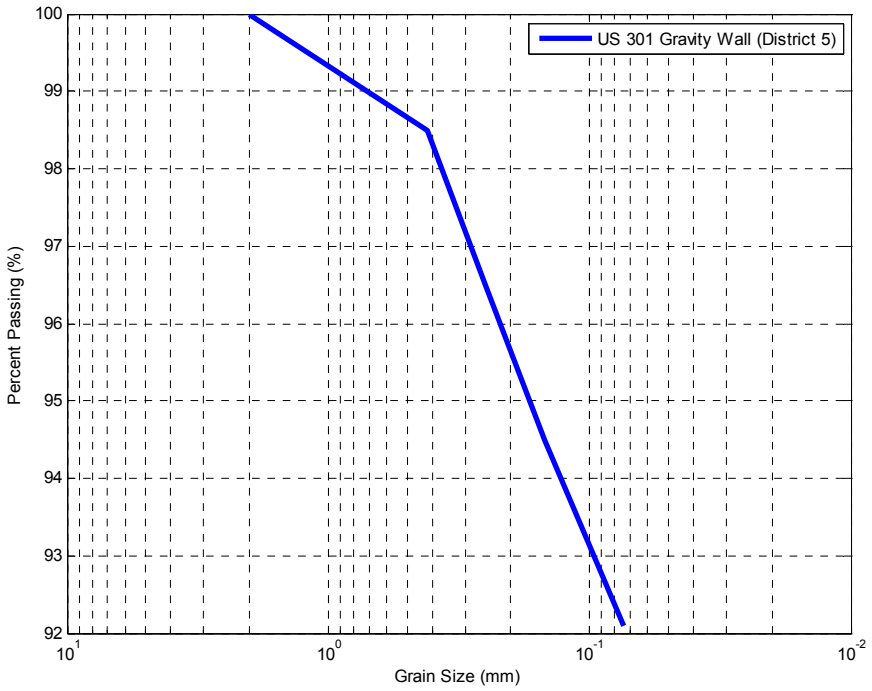

Figure B-59. Grain size distribution for D-5 (US 301) specimen

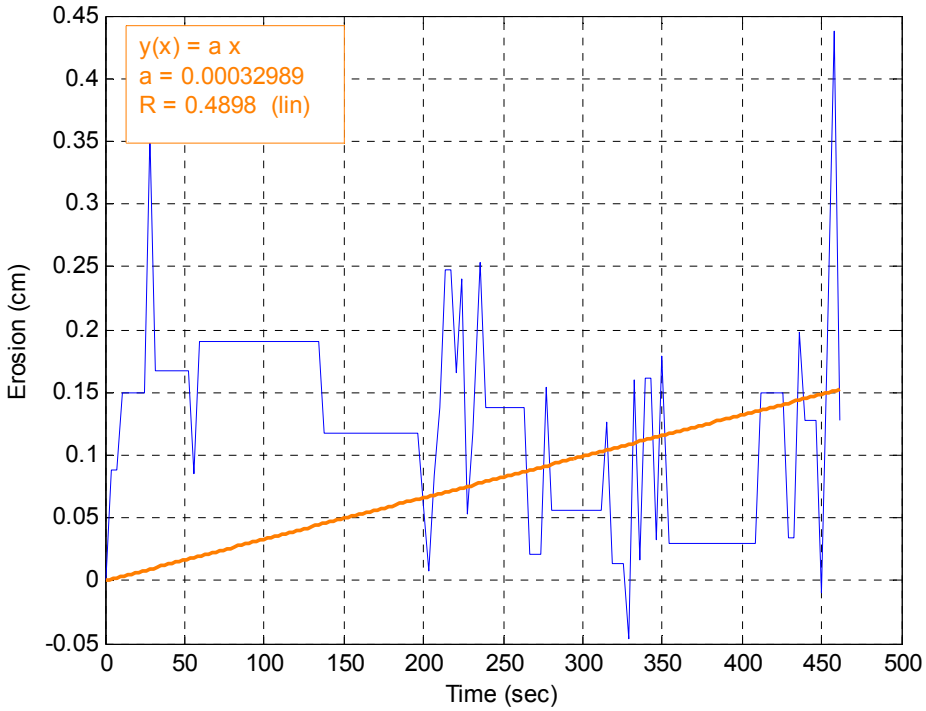

Figure B-60. Erosion versus time for specimen JCB 12'-14' at 6.72 Pa

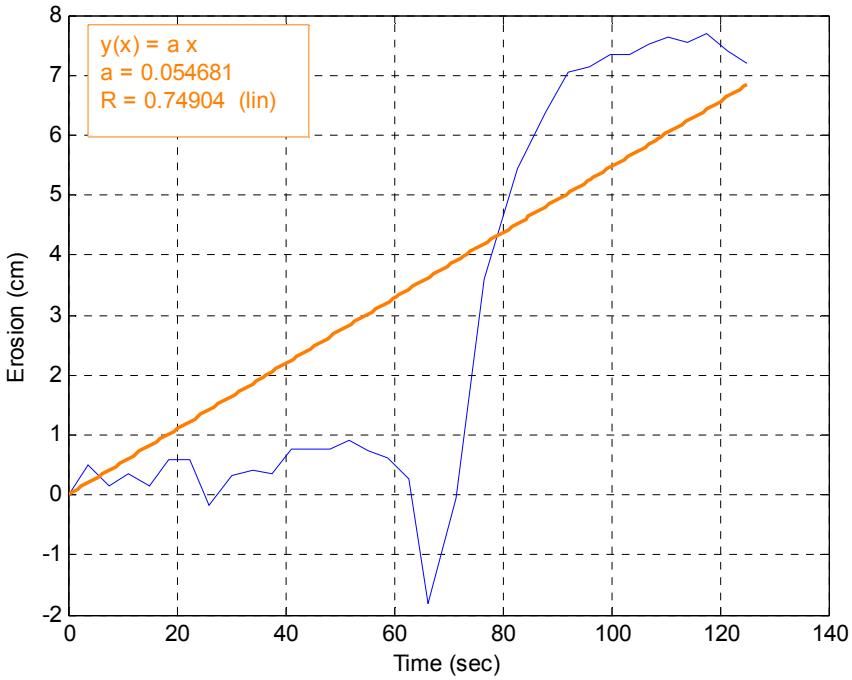

Figure B-61. Erosion versus time for specimen JCB 12'-14' at 10.37 Pa

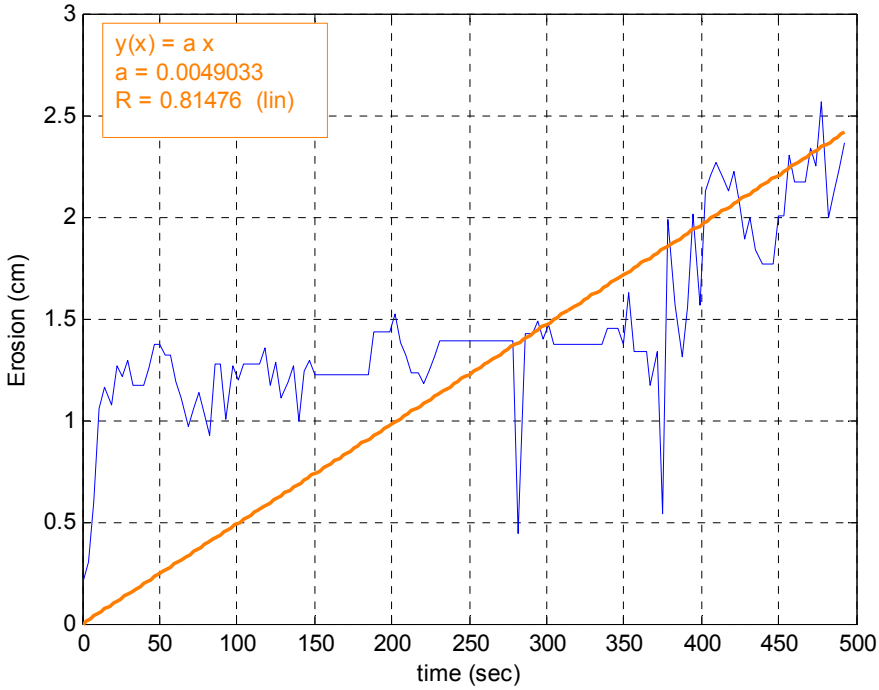

Figure B-62. Erosion versus time for specimen JCB 12'-14' at 7.37 Pa

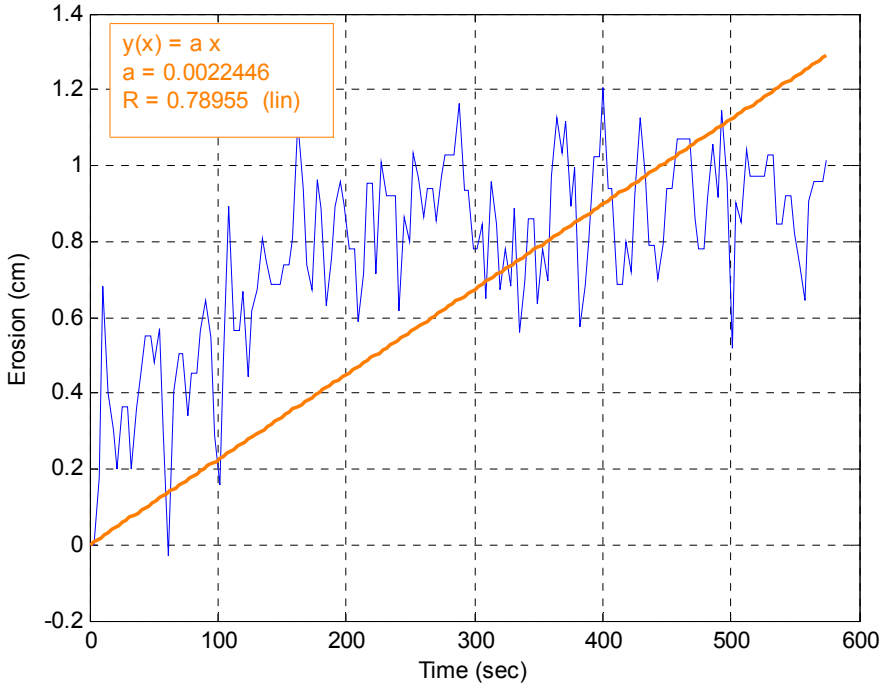

Figure B-63. Erosion versus time for specimen JCB 12'-14' at 8.06 Pa

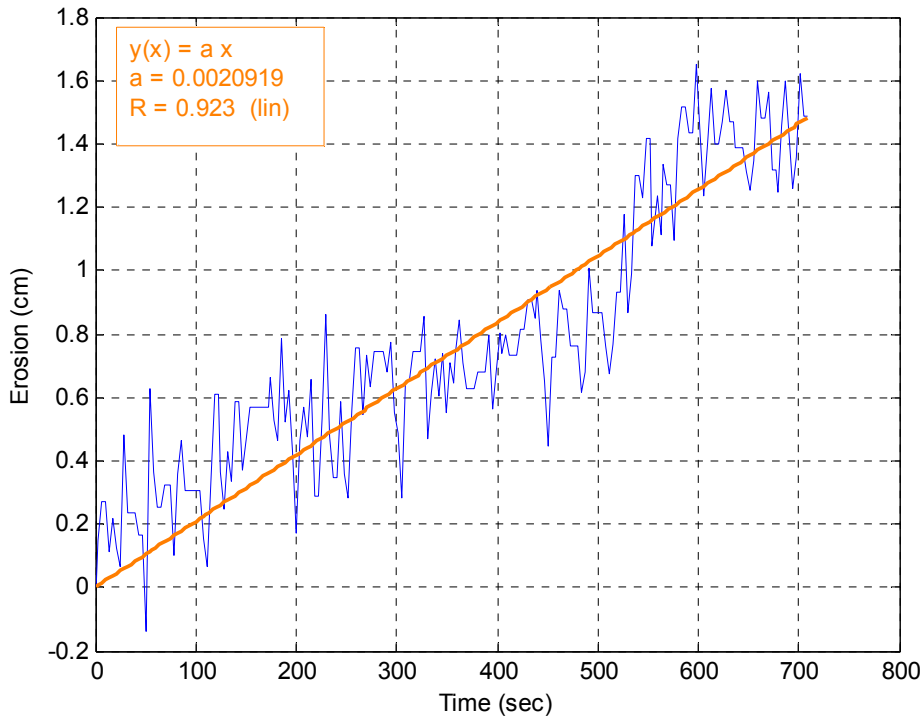

Figure B-64. Erosion versus time for specimen JCB 12'-14' at 8.79 Pa

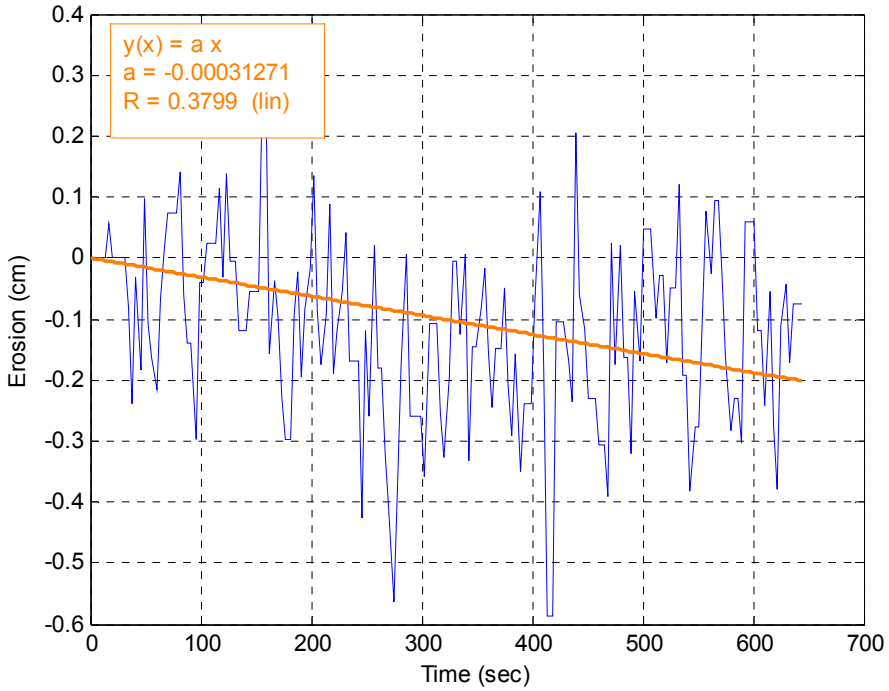

Figure B-65. Erosion versus time for specimen JCB 12'-14' at 9.56 Pa

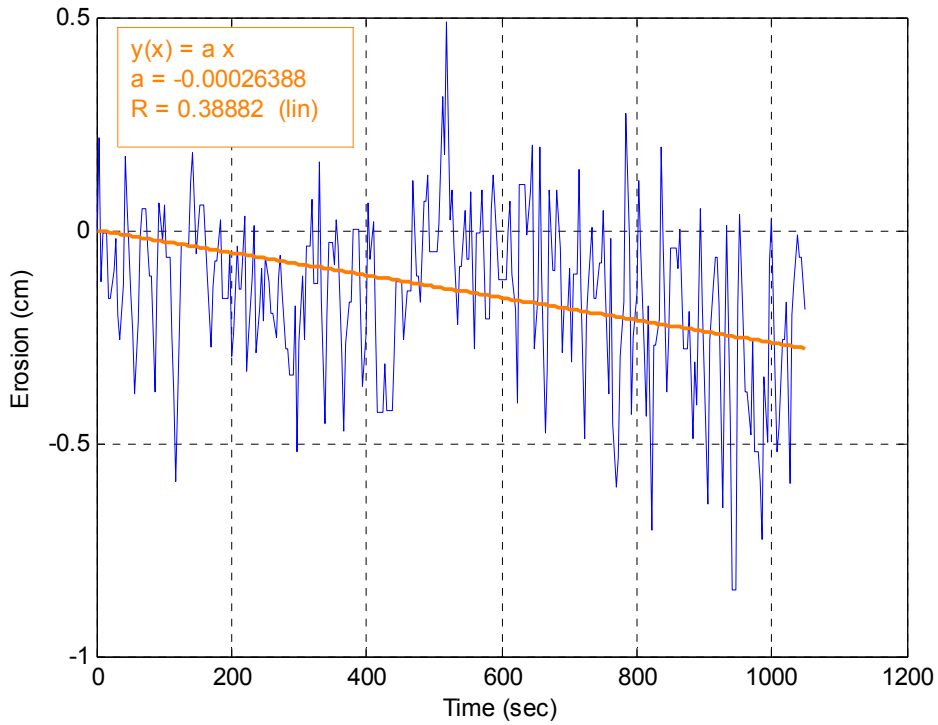

Figure B-66. Erosion versus time for specimen JCB 12'-14' at 10.37 Pa

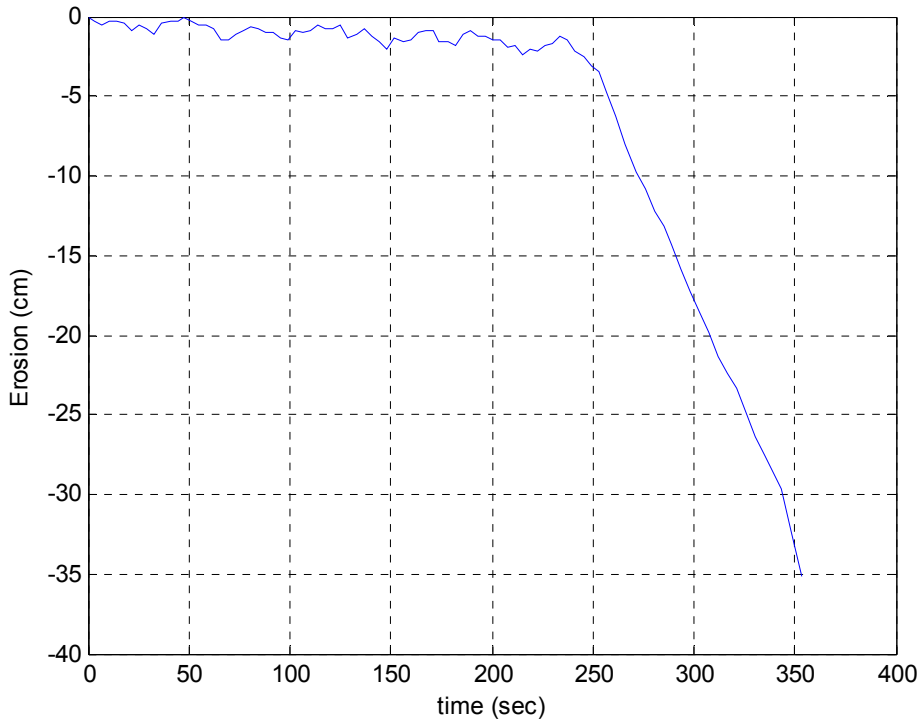

Figure B-67. Erosion versus time for specimen JCB 12'-14' at 10.37 Pa

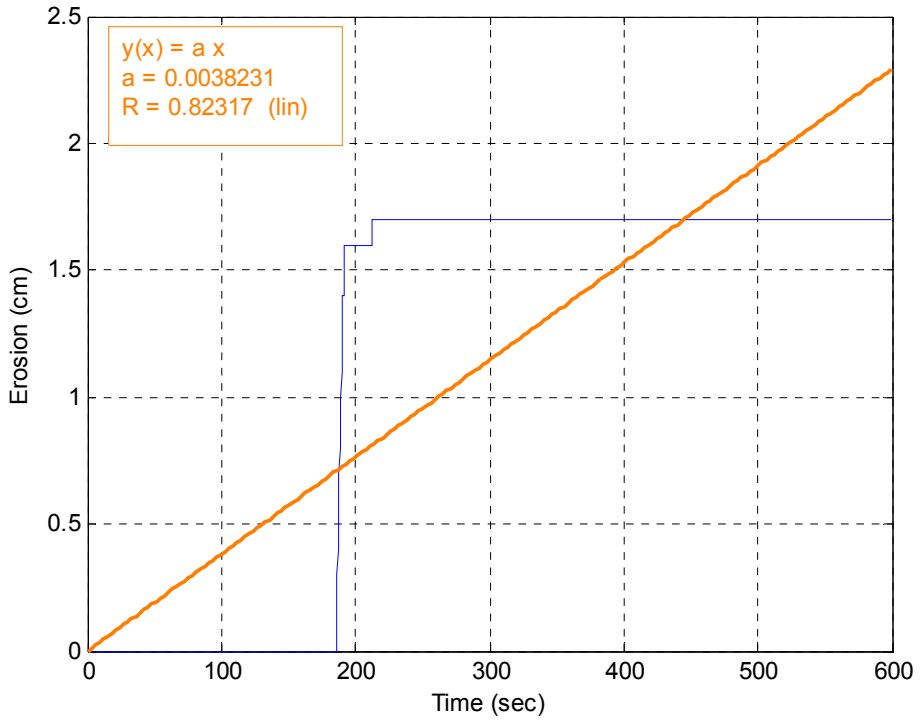

Figure B-68. Erosion versus time for specimen JCB 10'-12' at 52.60 Pa

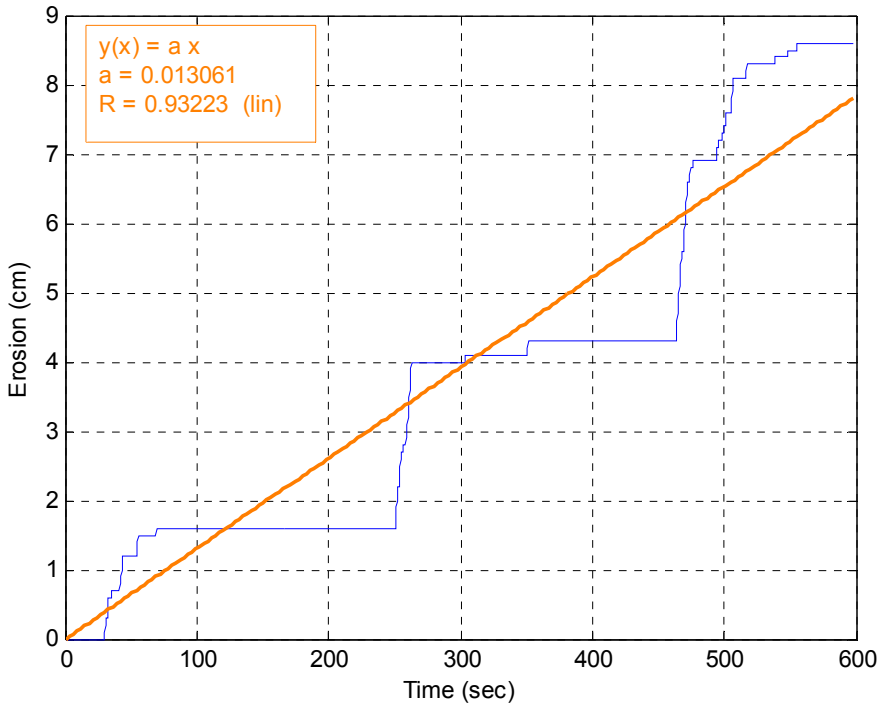

Figure B-69. Erosion versus time for specimen JCB 10'-12' at 63.03 Pa

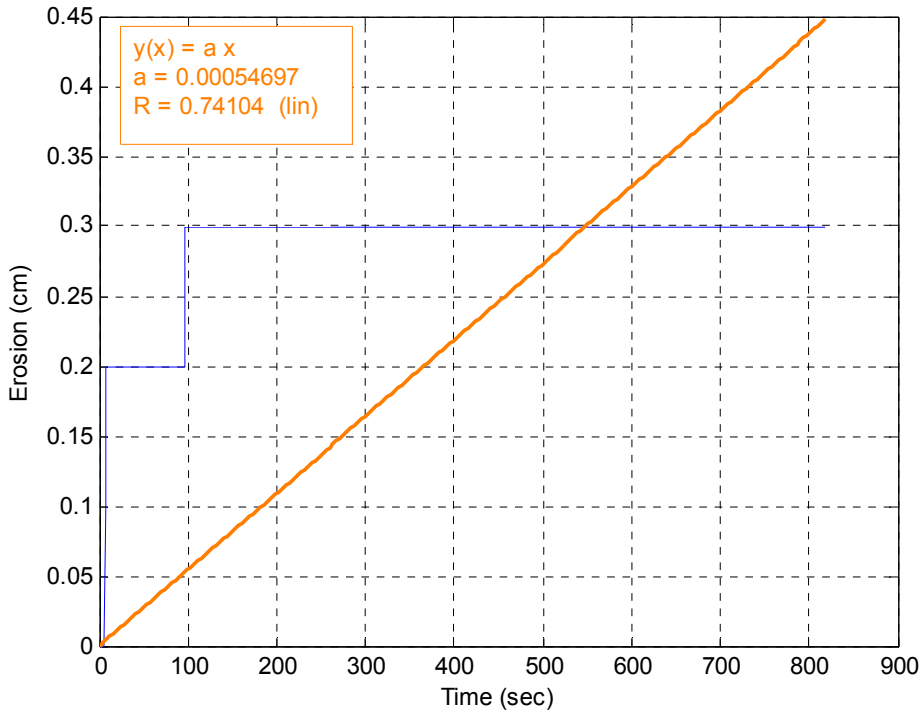

Figure B-70. Erosion versus time for specimen JCB 10'-12' at 60.86 Pa

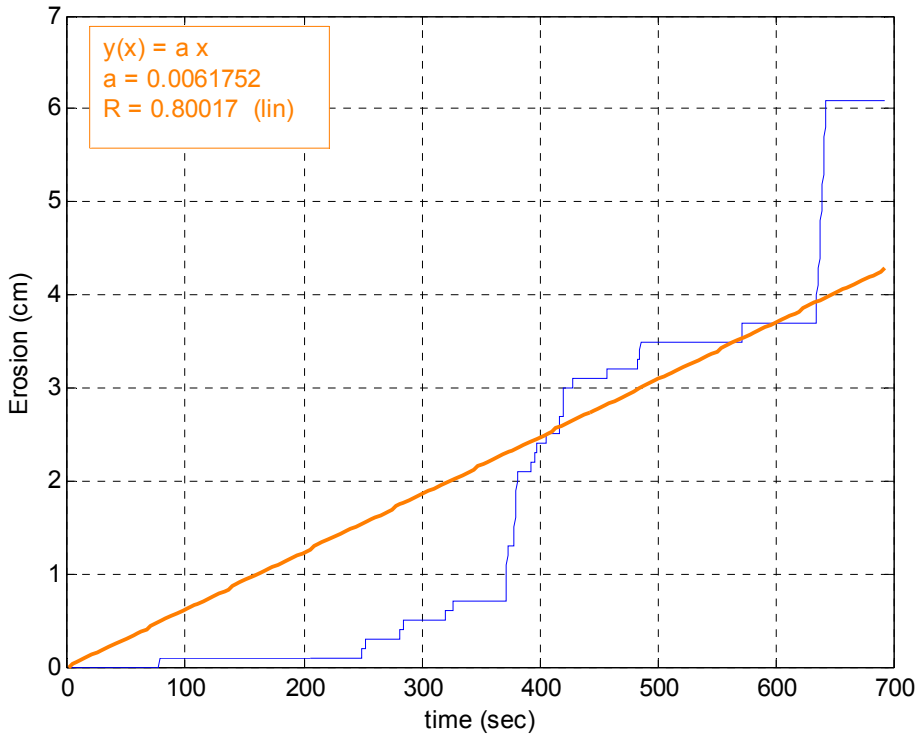

Figure B-71. Erosion versus time for specimen JCB 10'-12' at 58.74 Pa

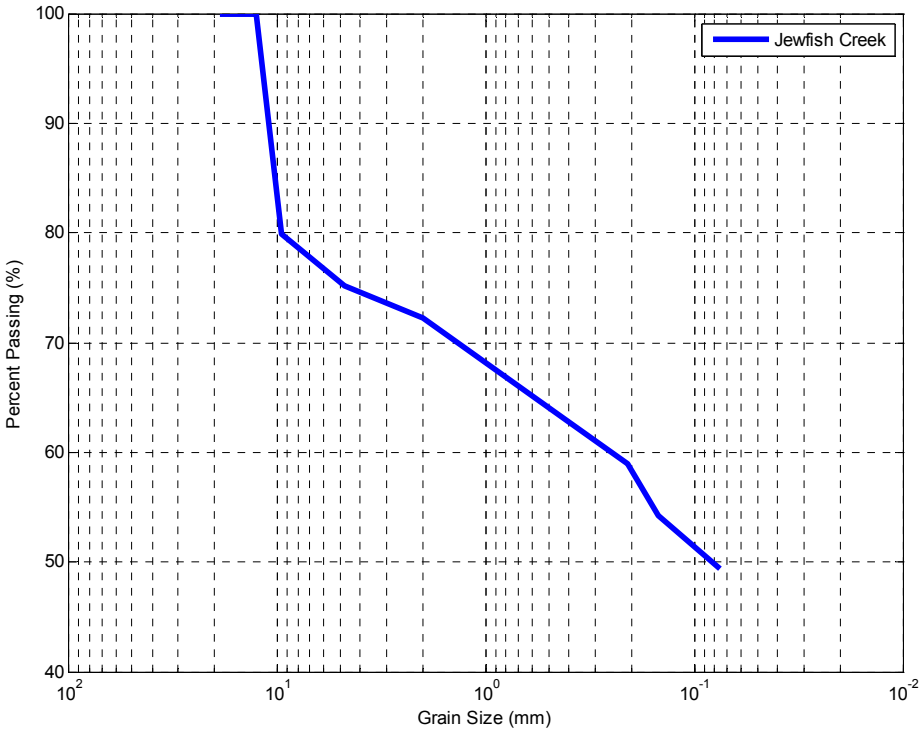

Figure B-72. Jewfish Creek grain size distribution

APPENDIX C
RAW EROSION DATA FOR OUT-OF-STATE SPECIMENS

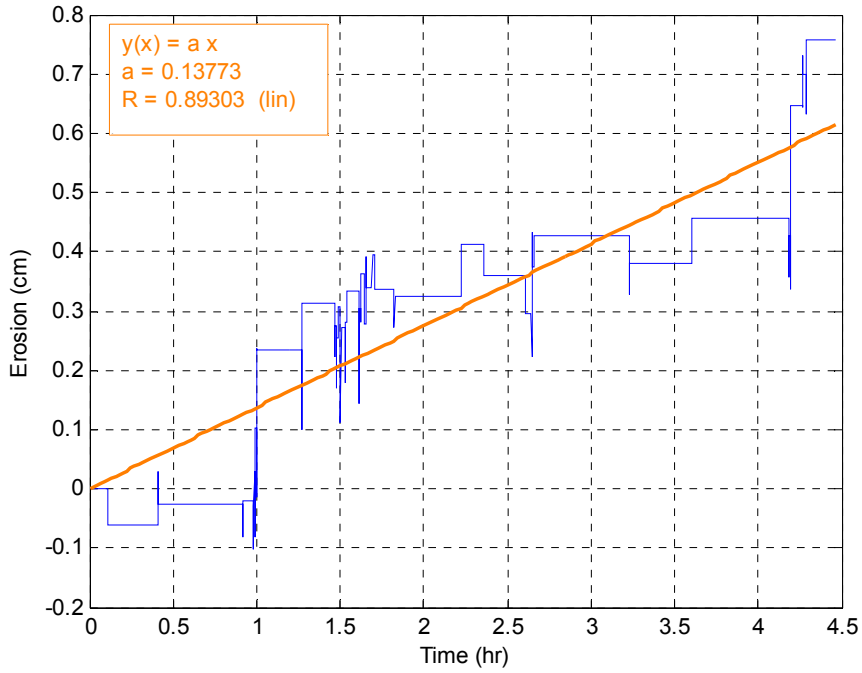

Figure C-1. Erosion versus time for specimen OS-35 60-62 top at 4.05 Pa

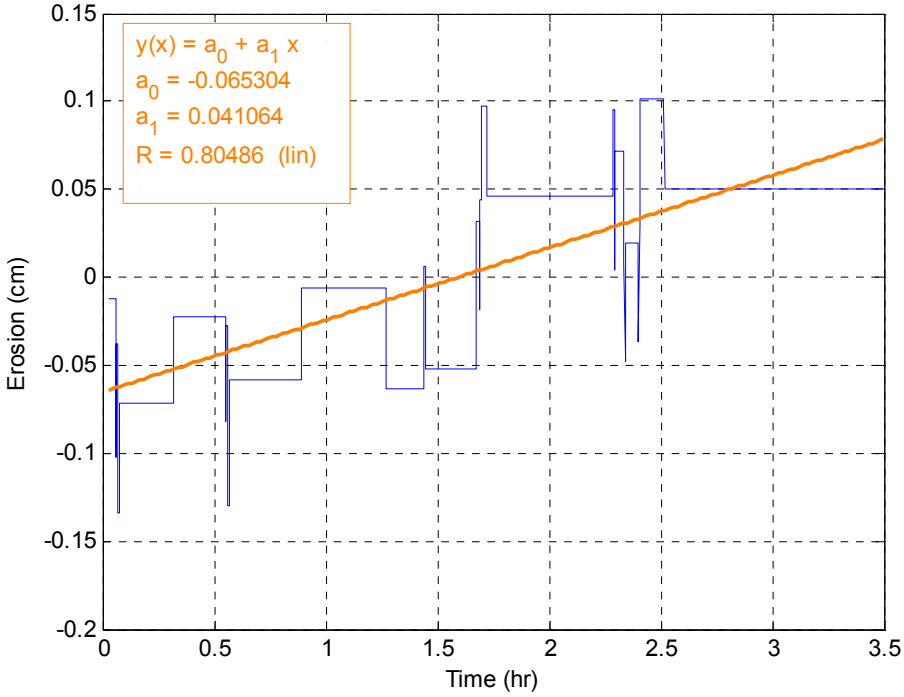

Figure C-2. Erosion versus time for specimen OS-35 60-62 top at 6.72 Pa

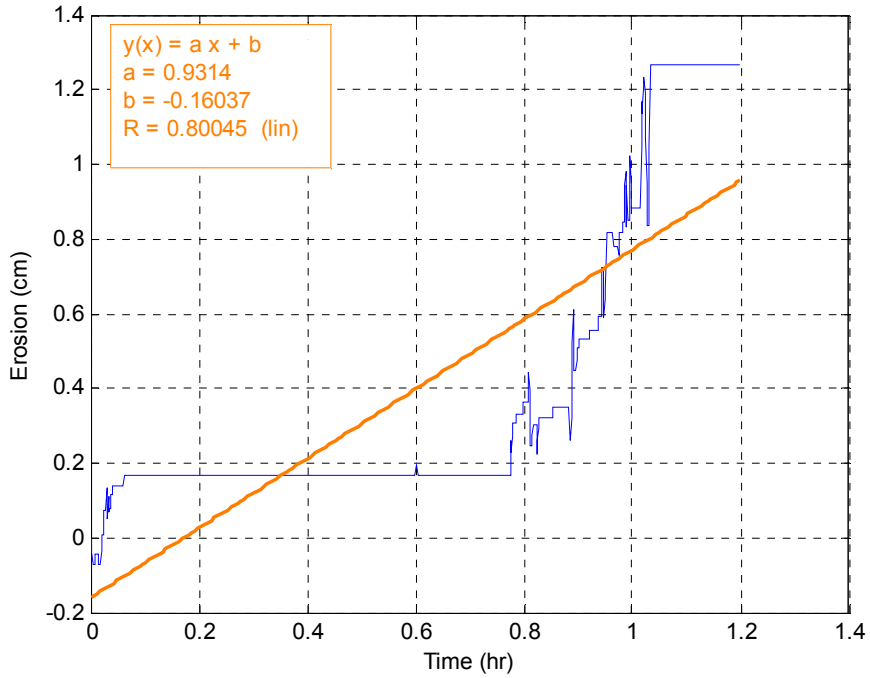

Figure C-3. Erosion versus time for specimen OS-35 60-62 top at 8.06 Pa

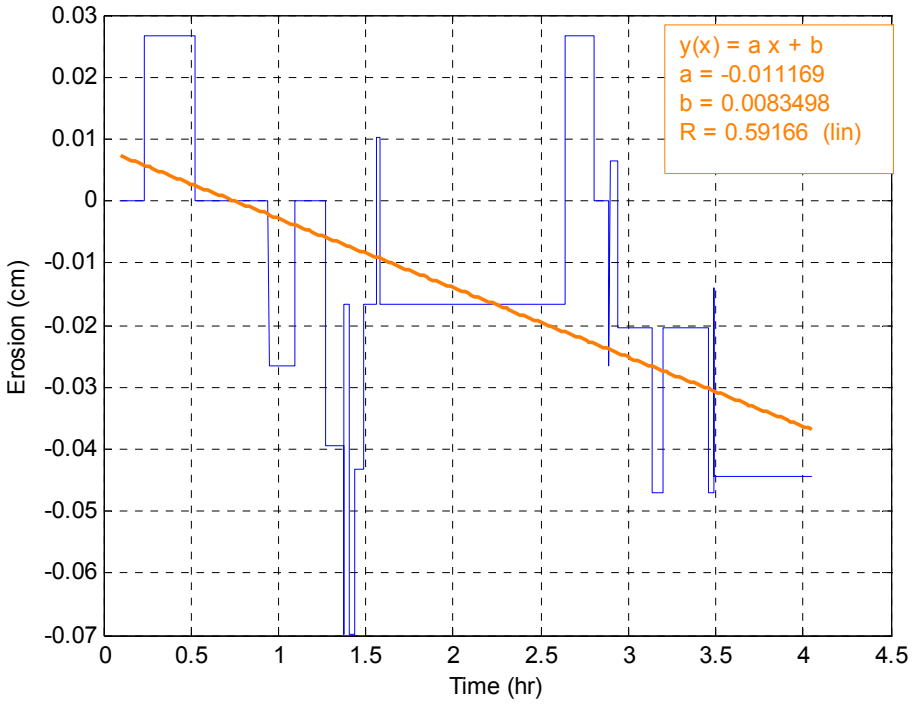

Figure C-4. Erosion versus time for specimen OS-35 60-62 bottom at 4.0 Pa

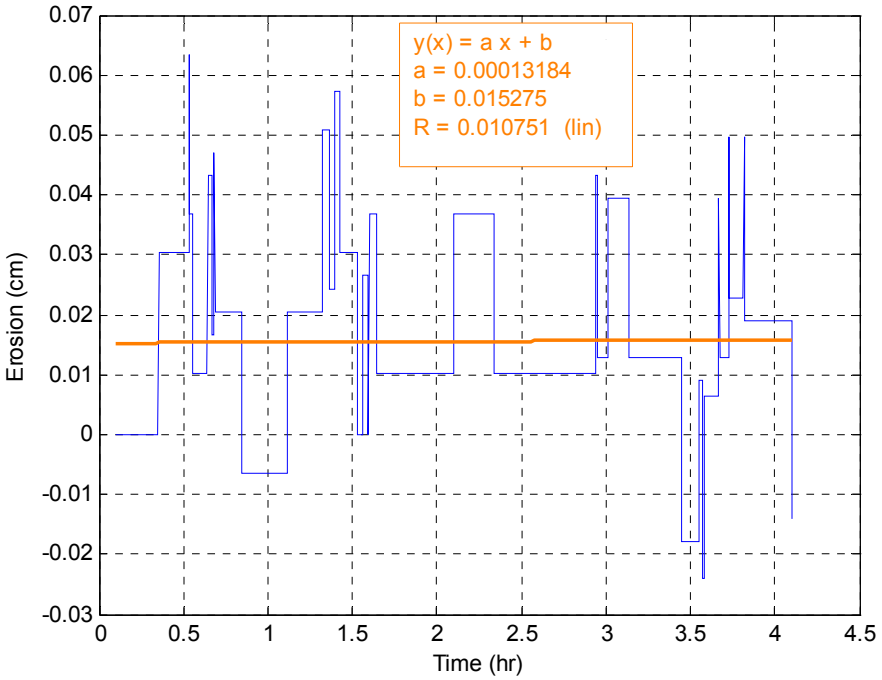

Figure C-5. Erosion versus time for specimen OS-35 60-62 bottom at 6.0 Pa

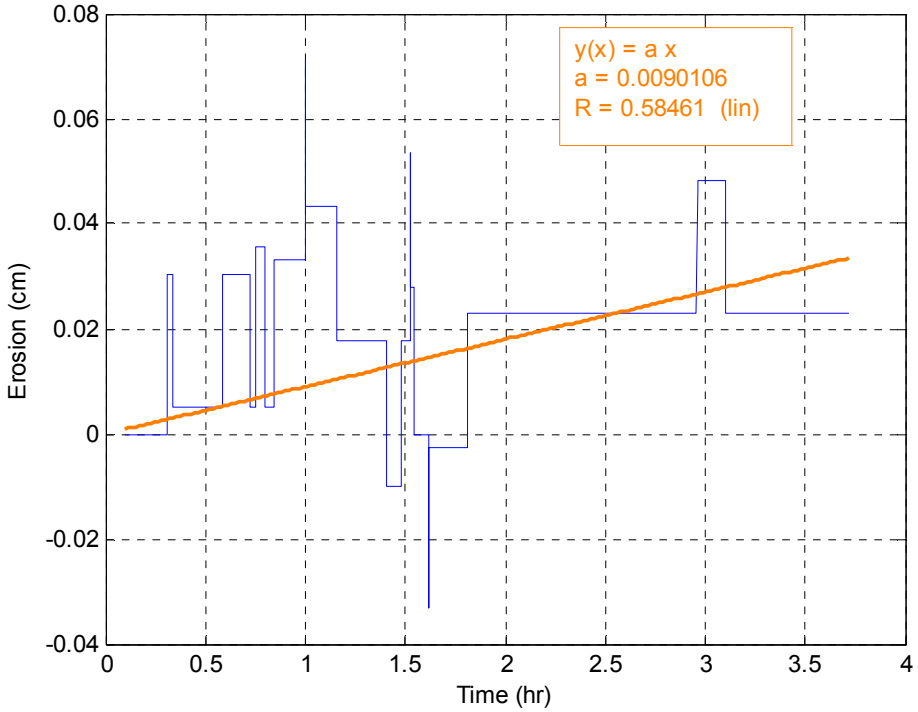

Figure C-6. Erosion versus time for specimen OS-35 60-62 bottom at 10.0 Pa

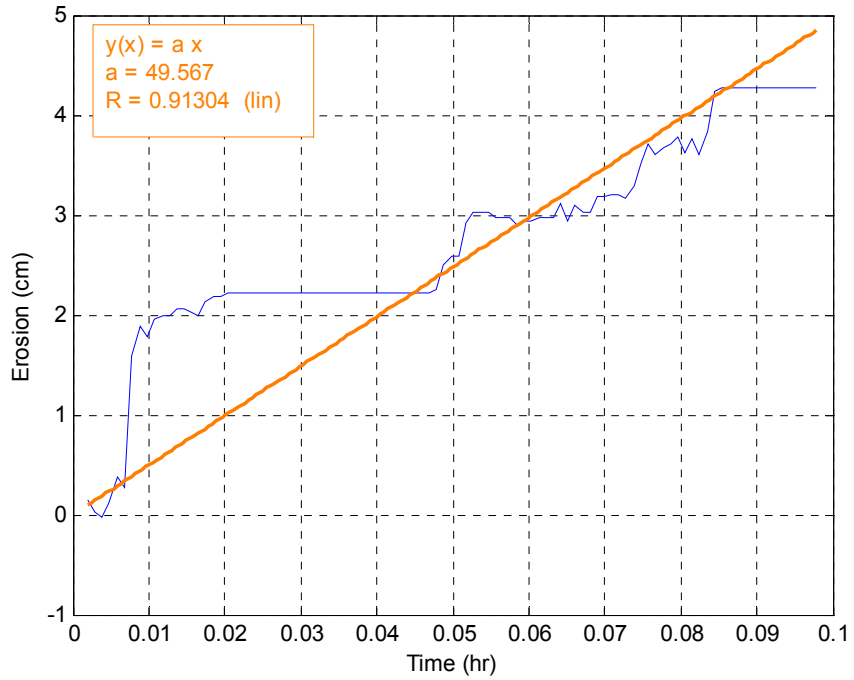

Figure C-7. Erosion versus time for specimen OS-35 60-62 bottom at 13.02 Pa

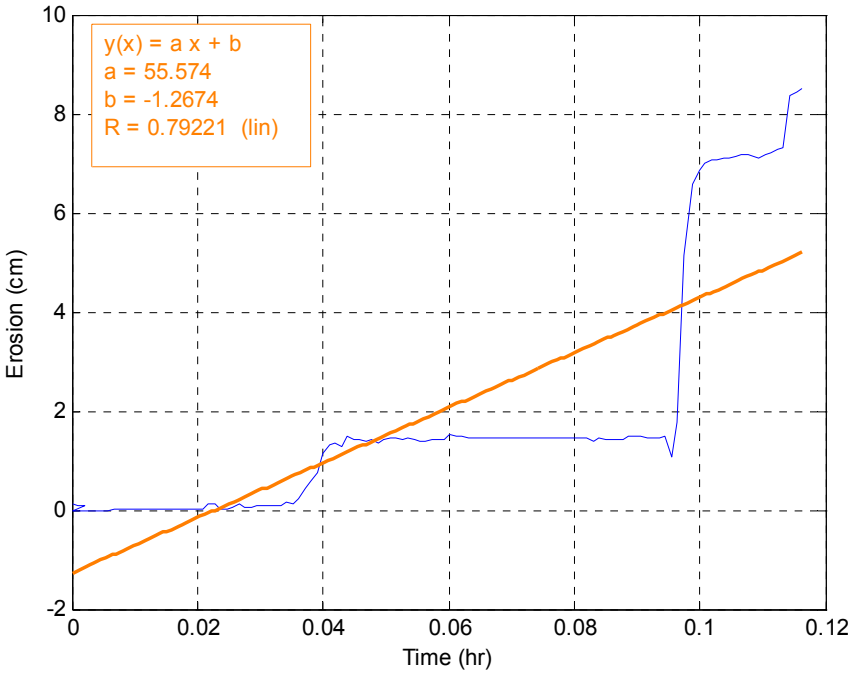

Figure C-8. Erosion versus time for specimen OS-35 60-62 bottom at 17.54 Pa.

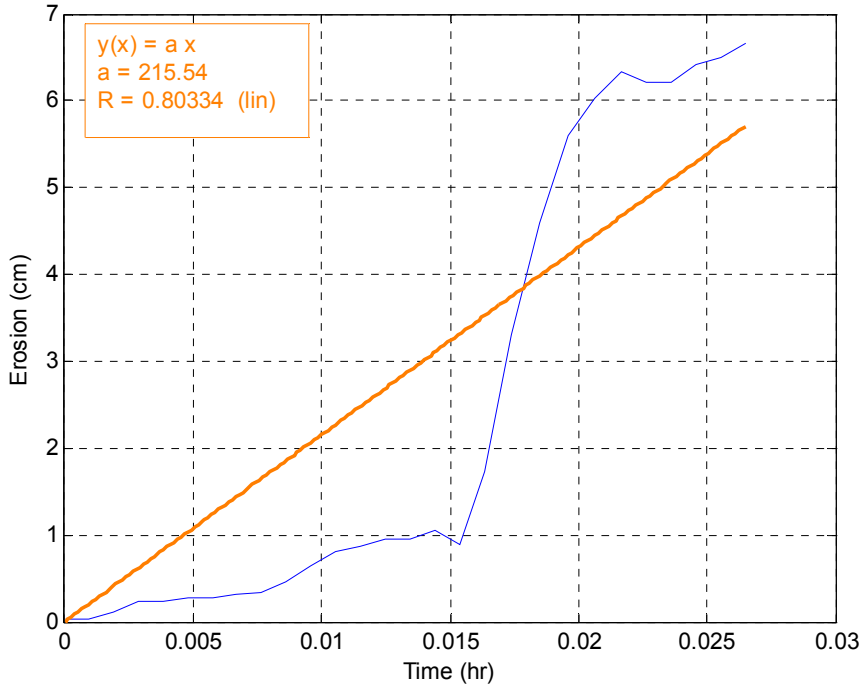

Figure C-9. Erosion versus time for specimen OS-35 60-62 bottom at 25.00 Pa

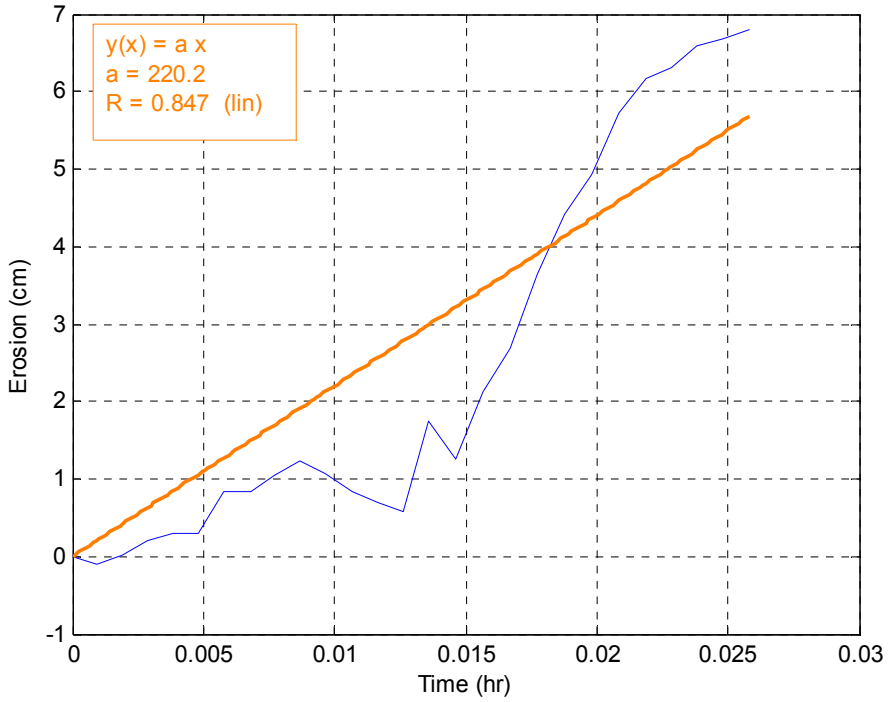

Figure C-10. Erosion versus time for specimen OS-34 52-54 top at 5.37 Pa

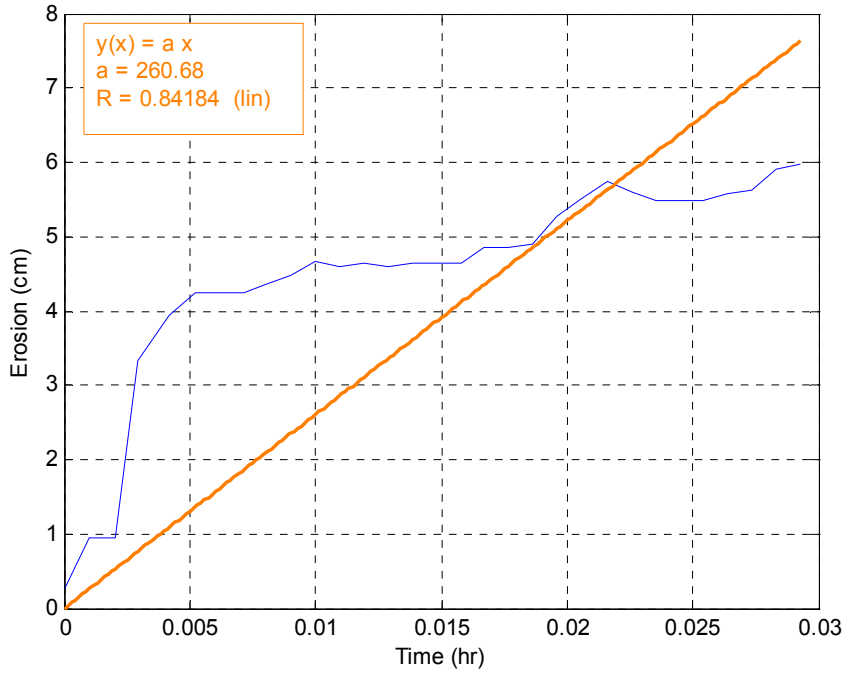

Figure C-11. Erosion versus time for specimen OS-34 52-54 top at 10.00 Pa

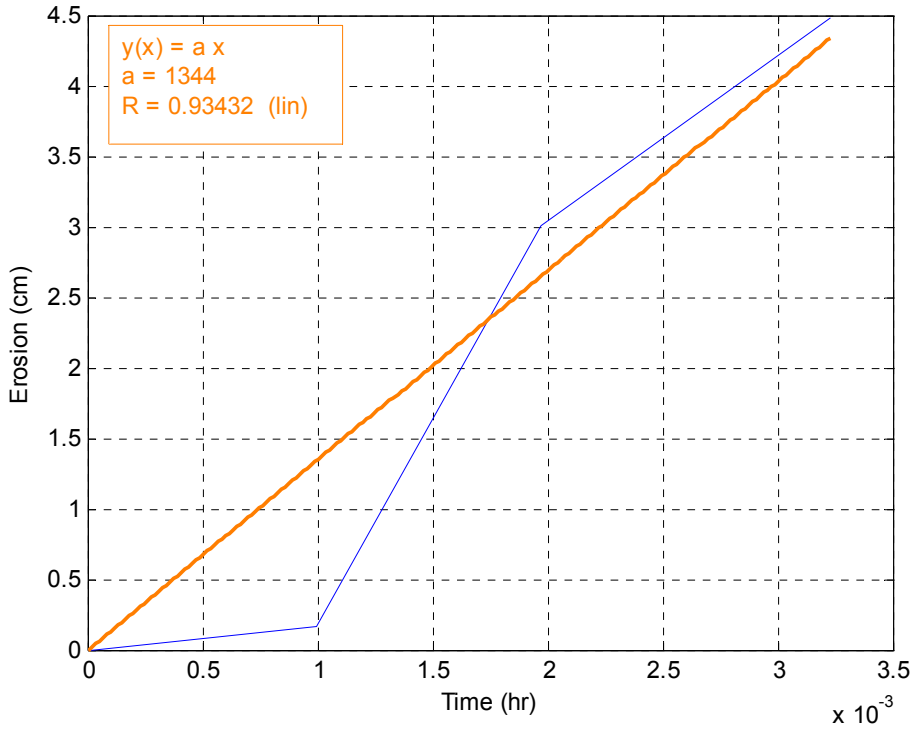

Figure C-12. Erosion versus time for specimen OS-34 52-54 top at 15.00 Pa

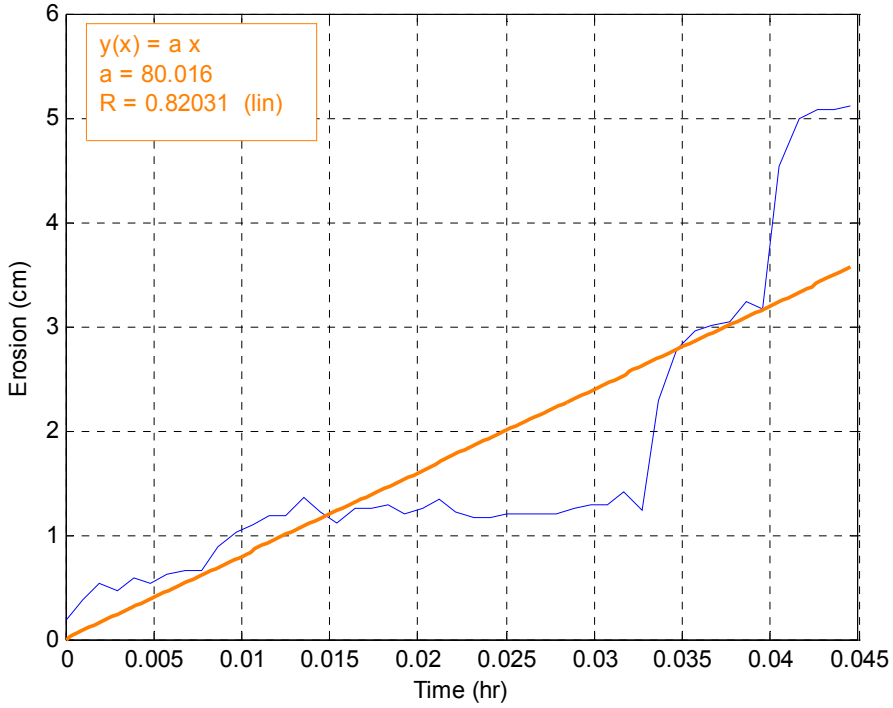

Figure C-13. Erosion versus time for specimen OS-34 52-54 bottom at 5.00 Pa

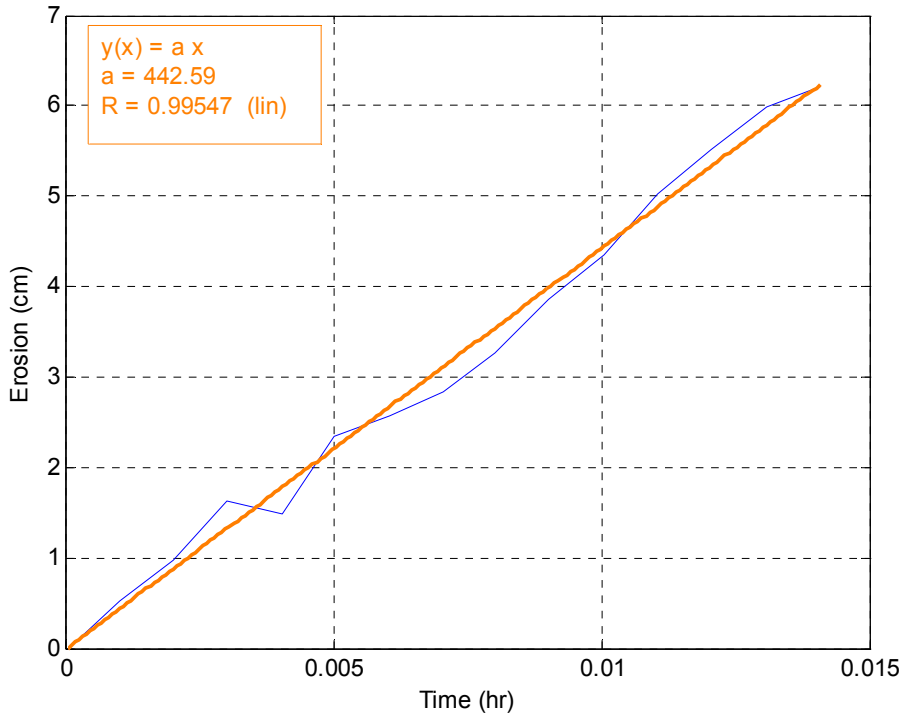

Figure C-13. Erosion versus time for specimen OS-34 52-54 bottom at 10.00 Pa

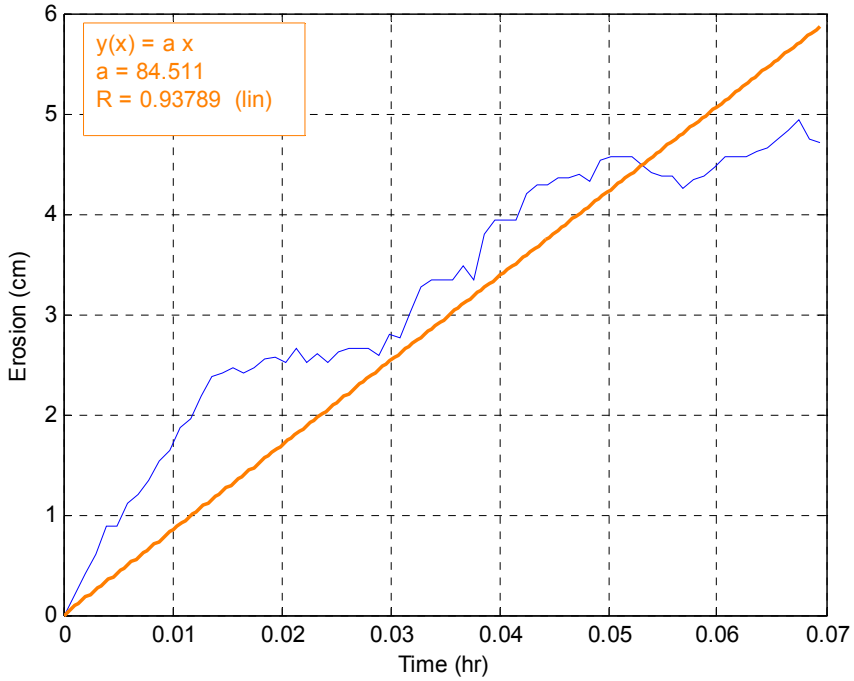

Figure C-14. Erosion versus time for specimen OS-34 52-54 bottom at 15.00 Pa

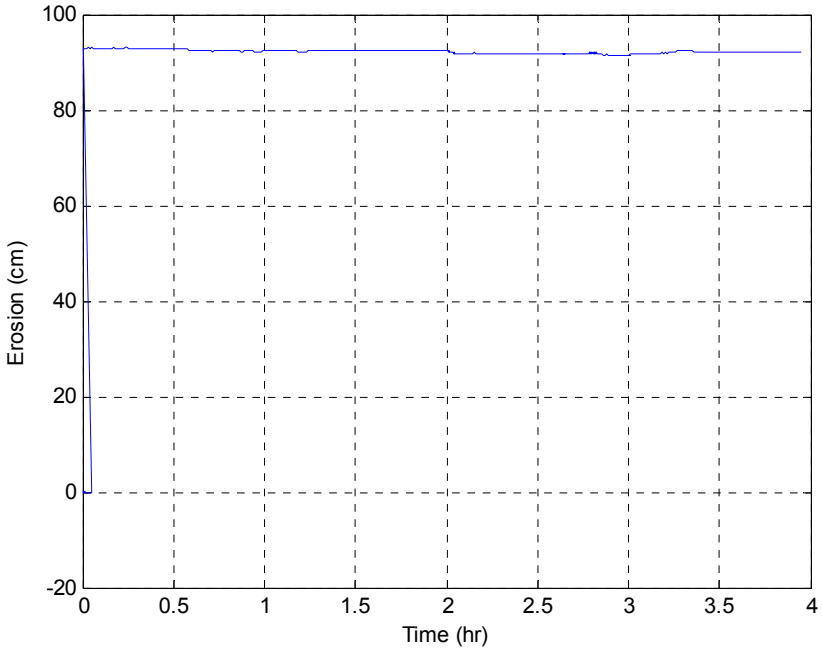

Figure C-15. Erosion versus time for specimen OS-51 24/24 top at 5.0 Pa (note, large cobble obstructed erosion during test; data is not believed to be indicative of actual erosion conditions; data not used in erosion function development)

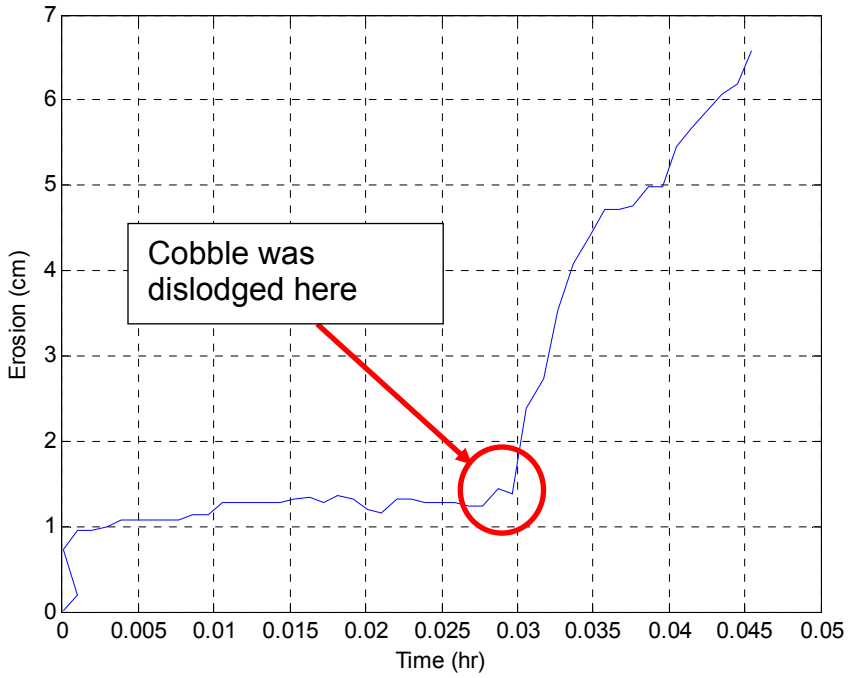

Figure C-16. Erosion versus time for specimen OS-51 top at 10.0 Pa. Note, two distinctive erosion rates were observed – one with large cobble and one without large cobble; due to layering, data not used in erosion function development

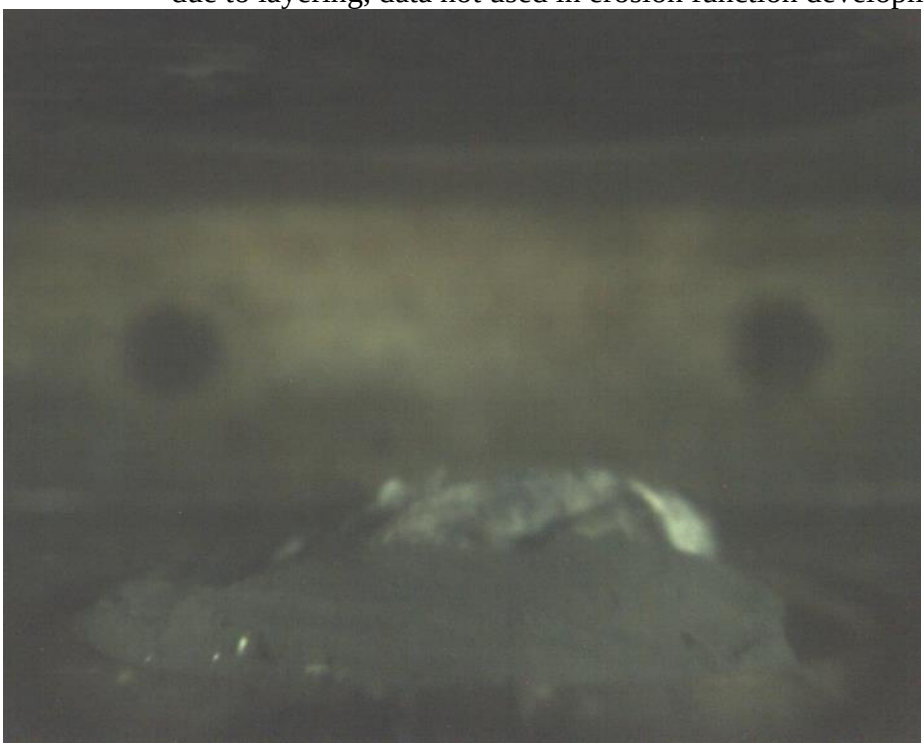

Figure C-17. Photograph of large cobble

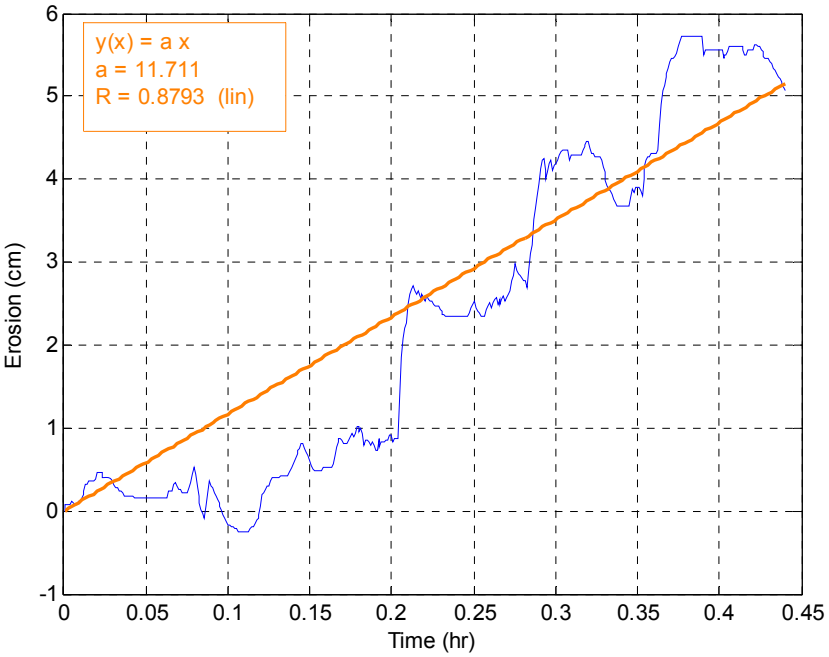

Figure C-18. Erosion versus time for specimen OS-51 24/24 top at 5.0 Pa without cobble obstruction

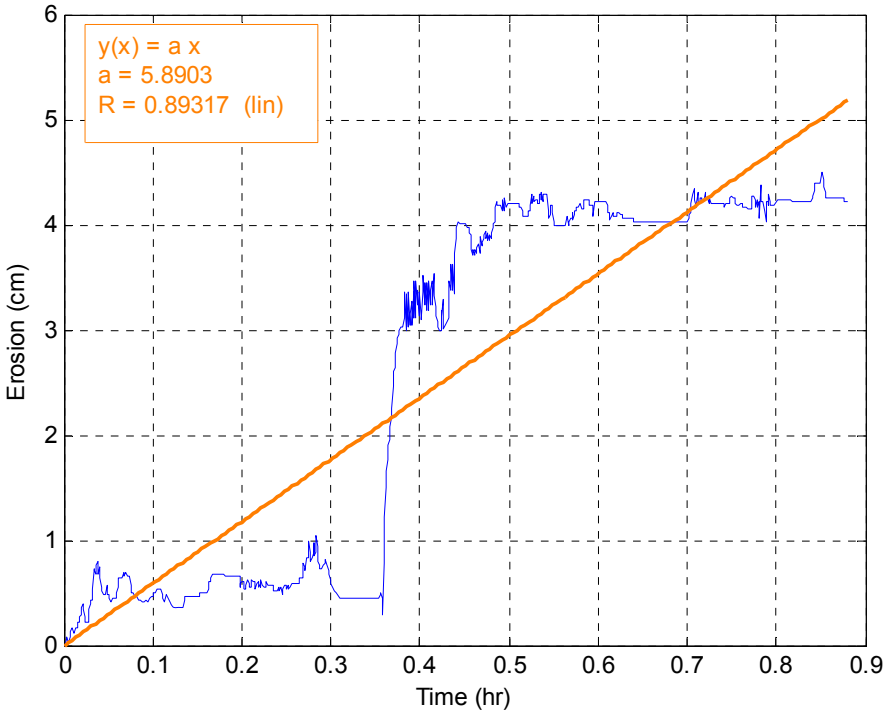

Figure C-19. Erosion versus time for specimen OS-51 24/24 top at 10.0 Pa (note, specimen encountered stiff shell layer that appeared to obstruct erosion)

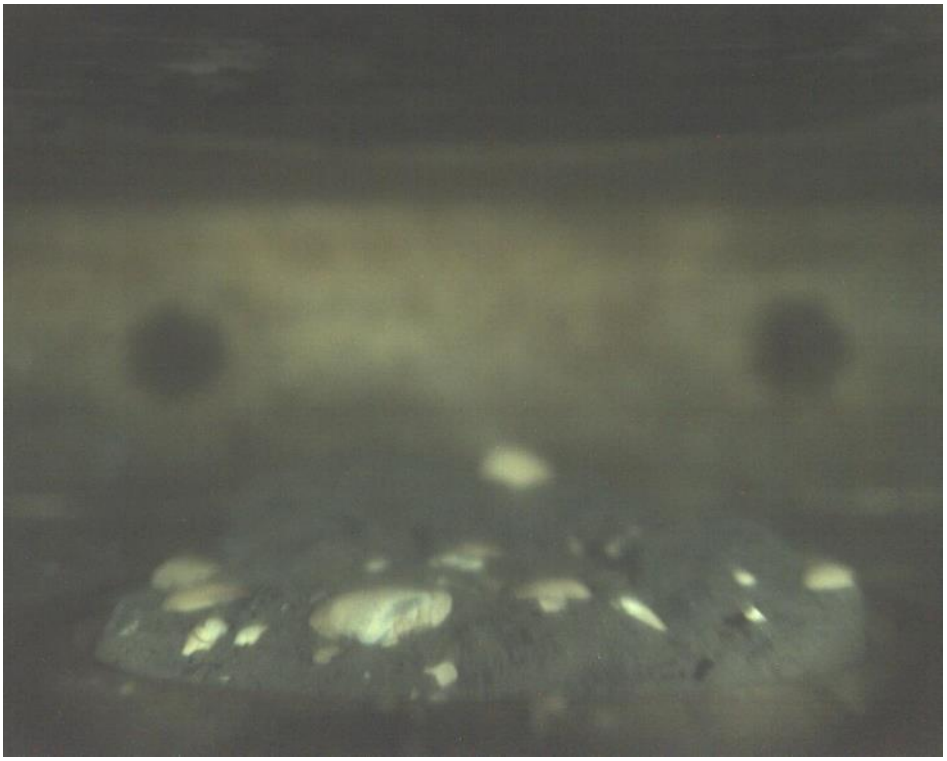

Figure C-20. Photograph of shell layer that appeared to obstruct erosion in OS-51 top

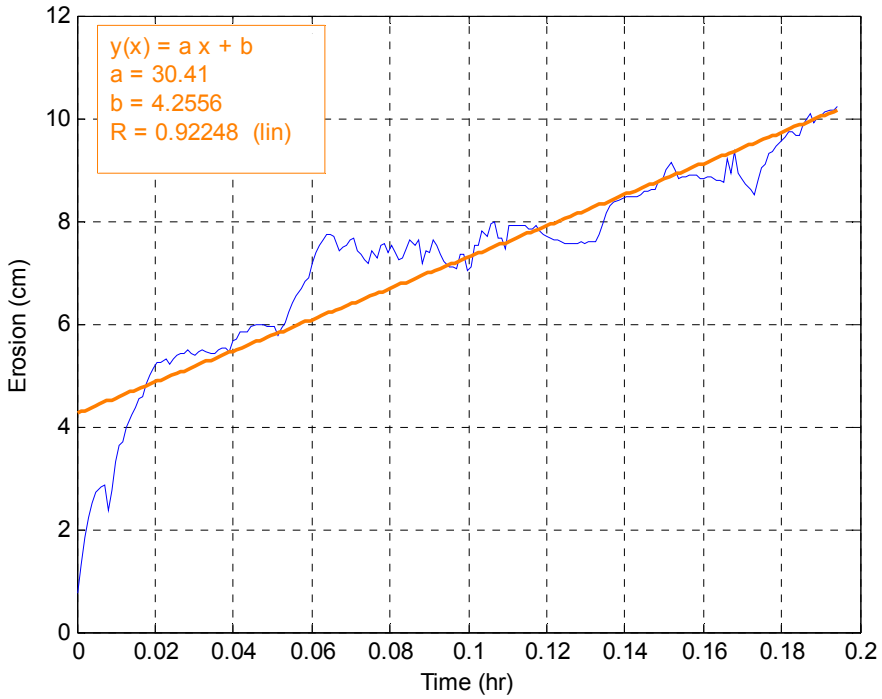

Figure C-21. Erosion versus time for specimen OS-51 24/24 top at 15.0 Pa

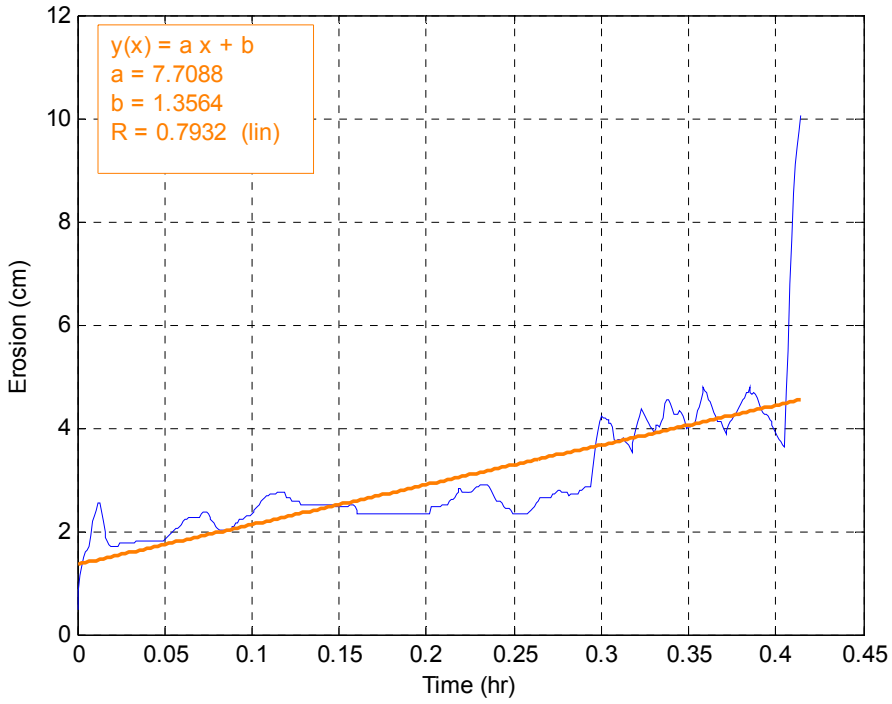

Figure C-22. Erosion versus time for specimen OS-51 24/24 bottom at 5.0 Pa

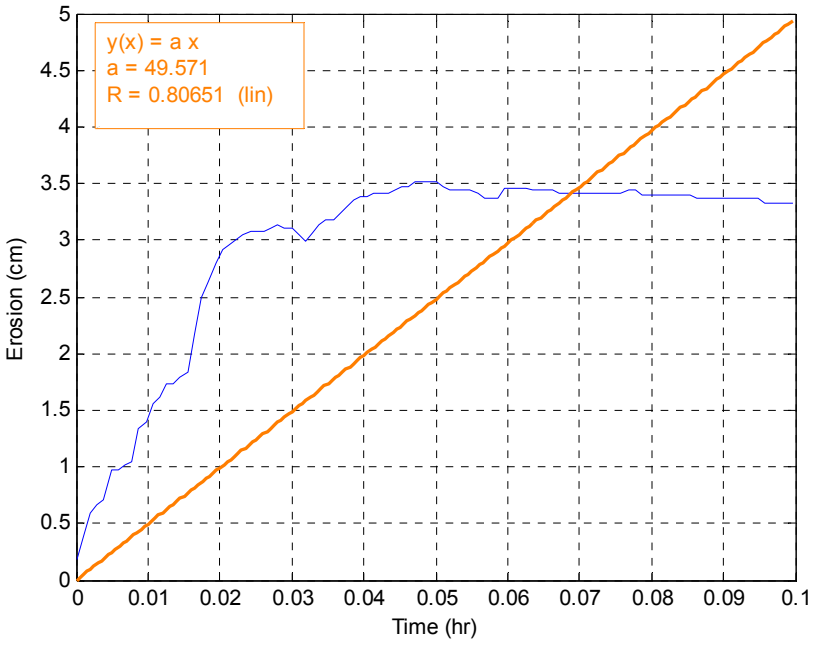

Figure C-23. Erosion versus time for specimen OS-51 24/24 bottom at 10.0 Pa

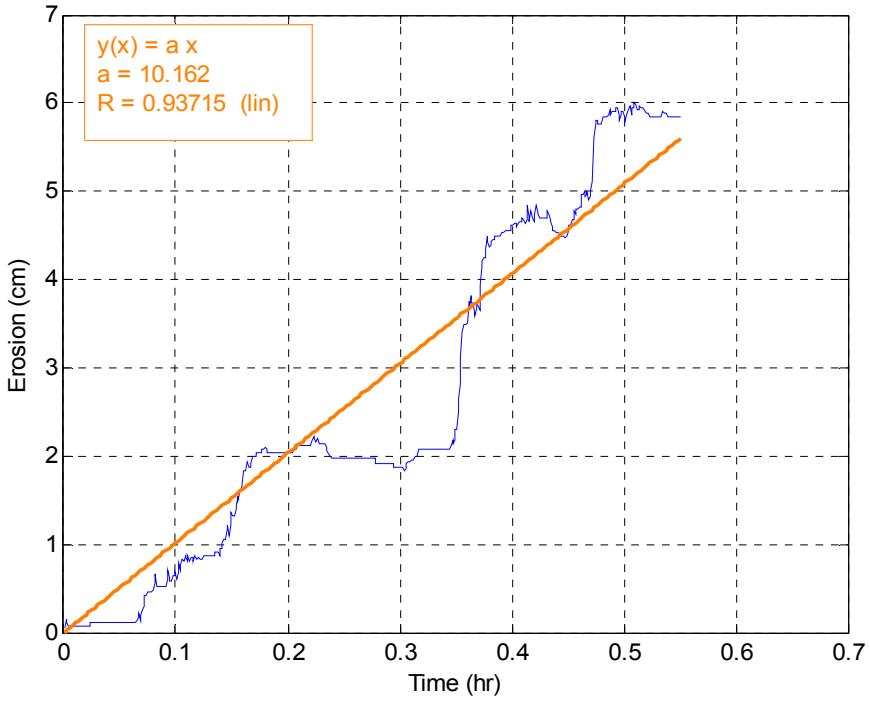

Figure C-24. Erosion versus time for specimen OS-23 U-1 30-32 at 5.0 Pa

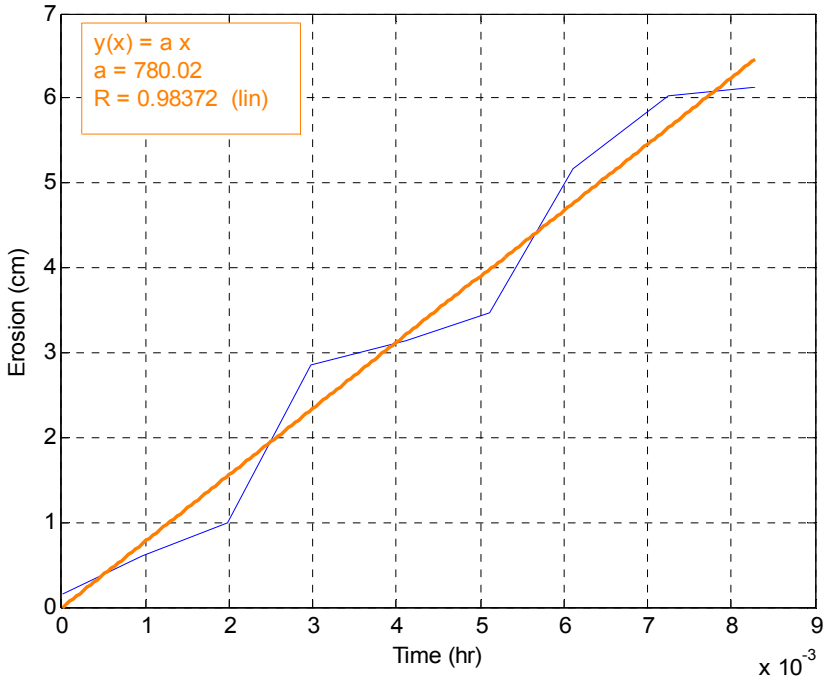

Figure C-25. Erosion versus time for specimen OS-23 U-1 30-32 at 10.0 Pa

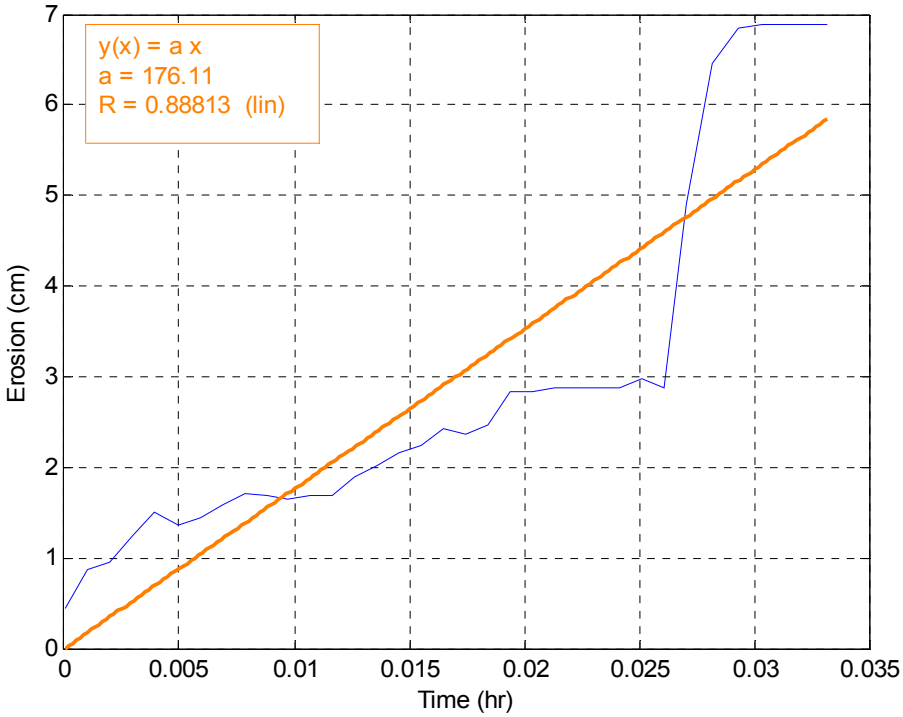

Figure C-26. Erosion versus time for specimen OS-23 U-1 30-32 at 15.0 Pa

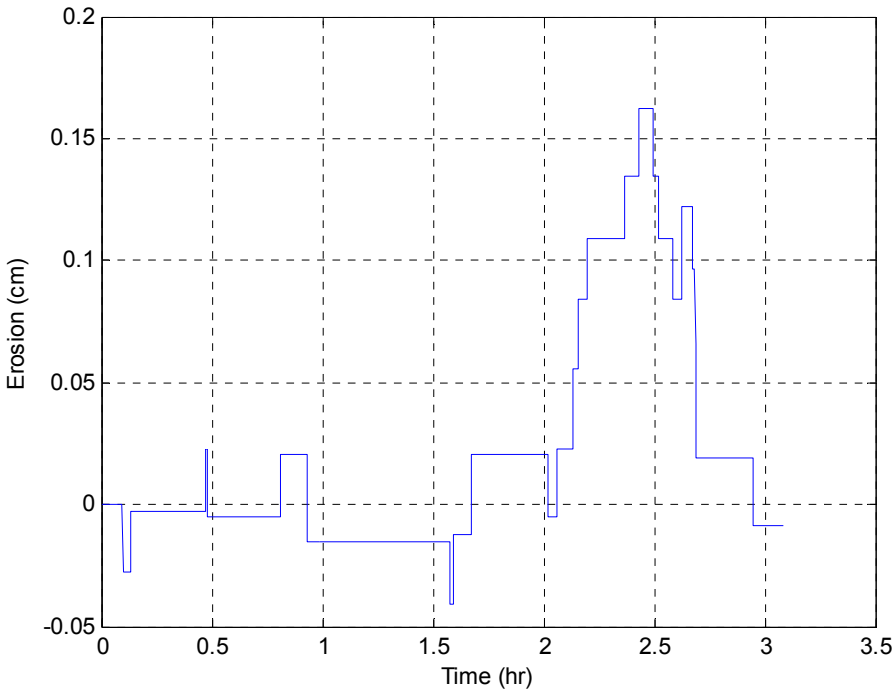

Figure C-27. Erosion versus time for specimen OS-23 U-1 30-32 at 4.0 Pa

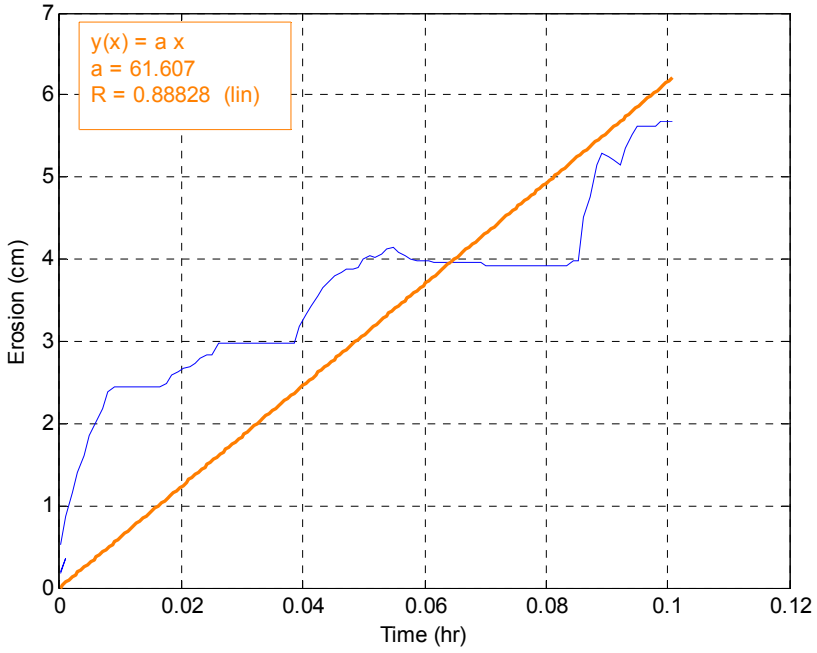

Figure C-28. Erosion versus time for specimen OS-23 U-1 30-32 at 8.0 Pa

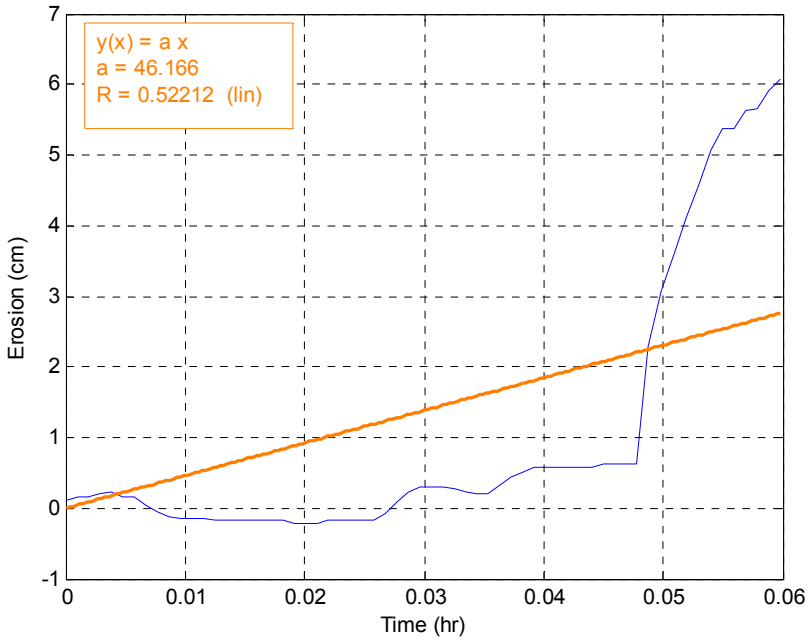

Figure C-29. Erosion versus time for specimen OS-23 U-1 30-32 at 12.0 Pa

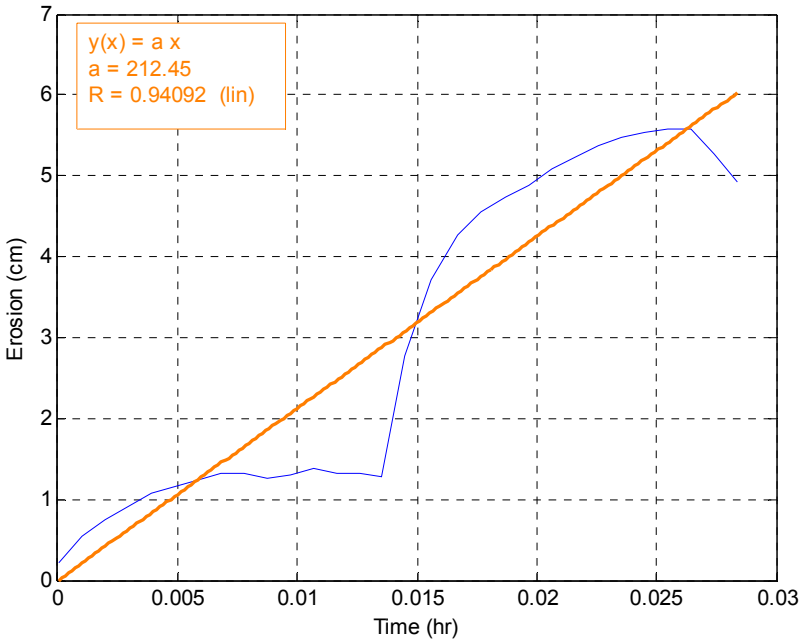

Figure C-30. Erosion versus time for specimen OS-23 U-1 30-32 at 18.0 Pa

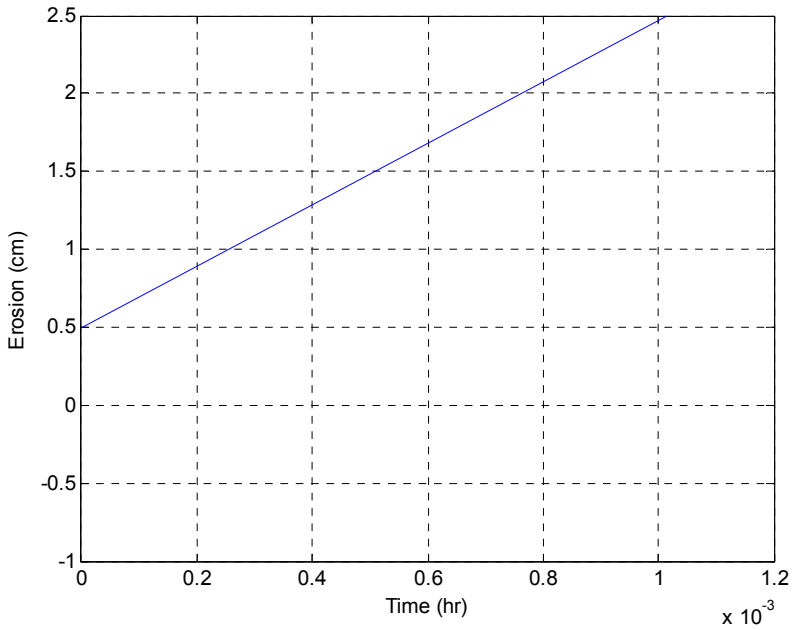

Figure C-31. Erosion versus time for specimen OS-23 U-1 30-32 at 22.0 Pa

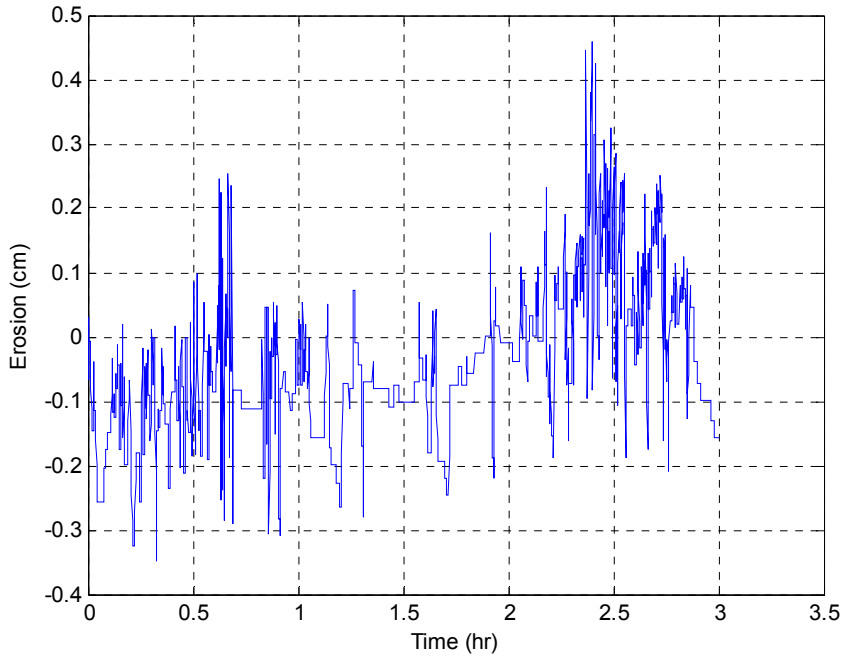

Figure C-32. Erosion versus time for specimen OS-34 U-2 63-66 top at 5.0 Pa

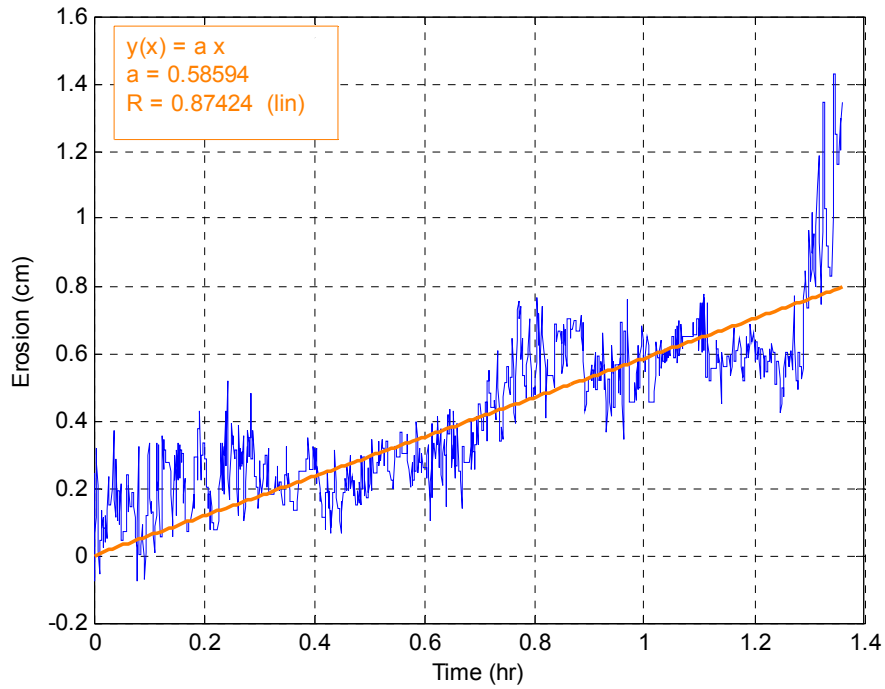

Figure C-33. Erosion versus time for specimen OS-34 U-2 63-66 top at 10.0 Pa

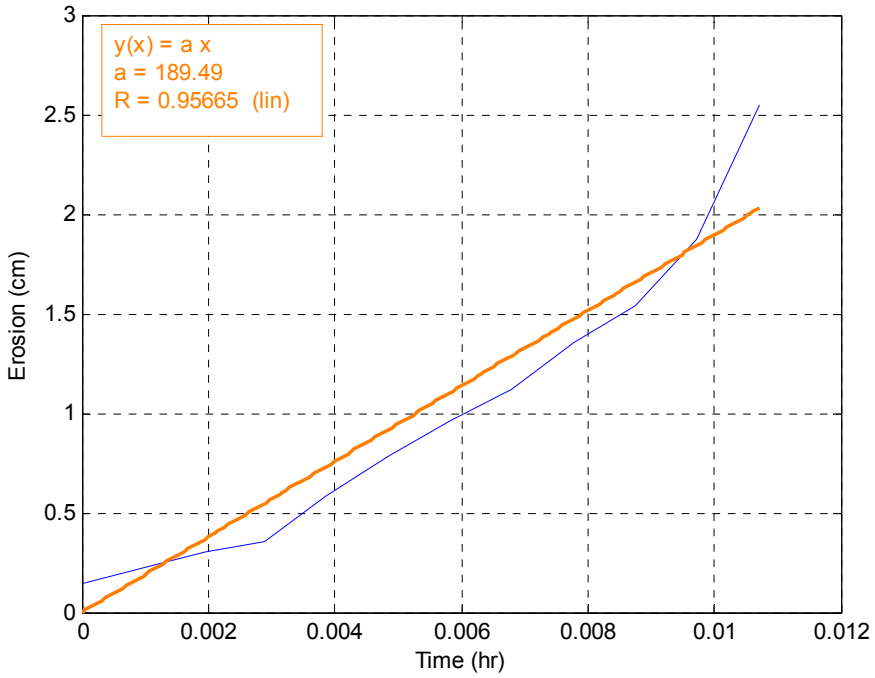

Figure C-34. Erosion versus time for specimen OS-34 U-2 63-66 top at 15.0 Pa

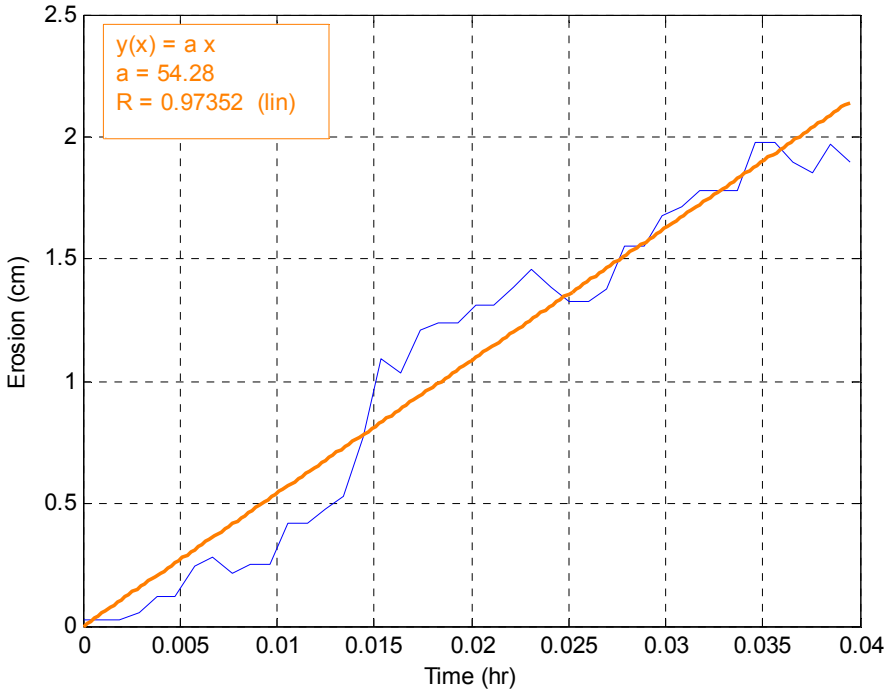

Figure C-35. Erosion versus time for specimen OS-34 U-2 63-66 top at 8.0 Pa

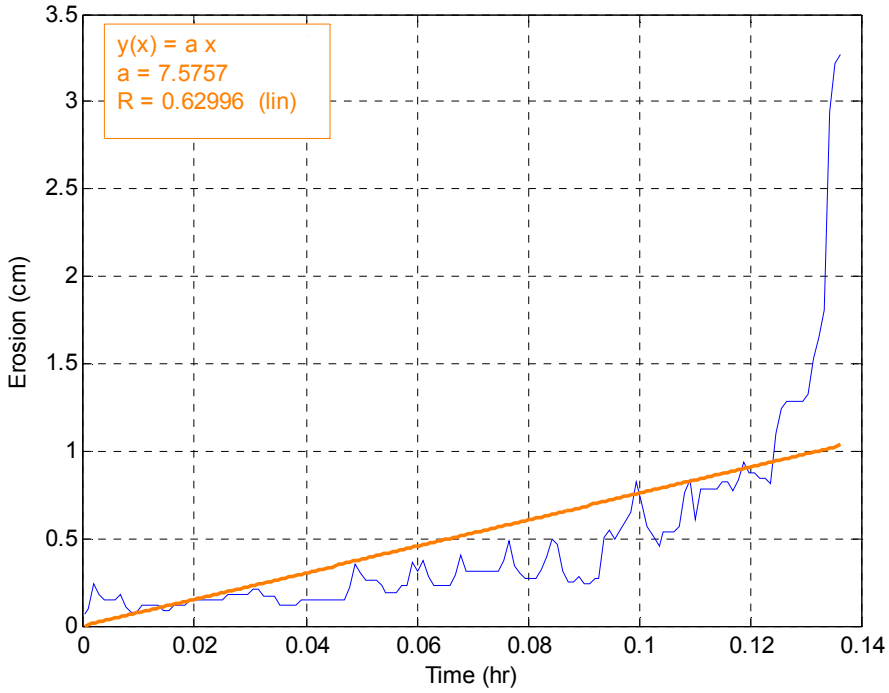

Figure C-36. Erosion versus time for specimen OS-34 U-2 63-66 top at 12.0 Pa

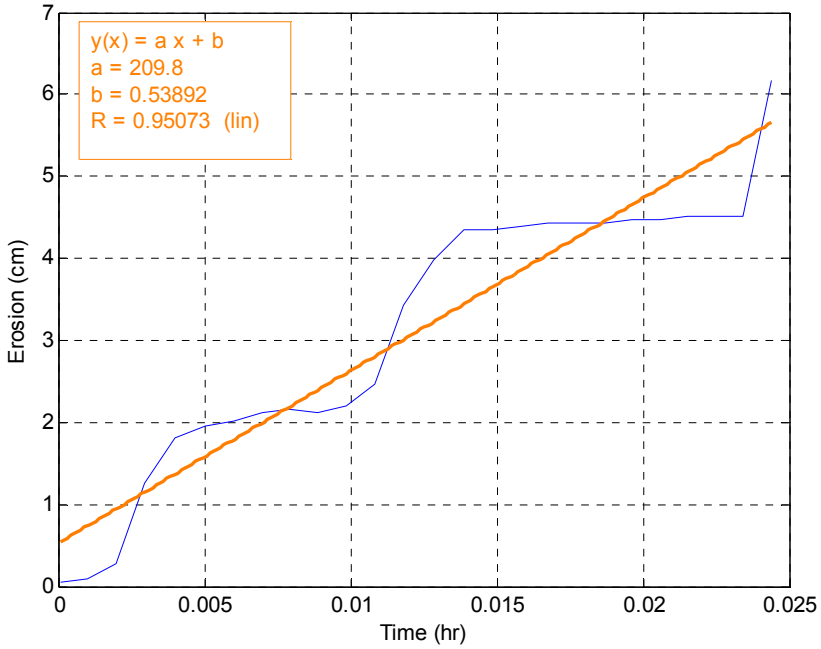

Figure C-37. Erosion versus time for specimen OS-34 U-2 63-66 bottom at 15.0 Pa

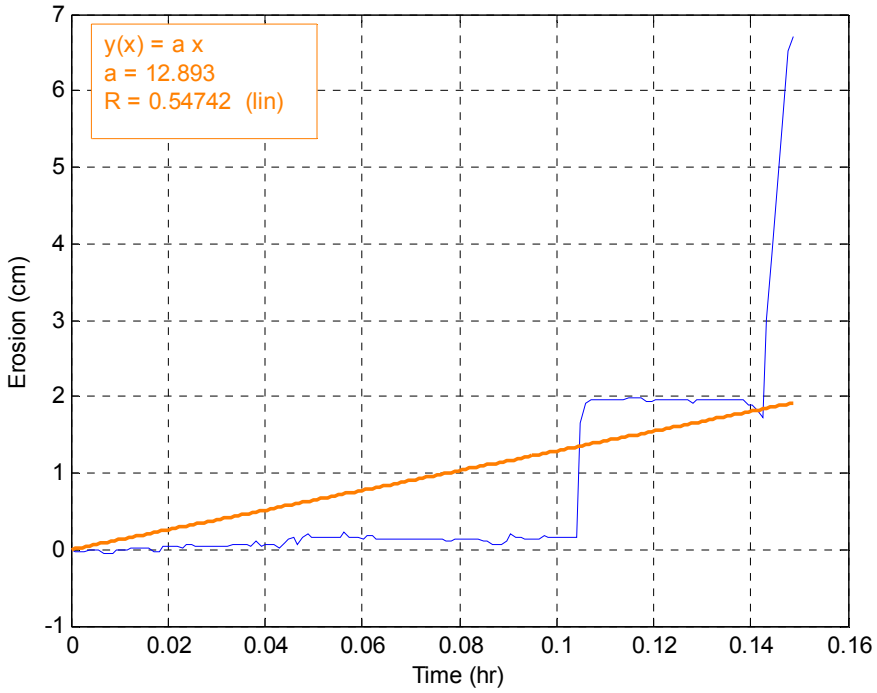

Figure C-37. Erosion versus time for specimen OS-34 U-2 63-66 bottom at 12.0 Pa

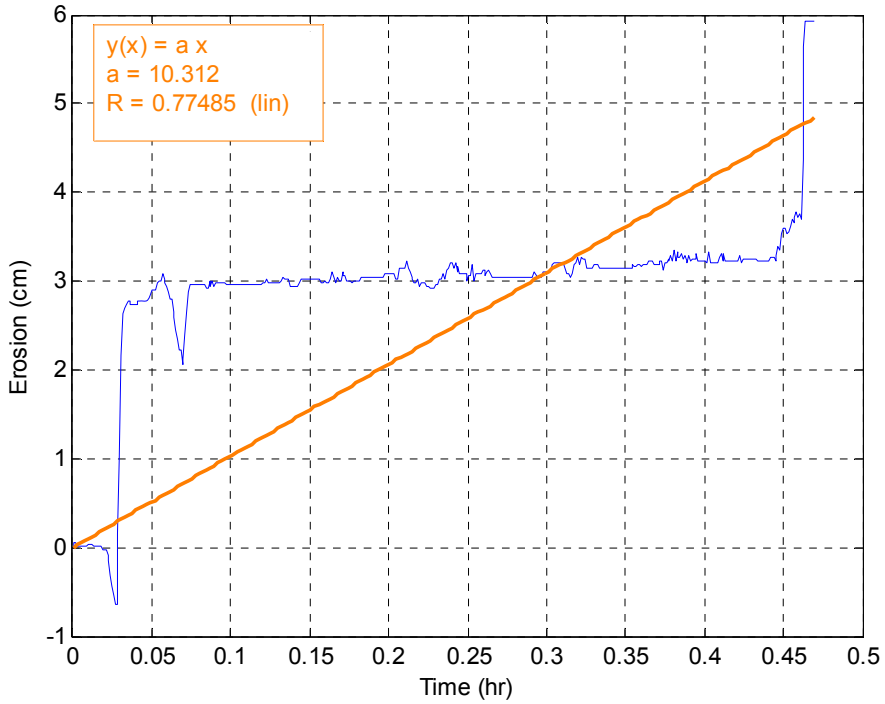

Figure C-38. Erosion versus time for specimen OS-34 U-2 63-66 bottom at 8.0 Pa

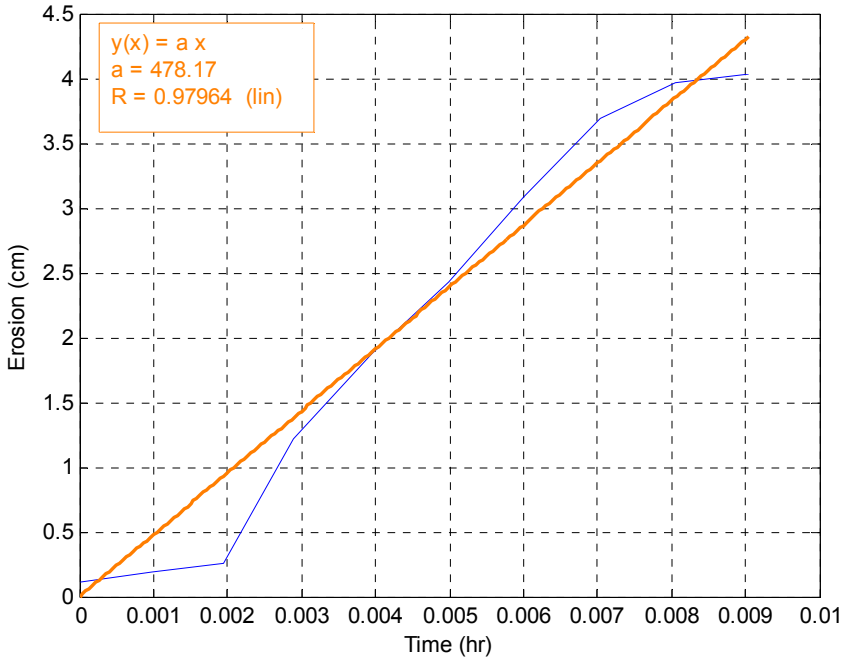

Figure C-39. Erosion versus time for specimen OS-33 top at 5.0 Pa (data omitted from erosion function due to suspected surface disturbances from transport)

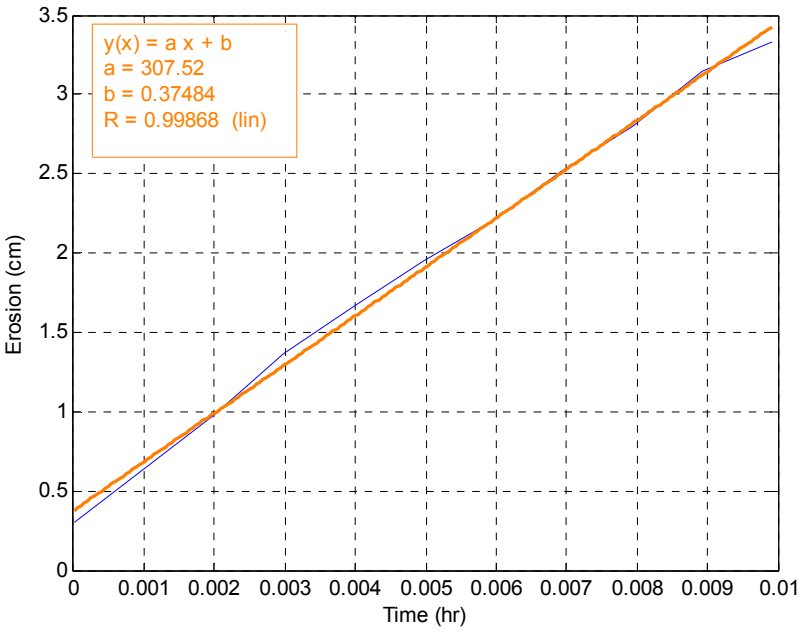

Figure C-40. Erosion versus time for specimen OS-33 top at 7.5 Pa (data omitted from erosion function due to suspected surface disturbances from transport)

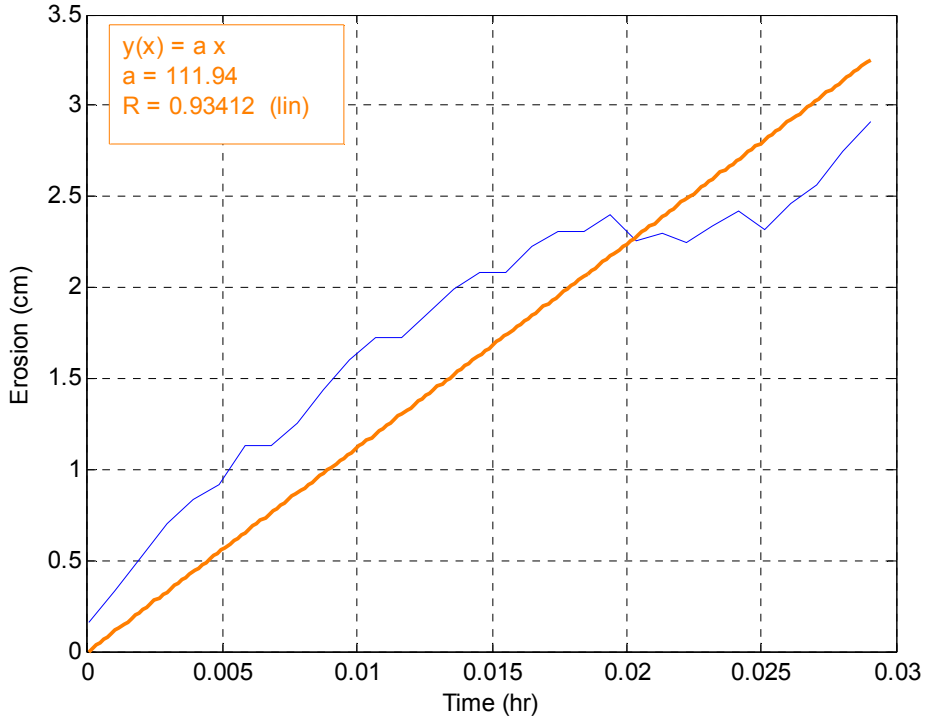

Figure C-41. Erosion versus time for specimen OS-33 top at 10.0 Pa

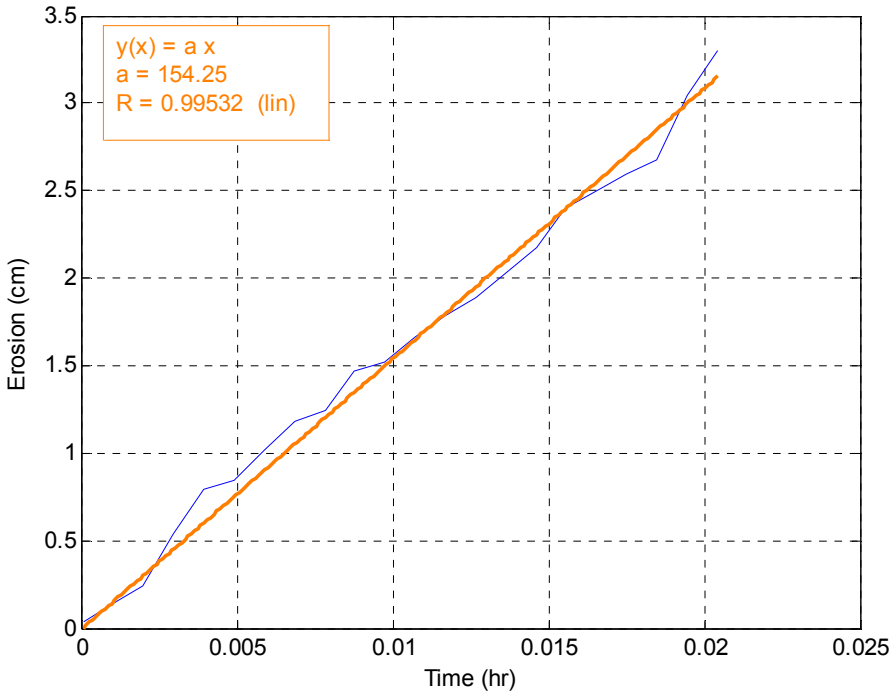

Figure C-42. Erosion versus time for specimen OS-33 top at 12.5 Pa

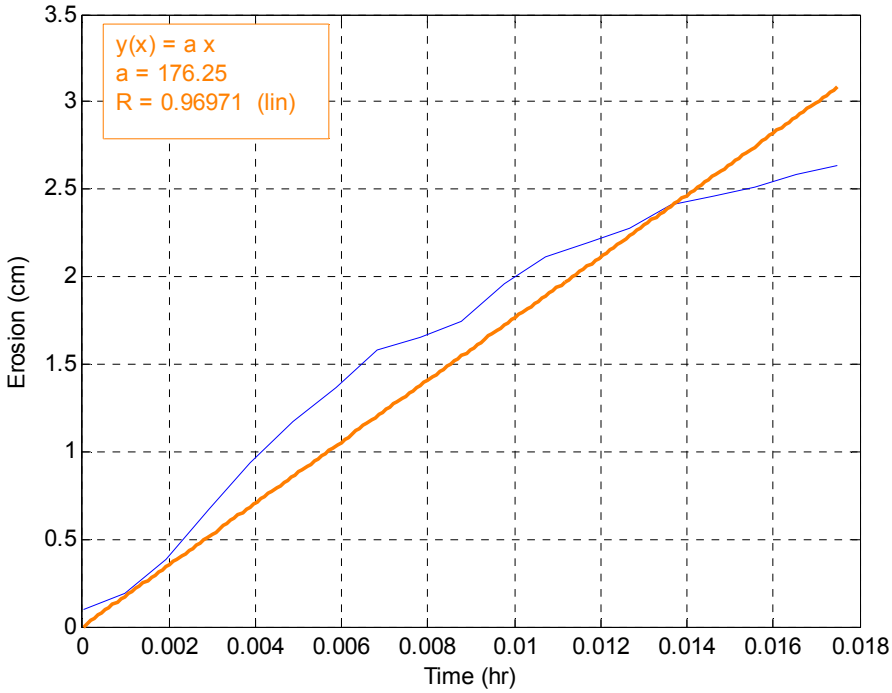

Figure C-43. Erosion versus time for specimen OS-33 top at 15.0 Pa

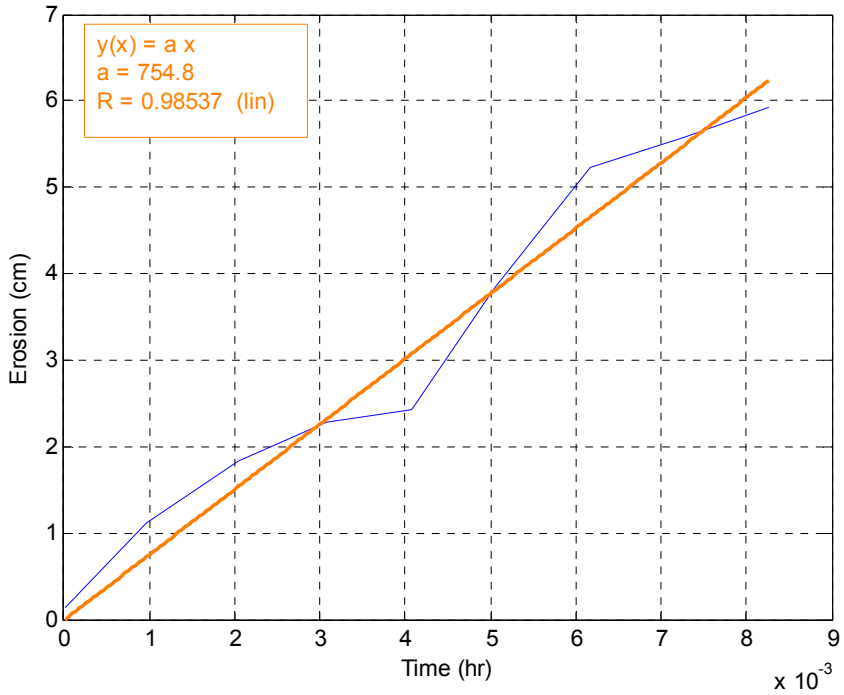

Figure C-44. Erosion versus time for specimen OS-33 top at 17.5 Pa (data omitted from erosion function due to irregular erosion; large "chunk" was removed indicating anomalous layer)

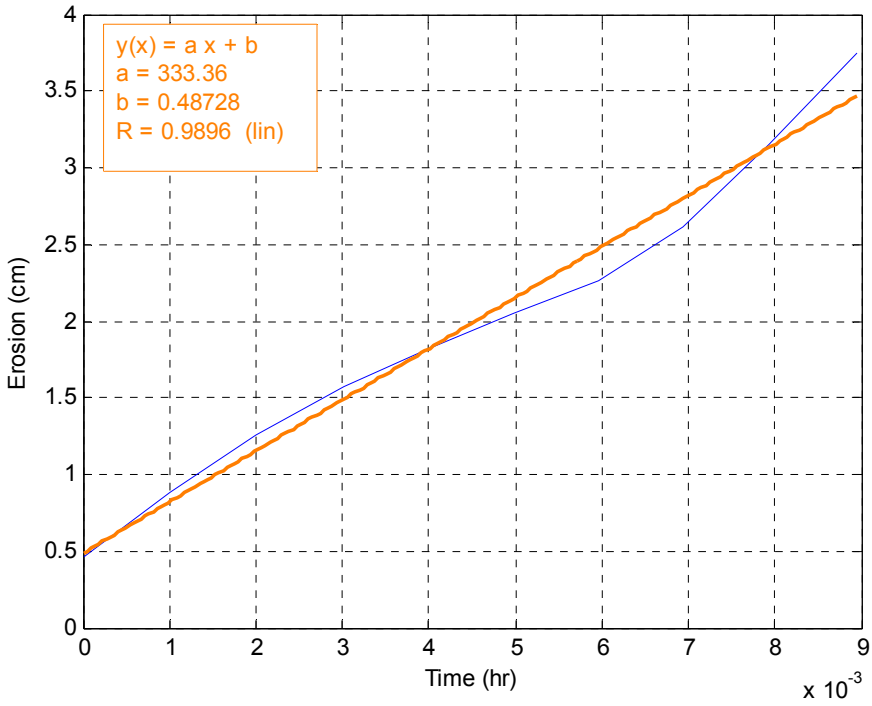

Figure C-45. Erosion versus time for specimen OS-33 top at 20.0 Pa

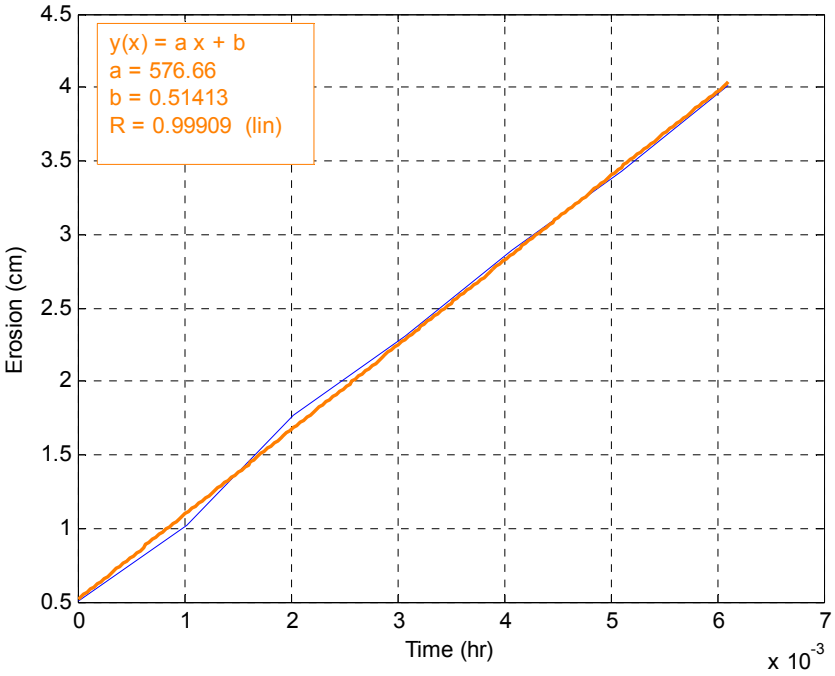

Figure C-46. Erosion versus time for specimen OS-33 top at 22.5 Pa

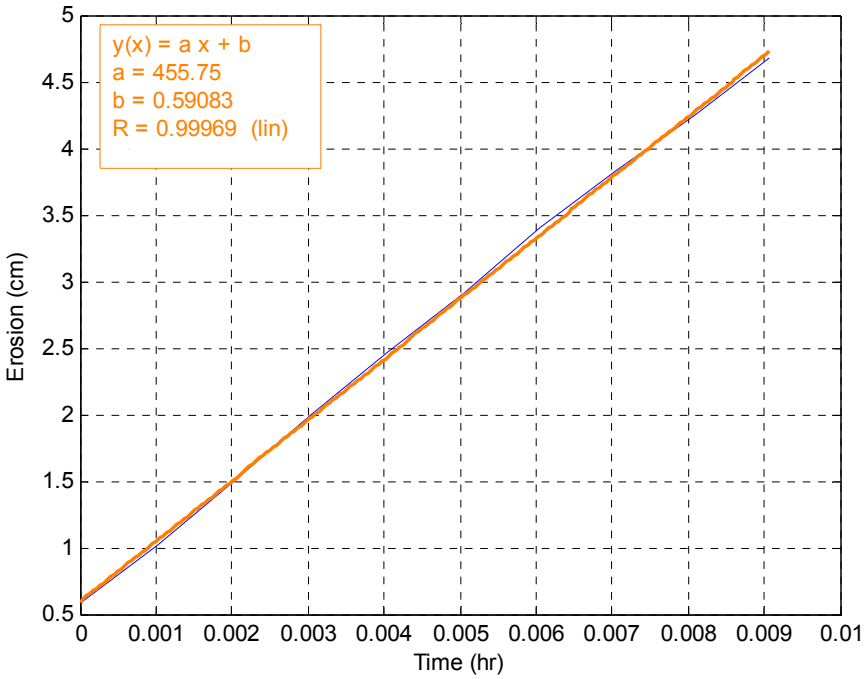

Figure C-47. Erosion versus time for specimen OS-33 top at 25.0 Pa

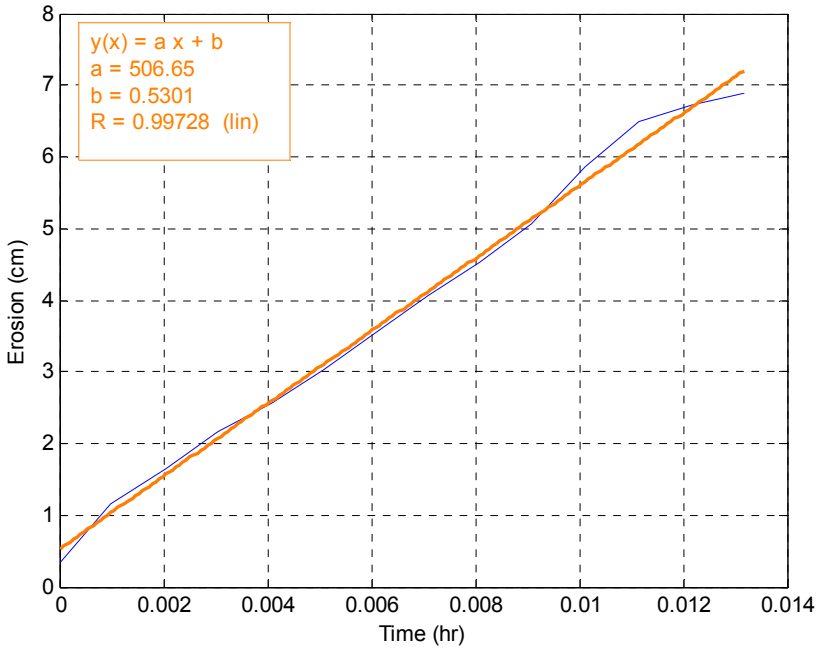

Figure C-48. Erosion versus time for specimen OS-33 top at 27.5 Pa

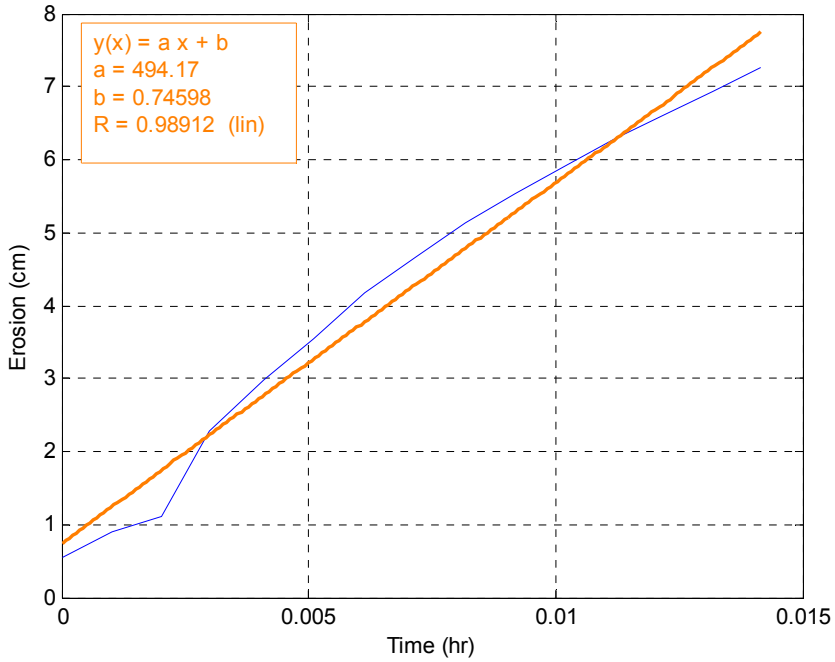

Figure C-49. Erosion versus time for specimen OS-33 top at 30.0 Pa

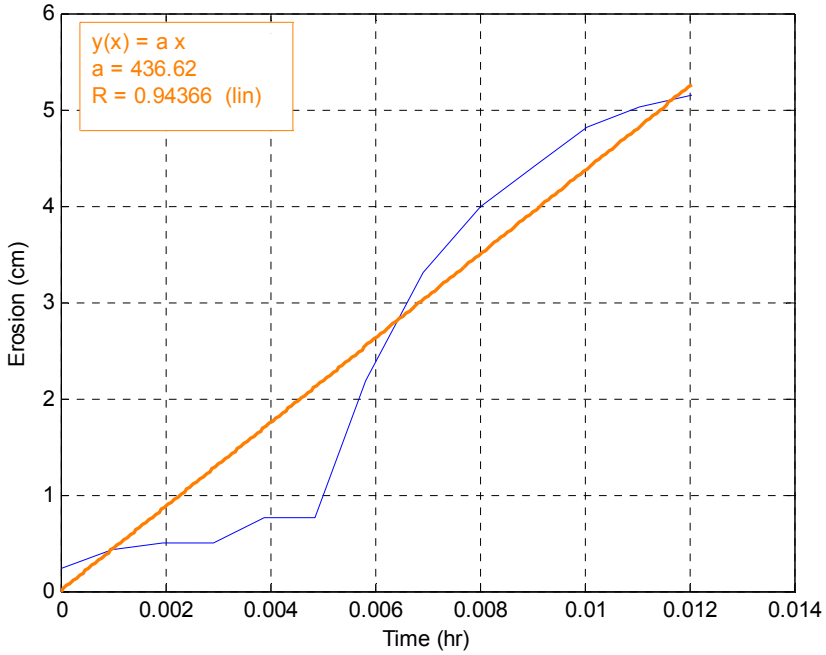

Figure C-50. Erosion versus time for specimen OS-33 bottom at 5.0 Pa (data removed from erosion function due to suspected surface damage)

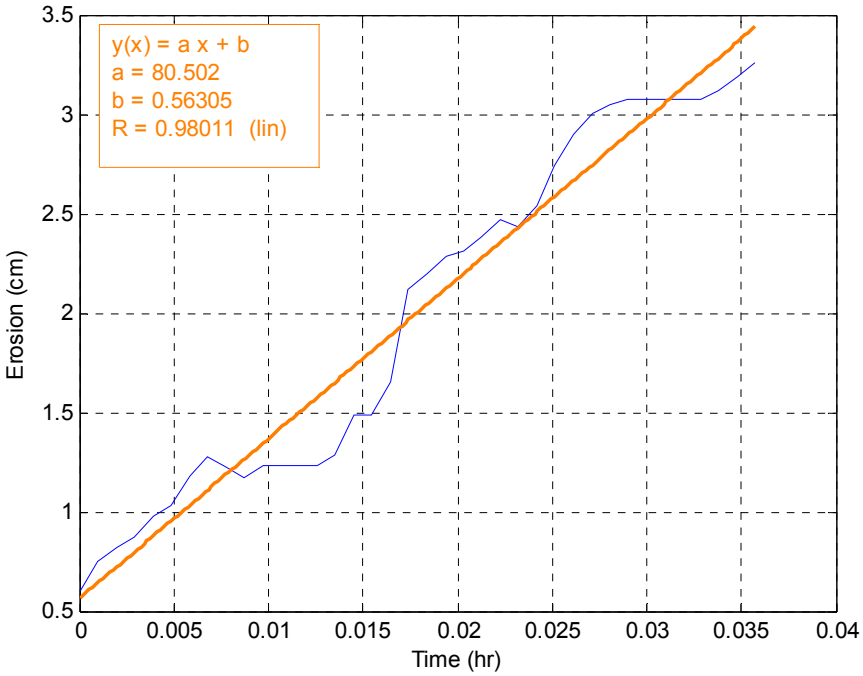

Figure C-51. Erosion versus time for specimen OS-33 bottom at 15.0 Pa

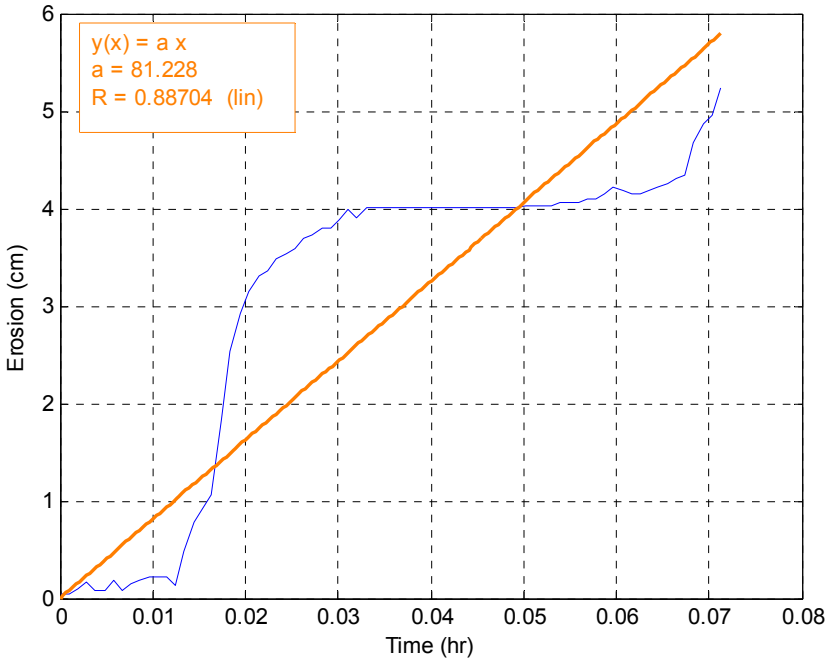

Figure C-52. Erosion versus time for specimen OS-33 bottom at 20.0 Pa

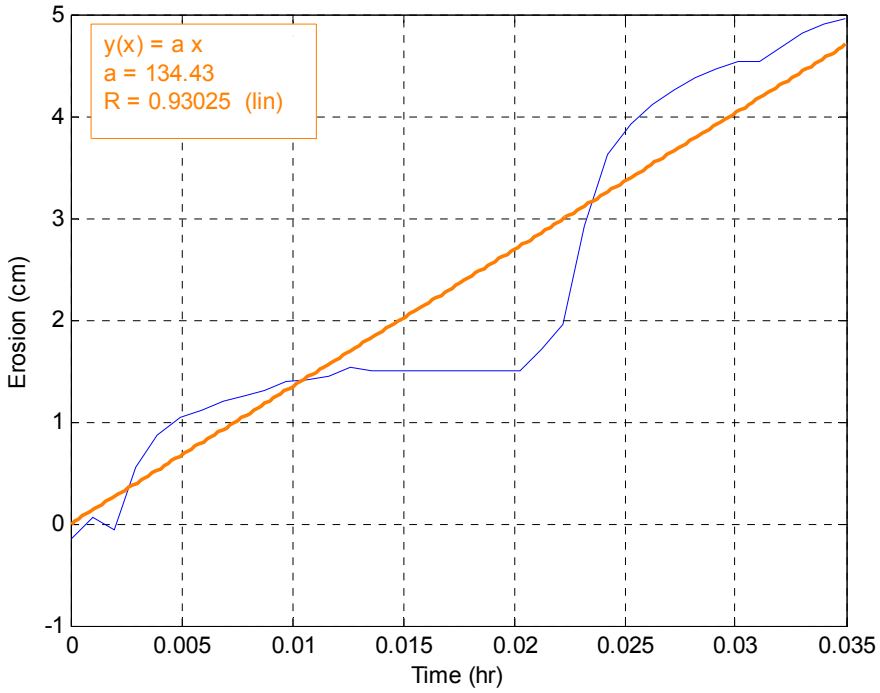

Figure C-53. Erosion versus time for specimen OS-33 bottom at 25.0 Pa

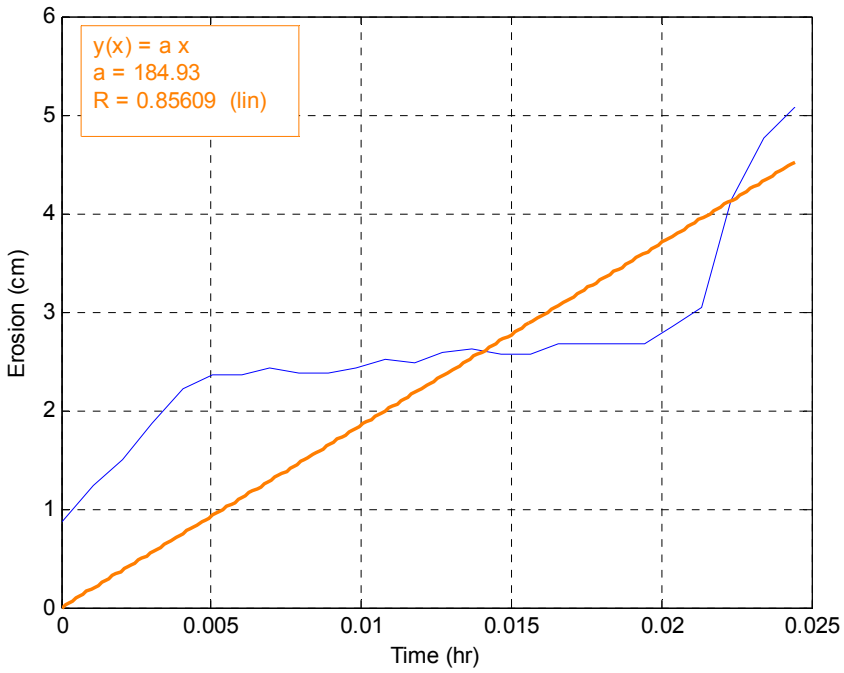

Figure C-54. Erosion versus time for specimen OS-33 bottom at 30.0 Pa

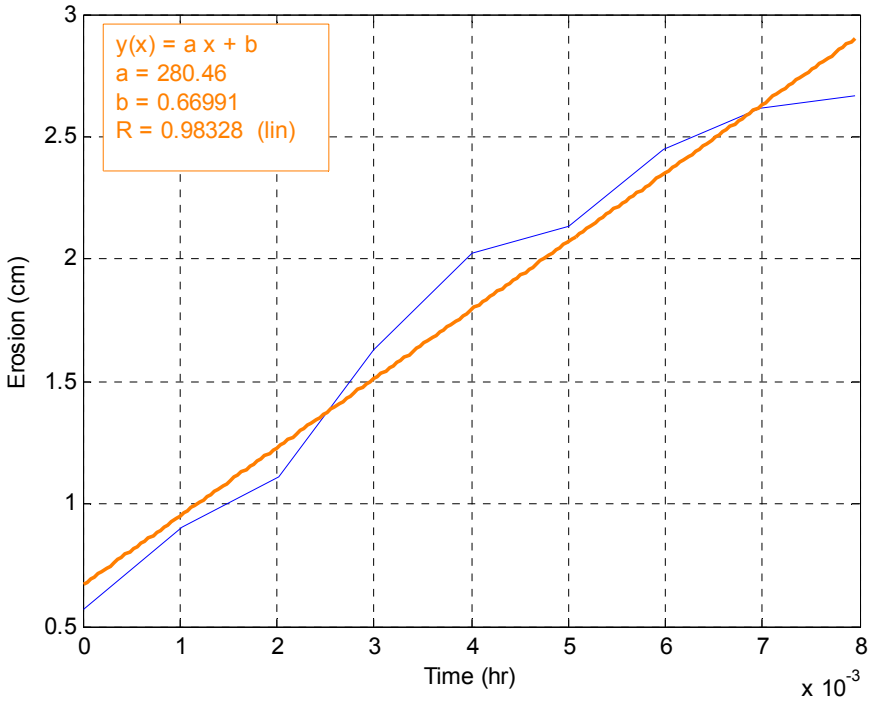

Figure C-55. Erosion versus time for specimen OS-35 46-48 bottom at 5.0 Pa

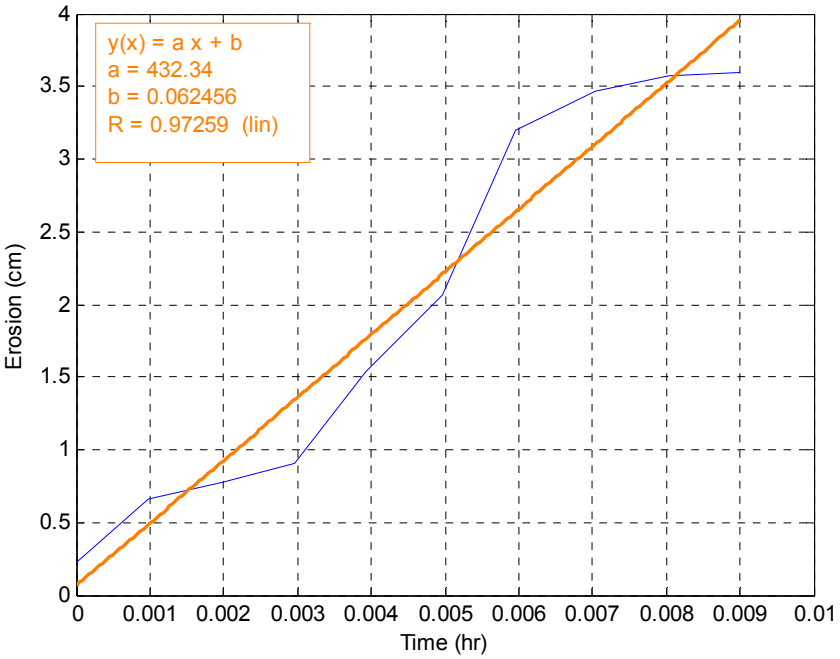

Figure C-56. Erosion versus time for specimen OS-35 46-48 bottom at 20.0 Pa

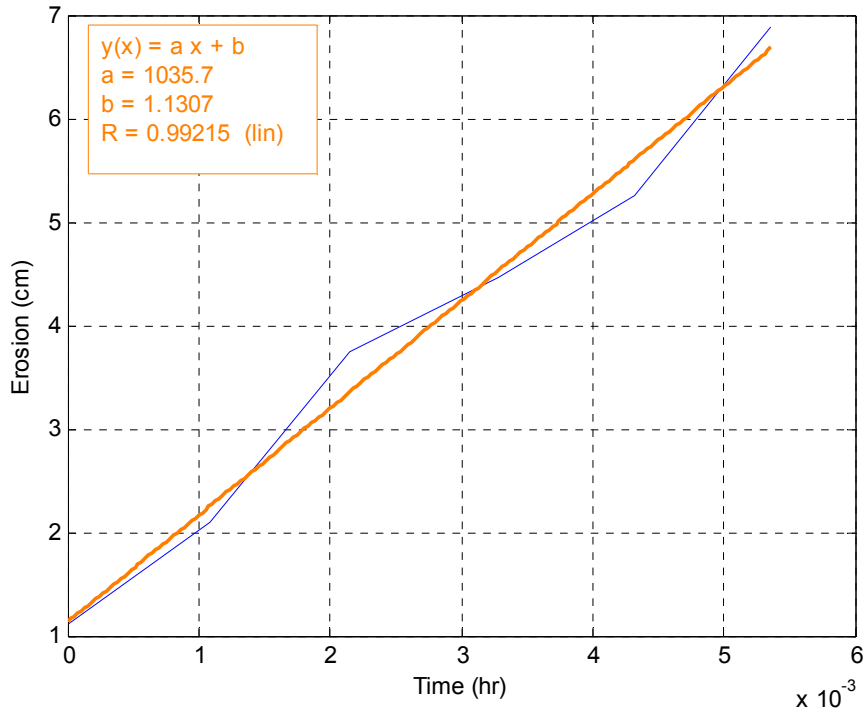

Figure C-57. Erosion versus time for specimen OS-35 46-48 bottom at 30.0 Pa

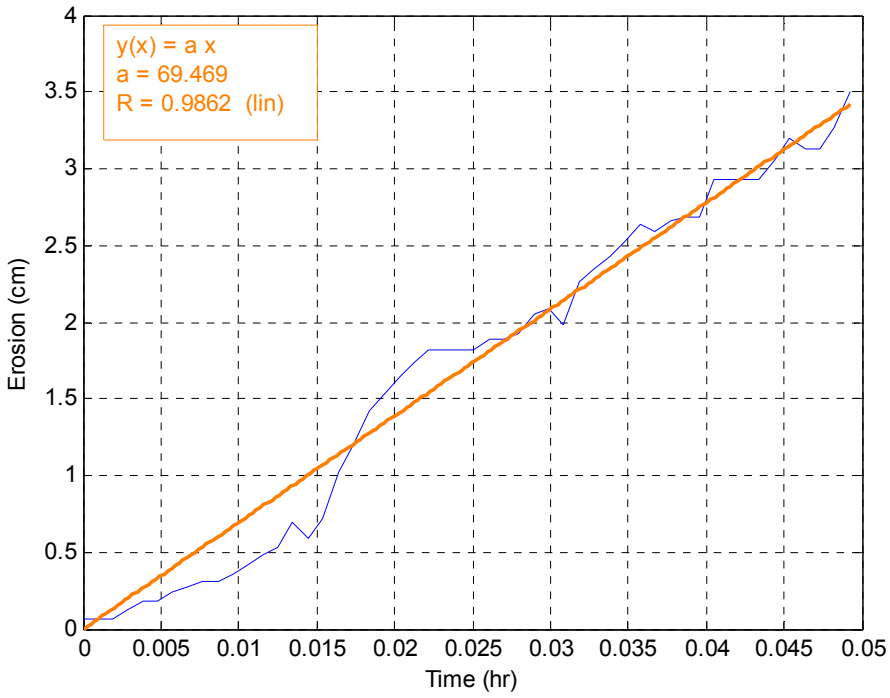

Figure C-58. Erosion versus time for specimen OS-44 bottom at 5.0 Pa

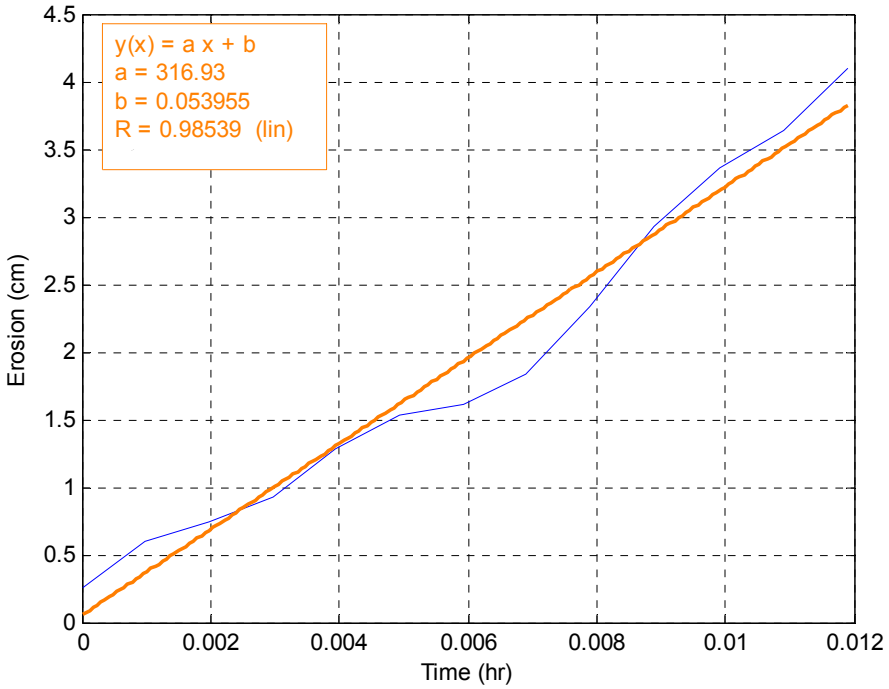

Figure C-59. Erosion versus time for specimen OS-44 bottom at 10.0 Pa

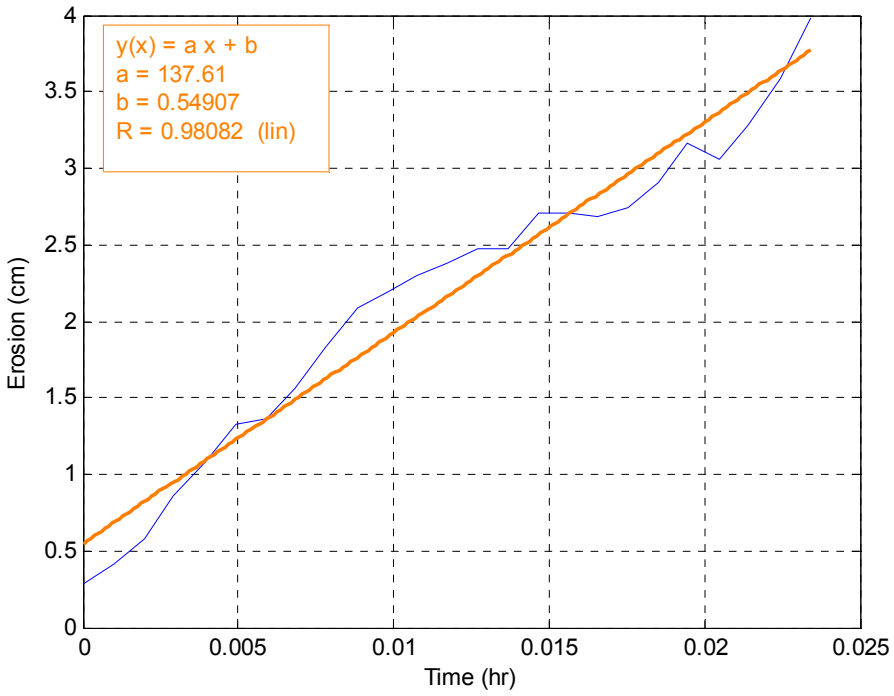

Figure C-60. Erosion versus time for specimen OS-44 bottom at 15.0 Pa

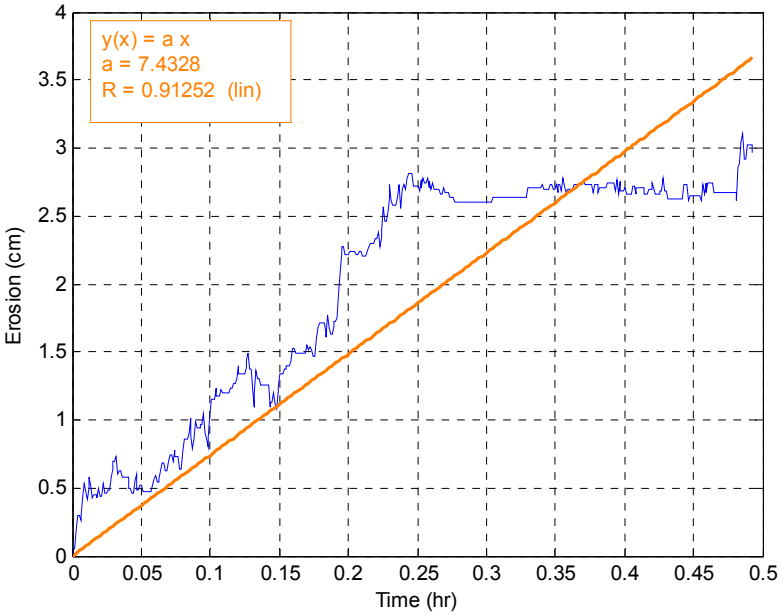

Figure C-61. Erosion versus time for specimen OS-44 bottom at 7.5 Pa

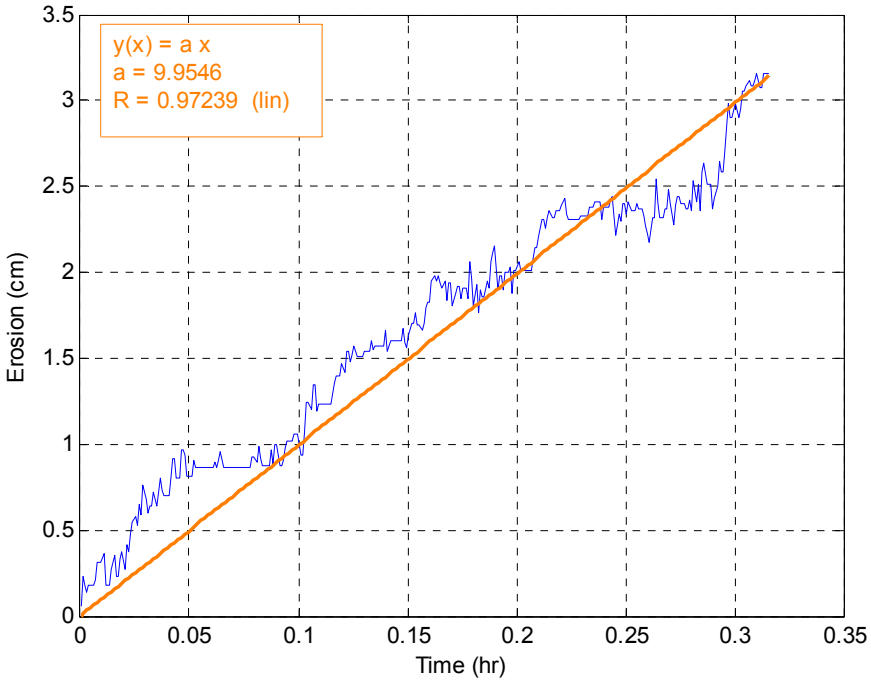

Figure C-62. Erosion versus time for specimen OS-44 bottom at 12.5 Pa

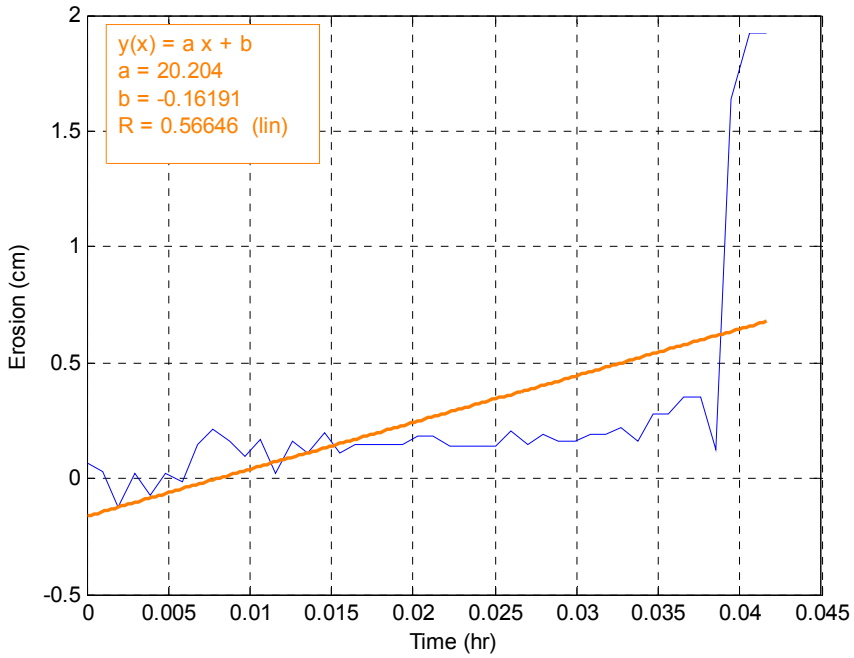

Figure C-63. Erosion versus time for specimen OS-44 at 17.5 Pa

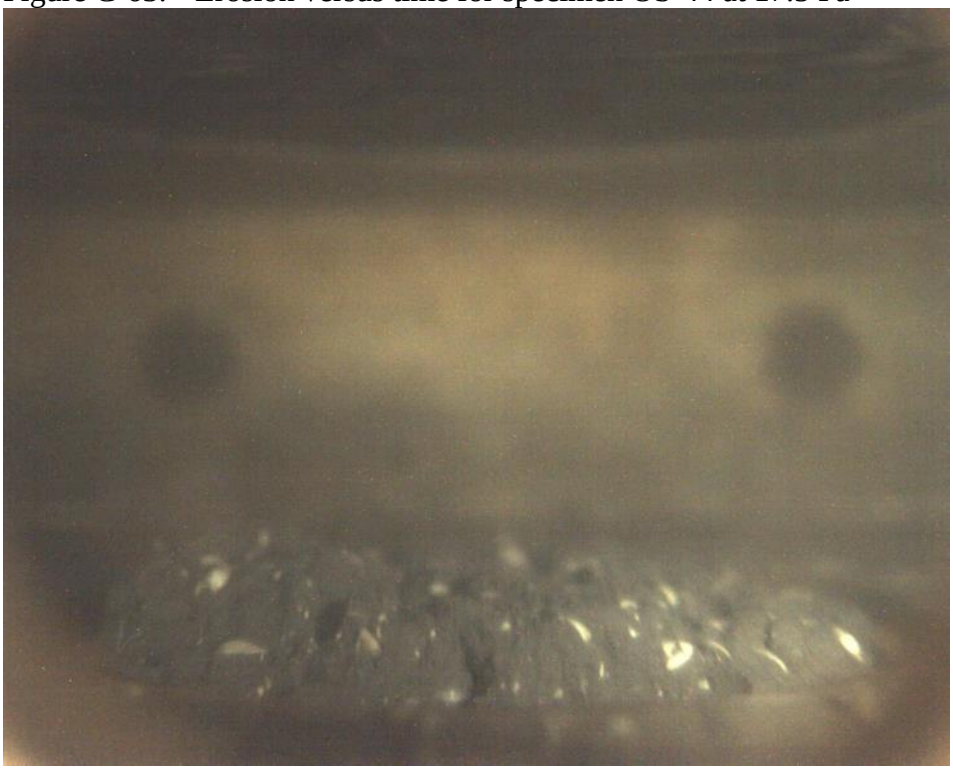

Figure C-64. Photograph of shell layer that is believed to be responsible for slow erosion in Figs. C-61 through C-63.

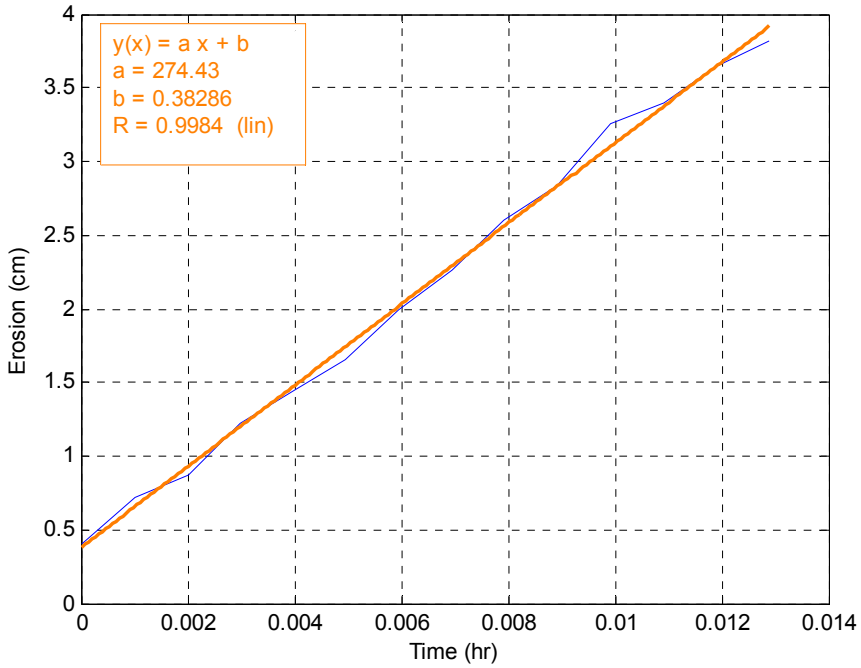

Figure C-65. Erosion versus time for specimen OS-44 very bottom at 17.5 Pa

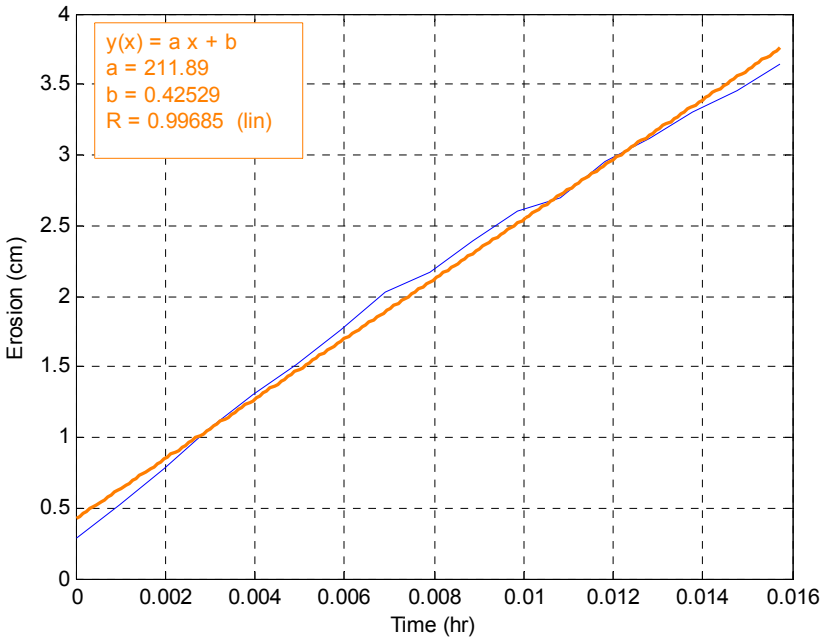

Figure C-66. Erosion versus time for specimen OS-44 very bottom at 20.0 Pa

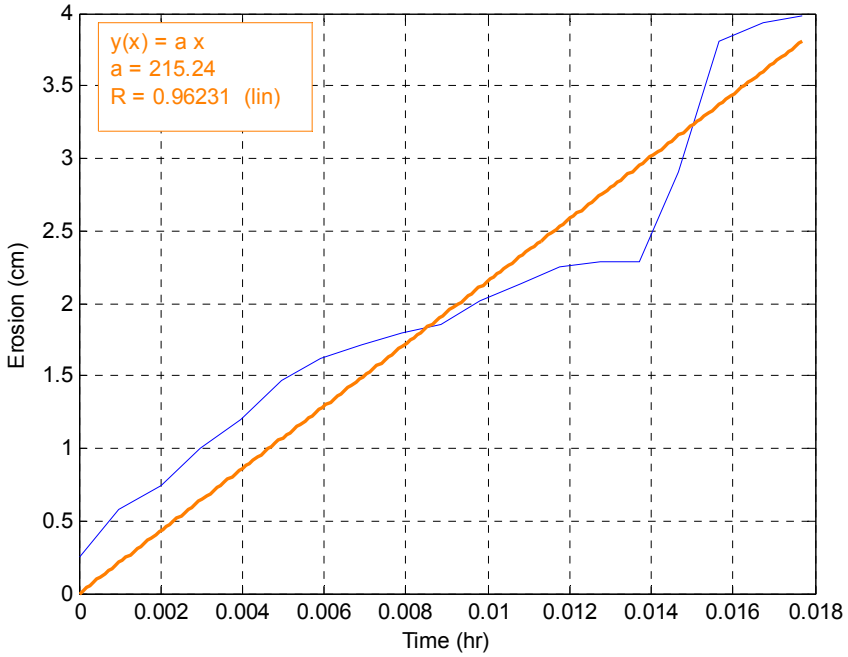

Figure C-66. Erosion versus time for specimen OS-44 very bottom at 20.0 Pa

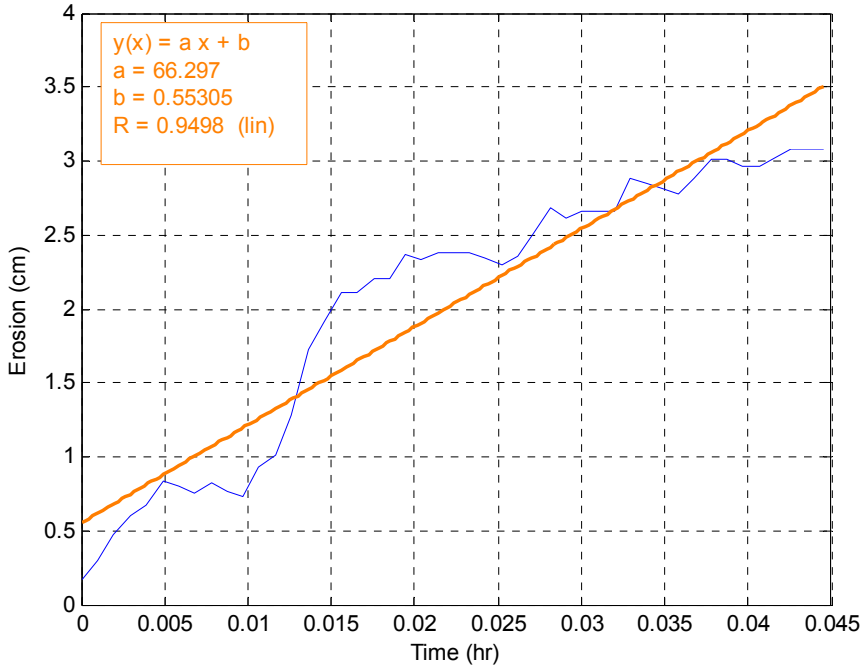

Figure C-67. Erosion versus time for specimen OS-28 top at 5.0 Pa

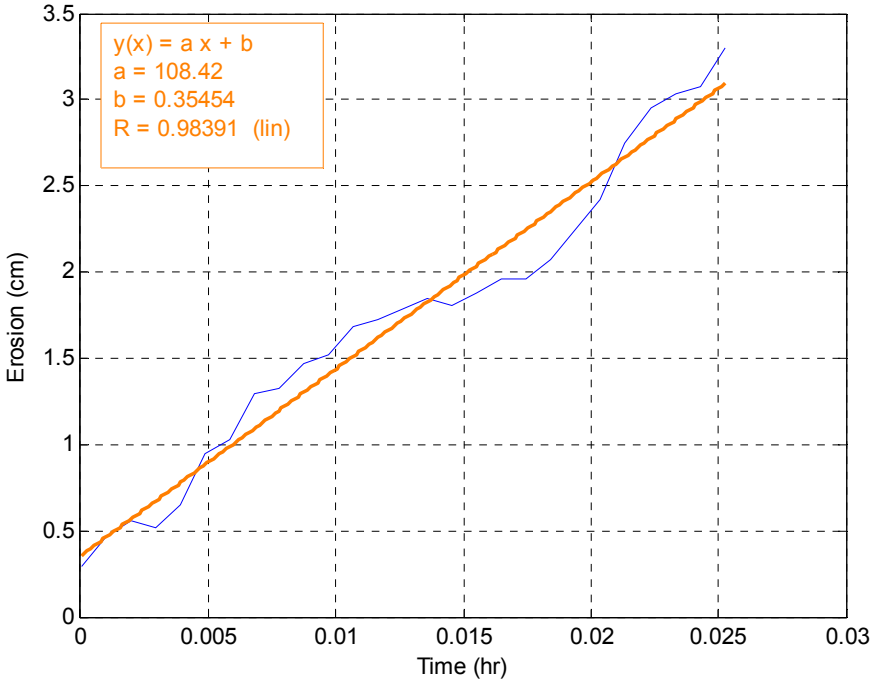

Figure C-68. Erosion versus time for specimen OS-28 top at 10.0 Pa

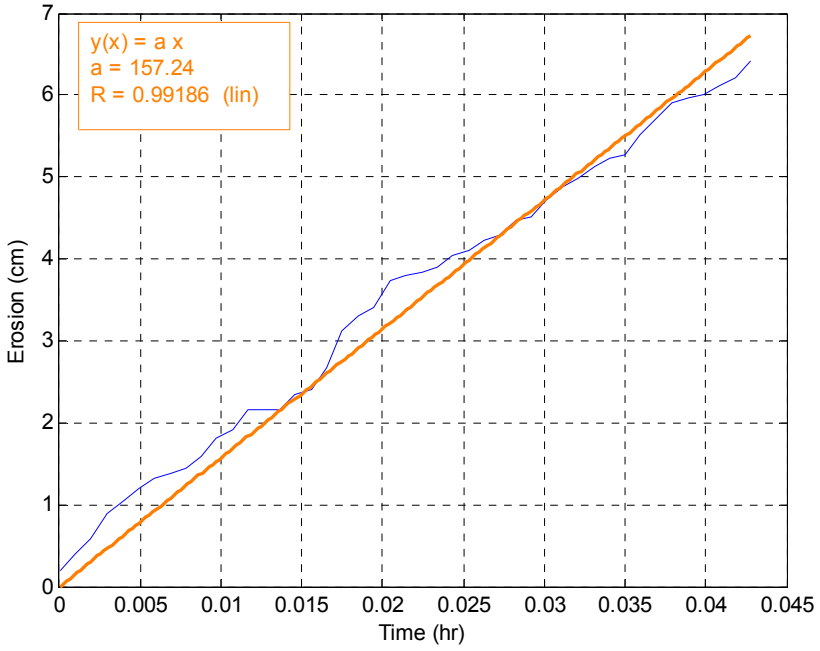

Figure C-69. Erosion versus time for specimen OS-28 top at 15.0 Pa

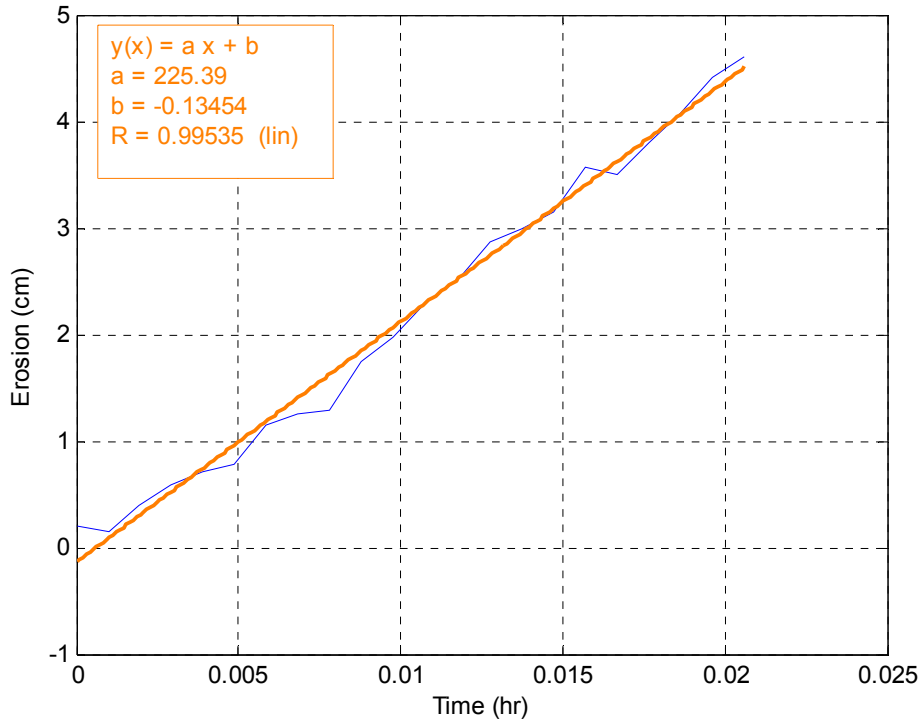

Figure C-70. Erosion versus time for specimen OS-28 top at 20.0 Pa

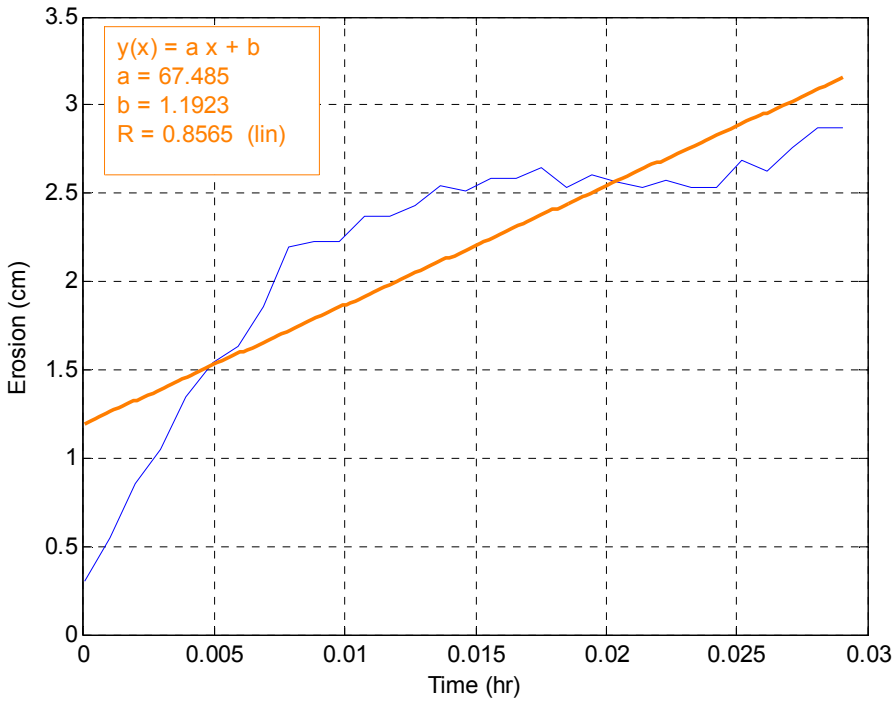

Figure C-71. Erosion versus time for specimen OS-28 top at 25.0 Pa

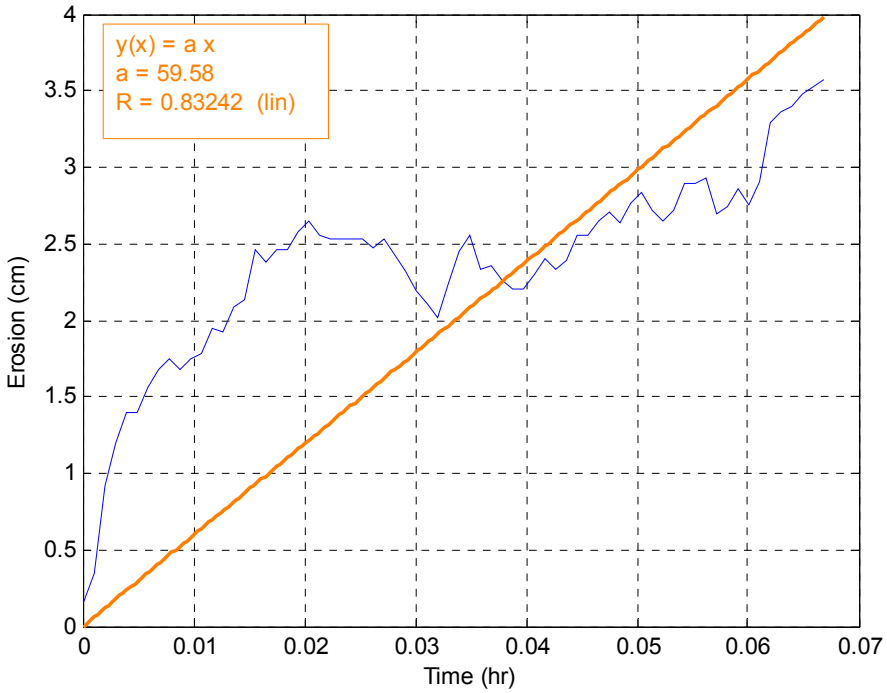

Figure C-72. Erosion versus time for specimen OS-28 bottom at 7.5 Pa

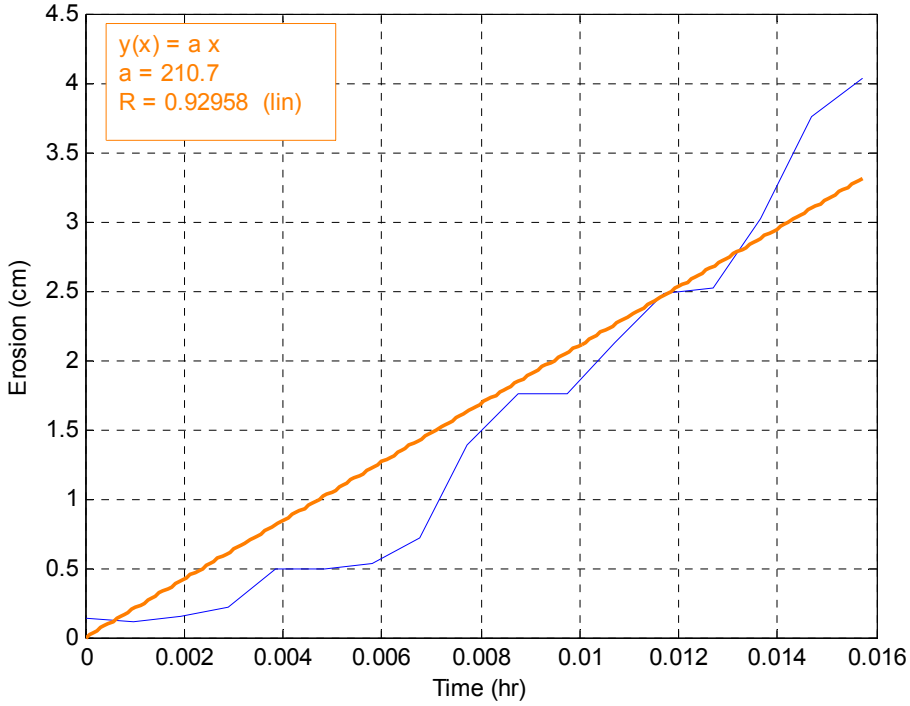

Figure C-73. Erosion versus time for specimen OS-28 bottom at 12.5 Pa

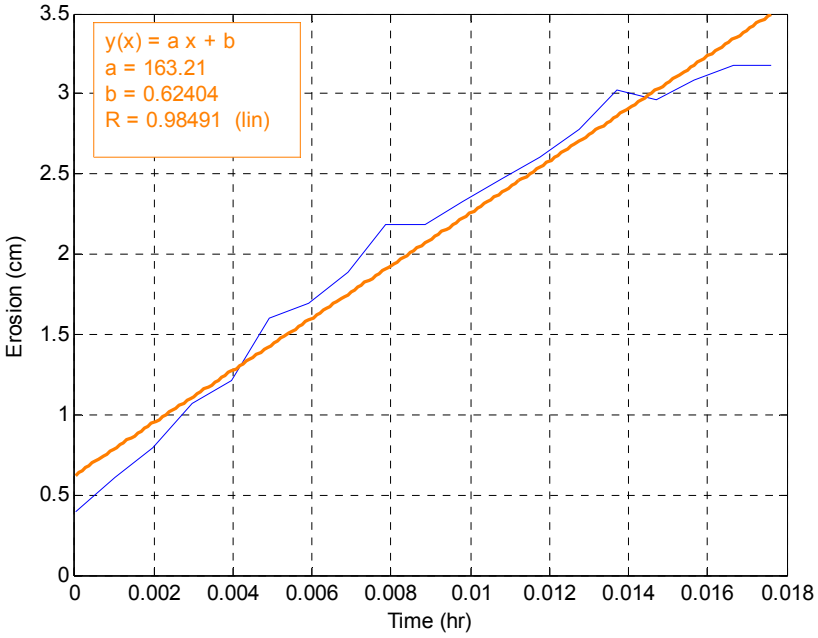

Figure C-74. Erosion versus time for specimen OS-28 bottom at 17.5 Pa

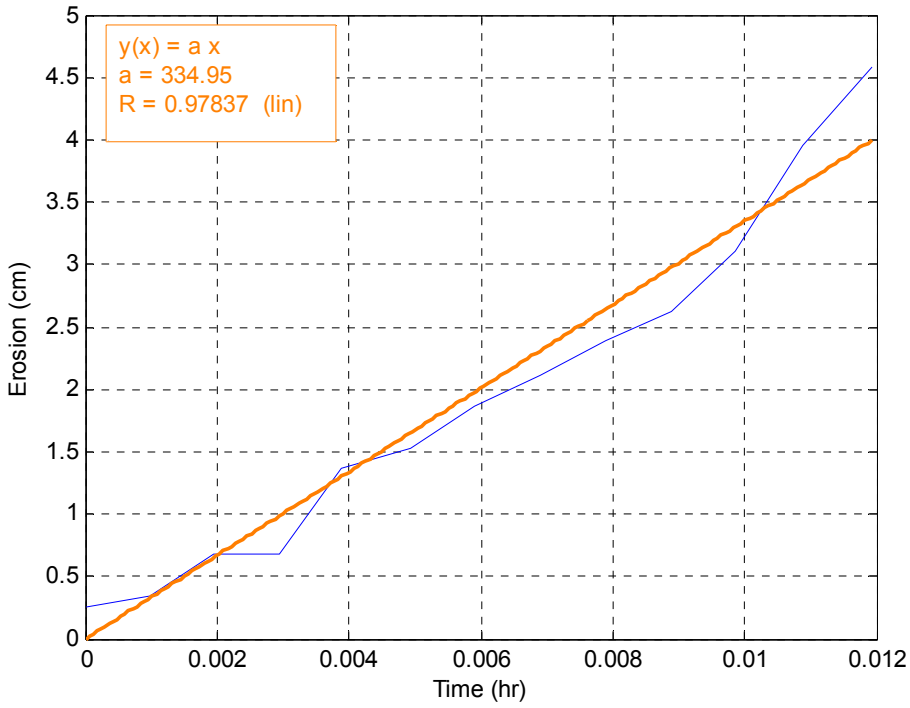

Figure C-75. Erosion versus time for specimen OS-28 bottom at 22.5 Pa

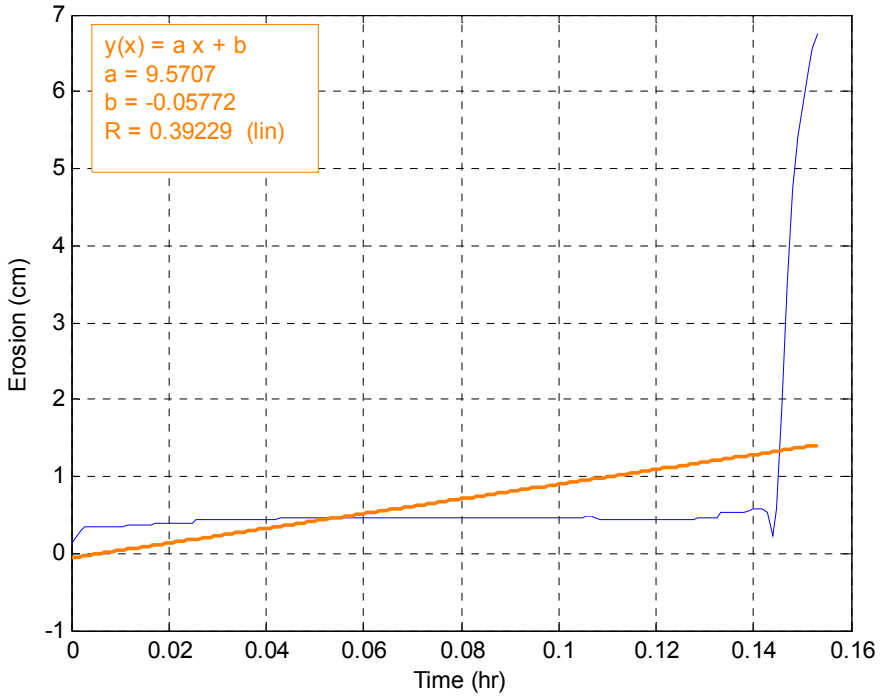

Figure C-76. Erosion versus time for specimen OS-104 bottom at 5.0 Pa

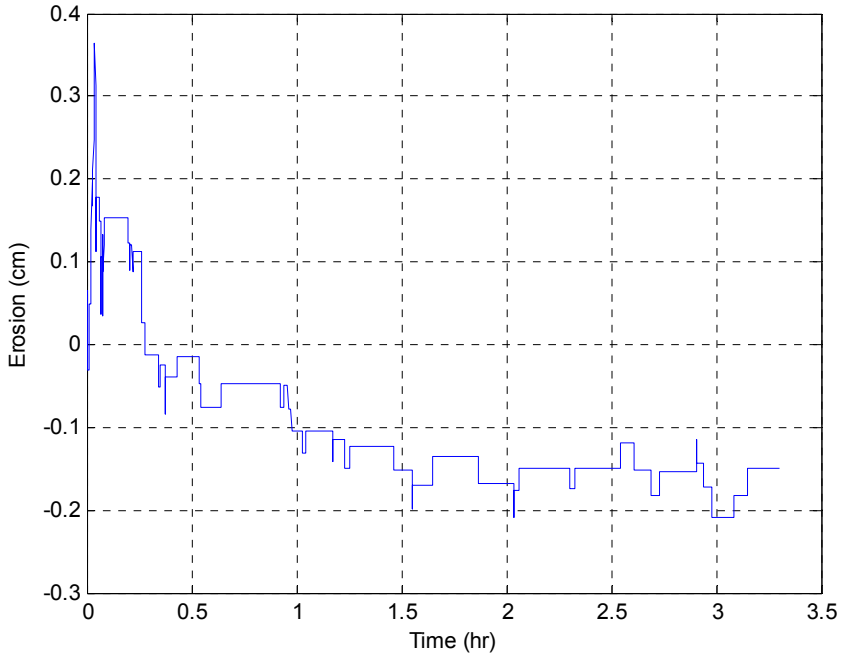

Figure C-77. Erosion versus time for specimen OS-104 bottom at 10.0 Pa

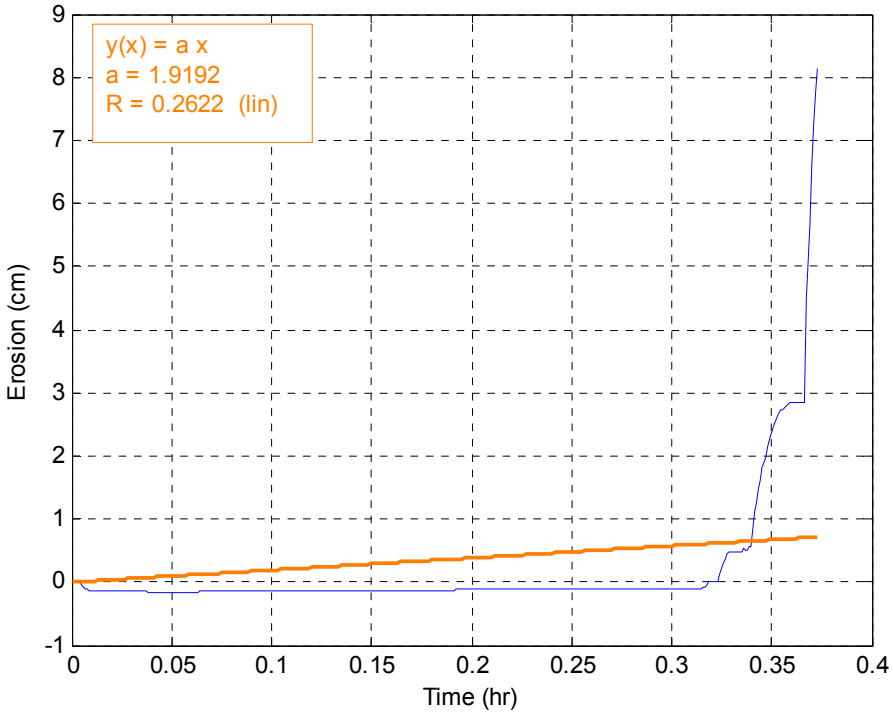

Figure C-78. Erosion versus time for specimen OS-104 bottom at 15.0 Pa

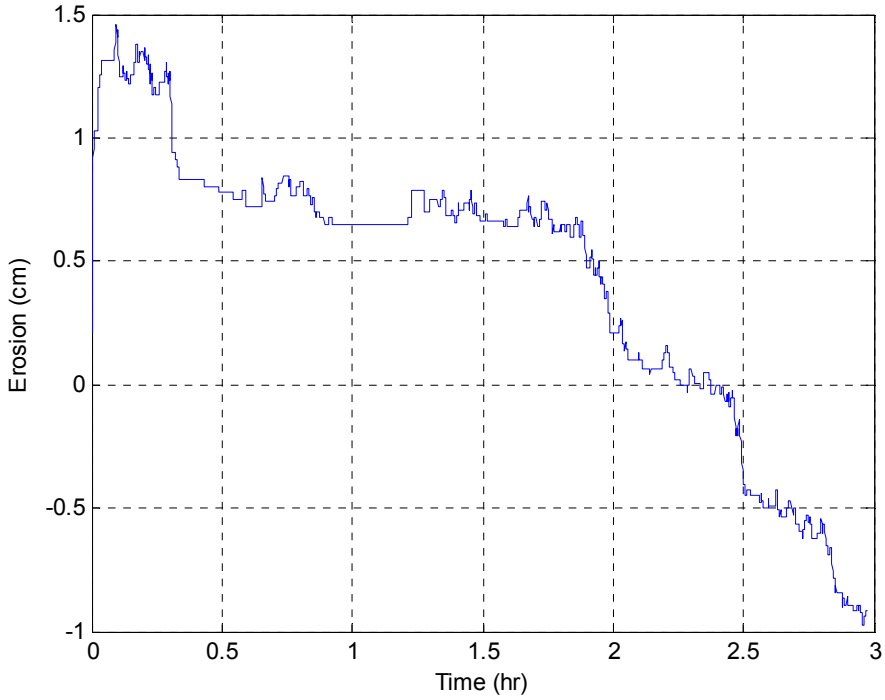

Figure C-79. Erosion versus time for specimen OS-104 bottom at 20.0 Pa

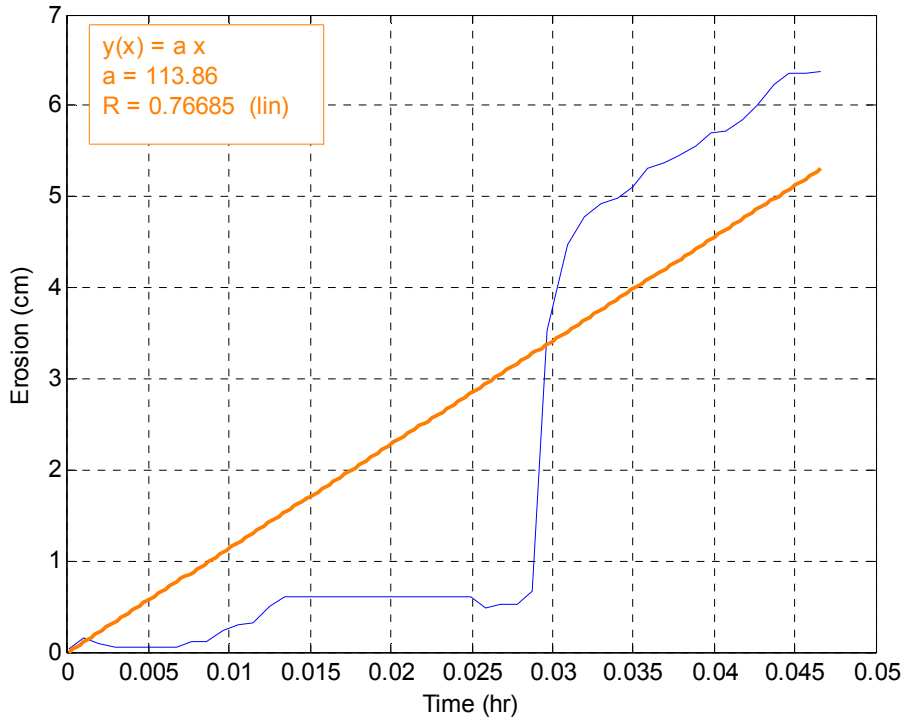

Figure C-80. Erosion versus time for specimen OS-104 bottom at 25.0 Pa

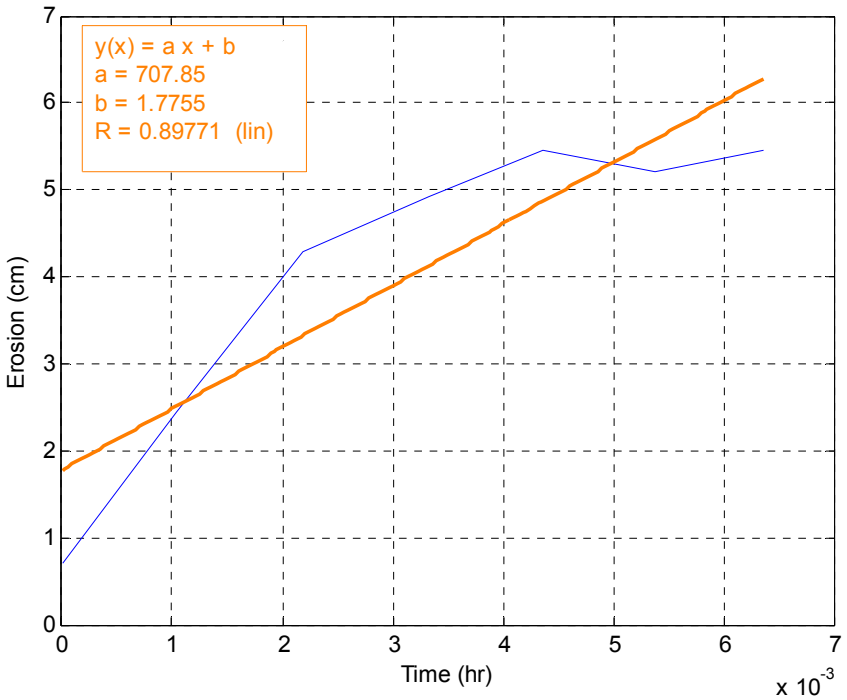

Figure C-81. Erosion versus time for specimen OS-104 bottom at 30.0 Pa

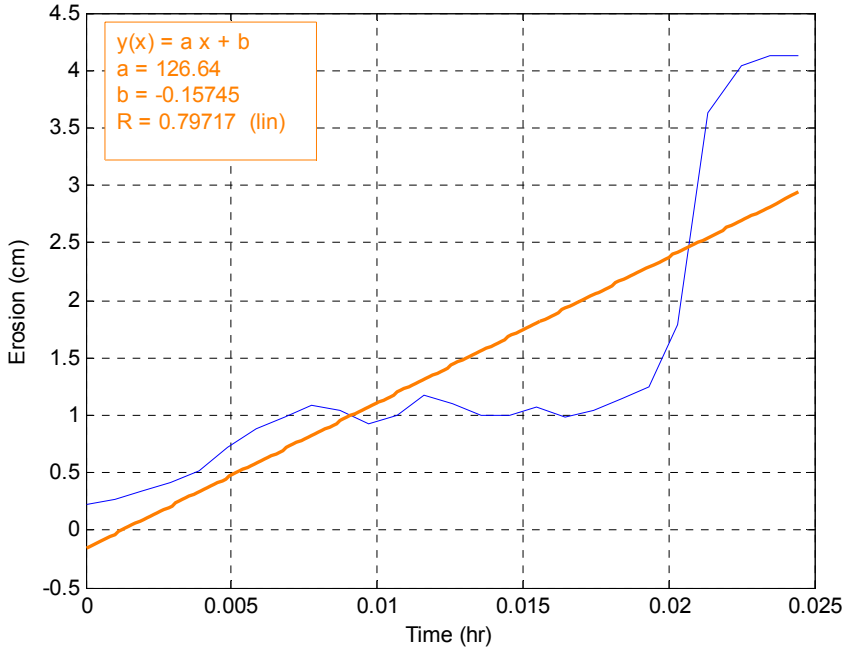

Figure C-82. Erosion versus time for specimen OS-104 bottom at 27.5 Pa

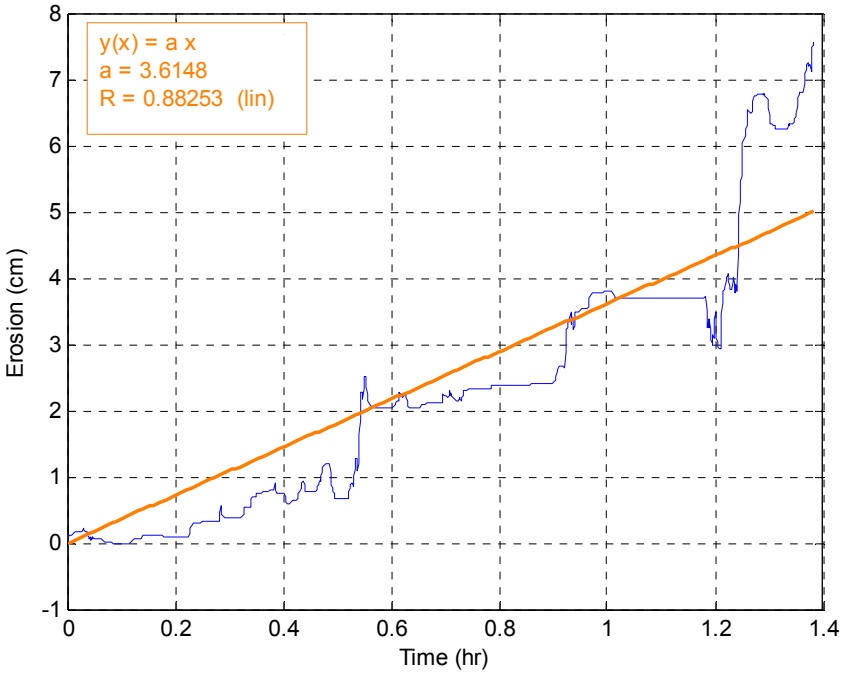

Figure C-83. Erosion versus time for specimen OS-104 top at 7.50 Pa

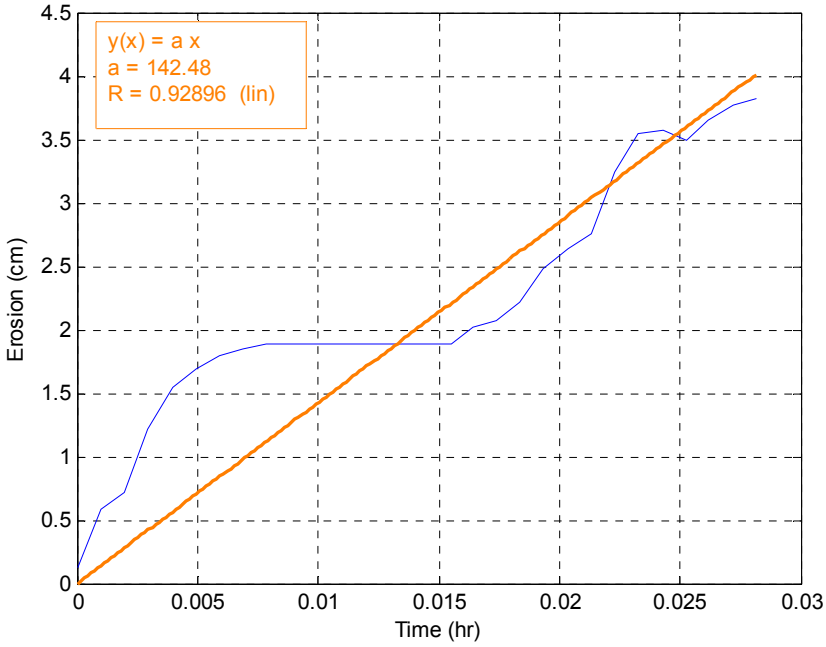

Figure C-83. Erosion versus time for specimen ZTC-104 top at 17.5 Pa

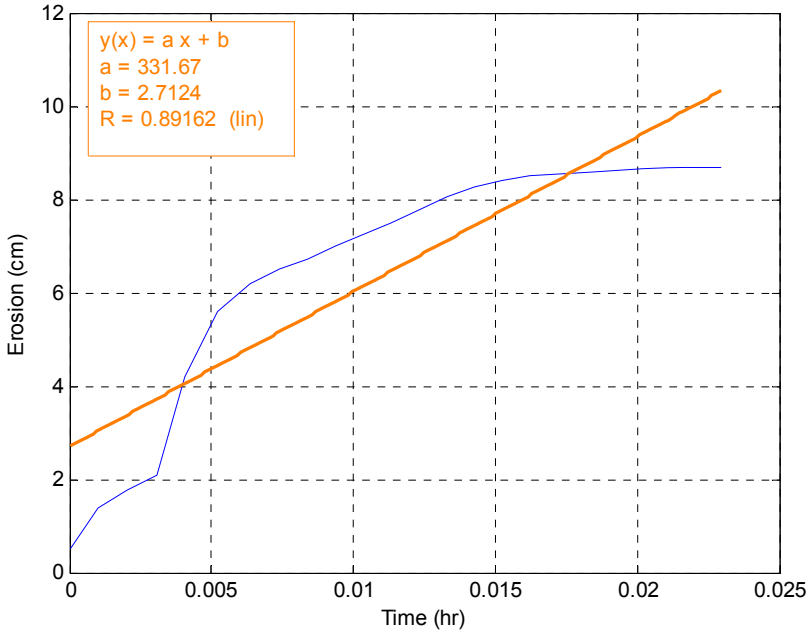

Figure C-84. Erosion versus time for specimen OS-104 bottom at 22.5 Pa

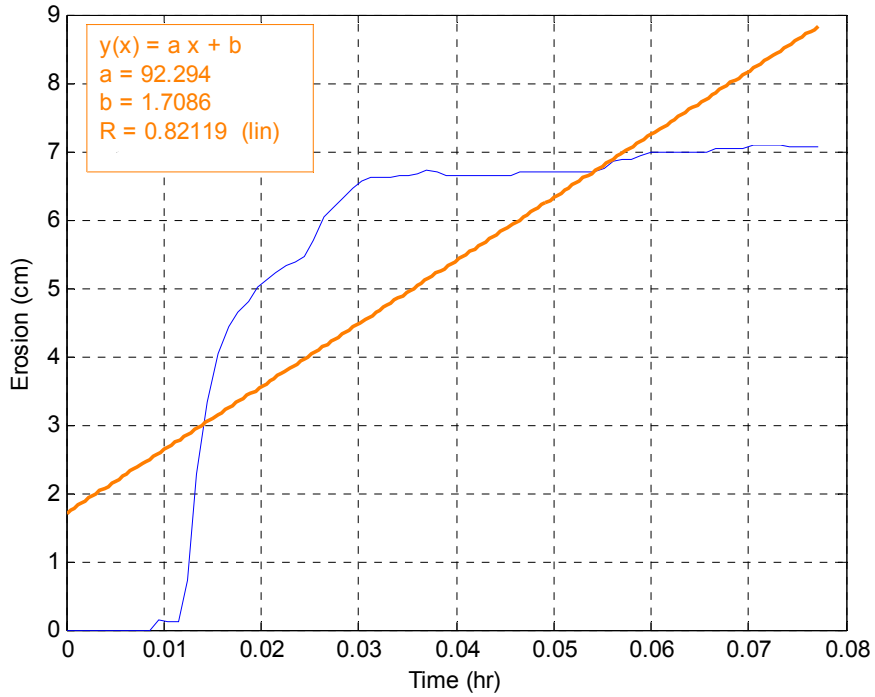

Figure C-85. Erosion versus time for specimen OS-104 bottom at 20.0 Pa

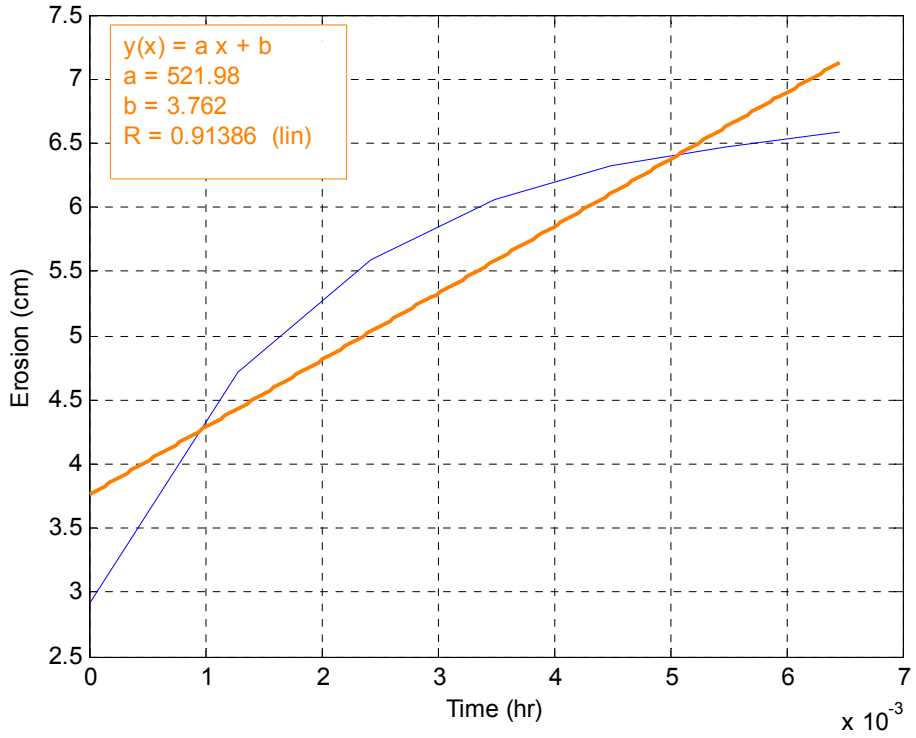

Figure C-86. Erosion versus time for specimen OS-104 bottom at 25.0 Pa

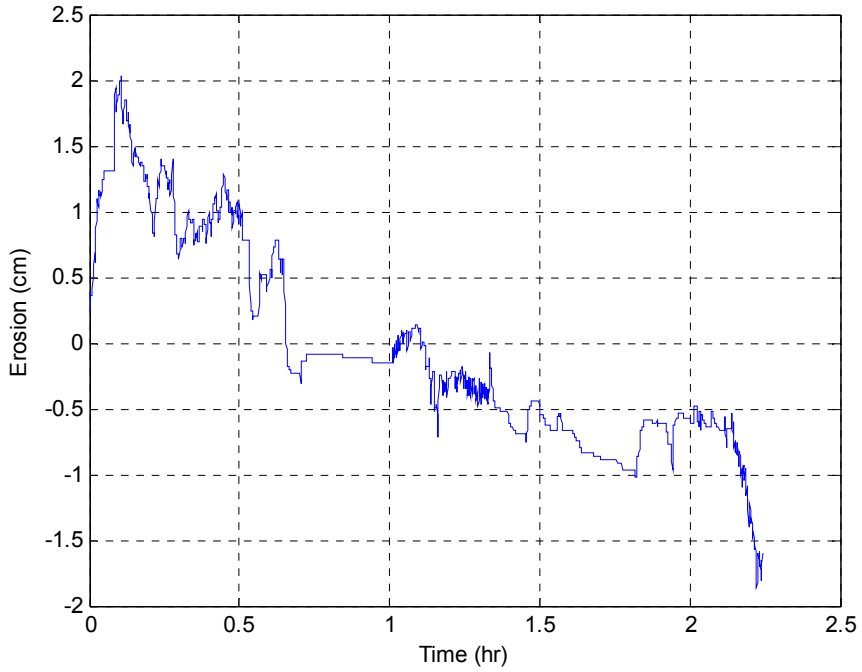

Figure C-87. Erosion versus time for specimen OS-26 at 5.0 Pa

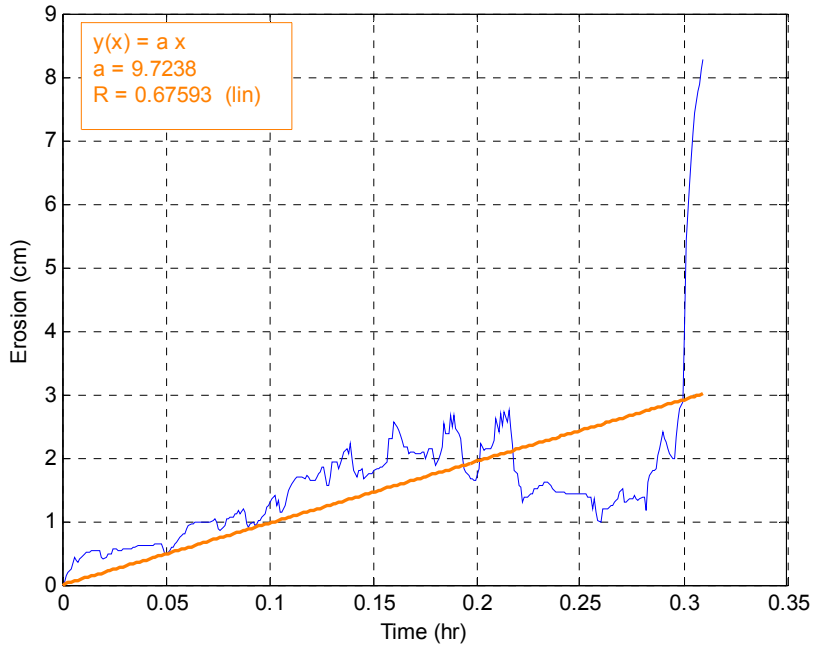

Figure C-88. Erosion versus time for specimen OS-26 at 10.0 Pa

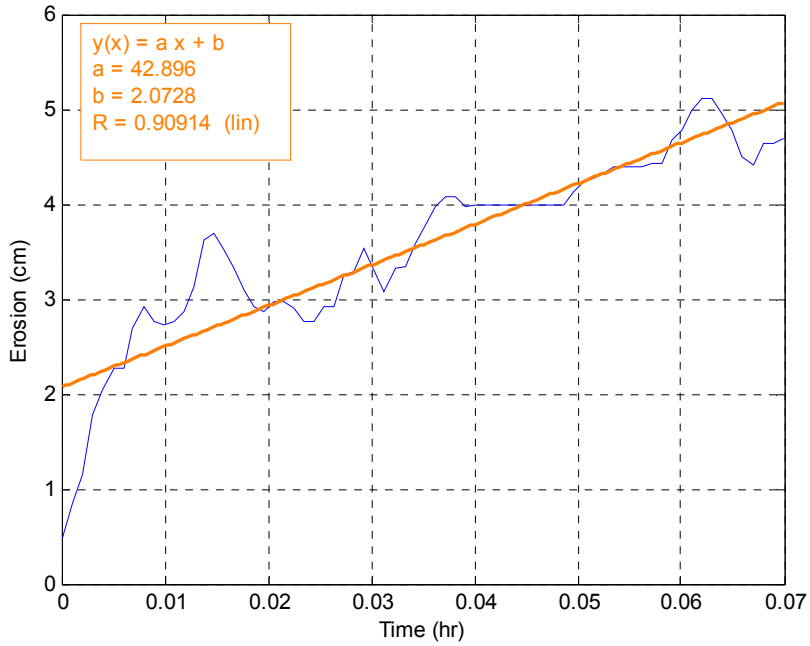

Figure C-89. Erosion versus time for specimen OS-26 at 15.0 Pa

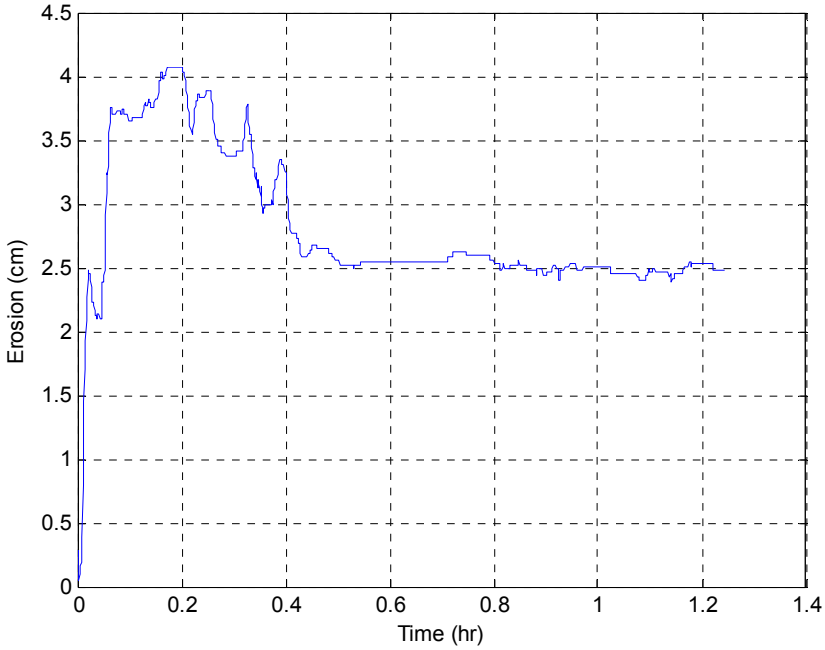

Figure C-90. Erosion versus time for specimen OS-26 at 12.50 Pa

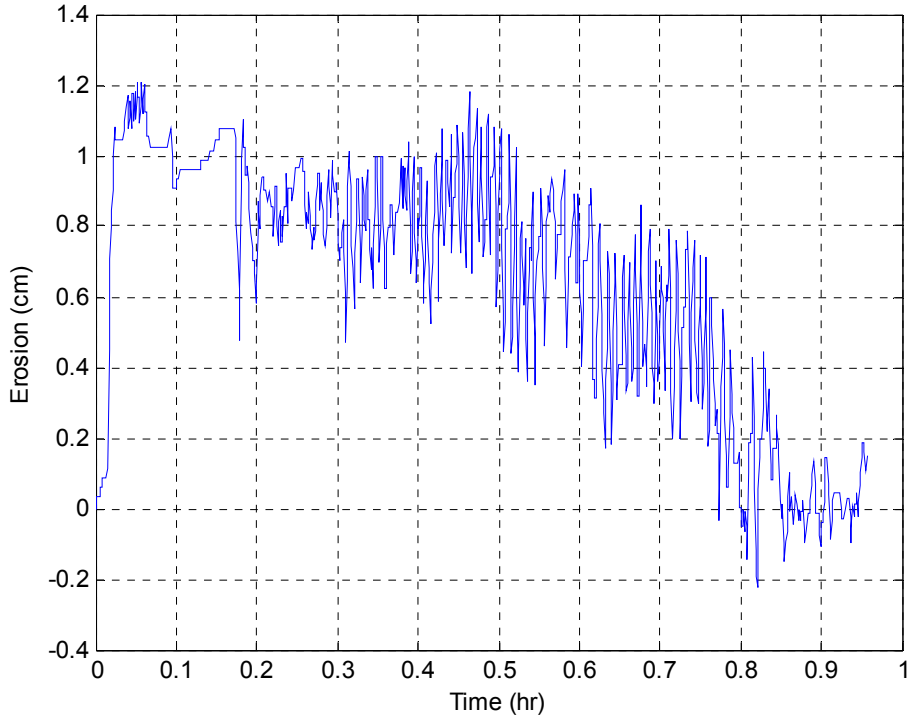

Figure C-91. Erosion versus time for specimen OS-26 at 7.50 Pa

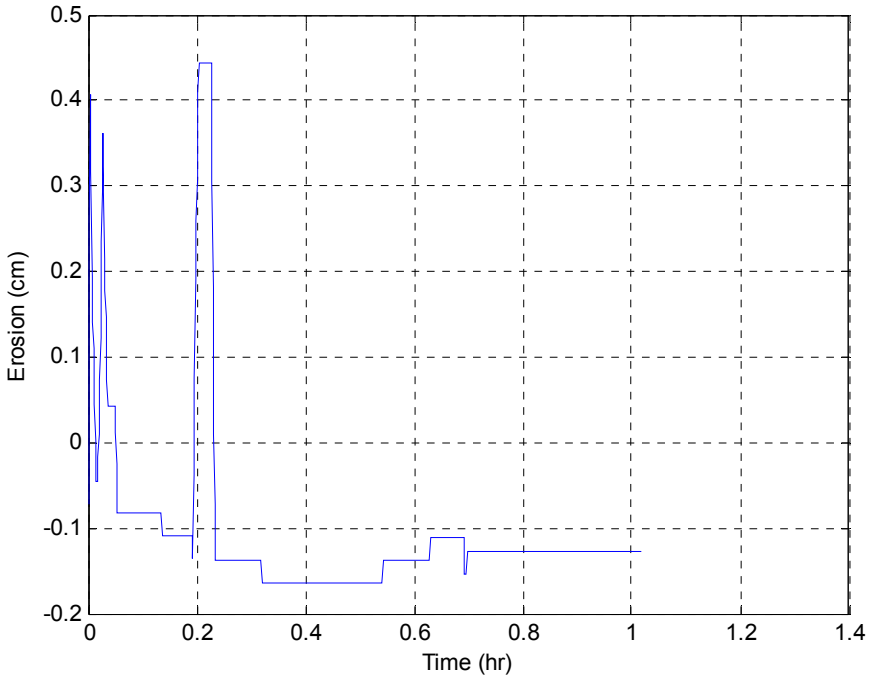

Figure C-92. Erosion versus time for specimen OS-102 top at 5.0 Pa

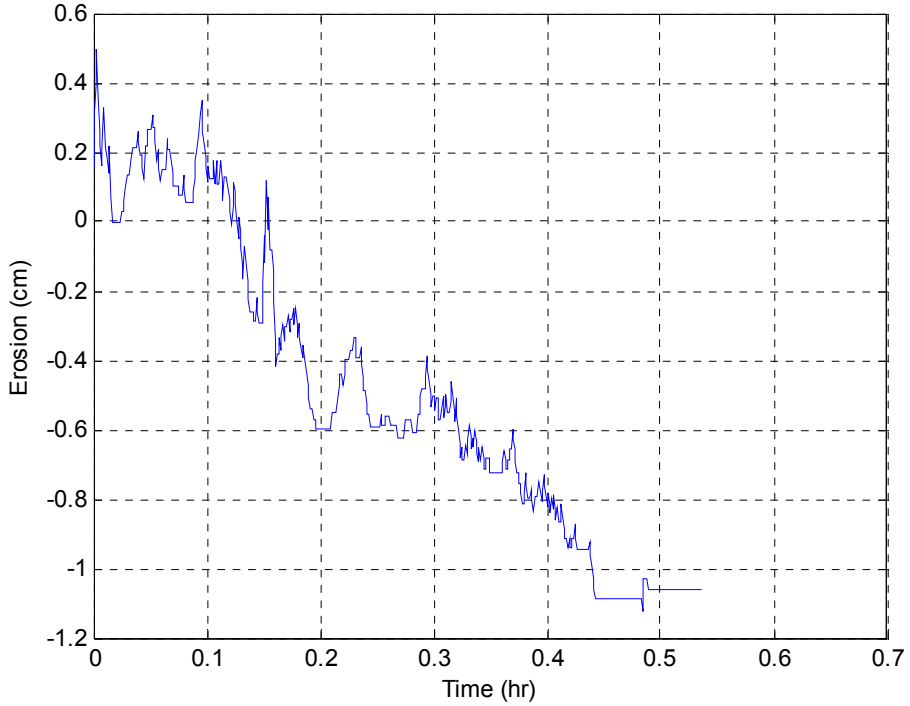

Figure C-93. Erosion versus time for specimen OS-102 top at 10.0 Pa

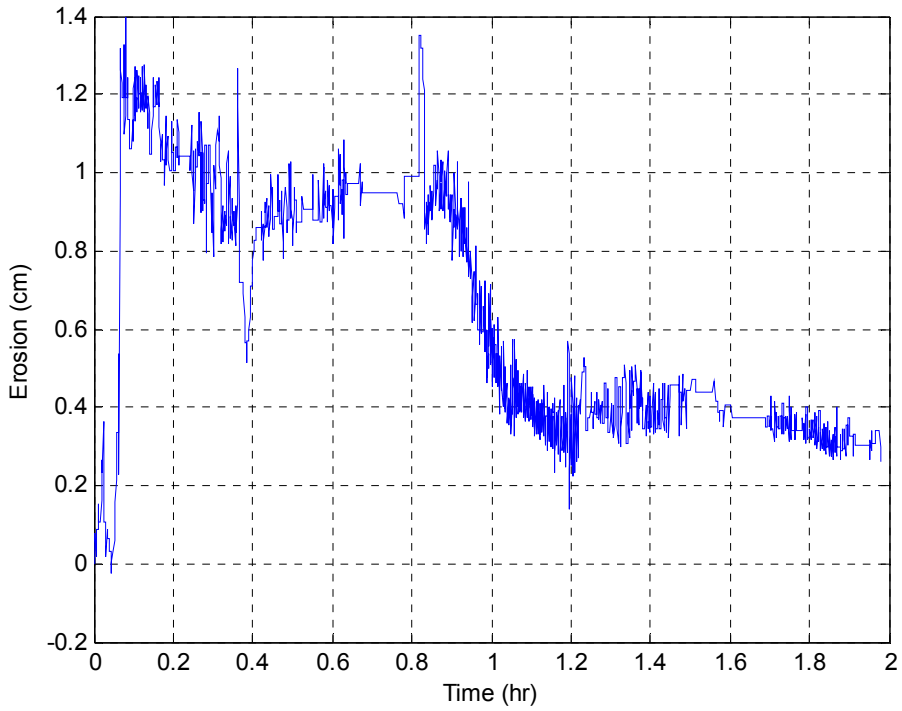

Figure C-94. Erosion versus time for specimen OS-102 top at 15.0 Pa

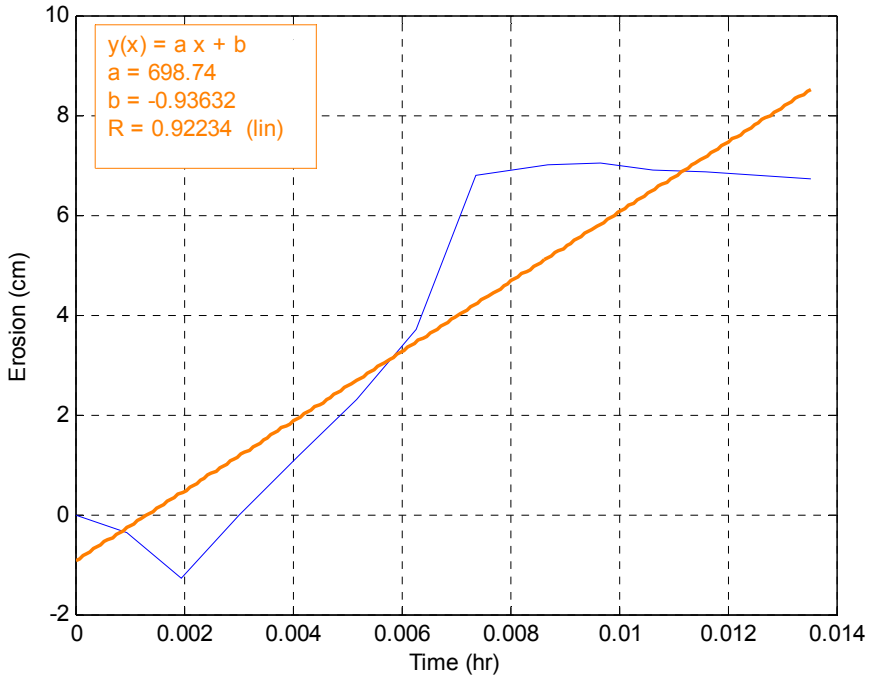

Figure C-95. Erosion versus time for specimen OS-102 top at 20.0 Pa. Note: a large piece of wax (from sealing the Shelby tube) may have affected results

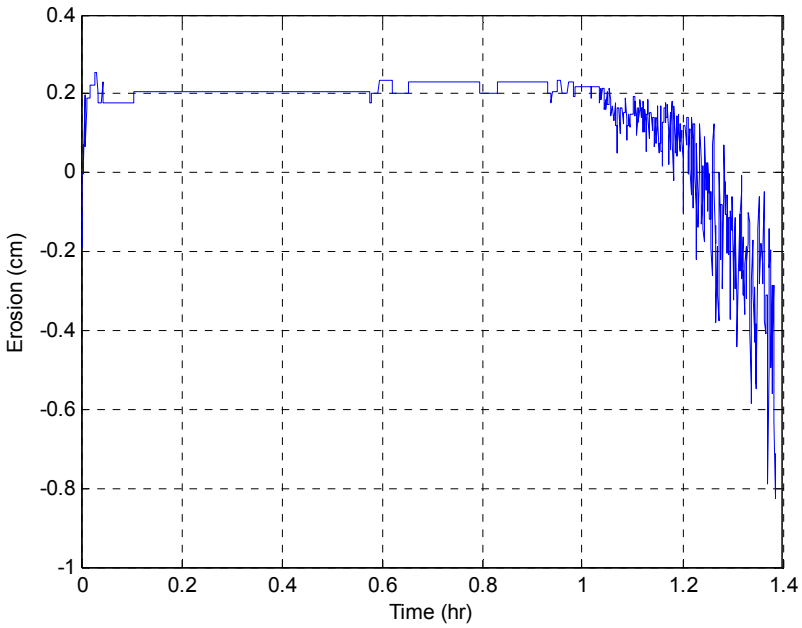

Figure C-96. Erosion versus time for OS-102 top at 20.0 Pa after wax removal. Note, by the end of the test, ultrasonic signals were absorbed by specimen

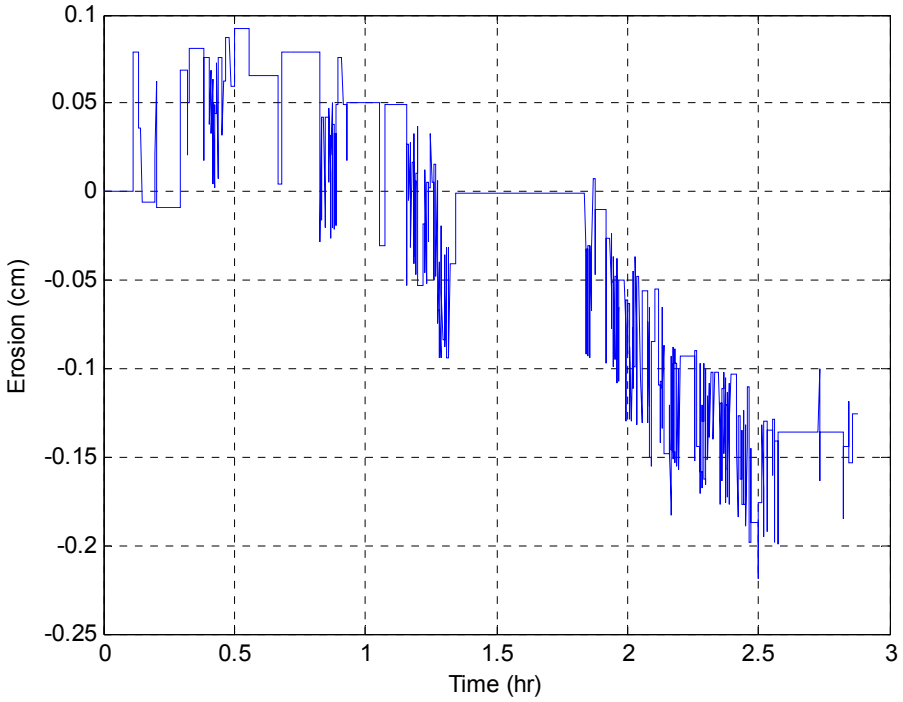

Figure C-97. Erosion versus time for OS-102 top at 25.0 Pa.

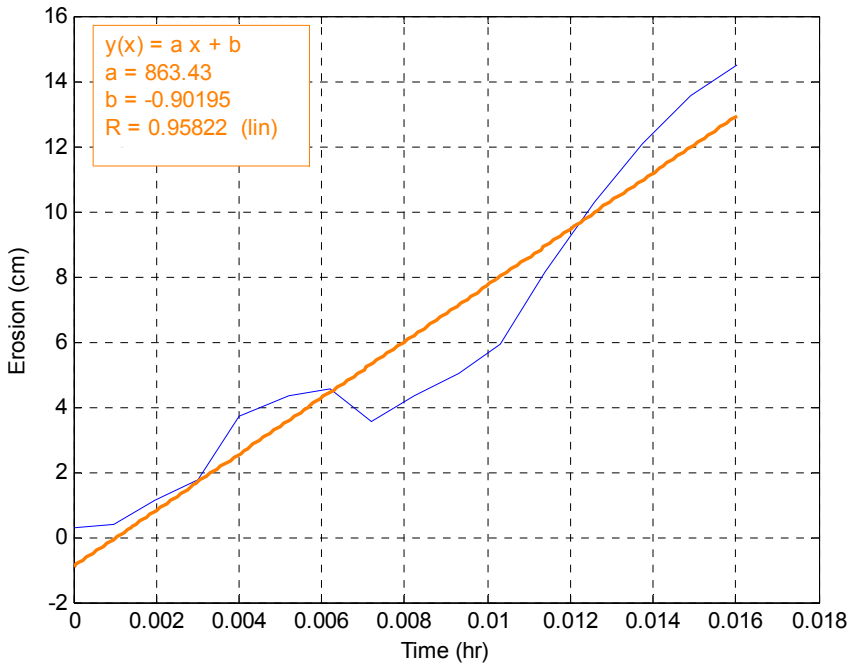

Figure C-98. Erosion versus time for OS-102 top at 30.0 Pa

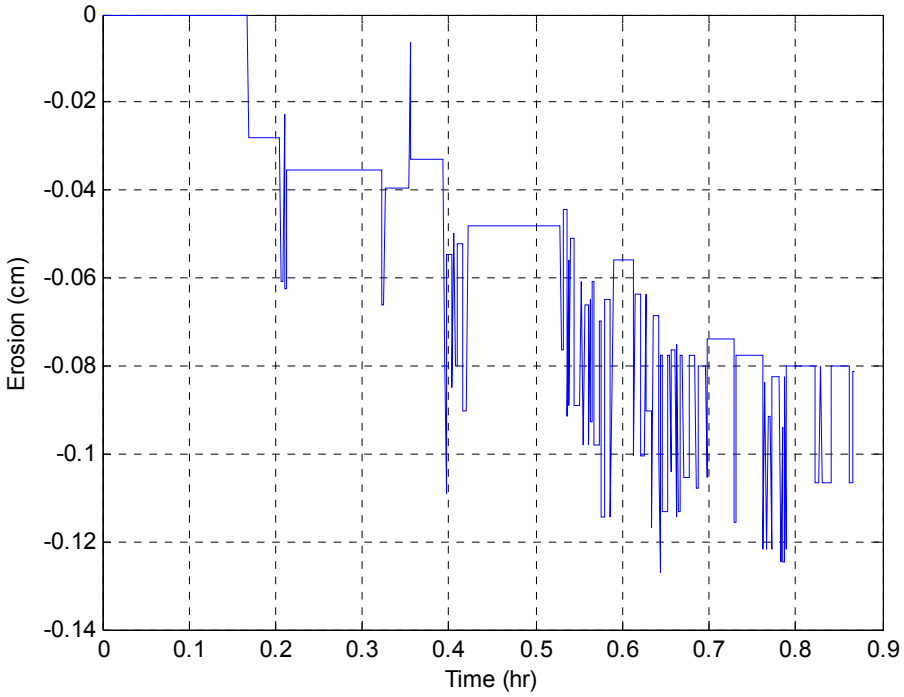

Figure C-99. Erosion versus time for OS-102 bottom at 5.0 Pa

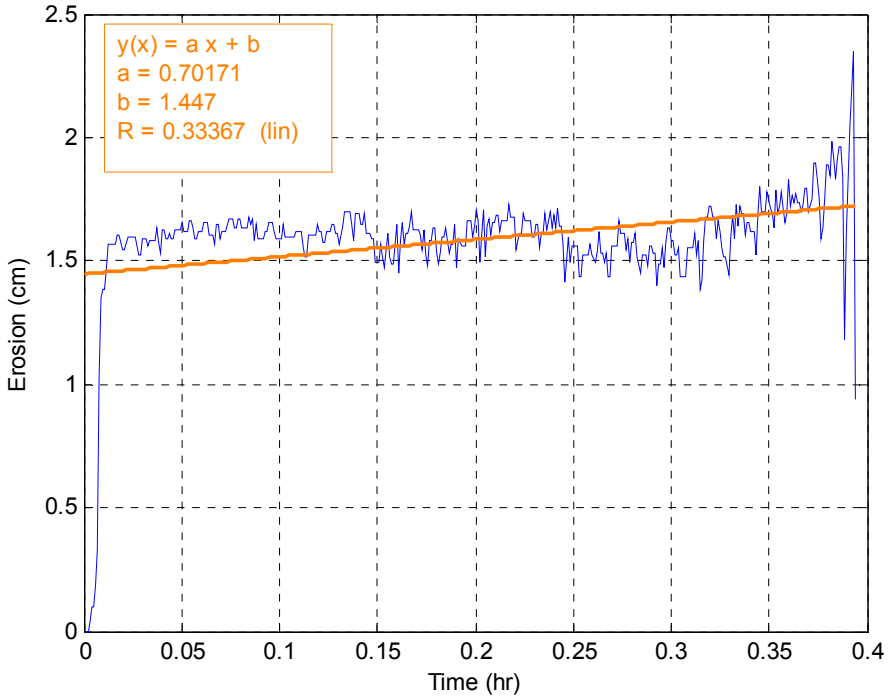

Figure C-100. Erosion versus time for OS-102 bottom at 35.0 Pa

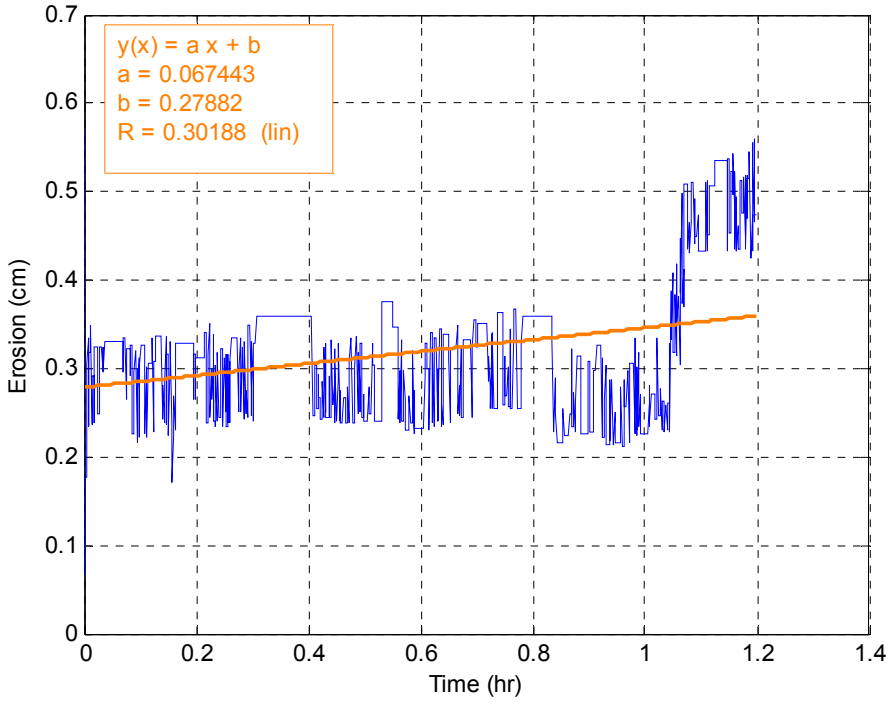

Figure C-101. Erosion versus time for OS-102 bottom at 35.0 Pa (test 2)

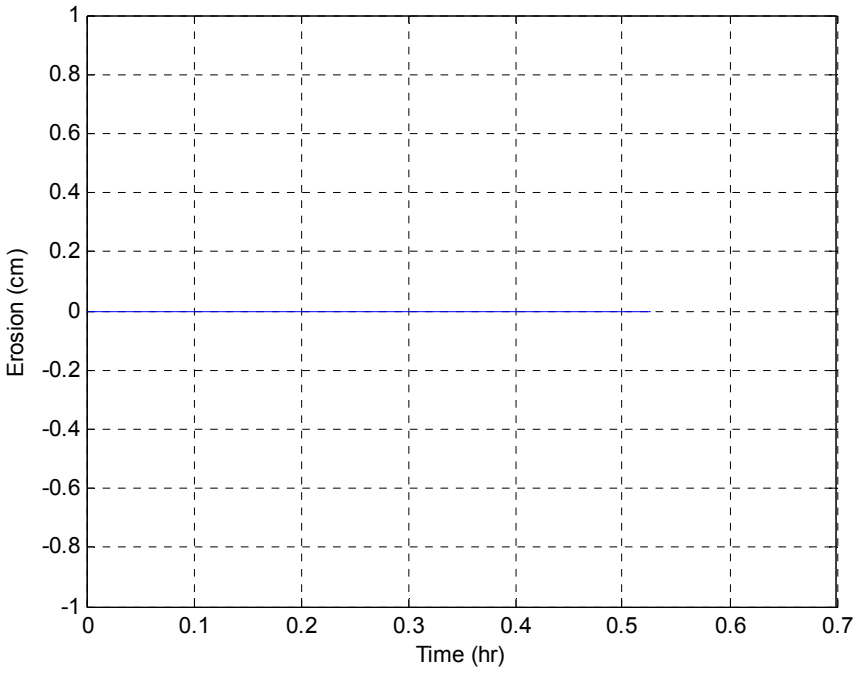

Figure C-102. Erosion versus time for OS-102 bottom at 35.0 Pa (test 3)

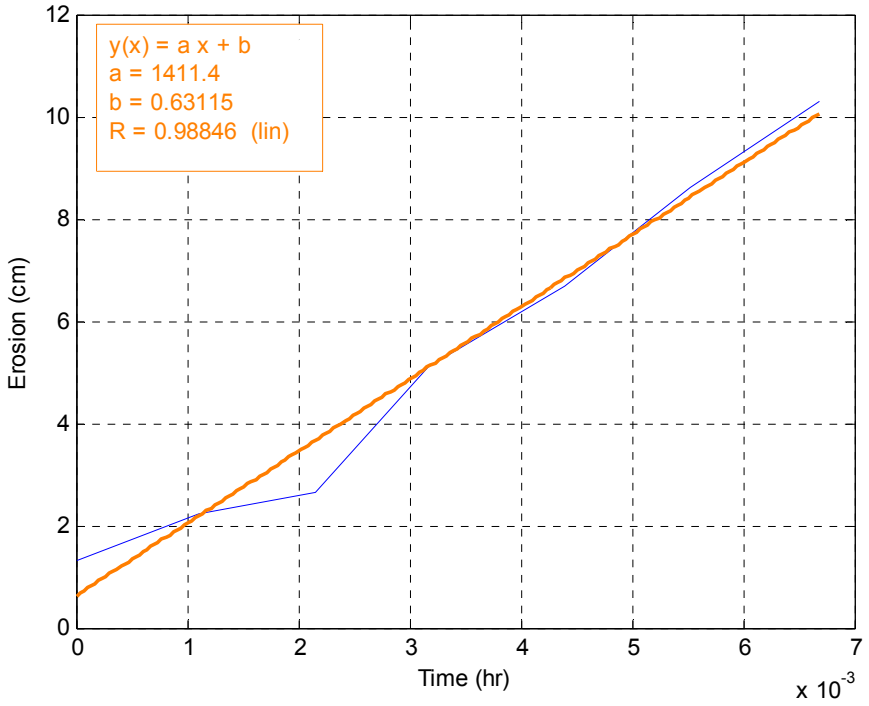

Figure C-103. Erosion versus time for OS-102 bottom at 35.0 Pa (test 4)

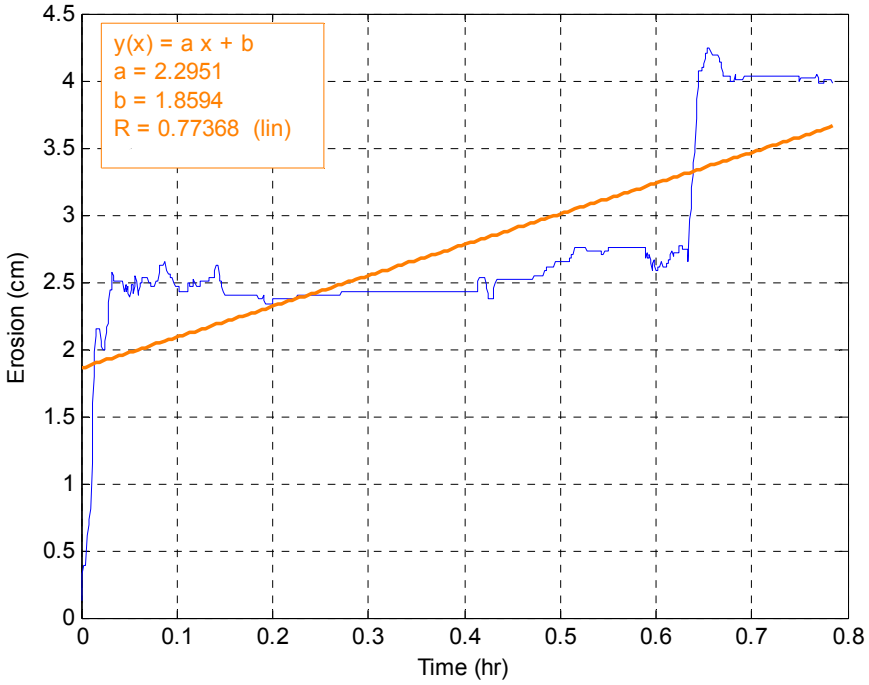

Figure C-104. Erosion versus time for OS-102 bottom at 27.57 Pa

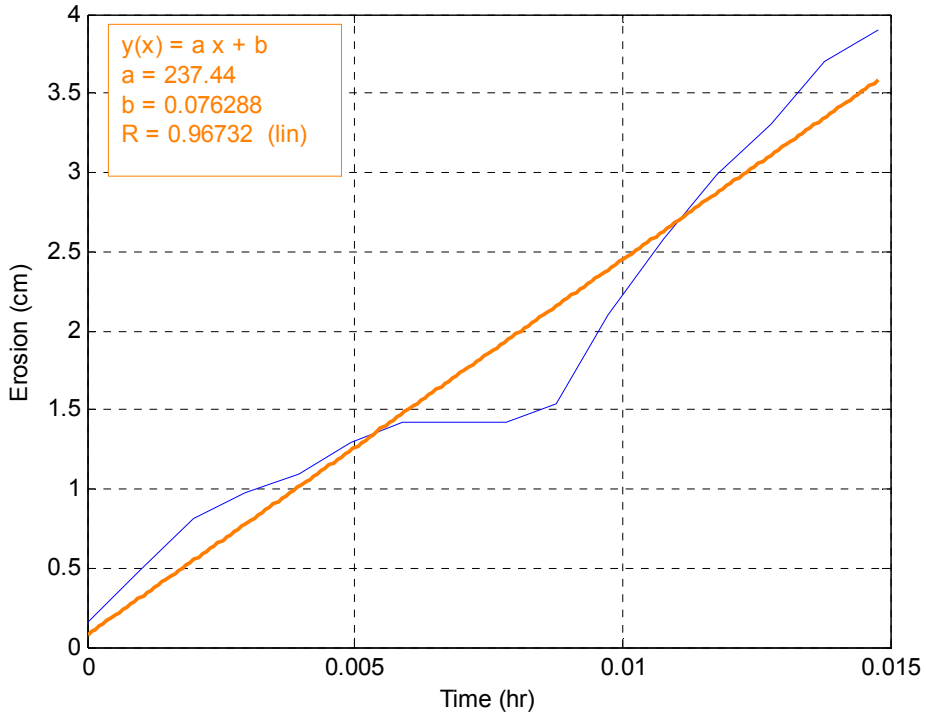

Figure C-105. Erosion versus time for OS-102 bottom at 30.0 Pa

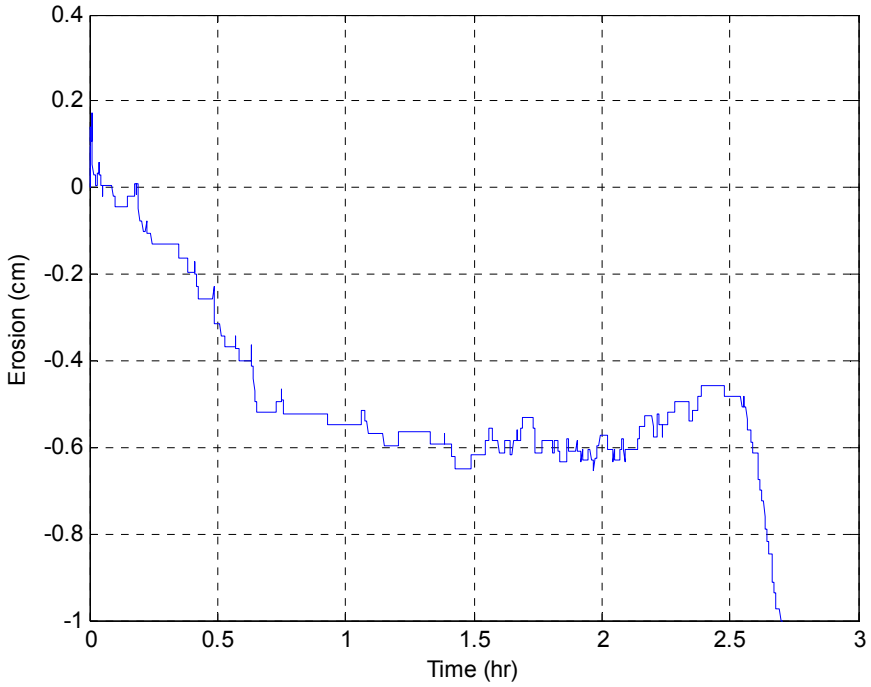

Figure C-106. Erosion versus time for OS-5 top at 5.0 Pa

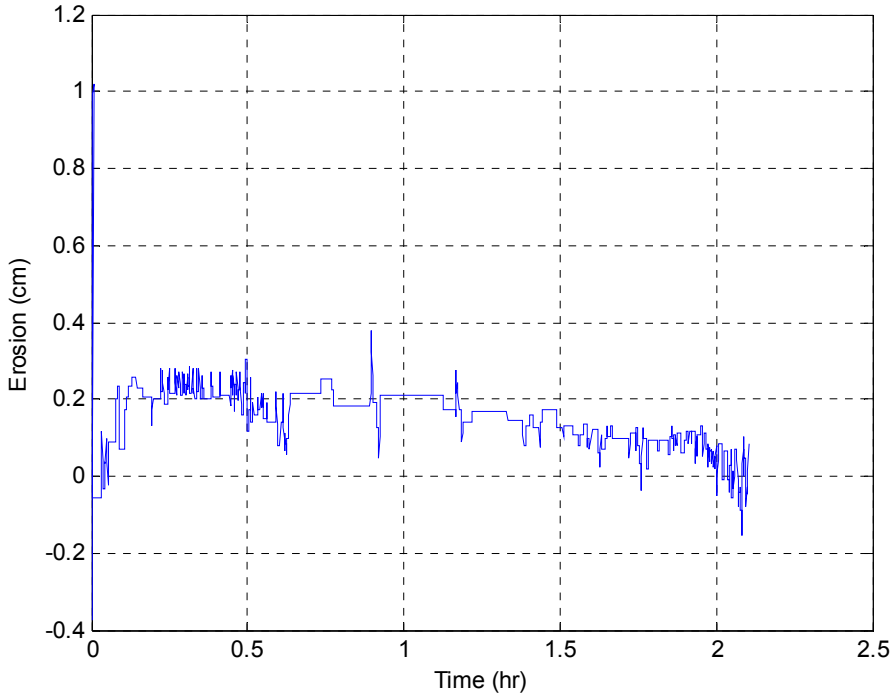

Figure C-107. Erosion versus time for OS-5 top at 15.0 Pa

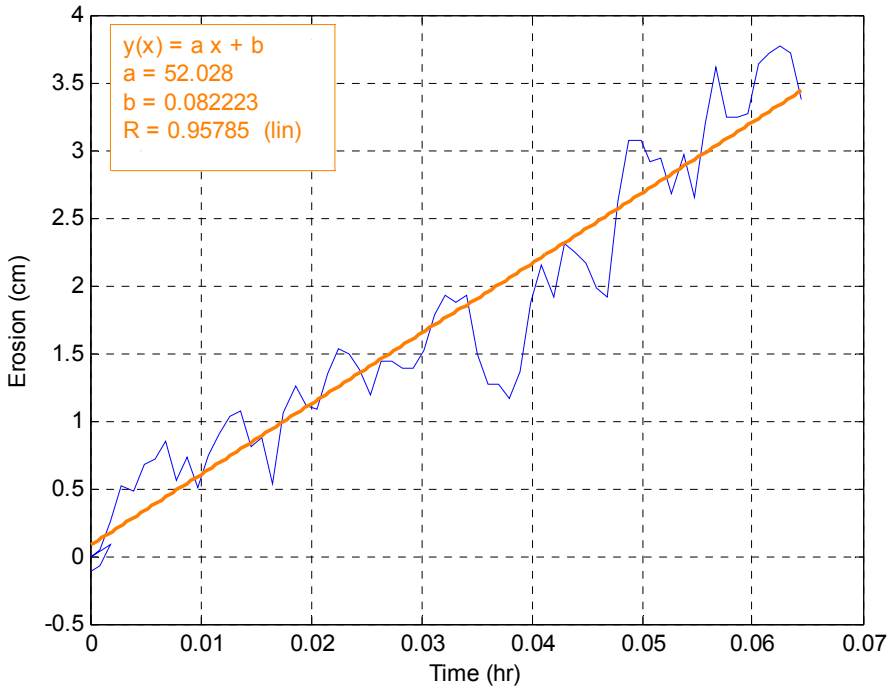

Figure C-108. Erosion versus time for OS-5 top at 25.0 Pa

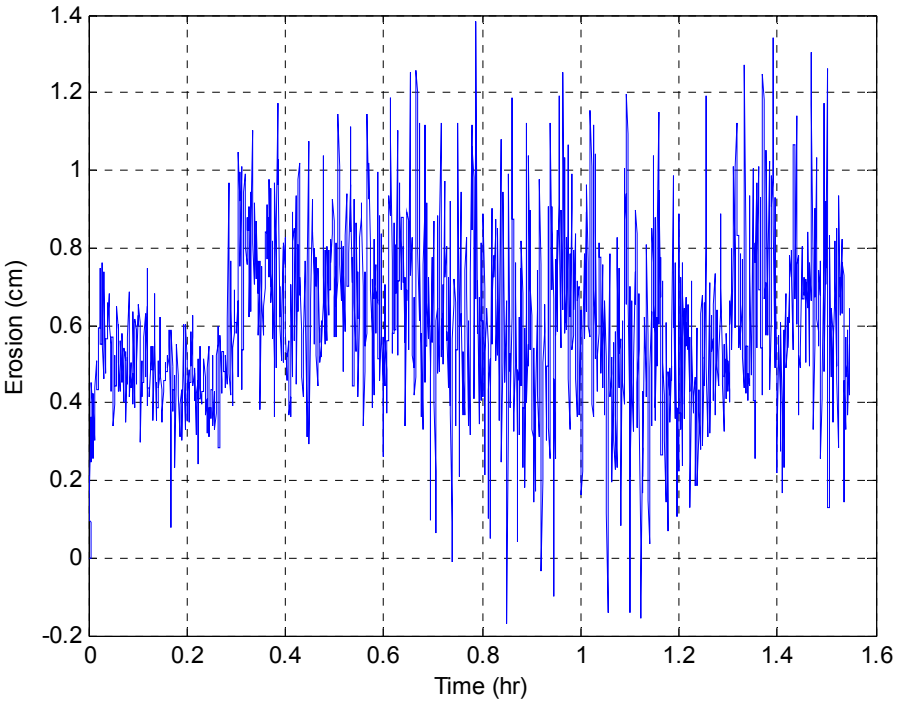

Figure C-109. Erosion versus time for OS-5 top at 40.02 Pa

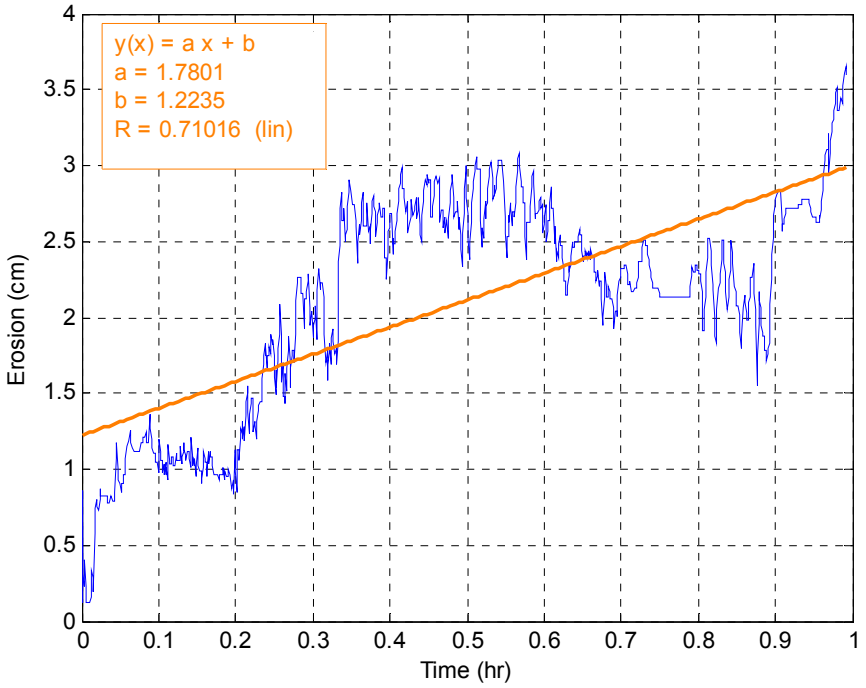

Figure C-110. Erosion versus time for OS-5 top at 45.0 Pa

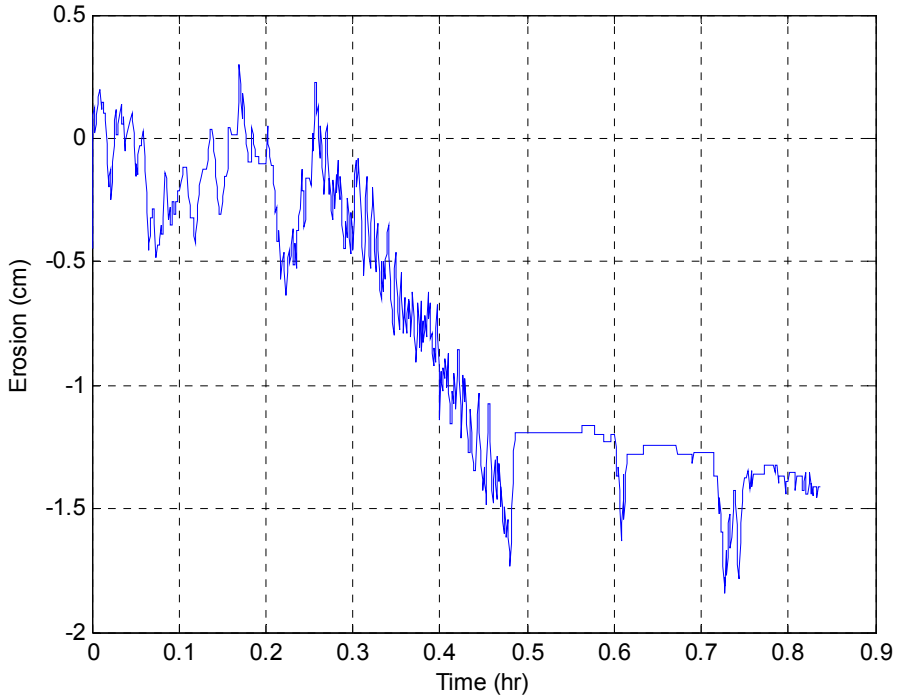

Figure C-111. Erosion versus time for OS-5 top at 50.0 Pa

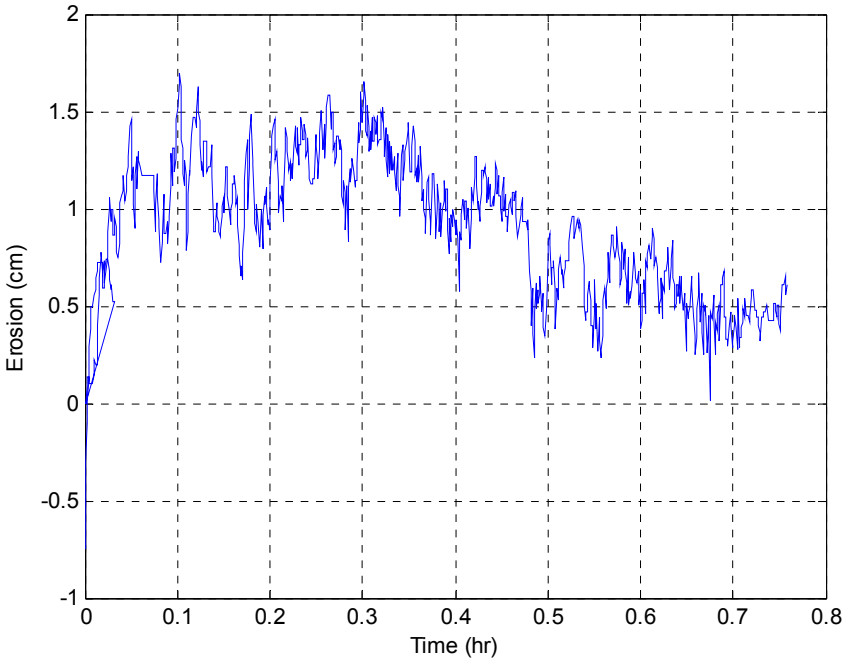

Figure C-112. Erosion versus time for OS-5 top at 63.0 Pa

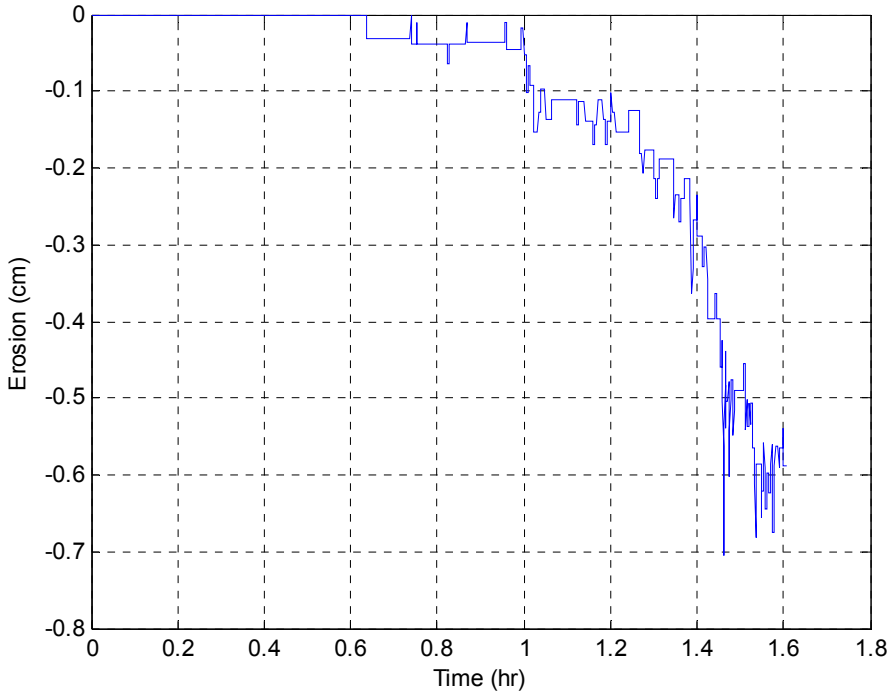

Figure C-113. Erosion versus time for OS-6 top at 5.0 Pa

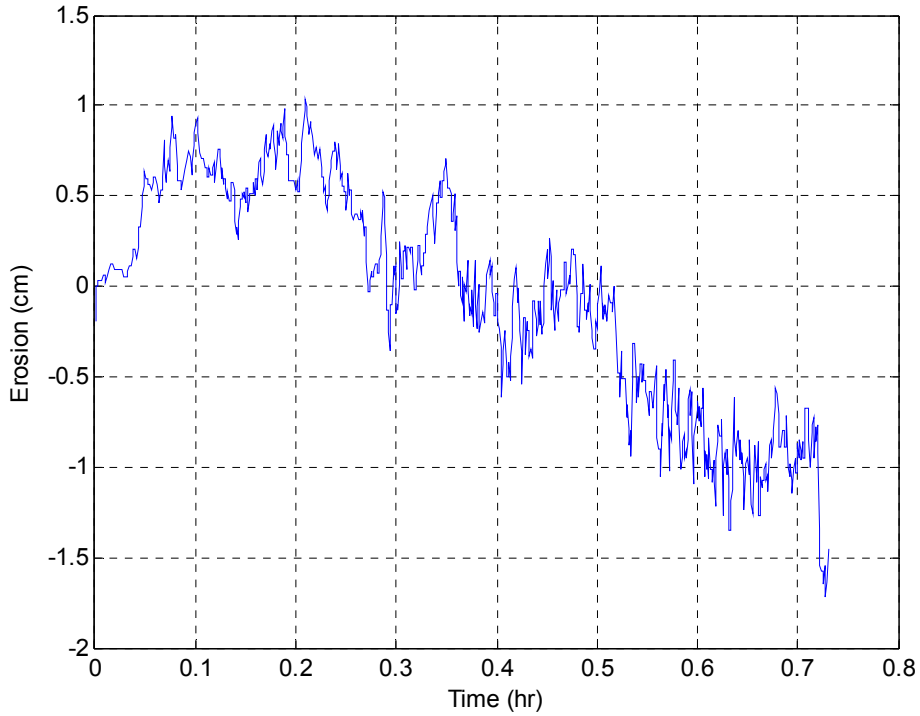

Figure C-114. Erosion versus time for OS-6 top at 10.0 Pa

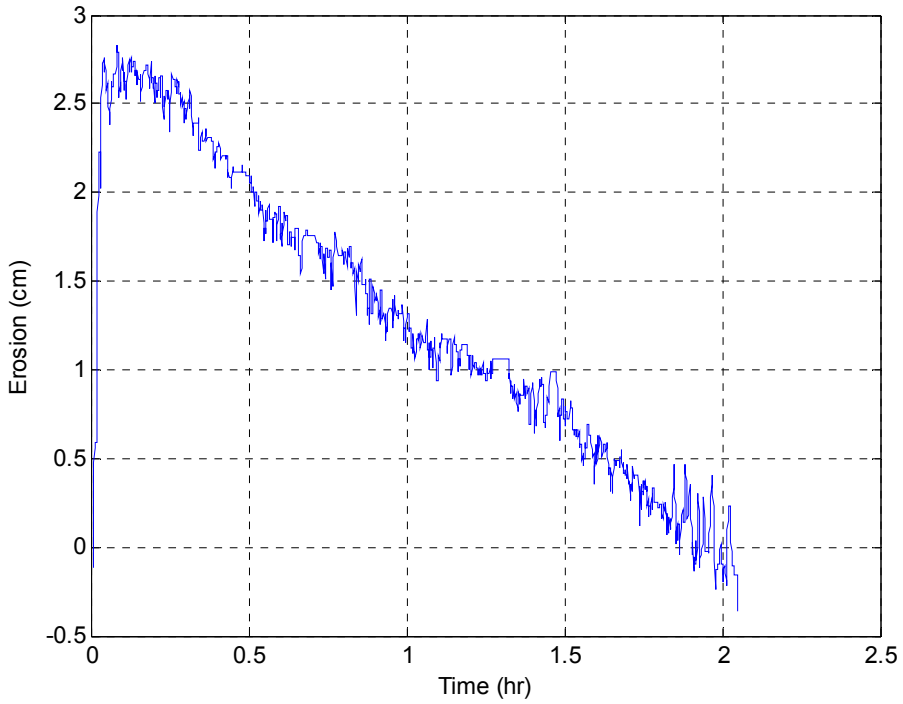

Figure C-115. Erosion versus time for OS-6 at 15.0 Pa

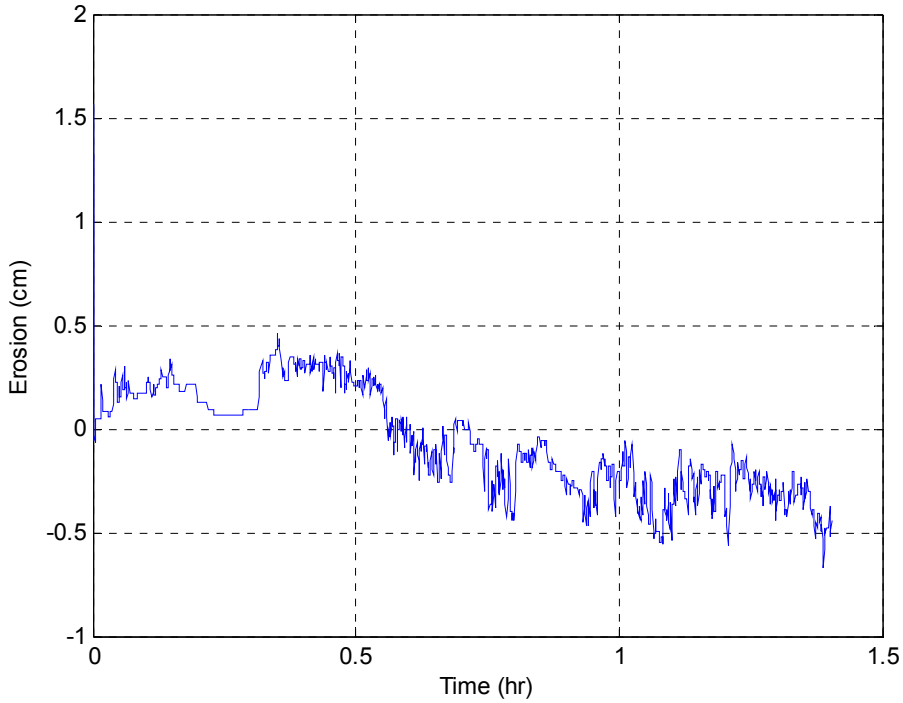

Figure C-116. Erosion versus time for OS-6 at 20.0 Pa

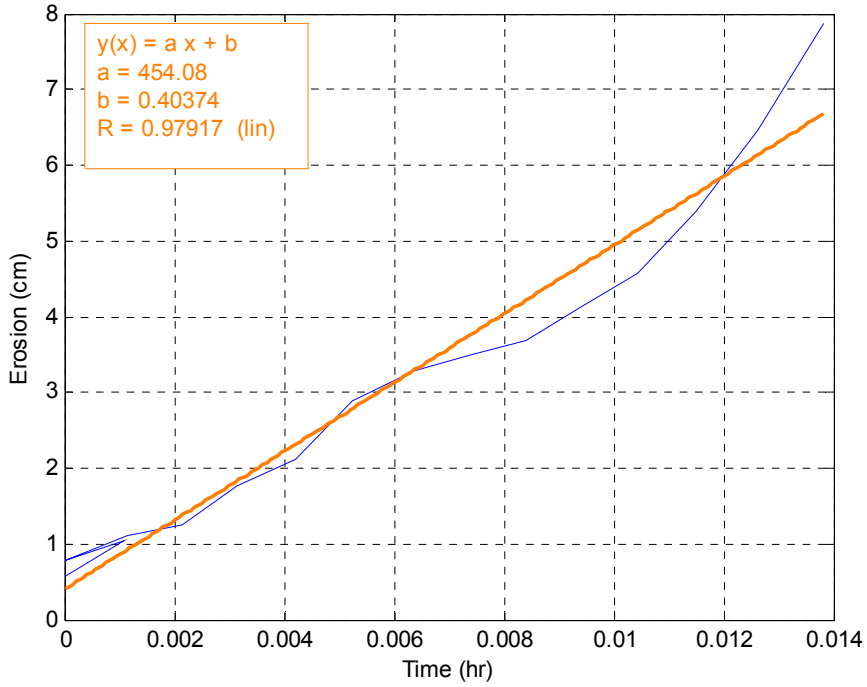

Figure C-117. Erosion versus time for OS-6 at 45 Pa

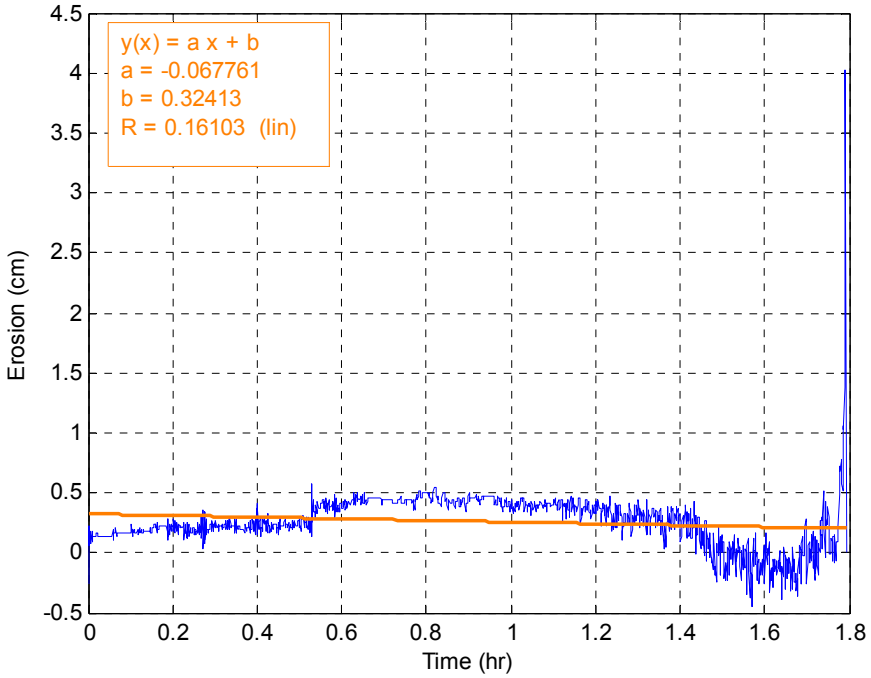

Figure C-118. Erosion versus time for OS-42 top at 5.0 Pa

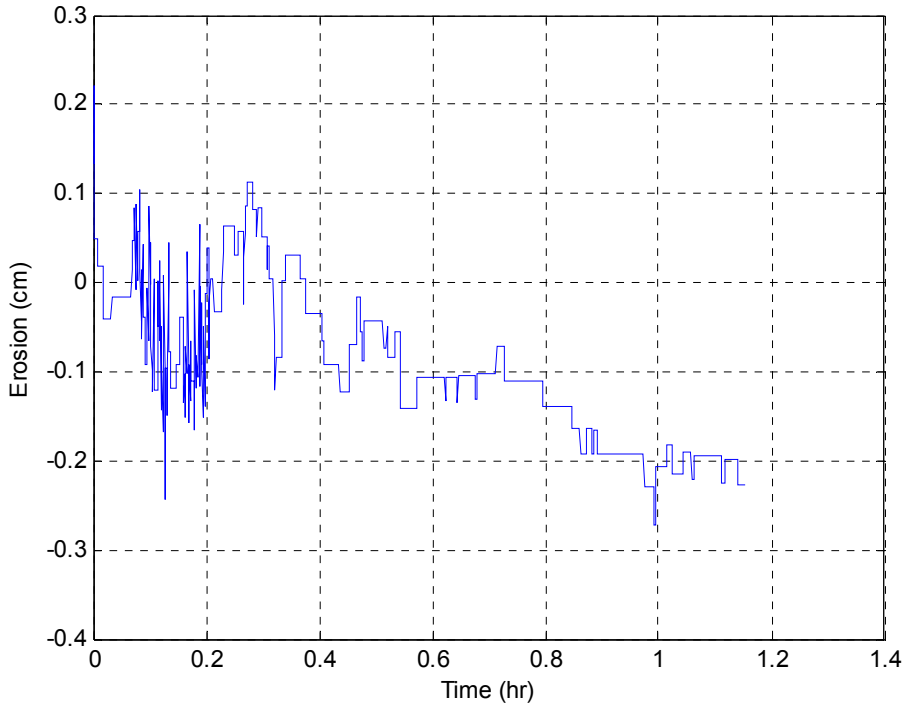

Figure C-119. Erosion versus time for OS-42 top at 10.0 Pa

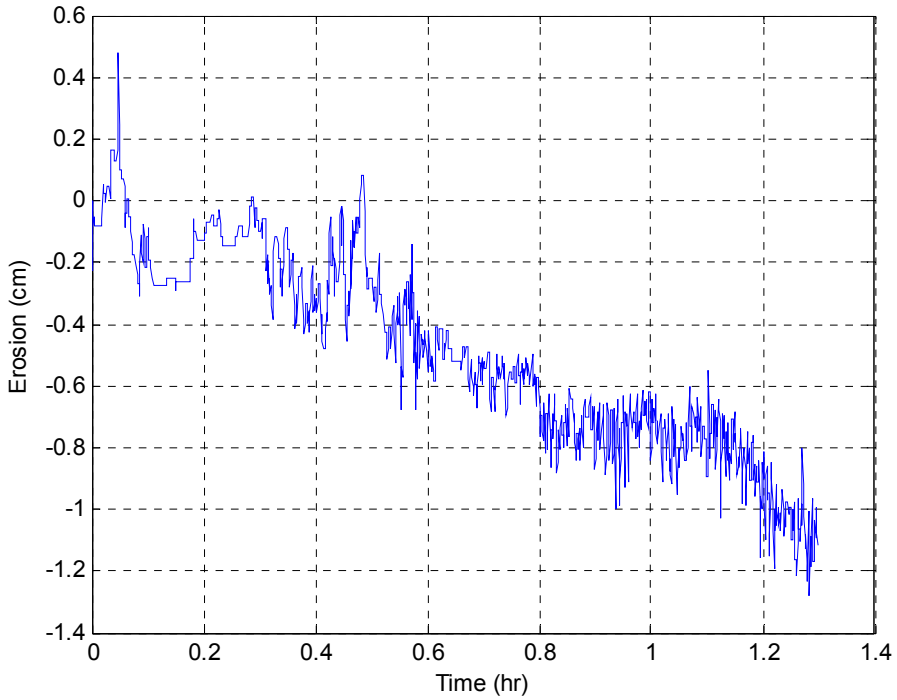

Figure C-120. Erosion versus time for OS-42 top at 15.0 Pa

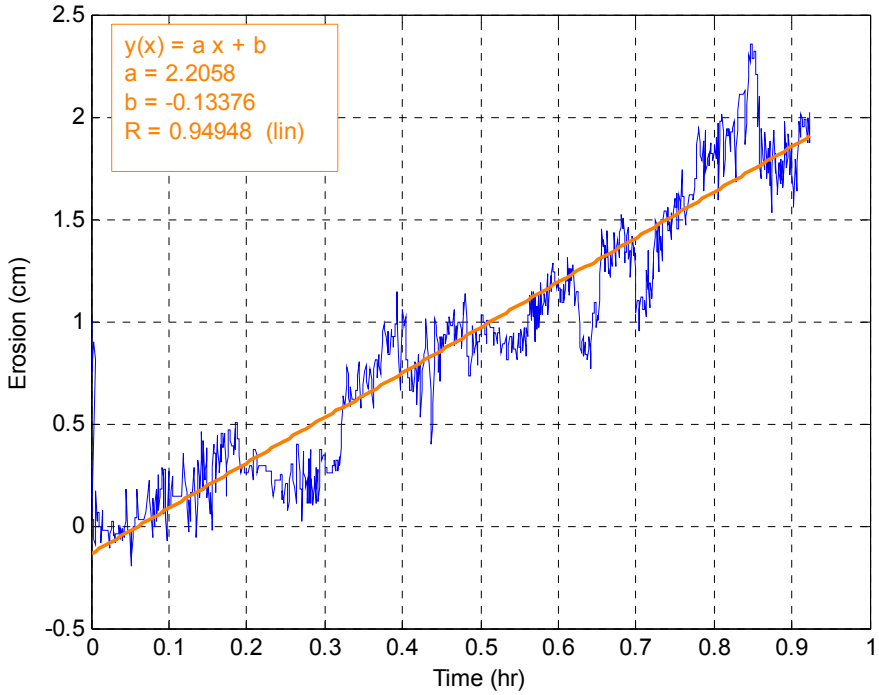

Figure C-121. Erosion versus time for OS-42 top at 20.0 Pa

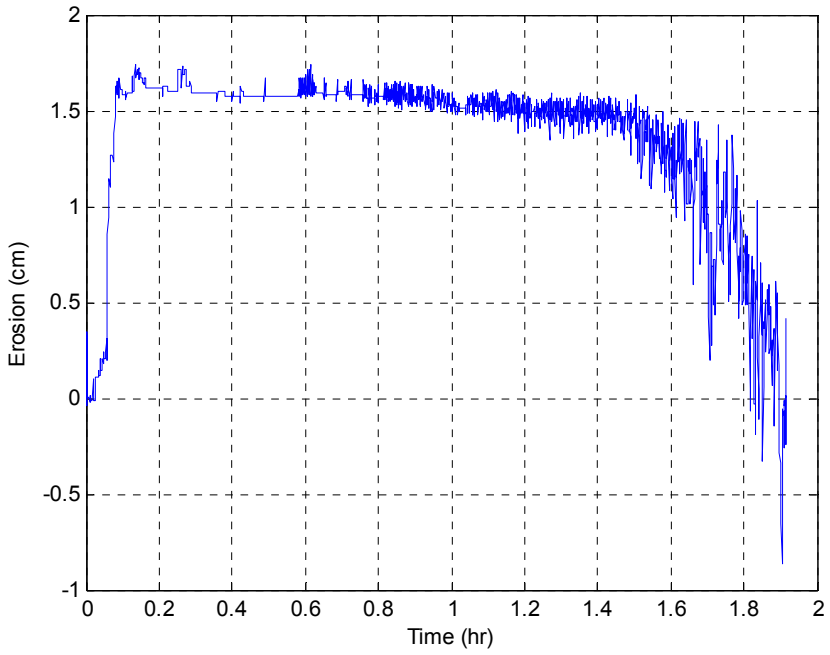

Figure C-121. Erosion versus time for OS-42 top at 25.0 Pa

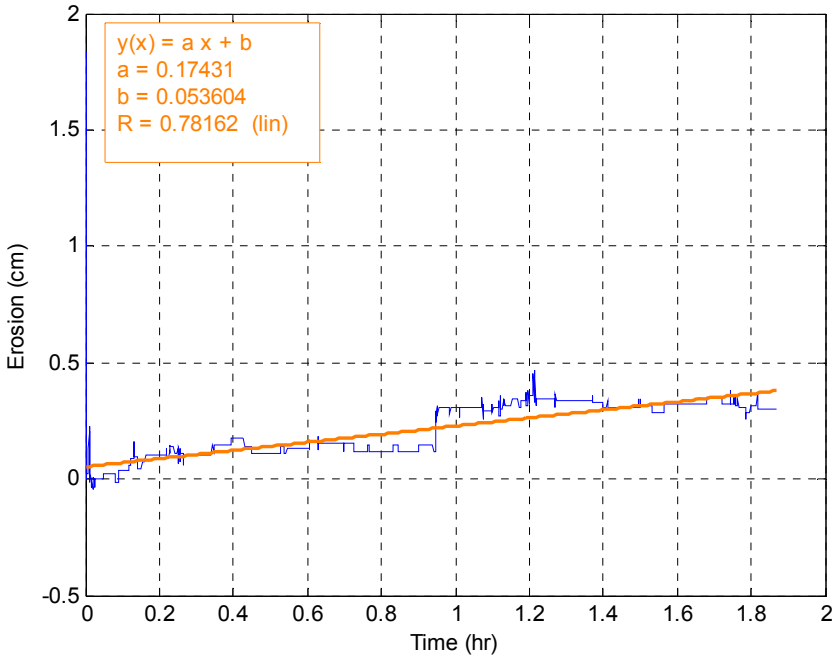

Figure C-123. Erosion versus time for OS-42 top at 30.0 Pa

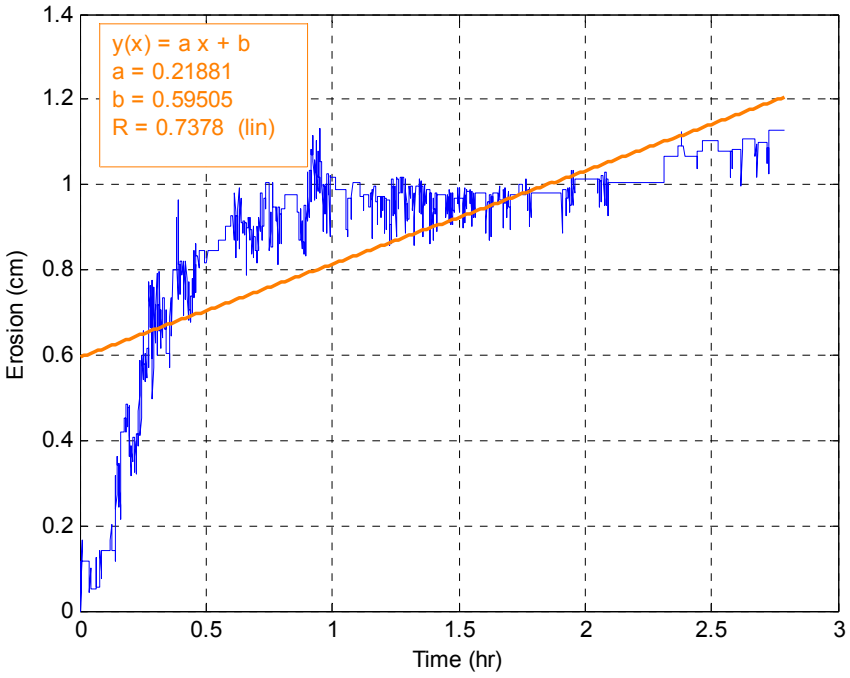

Figure C-124. Erosion versus time for OS-42 top at 35.0 Pa

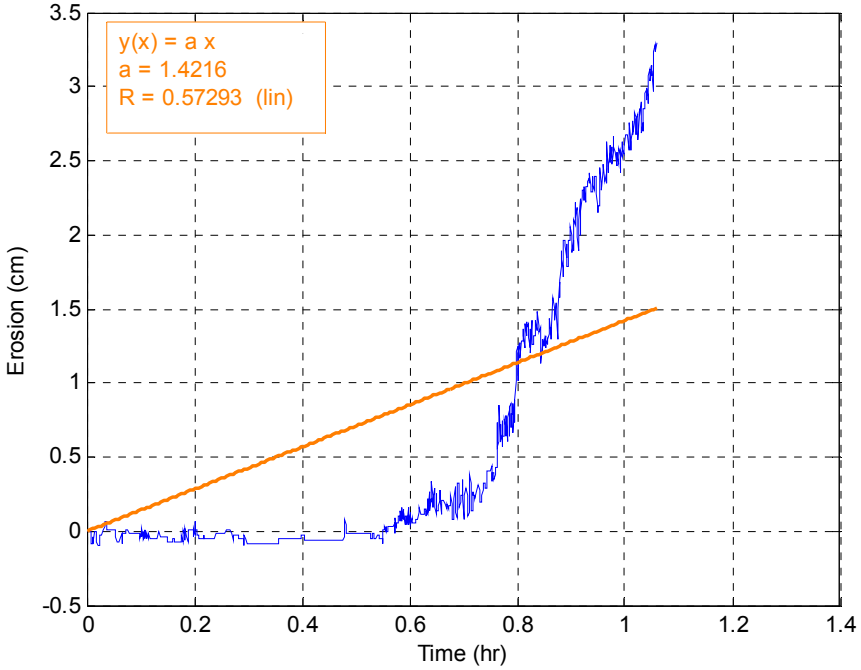

Figure C-125. Erosion versus time for OS-42 top at 40.0 Pa

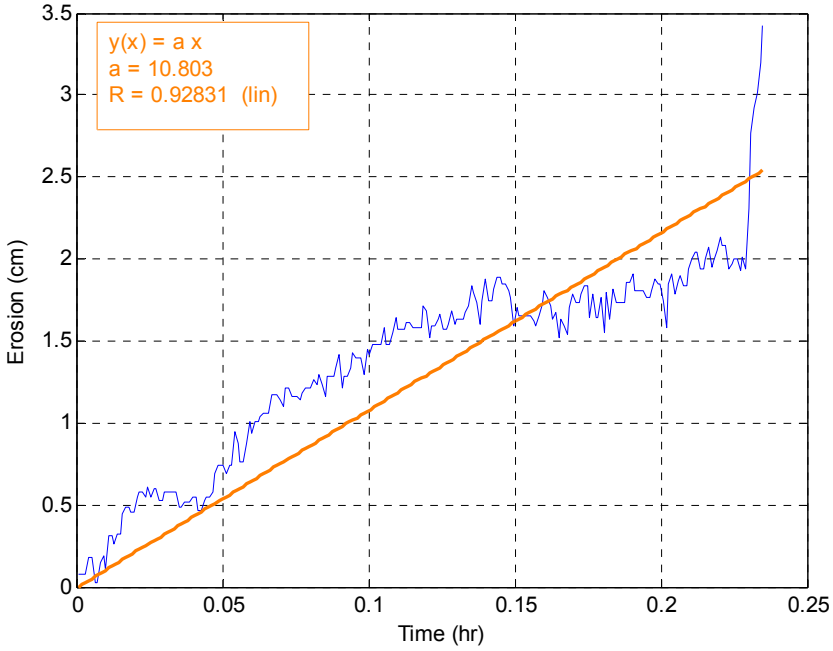

Figure C-126. Erosion versus time for OS-42 top at 45.0 Pa

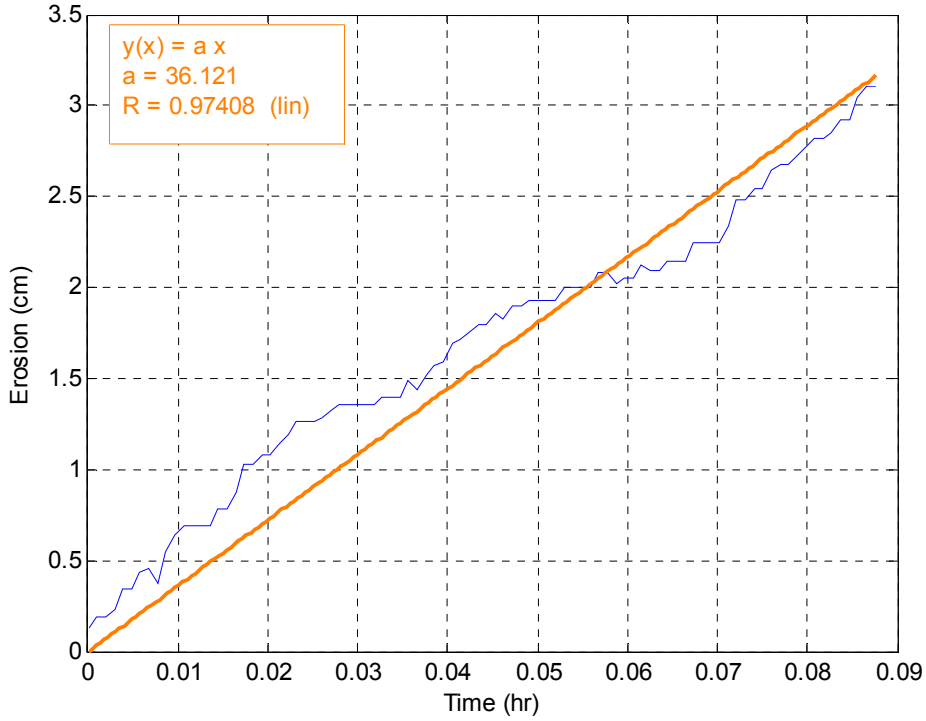

Figure C-127. Erosion versus time for OS-42 top at 50.0 Pa

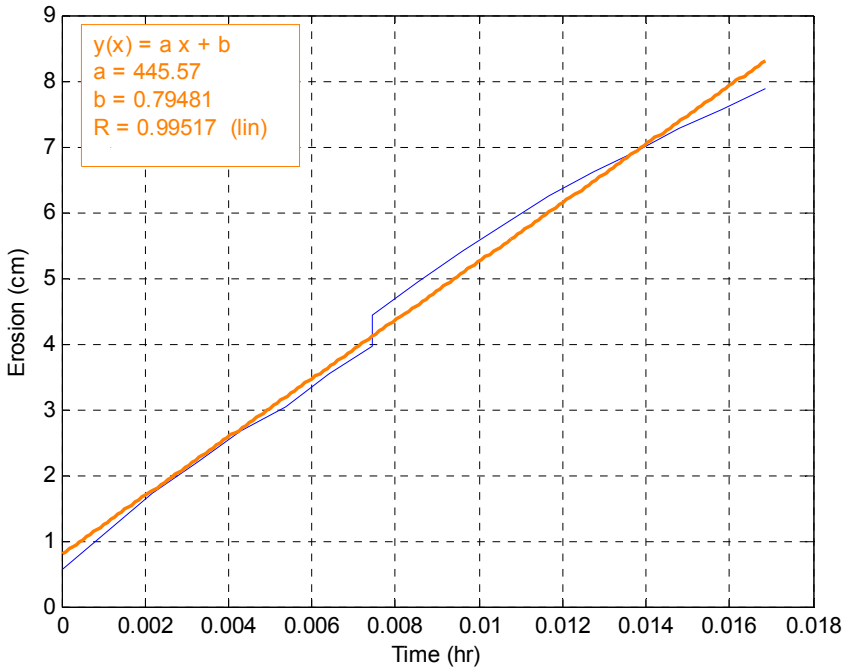

Figure C-128. Erosion versus time for OS-42 top at 63.0 Pa

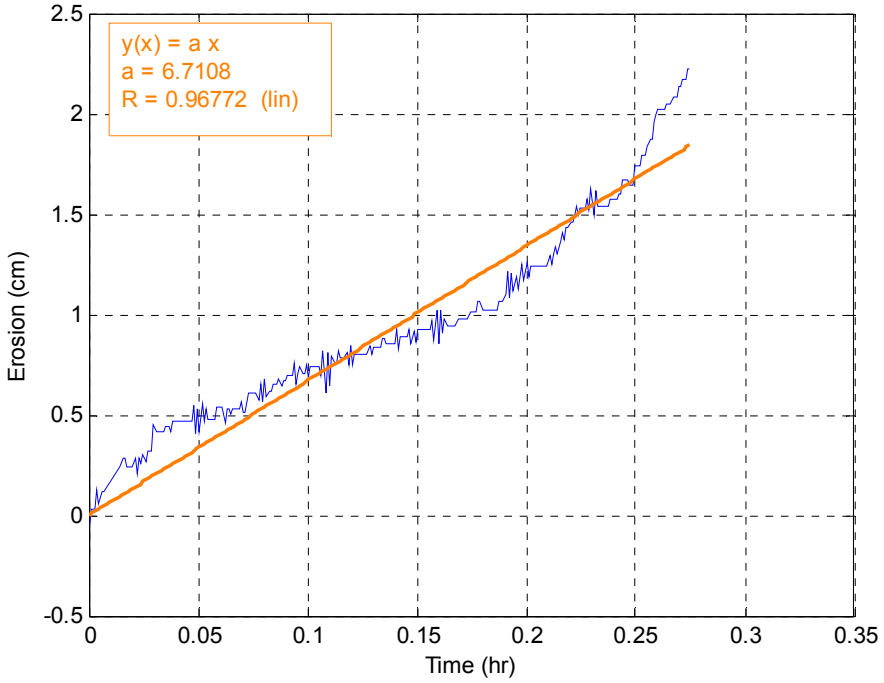

Figure C-129. Erosion versus time for OS-42 bottom at 5.0 Pa

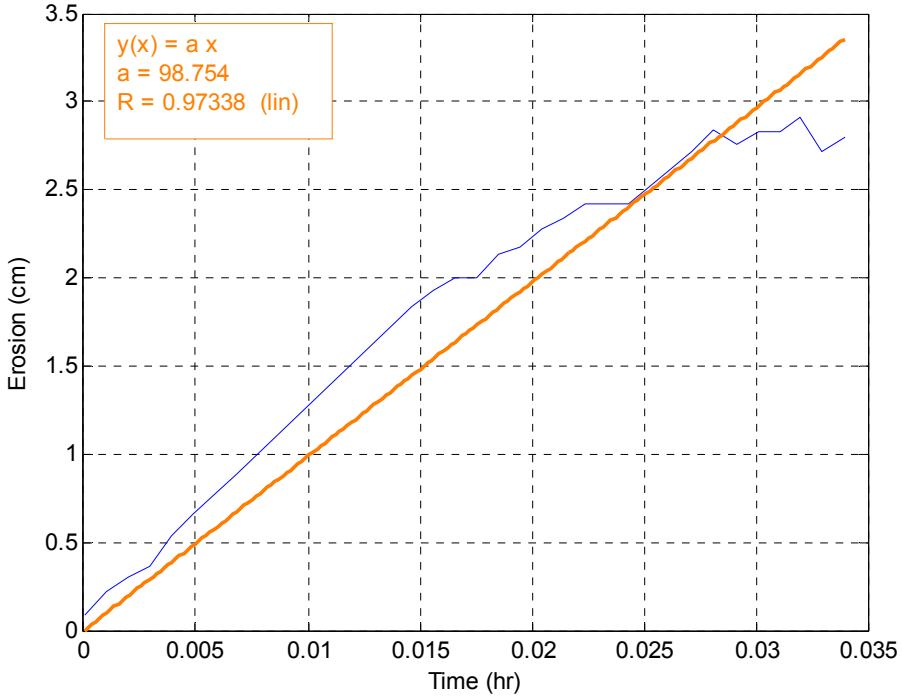

Figure C-130. Erosion versus time for OS-42 bottom at 10.0 Pa

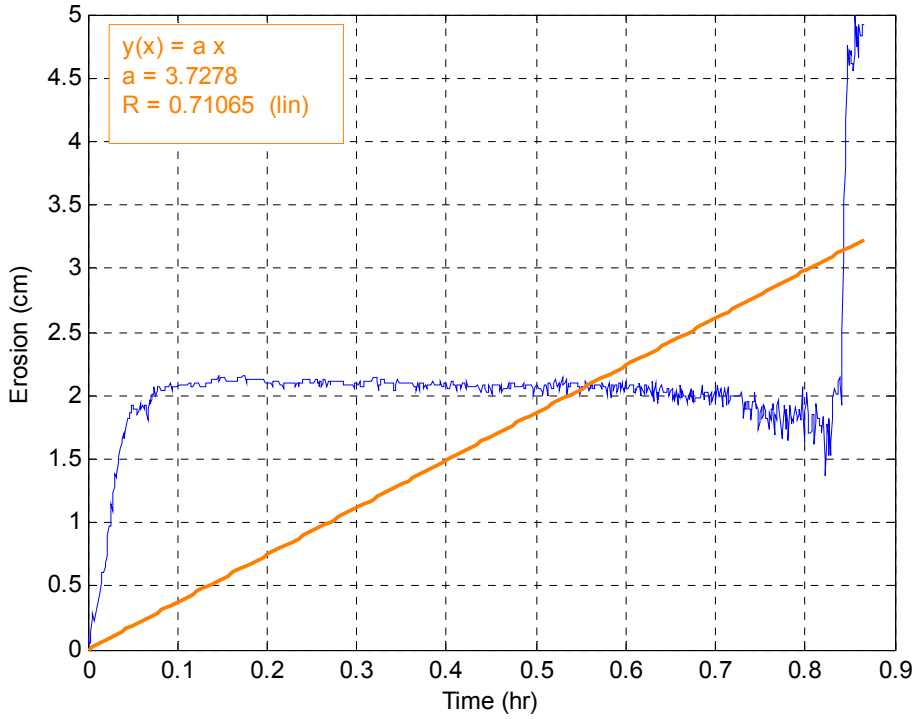

Figure C-131. Erosion versus time for OS-42 bottom at 15.0 Pa

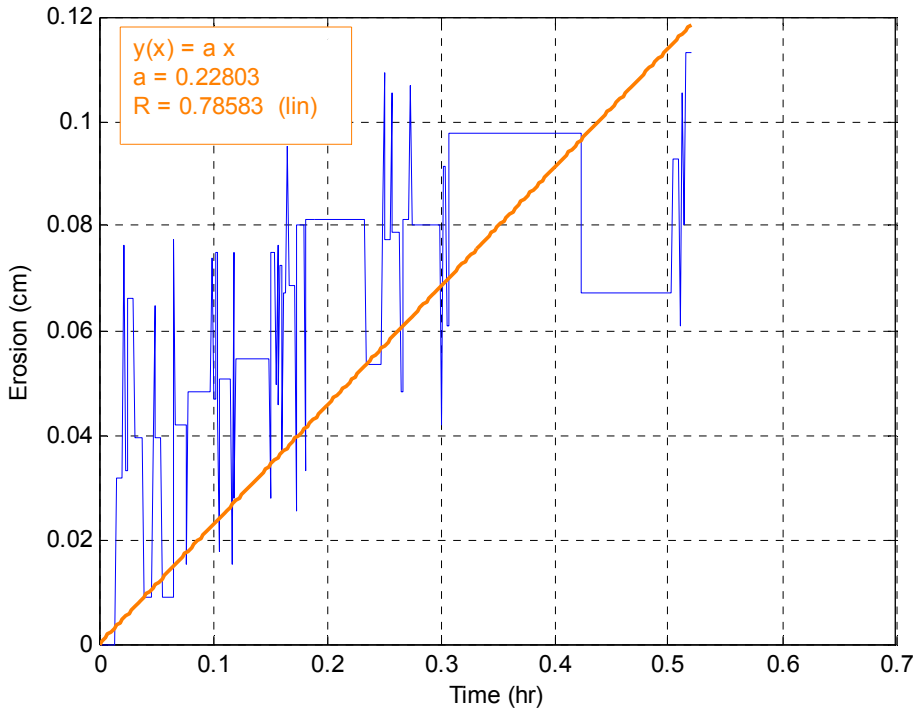

Figure C-132. Erosion versus time for OS-42 bottom at 20.0 Pa

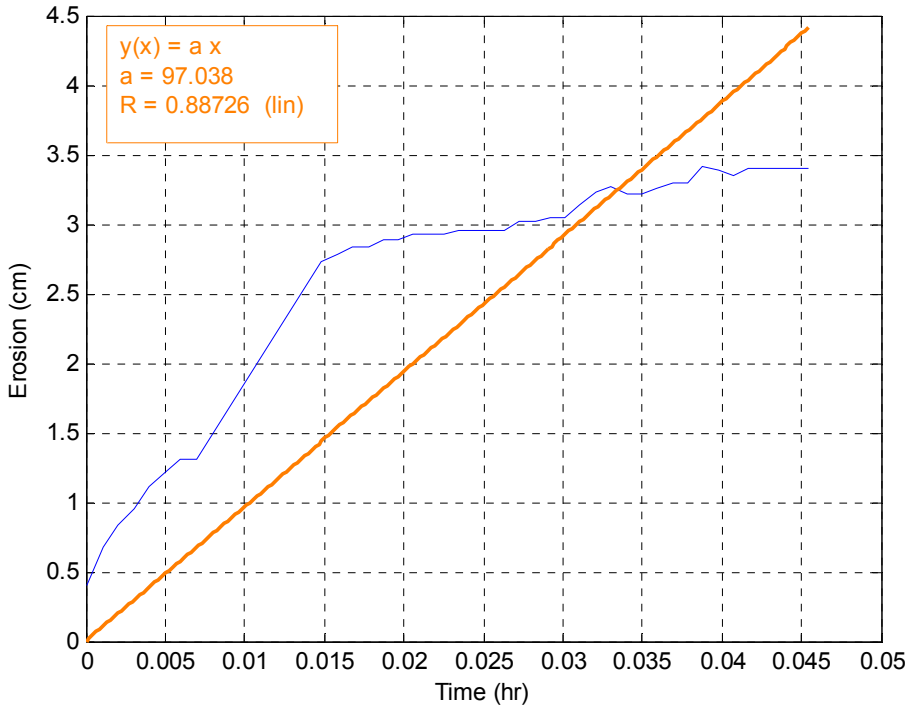

Figure C-133. Erosion versus time for OS-42 bottom at 55.0 Pa

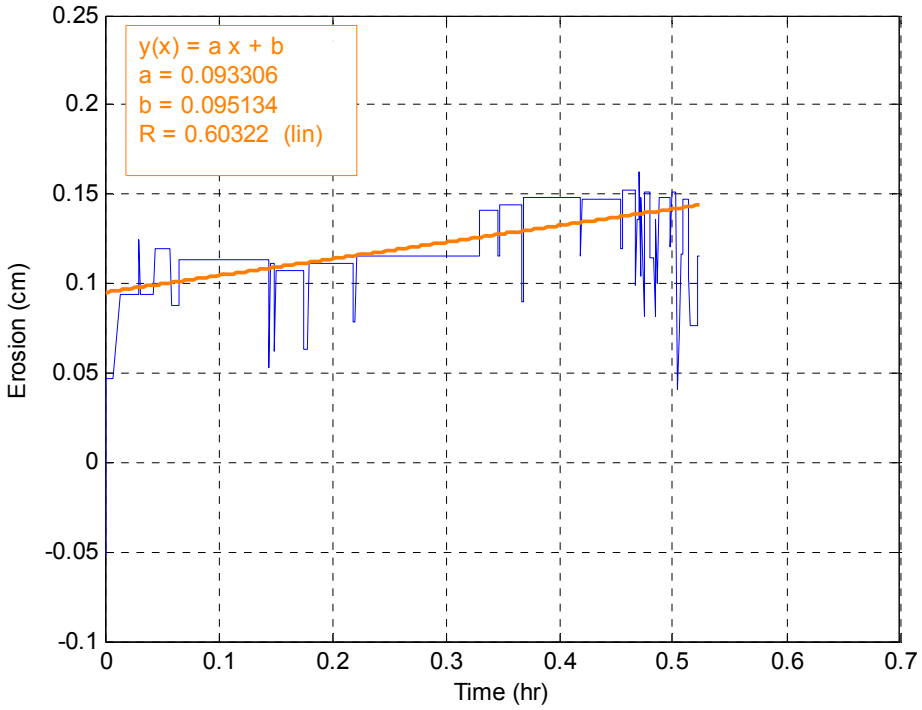

Figure C-134. Erosion versus time for OS-66 top at 10.0 Pa

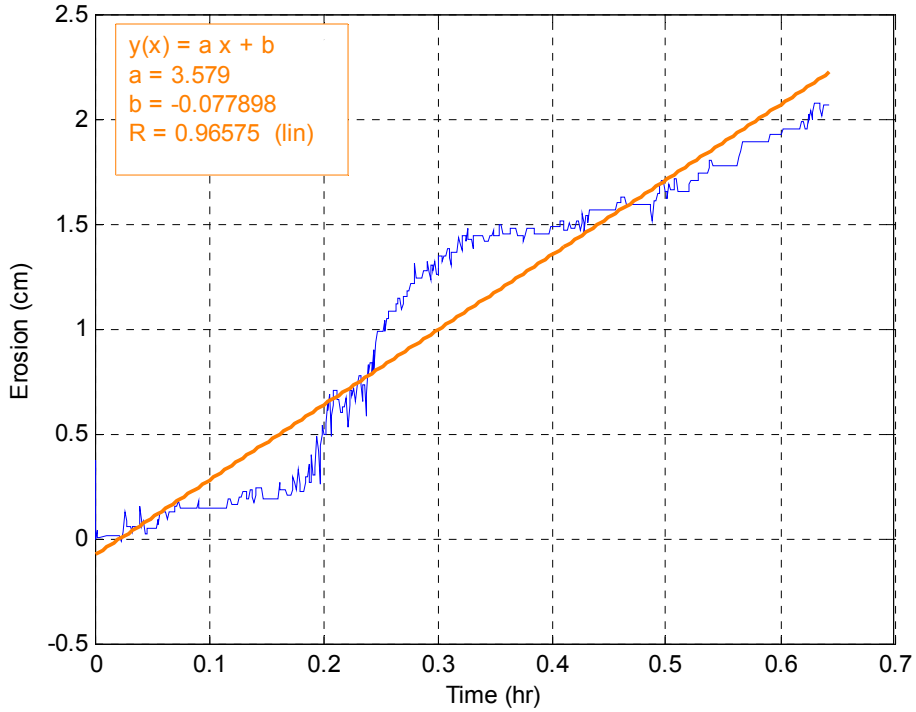

Figure C-135. Erosion versus time for OS-66 top at 20.0 Pa

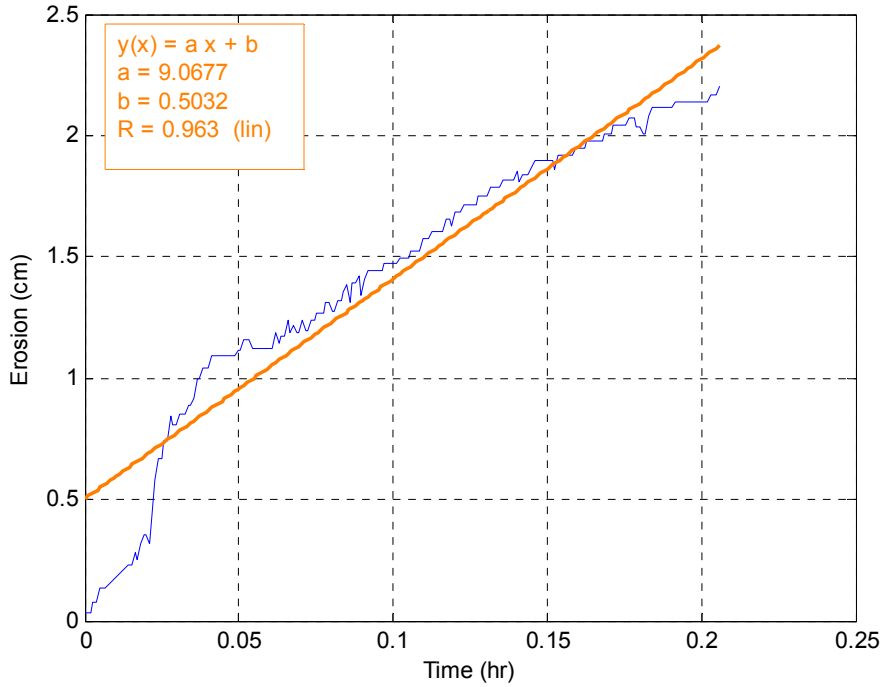

Figure C-136. Erosion versus time for OS-66 top at 30.0 Pa

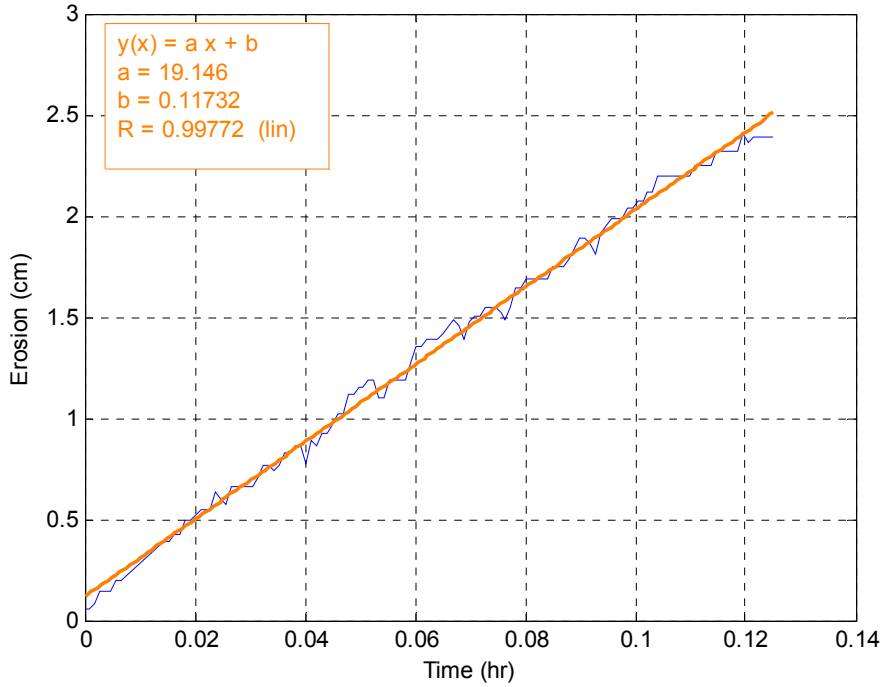

Figure C-137. Erosion versus time for OS-66 top at 40.0 Pa

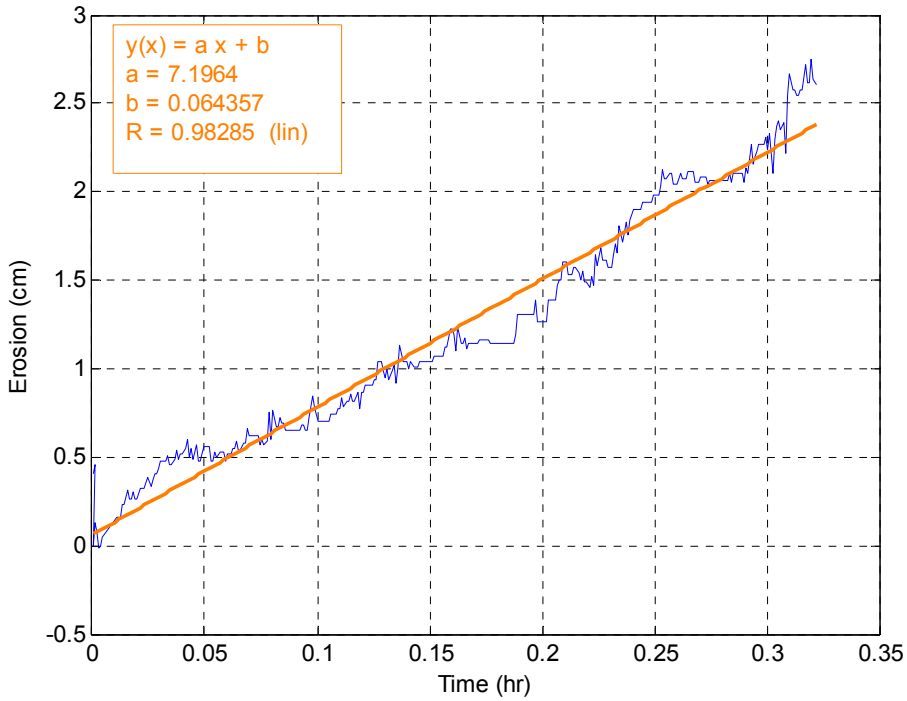

Figure C-138. Erosion versus time for OS-66 top at 25.0 Pa

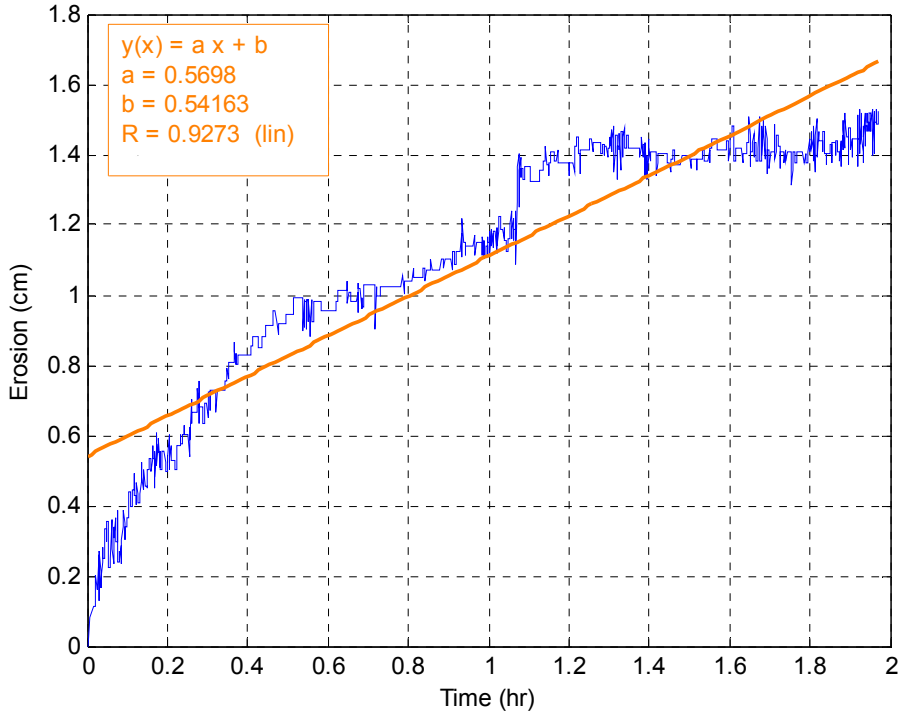

Figure C-139. Erosion versus time for OS-66 top at 27.5 Pa

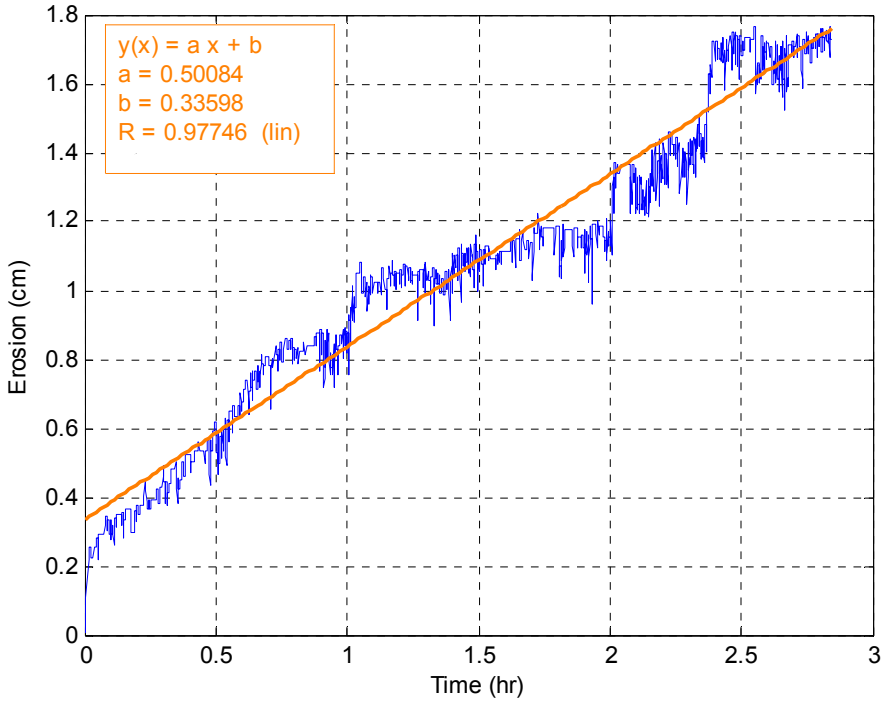

Figure C-140. Erosion versus time for OS-66 top at 35.0 Pa

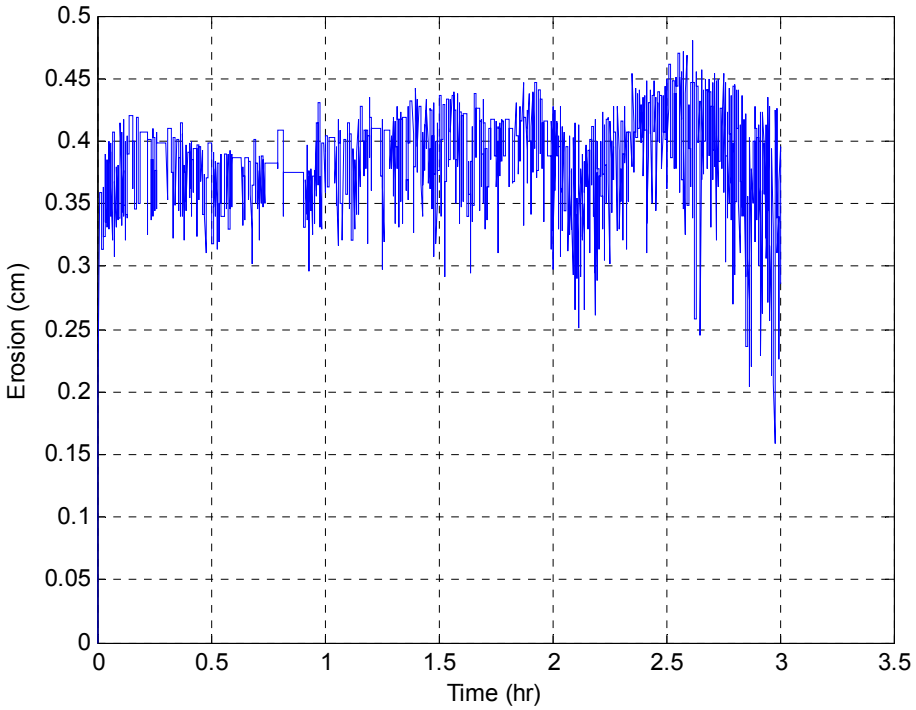

Figure C-141. Erosion versus time for OS-66 bottom at 40.0 Pa (note – no movement, which apparently confirms existence of layer).

APPENDIX D
EROSION FUNCTIONS FOR FLORIDA SPECIMENS

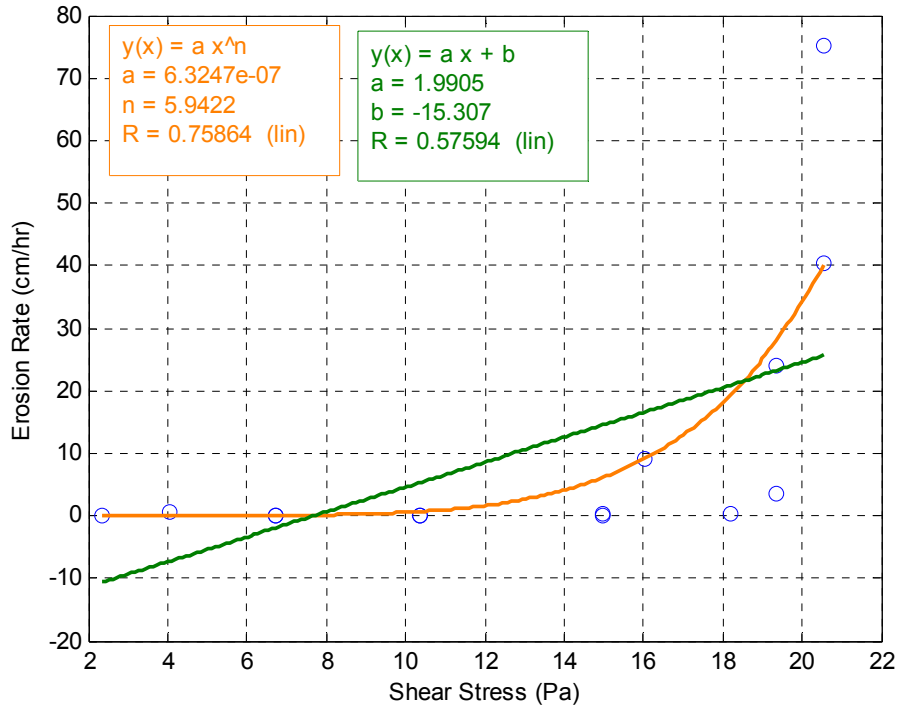

Figure D-1. Erosion rate versus shear stress for specimen AS-UF1

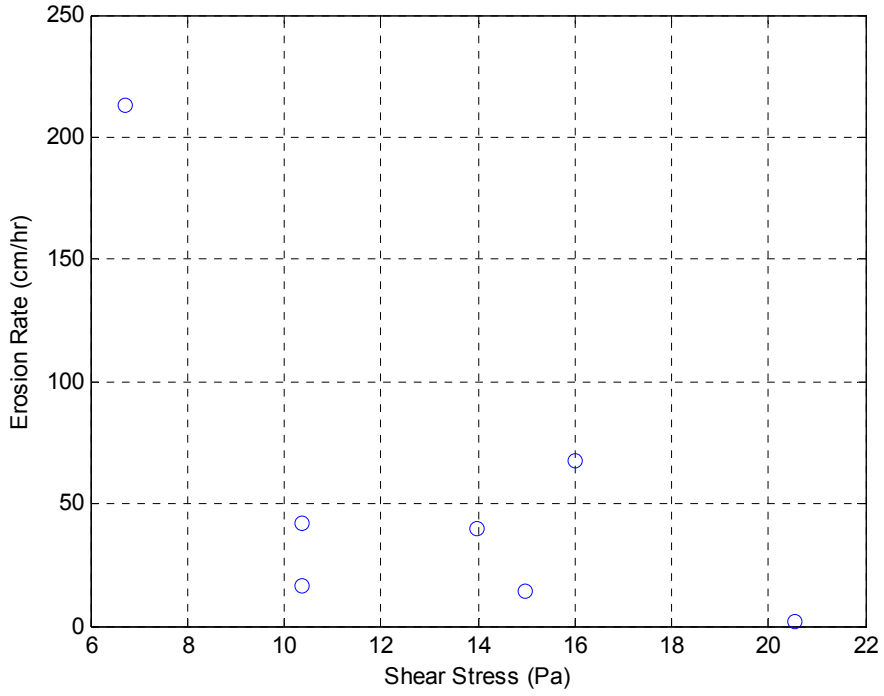

Figure D-2. Erosion rate versus shear stress for specimen AS-UF4

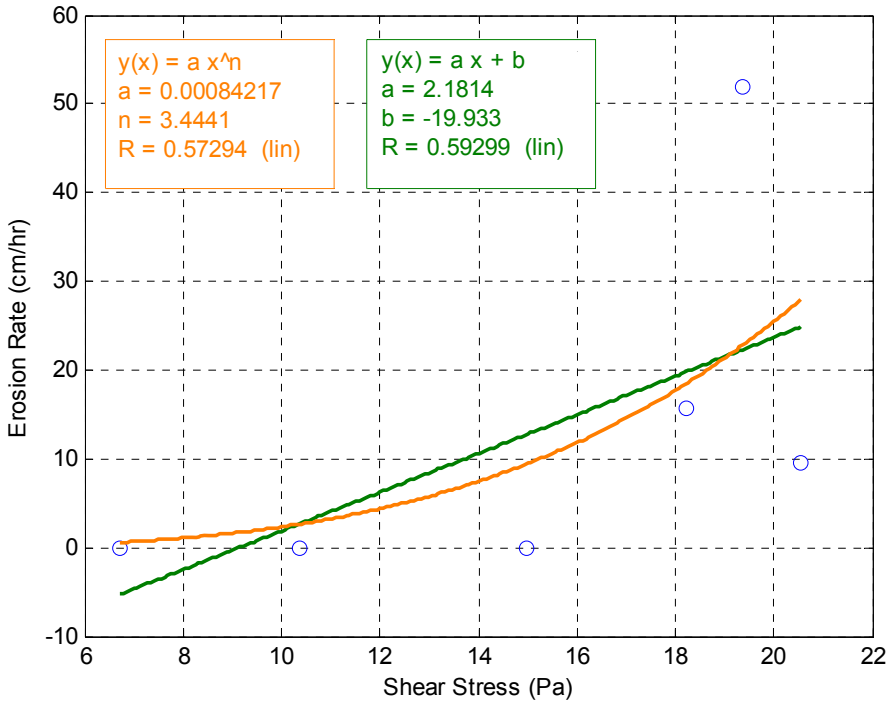

Figure D-3. Erosion rate versus shear stress for specimen AS-100

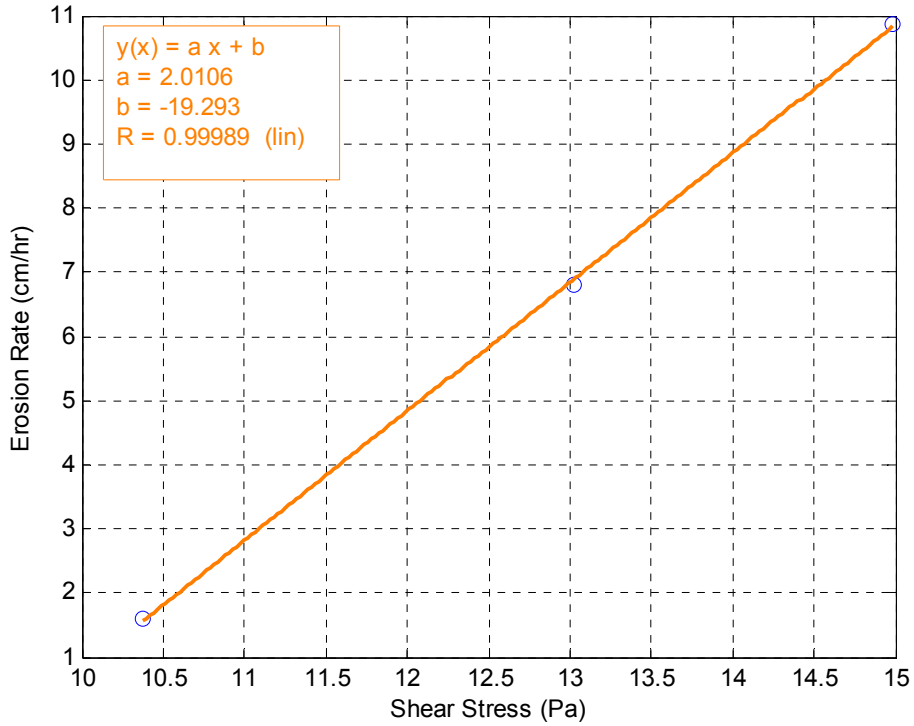

Figure D-4. Erosion rate versus shear stress for specimen RR B-1E

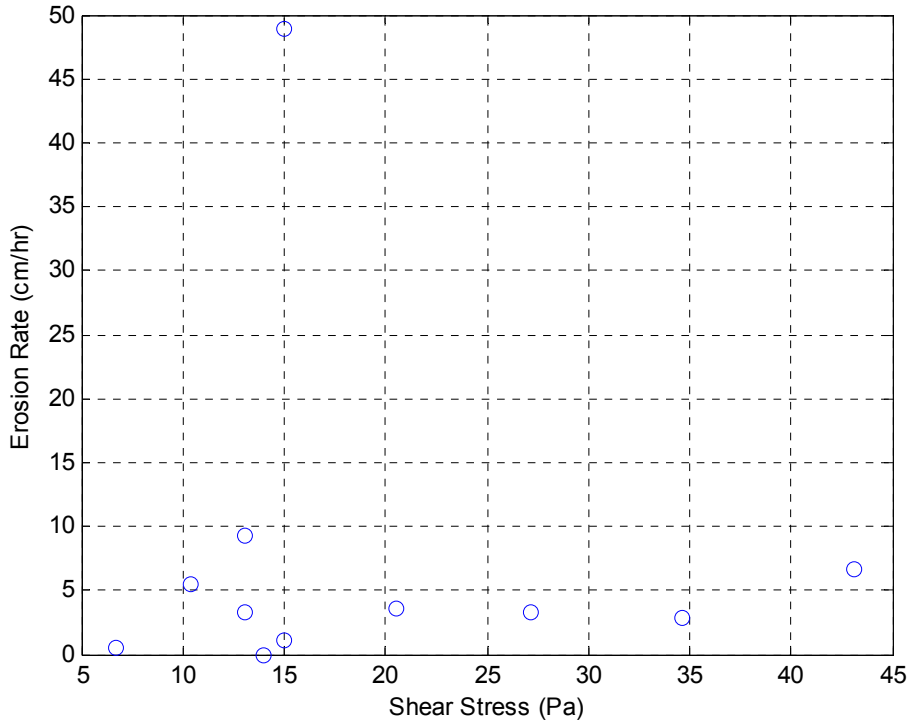

Figure D-5. Erosion rate versus shear stress for specimen RR B-3 9'-11'

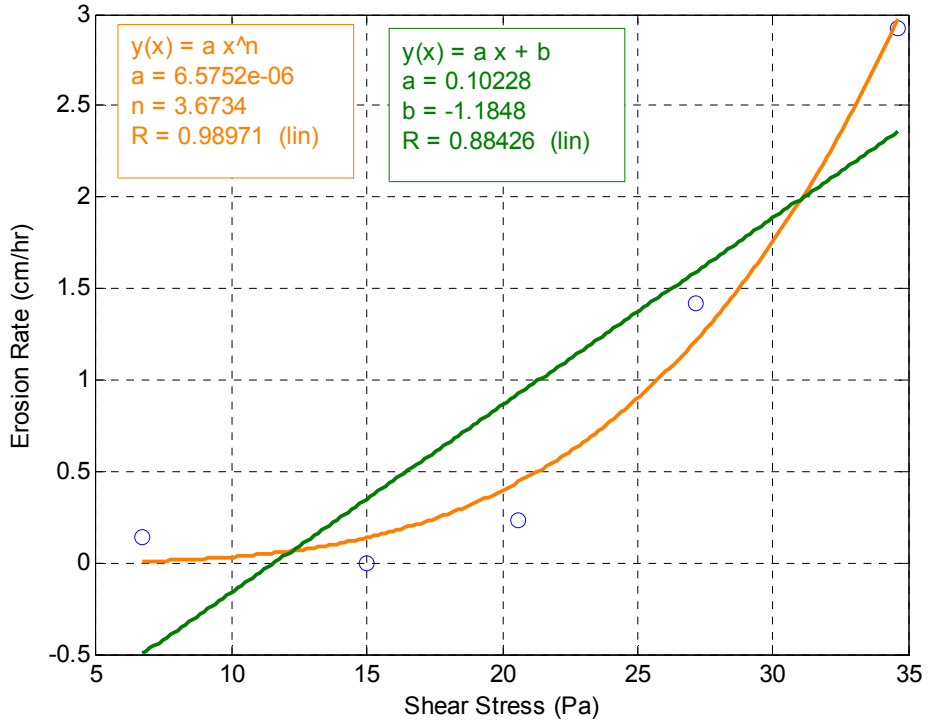

Figure D-6. Erosion rate versus shear stress for specimen D-5 S-2

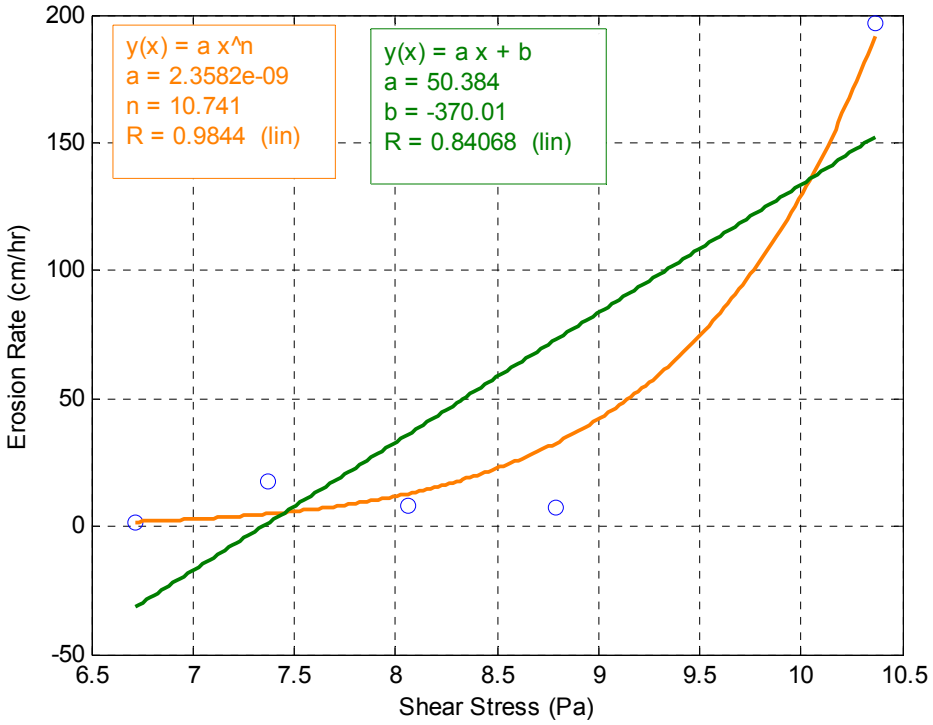

Figure D-7. Erosion rate versus shear stress for specimen JBC 12'-14'

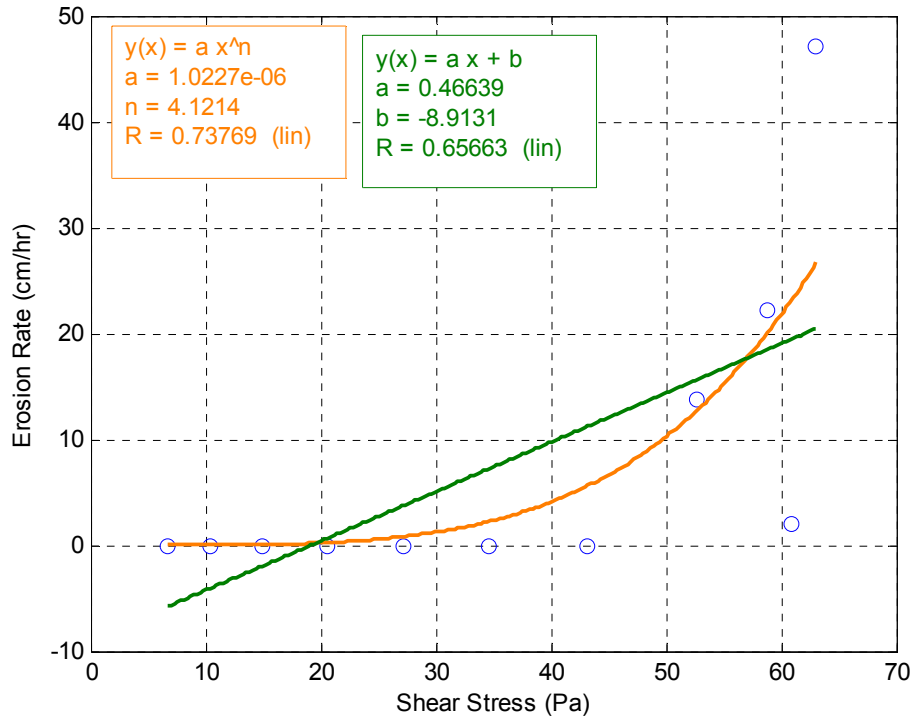

Figure D-8. Erosion rate versus shear stress for specimen JBC 10'-12' (dry)

APPENDIX E
EROSION FUNCTIONS FOR OUT-OF-STATE SPECIMENS

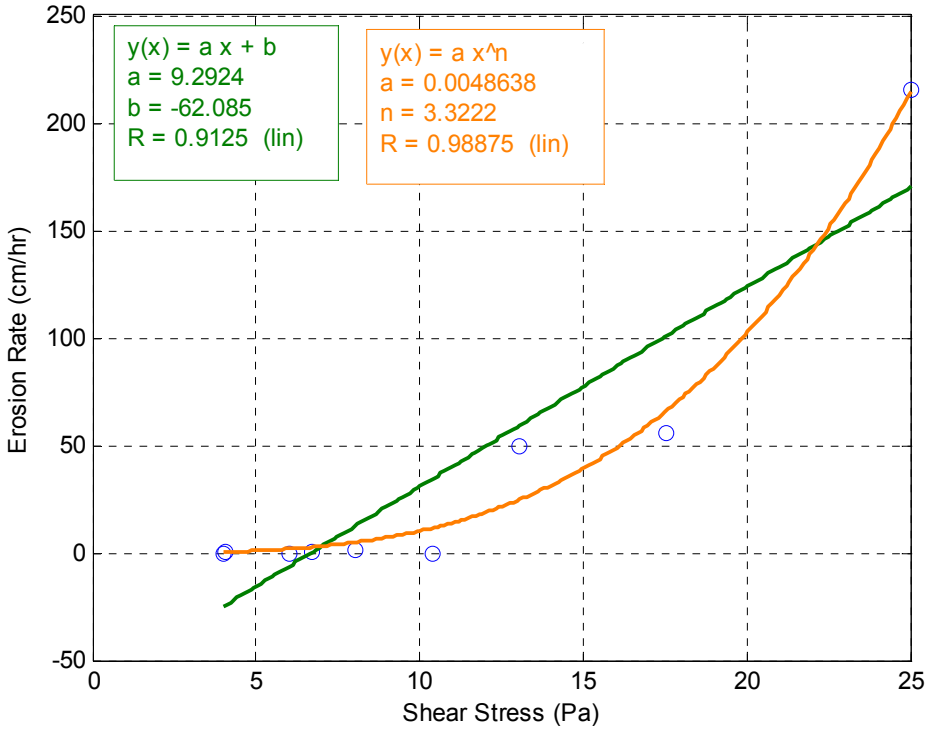

Figure E-1. Erosion rate versus shear stress for OS-35 60-62

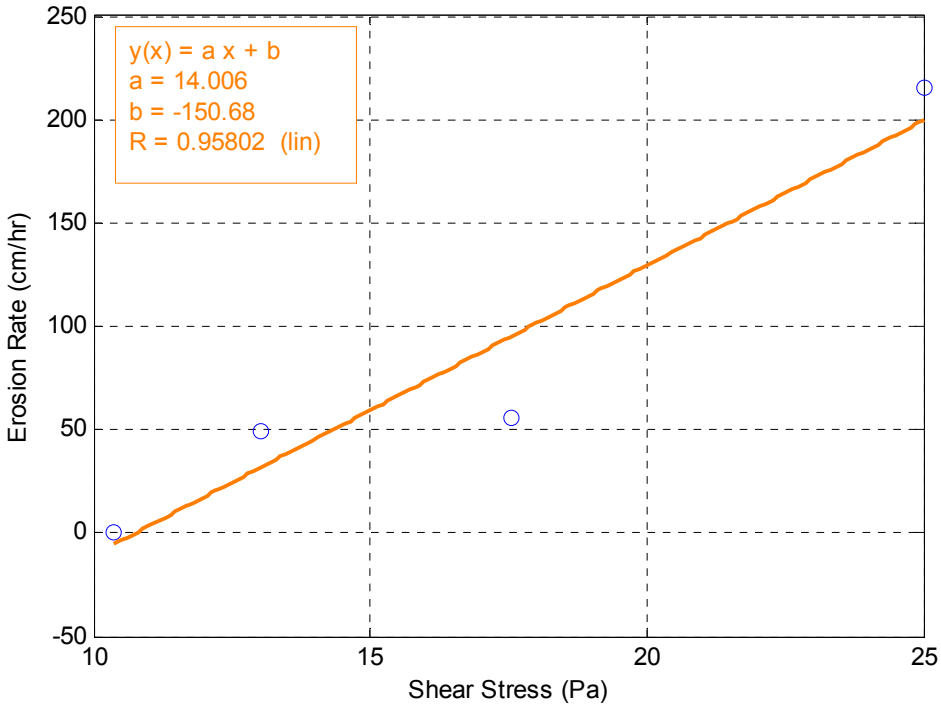

Figure E-2. Erosion versus shear stress for OS-35 60-62 with lower data points removed

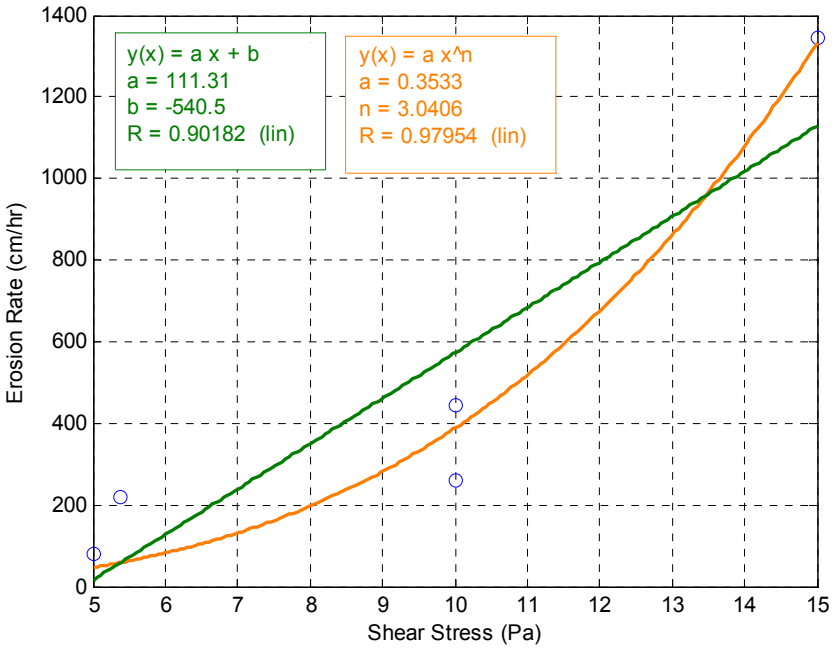

Figure E-3. Erosion rate versus shear stress for OS-34 52-54 (Note, last raw data point was eliminated because specimen noticeably stiffened as a function of depth)

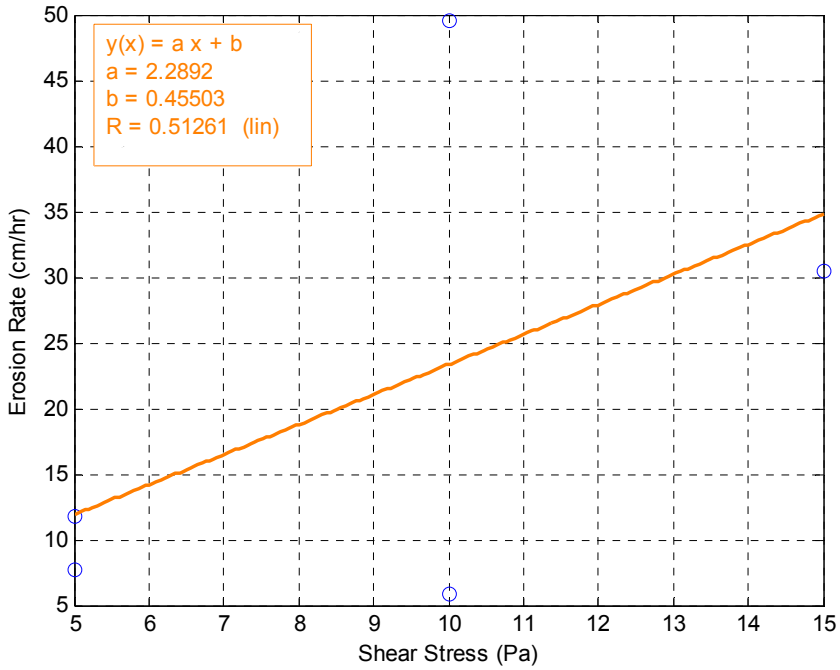

Figure E-4. Erosion rate versus shear stress for OS-51. Note, specimen was *highly* layered – hence the very poor correlation shown here

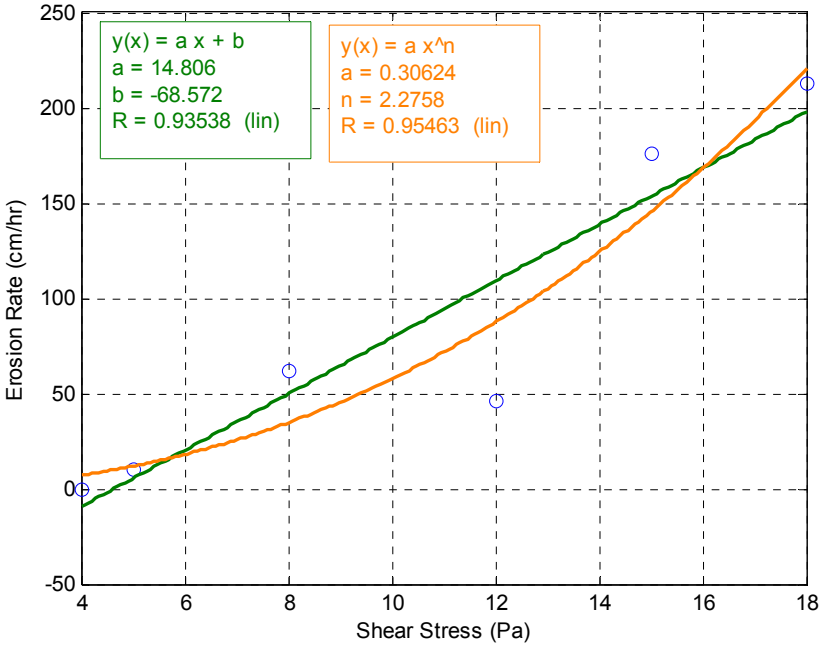

Figure E-5. Erosion rate versus shear stress for OS-23 U-1 30-32

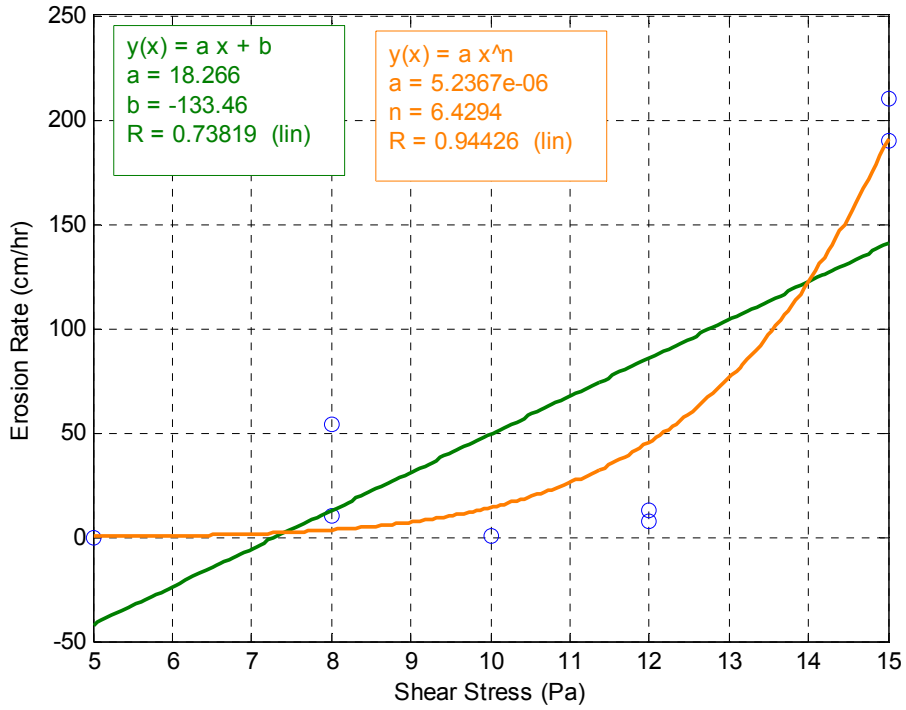

Figure E-6. Erosion versus shear stress for OS-34 U-2 63-66

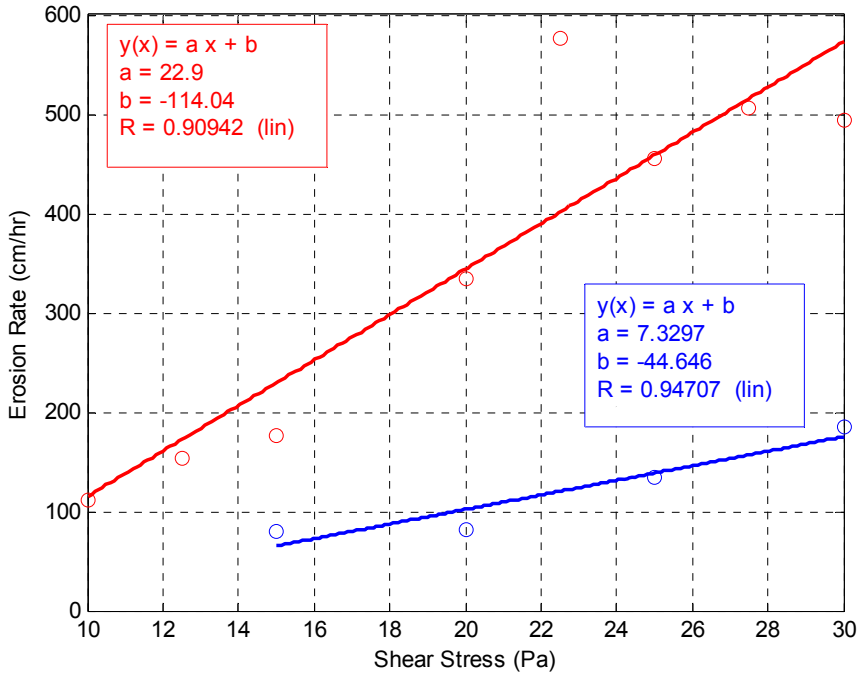

Figure E-7. Erosion versus shear stress for specimen OS-33; note the two distinct layers between top and bottom tests (top in red, bottom in blue)

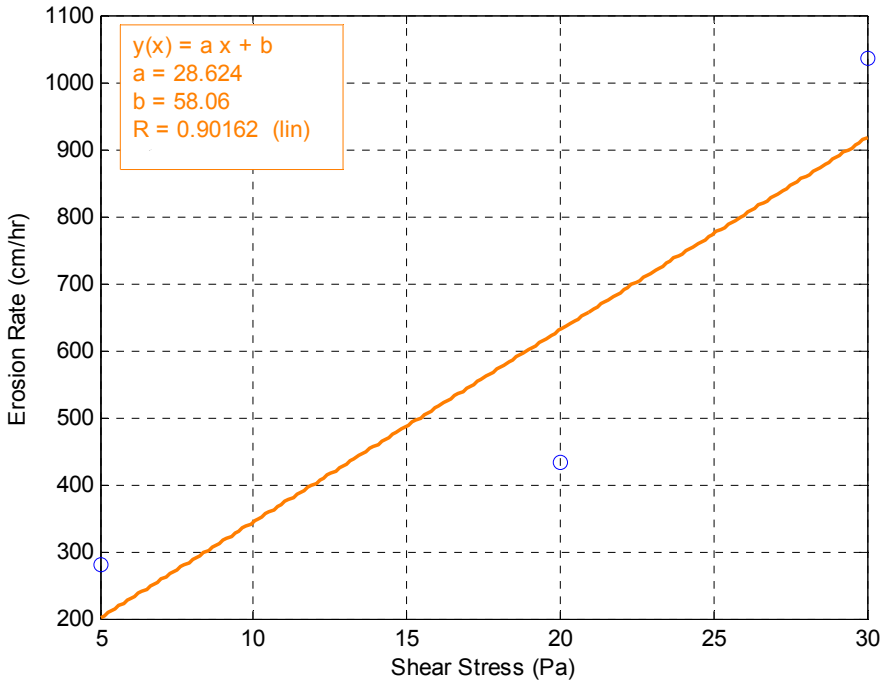

Figure E-8. Erosion versus shear stress for specimen OS-35 46-48

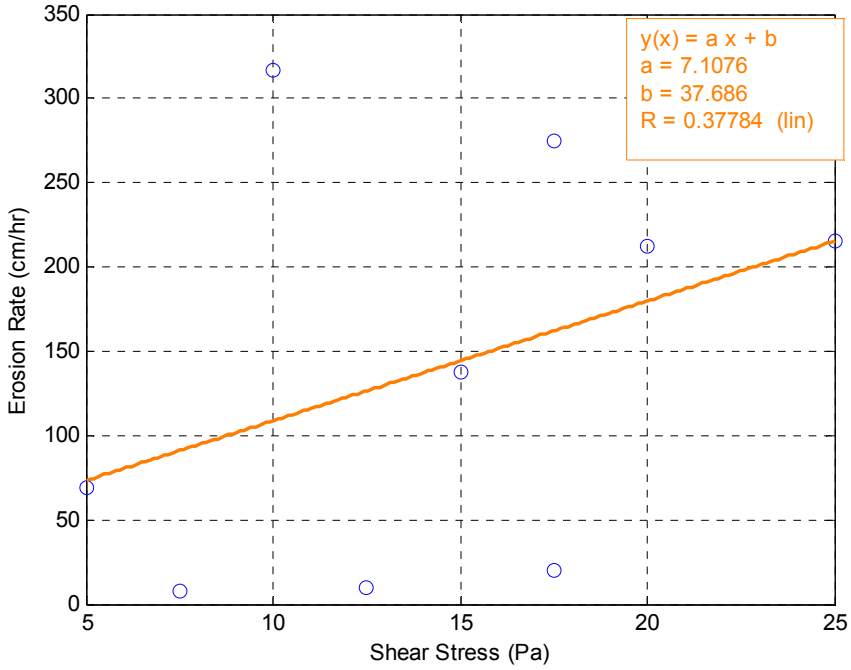

Figure E-9. Erosion versus shear stress for specimen OS-44 using all data points.

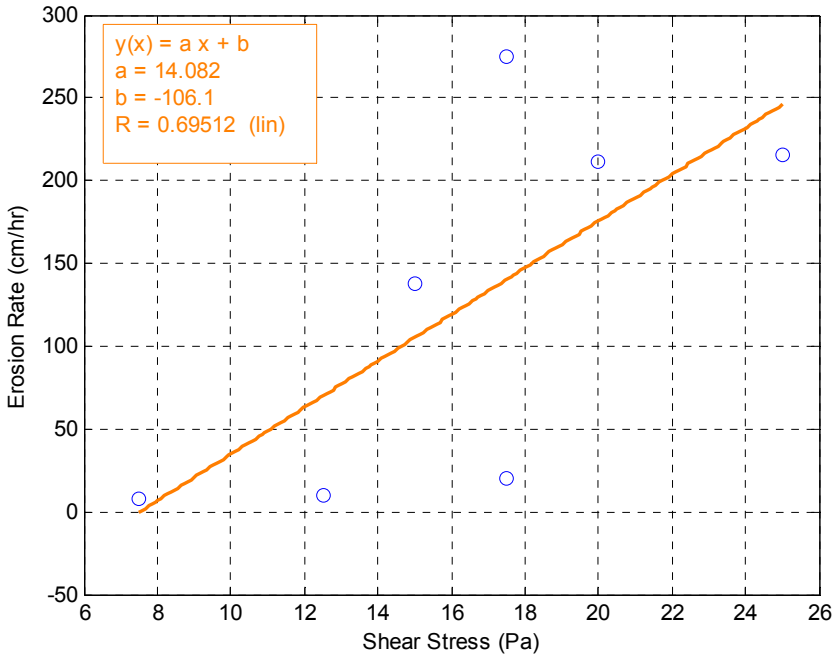

Figure E-10. Erosion versus shear stress for specimen OS-44 eliminating the 5.0 and 10.0 Pa data points (sample noticeably stiffened within approximately 8.0 cm).

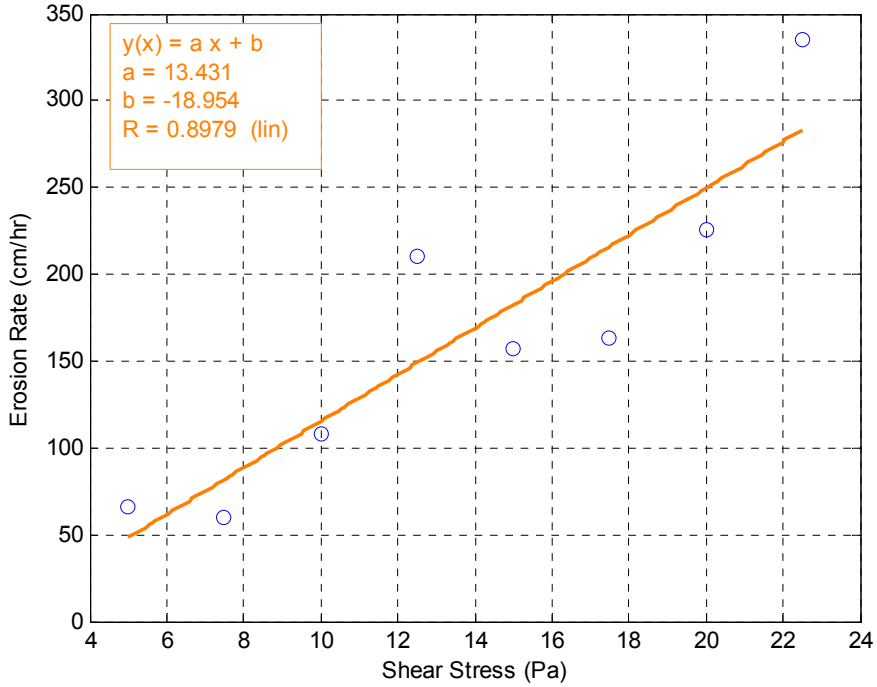

Figure E-11. Erosion versus shear stress for specimen OS-28

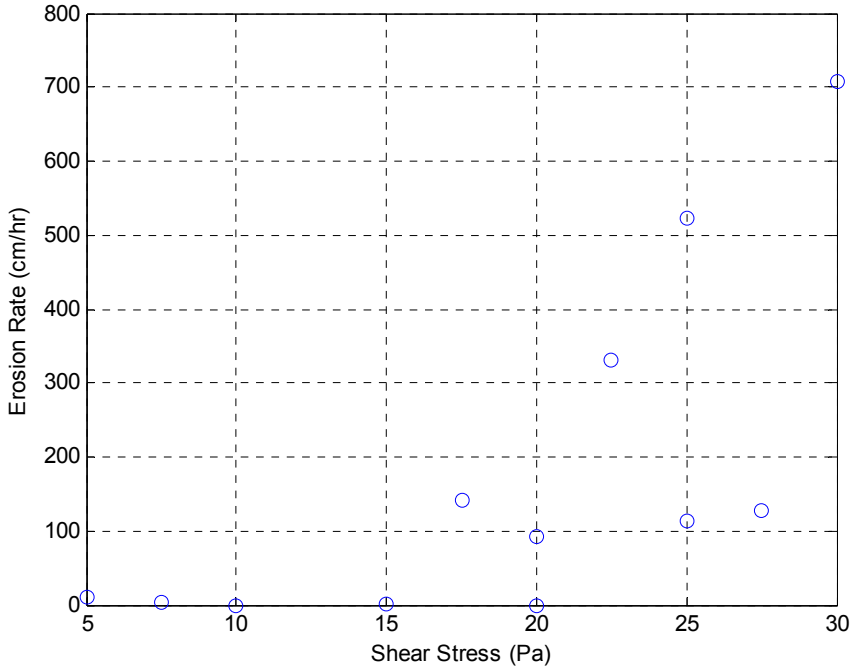

Figure E-12. Erosion versus shear stress for specimen OS-104 (all data points)

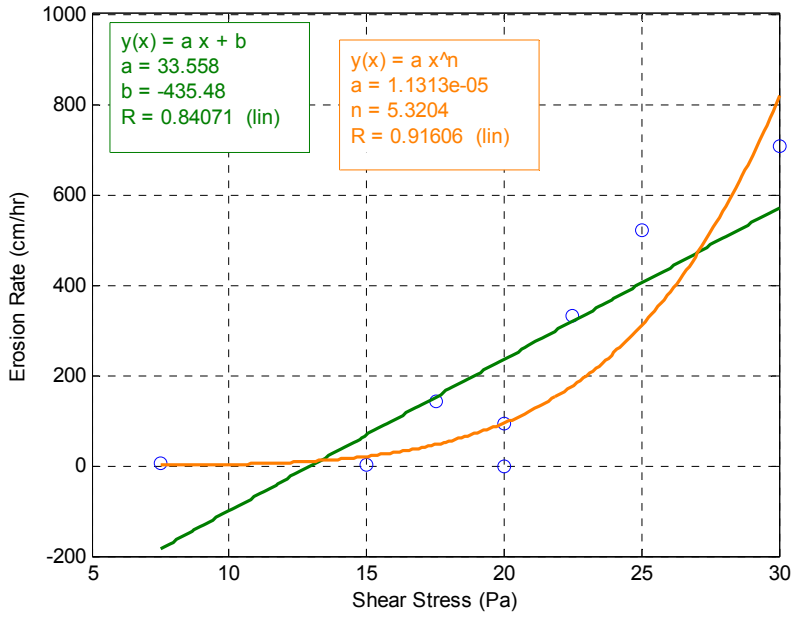

Figure E-13. Erosion versus shear stress for specimen OS-104 (zero-points removed and two alternating layers near bottom of sample where it stiffened removed probably OK because it is (1) conservative; and (2) near the bottom

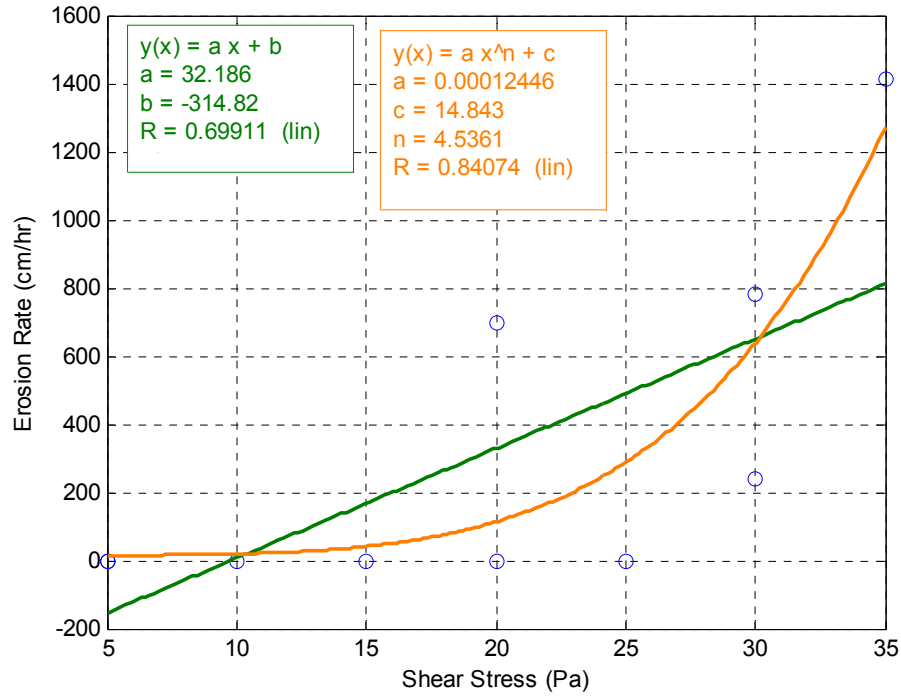

Figure E-14. Erosion versus time for specimen OS-102 (similar to E-13 – zero-points at higher stresses are removed due to stiff layering that was observed).

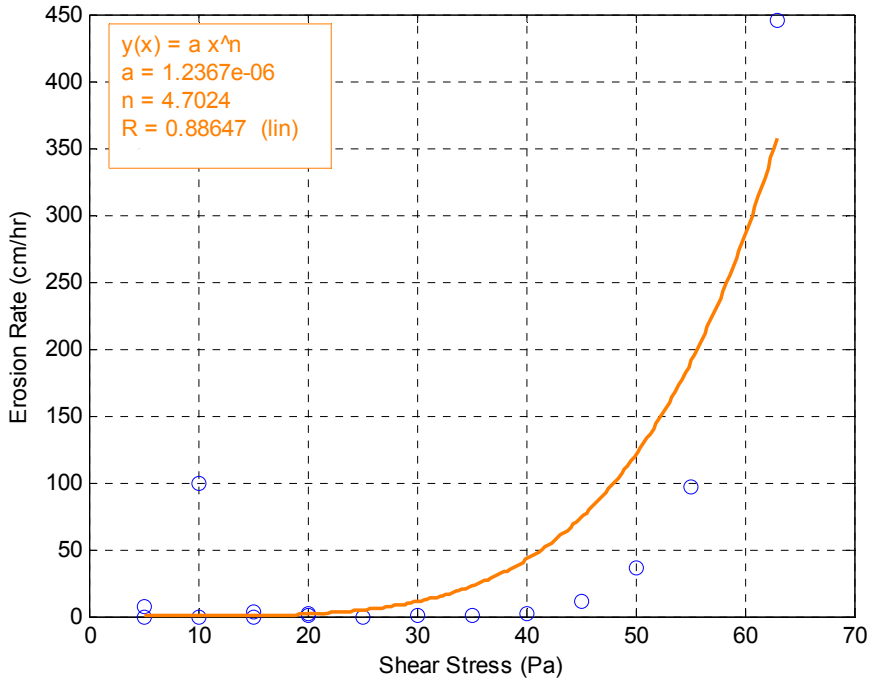

Figure E-15. Erosion versus time for specimen OS-42 (all data points)

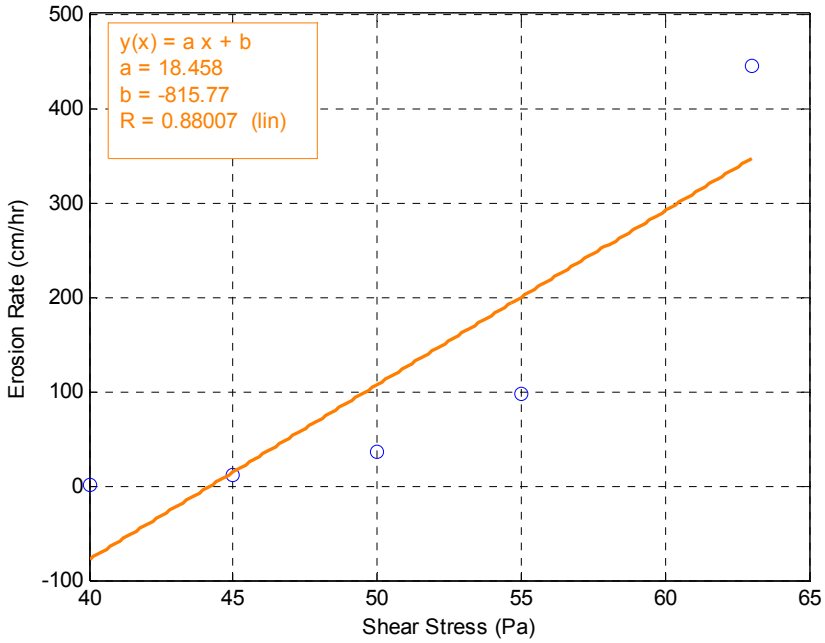

Figure E-16. Erosion versus time for specimen OS-42 (similar to previous figures, zero-points removed; so that critical shear stress could be developed).

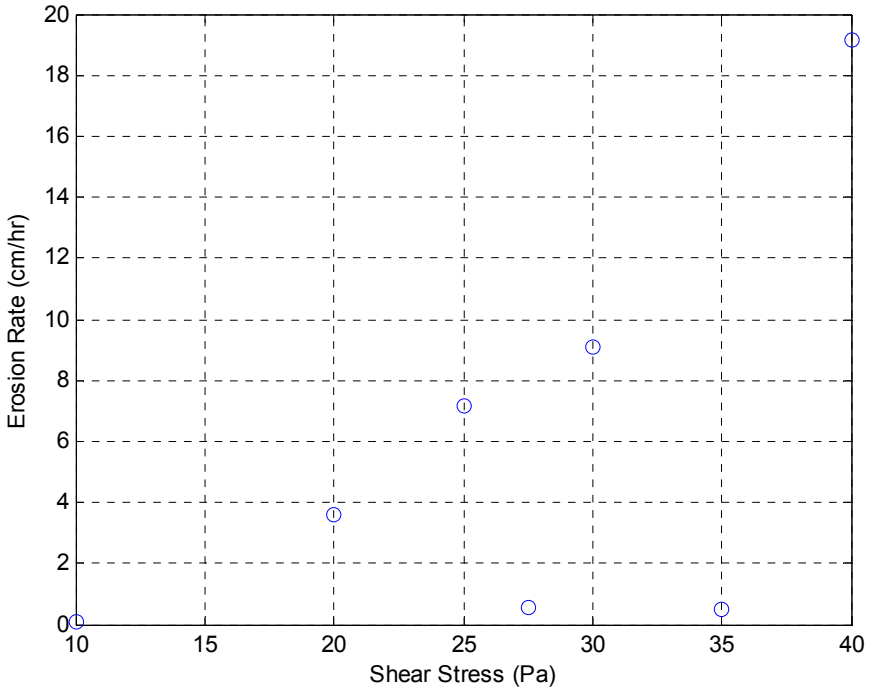

Figure E-17. Erosion versus time for specimen OS-66 (all data points)

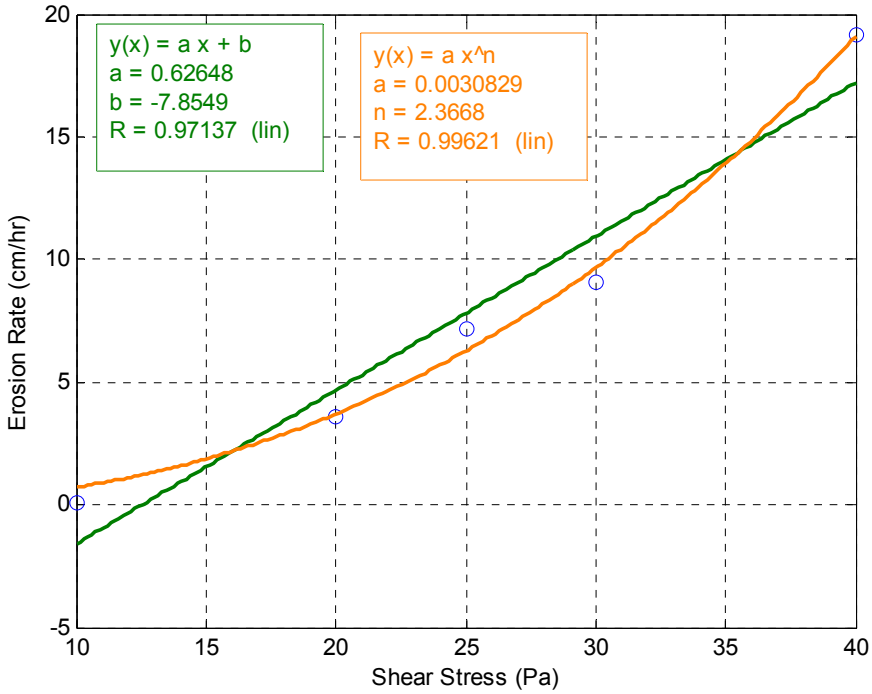

Figure E-18. Erosion versus time for specimen OS-66 (data points removed at apparent "layer" so that erosion function could be developed)